LARGE-EDDY SIMULATIONS OF HIGH-PRESSURE SHEAR COAXIAL FLOWS RELEVANT FOR H_2/O_2 ROCKET ENGINES

A Dissertation
Presented to
The Academic Faculty

by

Matthieu M. Masquelet

In Partial Fulfillment
of the Requirements for the Degree
Doctor of Philosophy in the
School of Aerospace Engineering

Georgia Institute of Technology
May 2013

LARGE-EDDY SIMULATIONS OF HIGH-PRESSURE SHEAR COAXIAL FLOWS RELEVANT FOR H_2/O_2 ROCKET ENGINES

Approved by:

Professor Suresh Menon,
Committee Chair
School of Aerospace Engineering
Georgia Institute of Technology

Professor Suresh Menon, Adviser
School of Aerospace Engineering
Georgia Institute of Technology

Professor Stephen Ruffin
School of Aerospace Engineering
Georgia Institute of Technology

Professor Jerry Seitzman
School of Aerospace Engineering
Georgia Institute of Technology

Professor Vigor Yang
School of Aerospace Engineering
Georgia Institute of Technology

Doctor Joseph Oefelein
Combustion Research Facility
Sandia National Laboratories

Date Approved: January 2013

DEDICATION

To my wife, families and friends, all those who have kept believing in me and without whom this would not have been possible.

ACKNOWLEDGEMENTS

During my long stay at the Computational Combustion Laboratory, I had several opportunities to study incredibly interesting and complex problems, all related to my childhood dream, rockets. And so I could not be more grateful to my advisor, Pr. Suresh Menon for giving me these chances, stimulating me through numerous discussions and helping me completing this PhD. Thanks to him, to his persuasion and to our hard work, I have been so lucky to work with 3 major space programs over the last 10 years. So of course lots of gratitude flow towards EADS Astrium, NASA and JAXA for funding this research. To top it all, I feel very honored to have such distinguished committee members. I would like to thank all of them, Dr. Seitzman, Dr. Ruffin, Dr. Oefelein, Dr. Yang and once again Dr. Menon for the time they took to evaluate and review this work. But the CCL is more than just a place to conduct thesis research, it's also a place where one can meet truly remarkable people from all over the world, a place open nearly 24/7, a place where we can talk software development, French politics and Turkish soccer, a place where ideas flow constantly. A truly fascinating work environment. Having stayed there for 10 years and becoming almost part of the furniture, I cannot individually thank all those who helped me along the way but I will highlight the most remarkable ones. Starting with Dr. Christopher Stone and Dr. Vaidyanathan Sankaran, the senior people when I first joined and from whom I learned so much. I now know how you feel when I was bombarding you with questions ! As a bonus Dr. Stone played quite a role in my meeting of my wife, so I am forever in debt to him. Speaking of senior staff and post-docs, I would like to thank Dr. Jung Choi, Dr. Srikant Srinavasan, Dr. Nicolas Guézennec, Dr. Victor Granet and Dr. Patricia Sierra for bringing their outside experience to the CCL and myself, it was incredibly helpful. To the rest of my fellow past and present CCL members, I hope I managed to help you a little bit along the way because you helped me a lot. A lot of what we do is interlocked and we need to keep supporting each other. It was a pleasure to work with you all. And while on the one

hand, completing a PhD can be a long and lonely soul-searching journey, on the other hand, it's only possible because of the support of others. And so special thanks are due to those who became my friends along the way, whether they were colleagues or simply connected closely or not to Georgia Tech. First, the French gang (Gilles, Nathalie, Franklin, Rémi, Diane, Léon, Hélène, Christophe, Florent, Yannick, Delphine), whether we were polluting the CCL with our French talk, dining at 11 pm, playing coinche at the Local, watching the Thrashers or arguing about politics and movies, I was incredibly lucky to have you alongside me. The same can be said for the non-French members of the group, who had to suffer from some of our idiosyncracies: my roommates Chris, Justin, Zack and Stéphane, Pedro, Stephani, Aurelija, Callie, thank you all for not giving up on the Frenchies ! Going through the melting pot of the CCL, it was a pleasure to enjoy (a little) time outside the lab by partying with Turkish people (Ayse, Baris, Nurhak, Orcun), doing some sports with American people (Joey for the soccer, Tim and Andy for the cycling) and generally enjoying life and discovering new cultures with people like Martin, Kenji, Satoshi and many others. Further away, Gatou, Nuw', Cyprien, Kris, Gegeor, Fred, Bouli, So, Laure, despite being in France or some other remote locations, you were never really far in my heart, at most a phone call away and every time we would meet again in person, it was like we had never been separated. Finally, I had the chance to have two families supporting me along the way: my family, Maman, Papa et Bibiche, back in Yerres who are still confused as to why it took so long for me to finish but never stopped believing in me and supporting me, and the family of my dear wife Reah in Peachtree City, Jolene, Walt, Wesley, Chris and Laura who have welcomed me in their lives and made me feel at home whenever I visited them. So finally of course, an astronomically-sized gratitude to my wife Reah who has showed a truly incredible amount of patience with me and my never-ending research and who provides me everyday with the love, joy and energy to accomplish anything.

TABLE OF CONTENTS

LIST OF TABLES

LIST OF FIGURES

LIST OF SYMBOLS OR ABBREVIATIONS

AFRL	Air Force Research Laboratory.
ANN	Artificial Neural Network.
AUSM	Advection Upstream Splitting Method.
CCL	Computational Combustion Laboratory.
CFD	Computational Fluid Dynamics.
CPG	Calorically Perfect Gas.
CSP	Corresponding States Principle.
CUIP	Constellation University Institutes Project.
DNS	Direct Numerical Simulation.
EoS	Equation of State.
ESA	European Space Agency.
FDS	Flux-Difference Splitting.
FFSC	Full Flow Staged Combustion.
GH_2	Gaseous Hydrogen.
GOX	Gaseous Oxygen.
HLL	Harten-Lax-van Leer.
IG	Ideal Gas.
IK	Irving-Kirkwood.
JAXA	Japan Aerospace eXploration Agency.
LDKM	Localized Dynamic k^{sgs} Model.
LEM	Linear-Eddy Model.
LES	Large Eddy Simulation.
LOX	Liquid Oxygen.
LRE	Liquid Rocket Engine.
MCC	Main Combustion Chamber.
MCL	Monotonized Central Limiter.
MUSCL	Monotone Upstream-centered Schemes for Conservation Laws.

NASA National Aeronautics and Space Administration.

OFHC Oxygen-Free High thermal conductivity Copper.

PG Perfect Gas.

PR EoS Peng-Robinson Equation of State.

RANS Reynolds-Averaged Navier Stokes.

RG Real Gas.

RK EoS Redlich-Kwong Equation of State.

RLV Reusable Launch Vehicle.

RP-1 Rocket Propellant-1 or Refined Petroleum-1.

SML Spatial Mixing Layer.

SSME Space Shuttle Main Engine.

TML Temporal Mixing Layer.

TPG Thermally Perfect Gas.

TVD Total Variation Diminishing.

VTPR EoS Volume-Translated Peng-Robinson Equation of State.

k Boltzmann's Constant, 1.38065 $\times 10^{-23}$ J.K^{-1}.

R_u Universal Gas Constant, 8.31451 J.mol^{-1}.K^{-1}.

α_v $\frac{1}{v}\left(\frac{\partial v}{\partial T}\right)_p = -\frac{1}{\rho}\left(\frac{\partial \rho}{\partial T}\right)_p$: Coefficient of thermal expansion, K^{-1}.

μ^{dp} Dipole moment, debyes.

κ_s Adiabatic compressibility, Pa^{-1}.

κ_T $-\frac{1}{v}\left(\frac{\partial v}{\partial p}\right)_T = \frac{1}{\rho}\left(\frac{\partial \rho}{\partial p}\right)_T$: Isothermal compressibility, Pa^{-1}.

λ Thermal conductivity, W.(m.K)$^{-1}$.

ω Acentric factor, dimensionless.

ρ Density, kg.m^{-3}.

τ Viscous stress, Pa.

k Species k specific quantity.

m Mixture averaged quantity.

0 Low-pressure quantity.

a Massic Helmholtz free energy, J.kg^{-1}.

C_V	Molar heat capacity at constant volume, J.mol^{-1}.K^{-1}.
D_i	Diameter of the central jet (see Fig. 1), m.
$\mathcal{D}_{k,m}$	Pseudo binary diffusion coefficient between species k and the mixture, m^2.s^{-1}.
E	Internal energy, J.mol^{-1}.
e	Massic internal energy, J.kg^{-1}.
e_T	Massic total energy = massic internal energy + massic kinetic energy, J.kg^{-1}.
$\mathbf{F}$	Flux vector.
$\boldsymbol{\mathcal{F}}$	Vector of conservative fluxes.
g	Massic Gibbs free energy, J.kg^{-1}.
h	Massic enthalpy, J.kg^{-1}.
h_k	Massic enthalpy of formation of species k, J.kg^{-1}.
j_k	Mass diffusion flux for species k, W.m^{-2}.
$\boldsymbol{\mathcal{L}}$	Vector of wave amplitudes.
L_{dc}	Dark core length (see Fig. 1), m.
M	Molar Weight, kg.mol^{-1}.
MW	Molecular Weight, g.mol^{-1}.
N_S	Number of species in the system, dimensionless.
p	Pressure, Pa.
q	Heat diffusion flux, W.m^{-2}.
$\mathbf{Q}$	State vector.
$\mathbf{S}$	Source term vector.
T	Temperature, K.
t_{post}	Thickness of the central jet sleeve (see Fig. 1), m.
u	Velocity, m.s^{-1}.
$\boldsymbol{U}$	Vector of primitive variables.
$\boldsymbol{\mathcal{U}}$	Vector of conservative variables.
V	Molar volume, m^3.mol^{-1}.
v	Specific volume, m^3.kg^{-1}.
$\mathcal{V}_{i,k}$	Diffusion velocity of species k in the direction i, m.s^{-1}.

X_k	Mole fraction of species k, dimensionless.
Y_k	Mass fraction of species k, dimensionless.
Z	Compressibility factor, dimensionless.

SUMMARY

The understanding and prediction of transient phenomena inside Liquid Rocket Engines (LREs) have been very difficult because of the many challenges posed by the conditions inside the combustion chamber. This is especially true for injectors involving liquid oxygen LOX and gaseous hydrogen GH_2. A wide range of length scales needs to be captured from high-pressure flame thicknesses of a few microns to the length of the chamber of the order of a meter. A wide range of time scales needs to be captured, again from the very small timescales involved in hydrogen chemistry to low-frequency longitudinal acoustics in the chamber. A wide range of densities needs to be captured, from the cryogenic liquid oxygen to the very hot and light combustion products. A wide range of flow speeds needs to be captured, from the incompressible liquid oxygen jet to the supersonic nozzle. Whether one desires to study these issues numerically or experimentally, they combine to make simulations and measurements very difficult whereas reliable and accurate data are required to understand the complex physics at stake. This thesis focuses on the numerical simulations of flows relevant to LRE applications using Large Eddy Simulations (LES). It identifies the required features to tackle such complex flows, implements and develops state-of-the-art solutions and apply them to a variety of increasingly difficult problems.

More precisely, a multi-species real gas framework is developed inside a conservative, compressible solver that uses a state-of-the-art hybrid scheme to capture at the same time the large density gradients and the turbulent structures that can be found in a high-pressure liquid rocket engine. Particular care is applied to the implementation of the real gas framework with detailed derivations of thermodynamic properties, a modular implementation of select equations of state in the solver. and a new efficient iterative method. Several verification cases are performed to evaluate this implementation and the conservative properties of the solver. It is then validated against laboratory-scaled flows relevant to rocket engines,

from a gas-gas reacting injector to a liquid-gas injector under non-reacting and reacting conditions. All the injectors considered contain a single shear coaxial element and the reacting cases only deal with H_2-O_2 systems.

A gaseous oyxgen-gaseous hydrogen (GOX-GH_2) shear coaxial injector, typical of a staged combustion engine, is first investigated. Available experimental data is limited to the wall heat flux but extensive comparisons are conducted between three-dimensional and axisymmetric solutions generated by this solver as well as by other state-of-the-art solvers through a NASA validation campaign. It is found that the unsteady and three-dimensional character of LES is critical in capturing physical flow features, even on a relatively coarse grid and using a 7-step mechanism instead of a 21-step mechanism. The predictions of the wall heat flux, the only available data, are not very good and highlight the importance of grid resolution and near-wall models for LES.

To perform more quantitative comparisons, a new experimental setup is investigated under both non-reacting and reacting conditions. The main difference with the previous setup, and in fact with most of the other laboratory rigs from the literature, is the presence of a strong co-flow to mimic the surrounding flow of other injecting elements. For the non-reacting case, agreement with the experimental high-speed visualization is very good, both qualitatively and quantitatively but for the reacting case, only poor agreement is obtained, with the numerical flame significantly shorter than the observed one. In both cases, the role of the co-flow and inlet conditions are investigated and highlighted. A validated LES solver should be able to go beyond some experimental constraints and help define the next direction of investigation. For the non-reacting case, a new scaling law is suggested after a review of the existing literature and a new numerical experiment agrees with the prediction of this scaling law. A slightly modified version of this non-reacting setup is also used to investigate and validate the Linear-Eddy Model (LEM), an advanced sub-grid closure model, in real gas flows for the first time. Finally, the structure of the trans-critical flame observed in the reacting case hints at the need for such more advanced turbulent combustion model for this class of flow.

CHAPTER I

INTRODUCTION

1.1 Scope and motivation

Space programs all over the world are at a crossroad. What used to be a three-player race (USSR, USA and to a lesser extent Europe) funded by huge national programs has become a more diverse race. While early spaceflight programs served as technology demonstrators for military InterContinental Ballistic Missiles (ICBMs), they quickly developed into independent human exploration projects. Over the last 50 years, they branched out into many fields such as robotic exploration, commercial exploitation of space, space tourism, science experiments or scientific and military Earth-monitoring. Large national institutions such as NASA or ESA are still very much involved, but new countries have joined the fray, such as Japan, China, India and South Korea. Moreover, private companies such as Scaled Composite/Virgin Galactic, SpaceX, XCOR and many others are now able to access lower Earth orbits for space tourism or commercial cargo. They have become a rapidly growing segment of the industry and there are already concrete plans [1] for mining asteroids in the not so distant future. This diversity has allowed many different propulsion systems to be tested but for the moment, liquid rocket engines, and in particular engines using hydrogen (H_2) and oxygen (O_2) as propellants, remain one of the most popular technology used to escape Earth's gravitational pull.

There are many components in a modern liquid rocket engine. Depending on the rocket engine design, it can include tanks, turbo-pumps, pre-burners operating far from stoichiometry, gas turbines and/or cooling channels for example. All components present their own engineering challenges but the thrust chamber is one of the most important: it finally converts the propellants into the thrust that defines a rocket engine. This thrust chamber consists of an injector plate, with a single (for sub-scale laboratory tests) or hundreds (for some first stage engines) of injecting elements, a combustion chamber and a nozzle. The

current study will focus on the simplest of thrust chambers, with a single shear coaxial element. However, this simplest of rocket engine configuration is still extremely complex and poses significant challenges as the current understanding of all the physical processes inside the combustion chamber remains limited.

In the past, this limited understanding has led to the exorbitant cost of developing new rocket engines. Simple empirical design tools and lack of good diagnostics and monitoring have resulted in many catastrophic failures during the testing phase. This try-fail-fix cycle represents 75% of the development cost of large engines such as the F-1 engine for the Saturn V rocket and costs billions of dollars [167]. More recently, there were 18 major combustion device failures during the development of the Space Shuttle Main Engine [316]. These failures were caused by the onset of combustion instabilities which, given the large operating pressures of the combustion chamber (from 60 to 200 bar in many engines), generate huge mechanical stresses. While this huge cost was somewhat bearable during the space race of the 20^{th}century, economic constraints and the commercialization of space demand more cost-effective methods. As a consequence, relatively few new engines have been developed in the last decade and private companies prefer to rely on existing, older designs for their launch vehicles. And even these existing designs need scaling to meet the requirements of the launch vehicle and this scaling can also lead to costly testing [108].

Recent advances in experimental and numerical capabilities have the potential to significantly reduce the time and money required to design new engines. Computational Fluid Dynamics (CFD) solvers should be able to identify and maybe even solve many design issues before full scale testing is conducted. This cannot be achieved with current zero- or one-dimensional tools as they lack the physical models for these predictions. On the other hand, CFD solvers need to prove their robustness, accuracy and efficiency before they can be used as design tools. This is where new diagnostic techniques can help by providing detailed measurements in both space and time to validate CFD predictions. Currently, these detailed measurements are limited to sub-scale, laboratory-size chambers.

Since the scaling techniques available [108] are usually not able to predict both the performance and the stability of the full scale engines based only on sub-scale data, this is

only the first step of a long process. Given the unsteady and three-dimensional nature of the combustion instabilities that eventually need to be detected, these new numerical tools need to have these same characteristics and solve the three-dimensional, unsteady equations of motion inside the combustion chamber.

As mentioned earlier, the physics at play in a typical rocket engine are very complex. Because the reactants are usually injected at very low, cryogenic, temperatures under high pressure, the density of mass and energy can locally be very large, making for difficult optical access and difficult numerical modeling. In particular, the fluids can be so dense that the ideal gas assumption no longer applies. Even though these conditions are often described as high-pressure, it is the density of the fluid that brings in new physics, not high-pressure per se. However, the high pressure does impact the kinetics of the combustion which itself interacts with a highly turbulent flow. Some of these characteristics are also starting to be of interest to the aircraft engine community and the gas turbine community as the pressure inside these combustion systems is increased to achieve higher performance and/or efficiency. However the specific issues associated with the thermodynamic and thermochemical behavior of hydrocarbons under such high pressures are beyond the scope of this work.

So the purpose of this thesis is to develop a numerical tool for robust, accurate and efficient calculations of liquid rocket engine flows and to better understand the physics at play in these flows. To this end, several single-element, shear coaxial injectors are studied under non-reacting and reacting conditions and so a background on this particular configuration is provided first in this chapter. This is followed by a review of previous experimental and numerical works studying shear coaxial injectors under high pressure. This allows us to define the specific objectives of this thesis, presented at the end of this chapter.

1.2 Background on high-pressure shear coaxial injectors

1.2.1 Shear coaxial injectors in liquid rocket engines

There has always been a natural desire to increase the operating pressure of combustion devices. This trend can be found in the fields of aircraft engines, gas turbines, internal combustion engines as well as rocket engines. There are potential benefits to this increase,

Table 1: Principal thermodynamic properties for species relevant to rocket applications.

Species	T_c(K)	p_c(bar)	MW (g.mol^{-1})	$I_{sp,th}$ with LOX
O_2	154.6	50.4	32.0	N/A
H_2	33.2	13.1	2.0	455
CH_4	190.6	46.0	16.0	368
RP-1	675.0	21.7	≈ 170	358
N_2	126.2	34.0	28.0	N/A
H_2O	647.1	220.0	34.0	N/A

including better performance and efficiency or the possibility to build a more compact system. There are also concrete drawbacks, such as increased heat load, more complex, more expensive experiments during the design phase and more damaging combustion instabilities when they occur. Because performance is more critical in liquid rocket engines than for other combustion devices, the operating pressures in large-thrust combustion chambers have been above 50 bar since the 60's with the F-1 and J-2 engines and have surpassed 200 bar for the Space Shuttle Main Engine or the largest Russian RP-1 engines. This 50 bar limit is important because it is at or above the critical pressure p_c of most usual rocket propellants as shown in Table 1, which lists the main thermodynamic properties of species relevant to this work and/or to rocket engines applications in general. The specific impulses given, which measures the efficiency of a rocket engine, correspond to best-possible conditions [112].

The systems of interest for this work use shear coaxial elements to inject an annular stream of fuel around a round jet of oxygen. They are the most popular elements in liquid rocket engines and have been investigated extensively in the literature as will be shown in the next sections. Some engines such as the Space Shuttle Main Engine use a staged combustion cycle where the reactants go through preburners and thus enter the combustion chamber as hot gases. In this case, whether or not the chamber operating pressure p_{ch} is above the critical pressure p_c has little influence on the physics involved in the mixing and combustion processes. This gas-gas injection results in a simpler configuration that will be studied first in Chapter 4. On the other hand, other rocket engine cycles inject at least most of the oxygen close to its storage temperature. This temperature is usually very low, i.e. cryogenic, in order to limit the volume of the storage tanks, and is thus at or below the

critical temperature T_c for oxygen. This has a dramatic influence on the physics at play in the combustion chamber as it has been widely reported experimentally: instead of the classical liquid jet breakup observed at sub-critical pressures, a more gas-like behavior is observed around the oxygen jet. This is depicted in Figure 1, where a central round jet of diameter D_i, possibly liquid, is surrounded by an annular stream of outer diameter D_o. The outer fluid is usually gaseous and its bulk velocity u_o is usually larger than the bulk velocity u_i for the round jet. In general, the subscript i in this context refers to the central, round jet quantities, the subscript o refers to the outer, annular jet quantities while the subscript ch refers to the chamber properties. Both streams are separated by a post sleeve of thickness t_{post}. While the origin of the axial coordinates is located in the dump plane of the chamber, the exit plane of the post sleeve might be recessed by a distance l_{rec} from the dump plane. A widely used metric for shear coaxial injectors is the dark core length, indicated as L_{dc} in Figure 1. It can be defined as the near-liquid part of the jet, which would appear black in a backlit image, a common visualization technique for this kind of flow. It loosely corresponds to the potential core of the inner jet for gaseous coaxial streams. Finally, some laboratory configurations include a coflow around the coaxial element to mimic the flow for the many other elements that would compose a showerhead injector in a full-scale engine. Figure 1 also illustrates the two different breakup behaviors for the central jet, the super-critical one on the left and the classical, sub-critical one on the right. But before reviewing the body of experimental and numerical data on this topic, a quick introduction on these non-ideal thermodynamics is given. More details will be given later on in Chapter 2.5.

1.2.2 Primer on real gas thermodynamics

Once limited to liquid rocket engines, the study of fluid mechanics and combustion processes under high pressure conditions is spreading to many other applications. For example, the operating conditions of modern internal combustion engines and gas turbines tend towards higher pressures for power and size efficiency reasons. When these high pressures are coupled with low-to-moderate injection temperatures, sufficiently high densities are reached that the fluid of interest can no longer be considered an ideal gas(IG). Instead, a real gas formulation

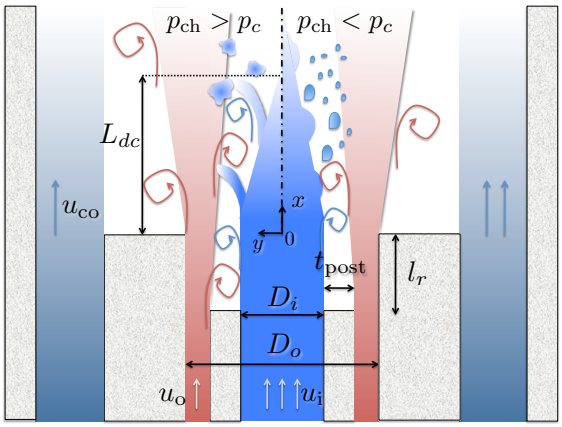

Figure 1: Schematic representation of a shear coaxial injector element with illustration of the central jet breakup process under super-critical conditions on the left and under sub-critical conditions on the right.

should be used in order to model its behavior.

The term "real gas" can take several meanings in the context of gas dynamics. In any case, it signifies a departure from the hypothetical ideal gas or perfect gas (PG) behavior which assumes the constituent molecules[1] have no volume and do not exhibit interaction forces among them except during elastic collisions. These two assumptions lead to the two governing equations for the thermodynamic ideal gas, the "pressure" or "standard" equation of state EoS (Eq. 1.2.1) and the "calorific" or "thermal" EoS (Eq. 1.2.2):

$$pV = R_u T \tag{1.2.1}$$

$$E = C_V T \tag{1.2.2}$$

where p is the pressure, V is the molar volume, R_u is the universal gas constant, T is the temperature, E is the molar internal energy, C_V is the molar heat capacity at constant volume and is assumed constant.

High temperature real gas effects are mostly concerned with the calorific EoS. Real molecules have a much more complex structure than the "point mass" model of the ideal gas law. They are particles with a finite volume and thus a moment of inertia. They can have

[1]We adopt here the gas kinetics point of view, where any fluid particle, mono-atomic or poly-atomic, is called a molecule.

chemical bonds which can store vibrational energy. They are surrounded by an electronic cloud. At sufficiently high temperatures, these different aspects of the molecular structure start to affect the the calorific EoS.[2] On the other hand, the IG pressure EoS remains valid under these conditions.

This is not the case for the sort of real gas effects that will be considered here. By including inter-molecular forces outside collisions and by dropping the point-mass assumption, the volume occupied by the molecules at a given temperature and pressure is modified (new pressure EoS) and the work done by the traveling molecules in these force fields also affects the different transfers of energy (new calorific EoS). Depending on the magnitude of these inter-molecular forces, the fluid behaves more like a gas or more like a liquid. Concepts such as surface tension or latent heat of vaporization no longer apply if the pressure is high enough. In addition to these thermodynamics changes, the high pressures encountered in these modern systems have also repercussions on the transport properties of the fluid, hence influencing the mixing processes, and on the chemistry, therefore influencing the combustion processes. More detailed information, especially on the mathematical formulation of these equations of states, is given in Section 2.5, but this introduction is necessary to better understand the existing body of work on high-pressure coaxial injectors.

Going back to the injection regimes mentioned in the previous section, the phase diagram of oxygen shown in Figure 2 is used to define them more precisely. For a multi-species coaxial flow, this is not perfectly representative of the flow: this two-dimensional diagram only represents a slice of the possible thermodynamic states, with other dimensions representing the mixing with other species. However, when considering a mixing case where the other species are injected in a gaseous state, most of the non-ideal behavior occurs close to this plane. And of course, in the case of coaxial streams with a single species, it represents all possible thermodynamic states. So in the end, the $p - T$ diagram in Figure 2 is a good representation of the thermodynamic states in a coaxial injector with liquid oxygen and it

[2]Note that a thermally perfect gas (TPG) formulation, which allows for some evolution of the specific heat with temperature, captures some of these departures from the calorific EoS. Since the TPG formulation is used as a building block for our real gas formulation, some of the high temperature real gas effects are implicitly taken into account. Most notably, electronic energy is usually neglected.

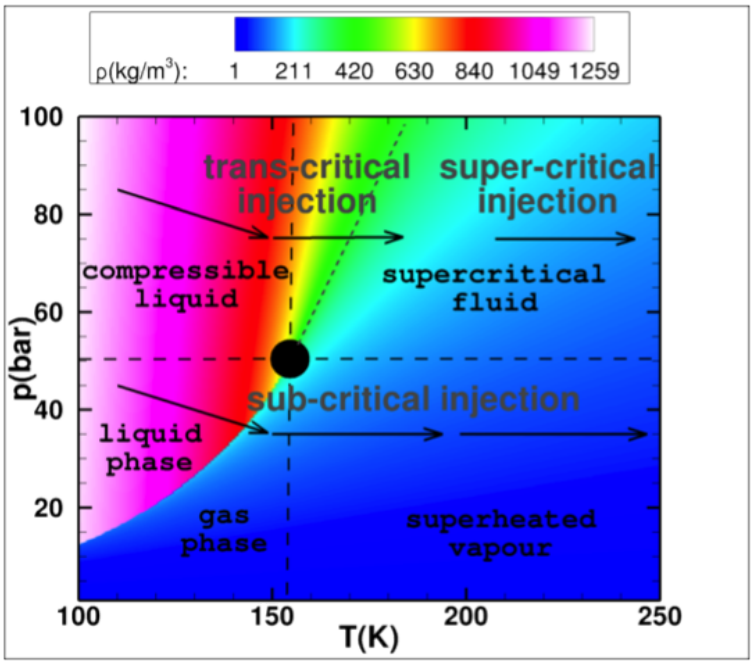

Figure 2: Phase diagram of oxygen in the $p-T$ space. The black dot represents the critical point at the intersection of the long-dash lines for the critical temperature and pressure. The short-dash line is the pseudo-boiling line [229] or Widom line [281] and corresponds approximately to the region of maximum specific heat at constant pressure. The density is represented by the colored contours in the background.

helps distinguish the two regimes mentioned above by following the thermodynamic path of an oxygen fluid particle as it enters the combustion chamber. When the operating pressure is below the critical pressure of oxygen, the liquid oxygen has to go through the classical vaporization transition after it heats up to the boiling temperature at the given pressure. This discrete phase change is characterized by discontinuous thermodynamic properties between the liquid and the gas phase. In particular, the surface tension at the interface between the two phases is responsible for the multi-phase breakup and atomization processes observed experimentally at sub-critical pressures. On the other hand, when the operating pressure is above the oxygen critical pressure, oxygen enters the combustion chamber as a compressible liquid, slightly mechanically different from the incompressible liquid at sub-critical pressures. From an energy point of view, instead of requiring a large, discrete amount of energy (the latent heat of vaporization) to go from liquid to gas phase, an equivalent amount of energy is necessary to transition continuously from the compressed liquid phase to the super-critical fluid phase as the fluid heats up from a sub-critical temperature ($T < T_c$) to a super-critical temperature ($T > T_c$). This transition has been called a trans-critical event in the 1990's [337, 217], and thus injection conditions that require a species to undergo this transition correspond to a trans-critical injection. During this trans-critical event, there is no surface tension effect between the two phases, which is why experimentally, a more gas-like behavior is observed. A more detailed review of these experimental findings is presented in the next section.

1.3 Literature review

For an overview of the state-of-the-art in super-critical combustion prior to 2006, the reader is referred to a previous work [175] which contains an exhaustive review of the theoretical, experimental and numerical knowledge on coaxial super-critical flame, with a focus on oxygen-hydrogen injection under typical rocket conditions. The following sections will simply update this existing review. There also exist broad reviews of high-pressure mixing processes by Bellan [15] and Oschwald et al. [229].

1.3.1 Review of the mixing experimental data

The dark core mentioned earlier in the description of the coaxial injector has been the focus point of many experimental and theoretical studies in the past. The accurate prediction of the dark core length under arbitrary conditions, is an important stepping stone for the understanding of the combustion dynamics inside rocket engines as proposed by Chehroudi [35]. While Chehroudi focuses on impinging jets, the dark core length of coaxial elements is also of interest and is the focus of this study. Shear coaxial injecting elements are one of the most popular injector design for liquid rocket engines and their mixing properties have been extensively studied in the past whether in low-pressure gas-gas settings [327, 10] or in low-pressure multi-phase gas-liquid settings[328, 143]. In parallel, and particularly over the last few years, there have been extensive efforts to study non-reacting coaxial jets in conditions relevant to liquid rocket engine applications [228, 52, 148, 149, 252, 90, 304, 160, 309]. The studies cited are limited to non-reacting setups where the chamber pressure is above the critical pressure of species injected through the central jet. One common point to all these studies, whether sub-critical or super-critical, was to find a relationship between the dark or potential core length L_{dc} and a non-dimensional parameter defining the coaxial flow. The momentum flux ratio J was chosen as such parameter over the velocity ratio VR $= u_{\mathrm{o}}/u_{\mathrm{i}}$[3]:

$$J = \frac{\rho_o u_o^2}{\rho_i u_i^2} \tag{1.3.1}$$

Most of the dark core length data [52, 148, 149, 252, 90, 160, 309] was obtained through high-speed back-lit images, where the high density fluid does not let the light go through and appears black. The normalized density can be used as a marker for the dark core length and will be used later on in the analysis of the numerical results. It is defined as:

$$\rho^* = \frac{\rho - \rho_{\mathrm{ch}}}{\rho_i - \rho_{\mathrm{ch}}} \tag{1.3.2}$$

The dark core length for the Oschwald data is estimated from the density profiles obtained through Raman scattering. The end of the dense jet is assumed to be located where $\rho^* = 0.5$. The dark core data from Tani et al. were obtained through time-averaged shadowgraph

[3]This section adopts the same notation as the one introduced through Figure 1.

images.

Over a range of momentum flux ratios typical of full-scale liquid rocket engines, Figure 3 shows a scatter plot of the experimental data along with a few important correlations between L_{dc} and J. These scaling laws are selected here to illustrate the different regimes that could control the dark core length. Rehab et al. [247], using incompressible coaxial water streams, suggested one of the first general correlation which was later further generalized by Lasheras et al. [143] to take into account variable density flows:

$$\frac{L_{dc}}{D} \approx \frac{6}{\sqrt{J}\left(1 - \frac{1}{VR}\right)} \tag{1.3.3}$$

The validity of this correlation under super-critical and compressible conditions is questionable but it provides both historical perspective and asymptotic behavior for the data of interest. Interestingly, Rehab et al. propose that a larger annular gap should result in a longer dark core for the same velocity ratio because the entrainment rate is weaker over the length of the jet. However, the available experimental data for super-critical conditions, and especially the data by Rodriguez et al.[253] and Teshome [309], suggest the opposite trend, with cores with a thin lip being usually longer than with a large lip over similar values of momentum flux ratio.

Using their own near- or super-critical experimental data, Davis et al. [53] find the following correlation, deemed a single-phase correlation:

$$\frac{L_{dc}}{D} \approx \frac{12}{\sqrt{J}} \tag{1.3.4}$$

Note that this corresponds to the Lasheras correlation 1.3.3 shown above with a low velocity ratio of 2 which is usually obtained when both streams are in the same phase. On the other hand, using their sub-critical data, Davis et al. find a different two-phase correlation, with a lower exponent for the dependence on the momentum flux ratio:

$$\frac{L_{dc}}{D} \approx \frac{25}{J^{0.2}} \tag{1.3.5}$$

This expression does not contain any dependence on surface tension and seems to go against the Lasheras et al. correlation 1.3.3 where for liquid-gas streams, the velocity ratio is usually large and thus L_{dc}/D should be converging towards $6/\sqrt{J}$. Actually, Lasheras et al. offer

a correlation for two-phase flows with a surface tension dependence that converges towards $6/\sqrt{J}$ as surface tension disappears. As noted by Leyva et al. [148], this second branch of sub-critical data that follows Eq. 1.3.5 is striking and hints at dependencies other than just the momentum flux ratio. While the data from Rodriguez et al. [253] seems to rule out a strong dependence on lip thickness, there are many other factors that could influence the jet breakup such as the Reynolds number, the presence of a co-flow or the presence of a recess. Also, as shown in Eq. 1.3.3, the dependency on the density and velocity ratio might not be as simple as the one implied by the use of the momentum flux ratio. This could explain the difference of behavior between the water-air coaxial jets and the more recent high-pressure data. For example the atmospheric water-air jets require a velocity ratio of 100 for a momentum flux of 10 whereas for the high-pressure jets, the smaller density ratio means the velocity ratio is of the order of 10 for a momentum flux ratio of 10. Overall the selected super-critical experimental data is bounded on the lower end by the high velocity ratio correlation of Lasheras et al. and on the upper end by the 2-phase correlation by Davis et al. While a significant number of experiments lie around the 1-phase Davis correlation, there is considerable scatter in the data when plotted against the momentum flux ratio only.

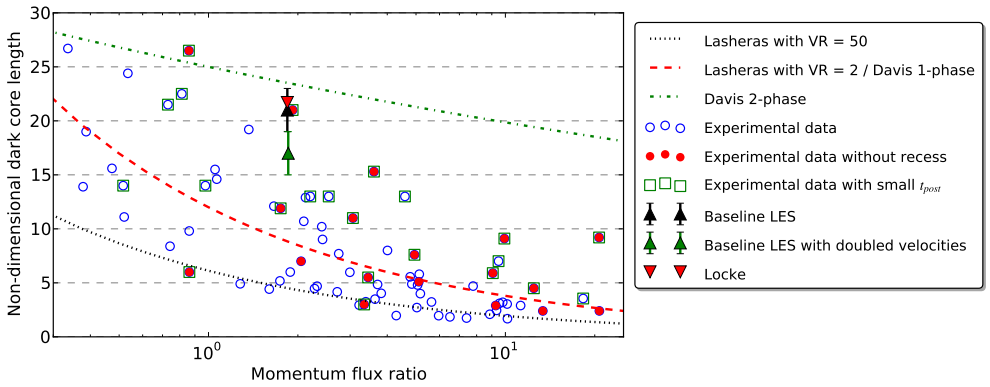

Figure 3: Experimental data for shear coaxial non-reacting flows under super-critical conditions with respect to the inner jet species.

The following series of plots, Figures 4 to 10, show the main metric, the observed dark core length normalized by the inner jet diameter $\frac{L_{dc}}{D_i}$, versus a possible list of variables on

which the dark core length might depend:

- the momentum flux ratio $J = \frac{\rho_o u_o^2}{\rho_i u_i^2}$
- the area ratio $\frac{A_o}{A_i}$, comparing the injection area for the round stream and the annular stream
- the density ratio $\mathrm{DR} = \frac{\rho_i}{\rho_o}$
- the normalized recess length $\frac{l_r}{D_i}$
- the shear Reynolds number $\mathrm{Re}_s = \frac{\rho_m |u_o - u_i| t_{\mathrm{post}}}{\mu_m}$. This Reynolds number is selected by analogy with the Weber number dependence observed under sub-critical pressures [160]. That Weber number uses the shear velocity $|u_o - u_i|$ but its length scale is the jet diameter. Here the post thickness allows the Reynolds number to incorporate some geometrical effect too and appears to be a more logical length to estimate the initial shear between the two coaxial streams.
- the post thickness normalized by the round jet diameter $\frac{t_{\mathrm{post}}}{D_i}$
- the velocity ratio $\frac{u_o}{u_i}$

Note that because of their definitions, $J = \mathrm{VR}^2/\mathrm{DR}$: to maintain the same J, both velocity and density ratios have to increase or decrease together. It is done to qualitatively detect possible trends over all the available data even if the comparison between some of the data is difficult because the methods to measure the dark core length are different or because other parameters such as the presence of a co-flow are not taken into account. The reference for each data point is indicated on each plot to detect potential outliers, even if this makes a precise reading of the data more difficult. Again, the emphasis here is on qualitative trends. Whether a linear or a logarithmic scale is used for each plot depends on which scale displays the possible trend more clearly.

The first plot, Figure 4, shows the dark core length as a function of momentum flux ratio J in a log-log representation. Since J is used on the x-axis, the experimental points are colored by the shear Reynolds number Re_s. In all subsequent plots, the data points

will be colored by J. As already mentioned, the dark core length is thought to depend strongly on J and the trend is apparent here. There appears to be quite a bit of scatter for the Reynolds number dependence, with higher Reynolds number not always producing a shorter core for a given range of J. This will be further examined later on. Also, one data point from Rodriguez et al. [253] appears to be an outlier compared to the rest of the data. For that case, the inner jet velocity is actually larger than the annular stream velocity and so this point will be discarded for further analysis as it is not representative of the flow conditions in a typical rocket engine.

The next plot, Figure 5, shows the dark core length as a function of area ratio J in a semi-log representation. There is no clear trend in the data, especially since the lower values of area ratio appear to be limited to larger momentum flux ratios.

The next plot, Figure 6, shows the dark core length as a function of the density ratio DR in a log-log representation. It appears that larger density ratios result in longer dark cores, on top of the dependence on the momentum flux ratio. For the same momentum flux ratio, the observed dark core length seem to increase with increasing density ratio. The experimental data from Tani et al. and Oschwald et al. are outliers here since they deal with the mixing of a dense species (O_2 or N_2) with a light species (H_2 or He). However, they seem to follow a similar trend than the rest of the experimental data.

The next plot, Figure 7, shows the dark core length as a function of the normalized recess length l_r/D_i. The fact that a recessed injector displays quicker mixing than a non-recessed one has been well established in the literature for reacting flows [30] and has been confirmed in cold flow conditions by Tani et al. [304] and Graham et al. [90]. However, the trend is only slightly visible in the overall current experimental data.

The next plot, Figure 8, shows the dark core length as a function of the shear Reynolds number Re_s. While there is a definite trend of shorter cores with increasing Reynolds number, some of that effect might be due to the momentum flux ratio as both J and Re_s usually increase together. This will be further investigated in the second part of this analysis.

The next plot, Figure 9, shows the dark core length as a function of normalized post thickness t/D_i in a log-log representation. There is no clear trend in the data, only a hint

that dark core might be slightly shorter with larger post thickness.

The last plot, Figure 10, shows the dark core length as a function of velocity ratio VR in a log-log representation. While the overall trend is for shorter cores with increasing velocity ratios, it appears that for a constant J, increasing the velocity ratio actually lengthens the dark core. In that case, this is probably because the density ratio DR dependence is stronger than the velocity ratio dependence: for a constant J, DR has to increase if VR increases, resulting in a longer core as seen in Figure 6.

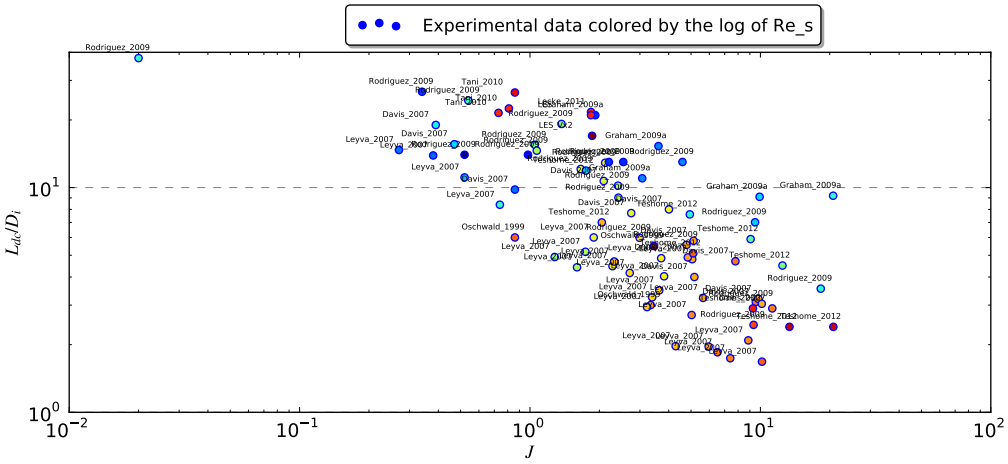

Figure 4: Plot of the experimental data for super-critical shear coaxial mixing. The normalized dark core length is plotted against the momentum flux ratio on a log-log scale. Data points are colored by the shear Reynolds number.

Given these observations, a restricted dataset is constructed that removes the data from Tani et al. and Oschwald et al. because of the different method of measuring the dark core length and because the flow conditions are so different from the rest of the data that there is a risk they skew any regression analysis. However this highlights a need to expand the body of experimental data to cover a larger range of conditions, especially since the Tani et al. and the Oschwald et al. data are actually closer to the conditions in real rocket engines. The data point from Rodriguez et al. where the velocity gradient is inverted is also removed.

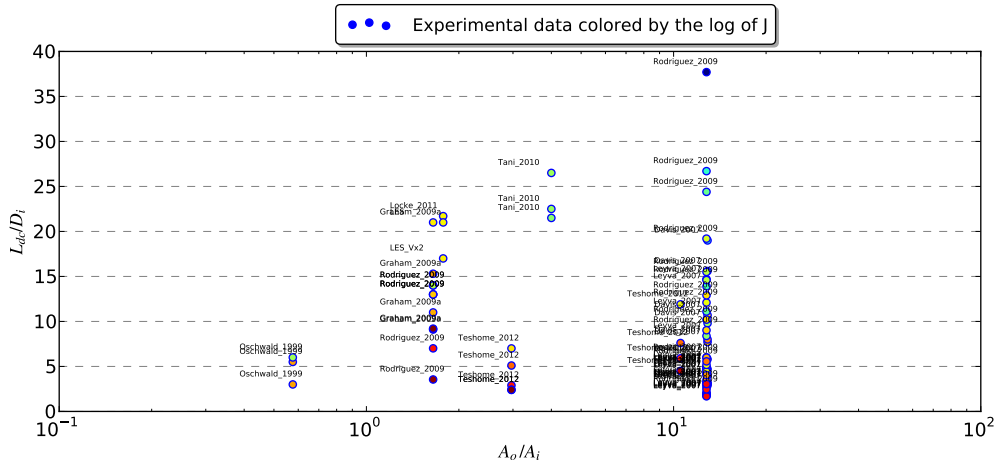

Figure 5: Plot of the experimental data for super-critical shear coaxial mixing. The normalized dark core length is plotted against the area ratio on a semi-log scale. Data points are colored by the momentum flux ratio.

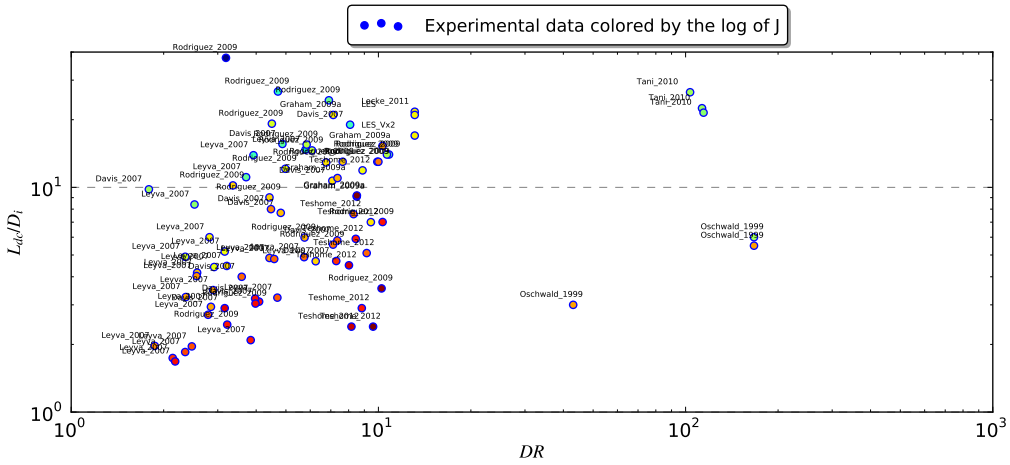

Figure 6: Plot of the experimental data for super-critical shear coaxial mixing. The normalized dark core length is plotted against the density ratio on a log-log scale. Data points are colored by the momentum flux ratio.

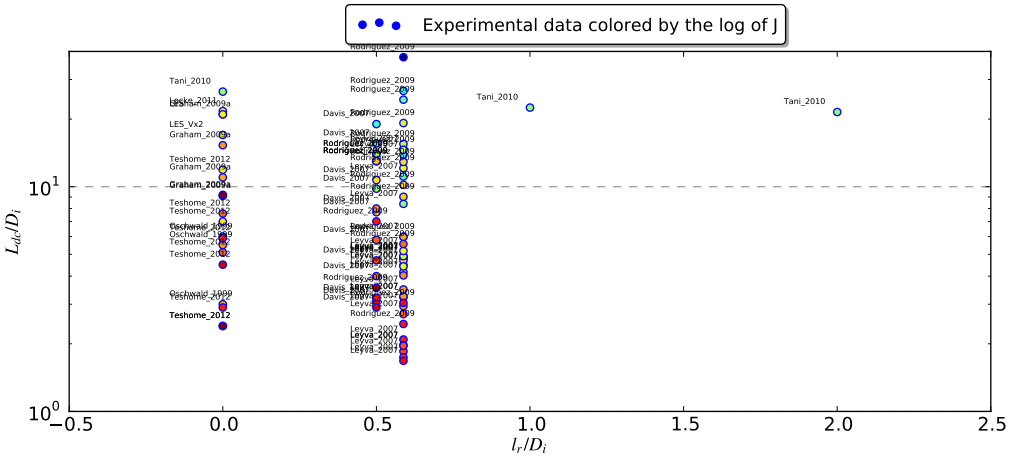

Figure 7: Plot of the experimental data for super-critical shear coaxial mixing. The normalized dark core length is plotted against the normalized recess length on a log-log scale. Data points are colored by the momentum flux ratio.

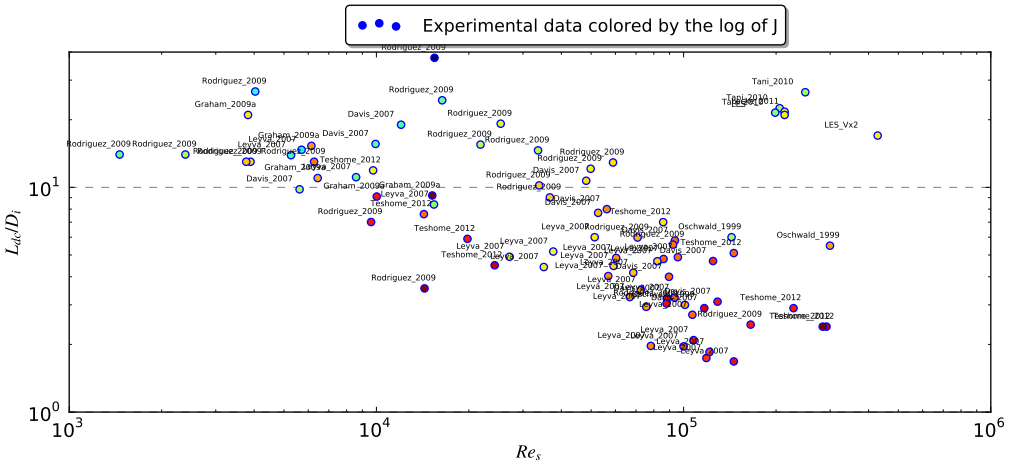

Figure 8: Plot of the experimental data for super-critical shear coaxial mixing. The normalized dark core length is plotted against the shear Reynolds number on a log-log scale. Data points are colored by the momentum flux ratio.

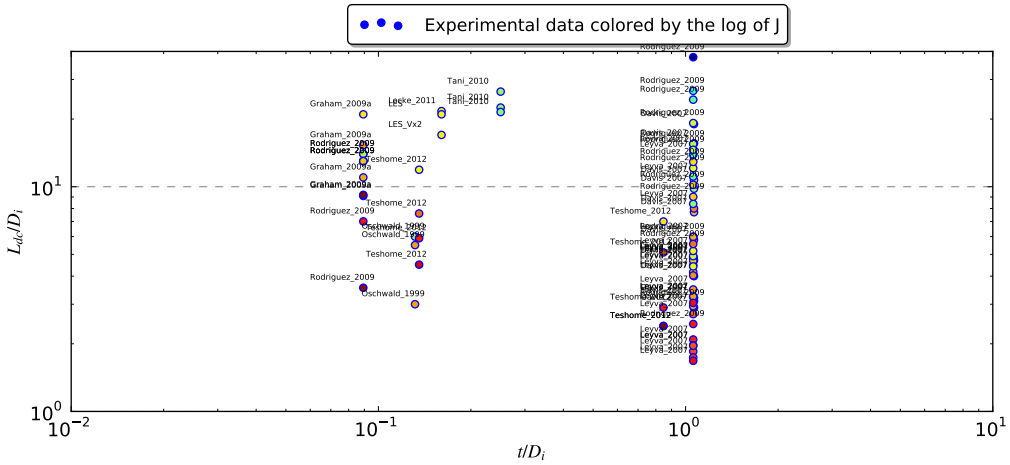

Figure 9: Plot of the experimental data for super-critical shear coaxial mixing. The normalized dark core length is plotted against the normalized post thickness on a log-log scale. Data points are colored by the momentum flux ratio.

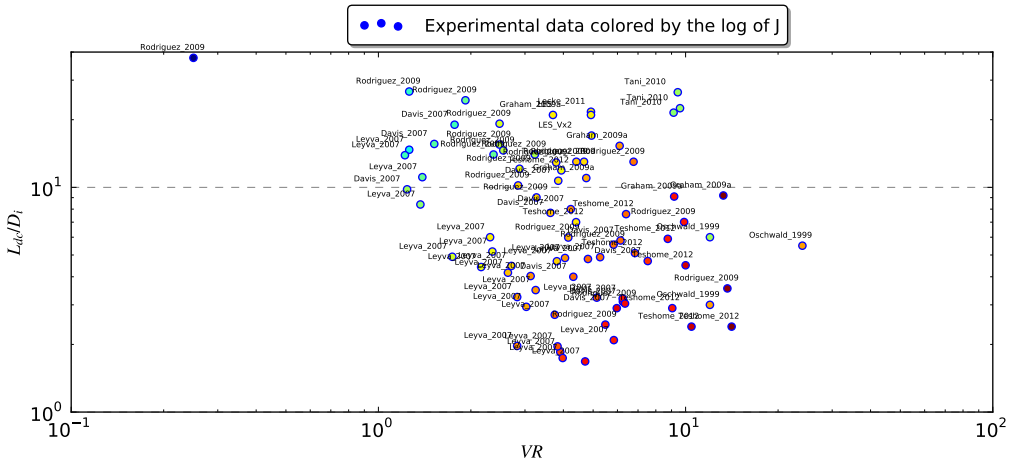

Figure 10: Plot of the experimental data for super-critical shear coaxial mixing. The normalized dark core length is plotted against the velocity ratio on a log-log scale. Data points are colored by the momentum flux ratio.

The remaining dataset contains data for both near-critical and super-critical pressures as it postulated that they would follow a similar behavior. Using a dataset containing only near-critical pressure data, Teshome [309] suggests a new correlation for the dark core length that incorporate geometric parameters:

$$\frac{L_{dc}}{D_i} = 11J^{-0.43}\left(\frac{t}{D_i}\right)^{-0.12}\left(\frac{A_o}{A_i}\right)^{0.15} \tag{1.3.6}$$

This correlation suggests that the dark core length would decrease with increasing post thickness and increase with increasing area ratio. Plotted against the current set of data, as shown in Figure 11, it does display a tighter fit than the simple momentum flux ratio correlation. However the fit is not as good as the one reported by Teshome for a more limited dataset.

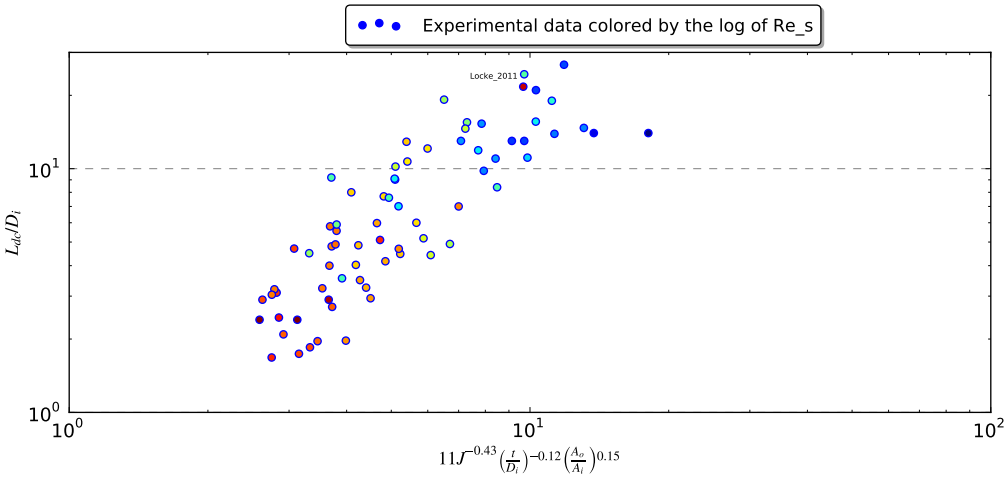

Figure 11: Plot of the experimental data for super-critical shear coaxial mixing. The normalized dark core length is plotted against the curvefit from Eq. 1.3.6 and points are colored by the shear Reynolds number.

Using the momentum flux ratio alone, the best fit through non-linear regression for the current data is:

$$\frac{L_{dc}}{D_i} = 12.05J^{-0.429} \tag{1.3.7}$$

This fit produces a residual standard error of 4.2 on L_{dc}/D_i and is shown in Figure 12. If one includes the shear Reynolds number in the correlation, the following fit is obtained:

$$\frac{L_{dc}}{D_i} = 57.20J^{-0.277}\mathrm{Re}_s^{-0.164} \tag{1.3.8}$$

Table 2: Characteristics of the fit $L_{dc}/D_i = CJ^{c1}\mathrm{Re}_s^{c2}$ presented in Eq. 1.3.8 as reported by the statistical package R [246].

	Estimate	Standard error	t value	$\Pr(>\|t\|)$
C	57.20389	26.40011	2.167	0.0337
c1	-0.27721	0.05901	-4.698	1.27e-05
c2	-0.16424	0.04936	-3.327	0.0014

The characteristics of the curvefit are listed in Table 2. This fit produces a residual standard error of 4.0, with 70 degrees of freedom, on L_{dc}/D_i, slightly better than the previous fit and is shown in Figure 13. The experimental point from Locke thus appears as an outlier, showing a longer core than the curvefit predicts. This could be due to the presence of a co-flow (the only experiment with such feature in the current dataset) or some other geometric parameters as all the other points were obtained on the same rig. Since the Locke experiment will be investigated numerically later on, some of these dependencies will be explored. In general, for all curvefits presented here, the residuals are large for longer dark cores given that most of the experimental data has produced short dark cores. Further adding variables to the fit produce p-values much larger than a reasonable significance level of 0.05 and so Eq. 1.3.8 is the best fit currently obtained. Unfortunately, most of the variables have at least some level of dependency between and a full non-linear multi-variate regression is beyond the scope of this work. So a definite answer cannot be obtained at this point but hopefully more experimental data will be available in the future to further investigate these trends.

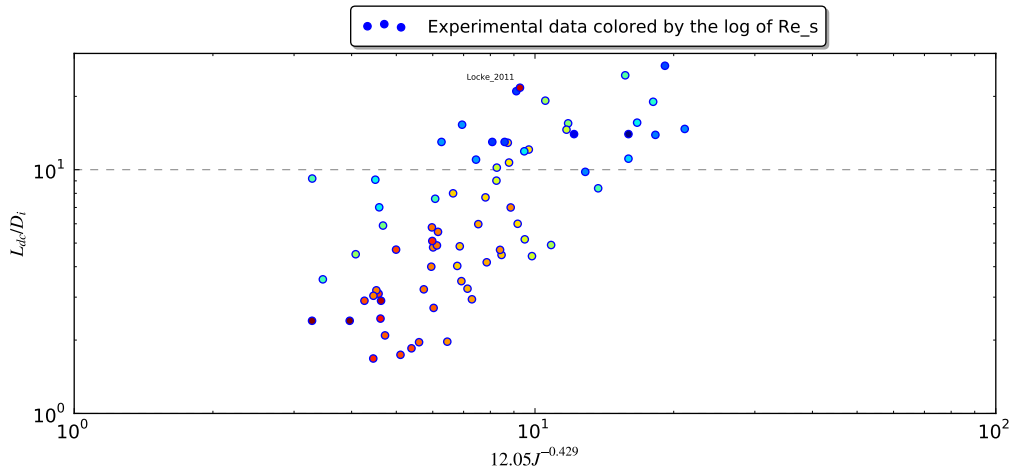

Figure 12: Plot of the experimental data for super-critical shear coaxial mixing. The normalized dark core length is plotted against the curvefit from Eq. 1.3.7 points are colored by the shear Reynolds number.

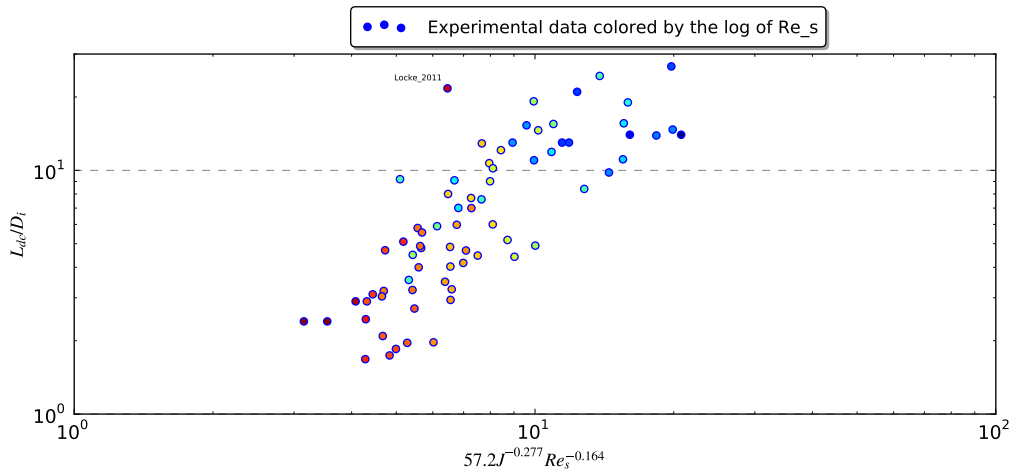

Figure 13: Plot of the experimental data for super-critical shear coaxial mixing. The normalized dark core length is plotted against the curvefit from Eq. 1.3.8 and points are colored by the shear Reynolds number.

1.3.2 Review of the reacting experimental data

A detailed picture of the super-critical flame produced by a shear coaxial element is shown in Section 6.4 where numerical predictions are qualitatively compared to the flame structure accepted by the experimental community [30]. A specific feature of O_2-H_2 injection is that the flame anchoring at the tip of the central jet sleeve is very stable. This has been observed experimentally in multiple rigs [113, 318, 160], while it has been shown to not be the case for O_2-CH_4 systems [284, 166, 165]. Physically, this is due to the much larger Damköhler number $\mathrm{Da} = \frac{\tau_{\mathrm{flow}}}{\tau_{\mathrm{chem}}}$ with hydrogen chemistry compared to methane or other hydrocarbons. The time-scales and length-scales in a super-critical H_2-O_2 coaxial flame were estimated by Ivancic and Mayer [113] to be around 1 μs and 1 μm near the flame anchoring. Since 2006, while there were no new findings fundamentally altering the understanding of the physical processes at play in a single super-critical flame, the experimental research has focused on gathering better data thanks to better instrumentation. Many earlier experiments provided limited visualization or no visualization at all and only global metrics such as the wall heat flux through the chamber walls. It will be shown in Chapter 4 that this greatly limits the validation process of numerical simulations. Two-dimensional high-speed visualizations through backlighting or shadowgraph imagery are now more commonplace [287, 160], which allows for a good qualitative picture of the instantaneous and time-averaged flow field. Techniques such as OH-PLIF can provide instantaneous (exposure time $< 1\mu$s) two-dimensional slices at sampling rates on the order of 10 Hz [318]. However, detailed local measurements at a high sampling rate of multiple scalars and velocity vectors is not available yet under rocket conditions as they are available for normal conditions through the TNF workshops [11]. Until these are available, the validation of CFD solvers for rocket engine applications will remain limited. Also, sub-scale multi-element injectors are also investigated in more details as they represent the logical step in complexity before the simulations of full-scale engines Finally, since the ultimate goal of this field of research in the understanding of combustion instabilities in liquid rocket engines, the interaction of super-critical flames with acoustic fields is actively being studied [250, 251] while some sub-scale chambers with natural combustion noise and/or instabilities are beginning to come under scrutiny [210].

1.3.3 Experimental work selected for this work

As mentioned previously, the improvement in the visualization techniques for high-pressure chambers is an important development towards the validation of CFD solvers. The first study that will be performed for this work, in Chapter 4, did not have access to any flow-field visualization and the shortcomings of this defect will be detailed there. For further validation of the solver and to get understanding of flows as relevant as possible to real rocket engines, the experiments from Locke [160] are selected. The main reasons for this choice are:

- the quality of the visualization data, where detailed high-speed backlit images are available to compare the instantaneous and time-averaged predictions of the numerical simulations
- the high speeds/flowrates that are closer to realistic conditions and are easier to model with a compressible solver
- the presence of a co-flow to mimic the surrounding flow of other injection elements in a full-scale configuration
- both non-reacting LOX-GOX, reacting GOX-GH2 and reacting LOX-GH2 experiments were run in the same chamber at different sub-critical and super-critical pressures. Even if this work will only investigate the super-critical LOX-GOX and LOX-GH2 cases, it will pave the way for future studies of the same setup.

Details on the geometry and flow conditions of each case will be given in the relevant chapters.

1.3.4 Previous computational efforts

From a numerical point of view, high-pressure mixing is essentially represented by temporal mixing layers (TML), spatial mixing layers (SML) and jets (both free jets and coaxial jets) [15]. The simple configuration of temporal mixing layers has allowed researchers to study in-depth the impact of non-ideal thermodynamics on the fluid mechanics using Direct

Numerical Simulations (DNS). The heavily stratified flow displays interesting properties such as the dampening of velocity fluctuations on the dense side and the redistribution of the turbulent kinetic energy parallel to the density interface [225, 223]. Also, significant backscatter of energy from the smallest scales to larger scales has been observed in these DNS, which might need to be modeled by the closure models for Large Eddy Simulations (LES) [224]. From a formulation point of view, real gas equation of states introduce new terms in the LES formulation and can also increase the magnitude of terms that were previously neglected [16]. To investigate these terms, DNS databases were built and used in *a priori* and *a posteriori* analyses of the validity of existing closure models for LES [307, 306, 273].

In parallel, similar analyses of temporal reacting mixing layers by Foster et al. [70, 69, 139, 168] identified sub-grid terms that should not be neglected in their H_2-O_2 configuration. However, practical sub-grid closure terms have yet to be used in simulations of realistic configurations. And while some of these closure issues can undoubtedly have an impact on the flow structure and dynamics, there is a need to first evaluate the basic capabilities of LES solvers to reproduce qualitatively and quantitatively practical flows relevant to liquid rocket engines.

Like for the experimental work, the focus here is on coaxial jets. However, there are a few general observations that can be made on the numerical aspects of non-ideal gas computations. Colonna et al. [40] argue that for real gas computations, since the cost of a single iteration is dramatically increased, an implicit time integration is much more efficient than an explicit scheme such as Runge-Kutta or MacCormack schemes. They also stress [41] that whenever available, analytic expressions for the various thermodynamic derivatives are much more efficient than numerical approximations based on finite differences. Their applications include the study on non-classical gas dynamics in real gases, such as rarefaction shocks and compression fans in regimes where non-classical behavior is observed [39, 204]. For the applications of interest of this study, the thermodynamic state is sufficiently removed from the critical point that these issues are not a concern. However, it is possible for some rocket engines conditions to approach this regime [148, 287]. These conditions simply won't be considered in this study.

For compressible applications and in particular rocket engine applications, two kinds of numerical approaches are possible: explicit, fully-conservative, fully-coupled methodologies and implicit, pre-conditioned ones. Liou and Steffen [158] introduced a new flux splitting scheme called Advection Upstream Splitting Method (AUSM) to overcome limitations of the Roe splitting method. This method was further improved over the years and a recent overview is provided by Liou [157]. Applications that displayed large density gradients were also a center of interest for this method, in particular for two-phase flows and cavitating flows [60]. This demonstrated that the AUSM method could be applied to non-ideal equations of state. These flux-splitting methods are generally coupled with time-derivative preconditioning to efficiently deal with both compressible and incompressible regions of the flow. However, generalization to these schemes to three-dimensional configurations can be difficult [25]. Also while there are clear advantages in terms of stability and convergence for these methods, the accurate capture of turbulent structures and its coupling with chemical processes is not always evident. For example, the two-dimensional solution of a coaxial GH_2-GO_2 injector shown by Lian et al. [152] displays a very thin flame that appears purely diffusive, with little hint of a turbulent flame brush. An intermediate method is to precondition the scheme as pioneered by Venkateswaran et al. [325] and extended to real gas flows by Zong et al. [349]. Alternatively, it is possible to extend the explicit MacCormack scheme to a semi-implicit method to significantly speed up at least part of the computation [170, 78].

1.3.4.1 Mixing studies

Very few numerical studies have focused on a shear coaxial injector configuration with transcritical injection of the central jet species. Gautam and Gupta [80, 79] have conducted joint experimental and numerical studies of cryogenic coaxial injectors but they only dealt with atmospheric pressure flows. If the scope is extended to single round jets, Zong et al. [346], Schmitt et al. [268] and Petit et al. [236] extensively studied the experiments by Mayer et al. [188] and performed detailed analyses of the jet spreading and decay rates using Large Eddy Simulation. Without any real gas-specific treatment of the sub-grid models, good agreement is obtained with the limited reliable available data. For this same round jet case,

Park [234] shows that Large Eddy Simulation is superior to Reynolds Averaged Navier-Stokes (RANS) methods for predicting the spreading rate of the super-critical jet. For a shear coaxial configuration under high-pressure, to the knowledge of the authors, only the mixing studies by Hosangadi et al. [104], Liu [159] and Candel et al.[31] are available and they all model the rig from the Air Force Research Laboratory [53] which has generated most of the experimental data on high-pressure coaxial injection to this day. Each work was able to reproduce at least qualitatively the experimental flow-field using LES or hybrid RANS-LES formulations, without any real gas-specific sub-grid modeling.

1.3.4.2 Reacting studies

Surprisingly, there is a larger set of numerical investigations for the more complex reacting shear coaxial configuration under super-critical conditions as it has more direct applications to actual rocket engines. Because of the importance of the flame anchoring mechanism, and because focusing on the splitter plate region limits the complexity and cost of the simulation, many studies have focused on the flame stabilization region [348, 110]. However, no detailed study of this region has been performed in three-dimensions and using isothermal wall boundary conditions. This is probably crucial to capture the flame anchoring of hydrocarbons as observed experimentally by Singla et al. [284]. The full-combustor LES simulations [218, 214, 215, 181, 184, 258, 267] have reproduced at least qualitatively the observed super-critical flames and have contributed to a better understanding of the flow dynamics inside a sub-scale rocket chamber. In parallel, a number of RANS studies have also been performed [244, 50] and have explored a large array of modeling options thanks to their low computational cost. For example, Poschner et al. show a small impact of the volume correction in a cubic equation of state while Cutrone et al. explore the impact of turbulent combustion modeling and kinetics on super-critical combustion cases. They show that for their RANS simulations, detailed kinetics including HO_2 and H_2O_2 were necessary to get qualitative agreement with the experimental flame. They also demonstrate the applicability of a flamelet model which has been studied extensively by different groups [347, 174, 134, 135, 140, 133] for its application for super-critical combustion. The

development of this flamelet model find its roots in numerous one-dimensional studies of high-pressure flames [232, 249, 242].

1.4 Objectives

As seen in the previous sections, numerical modeling of liquid rocket engine flows is a great challenge. Starting from an existing and well validated compressible Large-Eddy Simulation solver (referred to as LESLIE from here on out), the first goal of this study is to develop and extend features that are required to study liquid rocket engine flows. These features include physical models as well as computational frameworks and are detailed in the objectives below. With these new capabilities, the solver will be validated against increasing complex flows relevant to rocket applications. New understanding will be gained on the dominant physical processes in these flows thanks to the spatial and temporal information provided by Large-Eddy Simulations. In the end, the following objectives need to be achieved:

- **Study the unsteady and three-dimensional characteristics of a high-pressure GOX-GH_2 combustor**

  Coaxial injectors typically used in liquid rocket engines can present large density gradients when the propellants used are hydrogen and oxygen, as it is for this work. Even in the combustion chamber of a staged combustion engine, where propellants are introduced as hot gases, the density gradients are large enough that a locally dissipative scheme is needed. Away from the thin diffusion flame however, the turbulent structures need to be represented with little dissipation to capture the overall flow dynamics. Many numerical schemes do not combine these two characteristics and even the existing hybrid central-upwind scheme in LESLIE has not been tested and optimized for flows with strong density gradients. Also, the main experimental data available for such a sub-scale combustion chamber is the wall heat flux, highlighting the difficulty to visualize and measure the flow properties in high-pressure, reacting environments. Thus particular attention needs to be given to the near-wall turbulence.

  To solve the first issue, the hybrid numerical scheme developed by Génin [81] is extended here for flows with density gradients. The local, dynamic switch is based on the

value of the density gradients and its parameters are selected after extensive testing on canonical temporal mixing layers. Since the sub-scale chamber under investigation has been extensively studied, a comprehensive comparison with the experimental data and simulations from other state-of-the-art solvers is presented highlighting the strengths and shortcomings of the current approach.

- **Develop a multi-species real gas framework inside a conservative, compressible solver**

  For many rocket engine cycles, the oxygen is injected in the combustion at cryogenic temperatures. If the operating pressure in the combustion chamber is larger than the critical pressure of oxygen (around 56 bar), this means the oxygen is injected as a compressed liquid. Because surface tension vanishes under such regime, the oxygen will not break up and atomize like a conventional liquid jet and thus usual multi-phase methods cannot be used to model such flow. While a single phase formulation can solve such flow, the ideal gas equation of state and by extension the thermally perfect calorific equations of state are not able to represent the compressed liquid state and the transition to a gas as the density decreases.

  To represent these departures from ideal gas behavior, well-known cubic equations of states such as the Redlich-Kwong EoS and the Peng-Robinson EoS are selected as a compromise between cost and accuracy. In a similar fashion, a transport properties framework is implemented using the methods of Chung and Fuller alongside high-pressure corrections. The implementation of the thermodynamics is particularly challenging since iterative methods are required by the conservative solver to convert the conservative variables into the primitive ones. Their performance will be investigated in order to limit their computational cost.

  Both frameworks are first verified on the most basic level using experimental data available. This data is particularly scarce for high-pressure mixtures. The coupling of the real gas framework with the hybrid solver is further verified using high-pressure versions of standard test cases such as the Shu-Osher test or simple convection cases.

- **Perform three-dimensional Large Eddy Simulations of trans-critical shear coaxial flows with extensive experimental data to gain a better understanding of the physics involved.**

  A review of the literature has shown that three-dimensional Large Eddy Simulations are able to reproduce at least qualitatively single element shear coaxial flows, even without new sub-grid models. Newly available experimental data on non-reacting and reacting configurations should allow an in-depth validation of the current three-dimensional unsteady real gas solver, including quantitative comparisons on the prediction of the dark core length. This is an important global characteristic of a coaxial injector and there is significant interest in validating scaling laws that can be used to infer full-scale performance from sub-scale testing.

  The first study of a shear coaxial LOX-GOX injector contains extensive qualitative and quantitative comparisons between the numerical predictions and the different flow visualizations. It illustrates how numerical simulations can complement the available data and try to predict trends that future experiments could investigate. This mixing case is then slightly modified to demonstrate the application of the Linear-Eddy Model as a sub-grid closure for real gas flows. To the knowledge of the author, this would be the first application of the LEM in such flow. Finally, the full solver is tested on a reacting trans-critical flow involving the same injector as before. This study of a shear coaxial LOX-GH_2 injector highlights the additional complexities of reacting flows under liquid rocket engine conditions. However, the investigation of the LEM in a reacting trans-critical flow is beyond the scope of this work.

1.5 Thesis outline

This first chapter was dedicated first to background information on liquid rocket engines, why they are such complex systems to study and why better numerical tools are needed to understand them better. In particular, basic knowledge on coaxial injectors and real gas thermodynamics was given to help the reader understand the challenges and the goals of this work. After a review of the existing experimental data and previous numerical works,

a detailed list of objectives was presented.

Chapter 2 details the formulation used to solve these objectives, with an emphasis on the real gas framework. How this formulation is implemented in the CFD solver is described in Chapter 3. The main focus is on the hybrid upwind-central solver and how it behaves in a conservative approach with real gas thermodynamics.

The following chapter, Chapter 4, reviews the first application of the current approach, a gas-gas reacting shear coaxial injector. Despite the high operating pressure, no real gas thermodynamics are needed and the emphasis is on the capture of the wall heat flux. This chapter also contains an extensive comparison of the current results with other state-of-the-art solvers that modeled the same configuration. This puts in perspective the available experimental data and provides insight on the strengths and shortcomings of the current approach. In particular, this configuration is later revisited with a new turbulent sub-grid model to address some near-wall issues and the results are presented at the end of the chapter.

The next application focuses on the validation of the real gas solver by considering a non-reacting liquid-gas injector. The previous study had allowed the CFD community to make recommendations on a new experimental rig and the first stage is to investigate the LOX-GOX cold flow results. This single-species flow removes many assumptions made in the formulation and allows a focused study on the ability of the solver to deal with the trans-critical injection with the Redlich-Kwong equation of state while capturing the overall turbulence dynamics. Several qualitative and quantitative comparisons are made with experimental data and a demonstration is made of how LES can go beyond the current limitations of the experimental rig and hopefully provide guidelines for future experimental work. Finally, the LEM-LES methodology is applied to the same configuration after a slight modification of the conditions to allow for a multi-species flow.

The final application puts all the pieces together as a reacting liquid-gas injector is modeled. The feasibility of a full three-dimensional LES simulation with complex geometry is investigated. Insights are gained on the role of the boundary conditions and the flow confinement. Comparison with experimental data is not yet satisfactory but suggestions are

made to improve the current results.

Chapter 7 concludes the main body of this thesis by reviewing the objectives listed in this chapter, highlighting the contributions made over the course of this work. Perspectives on the current state of the solver are also given and recommendations for future work are provided to continue to improve the cost and accuracy of this CFD tool for liquid rocket engines.

A few Appendix chapters are also provided to serve as reference material, in particular for the real gas formulation.

CHAPTER II

FORMULATION

First, the general equations governing the fluid mechanics are described and the concept of LES filtering is introduced. In the next section, the closure of the terms introduced by the LES formulation is discussed. A section is dedicated to the Linear-Eddy Model as it has the potential to close many of these terms. Then the thermodynamic and transport properties relevant for high-density flows are described. The treatment of the boundary conditions is then detailed last. A description of the reaction mechanisms used for this work can be found in the Appendix H.

2.1 Exact governing equations for the fluid mechanics

For this work, the full Navier-Stokes are considered. They determine the motions of an unsteady, compressible, reacting, multi-species fluid through the conservation of mass, momentum, total energy and species. Notably, external forces such as gravity or electro-magnetism are neglected in the current solver and thus buoyancy or MagnetoHydroDynamics (MHD) cannot be simulated. Assuming the continuum assumption holds for the flow of interest and using the Einstein summation convention, the governing equations read:

$$\frac{\partial \rho}{\partial t} + \frac{\partial \rho u_i}{\partial x_i} = 0 \tag{2.1.1}$$

$$\frac{\partial \rho u_i}{\partial t} + \frac{\partial}{\partial x_j}\left(\rho u_i u_j + p\delta_{ij} - \tau_{ij}\right) = 0 \tag{2.1.2}$$

$$\frac{\partial \rho e_T}{\partial t} + \frac{\partial}{\partial x_i}\left(\left(\rho e_T + p\right) u_i + q_i^{\mathrm{IK}} - u_j \tau_{ij}\right) = 0 \tag{2.1.3}$$

$$\frac{\partial \rho Y_k}{\partial t} + \frac{\partial}{\partial x_i}\left(\rho Y_k u_i + j_{i,k}\right) = \dot{\omega}_k \tag{2.1.4}$$

Some simulations in this work will be performed in an axisymmetric configuration. While three-dimensional fluxes could be used in such configuration, it is more cost efficient to shut down the fluxes in the third direction and to replace them with additional terms in radial momentum equation. More details on this formulation can be found in previous works [175].

2.1.1 Equations of state

In the above equations, ρ is the density, u_i is a component of the Cartesian velocity vector, p is the pressure, τ is the viscous stress tensor, e_T is the total massic energy (internal energy e plus kinetic energy $\frac{u_i u_i}{2}$), q^{IK} is the heat diffusion flux in its "Irving-Kirkwood" form including the enthalpy flux by mass diffusion, Y_k is the mass fraction for species k and j_k is the mass diffusion flux for species k , k varying between 1 and N_S, the number of species considered in the mixture. The massic internal energy e can generally be expressed as a function of temperature, pressure and composition as will be described in the thermodynamics section. For thermally perfect gases, this reduces to:

$$\begin{aligned} e &= f(T, p, Y_k) \\ &= \sum_{k=1}^{N_S} Y_k e_k(T) \text{ for TPG} \end{aligned} \tag{2.1.5}$$

The relationship between internal energy and temperature is sometimes called the thermal or calorific equation of state(EoS). The thermal EoS alone cannot close the system of equations (2.1.1)-(2.1.2)-(2.1.3)-(2.1.4) since it introduces explicitely the temperature as a variable. An additional equation of state is required, linking the temperature, pressure and density. Assuming a mixture of ideal gases, this can be expressed as:

$$p = f(\rho, T, Y_k) \tag{2.1.6}$$

$$= \rho R_g T \tag{2.1.7}$$

The gas constant R_g is a simple function of the mixture composition:

$$R_g = R_u \sum_{k=1}^{N_S} \frac{Y_k}{MW_k} \tag{2.1.8}$$

with R_u the universal gas constant and MW the molecular weight. This simple forms of the thermal and standard equation state show a possible closure of the governing equations. However, for rocket engine applications, significant parts of the flow cannot be assumed to behave like an ideal gas and more complex relationships for Equations (2.1.5) and (2.1.6) are needed. More details will be given in the thermodynamics section, Section 2.5. All is left to define are the diffusion terms for momentum, heat and mass fluxes.

2.1.2 Momentum diffusion and stress tensor

The current work only deals with Newtonian fluids, where the stresses are linearly proportional to the rate of strain:

$$\tau_{ij} = \mu \left(\frac{\partial u_i}{\partial x_j} + \frac{\partial u_j}{\partial x_i} \right) + \lambda \frac{\partial u_k}{\partial x_k} \delta_{ij} \tag{2.1.9}$$

The dynamic viscosity μ, like most other derived quantities introduced in this section, is generally a function of two state variables (usually T and p) and the mixture composition. Note that even under conditions where thermodynamic departures from ideal gas are small, transport properties such as dynamic viscosity can display more significant pressure dependence. This is illustrated by Figure 14. Ideal gas thermodynamics and transport properties display of course no dependence on pressure, typical of the simpler expressions shown in Equations (2.1.5) and (2.1.6). But it can be seen that at 300 K and 100 bar, departures from ideal gas thermodynamics can reach 5% while departures from ideal gas transport properties exceed 10%. More details on the best ways to model these departures will be given in Sections 2.5 and 2.6.

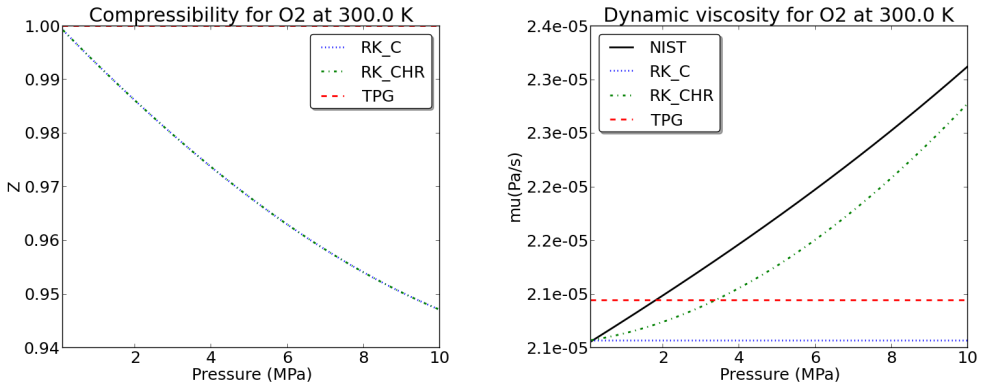

(a) Compressibility $Z = \frac{p}{\rho R_g T}$ (b) Dynamic viscosity μ

Figure 14: Examples of thermodynamic and transport properties departures from ideal gas behaviors with the compressibility factor (left) and dynamic viscosity (right) of oxygen at 300 K, between 1 bar and 100 bar. NIST denotes experimental data, TPG denotes ideal gas equation of state and transport properties, RK_C denotes real gas equation of state and low-pressure transport properties and RK_CHR denotes real gas equation of state and high-pressure transport properties.

The other viscosity coefficient in Eq. (2.1.9) is the volume viscosity. Stokes' hypothesis states that the coefficient of bulk viscosity, expressed as $\left(\lambda + \frac{2}{3}\mu\right)$, is null because the stress tensor should be traceless. An analysis of this hypothesis for real gas flows is given in Appendix G. To summarize, even with flows where the bulk viscosity is significantly non-zero, there is little effect on the flowfield. Thus, for the rest of this work, the Stokes' hypothesis is assumed to hold and the stress tensor can simply be expressed as:

$$\tau_{ij} = 2\mu\left(S_{ij} - \frac{1}{3}S_{kk}\delta_{ij}\right) \tag{2.1.10}$$

where S_{ij} is the local rate of strain tensor:

$$S_{ij} = \frac{1}{2}\left(\frac{\partial u_i}{\partial x_j} + \frac{\partial u_j}{\partial x_i}\right) \tag{2.1.11}$$

2.1.3 Heat and mass diffusion

2.1.3.1 General multi-component formulation

A complete description of the molar mass and heat diffusion fluxes can be obtained through Keizer's [124] fluctuation-dissipation theory and non-equilibrium thermodynamics and is shown here in its Irving-Kirkwood (IK) form:

$$\boldsymbol{J_k} = L_{kq}\nabla\frac{1}{R_u T} - \sum_{l=1}^{N_S} L_{kl}\nabla\frac{\mu_l}{R_u T} \tag{2.1.12}$$

$$\boldsymbol{Q}^{\mathrm{IK}} = L_{qq}\nabla\frac{1}{R_u T} - \sum_{l=1}^{N_S} L_{ql}\nabla\frac{\mu_l}{R_u T} \tag{2.1.13}$$

where $\boldsymbol{J_k}$ is the partial molar flux for species k, $\boldsymbol{Q}^{\mathrm{IK}}$ is the Irving-Kirkwood form of the heat flux and μ_l is the chemical potential of species l. In this form, the diffusion coefficients can be clearly identified:

- L_{kq} are the Soret diffusion elements.
- L_{kl} are the Fick diffusion elements.
- L_{qq} is the Fourier diffusion element.
- L_{ql} are the Dufour diffusion elements.

However, for a fluid mechanics application, it is preferable to express these diffusion fluxes with respect to the gradients of primitive variables such as T, p or X_k. Moreover, these diffusion elements are difficult to measure experimentally. For example, a thermal conductivity coefficient $\kappa_{kl}^{\mathrm{IK}} = L_{qq}/(R_u T^2)$ can be extracted from the Fourier diffusion element. But it does not correspond, for a mixture, to the thermal conductivity that can be measured experimentally or that is defined by the kinetic theory, partly because it is not the only coefficient of the temperature gradient. Consequently, manipulations are necessary to recast Equations 2.1.12 and 2.1.13 as the sum of temperature, pressure and species gradients terms. From general thermodynamics, one can derive:

$$\nabla \frac{\mu_l}{R_u T} = \frac{V_{,l} \nabla p - H_{,l} \nabla \ln T}{R_u T} + \frac{1}{X_l} \sum_{k=1}^{N_S - 1} \alpha_{lk}^{\mathcal{D}} \nabla X_k \tag{2.1.14}$$

where $V_{,l}$ and $H_{,l}$ are the partial molar volume and the partial molar enthalpy for species l and $\alpha_{lk}^{\mathcal{D}}$ is the mass diffusion factor. These quantities can be computed from first principles given an equation of state. After lengthy manipulations, it is possible to express the diffusion fluxes as the sum of fluxes caused by temperature, pressure and species gradients:

$$J_k = A_{j,k} \nabla T + B_{j,k} \nabla p + \sum_{\substack{l=1 \\ l \neq k}}^{N_S} C_{j,kl} \nabla X_l \tag{2.1.15}$$

$$Q^{\mathrm{BK}} = A_q \nabla T + B_q \nabla p + \sum_{\substack{l=1 \\ l \neq k}}^{N_S} C_{ql} \nabla X_l \tag{2.1.16}$$

The diffusion of mass due to species gradients and the diffusion of heat due to temperature gradients are respectively, the normal Fick's and Fourier's type of diffusion. The other terms are cross diffusion terms since the diffusion of a property is caused by gradients of other properties. The general derivation of the coefficients $A_{j,k}$, $B_{j,k}$, $C_{j,kl}$, A_q, B_q and C_{ql} as a function of the diffusion coefficients introduced above is beyond the scope of the current work for a multi-component mixture. The reader is referred to Bird [20], Palle [231] and Giovangigli et al. [85] for detailed discussions of the validity of the various forms of the diffusion fluxes, depending on whether they are approached from a statistical mechanics, a statistical thermodynamics or a macroscopic point of view. At this point, this formulation is computationally too expensive for applications in complex geometries and

detailed mechanisms. It has been successfully applied in simpler geometries and with a few species [162, 222, 232, 324] and it will have to be incorporated in the future for more complex applications. But for the present work, this cannot be afforded computationally and so a simplified approach to the diffusion fluxes is presented next.

2.1.3.2 Simplified transport properties

The heat diffusion flux and the mass diffusion flux, if solely based on Fick's and Fourier's types of diffusion, can be written as:

$$j_{i,k} = \rho Y_k \mathcal{V}_{i,k} = -\rho Y_k \frac{1}{X_k} \mathcal{D}_{k,m} \frac{\partial X_k}{\partial x_i} \tag{2.1.17}$$

$$q_i^{\mathrm{IK}} = -\lambda \frac{\partial T}{\partial x_i} + \sum_{k=1}^{N_S} j_{i,k} h_k \tag{2.1.18}$$

Here $\mathcal{V}_{i,k}$ is the diffusion velocity for species k in the i-th direction, X_k is the mole fraction for species k, λ is the thermal conductivity and h_k is the partial massic enthalpy of species k. $\mathcal{D}_{k,m}$ is the pseudo binary diffusion coefficient between the species k and the mixture and allows for a simpler representation of the species diffusive fluxes by neglecting multi-component diffusion:

$$\mathcal{D}_{k,m} = \frac{\sum_{k \neq j} Y_k}{\sum_{j \neq k} \frac{X_j}{\mathcal{D}_{k,j}}} \tag{2.1.19}$$

For simulations of three-dimensional combustion chambers and detailed kinetics, this is the only option whose computational cost is reasonable. The interdiffusional enthalpy flux is sometimes neglected in the literature but is included here as it prevents local violations of the entropy conditions when species with very different molecular weights mix [44]. The other main assumption in Equations 2.1.17 and 2.1.18 is that cross-diffusion is neglected. It is possible to include these terms in this simplified formulation without all the other cross-diffusion terms described in the previous section. It is recalled that the Soret effect represents the species diffusion induced by temperature gradients while the Dufour effect represents the heat flux caused by concentration gradients. For thermally perfect gas simulations, neglecting these effects is perfectly justified as densities are not large enough to make these cross-diffusion terms significant. For flows with significant departures from ideal gas, their impact is not well defined yet. Miller and Lou [199] first investigated this issue

using compressible mixing layers. They found that the Soret diffusion had an influence on the shear layer growth when the pressure gradients where aligned with the species gradients, which would occur at the edge of strong vortices. Using one-dimensional flame simulations with simplified kinetics, Palle et al. [233] found that the Soret diffusion had an effect on H_2-O_2 flames (temperature reduced by 200 K) but that the Dufour term had none. Using compressible H_2-O_2 mixing layers, Mahle et al. [171] found some significant differences in the instantaneous flowfields with and without cross-diffusion but for statistics, relative differences were below 10%. Using one-dimensional H_2-O_2 flame simulations with detailed kinetics, Ribert et al. [249] found very little effect at elevated pressured because of the large reaction rates. Similarly, a recent study of oxygen droplet evaporation at high pressure by Lafon et al. [141] found little influence of the cross-diffusion terms. Finally, Giovangigli et al. [86] analyzed planar trans-critical H_2-O_2-N_2 and found that while the Soret diffusion had a quantitative effect on the reactants diffusion fluxes, the flame structure was not significantly altered. Also, the heat diffusion flux does not include thermal radiation which is neglected for this study. It has been shown to play a role in liquid rocket engines using heavy hydrocarbons such as kerosene as fuel [26] because of the non-negligible soot formation that can occur. Since the current study focuses on hydrogen-oxygen engines, it is not included in the current equations. Despite these assumptions, exact mass conservation is not mathematically enforced in Eq. (2.1.17) as the net species diffusion flux $\sum_{k=1}^{N_S} \mathcal{V}_{i,k} Y_k$ is not necessarily zero. Thus a correction velocity needs to be added to the diffusion velocities so that the net diffusion is null:

$$\mathcal{V}_i^{\text{cor}} = -\sum_{k=1}^{N_S} Y_k \left(\frac{\mathcal{D}_{k,m}}{X_k} \frac{\partial X_k}{\partial x_i} \right) \tag{2.1.20}$$

The final expression for the mass diffusion flux is thus:

$$j_{i,k} = \rho Y_k \left(\mathcal{V}_{i,k} + \mathcal{V}_i^{\text{cor}} \right) \tag{2.1.21}$$

The evaluation of the mass diffusion coefficients and the thermal conductivity is detailed in Section 2.6. In general, these will be assumed to depend, like the dynamic viscosity, on temperature, pressure and mixture composition.

These are the equations that would be solved in a Direct Numerical Simulation (DNS). However, for engineering applications, DNS is too costly in terms of computational resources as it requires to resolve all scales of the flow. For turbulent combustion applications such as liquid rocket engines, the Batchelor and Kolmogorov scales are many orders of magnitude smaller than the combustion chamber and a DNS of such a chamber might never be feasible. Large Eddy Simulation (LES) was designed to solve this computational cost issue by modeling scales below a certain level. To achieve this, a spatial filtering of the governing Navier-Stokes equations is required.

2.2 LES formulation

Thanks to the Kolmogorov theory on turbulence, which introduced the separation of the flow scales and the universilaty of small scales at high Reynolds number, it is possible to imagine solving explicitely only some of large scales present in a flow. The small scales and the energy transfer from the large scales to the small scales would simply be modeled but not solved explicitely. This is the idea behind the Large Eddy Simulation (LES) formulation. Mathematically, this is achieved by filtering the Navier-Stokes equations described above and the filters used for this process are detailed next. The resulting LES equations are listed afterwards. They contain unclosed, sub-grid terms that cannot be solved explicitely but require modeling. This will be the focus of the next section.

2.2.1 Spatial and Favré averaging

Following Erlebacher et al. [65], the flow variables are decomposed into the resolved (super-grid scale) and unresolved (sub-grid scale) components by a spatial filtering operation, such that $f = \bar{f} + f"$, where the bar $(-)$ denotes resolved scale and the double prime (") denotes unresolved sub-grid scale quantities. This is performed using a filter kernel $G(\vec{x}, \vec{x}')$ over the computational domain Ω:

$$\bar{f}(\vec{x}, t) = \int_{\Omega} f(\vec{x}', t) G(\vec{x}, \vec{x}') \, \mathrm{d}\, \vec{x}' \tag{2.2.1}$$

where $\vec{x}$ and $\vec{x}'$) are position vectors. Practically, over a three-dimensional cartesian grid, this filter can be discretized as:

$$G(\vec{x},\vec{x}') = \prod_{i=1}^{3} g_i(x_i - x_i') \tag{2.2.2}$$

For the current solver, the one-dimensional filters g_i are top-hat, or box, filters that can be expressed as:

$$g_i(x_i - x_i') = \begin{cases} \frac{1}{\Delta_i} \text{ if } |x_i - x_i'| < \frac{\Delta_i}{2} 0 \text{ otherwise} \end{cases} \tag{2.2.3}$$

where Δ_i is the local one-dimensional filter size in the i-direction. The global filter size $\bar{\Delta}$ is computed as:

$$\bar{\Delta} = \sqrt[3]{\Delta_1 \Delta_2 \Delta_3} \tag{2.2.4}$$

For the current LES approach, the one-dimensional filter sizes are based on the local grid spacings and thus $\bar{\Delta}$ can be thought as a measure of the local grid cell size.

This spatial filtering is sufficient to derive LES equations and use the universal character of the small scales to model them. However, for a compressible formulation, the number of unclosed terms in the resulting LES equations can be reduced significantly by mass-weighting the spatial filter. This procedure is named Favré filtering and is used to establish the current LES formulation. A Favré-filtered variable will be denoted by a tilde from here on out:

$$\widetilde{f} = \frac{\overline{\rho f}}{\bar{\rho}} \tag{2.2.5}$$

2.2.2 Filtered Navier-Stokes equations

The generic procedure is to apply the spatial filtering first, then to use the commutative property of the spatial filter and the spatial derivative and finally to apply the Favré averaging.

Mass conservation

The filtered version of the continuity equation Eq. (2.1.1) is:

$$\frac{\partial \bar{\rho}}{\partial t} + \frac{\partial \bar{\rho} \widetilde{u_i}}{\partial x_i} = 0 \tag{2.2.6}$$

Momentum conservation

The filtered version of the momentum conservation equation Eq. (2.1.2) is:

$$\frac{\partial \bar{\rho}\widetilde{u_i}}{\partial t} + \frac{\partial}{\partial x_j}\left(\bar{\rho}\widetilde{u_i}\widetilde{u_j} + \bar{p}\delta_{ij} - \bar{\tau}_{ij} + \tau_{ij}^{\text{sgs}}\right) = 0 \tag{2.2.7}$$

where the sub-grid stress is defined as $\tau_{ij}^{\text{sgs}} = \bar{\rho}\left(\widetilde{u_i u_j} - \widetilde{u_i}\widetilde{u_j}\right)$. Like other sub-grid terms that will be introduced in this section, the sub-grid stress is related to the unresolved fluctuations at scales smaller than the local grid size $\bar{\Delta}$.

Energy conservation

The filtered version of the momentum conservation equation Eq. (2.1.3) is:

$$\frac{\partial \bar{\rho}\widetilde{e_T}}{\partial t} + \frac{\partial}{\partial x_j}\left(\bar{\rho}\widetilde{u_j}\widetilde{e_T} + \bar{p}\widetilde{u_j} + \overline{q_j^{IK}} - \widetilde{u_i}\bar{\tau_{ij}} + H_j^{\text{sgs}} + \sigma_j^{\text{sgs}}\right) = 0 \tag{2.2.8}$$

where the sub-grid terms are defined as $H_j^{\text{sgs}} = \bar{\rho}\left(\widetilde{e_T u_j} - \widetilde{e_T}\widetilde{u_j}\right) + \left(\overline{u_j p} - \bar{p}\widetilde{u_j}\right)$ and $\sigma_j^{\text{sgs}} = -\left(\overline{u_i \tau_{ij}} - \widetilde{u_i}\bar{\tau_{ij}}\right)$ The filtered heat flux vector can be expressed as:

$$\overline{q_j^{IK}} = -\lambda(\widetilde{T}, \bar{p}, \widetilde{Y_k})\frac{\partial \widetilde{T}}{\partial x_j} + \bar{\rho}\sum_{k=1}^{N_S}\widetilde{Y_k}h_k(\widetilde{T}, \bar{p}, \widetilde{Y_k})\widetilde{\mathcal{V}_{j,k}} + \sum_{k=1}^{N_S} q_{j,k}^{\text{sgs}} \tag{2.2.9}$$

The sub-grid heat transfer due to small-scale turbulent diffusion of species is equal to:

$$q_{j,k}^{\text{sgs}} = \bar{\rho}\left(Y_k\widetilde{h_k\mathcal{V}_{j,k}} - \widetilde{Y_k}\widetilde{h_k}\widetilde{\mathcal{V}_{j,k}}\right) \tag{2.2.10}$$

Species conservation

The filtered version of the species density conservation equation Eq. (2.1.4) is:

$$\frac{\partial \bar{\rho}\widetilde{Y_k}}{\partial t} + \frac{\partial}{\partial x_i}\left(\bar{\rho}\widetilde{u_i}\widetilde{Y_k} + \bar{\rho}\widetilde{u_i}\left(\widetilde{\mathcal{V}_{i,k}} + \widetilde{\mathcal{V}^{\text{cor}_i}}\right) + Y_{i,k}^{\text{sgs}} + \theta_{i,k}^{\text{sgs}}\right) = \overline{\dot{\omega_k}} \tag{2.2.11}$$

The sub-grid mass flux $Y_{i,k}^{\text{sgs}}$ and the sub-grid diffusive flux $\theta_{i,k}^{\text{sgs}}$ are equal to:

$$Y_{i,k}^{\text{sgs}} = \bar{\rho}\left(\widetilde{u_i Y_k} - \widetilde{u_i}\widetilde{Y_k}\right) \tag{2.2.12}$$

$$\theta_{i,k}^{\text{sgs}} = \bar{\rho}\left(\widetilde{\mathcal{V}_{i,k}Y_k} - \widetilde{\mathcal{V}_{i,k}}\widetilde{Y_k}\right) \tag{2.2.13}$$

Equations of state

Using the generic expressions for the equations of states, Eqs. (2.1.5) and (2.1.6), their filtered versions read:

$$\bar{p} = f(\bar{\rho}, \widetilde{T}, \widetilde{Y_k}) + p^{\text{sgs}} \tag{2.2.14}$$

$$\widetilde{e} = f(\bar{p}, \widetilde{T}, \widetilde{Y_k}) + e^{\text{sgs}} \tag{2.2.15}$$

The sub-grid pressure and energy are simply defined as:

$$p^{\text{sgs}} = f(\rho, \widetilde{T, Y_k}) - f(\bar{\rho}, \widetilde{T}, \widetilde{Y_k}) \tag{2.2.16}$$

$$e^{\text{sgs}} = f(p, \widetilde{T, Y_k}) - f(\bar{p}, \widetilde{T}, \widetilde{Y_k}) \tag{2.2.17}$$

2.3 Closure of the LES equations

The previous section described the $1 + N_{dim} + 1 + N_S + 2$ equations required to solve for the evolution of the $1 + N_{dim} + 1 + N_S + 2$ variables ($\bar{\rho}$, $\tilde{u}_i$, $\widetilde{E_T}$, $\widetilde{Y_k}$, $\widetilde{T}$ and $\bar{p}$) from prescribed initial conditions. However, these equations contain unknown, *unclosed* terms that need to be evaluated or modeled using flow variables. This section discusses several options for the closure of each term and most of them will use the concept of eddy, or turbulent, viscosity. This concept postulates that sub-grid energy dissipation comes from a flow viscosity ν_t, similar to the fluid viscosity that would dissipate energy at the Kolmogorov scale. Another way to think about this eddy viscosity is to consider the momentum transfer generated by turbulent eddies. Since this is analog to the momentum transfer by molecular viscosity, the Reynolds stress $\rho u_i' u_j'$, which represents that turbulent momentum transfer, can be proportional to a turbulent viscosity. The modeling of that turbulent viscosity will be detailed at the end of this section. Skipping the continuity equation which is fully closed, the discussion starts with the sub-grid kinetic energy transport equation.

2.3.1 Sub-grid kinetic energy transport equation

One particularity of the present LES modeling is that the sub-grid kinetic energy plays an important role in all unclosed transport equations, not only by providing a characteristic

velocity scale at the sub-grid level but also by creating transport terms of momentum and energy that are neglected in formulations that do not solve for this transport equation [208]. A complete derivation of the k^{sgs} transport equation is provided by Génin [81] and only a summary is given here. The first step is to filter the total kinetic energy $K = \frac{1}{2}u_i u_i$ equation, constructed from the original Navier-Stokes momentum equation multiplied by the actual velocity. Then the resolved kinetic energy $K_{\text{res}} = \frac{1}{2}\widetilde{u_i}\widetilde{u_i}$ equation is derived by multiplying the filtered momentum equation by the resolved filtered velocity. Substracting the total energy equation by the resolved one and then rearranging yields:

$$\frac{\partial \bar{\rho} k^{\text{sgs}}}{\partial t} + \frac{\partial}{\partial x_i}\left(\bar{\rho}\widetilde{u_i} k^{\text{sgs}}\right) = \mathcal{T}_{k^{\text{sgs}}} + \mathcal{Y}_{k^{\text{sgs}}} + \mathcal{P}_{k^{\text{sgs}}} - \mathcal{D}_{k^{\text{sgs}}} \tag{2.3.1}$$

$\mathcal{T}_{k^{\text{sgs}}}$ represents the diffusive transport of k^{sgs}. $\mathcal{Y}_{k^{\text{sgs}}}$ represents the pressure dilatation correction and is neglected in this work since the regions of interest in rocket engine applications are only slightly compressible. More details on how to model compressible effects in the k^{sgs} model are given by Génin [81]. $\mathcal{P}_{k^{\text{sgs}}}$ is the production term and there is an equivalent dissipation term in the resolved energy equation. Finally, $\mathcal{D}_{k^{\text{sgs}}}$ is the k^{sgs} dissipation term. The pressure diffusion term is neglected for the same reasons the pressure dilatation is neglected while the two other diffusive transport terms are modeled using gradient diffusion approximations:

$$\mathcal{T}_{k^{\text{sgs}}} = \frac{\partial}{\partial x_i}\left[\left(\frac{\bar{\rho}\nu_t}{\sigma_k} + \bar{\mu}\right)\frac{\partial k^{\text{sgs}}}{\partial x_i}\right] \tag{2.3.2}$$

By analogy with the Kolmogorov energy cascade and assuming that the cutoff scale, i.e. the local filter size, lies within the inertial range, the dissipation of k^{sgs} can be constructed through dimensional argument:

$$\mathcal{D}_{k^{\text{sgs}}} = \bar{\rho} C_\varepsilon \frac{\left(k^{\text{sgs}}\right)^{3/2}}{\bar{\Delta}} \tag{2.3.3}$$

Finally, the production term depends on the still-to-be-modeled sub-grid stress τ_{ij}^{sgs}:

$$\mathcal{P}_{k^{\text{sgs}}} = -\tau_{ij}^{\text{sgs}} \frac{\partial \widetilde{u_j}}{\partial x_i} \tag{2.3.4}$$

Given the expression of this production term, it is noted that no k^{sgs} can be created in a flow without the initial presence of some k^{sgs} if the sub-grid stress depends on k^{sgs}.

The evaluation of the model coefficients (C_ε,σ_k) introduced in this section will be discussed in Section 2.3.4.

2.3.2 Modeling the unclosed terms

Momentum equation closure

The only unresolved term in the momentum equation (Eq. (2.2.7)) is the sub-grid stress:

$$\tau_{ij}^{\text{sgs}} = \bar{\rho}\left(\widetilde{u_i u_j} - \widetilde{u}_i \widetilde{u}_j\right) \tag{2.3.5}$$

It corresponds to the momentum transfer by velocity fluctuations at scales smaller than the local grid size. To construct the sub-grid stress, two further assumptions are made. The first is that only the anisotropic part ($\langle u_i u_j \rangle - \frac{2}{3}k\delta_{ij}$ with $\langle\rangle$ a spatial averaging and k the unresolved part of the kinetic energy) of the sub-grid stress tensor is proportional to the resolved velocity gradients. The second is that, like for the viscous resolved stress, the anisotropic Reynolds-stress is proportional to the resolved strain rate and the eddy viscosity ν_t. Combining both assumptions yields:

$$\tau_{ij}^{\text{sgs}} = -2\bar{\rho}\nu_t\left(\widetilde{S_{ij}} - \frac{1}{3}\widetilde{S_{kk}}\delta_{ij}\right) + \rho\frac{2}{3}k^{\text{sgs}}\delta_{ij} \tag{2.3.6}$$

This highlights the importance of the sub-grid kinetic energy as it directly influences the momentum and the energy equation even if it is not used to compute the turbulent viscosity, as shown below.

Energy equation closure

The two unresolved terms of the energy equation (Eq. (2.2.8)), the sub-grid transport work H_i^{sgs} and the sub-grid viscous stress σ_i^{sgs}, are usually modeled together [292]:

$$H_i^{\text{sgs}} + \sigma_i^{\text{sgs}} = -\left(\bar{\rho}\nu_t + \bar{\mu}\right)\frac{\partial k^{\text{sgs}}}{\partial x_i} - \frac{\bar{\rho}\nu_t c_p}{\text{Pr}_t}\frac{\partial \bar{T}}{\partial x_i} + \widetilde{u}_j\tau_{ij}^{\text{sgs}} \tag{2.3.7}$$

Again here, the different methods to evaluate ν_t and Pr_t will be discussed below.

Species equation closure

There are also two unclosed terms in the species equations. While the diffusion term $\theta_{i,k}^{\text{sgs}}$

created by sub-grid fluctuations in species diffusion velocity is neglected in this study, the sub-grid diffusion of species mass, $Y_{i,k}^{\text{sgs}}$ is modeled using a gradient diffusion approach:

$$Y_{i,k}^{\text{sgs}} = -\frac{\bar{\rho}\nu_t}{\text{Sc}_t}\frac{\partial \widetilde{Y_k}}{\partial x_i} \tag{2.3.8}$$

Equation of state closure

The expressions for the sub-grid thermodynamic terms (Eq. 2.2.16 and Eq. 2.2.17) are obviously very dependent on the form of the equations of state used. For a thermally perfect gas, they simplify as:

$$p^{\text{sgs}} = \widetilde{\rho R_g T} - \widetilde{\rho}\widetilde{R_g}\widetilde{T} \tag{2.3.9}$$

$$= \bar{\rho}\widetilde{R_g T} - \bar{\rho}\widetilde{R_g}\widetilde{T} \tag{2.3.10}$$

$$= \bar{\rho}R_u \sum_{k=1}^{N_S} \frac{\widetilde{Y_k T} - \widetilde{Y_k}\widetilde{T}}{MW_k} \tag{2.3.11}$$

$$= \bar{\rho}R_u T^{\text{sgs}} \tag{2.3.12}$$

$$e^{\text{sgs}} = \sum_{k=1}^{N_S} Y_k\widetilde{e_k(T)} - \widetilde{Y_k}e_k(\widetilde{T}) \tag{2.3.13}$$

and they are usually neglected as previous works [77] have not found they play a significant role. For non-ideal gas mixtures, Selle et al. [273] showed that unknown thermodynamic variables could be computed from filtered variables with little error. This means that the assumption of $p^{\text{sgs}} = 0$ and $e^{\text{sgs}} = 0$ can be made, even though more evidence is needed for many-species mixtures and reacting flows. This will be the assumption retained for this work.

2.3.3 Eddy viscosity models

To complete the closure of the LES formulation, the turbulent viscosity needs to be computed and all closure coefficients need to be evaluated. Several methods are available to compute the eddy viscosity in a LES framework, starting with the simple Smagorinsky model [285]. The more complex ones try to address the well-known deficiencies of LES in near-wall regions.

Far away from the walls, the scale similarity hypothesis holds well. But close to the wall, the scales containing most of the energy decrease in size and should require additional resolution to be captured, with the filter size remaining smaller than the local inertial length scale. With structured grids, this resolution requirement results in cells with large aspect ratio close to the wall. Replacing the characteristic length of the cell by the distance to the wall for the explicit filter size is one possible solution to deal with this issue without additional resolution. This will be illustrated when describing the k^{sgs} model for eddy viscosity.

But the physics that control the exchange of energy between the resolved and the sub-grid scales near the wall do not respect all the assumptions behind the Large Eddy Simulation concept. In particular, significant anisotropic Reynolds-stresses are produced in the near-wall region. A dynamic model such as LDKM does help in this regard but in general, the wall shear stress remain over-predicted because of an overestimation of the turbulent viscosity near the wall. This is because the lack of inertial range and scale similarity near the wall violates the assumption behind the dynamics models.

2.3.3.1 k^{sgs} model

As described previously, in the current compressible LES formulation, the sub-grid kinetic energy equation is always solved, regardless of the turbulence modeling. It is however straightforward to build a turbulence model based on k^{sgs}. Through dimensional arguments, the eddy viscosity ν_t can be evaluated using a characteristic length scale, chosen as the minimum between local filter size $\bar{\Delta}$ and the distance to the nearest wall d_w, and a characteristic velocity scale, chosen as the square root of the sub-grid kinetic energy k^{sgs}. Using a model parameter C_ν, this yields:

$$\nu_t = C_\nu \min\left(\bar{\Delta}, d_w\right) \sqrt{k^{\text{sgs}}} \tag{2.3.14}$$

When using a constant value for C_ν, this is the default method used in the current LES solver. The evaluation of C_ν is discussed in the next Section alongside the other model parameters.

2.3.4 Evaluation of the model coefficients

Six closure coefficients have been introduced in the previous sections: C_ν, C_ε, C_w, σ_k, Pr_t and Sc_t. Their default, constant values are first presented before describing a method to compute at least some of them dynamically.

2.3.4.1 Constant values

Nominal values for C_ν and C_ε can be obtained through theoretical considerations, using a model Pao spectrum [34, 81]. Assuming a very large Reynolds number and thus a wide inertial range where viscous dissipative effects are neglected, one can derive constant, universal values of 0.067 and 0.916 respectively for C_ν and C_ε. Using such constant value of 0.067 is the default eddy viscosity method used in the current LES solver unless otherwise specified. Table 3 summarizes the nominal values for the model coefficients. For σ_k, Pr_t and Sc_t, simple theories such as the Reynolds analogy predict values of 1.0 for these coefficients. However, experimental works [121] on heat transfer have shown the turbulent Prandtl number to lie in a range of 0.7 to 0.9 for most gas flows and a value of 0.9 is adopted by default in this work. But the same experimental work shows that the turbulent Prandtl number can take very different values in different parts of the flow. The next section describes a method to compute at least some of these model coefficients locally and dynamically as the simulation progresses.

Table 3: Nominal values for the model coefficients of the current LES closure.

C_ν	C_ε	σ_k	Pr_t	Sc_t
0.067	0.916	1.0	0.9	1.0

2.3.4.2 The Localized Dynamic k^{sgs} Model (LDKM)

In this study, a compressible version of the localized dynamic k^{sgs} model (LDKM) [136, 192, 137] is employed to achieve closure for the models described in the previous sections. As in other dynamic models [83], the LDKM is based on the assumption of scale similarity in the inertial subrange. Provided that enough of the inertial subrange is resolved, stresses at the

cutoff (i.e., the grid size) can be related to stresses at (say) twice the cutoff (i.e., the test filter width). The test-scale field is constructed from the grid-scale field by applying a test filter which is characterized by $\widehat{\Delta}$ (typically, $\widehat{\Delta} = 2\overline{\Delta}$). A test filter shape which is consistent with the grid filter in form is preferred. In the present study, the top-hat filter based on the Simpson rule is employed for the test filter. This filter is consistent with finite-volume methods [270] and is implicit in the grid filter. For a detailed derivation of the method, the reader is referred to the work of Génin [81] and only a few highlights are given here.

The model coefficients C_ν and C_ε are obtained from the similarity of, respectively, the Leonard stress and the dissipation at the grid-filter and test-filter level. The prolonged presence of a negative model coefficient, described by Lund et al. [164] is avoided since the present model is based on the subgrid kinetic energy which is always positive. Finally, the dynamically determined C_ε does not vanish in the limit of high Re, a phenomenon that was observed in an earlier dynamic kinetic energy model formulation'[336]. These features of LDKM allows fully localized dynamic evaluation without encountering any numerical instability. Recently the dynamic evaluation of model coefficients was extended to the turbulent Prandtl number [81] and the current work can include this feature when using LDKM. Using once again a least-square method to eliminate the overs-specification of Pr_t, one obtains:

$$\frac{1}{\mathrm{Pr}_t} = -\frac{d_i n_i}{d_i d_i} \tag{2.3.15}$$

where n_i is the temperature-velocity correlation at the testscale level:

$$n_i = \langle \widetilde{u_i}\widetilde{T}\rangle - \langle \widetilde{u_i}\rangle\langle \widetilde{T}\rangle \tag{2.3.16}$$

and where d_i is:

$$d_i = C_\nu \sqrt{k^{\mathrm{test}}}\widehat{\Delta}\langle \frac{\partial \widetilde{T}}{\partial x_i}\rangle \tag{2.3.17}$$

Other coefficients such as C_w, σ_k or Sc_t could also computed dynamically using the same methodology but they are currently taken to assume their nominal values listed in Table 3 when using LDKM. Previous works using LDKM[205, 137] have shown that it is Galilean-invariant and that it satisfies the realizability conditions on the sub-grid stress developed by Schumann [271] and Vreman et al. [329] most of the time. However, for flows with strong

gradients, certain regions can become ill-behaved and it is safer to explicitely apply these realizability conditions. These boundings were summarized by Génin [81] as:

$$\tau_{11}^{\text{sgs}}, \tau_{22}^{\text{sgs}}, \tau_{33}^{\text{sgs}} \geq 0 \tag{2.3.18}$$

$$\det\left[\tau_{ij}^{\text{sgs}}\right] \geq 0 \tag{2.3.19}$$

$$C_\nu \leq \frac{\sqrt{k^{\text{sgs}}}}{\sqrt{3}\widetilde{S}\bar{\Delta}} \tag{2.3.20}$$

where $\widetilde{S} = \sqrt{\frac{1}{2}\widetilde{S}_{ij}\widetilde{S}_{ij}}$ is the strain rate magnitude.

2.3.5 Validation and perspectives

Since the current work deals with turbulent flows involving non-ideal gas, a few words are necessary to justify that no special treatment of the turbulence is required with real gas flows. Mathematically, the non-linearity of real gas equations of state does not affect the expression for the spatial and mass-weighted filtering. As long as the density has been properly computed, the Favré-filtering as described previously will produce correct values, with of course a bias towards the large density regions. Selle and Schmitt [274] confirmed that in homogeneous isotropic turbulence simulations, both DNS and LES, no peculiar behavior was observed for real gas conditions, with turbulent spectra for real gas conditions perfectly matching turbulent spectra for ideal gas conditions. Similar isotropic turbulence studies were conducted for this work and very brief results are presented here as they simply confirm the findings of Selle and Schmitt. Both DNS, on a 256^3 grid, and LES, on a 64^3 grid, were conducted from an initial field generated by a Kraichnan spectrum:

$$E(k) = u_{rms}^2 16\sqrt{\frac{2}{\pi}}\frac{k^4}{k_0^5}\exp\left(-2k^2/k_0^2\right) \tag{2.3.21}$$

For all simulations, the initial $\text{Re}_\lambda = u_{\text{rms}}\lambda/\nu$ is set at 80. For such relatively low values of Re_λ, the decay exponent is expected to lie in the range 1.15 to 1.45 [243] and to decrease towards 1 as the Reynolds number increases. A value of 1.3 is picked here to compare the decay of the kinetic energy as the simulation progresses. Figure 15 shows the evolution of the kinetic energy spectum for the DNS simulation under ideal gas conditions. Given the modest Reynolds number, the extent of the inertial range showing a -5/3 decay is

limited but it is appearent compared to the initial spectrum. More interesting is the decay rate of the kinetic energy in the domain, shown in Figure 16(a), which approaches a rate proportional to $\left(\frac{t}{\tau}\right)^{(-1.3)}$ with τ the eddy turn-over time. This same rate is observed for DNS of real gas conditions (Fig. 16(b)), LES of ideal gas conditions with LDKM (Fig. 16(c)) and LES of real gas conditions with LDKM (Fig. 16(d)). This confirms the fact that from the momentum closure point of view, real gas thermodynamics do not produce a different kind of turbulence. However, as noted by Selle and Schmitt, transport phenomena might affect local dissipation rates of scalars which could then get coupled with the thermodynamics. But such fundamental study is beyond the scope of this work.

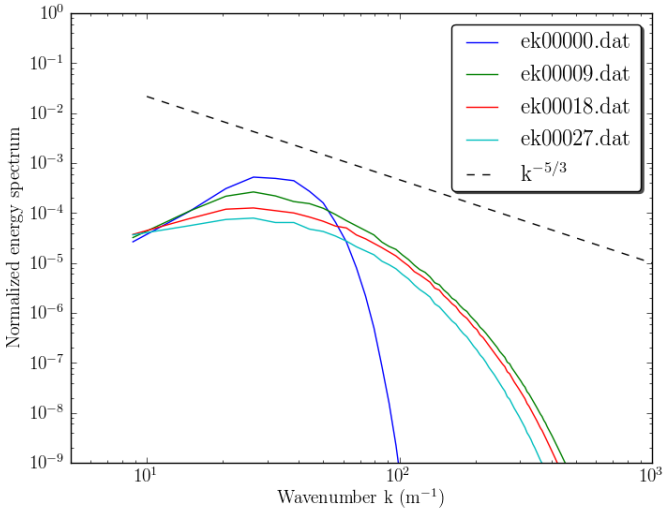

Figure 15: Evolution of the kinetic energy spectrum of a DNS of homogeneous isotropic turbulence with an initial Re_λ of 80.

Finally, numerous applications of non-reacting real gas flows with turbulence such as cooling channels in rockets, super-critical water for nuclear reactor cooling and basic studies of heated channels [14] that no specific turbulence model has ever been designed for non-ideal gas flows. Therefore, the current formulation is applied with confidence to a variety of rocket engine flows.

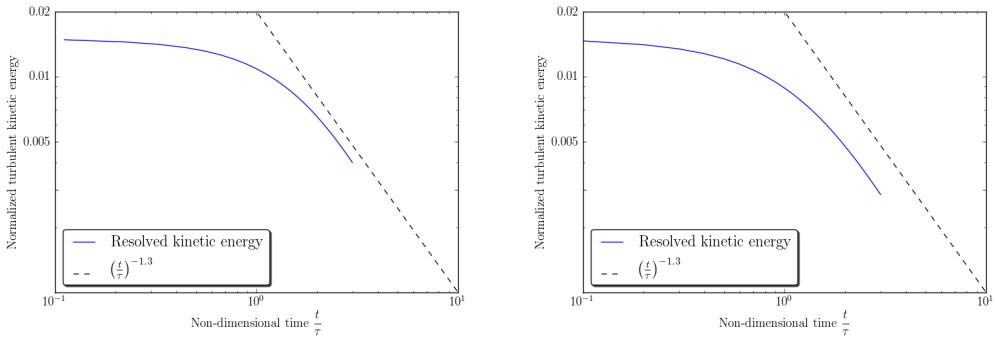

(a) DNS IG

(b) DNS RG

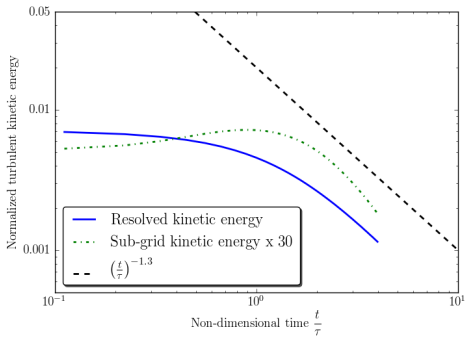

(c) LES-LDKM IG

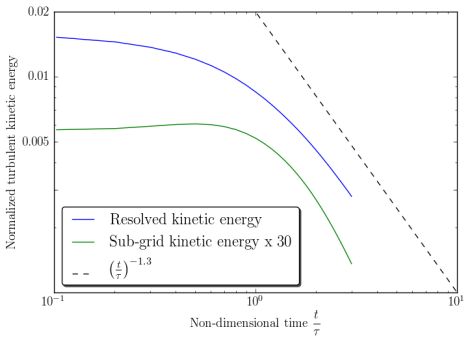

(d) LES-LDKM RG

Figure 16: Decay of the total kinetic energy in the computational domain for various numerical simulations of homogeneous isotropic turbulence with an initial Re_λ of 80.

2.3.6 Turbulent combustion modeling

The last remaining unclosed term in the LES equations is the filtered reaction in Equation 2.2.11. In this work, the raw reaction rates will be computed using multi-step, finite-rate chemistry mechanisms detailed in Appendix H. The mathematical integration of the system of differential equations that compose a reaction mechanism is described in Section 3.2.3. This section however deals with the possible interactions between turbulence and combustion which could cause the filtered reaction rate $\overline{\dot{\omega}_k}$ to differ significantly the raw reaction rate $\dot{\omega}_k$. For Large-Eddy Simulations, the smallest fluid mechanics scales resolved are, by definition, often larger than the Kolmogorov scale, the smallest length scale related to the fluid mechanics. However, scalar mixing and thus combustion, occurs at the Batchelor scale which is itself often smaller than the Kolmogorov scale. Therefore, from an LES point of view, the reaction rates generated are all sub-grid. How these different scales interact is at the heart of turbulent combustion modeling. Many reviews of the current state-of-the-art closures for LES applications exist and the reader is referred to them for more details [76, 238, 58].

To summarize, there are two main families of turbulent combustion models, flamelet models and finite-rate models. In the former, the flame is assumed to be infinitely thin and a new variable (mixture fraction for non-premixed flames, progress variable for premixed flames) is introduced as the main parameter for the property variations across the flame. This approach is strictly valid only for high Damköhler numbers which is the case as first approximation for H_2-O_2 rocket applications. Finite-rate models compute a reaction rate from the flow variables and modify it through a probability density function (PDF approach) or other phenomenological approach (Eddy Break-Up, Eddy Dissipation Concept, Partially Stirred Reactor). The simplest finite-rate model is actually to not modify the raw reaction rate at all and thus to neglect the effect of sub-grid mixing. This approach will be named laminar finite-rate from here on out. Several recent studies have compared the laminar finite-rate approximation to other models and/or experimental data, both in premixed and non-premixed settings. In particular, supersonic hydrogen combustion applications like SCRAMJET share many similarities with rocket engines. After reviewing the available closure models, Sun et al. [300] found that grid resolution was more influential on

the results than the turbulent combustion model and chose laminar finite-rate chemistry (8-step, 6-species mechanism) for their hybrid RANS/LES SCRAMJET study. They obtained qualitative agreement with their experiments. In a simulation of a reacting supersonic wall-jet, Edwards et al. [59] obtained good agreement with the experimental data with laminar chemistry, with a more advanced model such as the Gaussian quadrature providing little improvement with the detailed mechanisms used. Sozer et al. [293] conducted a comparison of a flamelet model with a laminar finite-rate model on a gas-gas shear coxial configuration similar to the one shown in Chapter 4 and found both approaches to not perform very well in the context of unsteady RANS simulations. While some significant differences could be observed between the two models near the walls, the overall flowfield predicted by both models were relatively similar. Finally, in a premixed setting and using simplified mechanisms, Fureby [75] obtained satisfactory results with the laminar approximation as long as the grid resolution was relatively fine.

In the configuration of interest for this work, the shear coaxial injector, the thickness of the sleeve between the oxygen and the hydrogen streams defines a length scale that is small with respect to the fluid mechanics, at most a few hundred microns for most injectors. Resolving this sleeve with even half a dozen points ensure that in the near field, the grid spacing is relatively fine with respect to the flow structures and the flame. One of the goal of this study is to evaluate whether this kind of resolution is sufficient to use the laminar finite-rate approximation for rocket engine applications. This will be done through two different reacting configurations, one where there is no significant departure from ideal gas and one where real gas equations of states are required to accurately model the flow. Moreover, the next section presents a more advanced sub-grid mixing model that could eventually replace the current laminar chemistry assumption.

2.4 Linear-Eddy Model

While the previous section provided simple closure models for species mixing and the filtered reaction rate, there could be a need for a more advanced closure for rocket engine applications, where strong non-idealities and complex turbulent-flame interactions can significantly affect mixing and reaction at the sub-grid level.

The Linear-Eddy Model (LEM) was developed [125, 131, 126, 127, 129] to solve, at their relevant length and time scales, the physical processes at the heart of turbulent combustion. These processes were identified as large scale advection, small scale mixing, molecular diffusion and chemical reaction. This model produces an accurate representation of turbulent reacting flows at a fraction of the cost of a Direct Numerical Simulation (DNS) because the LEM scalar field is described on a "one-dimensional" line while the DNS attemps to resolve all length and time scales in all three dimensions. However, the effect of turbulence on the scalars is still modeled using three-dimensional scaling laws and can mimic the effect of three-dimensional turbulent eddies on a flame.

By itself, LEM has been shown to produce similar scalar power spectra as a full three-dimensional simulation for the homogeneous mixing of a sustained mean gradient [127]. These scalar spectra also showed a strong Schmidt number dependence. Numerous other standalone LEM simulations originally demonstrated the credibility of LEM as an accurate and economic mixing model [128, 129] and more recent works [339, 275, 29] continue to show the relevance of standalone LEM on more complex problems.

The LEM approach applied to LES (referred to as LEM-LES, hereafter) was first applied to premixed and non-premixed combustion by [193] and since then has gone through several modifications [28, 191, 290, 34, 261, 275]. In this study, the goal is demonstrate that the LEM approach can be easily extended to real gas flows.

In LEM-LES, the governing filtered conservation equations for mass, momentum and energy are the same as previously described in Eqs. 2.2.6-2.2.7-2.2.8 and the same sub-grid models for the sub-grid stress can be used. Eulerian frame of reference). At this stage, no conservation equation for species is solved on the resolved LES grid.

The species/scalar field evolution is tracked using a **two-scale** numerical approach. In

this technique, turbulent convection of the scalars is split into two parts: **large scale advection** and **turbulent convection** at the small (sub-grid) scales. Large scale advection is the convection that happens above the unresolved scales and is modeled by using a Lagrangian scheme that explicitly transports mass across the finite-volume cell surfaces in a manner consistent with the mass transport in the continuity equation solved on the resolved grid. Small-scale advection is the turbulent stirring by scales smaller than the resolved grid. Turbulent convection at the sub-grid scales only transports fluid mass over sub-grid length scales.

2.4.1 Sub-grid Mixing Model Formulation

The two-scale approach for the transport of an exact scalar Ψ is derived by splitting the velocity field into a resolved velocity $\widetilde{u_k}$ and an unresolved, sub-grid velocity $u_k^{"}$:

$$\frac{\Psi^{n+1} - \Psi^*}{\Delta t_{LES}} = -\widetilde{u_k}\frac{\partial \Psi^*}{\partial x_k} - \left(u_k^{"}\right)^{face}\frac{\partial \Psi^*}{\partial x_k} \tag{2.4.1}$$

$$\Psi^* - \Psi^n = \int_t^{t+\Delta t_{LES}} \Big[- u_k^{"}\frac{\partial \Psi^n}{\partial x_k} + \frac{\partial}{\partial x_m}\Big(D_\Psi \frac{\partial \Psi^n}{\partial x_m}\Big) + \dot{w}_{\Psi^n}\Big] dt \tag{2.4.2}$$

Eq. 2.4.1 describes the large-scale three-dimensional Lagrangian convection of the scalar field and is implemented via the transfer of fluid between LES cells through the control volume surfaces. The second term on the RHS corresponds to the contribution of the sub-grid velocity field.

Eq. 2.4.2 includes the sub-grid mixing (first term in the integral), the diffusion process (D_Ψ is the molecular diffusion coefficient for scalar Ψ) and the possible source term through the reaction rate $\dot{w}_\Psi$. These processes occur within each LES cell during the LES integration time step and are solved on a one-dimensional line. The justifications for this approximation are:

- small scale turbulence is locally homogeneous and isotropic for a proper LES simulation
- heat-release and the associated thermal expansion are isotropic
- the model in its basic form has been shown [125] to capture the correct physics of scalar mixing at small-scales in homogeneous, isotropic turbulence

The intermediate scalar field Ψ^* is obtained after this step and will be the field convected through a Lagrangian process.

Therefore, within the context of LES, the LEM approach can be used to model the small scale processes in a reduced dimension while the large scales of the flow are calculated directly from the LES equations with an appropriate coupling procedure.

2.4.2 Sub-grid Reaction-Diffusion Model

The one-dimensional reaction-diffusion equations for the conservation of species and energy are written in non-conservative form and solved using a simple finite difference scheme. The main assumptions made to obtain these equations are:

- The pressure inside the LEM domain is assumed to be constant and equal to the LES pressure. In the absence of strong pressure gradients such as shocks, this is a reasonable assumption.
- As a consequence, the compressible effects of the sub-grid velocity field are neglected, allowing the use of a low-Mach formulation for the energy equation.
- The sub-grid viscous work is neglected in the energy equation.

$$\rho\frac{\partial Y_k}{\partial t} + F_{k,stir} + \frac{\partial}{\partial s}\left(-\rho Y_k\left(\mathcal{V}_{s,k} + \mathcal{V}_s^{\mathrm{cor}}\right)\right) = \dot{\omega}_k MW_k \tag{2.4.3}$$

$$\rho c_p\frac{\partial T}{\partial t} + F_{T,stir} - \frac{\partial}{\partial s}\left(-\rho Y_k h_k\left(\mathcal{V}_{s,k} + \mathcal{V}_s^{\mathrm{cor}}\right)\right) - \frac{\partial}{\partial s}(\kappa\frac{\partial T}{\partial s}) = -\sum_{k=1}^{N} h_k\dot{\omega}_k MW_k \tag{2.4.4}$$

In Eqs. 2.4.3 and 2.4.4, s denotes the coordinate direction on the one-dimensional domain, whose length is taken to be the local LES filter width Δ. The orientation of this one-dimensional domain is usually aligned with the direction of the largest scalar gradient but it does not have to be and is dependent of the particular application. While for a single scalar, the scalar gradient is aligned with the direction of most compressive strain rate in isotropic turbulence [33], the generalization to a multi-species situation is not evident. Also, h_k is the sensible enthalpy of the k-th species and MW_k is the molecular weight of the k-th species. The energy equation can be cast as a temperature equation through a low-Mach

number approximation that is valid for any equation of state and thus does not need to be modified for real gas flows. Similarly, the density in the sub-grid fiel is computed using the same equation of state as at the LES level. All thermodynamic and transport properties are computed using the real gas formulation described in Sections 2.5 and 2.6. These equations use the same concept of correction diffusion velocity as Section 2.1.3.2 and the velocity correction $\mathcal{V}_s^{\text{cor}}$ is computed using Eq.(2.1.20) based on the LEM field quantities.

The timescales involved in the diffusion-reaction processes at the LEM level can be very small, especially with configurations involving hydrogen. The timestep Δt_{chem} associated with the chemical reaction is related to the stiffness of the reaction mechanism. For simplified reaction mechanisms containing hydrogen, a timestep of the order of 1×10^{-10} s is not uncommon and if reactive radicals such as H_2O_2 and HO_2 are taken into account, chemical timescales can be as small as 1×10^{-12} s. The numerical stability limit of the diffusion equation sets the timestep Δt_{diff} associated with the molecular diffusion:

$$\Delta t_{\text{diff}} = C_{\text{diff}} \frac{(\Delta s)^2}{\max_{k=1,N} D_k} \tag{2.4.5}$$

In the above equation, C_{diff} is set at 0.25 for numerical stability and Δs is the LEM grid resolution.

2.4.3 Sub-grid Turbulent Stirring

Two terms remain to be described in Eqs. (2.4.3) and (2.4.4), $F_{k,stir}$ and $F_{T,stir}$, respectively the turbulent convection or stirring of the species k and of the temperature. The effects of the sub-grid velocity field on the sub-grid scalar fields are modeled numerically using stochastic re-arrangement events called *triplet maps* [131]. Each triplet map represents the action of an isotropic turbulent eddy on the sub-grid scalar field. Graphical descriptions of the triplet mapping can be found elsewhere [261, 275]. The scalar field obtained is continuous and preserves the LES Favre-filtered average, however its derivative is discontinuous. This increased scalar gradient has been shown to mimic the physical effect of three-dimensional

turbulence [130]. This triplet mapping can be defined mathematically as:

$$\Psi(x,t_o) = \begin{cases} \Psi^0(3x-2x_o,t_o) & x_o \le x \le x_o + l/3, \\ \Psi^0(-3x+4x_o+2l,t_o) & x_o + l/3x \le x \le x_o + 2l/3, \\ \Psi^0(3x-2x_o-2l,t_o) & x_o + 2l/3 \le x \le x_o + l, \\ \Psi^0(x,t_o) & \text{otherwise} \end{cases} \tag{2.4.6}$$

where $\Psi^0(x,t)$ is the initial scalar field, $\Psi(x,t)$ is the stirred scalar field, l is the size of the mapping event, x_o is the location of the mapping event and t_o is the time of the event. Three parameters are needed to implement the turbulent stirring events: the eddy size l, the eddy location x_o within the 1-D domain and the stirring frequency λ. All three parameters can be determined through a stochastic process based on physical laws. The eddy size in the range Δ to η (Kolmogorov scale) is determined randomly from an eddy size distribution $f(l)$, obtained using inertial range scaling in three-dimensional turbulence [33]:

$$f(l) = \frac{5}{3}\frac{l^{-8/3}}{(\eta^{-5/3} - \Delta^{-5/3})} \tag{2.4.7}$$

Here, η is determined from inertial range scaling law

$$\eta = N_\eta \frac{\Delta}{Re_\Delta^{3/4}}$$

where N_η is an empirical constant and Re_Δ is the sub-grid Reynolds number based on the sub-grid turbulence intensity, kinematic viscosity and the local LES filter width, Δ. This constant reduces the effective range of scales between Δ and η but does not change the turbulent diffusivity, as described by [289]: it is generally taken as 5.0. The event location is chosen randomly from a uniform distribution, and the event (mapping) rate (mean frequency per unit length) is implemented as a Poisson process in time ([131])

$$\lambda = \frac{54}{5}\frac{\nu Re_\Delta C_\lambda}{\Delta^3}\frac{[(\Delta/\eta)^{5/3} - 1]}{[1 - (\eta/\Delta)^{4/3}]} \tag{2.4.8}$$

C_λ represents the scalar turbulent diffusivity and is set to 0.067 following high Reynolds number phenomenological arguments by Chakravarthy and Menon [33]. The time interval between events then is given as:

$$\Delta t_{stir} = \frac{1}{\lambda\Delta} \tag{2.4.9}$$

where Δ is the length of the 1-D domain, which is also same as the local LES filter width. The mean rate parameter of the mapping event, λ, is not a function of length scale, l, which implies that the interval between the stirring events is the same for all length scales.

2.4.4 Large Scale Advection

After completing the previous steps of reaction, diffusion and stirring in each LES cell, the sub-grid scalar fields are advected by the LES-resolved velocity field through a Lagrangian implementation. This method involves the transfer of full or partial LEM cells between adjacent LES cells by matching the mass fluxes across the LES cell faces. The algorithm used for this work is identical to the one described by Sen [275] and the reader is referred there for further details.

One potentially overlooked issue is the contribution to large scale advection by unresolved turbulent eddies at the interface of LES cells. While briefly mentioned by Sen [275], its influence on the mixing was not well established. This splicing is due to unresolved eddies at the edge of LES cells and is illustrated by Figure 17. These eddies, of size smaller than Δ, can contribute to the scalar mixing between LES cells by randomly modifying the large-scale fluxes. They correspond to the second term on the RHS of Eq. 2.4.1. For this work, when the turbulent splicing is used, the flux across an LES face of size dS will be:

$$\dot{m}^{\text{sgs}}_{face} = \chi\sqrt{\frac{2k^{\text{sgs}}}{3}}\rho dS \tag{2.4.10}$$

with χ a uniform random variable between -1 and 1.

2.4.5 Volumetric expansion, regridding and sub-grid temperature

The final sub-grid process in the LEM is the volumetric expansion and/or compression. This process accounts for heat release and/or compressibility effect. It is modeled by expanding or compressing each linear-eddy cell in the sub-grid domain by $\Delta V^*_{LEM,i} = \rho^n_i/\rho^*_i$, where $\Delta V_{LEM,i}$ is the change in volume of LEM cell i. ρ^n_i and ρ^*_i are, respectively, the density of the "$i-th$" cell at the previous and the current time integration levels in the sub-grid simulation. Since the splicing algorithm currently assumes a uniform grid, the expanded/compressed grid needs to be regridded at the end of the LES timestep. This process does introduce

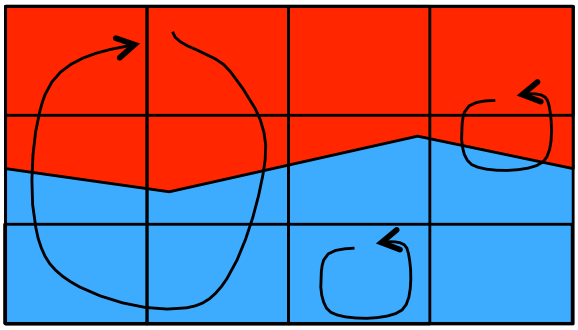

Figure 17: Illustration of the role of resolved and unresolved eddies for an LEM-LES of scalar mixing. Leftmost eddy corresponds to regular splicing, central eddy corresponds to sub-grid stirring and rightmost eddy corresponds to turbulent splicing.

some numerical dissipation by potentially smearing some of the small-scale scalar gradients but previous studies found the effect to be negligible [61]. Finally, since the energy equation solved at the sub-grid level is different from the energy equation at the LES level, the filtered temperature over the LEM line will not be equal to the Favré-filtered. While the divergence is usually small, long term drift is not desirable and the sub-grid temperature is periodically rescaled to match the Favré-filtered LES values.

2.5 Real gas framework

2.5.1 Generalities on equations of state

A "standard" or "pressure" equation of state (EoS) is an algebraic relation between the pressure p, the temperature T and a volume or a density. These quantities are equivalent for the extent of this work where the composition of the fluid is known. One way to express this relation is to use the compressibility factor Z, which can be considered as a function of either T and p or of T and the molar volume V:

$$Z = \frac{pV}{R_u T} = f_p(T, p) \tag{2.5.1}$$

$$= f_V(T, V) \tag{2.5.2}$$

In these expression, R_u is the universal gas constant. For the ideal gas law, $pV = R_u T$ and Z is simply equal to 1 no matter the choice of independent variables. However, the choice of independent variables is not arbitrary. If one desires to describe the behavior of a fluid in both its liquid and gaseous forms, the multiplicity of the volume/density roots (due to the liquid/vapor equilibrium) requires that an equation of the form of Eq. 2.5.2 be used. This explains the form of the popular cubic equations of states. But before going into more details on the mathematics of equations of states, an historical perspective is offered alongside the definition of some key thermodynamical concepts.

Historically, the concept of a fluid other than a pure gas or liquid started with the experiments of Cagniard de la Tour in the 1820's [27]. This was followed by 50 years of further experiments which are described in the historical review by Berche et al. [17] for the 150-year anniversary of Cagniard de la Tour's death. These experiments helped shaped the contours of what is now known as phase diagrams, which define the domains of existence of the different states (or phases) of matter for a pure component. The most popular diagrams, such as the p-T or the p-V diagrams, are two-dimensional but the actual possible states are represented by a surface, the *state surface*, in a three-dimensional space with usually p, T and V as axes. This is illustrated by Figure 18 from Carlès [32]. While the separation between the solid and liquid phases appears infinite, the *coexistence curve* between liquid and vapor phases is closed, indicating that liquid and vapor phases are actually two extremes of

a same continuum fluid phase. The "top" of that curve, the point that defines the maximum pressure and temperature at which phases can coexist, was named the *critical point* by Thomas Andrews [6]. The values of the state variables for a pure component at that point are the critical temperature, pressure and volume. These quantities were used by van der Waals in 1873 when he introduced the concept of the compressibility factor Z [320].

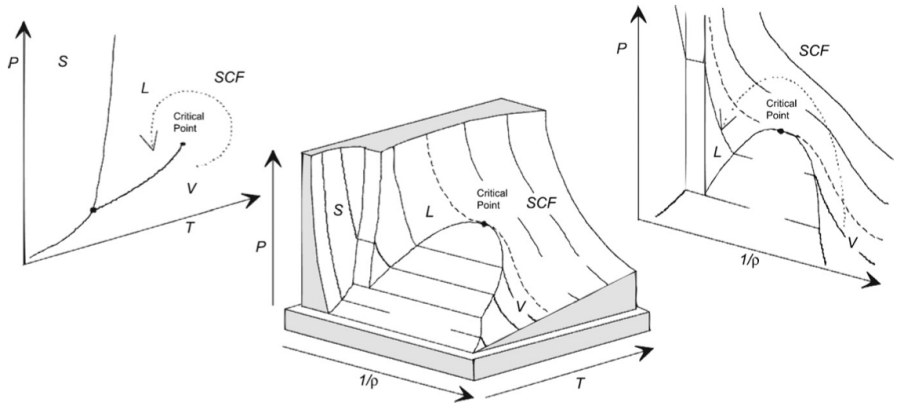

Figure 18: State surface of a pure component in a three-dimensional space (center). Possible states are solid (S), liquid (L), vapor (V) and super-critical fluid (SCF). Two-dimensional phase diagrams are shown on the sides. Figure from Carlès [32]

When non-dimensionalizing T and p by their critical counterparts T_c and p_c, a universal behavior of Z can be found across all fluids. This is called the *Corresponding States Principle* (CSP). It means that generalized compressibility charts can be drawn to estimate the behavior of any substance based on experimental data of only a few fluids. Such a chart is shown on Figure 21. This is actually quite accurate (with 5%) for most common fluids as long as the conditions are away from the critical point or the saturation curve. This CSP is limited because it takes into account only two parameters, the critical temperature and the critical pressure to normalize the fluid properties. But it recognizes that all fluid properties are dependent on intermolecular forces which are universal and can be described by a number of global parameters such as the critical properties. In order to deal with more irregular fluids polar substances like H_2O and in order to get a better match match close to the critical point, additional parameters can be considered for the non-dimensionalization. The most popular one is the *acentric factor* ω, introduced by Pitzer [239] in 1955. It is a

measure of the non-sphericity of the molecules.

Now that the critical quantities have been introduced, a more detailed description of the states of matter of interest for this work is needed. This time, a p-T diagram such as the one shown in Figure 19 is used as it makes it easier to identify the different phases a fluid can be in the context of rocket propellants. Oxygen is chosen here to illustrate this point, with its critical temperature of 154.6 K and its critical pressure of 50.43 bar, both indicated by dashed lines on Figure 19. The critical point is represented by the large black dot at the intersection of these dashed lines. The well-known liquid and gas/vapor phases can be found at low temperatures and pressures and are separated by the boiling line. Mechanically, this liquid phase is usually considered as incompressible while the gas/vapor phase is very much compressible. To go from one to the other requires a discrete phase change with discontinuous thermodynamic properties on each side. There is an obvious change in density shown in Figure 19 as the boiling line is crossed. In terms of energy, the difference between the vapor phase and the liquid phase corresponds to the latent heat of vaporization. As the temperature and pressure are increased above their critical values, the oxygen is now a *super-critical fluid* and the sharp interface of the boiling line is replaced by a smooth transition across the diagonal dotted line which has been called the *pseudo-boiling line* in the rocket engine community [229]. This pseudo-boiling line corresponds to the smooth transition between the *compressible liquid* region ($T < T_c$, $p > p_c$) and the super-critical fluid region ($T > T_c$, $p > p_c$). It is accompanied by a sharp but continuous peak of specific heat at constant pressure that mimics the discrete latent heat of vaporization. So if one would consider the mixing of two species at the same absolute temperature but with a reduced temperature below 1 for one species and above 1 for the other, one would observe a drop of temperature in the mixing region, similar to the drop in temperature observed in the gas surrounding an evaporating spray. This was observed with the current solver when simulating the experiments of Segal and Polikhov [272]. Recently, this pseudo-boiling line has received renewed attention in the thermodynamic community [189, 281] where it is proposed as a boundary for a phase transition inside the super-critical regime under the name of *Widom line*. For reduced pressures below 10, this Widom line corresponds

approximately to the critical isochore but this is no longer the case at very high pressures. According to Simeoni et al. [281], the Widom line and its extrapolated extension (once the peak of specific heat is too broad) defines "a well-defined partition between two completely different dynamical behaviours reminiscent of gas and liquid dynamic properties". Not only do some thermodynamic variables show large variations across that line, but the mechanical behavior of the fluid and in particular sound propagation is also affected. This might be linked to some of the bulk viscosity issues detailed in Appendix G.

In the context of a nearly-constant pressure system like a rocket or a gas turbine combustion chamber, a $p-T$ diagram like the one shown in Figure 19 helps define the different states of oxygen under rocket conditions. Sub- and super-critical injections are thus defined with respect to the critical pressure first and foremost. The injection temperature then helps differentiate whether the super-critical injection involves a trans-critical stage ($T_{inj} < T_c$) or whether a sub-critical injection involves a multi-phase flow ($T_{inj} < T_b(p)$), with $T_b(p)$ the boiling temperature such that $T_b(p_c) = T_c$. Note that the five phases listed in Figure 19, gas phase, liquid phase, superheated vapor, supercritical fluid and compressible are generic thermodynamic terms while the injection terms defined above are specific to constant-pressure combustion systems. Also this diagram does not help highlighting the regions where significant non-ideal gas effects are present. To illustrate this point more generally, a series of heptane $p-T$ diagrams is presented in Figure 20. Intuitively, one could think that real gas effects are limited to the super-critical fluid region but Figure 20(b) in fact shows that even the sub-critical vapor phase can display departures from the ideal gas behavior, i.e. $Z = 1$. And Figure 20(c) shows the extent of the pseudo-boiling line and the region where a significant trans-critical layer, characterized by large specific heats, could appear. The visual similarities between Figures 19 and 20(a) also illustrate the Corresponding State Principle: any $p-T$ diagram for any species, if properly scaled/translated, will look the same.

Equation of states are simply mathematical representations of the generalized compressibility charts mentioned previously. There are very complicated equations of state that to try to match the experimental data of the compressibility charts even near the critical point and

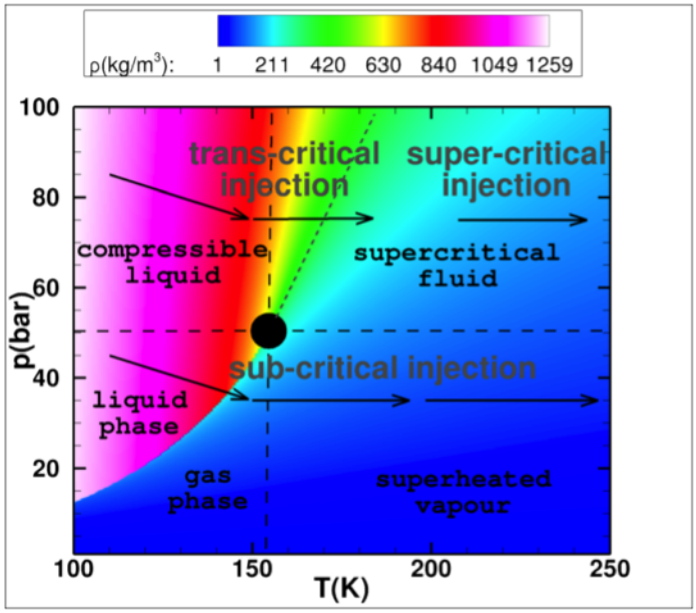

Figure 19: p-T diagram of oxygen generated with the Peng-Robinson equation of state. The color contours represent the predicted density in kg.m^{-3}.

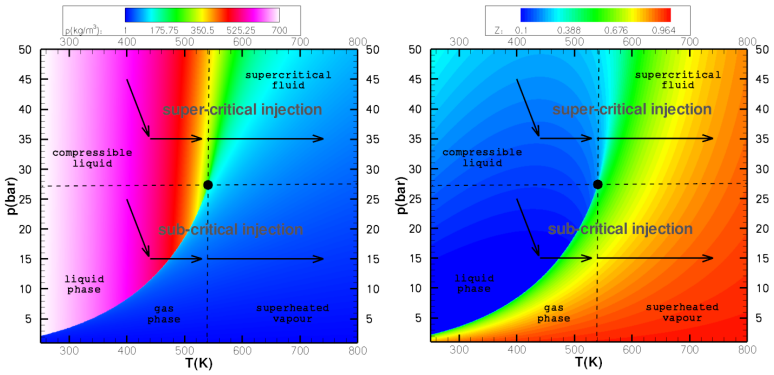

(a) Density (b) Compressibility

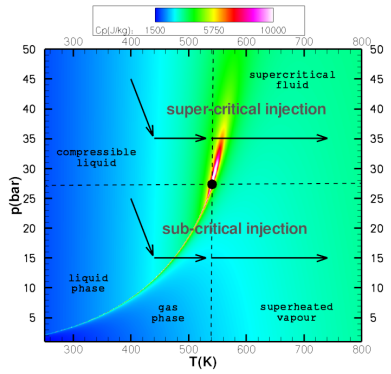

(c) Specific heat

Figure 20: p-T diagrams of heptane generated with the Peng-Robinson equation of state.

using more than a handful of normalization parameters. The Benedict-Webb-Rubin EoS is an example of such approach and it has been used in a few CFD solvers [97, 216]. However, its computational cost is very high since the equation can only be solved numerically given its high-order, non-linear terms. At the other hand of the spectrum, the virial EoS is very simple but can only represent small deviations from ideal gas behavior. It is unsuited to the purpose of this study, which is to model the injection of fluid in a compressed liquid state. As a compromise, the "analytical" equations of states, and more specifically, the "cubic" equation of states appear well suited to the CFD solver of interest. These qualifiers come from the fact that with these EoSs, V can be found analytically given T and p: the function f_V from Eq. 2.5.2 thus cannot have powers of V higher than 4. Given the complexity of solving quartic equations and given that cubic terms in V are necessary to describe both the gas and liquid phases behavior [241], the cubic equations of states are a popular choice for engineering computations.

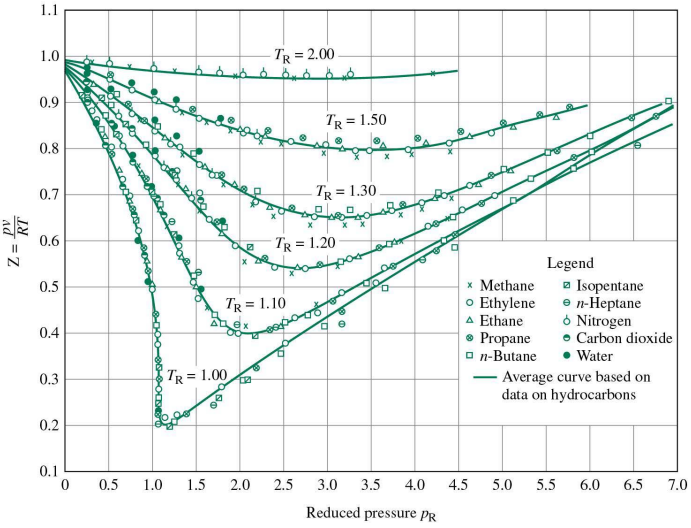

Figure 21: Generalized compressibility chart. [116]

For a given fluid, they take the general form :

$$p = \frac{R_u T}{V - b} - \frac{\Theta}{V^2 + \delta V + \varepsilon} \tag{2.5.3}$$

The reader is referred to the work of Poling et al. [241] for a nearly exhaustive list of cubic EoSs developed over the years and which adopt various expressions for Θ, b, δ and ε. It is

simply recalled that the van der Waals equation of state is a cubic equation of state with Θ set to a constant a and δ=ε=0. This equation, albeit simple, illustrates the physics modeled by cubic EoSs. Recall that this form of EoS differs from the ideal law because it takes into account some inter-molecular forces:

- The first term is $\frac{R_u T}{V-b}$ instead of $\frac{R_u T}{V}$ as it models the repulsive force that molecules exert on each other at short distance. The b term is proportional to the actual volume of the molecule. In the van der Waals model that considers molecules as hard spheres, b is equal to 4 times the volume of the molecule as each sphere cannot get closer than a distance of two radii from another sphere.

- The second additional term $-\frac{a}{V^2}$ models the long-range attractive forces between the molecules such as electrostatics forces, polarization or London dispersion forces. These forces are the glue that keep a gas together and that allow for the liquid state to exist. They decrease the pressure exercised by the fluid on the walls of a vessel, hence the negative sign for this term.

While the terms involved in later cubic EoSs are more complicated, they still model these two fundamental inter-molecular forces.

One limitation of classical cubic EoS is the well-known poor behavior very close to the critical point, where the various thermodynamics functions become either steep or ill-defined. While this can be addressed using for example crossover functions [138], it is assumed in this study that the fluids considered are not in the close neighborhood of the critical point. Since we will usually deal with constant pressure systems, that means we usually operate at pressures sufficiently far away from the fluid or the mixture critical pressure. Finally, since for fluid mechanics solver, density/volume is usually obtained through the conservation equations, numerical solvers will be required to obtain the other state variables. Unfortunately, this adds to the computational cost of the real gas framework.

Since this document will include a large quantity of thermodynamic derivations, a word needs to be said about the conventions adopted for notation. Mass and volume are extensive quantities, whose magnitude increases as the size of the system increases. On the other hand,

temperature and pressure are intensive quantities since their magnitude is independent of the extent of the system. In general, extensive quantities will be denoted by calligraphic upper case letters (mass $\mathcal{M}$, volume $\mathcal{V}$). Specific or massic quantities, which are extensive quantities divided by mass, are denoted by lower case letters (specific volume v, specific heat capacity at constant pressure c_p) whereas molar quantities are denoted by upper case letters (molar volume V, molar heat capacity at constant pressure C_p). The main source of conflict comes from the fact that originally, the real gas framework deals with molar quantities whereas the conservative flow solver used in this work favors massic quantities. The molecular weight MW with units g.mol^{-1} will be used from time to time even though the molar mass M with units kg.mol^{-1} should be the preferred quantity as it is the official SI unit. Below are listed some useful relationships:

$$\rho = \frac{\mathcal{M}}{\mathcal{V}} \text{ in kg.m}^{-3} \tag{2.5.4}$$

$$v = \frac{\mathcal{V}}{\mathcal{M}} \text{ in m}^3\text{.kg}^{-1} \tag{2.5.5}$$

$$V = vM \text{ in m}^3\text{.mol}^{-1} \tag{2.5.6}$$

$$\rho = \frac{1}{v} = \frac{M}{V} = 10^{-3}\frac{MW}{V} \tag{2.5.7}$$

Also recalled here are the conversions between mole fractions X_k and mass fractions Y_k and the different possible computations of the mixture molecular weight or molar weight. In general, and unless noted otherwise, subscript m indicates mixture-averaged quantities:

$$X_k = Y_k\frac{MW_m}{MW_k} = Y_k\frac{M_m}{M_k} \tag{2.5.8}$$

$$Y_k = X_k\frac{MW_k}{MW_m} = X_k\frac{M_k}{M_m} \tag{2.5.9}$$

$$MW_m = \frac{1}{\sum_k^{N_S}\frac{Y_k}{MW_k}} = \sum_k^{N_S} X_k MW_k \tag{2.5.10}$$

$$M_m = \frac{1}{\sum_k^{N_S}\frac{Y_k}{M_k}} = \sum_k^{N_S} X_k M_k \tag{2.5.11}$$

2.5.2 Redlich-Kwong equation of state

This equation of state was the first major improvement over the Van der Waals EoS. While not as accurate as more modern ones, its simple form and good accuracy over the super-critical regime make it appropriate for the studies of interest. Keeping in mind its poor performance in the liquid phase and its inability to accurately predict vapor-liquid equilibria, this EoS should provide a much more computationally efficient option, especially as the number of species increases. That is because the temperature dependent term only weakly depends on the mixture composition. It has not been used extensively by the CFD community, especially with LES. One of the only CFD study using it solved the axisymmetric Euler equations to model the expansion of a super-critical CO_2 jet and obtained reasonable agreement with experiments [132].

Similarly to Eq. 2.5.3, the pressure form of the RK EoS is:

$$p = \frac{R_u T}{V - B_m} - \frac{A_m}{V^2 + V B_m} \tag{2.5.12}$$

with the molar volume V in $\mathrm{m^3.mol^{-1}}$, A_m in $\mathrm{Pa.(m^3.mol^{-1})^2}$ or $\mathrm{J.m^3.mol^{-2}}$ and B_m in $\mathrm{m^3.mol^{-1}}$. R_u is the universal gas constant, whose value is taken as 8.31451 $\mathrm{J.mol^{-1}.K^{-1}}$. The mixture parameters A_m and B_m are computed from the critical properties of individual species through the use of various mixing rules detailed below. An alternate form of this equation introduces the compressibility factor Z:

$$p = Z \rho R_u \sum_{k=1}^{N_S} \frac{Y_k}{M_k} T = Z \rho R_m T \tag{2.5.13}$$

which can be expressed as:

$$Z = \frac{V}{V - B_m} - \frac{A_m \frac{V}{R_u T}}{V^2 + V B_m} \tag{2.5.14}$$

In terms of specific volume, this yields:

$$Z = \frac{v}{v - b_m} - \frac{a_m \frac{v}{R_m T}}{v\,(v + b_m)} \tag{2.5.15}$$

$$Z = \frac{1}{1 - \rho b_m} - \frac{a_m \frac{1}{R_m T}}{(1 + \rho b_m)} \tag{2.5.16}$$

with $a_m = A_m / M^2$ in $\mathrm{Pa.(m^3.kg^{-1})^2}$, $b_m = B_m / M$ in $\mathrm{m^3.kg^{-1}}$ and R_m the specific gas constant for the mixture in $\mathrm{J.kg^{-1}.K^{-1}}$. In the same fashion, Equation 2.5.12 can be recast

as:

$$p = \frac{R_m T}{v - b_m} - \frac{a_m}{(v^2 + v b_m)} \tag{2.5.17}$$

$$p = \frac{\rho R_m T}{1 - \rho b_m} - \frac{\rho^2 a_m}{(1 + \rho b_m)} \tag{2.5.18}$$

For a single fluid, the expressions for the parameters A_m and B_m are simply:

$$A_m = A = 0.42748 \frac{(R_u T_c)^2}{p_c} \alpha(T_r) \tag{2.5.19}$$

$$B_m = B = 0.08664 \frac{(R_u T_c)}{p_c} \tag{2.5.20}$$

where T_c and p_c are the critical temperature and pressure of the fluid of interest and where $\alpha(T)$ is a reduced temperature-dependent factor of the form [241]:

$$\alpha(T_r) = \sqrt{\frac{T_c}{T}} = \frac{1}{\sqrt{T_r}} \tag{2.5.21}$$

In this last expression, T_r is the reduced temperature of the fluid.

2.5.3 Peng-Robinson equation of state

Among the cubic EoSs listed by Poling et al. [241], the Peng-Robinson equation of state (PR EoS) is the most appropriate for this study. Like the RK EoS, it requires only the acentric factor on top of the critical properties and is thus easy to implement for a wide range of species. It provides slightly better accuracy than the RK EoS because of a more complex temperature dependence. As a consequence, energies and specific heats predictions are more accurate, an important feature for reacting flows. This equation of state has been investigated in the past for rocket engine applications and both Oefelein [213] and Congiunti et al. [42] praise its cost-accuracy compromise. Like the RK EoS, the PR EoS allows for a satisfactory modeling of compressed liquids, super-critical fluids and ideal gases with a single equation of state.

Similarly to Eq. 2.5.3, the pressure form of the PR EoS is:

$$p = \frac{R_u T}{V - B_m} - \frac{A_m}{V^2 + 2 V B_m - B_m^2} \tag{2.5.22}$$

with the molar volume V in $\mathrm{m^3.mol^{-1}}$, A_m in $\mathrm{Pa.(m^3.mol^{-1})^2}$ or $\mathrm{J.m^3.mol^{-2}}$ and B_m in $\mathrm{m^3.mol^{-1}}$. R_u is the universal gas constant, whose value is taken as 8.31451 $\mathrm{J.mol^{-1}.K^{-1}}$.

The mixture parameters A_m and B_m are computed from the critical properties of individual species through the use of various mixing rules detailed below. An alternate form of this equation introduces the compressibility factor Z:

$$p = Z\rho R_u \sum_{k=1}^{N_S} \frac{Y_k}{M_k} T = Z\rho R_m T \tag{2.5.23}$$

which can be expressed as:

$$Z = \frac{V}{V - B_m} - \frac{A_m \frac{V}{R_u T}}{V^2 + 2VB_m - B_m^2} \tag{2.5.24}$$

The denominator can be recast as:

$$V^2 + 2VB_m - B_m^2 = (V + B_m)^2 - 2B_m^2 \tag{2.5.25}$$

$$= \left(V + (1 - \sqrt{2})B_m\right)\left(V + (1 + \sqrt{2})B_m\right) \tag{2.5.26}$$

In terms of specific volume, this yields:

$$Z = \frac{v}{v - b_m} - \frac{a_m \frac{v}{R_m T}}{\left(v + (1 - \sqrt{2})b_m\right)\left(v + (1 + \sqrt{2})b_m\right)} \tag{2.5.27}$$

$$Z = \frac{1}{1 - \rho b_m} - \frac{a_m \frac{1}{R_m T}}{\left(1 + (1 - \sqrt{2})\rho b_m\right)\left(1 + (1 + \sqrt{2})\rho b_m\right)} \tag{2.5.28}$$

with $a_m = A_m/M^2$ in Pa.(m^3.kg^{-1})^2, $b_m = B_m/M$ in m^3.kg^{-1} and R_m the specific gas constant for the mixture in J.kg^{-1}.K^{-1}. In the same fashion, Equation 2.5.22 can be recast as:

$$p = \frac{R_m T}{v - b_m} - \frac{a_m}{(v^2 + 2vb_m - b_m^2)} \tag{2.5.29}$$

$$p = \frac{\rho R_m T}{1 - \rho b_m} - \frac{\rho^2 a_m}{(1 + 2\rho b_m - \rho^2 b_m^2)} \tag{2.5.30}$$

For a single fluid, the expressions for the parameters A_m and B_m are simply:

$$A_m = A = 0.457236 \frac{(R_u T_c)^2}{p_c} \alpha(T_r) \tag{2.5.31}$$

$$B_m = B = 0.077796 \frac{(R_u T_c)}{p_c} \tag{2.5.32}$$

where T_c and p_c are the critical temperature and pressure of the fluid of interest and where $\alpha(T)$ is a reduced temperature-dependent factor of the form [299, 344]:

$$\alpha(T_r) = \left(1 + f(\omega)\left(1 - \sqrt{T_r}\right)\right)^2 \tag{2.5.33}$$

In this last expression, T_r is the reduced temperature of the fluid and $f(\omega)$ is a polynomial function of the acentric factor ω of the fluid [313]:

$$f(\omega) = 0.379642 + 1.48503\omega - 0.164423\omega^2 + 0.016666\omega^3 \tag{2.5.34}$$

The remaining question is how the formulation presented above, seemingly only valid for a single fluid, can be applied to multi-component mixtures. Using the Corresponding States Principle (CSP), the next section introduces the mixing rules necessary for this multi-species real gas formulation.

2.5.4 Mixture formulation

2.5.4.1 Extending the Corresponding States Principle

There are two main ways to extend the formulations described in the previous section to mixtures of fluids. Coming from the molecular theory, one could add additional, higher-order cross terms to take into account the addition of multiple species. This is what is done for the virial equation of state for example. For the cubic equations of state, the Corresponding States Principle (CSP) is extended to a pseudo species that would represent the whole mixture. By properly defining pseudo-critical properties, the mixture behavior can be approximated with a single species and the formulations described earlier can be readily applied. In that case, the behavior of the mixture in a reduced state corresponds to the behavior of the pseudo-species in the same reduced state. The mixing rules required to defined the pseudo-critical properties are detailed next.

2.5.4.2 Mixing rules and binary interaction parameters

The mixing rules used in this study are based on the ones suggested by Harstad et al. [99], which themselves find their roots in the work of Wong and Sandler [335]. For a given parameter Q, the pseudo-property of the mixture has a quadratic dependence on the mole fractions of the individual species:

$$Q_m = \sum_{i=1}^{N_S} \sum_{j=1}^{N_S} X_i X_j Q_{ij} \tag{2.5.35}$$

The value of the pseudo-property for the couple of species (i, j) is usually computed using an arithmetic or a geometric mean but more complex, non-linear expressions such as an

harmonic mean can also be used. On top of this averaging, a binary interaction parameter k_{ij} can be included to take into account non-linear inter-molecular effects such as electrostatic interaction of permanent molecular dipoles. So a non-linear arithmetic pseudo-property would be expressed as $Q_{ij} = 0.5(Q_{ii} + Q_{jj})(1 - k_{ij})$ while a conventional geometric pseudo-property would be expressed as $Q_{ij} = \sqrt{Q_{ii}Q_{jj}}$. Finally, not all properties require the use of binary interaction parameters and usually only either the high-level EoS parameters or a low-level quantity such as temperature includes them for a given formulation.

For this work, conventional mixing rules are used for the main parameters of the PR EoS and the RK EoS:

$$A_m = \sum_{i=1}^{N_S} \sum_{j=1}^{N_S} X_i X_j A_{ij} \tag{2.5.36}$$

$$B_m = \sum_{i=1}^{N_S} X_i B_i \tag{2.5.37}$$

The individual elements A_{ij} and B_i are computed following Equations 2.5.31 and 2.5.32 for the PR EoS:

$$A_{ij} = 0.457236 \frac{(R_u T_{c,ij})^2}{p_{c,ij}} \alpha_{ij}(T_{r,ij}) = A^*_{ij} \alpha_{ij}(T_{r,ij}) \tag{2.5.38}$$

$$B_{ij} = 0.077796 \frac{(R_u T_{c,ij})}{p_{c,ij}} \tag{2.5.39}$$

with:

$$\alpha_{ij}(T_{r,ij}) = \left(1 + f(\omega_{ij}) \left(1 - \sqrt{\frac{T}{T_{c,ij}}}\right)\right)^2 \tag{2.5.40}$$

The individual elements A_{ij} and B_i are computed following Equations 2.5.19 and 2.5.20 for the RK EoS:

$$A_{ij} = 0.42748 \frac{(R_u T_{c,ij})^2}{p_{c,ij}} \alpha_{ij}(T_{r,ij}) = A^*_{ij} \alpha_{ij}(T_{r,ij}) \tag{2.5.41}$$

$$B_{ij} = 0.08664 \frac{(R_u T_{c,ij})}{p_{c,ij}} \tag{2.5.42}$$

with:

$$\alpha_{ij}(T_{r,ij}) = \sqrt{\frac{T}{T_{c,ij}}} \tag{2.5.43}$$

Another set of mixing rules is needed to compute the binary parameters $T_{c,ij}$, $p_{c,ij}$ and ω_{ij}, and the pseudo critical temperature introduces a binary interaction parameter:

$$T_{c,ij} = \sqrt{T_{c,i}T_{c,j}}\left(1 - k_{ij}^{\mathrm{PR}}\right) \tag{2.5.44}$$

$$p_{c,ij} = Z_{c,ij}\frac{R_u T_{c,ij}}{V_{c,ij}} \tag{2.5.45}$$

$$\omega_{ij} = \frac{1}{2}\left(\omega_i + \omega_j\right) \tag{2.5.46}$$

The computation of the binary critical pressure $p_{c,ij}$ requires additional mixing rules for the binary critical molar volume $V_{c,ij}$ and the critical binary compressibility $Z_{c,ij}$:

$$V_{c,ij} = \frac{1}{8}\left(V_{c,i}^{1/3}V_{c,j}^{1/3}\right)^3 \tag{2.5.47}$$

$$Z_{c,ij} = \frac{1}{2}\left(Z_{c,i} + Z_{c,j}\right) \tag{2.5.48}$$

Binary interaction parameters can be obtained through scarce experimental data and are otherwise assumed to be zero. For a table of the parameters used in this work and a discussion of the influence of the binary parameters on the model predictions, the reader is referred to Table 19 and Appendix B.

2.5.5 Equation of state derivatives

Here, various quantities will be derived from the basic equation of state and many will involve derivatives of thermodynamic quantities or of EoS parameters.

2.5.5.1 First derivatives of A_m

Redlich-Kwong EoS

$$\frac{\partial A_m}{\partial T} = \left(\frac{\partial A_m}{\partial T}\right)_{V,X} = \left(\frac{\partial A_m}{\partial T}\right)_{p,X} = \sum_{i=1}^{N_S}\sum_{j=1}^{N_S} X_i X_j A_{ij}^* \frac{\partial \alpha_{ij}}{\partial T}$$

$$= -\frac{1}{2T}\sum_{i=1}^{N_S}\sum_{j=1}^{N_S} X_i X_j A_{ij}^* \sqrt{\frac{T_{c,ij}}{T}}$$

$$\frac{\partial A_m}{\partial T} = -\frac{1}{2T}A_m \tag{2.5.49}$$

$$\left(\frac{\partial A_m}{\partial X_k}\right)_T = 2\sum_{i=1}^{N_S} X_i A_{ik} \tag{2.5.50}$$

Note that the quantity $A_m - T\frac{\partial A_m}{\partial T}$ reduces to:

$$A_m - T\frac{\partial A_m}{\partial T} = \frac{3A_m}{2} \tag{2.5.51}$$

Peng-Robinson EoS

$$\begin{aligned}\frac{\partial A_m}{\partial T} &= \left(\frac{\partial A_m}{\partial T}\right)_{V,X} = \left(\frac{\partial A_m}{\partial T}\right)_{p,X} = \sum_{i=1}^{N_S}\sum_{j=1}^{N_S} X_i X_j A_{ij}^* \frac{\partial \alpha_{ij}}{\partial T} \\ &= \sum_{i=1}^{N_S}\sum_{j=1}^{N_S} X_i X_j A_{ij}^* 2\left(-\frac{f(\omega_{ij})}{2}\sqrt{\frac{1}{TT_{c,ij}}}\right)\left(1 + f(\omega_{ij})\left(1 - \sqrt{\frac{T}{T_{c,ij}}}\right)\right) \\ &= -\frac{1}{T}\sum_{i=1}^{N_S}\sum_{j=1}^{N_S} X_i X_j A_{ij} \frac{f(\omega_{ij})\sqrt{\frac{T}{T_{c,ij}}}}{1 + f(\omega_{ij})\left(1 - \sqrt{\frac{T}{T_{c,ij}}}\right)} \quad \text{(See Palle [231])}\end{aligned} \tag{2.5.52}$$

$$\frac{\partial A_m}{\partial T} = -\frac{1}{\sqrt{T}}\sum_{i=1}^{N_S}\sum_{j=1}^{N_S} X_i X_j A_{ij}^* \frac{f(\omega_{ij})}{\sqrt{T_{c,ij}}}\left(1 + f(\omega_{ij})\left(1 - \sqrt{\frac{T}{T_{c,ij}}}\right)\right) \tag{2.5.53}$$

$$\left(\frac{\partial A_m}{\partial X_k}\right)_T = 2\sum_{i=1}^{N_S} X_i A_{ik} \tag{2.5.54}$$

2.5.5.2 Further derivatives of A_m

Redlich-Kwong EoS

$$\frac{\partial^2 A_m}{\partial T^2} = -\frac{1}{2T}\frac{\partial A_m}{\partial T} + \frac{1}{2T^2}A_m = \frac{3}{4T^2}A_m \tag{2.5.55}$$

$$\left(\frac{\partial^2 A_m}{\partial X_k \partial T}\right) = -\frac{1}{T}\sum_{i=1}^{N_S} X_i A_{ik} \tag{2.5.56}$$

$$\left(\frac{\partial^3 A_m}{\partial X_k \partial^2 T}\right) = \frac{1}{T^2}\sum_{i=1}^{N_S} X_i A_{ik} \tag{2.5.57}$$

Peng-Robinson EoS

$$\begin{aligned}\frac{\partial^2 A_m}{\partial T^2} &= -\frac{1}{2T}\frac{\partial A_m}{\partial T} + \frac{1}{\sqrt{T}}\sum_{i=1}^{N_S}\sum_{j=1}^{N_S} X_i X_j A_{ij}^* \frac{(f(\omega_{ij}))^2}{T_{c,ij}}\frac{1}{2\sqrt{T}} \\ \frac{\partial^2 A_m}{\partial T^2} &= \frac{1}{2T}\left(\sum_{i=1}^{N_S}\sum_{j=1}^{N_S} X_i X_j A_{ij}^* \frac{(f(\omega_{ij}))^2}{T_{c,ij}} - \frac{\partial A_m}{\partial T}\right)\end{aligned} \tag{2.5.58}$$

$$\left(\frac{\partial^2 A_m}{\partial X_k \partial T}\right) = -\frac{2}{\sqrt{T}} \sum_{i=1}^{N_S} X_i A_{ik}^* \frac{f(\omega_{ik})}{\sqrt{T_{c,ik}}} \left(1 + f(\omega_{ik}) \left(1 - \sqrt{\frac{T}{T_{c,ik}}}\right)\right) \tag{2.5.59}$$

$$\left(\frac{\partial^3 A_m}{\partial X_k \partial^2 T}\right) = \frac{1}{2T} \left(2 \sum_{i=1}^{N_S} X_i A_{ik}^* \frac{\left(f(\omega_{ik})\right)^2}{T_{c,ik}} - \left(\frac{\partial^2 A_m}{\partial X_k \partial T}\right)\right) \tag{2.5.60}$$

From the above epxressions, the following relationships can be deduced:

$$\frac{\partial A_m}{\partial T} = \frac{1}{2} \sum_{k=1}^{N_S} X_k \left(\frac{\partial^2 A_m}{\partial X_k \partial T}\right) \tag{2.5.61}$$

$$A_m = \frac{1}{2} \sum_{k=1}^{N_S} X_k \left(\frac{\partial A_m}{\partial X_k}\right)_T \tag{2.5.62}$$

2.5.5.3 Pressure partial derivatives

Redlich-Kwong EoS

The partial derivatives of pressure are easily obtained:

$$\left(\frac{\partial p}{\partial V}\right)_{T,X} = -\frac{R_u T}{\left(V - B_m\right)^2} + \frac{A_m \left(2V + B_m\right)}{\left(V^2 + V B_m\right)^2} \tag{2.5.63}$$

$$\left(\frac{\partial p}{\partial T}\right)_{V,X} = \frac{R_u}{V - B_m} + \frac{A_m}{2T \left(V^2 + V B_m\right)} \tag{2.5.64}$$

Peng-Robinson EoS

The partial derivatives of pressure are easily obtained:

$$\left(\frac{\partial p}{\partial V}\right)_{T,X} = -\frac{R_u T}{\left(V - B_m\right)^2} + \frac{2A_m \left(V + B_m\right)}{\left(V + (1 - \sqrt{2})B_m\right)^2 \left(V + (1 + \sqrt{2})B_m\right)^2} \tag{2.5.65}$$

$$\left(\frac{\partial p}{\partial T}\right)_{V,X} = \frac{R_u}{V - B_m} - \frac{\frac{\partial A_m}{\partial T}}{\left(V + (1 - \sqrt{2})B_m\right) \left(V + (1 + \sqrt{2})B_m\right)} \tag{2.5.66}$$

2.5.6 Departure functions for other thermodynamic quantities

The equations of state described above establish relationships between measurable quantities such as temperature, pressure or volume. Other thermodynamic properties are not measurable (except specific heat) but rather conceptual [212] and are only defined in a relative sense. There is no absolute value for the enthalpy of a system for example, only the change is relevant. Because these quantities are state properties, the changes in their values do not depend on the path taken between the initial and final states. It is therefore possible

to construct an artificial path that only requires relationships provided by the equation of state. Let Ψ be the value of some thermodynamic property of a pure component (or a mixture with a fixed composition) at some p and T. If Ψ° denotes the value of Ψ at the same temperature but in an *ideal-gas state* and *at a reference pressure* p°, then we call $\Psi - \Psi^\circ$ the departure function. More details on the derivation can be found in Poling et al. [241] as well as in the Appendix D.1 and the next paragraphs simply state the main results for the equations of state of interest for this work.

2.5.6.1 Internal energy

Classical thermodynamics show that for a mixture of fixed composition, the departure function of internal energy can be written as:

$$E - E^{\text{ig}} = -R_u T \int_V^\infty \left[T \left(\frac{\partial Z}{\partial T} \right)_V \right] \frac{dV}{V} \tag{2.5.67}$$

Note that the temperature and the composition are held constant when performing the integration. Also this integral exists because, as v tends towards ∞, $\left(\frac{\partial Z}{\partial T}\right)_V$ tends towards 0 quickly enough.

Redlich-Kwong EoS

Using Equation 2.5.14, one can compute derivatives of compressibility such as:

$$\left(\frac{\partial Z}{\partial T} \right)_V = \frac{3}{2} \frac{A_m}{R_u T^2 (V + B_m)} \tag{2.5.68}$$

Equation 2.5.67 then becomes:

$$E - E^{\text{ig}} = -\frac{3A_m}{2} \int_V^\infty \frac{dV}{V^2 + V B_m} \tag{2.5.69}$$

$$= -\frac{3A_m}{2B_m} \ln \left(\frac{V}{V + B_m} \right) \tag{2.5.70}$$

In a similar fashion than Miller [198], from now on, the quantity K_1 will be defined as:

$$K_1 = \frac{1}{B_m} \ln \left(\frac{V}{V + B_m} \right) \tag{2.5.71}$$

Peng-Robinson EoS

Using Equation 2.5.24, one can compute derivatives of compressibility such as:

$$\left(\frac{\partial Z}{\partial T}\right)_V = -\frac{V}{V^2 + 2VB_m - B_m^2}\left(\frac{\frac{\partial A_m}{\partial T}T - A_m}{R_u T^2}\right) \tag{2.5.72}$$

Equation 2.5.67 then becomes:

$$E - E^{\text{ig}} = -T\int_V^\infty \left[\frac{dv}{V^2 + 2VB_m - B_m^2}\left(\frac{A_m}{T} - \frac{\partial A_m}{\partial T}\right)\right] \tag{2.5.73}$$

$$= -\left(A_m - T\frac{\partial A_m}{\partial T}\right)\int_V^\infty \frac{dV}{\left(V + (1-\sqrt{2})B_m\right)\left(V + (1+\sqrt{2})B_m\right)} \tag{2.5.74}$$

$$= \left(A_m - T\frac{\partial A_m}{\partial T}\right)\frac{1}{2\sqrt{2}B_m}\ln\left(\frac{V + (1-\sqrt{2})B_m}{V + (1+\sqrt{2})B_m}\right) \tag{2.5.75}$$

$$= \left(A_m - T\frac{\partial A_m}{\partial T}\right)\frac{1}{\sqrt{2}B_m}\tanh^{-1}\left(\frac{V + B_m}{\sqrt{2}B_m}\right) \tag{2.5.76}$$

In a similar fashion than Miller [198], from now on, the quantity K_1 will be defined as:

$$K_1 = \frac{1}{2\sqrt{2}B_m}\ln\left(\frac{V + (1-\sqrt{2})B_m}{V + (1+\sqrt{2})B_m}\right) = \frac{1}{\sqrt{2}B_m}\tanh^{-1}\left(\frac{V + B_m}{\sqrt{2}B_m}\right) \tag{2.5.77}$$

Thus for both the RK EoS and the PR EoS the departure function can be written as:

$$E - E^{\text{ig}} = K_1\left(A_m - T\frac{\partial A_m}{\partial T}\right) \tag{2.5.78}$$

2.5.6.2 Enthalpy

It is straightforward to obtain the departure function for enthalpy since it is linked to the internal energy departure function through:

$$\begin{aligned} H - H^{\text{ig}} &= E - E^{\text{ig}} + (Z-1)\,R_u T \\ &= \left(A_m - T\frac{\partial A_m}{\partial T}\right)K_1 + (Z-1)R_u T \end{aligned} \tag{2.5.79}$$

Redlich-Kwong EoS

The expression for the RK EoS is simply:

$$H - H^{\text{ig}} = -\frac{3A_m}{2}K_1 + (Z-1)\,R_u T \tag{2.5.80}$$

2.5.6.3 Helmholtz and Gibbs free energy

For reaction mechanisms, it is often needed to use the partial Gibbs free energy to compute equilibrium constants and obtain backwards reaction rates from forward reaction rates.

First, we take a look at the departure function for the mixture Gibbs free energy G:

$$G - G^{\text{ig}} = A - A^{\text{ig}} + (Z-1)\,R_u T \tag{2.5.81}$$

where A is the Helmholtz energy. The departure function for the Helmholtz energy is similar to the one for internal energy (Eq. 2.5.67):

$$A - A^{\text{ig}} = -R_u T \left(\int_V^\infty (1-Z)\frac{dV}{V} + \ln Z \right) \tag{2.5.82}$$

This integral exists because, as V tends towards ∞, Z tends towards V quickly enough. So the final expressions for any EoS are simply:

$$A - A^{\text{ig}} = -R_u T \left(\ln\left(\frac{V-B_m}{V}\right) - \frac{A_m}{R_u T}K_1 + \ln Z \right) \tag{2.5.83}$$

$$= -R_u T \ln\left(Z\left(1 - \frac{B_m}{V}\right)\right) + A_m K_1 \tag{2.5.84}$$

$$G - G^{\text{ig}} = R_u T \left(Z - 1 - \ln\left(Z\left(1 - \frac{B_m}{V}\right)\right)\right) + A_m K_1 \tag{2.5.85}$$

2.5.6.4 Heat capacities

Using the direct definition of the constant specific heat at constant volume, one gets:

$$C_V = \left(\frac{\partial E}{\partial T}\right)_V = -T\frac{\partial^2 A_m}{\partial T^2}K_1 + C_V^{\text{ig}} \tag{2.5.86}$$

The specific heats are linked by their thermodynamic definition, which yields $C_p^{\text{ig}} - C_V^{\text{ig}} = R_u$ for an ideal gas:

$$C_p = C_V - T\left(\frac{\partial V}{\partial T}\right)_p^2 \Bigg/ \left(\frac{\partial V}{\partial p}\right)_T \tag{2.5.87}$$

$$= C_V - T\left(\frac{\partial p}{\partial T}\right)_V^2 \Bigg/ \left(\frac{\partial p}{\partial V}\right)_T \tag{2.5.88}$$

The final expression for the specific heat at constant pressure is thus:

$$C_p = -T\frac{\partial^2 A_m}{\partial T^2}K_1 + C_V^{\text{ig}} - T\left(\frac{\partial p}{\partial T}\right)_V^2 \Bigg/ \left(\frac{\partial p}{\partial V}\right)_T \tag{2.5.89}$$

$$= -T\frac{\partial^2 A_m}{\partial T^2}K_1 + C_p^{\text{ig}} - R_u - T\left(\frac{\partial p}{\partial T}\right)_V^2 \Bigg/ \left(\frac{\partial p}{\partial V}\right)_T \tag{2.5.90}$$

Please note that since one can show that:

$$T\int_v^\infty \left[\left(\frac{\partial^2 p}{\partial T^2}\right)_v\right]_T dV = -T\frac{\partial^2 A_m}{\partial T^2}\int_v^\infty \frac{dV}{V^2 + 2VB_m - B_m^2} \quad = T\frac{\partial^2 A_m}{\partial T^2}K_1 \tag{2.5.91}$$

equation (6-5.3) from Poling et al. [241] is recovered. Also, all these expressions are independent of the chosen EoS.

2.5.6.5 Speed of sound

The speed of sound c in a medium can be defined in general by:

$$c^2 = \left(\frac{\partial p}{\partial \rho}\right)_s \tag{2.5.92}$$

This can be mathematically manipulated into:

$$c = \sqrt{-v^2 \left(\frac{\partial p}{\partial v}\right)_s} = v\sqrt{-\frac{\left(\frac{\partial T}{\partial v}\right)_s}{\left(\frac{\partial T}{\partial p}\right)_s}} \tag{2.5.93}$$

Using the Maxwell relations (see Appendix D.1.11, D.1.12, D.1.14 and D.1.13), the differentiation of entropy (see Equations D.1.15 and D.1.16) can be written as:

$$ds = \frac{C_v}{T}dT + \left(\frac{\partial p}{\partial T}\right)_v dv = \frac{C_p}{T}dT - \left(\frac{\partial v}{\partial T}\right)_p dp \tag{2.5.94}$$

Using the isentropic assumption, it can be shown that:

$$\left(\frac{\partial T}{\partial v}\right)_s = -\frac{T}{C_v}\left(\frac{\partial p}{\partial T}\right)_v \tag{2.5.95}$$

$$\left(\frac{\partial T}{\partial p}\right)_s = \frac{T}{C_p}\left(\frac{\partial v}{\partial T}\right)_p \tag{2.5.96}$$

Equation 2.5.93 can thus be written as:

$$c = v\sqrt{\frac{C_p}{C_v}\frac{\left(\frac{\partial p}{\partial T}\right)_v}{\left(\frac{\partial v}{\partial T}\right)_p}} \tag{2.5.97}$$

Using the triple product rule (see Equation D.1.1, this simplifies into:

$$c = v\sqrt{-\frac{C_p}{C_v}\left(\frac{\partial p}{\partial v}\right)_T} \tag{2.5.98}$$

This can be recast in terms of density and the ratio γ of specific heats:

$$c = \sqrt{\gamma\left(\frac{\partial p}{\partial \rho}\right)_T} \tag{2.5.99}$$

which is equivalent to the familiar $c = \sqrt{\gamma RT}$ for ideal gases. In general, it can be shown that the ratio γ of specific heats is:

$$\gamma = \frac{C_p}{C_v} = \left(\frac{\partial p}{\partial v}\right)_s \left(\frac{\partial v}{\partial p}\right)_T = \frac{\kappa_T}{\kappa_s} \tag{2.5.100}$$

The adiabatic (isentropic) bulk modulus κ_s for fluids is:

$$\kappa_s = -v\left(\frac{\partial p}{\partial v}\right)_s = -\rho\left(\frac{\partial p}{\partial \rho}\right)_s \tag{2.5.101}$$

It is also called the isentropic compressibility and can be expressed in terms of the expansivity α_v and the isothermal compressibility κ_T:

$$\kappa_s = \kappa_T - \frac{vT\alpha_v^2}{C_p} \tag{2.5.102}$$

These new quantities are defined as:

$$\alpha_v = -\frac{\left(\frac{\partial p}{\partial T}\right)_v}{v\left(\frac{\partial p}{\partial v}\right)_T} \quad \kappa_T = -\frac{1}{v\left(\frac{\partial p}{\partial v}\right)_T} \tag{2.5.103}$$

For an isotropic, continuous and non-dispersive medium, the speed of sound can usually be expressed in the form:

$$c = \sqrt{\frac{C_{\text{stiff}}}{\rho}} \tag{2.5.104}$$

where C_{stiff} is a coefficient of stiffness, equivalent to the modulus of bulk elasticity for fluid mediums. The adiabatic bulk modulus plays this role here no matter which EoS is chosen:

$$\kappa_s = \rho c^2 \tag{2.5.105}$$

2.5.6.6 Partial molar quantities and fugacity

The thermodynamic extensive properties of a mixture can always be obtained by summing contributions from the partial properties of each component of the mixtures. But since real gas models take into account inter-molecular effects, the partial properties of a species is not obtained easily from the mixture value of this property. Mathematically, this means for a general molar property F function of T, p and the molar composition X_k:

$$F_{,l}(T, p, X_k) \neq X_l F(T, p, X_k) \tag{2.5.106}$$

More generally, the partial molar property $F_{,l}$, which is an intensive property, is defined from the total property $\mathcal{F}$, which is an extensive property, as:

$$F_{,l}(T, p, X_k) = \left(\frac{\partial \mathcal{F}}{\partial N_l}\right)_{T,p,N_{k,k\neq l}} \tag{2.5.107}$$

Three main consequences can be obtained from this definition [286]:

1. A general form of the Gibbs-Duhem equation assuming the system is at equilibrium:

$$\sum_{l=1}^{N_S} X_l dF_{,l} + \left(\frac{\partial F}{\partial T}\right)_{p,X_k} dT + \left(\frac{\partial F}{\partial p}\right)_{T,X_k} dp = 0 \tag{2.5.108}$$

2. An expression for the additive rule for mixture properties mentioned earlier:

$$F(T, p, X_k) = \sum_{l=1}^{N_S} X_l F_{,l}(T, p, X_k) \tag{2.5.109}$$

3. A relation for the pure component limit, with $F^o_{,l}$ the molar property of pure component l, which depends only on T and p:

$$\lim_{X_l \to 1} F_{,l}(T, p, X_k) = F^o_{,l}(T, p) \tag{2.5.110}$$

The partial molar volume $V_{,l}$ and the partial molar enthalpy $H_{,l}$ appear in the governing equations of the flow and thus need to be computed for the PR EoS. In the Appendix D.2.1, it is shown that the partial molar volume can be expressed as:

$$V_{,l} = -\left(\frac{\partial V}{\partial p}\right)_{T,X} \left(\frac{R_u T}{V - B_m} + \frac{B_l R_u T}{(V - B_m)^2} - \frac{2\sum_{k=1}^{N_S} X_k A_{lk}}{V^2 + 2VB_m - B_m^2} + \frac{2A_m(V - B_m)B_l}{(V^2 + 2VB_m - B_m^2)^2}\right) \tag{2.5.111}$$

Similarly, the partial molar enthalpy can be obtained from the departure function obtained in Eq. 2.5.79:

$$\begin{aligned} H_{,l} &= \left(\frac{\partial \mathcal{H}}{\partial N_l}\right)_{T,p,N_{k,k\neq l}} \\ &= H_l^{\text{ig}} + pV_{,l} - R_u T + K_1 \left(\frac{\partial \left(A_m - T\frac{\partial A_m}{\partial T}\right)}{\partial X_l}\right)_{T,p,N_{k,k\neq l}} \\ &+ \left(A_m - T\frac{\partial A_m}{\partial T}\right)\left(\frac{\partial K_1}{\partial X_l}\right)_{T,p,N_{k,k\neq l}} \qquad (2.5.112) \\ &= H_l^{\text{ig}} + pV_{,l} - R_u T + K_1 \left(\frac{\partial A_m}{\partial X_l} - T\frac{\partial^2 A_m}{\partial X_l \partial T} - \left(A_m - T\frac{\partial A_m}{\partial T}\right)\frac{B_l}{B_m}\right) \\ &+ \left(A_m - T\frac{\partial A_m}{\partial T}\right)\frac{V_{,l} - V\frac{B_l}{B_m}}{V^2 + 2VB_m - B_m^2} \qquad (2.5.113) \end{aligned}$$

The partial molar specific heat at constant pressure is then derived easily:

$$\begin{aligned} C_{p,l} &= \left(\frac{\partial H_{,l}}{\partial T}\right)_p \\ &= p\left(\frac{\partial V_{,l}}{\partial T}\right)_p - R_u + K_1\left(-T\frac{\partial^3 A_m}{\partial X_l \partial T^2} + \frac{B_k}{B_m}T\frac{\partial^2 A_m}{\partial T^2}\right) \qquad (2.5.114) \\ &- T\frac{\partial^2 A_m}{\partial T^2}\frac{V_{,l} - V\frac{B_k}{B_m}}{V^2 + 2VB_m - B_m^2} \qquad (2.5.115) \end{aligned}$$

The fugacity could be computed in a similar fashion but it is not needed in the current formulation because of the simplified transport properties.

2.5.7 Conversion between state variables

The equation of state is used at various locations of the flow solver in order to obtain the needed unknown state variable from the known ones. The following subsections describe the equations and sometimes algorithms used for each case. The mixture composition is always assumed to be known.

2.5.7.1 Computing pressure from temperature and density

The pressure is obtained trivially from Equation 2.5.18 or from Equation 2.5.30 depending on the chosen EoS. The factors a_m and b_m are computed from the known composition and temperature.

2.5.7.2 *Computing density from temperature and pressure*

The compressibility factor cannot be expressed simply in function of the temperature and pressure only. Instead, it is expressed as a solution of a cubic equation (hence the name cubic equation of state):

$$Z^3 + \alpha Z^2 + \beta Z + \gamma = 0 \tag{2.5.116}$$

with, for the RK EoS:

$$\begin{aligned}
\alpha &= -1 \\
\beta &= \frac{a_m p - (b_m p)^2}{(R_u T)^2} - \frac{b_m p}{R_u T} \\
\gamma &= -\frac{a_m b_m p^2}{(R_u T)^3}
\end{aligned}$$

and with, for the PR EoS:

$$\begin{aligned}
\alpha &= -1 + \frac{b_m p}{R_u T} \\
\beta &= \frac{a_m p - 3(b_m p)^2}{(R_u T)^2} - \frac{2 b_m p}{R_u T} \\
\gamma &= -\frac{a_m b_m p^2}{(R_u T)^3} + \frac{(b_m p)^2}{(R_u T)^2} + \frac{(b_m p)^3}{(R_u T)^3}
\end{aligned}$$

Such cubic equation with real coefficients has at least one real root and may have three real roots. Efficient root-finding algorithms are widely available and one of them [206] is detailed here:

1. Compute Q and R such as:

$$\begin{aligned}
Q &= \frac{\alpha^2 - 3\beta}{9} \\
R &= \frac{2\alpha^3 - 9\alpha\beta + 27\gamma}{54}
\end{aligned}$$

2. The sign of $Q^3 - R^2$ determines the number of real roots.

   - If $Q^3 - R^2 \geq 0$, then the cubic equation has three real roots:

$$\begin{aligned}
Z_1 &= -2\sqrt{Q}\cos\left(\frac{\theta}{3}\right) - \frac{\alpha}{3} \\
Z_2 &= -2\sqrt{Q}\cos\left(\frac{\theta + 2\pi}{3}\right) - \frac{\alpha}{3} \\
Z_3 &= -2\sqrt{Q}\cos\left(\frac{\theta + 4\pi}{3}\right) - \frac{\alpha}{3}
\end{aligned}$$

with

$$\theta = \arccos\left(\frac{R}{Q^{3/2}}\right)$$

The compressibility factor Z is then the largest positive root among (Z_1, Z_2, Z_3).

- If $Q^3 - R^2 < 0$, then the cubic equation has only one real root:

$$Z = -\text{sign}(R)\left\{\left[\left(R^2 - Q^3\right)^{1/2} + |R|\right]^{1/3} + \frac{Q}{\left[\left(R^2 - Q^3\right)^{1/2} + |R|\right]^{1/3}}\right\} - \frac{\alpha}{3} \tag{2.5.117}$$

Once the compressibility factor is known, the density is simply obtained through:

$$\rho = \frac{p}{ZR_u \sum_{k=1}^{N_S} \frac{Y_k}{W_k} T} \tag{2.5.118}$$

2.5.7.3 Computing temperature from density and pressure

This situation arises with upwind schemes when the temperature at the cell interface needs to be computed from the reconstructed pressure, density and composition. In this case, the equation that needs to be solved is:

$$ZT = \frac{p}{\rho R_u \sum_{k=1}^{N_S} \frac{Y_k}{M_k}} = \frac{p}{\rho R_m} \tag{2.5.119}$$

In Equation 2.5.119, since Z cannot be expressed as a function of p and ρ easily, the left-hand side is essentially a complex function of T. Only an iterative method such as the Newton-Raphson method can efficiently solve this equation. Let f be a function of T only such as $f = ZT - \frac{p}{\rho R_m}$. The term $\frac{p}{\rho R_m}$ is known in this case. Since only the temperature satisfying $f(T) = 0$ is of interest, this can be recast as $f(T) = Z\rho R_m T - p$. Essentially, the convergence criterion is whether the guessed pressure is equal to the known pressure. The analytical derivative is easily computed. For the RK EoS, it writes:

$$\frac{\mathrm{d}\, f}{\mathrm{d}\, T} = \left(\frac{\partial p}{\partial T}\right)_{v,X} = \frac{R_u}{v - b_m} - \frac{\frac{\mathrm{d}\, a_m}{\mathrm{d}\, T}}{(v^2 + v b_m)} \tag{2.5.120}$$

For the PR EoS, it writes:

$$\frac{\mathrm{d}\, f}{\mathrm{d}\, T} = \left(\frac{\partial p}{\partial T}\right)_{v,X} = \frac{R_u}{v - b_m} - \frac{\frac{\mathrm{d}\, a_m}{\mathrm{d}\, T}}{(v^2 + 2v b_m - b_m^2)} \tag{2.5.121}$$

A simple Newton-Raphson method with scaling can be used to solve this equation:

$$T^{n+1} = T^n + \frac{dT}{1 + |dT * S_N|} \text{ with } dT = -\frac{f(T^n)}{\frac{\mathrm{d}f}{\mathrm{d}T}} \tag{2.5.122}$$

The convergence criterion is usally set to 1×10^{-4} and the scaling factor S_N to 1×10^{-5}.

2.5.7.4 Computing temperature and pressure from density and energy

While implicit or semi-implicit schemes can avoid most of the conversions from conservative variables to primitive variables through preconditioning [325, 190, 262], explicit schemes solving the fully conservative Navier-Stokes equations have to compute the local temperature and pressure from the energy/enthalpy and the density unless they use interpolation techniques such as curvefits [198] or Artificial Neural Networks (ANN). Two methods will be described thereafter:

- A method where simultaneous Newton-Raphson solvers are run with temperature and pressure updated until the computed energy/enthalpy and density computed match the ones obtained from the conservative variables. This is largely inspired from the works of Bellan et al. [226]. This will be referred as the dual-variable iteration method from here on out.
- A new method where only one Newton-Raphson solver is needed as it is possible to express the energy/enthalpy only with respect to density and temperature. Pressure is computed independently after convergence on temperature. This will be referred as the single-variable iteration method in the following.

Dual-variable iteration method

For the sake of brevity of this chapter, the detailed description of this method is given in Appendix D.2.

Single-variable iteration method

Coming from the conservation equations (2.1.1,2.1.3,2.1.4), internal energy, density and composition of the fluid mixture are known. From these conserved variables, primitive

variables need to be computed as these primitive variables appear directly (pressure transport terms, molecular heat transfer) and indirectly (various thermodynamic and transport properties) in the conservation equations. Unlike for ideal gas equation of state, the thermodynamic variable e is a function of two other variables, not just one. In order to avoid a complex iterative solver on both temperature and pressure, the internal energy needs to be expressed as a function of ρ and T. Since the density is known, this becomes a simple 1-equation/1-unknown system. Recasting the departure function obtained in Equation 2.5.76, the internal energy can be expressed as:

$$E(T,v) = E^{\text{ig}}(T) + \left(A_m(T) - T\frac{\partial A_m(T)}{\partial T}\right) K_1(v) \tag{2.5.123}$$

Several algorithms can be used to solve the non-linear equation of interest

$$F(T) = E^* - E(T,v^*) = 0$$

where superscript $*$ represents known quantities. If convergence speed is of primary importance, the Householder's numerical methods are a good choice. Robust convergence is expected for such a thermodynamic solver since the initial guesses for temperatures, coming from previous timesteps and/or nearby points in the computational domain should provide a reasonable estimate. Another argument for this class of methods is that the thermodynamic functions considered are smooth away from the critical point (where in any case the Peng-Robinson or any other cubic equation of state breaks down) and are easily derivable analytically. The Householder's method of order 1 is simply the Newton-Raphson method for which a large literature is available for best practices and various acceleration techniques. For this method, only the first-order derivative is required. For the equation considered, since the density/molar volume can be considered constant, this yields alongside Equation 2.5.86:

$$\left(\frac{\partial F}{\partial T}\right)_v = -\left(\frac{\partial E(T,v^*)}{\partial T}\right)_v = -C_V \tag{2.5.124}$$

$$= -C_V^{\text{ig}} + T\frac{\partial^2 A_m}{\partial T^2} K_1(v^*) \tag{2.5.125}$$

The 1-D algorithm used is shown in Algorithm 1. It is made possible by the fact that the departure functions for the energy and specific heat do not depend explicitely on p and can

be expressed as a function of T and v.

Algorithm 1 Algorithm for the temperature solver when E and ρ are known.

```
{E and ρ are known}
{Properties that do not depend on T are computed for the whole 1D line}
{The convergence depends on ϵ and α.}
for i = i1 to i2 do
  while error > ϵ .AND. iter < itermax do
    iter = iter + 1
    C = 1/(1+|DT*α|) {Acceleration technique}
    T_guess = T_guess + DT * C
    {Check if iteration is stuck in a limit cycle. If so, give it a little nudge.}
    {Compute ideal gas properties}
    {Compute departure functions Eqs. 2.5.76 and 2.5.86.}
    {This is possible since they do not depend on p explicitely}
    f0 = E* - E(T_guess, v*)
    DT = -f0/C_V(T_guess, v*)
    error = |f0|/Rg
  end while
end for
{Pressure can now be computed through Eq. 2.5.22}
```

Similarly to the previous section, it can happen that the known quantities are enthalpy and density, for example in the upwind scheme. It starts with the following expression for the enthalpy:

$$H(T,v) = H^{\text{ig}}(T) + \left(A_m(T) - T\frac{\partial A_m(T)}{\partial T}\right) K_1(v) + (Z-1)R_u T \tag{2.5.126}$$

According to Equation 2.5.24, compressibility can be expressed in function of T and v. This is once again a 1-equation/1-unknown system that needs to be solved through an iterative method. The derivative of the objective function

$$F(T) = H^* - H(T,v^*) = 0$$

is a little bit more complex than for the enthalpy:

$$\begin{aligned}\left(\frac{\partial F}{\partial T}\right)_v &= -\left(\frac{\partial H(T,v^*)}{\partial T}\right)_v \\ &= -C_V - \frac{v^*\alpha_v}{\kappa_T} \quad \text{per Eq.D.2.31} \\ &= -C_V - v^*\left(\frac{\partial p}{\partial T}\right)_v\end{aligned} \tag{2.5.127}$$

As can be seen from Equation 2.5.22, $\left(\frac{\partial p}{\partial T}\right)_v$ can be expressed very easily as a function of T and v only:

$$\left(\frac{\partial p}{\partial T}\right)_v = \frac{R_u}{v - B_m} - \frac{\frac{\partial A_m}{\partial T}}{v^2 + 2vB_m - B_m^2} \tag{2.5.128}$$

In this case, the algorithm described in Algorithm 1 changes very little.

The performances of these methods are evaluated in Section 3.5.1. Verification of the implementation on single species and mixture properties can be found in Appendix D.3 and Appendix B.

2.6 Transport properties

Following the simplifying assumptions made in Section 2.1.3.2 such as neglecting cross-diffusion and multi-component diffusion, three main quantities remain to be defined in this section: the viscosity, the thermal conductivity and binary diffusion coefficients. The methodology developed by Chung et al. [36], which is based on the same Corresponding State Principles (CSP) as the cubic equations of state, is selected for the viscosity and the thermal conductivity. It has been recognized in the literature has the most effective method in terms of computational cost and accuracy [241, 42] while still allowing the modeling of a large number of species from first principles. Most of the species-dependent quantities required are also used for the cubic equations of state which makes the implementation easier. Also, its main input variables are temperature and molar volume, i.e. density, a set of variables well suited for CFD applications. For the diffusion coefficients, the method of Fuller et al. [74] is chosen even though it requires additional input data such as atomic diffusion volumes. However, this data is easily available for the species of interest and the additional accuracy of this method [241] comes with no additional cost compared to its alternatives. For the extension to diffusion coefficients at high pressures, a field that lacks robust models, the empirical correlation of Riazi and Whitson [248] was chosen over the Takahashi method [301] for its ease of use and because its main shortcoming (wrong asymptotic behavior at low pressures) is irrelevant for the current application. Note that the thermodynamic framework and the transport properties framework are independent and thus it is possible to run any EoS (CPG, TPG or RG) with any transport properties framework such as a simple Sutherland's law model or the all-pressure formulation presented here.

2.6.1 Viscosity

This section deals with the computation of molecular viscosity. The volume viscosity is neglected for this work as mentioned in Section 2.1.2 and shown in Appendix G. The expression proposed by Chung is:

$$\mu = \mu^* \frac{36.344 \times 10^{-7} \sqrt{MW_m T_{c,m}}}{V_{c,m}^{2/3}} \tag{2.6.1}$$

where μ is the mixture viscosity in N.s.m^{-2} and $V_{c,m}$ is a critical volume of the mixture computed as $V_{c,m} = (\sigma_m/0.809)^3$ in cm^3.mol^{-1}. For consistency, it is recommended that the Lennard-Jones parameter σ be computed from the critical volume instead of being inputted independently and potentially not being consistent with the critical volume:

$$\sigma_m = \sum_i \sum_j X_i X_j \sigma_{ij} \tag{2.6.2}$$

$$\sigma_{ij} = \sqrt{\sigma_i \sigma_j} \tag{2.6.3}$$

$$\sigma_i = 0.809 V_{c,i}^{1/3} \tag{2.6.4}$$

Note that the expression for σ_{ij} (Eq. 2.6.3) could include a binary interaction parameter.

Going back to Equation 2.6.1:

$$\mu^* = \frac{\sqrt{T_m^*}}{\Omega_v} \left(F_{c,m} \left[G_2^{-1} + E_6 y \right] \right) + \mu^{**} \tag{2.6.5}$$

The dimensionless temperature T^*, the other Lennard-Jones parameter $\frac{\varepsilon}{k}$ and the collision integral Ω_v are related by:

$$T_m^* = \frac{T}{\frac{\varepsilon_m}{k}} \tag{2.6.6}$$

$$\frac{\varepsilon_m}{k} = \frac{\sum_i \sum_j X_i X_j \frac{\varepsilon_{ij}}{k} \sigma_{ij}^3}{\sigma_m^3} \tag{2.6.7}$$

$$\frac{\varepsilon_{ij}}{k} = \sqrt{\frac{\varepsilon_i}{k} \frac{\varepsilon_j}{k}} \tag{2.6.8}$$

$$\frac{\varepsilon_i}{k} = \frac{T_{c,i}}{1.2593} \tag{2.6.9}$$

$$\Omega_v = A(T^*)^{-B} + Ce^{-DT^*} + Ee^{-FT^*} \tag{2.6.10}$$

where k is the Boltzmann constant and the other constants are [101]:

$$A = 1.16145 \qquad B = 0.14874$$

$$C = 0.52487 \qquad D = 0.77320$$

$$E = 2.16178 \qquad F = 2.43787$$

Note that the expression for $\frac{\varepsilon_{ij}}{k}$ (Eq. 2.6.8) could include a binary interaction parameter.

The function $F_{c,m}$ takes into account the shape and polarity of the molecules through its dependencies on the acentric factor ω, the dimensionless dipole moment μ_r and the

association factor κ:

$$F_{c,m} = 1 - 0.2756\omega_m + 0.059035\mu_{r,m}^4 + \kappa_m$$

Additional mixing rules are required for these mixture parameters:

$$MW_m = \left(\frac{\sum_i \sum_j X_i X_j \frac{\varepsilon_{ij}}{k} \sigma_{ij}^2 \sqrt{MW_{ij}}}{\frac{\varepsilon_m}{k} \sigma_m^2} \right)^2 \tag{2.6.11}$$

$$MW_{ij} = \frac{2}{\frac{1}{MW_i} + \frac{1}{MW_j}} \tag{2.6.12}$$

$$\omega_m = \frac{\sum_i \sum_j X_i X_j \omega_{ij} \sigma_{ij}^3}{\sigma_m^3} \tag{2.6.13}$$

$$\omega_{ij} = \frac{\omega_i + \omega_j}{2} \tag{2.6.14}$$

The reduced dipole moment is computed from the physical dipole moment μ^{dp} in debyes:

$$\mu_{r,m} = 0.1313 \frac{\mu_m^{dp}}{\sqrt{V_c T_c}} \tag{2.6.15}$$

$$\left(\mu_m^{dp}\right)^4 = \sigma_m^3 \sum_i \sum_j \left(\frac{X_i X_j (\mu_i^{dp})^2 (\mu_j^{dp})^2}{\sigma_{ij}^3} \right) \tag{2.6.16}$$

$$\kappa_m = \sum_i \sum_j X_i X_j \kappa_{ij} \tag{2.6.17}$$

$$\kappa_{ij} = \sqrt{\kappa_i \kappa_j} \tag{2.6.18}$$

Table 4 summarizes the non-zero values of these coefficients for the current species of interest.

Table 4: Non-zero values of the parameters used for the viscosity computations for the species used in this work.

Species	κ	μ^{dp}
H_2O	0.076	1.8
HO_2	0.0	2.09

Finally, the high-pressure/high-density correction terms are expressed as:

$$
\begin{aligned}
y &= \frac{v_c}{6v} \\
G_1 &= \frac{1-0.5y}{(1-y)^3} \\
G_2 &= \frac{E_1\left[\left(1-e^{-E_4 y}\right)/y\right] + E_2 G_1 e^{E_5 y} + E_3 G_1}{E_1 E_4 + E_2 + E_3} \\
\mu^{**} &= E_7 y^2 G_2 e^{E_8 + \frac{E_9}{T^*} + \frac{E_{10}}{(T^*)^2}}
\end{aligned}
$$

The low-pressure viscosity is readily available if y is set to 0, it will be useful for the computation of the thermal conductivity. The parameters E_1 to E_{10} are a linear function of the accentric factor ω:

$$
\begin{aligned}
E_1 &= 6.324 + 50.412\omega & E_2 &= 0.00121 - 0.001154\omega \\
E_3 &= 5.283 + 254.209\omega & E_4 &= 6.623 + 38.096\omega \\
E_5 &= 19.745 + 7.630\omega & E_6 &= -1.9 - 12.537\omega \\
E_7 &= 24.275 + 3.45\omega & E_8 &= 0.7972 - 1.117\omega \\
E_9 &= -0.2382 + 0.06770\omega & E_{10} &= 0.06863 + 0.3479\omega
\end{aligned}
$$

One shortcoming of Chung's method is that, like other methods based on the corresponding states principle, it is not interpolative, meaning the mixture viscosity does not tend asymptotically towards the pure component viscosities. Also, it appears that Chung's formulation does not behave well with substances having negative acentric factor such as hydrogen. The acentric factor for these substances is thus set to 0 even if a different value can be used at the same time for thermodynamic computations.

2.6.2 Thermal conductivity

The computation of the viscosity and the thermal conductivity are actually linked as one can see in the following estimation:

$$
\lambda = \frac{31200\mu^0\Psi}{M}\left(\frac{1}{G_2} + B_6 y\right) + qB_7 y^2 \sqrt{T_{r,m}} G_2 \tag{2.6.19}
$$

where λ is the thermal conductivity in W.(m.K)$^{-1}$, the superscript 0 in μ^0 denotes the low-pressure viscosity mentioned earlier and q is defined as:

$$q = 1.134 \times 10^{-5} \sqrt{\frac{T_{c,m}}{MW_m V_{c,m}^{4/3}}}$$

and Ψ is a function of the molar heat capacity at constant volume C_V, the acentric factor ω and the reduced temperature T_r:

$$\Psi = 1 + \alpha \frac{0.215 + 0.28288\alpha - 1.061\beta + 0.26665Z}{0.6366 + \beta Z + 1.061\alpha\beta} \tag{2.6.20}$$

with:

$$\alpha = \frac{C_{v,m}}{R_u} - \frac{3}{2}$$

$$\beta = 0.7862 - 0.7109\omega_m + 1.3168\omega_m^2$$

$$Z = 2.0 + 10.5T_{r,m}^2$$

The other parameters are very similar to the ones used for the viscosity, allowing an easy implementation:

$$y = \frac{V_c}{6v}$$

$$G_1 = \frac{1 - 0.5y}{(1-y)^3}$$

$$G_2 = \frac{B_1\left[\left(1 - e^{-B_4 y}\right)/y\right] + B_2 G_1 e^{B_5 y} + B_3 G_1}{B_1 B_4 + B_2 + B_3}$$

$$B_1 = 2.4166 + 0.74824\omega$$

$$B_2 = -0.50924 - 1.5094\omega$$

$$B_3 = 6.6107 + 5.6207\omega$$

$$B_4 = 14.543 - 8.9139\omega$$

$$B_5 = 0.79274 + 0.82019\omega$$

$$B_6 = -5.8634 + 12.801\omega$$

$$B_7 = 91.089 + 128.11\omega$$

The mixing rules used to compute the mixture properties are also the same ones than for the viscosity computation.

2.6.3 Mass diffusion coefficients

Fuller et al. [74] modified the classical expression from Chapman and Enskog that was derived from the Boltzmann equation and kinetic theory:

$$\mathcal{D}_{ij} = \frac{C_D T^{1.75}}{p\sqrt{MW_{ij}}\left((\Sigma_v)_i^{1/3} + (\Sigma_v)_j^{1/3}\right)^2} \tag{2.6.21}$$

The pressure dependency satisfies the phenomenological law that $p\mathcal{D}$ or $\rho\mathcal{D}$ is constant at low pressures. The atomic diffusion volumes Σ_v are an additional input to the model compared to the original theory but they produce better results, avoid the expensive computation of a collision integral and can be easily estimated using a group contribution method if they are not included (see Table 11-1 from Poling [241]). The constant C_D is equal to 0.00143 for a diffusion coefficient in cm^2/s and the pressure p in bar. The averaged molecular weight is computed through a geometric mean $MW_{ij} = \frac{2}{\frac{1}{MW_i}+\frac{1}{MW_j}}$.

For high-pressure regimes where the density is large enough, the assumption of $p\mathcal{D}$ or $\rho\mathcal{D}$ being constant with increasing pressure is no longer valid. Instead, these quantities decrease with either increasing pressure or increase density. Very few models exist because of the scarcity of experimental data and the one chosen for this work is the one by Riazi and Whitson [248]:

$$\frac{\rho\mathcal{D}_{ij}}{(\rho\mathcal{D}_{ij})^o} = 1.07\left(\frac{\mu}{\mu^o}\right)^{(-0.27-0.38\omega-(0.05+0.1\omega)p_r)} \tag{2.6.22}$$

Other possible models for high-pressure mass diffusion coefficients include the empirical correlation by Takahashi [301] and the more fundamental work by Harstad and Bellan [98]. This latter particularly highlights the lack of consistent and reliable data at high-pressures for conditions relevant to rocket engine applications.

2.6.4 Verification

The thermal conductivity evaluation is verified against the experimental data from Yorizane et al. [342] which considers high-pressure binary mixtures of argon and carbon dioxide at 298

K. This experimental data corresponds to Figure 10-7 from Poling [241] where it is compared with the empirical curvefits from Stiel and Thodos [295]. Figure 22 shows the predictions of the current Chung's method versus available data at pressures from 11 bar to 71 bar. While the Chung's method is not as accurate as the empirical method of Stiel and Thodos, it does capture the non-linear trends at high pressures correctly. Note that this is an extreme case for the current work since the carbon dioxide critical point is (T_c=304.1 K,p_c=73.7 bar) and the argon critical point is (T_c=150.9 K,p_c=49.0 bar). So the higher-pressure curves do correspond to a super-critical regime where the Chung's formulation is known to behave properly while the lower-pressure curves correspond to a sub-critical liquid regime where the Chung's methodology and the cubic equation of state are known to struggle.

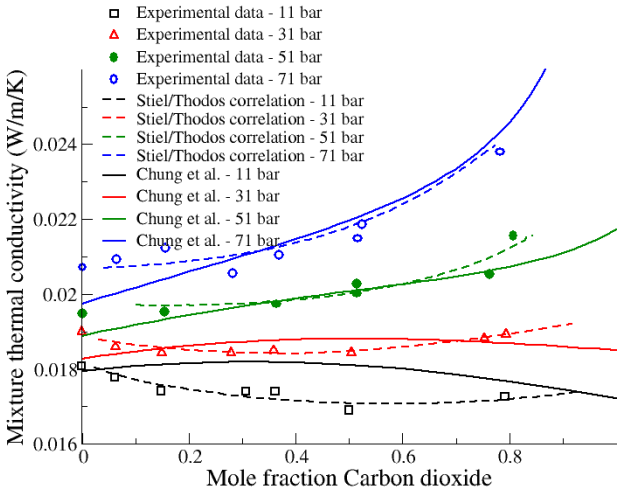

Figure 22: High-pressure thermal conductivities for mixture of argon and carbon dioxide at 298 K.

To test the current implementation of the computation of binary mass diffusion coefficients, the experimental data from Takahashi et al. [302] is considered. This data is also shown in Figure 11-4 in Poling [241]. It contains measurements of the binary diffusion coefficient between carbon dioxide and ethylene over a range of pressures. This coefficient is measured using traces of CO_2 into a carrier of C_2H_4 and using traces of C_2H_4 into a carrier of CO_2. Figure 23 shows the comparison between the experimental data and the

current formulation, referred to as the Fuller-Riazi data. At low to moderate pressures, the speed of diffusion of CO_2 into C_2H_4 is of course equal to the speed of diffusion of C_2H_4 into CO_2 and the pressure dependence of the binary diffusion coefficient can be approximated by assuming $p\mathcal{D}_{ij}$ is a constant. However, at higher pressures, not only does this approximation not hold anymore, but the binary diffusion coefficient depends on the carrier gas. This is due to the influence of intra-molecular forces and would be taken into account by a more complex transport formulation as shown in Section 2.1.3.1 and as reviewed by Lam[142]. The current implementation captures accurately the first part of the transition from the low-pressure regime to the high-pressure regimes but shows significant error when the diffusion coefficient starts to depend on the carrier gas.

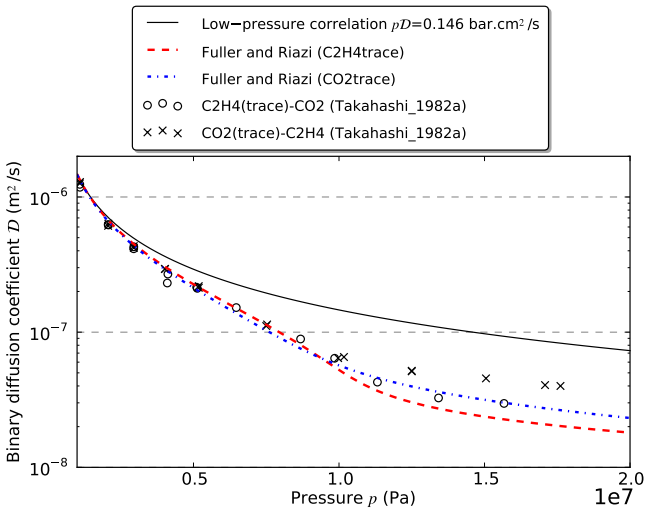

Figure 23: Effect of pressure and carrier gas on the binary diffusion coefficient of the CO_2-C_2H_4 system at 323.2 K

2.7 Boundary conditions

Many mechanisms in turbulent reacting flows are strongly coupled with acoustic waves. For example, a flame produces noise which itself can perturb the flame. Also, turbulence interacts with acoustic waves in various ways. For instance, velocities induced by acoustic oscillations can be of the same order as turbulent velocities. Finally, in closed combustion chambers such as in a gas turbine or in a rocket engine, combustion instabilities can arise from the coupling between pressure oscillations and heat release and impact the engine life cycle or even lead sometimes to catastrophic failures. A proper description of acoustic wave behavior through the boundaries of the computational domain is thus critical and this section presents the method used in the current work to prescribe accurate boundary conditions.

2.7.1 General formulation

As described by Thompson [310], the central concept of the treatment of boundary conditions *"is that hyperbolic systems of equations represent the propagation of waves and that at any boundary some of the wave are propagating into the computational domain while other are propagating out of it. The outward propagating waves have their behavior defined entirely by the solution at and within the boundary and no boundary can be specified for them. The inward propagating waves depend on the solution exterior to the [domain] and therefore require boundary conditions to complete the specification of their behavior."* This section describes how to write the conservation equations into a set of wave equations which represents the waves propagating at characteristic velocities.

Following the compressible Navier-Stokes equations introduced earlier, the conservation equations are recast with the viscous terms on the right-hand side:

$$\frac{\partial \rho}{\partial t} + \frac{\partial \rho u_i}{\partial x_i} = 0 \tag{2.7.1}$$

$$\frac{\partial \rho u_i}{\partial t} + \frac{\partial}{\partial x_j}\left(\rho u_i u_j + p\delta_{ij}\right) = \frac{\partial \tau_{ij}}{\partial x_j} \tag{2.7.2}$$

$$\frac{\partial \rho e_T}{\partial t} + \frac{\partial}{\partial x_i}\left(\left(\rho e_T + p\right) u_i\right) = \frac{\partial}{\partial x_i}\left(-q_i^{\mathrm{IK}} + u_j \tau_{ij}\right) \tag{2.7.3}$$

$$\frac{\partial \rho Y_k}{\partial t} + \frac{\partial \rho Y_k u_i}{\partial x_i} = -\frac{\partial j_{i,k}}{\partial x_i} \quad \text{with } k = 1 \ldots N_S \tag{2.7.4}$$

The vector $\boldsymbol{\mathcal{U}}$ of conservative variables is introduced with the equation:

$$\frac{\partial \boldsymbol{\mathcal{U}}}{\partial t} + \frac{\partial \boldsymbol{\mathcal{F}}^1}{\partial x_1} + \frac{\partial \boldsymbol{\mathcal{F}}^2}{\partial x_2} + \frac{\partial \boldsymbol{\mathcal{F}}^3}{\partial x_3} + \boldsymbol{\mathcal{D}} = 0 \tag{2.7.5}$$

where $\mathcal{F}^k$ is the vector of fluxes in the k direction and $\mathcal{D}$ is a vector of inhomogeneous terms. Considering the characteristic analysis in the x_1 direction, the transverse and inhomogeneous terms can be grouped together in order to focus on a single direction. These terms can be brought back later if needed:

$$\frac{\partial \boldsymbol{\mathcal{U}}}{\partial t} + \frac{\partial \boldsymbol{\mathcal{F}}^1}{\partial x_1} + \boldsymbol{\mathcal{C}} = 0 \tag{2.7.6}$$

The conservation equations (Eqs. (2.7.1)-(2.7.4)) impose the definitions of $\boldsymbol{\mathcal{U}}$ and $\boldsymbol{\mathcal{F}}$ but the choice of the vector $\boldsymbol{U}$ of primitive variables is somewhat arbitrary. Like Baum et al. [12] or Okong'o et al. [220] and unlike Poinsot et al. [240], pressure is chosen over temperature as a convenient primitive variable:

$$\boldsymbol{\mathcal{U}} = \begin{pmatrix} \rho \\ \rho e_T \\ \rho u_i \\ \rho Y_k \end{pmatrix} \quad \boldsymbol{\mathcal{F}} = \begin{pmatrix} \rho u_i \\ (\rho E + p) u_i \\ \rho u_i u_j \\ \rho Y_k u_i \end{pmatrix} \quad \boldsymbol{U} = \begin{pmatrix} \rho \\ p \\ u_i \\ Y_k \end{pmatrix} \tag{2.7.7}$$

It is possible to rewrite Eq. (2.7.6) so that only the primitive variables appear:

$$\frac{\partial \boldsymbol{U}}{\partial t} + A^1 \frac{\partial \boldsymbol{U}}{\partial x_1} + \boldsymbol{C} = 0 \tag{2.7.8}$$

with $A^k = P^{-1} Q^k$ the product of the Jacobian matrices P and Q^k such as:

$$P_{ij} = \frac{\partial \mathcal{U}_i}{\partial U_j} \qquad Q^k_{ij} = \frac{\partial \mathcal{F}^k_i}{\partial U_j} \tag{2.7.9}$$

Assuming the matrix A^k is not singular, its m-th eigenvalue λ_m can be introduced alongside its corresponding left and right eigenvectors l_m and r_m. Equation (2.7.8) can then be written as:

$$\frac{\partial \boldsymbol{U}}{\partial t} + S \boldsymbol{\mathcal{L}} + C' = 0 \tag{2.7.10}$$

where the vector $\boldsymbol{\mathcal{L}}$ contains the wave amplitudes $\mathcal{L}_m$ corresponding to each wave speed λ_m. The matrix S has the right eigenvectors r_m as its columns. The matrix C' is made of the transformed transverse and inhomogeneous terms.

It is possible to show without any loss of generality that the wave speeds and wave amplitudes do not depend on the equation of state since the governing Euler equations (Eqs. (2.7.1)-(2.7.4) with the right-hand sides set to 0) can be written as:

$$\frac{\partial u_i}{\partial t} + u_j \frac{\partial u_i}{\partial x_j} + \frac{1}{\rho}\frac{\partial p}{\partial x_i} = 0 \tag{2.7.11}$$

$$\frac{\partial \rho}{\partial t} + u_j \frac{\partial \rho}{\partial x_j} + \rho \frac{\partial u_j}{\partial x_j} = 0 \tag{2.7.12}$$

$$\frac{\partial p}{\partial t} + u_j \frac{\partial p}{\partial x_j} + \rho c^2 \frac{\partial u_j}{\partial x_j} = 0 \tag{2.7.13}$$

$$\frac{\partial Y_k}{\partial t} + u_j \frac{\partial Y_k}{\partial x_j} = 0 \tag{2.7.14}$$

The speed of sound c, which is actually the isentropic speed of sound, is given by:

$$c^2 = \left(\frac{\partial p}{\partial \rho}\right)_{e,Y_k} + \frac{p}{\rho^2}\left(\frac{\partial p}{\partial e}\right)_{\rho,Y_k} = \frac{1}{\rho \kappa_s} \tag{2.7.15}$$

The derivation is available in Appendix E.1. The generic, EoS-independent wave amplitudes / wave speeds couple in the x_1 direction are:

$$\mathcal{L}_1 = \left(\frac{u_1 - c}{2}\right)\left(\frac{\partial p}{\partial x_1} - \rho c \frac{\partial u_1}{\partial x_1}\right) \quad \text{for } \lambda_1 = u_1 - c \tag{2.7.16}$$

$$\mathcal{L}_2 = u_1 \left(\frac{\partial \rho}{\partial x_1} - \frac{1}{c^2}\frac{\partial p}{\partial x_1}\right) \quad \text{for } \lambda_2 = u_1 \tag{2.7.17}$$

$$\mathcal{L}_3 = u_1 \left(\frac{\partial u_2}{\partial x_1}\right) \quad \text{for } \lambda_3 = u_1 \tag{2.7.18}$$

$$\mathcal{L}_4 = u_1 \left(\frac{\partial u_3}{\partial x_1}\right) \quad \text{for } \lambda_4 = u_1 \tag{2.7.19}$$

$$\mathcal{L}_5 = \left(\frac{u_1 + c}{2}\right)\left(\frac{\partial p}{\partial x_1} + \rho c \frac{\partial u_1}{\partial x_1}\right) \quad \text{for } \lambda_5 = u_1 + c \tag{2.7.20}$$

$$\mathcal{L}_{5+k} = u_1 \left(\frac{\partial Y_k}{\partial x_1}\right) \quad \text{for } \lambda_{5+k} = u_1 \text{ with } k = 1 \ldots N_S \tag{2.7.21}$$

Plugging in these relations into the governing equations (Eqs. (2.7.11)-(2.7.14)) yields:

$$\frac{\partial u_1}{\partial t} + \frac{\mathcal{L}_5 - \mathcal{L}_1}{\rho c} = 0 \tag{2.7.22}$$

$$\frac{\partial u_2}{\partial t} + \mathcal{L}_3 = 0 \tag{2.7.23}$$

$$\frac{\partial u_3}{\partial t} + \mathcal{L}_4 = 0 \tag{2.7.24}$$

$$\frac{\partial \rho}{\partial t} + \frac{1}{c^2}\left(\mathcal{L}_5 + \mathcal{L}_1\right) + \mathcal{L}_2 = 0 \tag{2.7.25}$$

$$\frac{\partial p}{\partial t} + \mathcal{L}_5 + \mathcal{L}_1 = 0 \tag{2.7.26}$$

$$\frac{\partial Y_k}{\partial t} + \mathcal{L}_{5+k} = 0 \text{ with } k = 1 \dots N_S \tag{2.7.27}$$

It is then straightforward to obtain the time variations of the conservative variables in function of the wave amplitudes:

$$\frac{\partial \rho u_1}{\partial t} + u_1 d_4 + \rho d_1 = 0 \tag{2.7.28}$$

$$\frac{\partial \rho u_2}{\partial t} + u_2 d_4 + \rho d_2 = 0 \tag{2.7.29}$$

$$\frac{\partial \rho u_3}{\partial t} + u_3 d_4 + \rho d_3 = 0 \tag{2.7.30}$$

$$\frac{\partial \rho}{\partial t} + d_4 = 0 \tag{2.7.31}$$

$$\begin{aligned}\frac{\partial \rho e_T}{\partial t} + \left(e_T + \frac{p}{\rho}\right) + \rho u_1 d_1 + \rho u_2 d_2 + \rho u_3 d_3 \\ + \sum_{k=1}^{N_S} \rho d_{5+k} \left(\frac{\partial e}{\partial Y_k}\right)_{\rho,p,Y_{l,l\neq k}} + \frac{c_p}{\alpha_v} d_5 = 0\end{aligned} \tag{2.7.32}$$

$$\frac{\partial \rho Y_k}{\partial t} + Y_k d_4 + \rho d_{5+k} = 0 \text{ with } k = 1 \dots N_S \tag{2.7.33}$$

with the vector $\boldsymbol{d}$ as:

$$\boldsymbol{d} = \begin{pmatrix} \frac{\mathcal{L}_5 - \mathcal{L}_1}{\rho c} \\ \mathcal{L}_3 \\ \mathcal{L}_4 \\ \frac{1}{c^2}\left(\mathcal{L}_5 + \mathcal{L}_1\right) + \mathcal{L}_2 \\ \mathcal{L}_5 + \mathcal{L}_1 \\ \mathcal{L}_{5+k} \end{pmatrix} \tag{2.7.34}$$

Note that the energy equation was obtained by developing the $\frac{\partial \rho e_T u_j}{\partial x_j}$ term as follows:

$$\begin{aligned}
\frac{\partial \rho e_T u_j}{\partial x_j} &= -\frac{\partial \rho e_T}{\partial t} = -\frac{\partial \rho e}{\partial t} - \frac{1}{2}\frac{\partial \rho u_i u_i}{\partial t} \\
&= -\left(\frac{\partial \rho e}{\partial \rho}\right)_{p,Y_k}\frac{\partial \rho}{\partial t} - \left(\frac{\partial \rho e}{\partial p}\right)_{\rho,Y_k}\frac{\partial p}{\partial t} \\
&\quad - \sum_k^{N_S}\left(\frac{\partial \rho e}{\partial Y_k}\right)_{\rho,p}\frac{\partial Y_k}{\partial t} - \rho u_i \frac{\partial u_i}{\partial t} - \frac{1}{2}u_i u_i \frac{\partial \rho}{\partial t} \\
&= \left(\frac{\partial \rho e}{\partial \rho}\right)_{p,Y_k} d_4 + \left(\frac{\partial \rho e}{\partial p}\right)_{\rho,Y_k} d_5 + \sum_k^{N_S}\rho\left(\frac{\partial e}{\partial Y_k}\right)_{\rho,p} d_{5+k} \\
&\quad + \rho u_1 d_1 + \rho u_2 d_2 + \rho u_3 d_3 + \frac{1}{2}u_i u_i d_4 \\
&= \left(\frac{\partial \rho e_T}{\partial \rho}\right)_{p,Y_k} d_4 + \left(\frac{\partial \rho e}{\partial p}\right)_{\rho,Y_k} d_5 \\
&\quad + \sum_k^{N_S}\rho\left(\frac{\partial e}{\partial Y_k}\right)_{\rho,p} d_{5+k} + \rho u_1 d_1 + \rho u_2 d_2 + \rho u_3 d_3
\end{aligned}$$

The energy derivatives are given in Appendix E.1. Other useful relations which govern variables such as temperature or flow rate can be obtained similarly (see Appendix F):

$$\frac{\partial T}{\partial t} + \frac{T\alpha_v\left(\mathcal{L}_5 + \mathcal{L}_1\right)}{\rho c_p} - \frac{\mathcal{L}_2}{\rho \alpha_v} + \frac{1}{\alpha_v}\sum_k^{N_S}\mathcal{L}_{5+k}\frac{\rho_{,k}}{\rho} = 0 \tag{2.7.35}$$

$$\frac{\partial \rho u_1}{\partial t} + \frac{\left(\mathrm{Ma}+1\right)\mathcal{L}_5 + \left(\mathrm{Ma}-1\right)\mathcal{L}_1}{c} + u_1\mathcal{L}_2 = 0 \tag{2.7.36}$$

The number of boundary conditions that need to be prescribed is equal to the number of the incoming waves in the computational domain [310]. Thus, for a subsonic inflow, since only λ_1 is negative, all the other waves are propagating inside the domain and thus need to be prescribed. On the other hand, for a subsonic outflow, only $\mathcal{L}_1$ needs to be set as all the other waves escape the computational domain.

2.7.2 Subsonic reflecting inflow

As it was just mentioned, $4 + N_S$ variables need to be set. Usually, the temperature and the mixture composition are fixed. It is then possible to either set the velocities or set the mass flowrates (each counting for 3 variables obviously):

- If the velocities are set, then $\mathcal{L}_5 = \mathcal{L}_1$ and $\mathcal{L}_3 = \mathcal{L}_4 = \mathcal{L}_{5+k} = 0$. $\mathcal{L}_2$ is set through the temperature equation (Eq. 2.7.35) while only $\mathcal{L}_5$ is computed from the flow inside

the domain:

$$\mathcal{L}_5 = (u_1 + c)\left(\frac{\partial p}{\partial x_1} + \rho c \frac{\partial u_1}{\partial x_1}\right) \tag{2.7.37}$$

$$\mathcal{L}_2 = \frac{T\alpha_v^2\left(\mathcal{L}_5 + \mathcal{L}_1\right)}{c_p} \tag{2.7.38}$$

- If the mass flowrates are set, then a relationship between $\mathcal{L}_5$ and $\mathcal{L}_1$ is needed. Using Equation 2.7.36:

$$\mathcal{L}_5\left(u_1 + c\right) + \mathcal{L}_1\left(u_1 - c\right) = -u_1 c^2 \mathcal{L}_2 \tag{2.7.39}$$

Using once again the temperature equation yields:

$$\mathcal{L}_5\left(u_1 + c\right) + \mathcal{L}_1\left(u_1 - c\right) = -\frac{u_1 c^2 T\alpha_v^2\left(\mathcal{L}_5 + \mathcal{L}_1\right)}{c_p} \tag{2.7.40}$$

$$\mathcal{L}_5\left(u_1 + c + \frac{u_1 c^2 T\alpha_v^2}{c_p}\right) = \mathcal{L}_1\left(-u_1 + c - \frac{u_1 c^2 T\alpha_v^2}{c_p}\right) \tag{2.7.41}$$

$$\mathcal{L}_5\left(\mathrm{Ma} + 1 + \frac{u_1 c T\alpha_v^2}{c_p}\right) = \mathcal{L}_1\left(-\mathrm{Ma} + 1 - \frac{u_1 c T\alpha_v^2}{c_p}\right) \tag{2.7.42}$$

$$\mathcal{L}_5 = \mathcal{L}_1 \frac{1 - \mathrm{Ma} - \frac{u_1 c T\alpha_v^2}{c_p}}{1 + \mathrm{Ma} + \frac{u_1 c T\alpha_v^2}{c_p}} \tag{2.7.43}$$

For the transverse flowrates, the equations are much simpler:

$$\mathcal{L}_3 = -\frac{u_2}{\rho}\left(\mathcal{L}_2 + \frac{\mathcal{L}_5 + \mathcal{L}_1}{c^2}\right) \tag{2.7.44}$$

$$\mathcal{L}_4 = -\frac{u_3}{\rho}\left(\mathcal{L}_2 + \frac{\mathcal{L}_5 + \mathcal{L}_1}{c^2}\right) \tag{2.7.45}$$

$$\tag{2.7.46}$$

Note that with the ideal gas EoS, this simplifies to:

$$\mathcal{L}_1 = \mathcal{L}_5 \frac{1 + \gamma \mathrm{Ma}}{1 - \gamma \mathrm{Ma}} \tag{2.7.47}$$

2.7.3 Subsonic non-reflecting inflow

To obtain proper physical models for the relaxation factor for each variables, additional assumptions are required. For example, one has to assume that the temperature fluctuations are only caused by entropic waves and not by acoustic waves. Thus, the temperature variation in Eq. 2.7.35 cannot depend on the acoustic waves amplitudes $\mathcal{L}_1$ and $\mathcal{L}_5$:

$$\frac{\partial T}{\partial t} - \frac{\mathcal{L}_2}{\rho \alpha_v} = 0 \tag{2.7.48}$$

Since the desired response is of the form $T_\infty - e^{-Kt}(T_0 - T_\infty)$, which is a solution of the system $\frac{\partial T}{\partial t} = -K(T - T_\infty)$, the following relation holds:

$$\mathcal{L}_2 = -\rho\alpha_v K\left(T - T_\infty\right) \tag{2.7.49}$$

Similarly, for the acoustic wave amplitude, one obtains:

$$\mathcal{L}_5 = \rho c\frac{1 - \mathrm{Ma}^2}{2}K\left(u - u_\infty\right) \tag{2.7.50}$$

Note that K in these 2 equations has a dimension of a frequency and in practice, should be proportional to $\frac{c}{l_c}$, with l_c a characteristic acoustic length in a direction normal to the boundary.

For reacting rocket applications, it is important to have boundary conditions that, at the same time:

- conserve the mass flow rate over time so that the combustion is not perturbed by overall changes in the mixture ratio
- allow control of the reflectivity of the inlets. While the feedback from the feed lines to the chamber needs to be modeled correctly using reflective boundary conditions, initial transients for example require that unphysical waves exit the domain without perturbing the mass flow rate

So following a similar logic as before for the acoustic wave amplitude, one obtains:

$$\mathcal{L}_5 = c\frac{1 - \mathrm{Ma}^2}{2}K\left(\rho u - (\rho u)_\infty\right) \tag{2.7.51}$$

Looking over the literature, it is unclear whether such constant-mass, non-reflecting boundary condition for an arbitrary equation of state is widely used but it is important to include it for the rocket engine flows of interest in this work.

2.7.4 Subsonic non-reflecting outflow

This time, all the wave amplitudes are computed using one-sided differences except for $\mathcal{L}_1$. In order to ensure a well-posed problem, Baum et al. [12] suggested $\mathcal{L}_1 = K\left(p - p_\infty\right)$ where K is a parameter which determines the rate at which the average pressure in the domain

relaxes towards the imposed far-field pressure. K can be set as a constant or can be a function of the Mach number across the boundary.

CHAPTER III

NUMERICAL IMPLEMENTATION AND VERIFICATION

As mentioned in the introduction, solving the Navier-Stokes equation under the flow conditions typically found in a rocket engine is very challenging. This chapter presents the numerical methods used to overcome these issues. A brief introduction to the finite volume method is presented first alongside the time integration schemes, including the ones used to compute the chemical source terms. The spatial integration scheme is discussed next. It needs to be stable around the very large density gradients between the non-premixed reactant streams while capturing the turbulent structures that are crucial for the subsequent mixing and burning of these reactants. To this end, the current flow solver uses a hybrid scheme which switches locally and dynamically between a central scheme and an upwind scheme. This central scheme, similar to the historical MacCormack scheme [169], will be described first. The details of the upwind scheme will be then discussed before finally characterizing the local and dynamic switch between the two schemes. The properties of this scheme are then evaluated on simple one-dimensional test cases. The last section discusses a few other numerical issues such as the code performance and the real gas iterative solvers.

3.1 The finite volume method

The Navier-Stokes equations describing the flow evolution and introduced in Chapter 2 can be recast as:

$$\frac{\partial}{\partial t}\mathbf{Q} + \frac{\partial}{\partial x}\mathbf{F}_x + \frac{\partial}{\partial y}\mathbf{F}_y + \frac{\partial}{\partial z}\mathbf{F}_z = \mathbf{S} \tag{3.1.1}$$

Equation 3.1.1 describes the time evolution of the state vector $\mathbf{Q}$ following the principles of conservation of mass, momentum and energy. $\mathbf{F}$ represents the fluxes of the state vector through the faces of the computational cells that are used to discretized the computational domain. The source terms $\mathbf{S}$ can produce or destroy these state variables. Each computational cell has a volume $\mathcal{V}_{\text{cell}}$ and its interface with its surrounding cells has an area $\mathcal{A}_{\text{cell}}$.

Integrating Eq. 3.1.1 over a given computational cell yields:

$$\iiint_{\mathcal{V}_{\text{cell}}} \frac{\partial}{\partial t}\mathbf{Q}dV + \iiint_{\mathcal{V}_{\text{cell}}} \left(\frac{\partial}{\partial x}\mathbf{F}_x + \frac{\partial}{\partial x}\mathbf{F}_y + \frac{\partial}{\partial x}\mathbf{F}_z\right) dV = \iiint_{\mathcal{V}_{\text{cell}}} \mathbf{S}dV \tag{3.1.2}$$

This can be further transformed using the property of commutativity between the spatial integration and the time differentation and applying the Green's theorem:

$$\frac{\partial}{\partial t}\iiint_{\mathcal{V}_{\text{cell}}} \mathbf{Q}dV + \oint_{\mathcal{A}} (\mathbf{F}_x \cdot d\mathbf{A}_x + \mathbf{F}_y \cdot d\mathbf{A}_y + \mathbf{F}_z \cdot d\mathbf{A}_z) = \iiint_{\mathcal{V}_{\text{cell}}} \mathbf{S}dV \tag{3.1.3}$$

where $\mathbf{A}_x$, $\mathbf{A}_y$ and $\mathbf{A}_z$ represent the vector component of the normals to the cell faces. To complete the discretization of the governing equations, each computational cell is assumed to be an hexahedron with quadrilateral faces, whose topology is equivalent to a cube. This is commonly called a curvilinear or structured grid. In such grid, a computational cell can be identified by its coordinates (i, j, k) and its 6 faces are by convention located at $(i \pm \frac{1}{2}, j, k)$, $(i, j \pm \frac{1}{2}, j, k)$ and $(i, j, k \pm \frac{1}{2})$. Discretizing the Cartesian fluxes into the fluxes through each face of surface $\mathcal{A}_k$ and considering now $\mathbf{Q}$ and $\mathbf{S}$ as volume-averaged over the cell yields:

$$\delta\mathbf{Q} = -\frac{\Delta t}{\mathcal{V}_{\text{cell}}} \sum_{k=1\ldots6} \mathbf{F}_k \Sigma_k + \mathbf{S}\Delta t \tag{3.1.4}$$

with $\mathbf{F}_k = F_x\vec{n}_x + F_y\vec{n}_y + F_z\vec{n}_z$ the flux normal to the surface k.

3.2 Temporal integration schemes

3.2.1 MacCormack time integration

The time integration of Eq. 3.1.4 is performed using the MacCormack time integration method [169], equivalent to a two-stage Runge-Kutta method. The integration of the temporal derivative is split into two integration stages with the use of finite difference:

- A predictor stage: $\mathbf{Q}^\star = \mathbf{Q}^n + d\mathbf{Q}^n$
- A corrector stage: $\mathbf{Q}^{n+1} = \frac{1}{2}\left(\mathbf{Q}^n + \mathbf{Q}^\star + d\mathbf{Q}^\star\right)$

where the $d\mathbf{Q}$ increments are computed following Eq. 3.1.4 using the appropriate know state vector $\mathbf{Q}^n$ or $\mathbf{Q}^\star$. The superscript $\star$ indicates that the quantities are being evaluated using intermediate, predictor values while the superscript n denotes quantities computed using values from the previous time-step. These state vectors and their associated fluxes are

evaluated alternatively using forward (+) or backward (−) differencing. This order varies between each time-step and within the predictor-corrector loop. It is done as to achieve a central scheme while avoiding directional biasing and will be described in Section 3.3.2. The resulting integration is second-order accurate in time as the error scales as $(\Delta t)^2$.

3.2.2 Timestep determination

Since the time integration follows an explicit algorithm, there are stability and accuracy constraints on how large the time-step Δt can be set. To achieve time-accurate simulations, an upper bound is set by the physical time-scale of the modeled process and the whole computational domain needs to be integrated over the same time-step. Numerical theory [305] defines the maximum stable time-step as:

$$\Delta t = \mathrm{CFL} \times \min\left(\frac{\mathrm{V}}{v_w}\right) \tag{3.2.1}$$

where CFL is the Courant-Friedrich-Levy number and v_w is a wave velocity and determines how quickly information travels in the computational domain. For this explicit scheme to be stable, the local time-step cannot allow information to propagate further than a fraction of the local grid size over a single integration. This is the physical significance of Eq. 3.2.1. Information can propagate in the fluid through several physical processes such as advection, pressure fluctuations (acoustics), thermal diffusion, viscous diffusion or mass diffusion. Usually the propagation thanks to advection and acoustics are grouped together into an equivalent inviscid (or convective) velocity v_c:

$$v_c = |\mathbf{u} \cdot d\mathbf{A}_i| + |\mathbf{u} \cdot d\mathbf{A}_j| + |\mathbf{u} \cdot d\mathbf{A}_k| + c|d\mathbf{A}| \tag{3.2.2}$$

where $|\mathbf{u} \cdot d\mathbf{A}_i|$ represents the absolute value of the velocity in the i-direction and $|d\mathbf{A}|$ represents the magnitude of the surface normal vectors. For the diffusion processes, let us consider a simple parabolic, one dimensional partial differential equation:

$$\frac{\partial U}{\partial t} = -\lambda \frac{\partial^2 U}{\partial x^2} \tag{3.2.3}$$

Technically, such equation implies instantaneous propagation of disturbances and thus an infinite propagation velocity. However, numerical analysis reveals that for explicit time

integration, an equivalent speed of transmission of information through diffusion is:

$$v_d = K\lambda \frac{|d\mathbf{A}|^2}{\mathrm{V}} \tag{3.2.4}$$

where K is an experimental constant whose value needs to be greater or equal than 2 [7]. For the diffusion of momentum, $\lambda = \nu$, the kinematic viscosity. For the diffusion of species, a valid approximation is $\lambda = \max(\mathcal{D}_{i,m})$, the largest mixture diffusion coefficient. For the energy equation, we have $\rho c_V \frac{\partial T}{\partial t} = -\kappa \frac{\partial^2 T}{\partial x^2}$ and thus $\lambda = \frac{\kappa}{\rho c_V}$ which is equal to $\frac{\gamma\mu}{\rho \mathrm{Pr}}$ for a calorically perfect, constant-Prandtl gas. For gases, usually $\gamma/\mathrm{Pr} > 1$ and diffusion of temperature is faster than momentum diffusion. Also, unless very light species are involved, diffusion of temperature is faster than species diffusion. However, these assumptions might not hold in every situation with real gases and detailed reaction mechanisms involving Hand H_2 so a more general definition for v_d is adopted. From previous works using the MacCormack integration technique, K is set to 2 [296] and the coefficient for each type of diffusion is evaluated with only the largest one being retained:

$$v_d = 2\max(\lambda) \frac{|d\mathbf{A}|^2}{\mathrm{V}} \tag{3.2.5}$$

The final expression for the maximum stable time step is thus:

$$\Delta t = \mathrm{CFL} \times \min\left(\frac{\mathrm{V}}{v_c + v_d}\right) \tag{3.2.6}$$

Typically, when the local mesh Reynolds number is large, $v_c \gg v_d$ and viscous effects can be neglected in the stability analysis. This might no longer true in the near-wall region or near a flame anchor point for example, where local velocity is low and grid spacing can become really small. Finally, the optimal CFL number in Eq. 3.2.6 cannot be determined exactly but from experience [296], a good approximation is $1/N$ where N is the spatial accuracy of the MacCormack scheme, that is $N = 2$ or 4 in this study. No particular numerical instability was observed using a CFL of 0.5 with the hybrid scheme described in the following sections.

3.2.3 Integration of the chemical source terms

Independent of the turbulent combustion models that look at the interaction between the flame and the turbulence, purely mathematical solutions are required to accurately integrate

the source terms that appear on the right-hand side of the species equations. Different methods are available in the current solver and which one is used depends on the magnitude of the chemical time scales with respect to the fluid mechanics timestep derived in Eq. 3.2.6 as well as a usual cost-accuracy compromise. The two main methods are:

- the Variable-coefficient Ordinary Differential Equations solver in its double precision version (DVODE) [24]. When the DVODE solver is used, the stiff method with internally generated full Jacobian is chosen.

- a simple explicit Euler method provides a lower-cost alternative to the DVODE solver. As it will be shown, it provides a good cost-accuracy compromise for a number of iterations usually comprised between 1 and 20. Obviously, with a single iteration, this means the chemical source term is assumed to be constant over the LES timestep, which is only valid when the chemical time scales are of the order of the fluid mechanics time scales.

A general method for computing the chemical timescales is presented by Eppard [64] and can be used offline to evaluate the timescales over an instantaneous flow-field. This will be illustrated in Chapter 4.

3.3 Spatial integration schemes

As it has already been mentioned, a typical flow inside a liquid rocket engine is characterized by large density gradients between a weakly compressible liquid and a high-speed compressible turbulent gas stream. Focusing on the density gradients, there are two main types of numerical methods to treat them:

- The sharp interface methods come from a multi-phase background. The fluids are assumed to be immiscible and the interface is capture through various methods such volume-of-fluid, level-set or front-tracking.

- The diffused interface methods where the interface is not tracked directly and the same equation of state is used on both sides. Instead the numerical scheme chosen tries to maintain the interface sharp but finite. The numerical schemes include Essentially

Non-Oscillatory (ENO) schemes [279], their derivatives such as WENO (Weighted Essentially Non-Oscillatory) schemes [118, 278] or WCNS (Weighted Compact Nonlinear Schemes) [209] or Discontinuous Galerkin (DG) methods [92].

The diffuse interface methods for multi-phase flows or flows with large density gradients intersect with the shock-capturing methods used for compressible flows. While low-order upwind, shock-capturing schemes are very dissipative and cannot accurately resolve structures in smooth regions of the flow, hybrid central-upwind schemes [81] can accurately capture both flow discontinuities such as shocks and smooth structures such as turbulence. The idea here is to use such a hybrid scheme to deal with the large density gradients encountered in high-pressure liquid rocket engine flows. The work by Genin is the basis for this work and only a few highlights and key points related to the current application will be recalled here.

3.3.1 Hybrid scheme for turbulent flows with large density gradients

Following the finite volume method from the previous section, the fluxes through the cell faces need to be evaluated in order to advance the time integration. To capture both the large density gradients at the edges of compressed liquid jets and the turbulent structures in the shear layers surrounding said jets, a hybrid flux evaluation is required:

$$\mathbf{F}_{i+\frac{1}{2}} = \Lambda_{i+\frac{1}{2}}\mathbf{F}^{c}_{i+\frac{1}{2}} + (1-\Lambda_{i+\frac{1}{2}})\mathbf{F}^{u}_{i+\frac{1}{2}} \tag{3.3.1}$$

$\mathbf{F}^c$ is the flux obtained through a central scheme with low dissipation to capture smooth turbulent structures and $\mathbf{F}^u$ is the flux obtained through a upwind scheme to capture large, sharp density gradients. For this work, the switch variable Λ can only be valued as 0 or 1 so that the scheme actually switches between the flux evaluations and does not blend them. The main reason behind this is to avoid computing the flux evaluation twice for the same cell. Following the recommendations from Genin [81], the flow sensor used to detect discontinuities or large gradients of variable ϕ is given by:

$$S_{\phi,i} = \begin{cases} \frac{|\phi_{i+1}-2\phi_i+\phi_{i-1}|}{|\phi_{i+1}-\phi_i|+|\phi_i-\phi i-1|} - C_{\phi}^{\text{cutoff}} & \text{if } |\phi_{i+1}-2\phi_i+\phi_{i-1}| \geq \epsilon_{\phi}\phi_i \\ -C_{\phi}^{\text{cutoff}} & \text{otherwise} \end{cases} \tag{3.3.2}$$

For the current applications, the variable ϕ is either pressure p or density ρ. Upwinding is desired at the edges of the liquid jets (density sensor) but also inside them when the compressible solver can generate large pressure fluctuations due to the nearly incompressible nature of the fluid there. Note that the sensors will pick up both rapid variations and significant gradients. The optimization of these parameters for the current work and in particular real gas flows is shown in Appendix J. Unless otherwise specified, the default values from here on out are $(\epsilon_\rho, \epsilon_p, C_\rho^{\text{cutoff}}, C_p^{\text{cutoff}}) = (0.05, 0.05, 0.125, 0.5)$. More aggressive upwinding is obtained by decreasing the values of ϵ_ϕ. Finally, the switch function is defined as:

$$\Lambda_{i+\frac{1}{2}} = \begin{cases} 1 & \text{if } \max(S_{\rho,i}, S_{\rho,i+1}, S_{p,i}, S_{p,i+1}) \leq 0 \\ 0 & \text{otherwise} \end{cases} \tag{3.3.3}$$

3.3.2 MacCormack central scheme

A central scheme needs to be selected to capture the smooth, turbulent features of the flows of interest. Compact schemes are well suited for such applications, especially incompressible flows and single-species flows. The do suffer from a high computational cost and complex implementation because of filtering requirements. Recent developments in compact schemes [68] might overcome some of these issues for applications in complex geometries but for this work, a simpler central scheme is chosen. While pure central schemes exhibit numerical oscillations naturally and require either filtering or artificial dissipation, the MacCormack method [169] includes built-in dissipation by using two stages for the time integration, as described in Section 3.2.1. For each of this stage, the spatial integration will have a different bias, resulting in a central scheme with some built-in dissipation. For the original MacCormack method, which can be shown to be second-order accurate in space and time [81], backward (denoted by a $-$ superscript) and forward (denoted by a $+$ superscript) first order extrapolations are used alternatively to get the properties and fluxes at the cell interface:

$$\mathbf{F}^+_{i+\frac{1}{2}} = \mathbf{Q}_{i+1}\mathbf{u}_{i+1} \tag{3.3.4}$$

$$\mathbf{F}^-_{i+\frac{1}{2}} = \mathbf{Q}_{i}\mathbf{u}_{i} \tag{3.3.5}$$

Table 5: Sequence of alternating extrapolation biases for the MacCormack spatial and temporal scheme.

Iteration	I-direction Predictor/Corrector	J-direction Predictor/Corrector	K-direction Predictor/Corrector
n	+/-	+/-	+/-
n+1	-/+	+/-	+/-
n+2	+/-	-/+	+/-
n+3	-/+	-/+	+/-
n+4	+/-	+/-	-/+
n+5	-/+	+/-	-/+
n+6	+/-	-/+	-/+
n+7	-/+	-/+	-/+

The alternative combination of extrapolations within the MacCormack predictor/corrector stages lead to a higher-order scheme if the correct backward/forward sequence is followed. For the current first-order extrapolation, a sequence such as the one shown in Table 5 results in a second-order accurate scheme in space. It can be seen that the I-direction bias changes every iteration while it changes every two iterations for the J-direction and every four iterations for the K-direction. This works especially well when the main flow direction is in the I-direction. While this central scheme can be extended to higher orders [102], only some simple test cases shown in this will use a central scheme higher than second-order, and the reader is referred to the work of Genin [81] for a derivation of fourth-order MacCormack scheme used for this work.

3.3.3 Upwind flux-difference splitting scheme

Even with its built-in dissipation and additional artificial dissipation such as the one by Jameson [115], the MacCormack central scheme by itself cannot be applied to all high-pressure liquid rocket engine flows. Previous efforts [175, 181] were able to achieve super-critical injection in a rocket configuration, but the gradients associated with a trans-critical injection were too large for this central scheme to handle. Instead, an upwind method is required in the regions of large gradients. The approach selected for this work is a flux-difference splitting (FDS) scheme because of its low computational overhead and of

its capability in non-cartesian grids. The inherently low order of the scheme can be increased by using a Monotone Upstream Centered Scheme for Conservation Laws (MUSCL) re-construction technique. This technique evaluates the left and right states at each cell interface, setting up the resolution of a Riemann problem. For this study, an approximate Riemann solver of type HLL is chosen as exact Riemann solvers are too computationally intense for arbitrary equations of state.

3.3.3.1 MUSCL interpolation

Through the MUSCL approach from van Leer [322], the left and right states at a cell interface in direction i can be expressed in the most general fashion as:

$$U^L_{i+\frac{1}{2}} = U_i + \frac{\epsilon(1-\xi_i)}{4}\left[(1-\kappa)\,\phi(r^+_{i-\frac{1}{2}}) + (1+\kappa)\,\phi(\frac{1}{r^+_{i-\frac{1}{2}}})\phi(r^+_{i-\frac{1}{2}})\right](U_i - U_{i-1}) \tag{3.3.6}$$

$$U^R_{i+\frac{1}{2}} = U_{i+1} - \frac{\epsilon(1-\xi_{i+1})}{4}\left[(1-\kappa)\,\phi(r^-_{i+\frac{3}{2}}) + (1+\kappa)\,\phi(\frac{1}{r^-_{i+\frac{3}{2}}})\phi(r^-_{i+\frac{3}{2}})\right](U_{i+2} - U_{i+1}) \tag{3.3.7}$$

This includes the use of a limiter ϕ to ensure the monotonicity of the reconstruction technique. The extrapolated values at the cell interface cannot create local extrema of the given field. Mathematically, this limit on the extrapolated values is evaluated through the variable r:

$$r^+_{i+\frac{1}{2}} = \frac{U_{i+2} - U_{i+1}}{U_{i+1} - U_i} \tag{3.3.8}$$

$$r^-_{i+\frac{1}{2}} = \frac{U_i - U_{i-1}}{U_{i+1} - U_i} = \frac{1}{r^+_{i-\frac{1}{2}}} \tag{3.3.9}$$

Several simplifications can be applied to the general expressions of Equations 3.3.6 and 3.3.7. The coefficients ξ_i are use to "flatten" post-shock oscillations in compressible flows with strong shocks. For rocket applications, this is not an issue and so these coefficients can be assumed to be null. A basic, first-order piecewise constant FDS scheme is obtained with $\epsilon = 0$ while higher order can be achieved with $\epsilon = 1$. In the general case, the order of the scheme is then controlled by κ, with possible values of -1 (second-order upwind), 1 (second-order central) and $\frac{1}{3}$ (third-order upwind biased). However, depending on the limiter ϕ

that is used, this dependency on κ can disappear. For this work, the Monotonized Central Limiter (MCL) by van Leer [321] is selected for its ability to not sharpen excessively large gradients, an unnecessary feature when not dealing with shocks [81]. One of the property of the MCL is that it is symmetric: $\frac{\phi(r)}{r} = \phi\left(\frac{1}{r}\right)$. Taking all this into account, Equations 3.3.6 and 3.3.7 become:

$$U^L_{i+\frac{1}{2}} = U_i + \frac{\epsilon}{2}\phi(r^+_{i-\frac{1}{2}})\,(U_i - U_{i-1}) \tag{3.3.10}$$

$$U^R_{i+\frac{1}{2}} = U_{i+1} - \frac{\epsilon}{2}\phi(r^-_{i+\frac{3}{2}})\,(U_{i+2} - U_{i+1}) \tag{3.3.11}$$

Another property of the MCL is that it satisfies the Total Variation Diminishing (TVD) condition, which states that the total variation $\sum_i |U_{i+1} - U_i|$ decreases for each iteration. This leads to a so-called monotonic scheme [100]. For real gas applications, κ and ϵ are actually dependent on the compressibility of the gas. If the fluid is clearly in a compressed liquid state ($Z < 0.8$ usually), the order of the upwind scheme can be dropped in order to dissipate large pressure oscillations that the compressible solver can generate when the fluid becomes less compressible. This will be illustrated in the Chapter 5 where Figure 65 shows the extent of the MUSCL scheme for a typical trans-critical flow. When using the MCL that means the scheme drops to first order in the compressed liquid. Also, for the current application, the reconstruction technique is applied to the set of primitive variables $(\bar{\rho}, \widetilde{u}_i, \bar{p}, \bar{\rho}_k)$. While the reconstruction technique described above guarantees the monotonicity for each of these primitive variables, care must be applied to ensure the TVD condition over all variables and to make sure the gradient does not change sign at the interface. The latter is enforced by monitoring the sign of $(U_{i+1} - U_i)(U^R_{i+\frac{1}{2}} - U^L_{i+\frac{1}{2}})$. If it becomes negative, the MUSCL reconstruction is over-written by the following expressions [81]:

$$U^{L,\text{new}}_{i+\frac{1}{2}} = \frac{1}{2}\left(U^{L,\text{old}}_{i+\frac{1}{2}} + U^{R,\text{old}}_{i+\frac{1}{2}}\right) = U^{R,\text{new}}_{i+\frac{1}{2}} \tag{3.3.12}$$

The monotonicity of variables outside of $(\bar{\rho}, \widetilde{u}_i, \bar{p}, \bar{\rho}_k)$ also need to be enforced. For temperature, which is used in the Riemann solver described below, the following kind of relationship needs to be verified:

$$\max(T_i, T_{i+1}) \geq T^L_{i+\frac{1}{2}} \geq \min(T_i, T_{i+1}) \tag{3.3.13}$$

If it is not the case, one of density or pressure interpolated values needs to be modified. Genin [81] recommends modifying the pressure interpolation for supersonic flows containing shocks however for real gas applications, it was found that recomputing the extrapolated density based on the new temperature $T^L_{i+\frac{1}{2}}$ produced less numerical oscillations. This will be the method used for this work. Similarly, species mass fractions also need to be monotonic. The most stable solution is to compare the limiters used for the density and each partial density $\bar{\rho}_k$ and to apply the most limiting reconstruction among these to all densities. Mathematically, denoting $\bar{\rho}_0$ the regular density $\bar{\rho}$, this is expressed as:

$$\bar{\rho}^L_{k,i+\frac{1}{2}} = \bar{\rho}_{k,i} + \frac{\epsilon}{2} \min_{k=0...N_S} \left(\phi(r^+_{i-\frac{1}{2}}(\bar{\rho}_k)) \right) (\bar{\rho}_{k,i} - \bar{\rho}_{k,i-1}) \tag{3.3.14}$$

$$\bar{\rho}^R_{i+\frac{1}{2}} = \bar{\rho}_{i+1} - \frac{\epsilon}{2} \min_{k=0...N_S} \left(\phi(r^-_{i+\frac{3}{2}}(\bar{\rho}_k)) \right) (\bar{\rho}_{k,i+2} - \bar{\rho}_{k,i+1}) \tag{3.3.15}$$

3.3.3.2 Approximate Riemann solver

The Riemann problem deals with the solution of a conservation equation over an initial field that is piecewise constant with a central discontinuity. Mathematically, this can be summarized by:

$$u(x, t = 0) = \begin{cases} u_L \quad \text{for} \quad x < 0 \\ \\ u_R \quad \text{for} \quad x >= 0 \end{cases} \tag{3.3.16}$$

Physically, this could be thought as two gases with different temperatures/densities separated initially by an infinitely thin wall. At time $t = 0$, the wall is removed and the resulting evolution is computed. The numerical method used to compute this solution is called a Riemann solver. There are two classes of Riemann solvers:

- For a linear conservation equation, or for a non-linear conservation equation with very simple thermodynamics, it is possible to compute an exact solution to the Riemann problem. This gets very computationally expensive when the wave speeds depend strongly on the flow conditions, requiring complex iterative methods. For more details, the reader is referred to the large body of work discussing the original Godunov solver [88].

- For most practical applications, approximate Riemann solvers have been designed to reduce the computational cost. This is especially valuable for high-temperature flows, magneto-hydrodynamics and flows with real gas effects.

For this study, the HLLC modification by Toro [311] of the original HLL approximate solver by Harten et al. [100] is selected. The original HLL solver was developed by Harten, Lax and van Leer and expressed the hyperbolic system of conservation laws in an integral form. It was limited to 2 initial waves emanating from a discontinuity, with the wave speeds the main unknowns of the solver. This worked well for shocks but was very dissipative for contact discontinuities. The contact wave was added by Toro to create the HLLC solver, with a contact wave speed approximated by the particle velocity, that is the velocity at which a particle would oscillate when an acoustic wave travels by:

$$u^* = \frac{1}{2}(u_L + u_R) - \frac{1}{2}\frac{p_R - p_L}{\frac{1}{2}(\rho_L + \rho_R)\frac{1}{2}(c_L + c_R)} \tag{3.3.17}$$

This is similar to the wave speed proposed by Davis [55] and adopted here for this work. It illustrates the fact that the middle wave speed can be expressed without recomputing other state variables and/or a new speed of sound [62, 254] which is computationally expensive for real gas computations. One of the shortcoming of the Davis method is that it is more dissipative but it is not critical for the current subsonic rocket applications as it would be for a shock-capturing application. Once again, for a more complete derivation of the model, the reader is referred to Genin [81]. The formulation of the hybrid scheme being now complete, the next section will verify its implementation using classical one-dimensional cases.

3.4 One-dimensional verification of the schemes

3.4.1 Extending the Shu-Osher testcase

The Shu-Osher problem [279] is a classical test that has been extensively used in the validation of numerical schemes for compressible turbulent flows, including the current hybrid spatial scheme [81]. It was designed to evaluate the ability of a code to simultaneously capture shocks and smooth variations of the flowfield with accuracy. This is done by computing the propagation of a shock wave through afield of fluctuating density. The original setup

uses non-dimensional quantities and is thus not applicable for non-ideal equations of state. The current solver has already been validated using this non-dimensional setup using the calorically perfect equation of state [81]. This setup needs to be modified to consider the passage of a shock wave through compressed nitrogen that exhibits non-ideal compressibility in both pre- and post-shock regions. Two different cases will be run:

- A dimensional weakly non-ideal case to compare the results with the on obtained by Terashima et al. [308] with a high-order scheme
- A dimensional strongly non-ideal case to investigate the performance of the solver in more compressible regimes

For all the results presented in this section, the hybrid scheme uses very similar parameters than the ones used for the rocket injector flows later on. In particular, no flattening procedure is performed and the hybrid switch coefficients are $(\epsilon_\rho, \epsilon_p, C_\rho^{\text{cutoff}}, C_p^{\text{cutoff}}) = (0.025, 0.025, 0.0625, 0.25)$. Also, the Davis estimate for the middle wave-speed is chosen over the Einfeldt one since it doesn't require an extra costly computation of the sound speed from conservative variables in the Roe-averaged state.

3.4.1.1 Slightly non-ideal test case

The first set of dimensional initial conditions correspond to the ones used by Terashima et al. [308] for a similar super-critical test with a shock wave with a Mach number $M = 1.36$. They are expressed in terms of (u, ρ, p) as these are the natural variables for the Rankine-Hugoniot relations that govern the conditions across a shock. The left and right initial states are:

$$(u, \rho, p) = \begin{cases} \left(815.15, 192.85, 41.333 \times 10^6\right) & \text{for } -5 \leq x \leq -4 \\ \left(0.00, 50.0(1.0 + 0.2\sin(5x), 4.0 \times 10^6\right) & \text{for } -4 < x \leq +5 \end{cases} \tag{3.4.1}$$

Following the approach by Terashima et al., the discontinuity is smoothed using an error function:

$$U = (1 - f_s)\, U_{\text{left}} + f_s U_{\text{right}} \quad \text{with} \quad f_s = 0.5 + 0.5\,\text{erf}\left(\frac{s}{C_\varepsilon \Delta x}\right) \tag{3.4.2}$$

where s is the signed distance from the interface, erf is the Gauss error function, Δx is the local grid spacing and C_ε is the smoothing parameter. A value of 3 is usually considered as adequate to smooth the interface [209].

The fluid is simply pure nitrogen. The non-ideality of this case is limited with a compressibility factor varying from $Z = 0.95$ in the pre-shock region to $Z = 1.15$ in the post-shock region and this case is mostly performed to establish a comparison with a high-order scheme such as the sixth-order compact scheme with Local Artificial Viscosity by Terashima et al. [308]. For the original, non-dimensional Shu-Osher test case, Shu and Osher show the profiles at $t = 1.8$, with the shock front being located around $x = 2.4$ after starting from $x = -4$. For their super-critical case, Terashima et al. perform their simulation up to $t = 5.903$ ms, time over which the shock wave travels approximately 6 meters. The boundary conditions for this case are summarized in Table 6.

Table 6: Boundary conditions for the slightly non-ideal extension of the Shu-Osher test case

Inlet $x = -5$m:	**Supersonic Dirichlet inflow** Velocity : $\boldsymbol{U = 815.153139493\, m/s}$ Temperature: $\boldsymbol{T = 619.839853\, K}$ Pressure: $\boldsymbol{p = 41333330.0\, Pa}$ Species: $\boldsymbol{Y_{N_2} = 1.0}$
Outlet $x = 5$m:	**Supersonic Neumann outflow**
Wall in J and K:	**slip**

As mentioned previously, this case is mostly performed to establish a comparison with a high-order scheme such as sixth-order compact scheme with Local Artificial Viscosity by Terashima et al. [308]. Given the lower order of the McCormack scheme, twice as many points are used for the current simulations compared to the ones from Terashima et al.. The coarse grid (401 pts) results are shown in Figure 24 and show a pretty good match between the current simulation and the reference one. As mentioned earlier, the fact that different equations of state are used explains some of the discrepancies observed. Since the densities are imposed as initial conditions, the differences in density prediction from the various equations of states result in different initial temperatures. Similarly, the PR EOS

matches the ratio of specific heats from the SRK EOS from Terashima et al. in the the pre-shock region but the RK EOS does not. The rest of the discrepancies can be attributed to the numerical schemes used. While the current hybrid scheme is clearly more dissipative than the high-order scheme used by Terashima et al., both the main shock and the small scale structures behind it are captured quite accurately. The largest errors can be observed on either side of the train of compression waves with numerical oscillations on the left and a delayed formation of the weak shock behind the small structures. Overall, the results are satisfying and display similar characteristics than the ideal gas simulations.

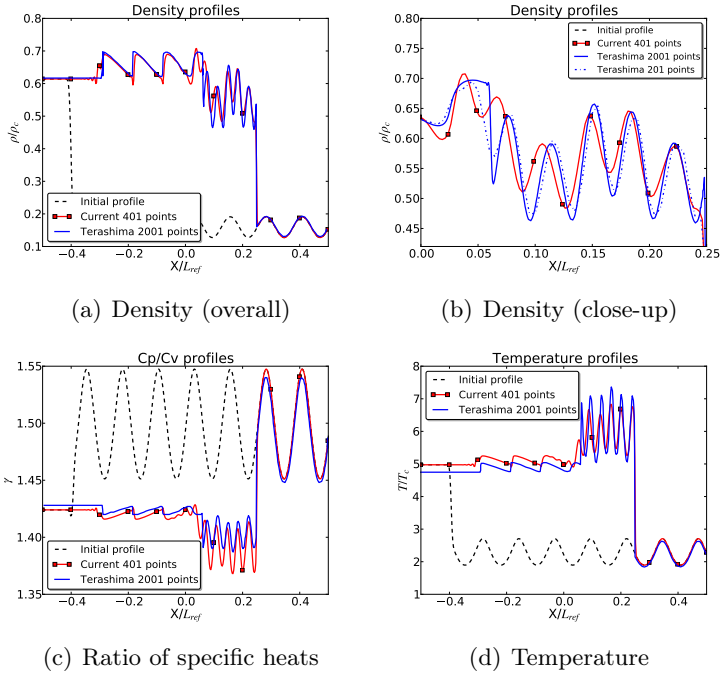

(a) Density (overall)

(b) Density (close-up)

(c) Ratio of specific heats

(d) Temperature

Figure 24: Results for the weakly non-ideal Shu-Osher test with 401 points and the Peng-Robinson equation of state.

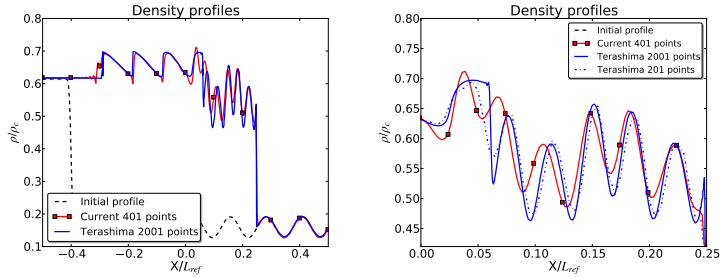

(a) Density (overall)

(b) Density (close-up)

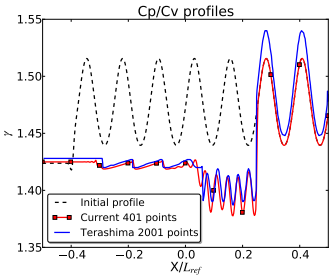

(c) Ratio of specific heats

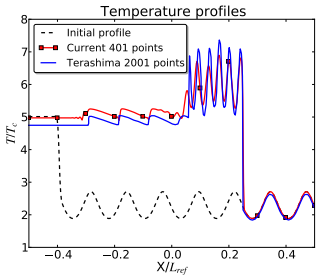

(d) Temperature

Figure 25: Results for the weakly non-ideal Shu-Osher test with 401 points and the Redlich-Kwong equation of state.

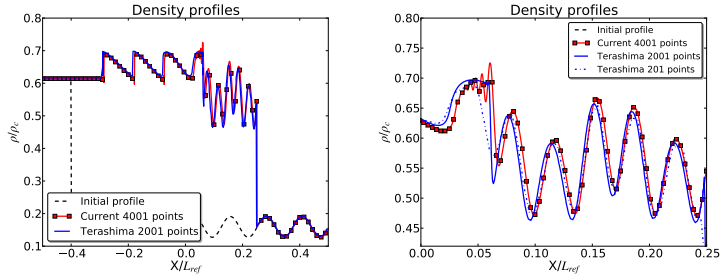

(a) Density (overall)

(b) Density (close-up)

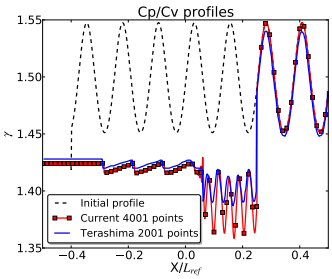

(c) Ratio of specific heats

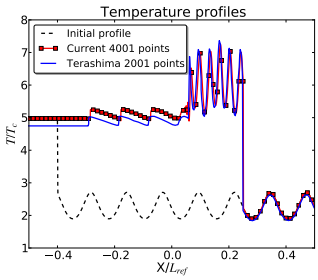

(d) Temperature

Figure 26: Results for the weakly non-ideal Shu-Osher test with 4001 points and the Peng-Robinson equation of state.

3.4.1.2 Strongly non-ideal test case

The temperature in the pre-shock region is set at 130 K for nitrogen. Setting it lower and thus closer or below the critical temperature of 126 K results in convergence issues as the thermodynamic derivatives for the cubic equations of state start diverging in that region. There are actually non-classical behaviors to be observed near the critical region of some fluids but more complex and more accurate equations of states are required [204] and this is beyond the scope of this study.

Like for the Terashima case, the fluid is pure nitrogen and smoothed using the error function (Eq. 3.4.2) and $C_\varepsilon = 3$.

$$(u, \rho, p) = \begin{cases} \left(434.49481, 192.85, 41.333 \times 10^6\right) & \text{for } -5 \leq x \leq -4 \\ \left(0.00, 50.0(1.0 + 0.2\sin(5x), 4.0 \times 10^6\right) & \text{for } -4 < x \leq +5 \end{cases} \tag{3.4.3}$$

The velocity is initialized a little differently here. The pre- and post-shock values of the velocity are computed and they are then translated in the frame of reference of the pre-shock fluid. The simulation time is set to $t = 10.38$ ms, the time it takes for the shock wave to travel 80% of the distance from its initial location to the end of the domain. The boundary conditions for this case are summarized in Table 7.

Table 7: Boundary conditions for the strongly non-ideal extension of the Shu-Osher test case

Inlet $x = -5$m:	**Supersonic Dirichlet inflow** Velocity : $\boldsymbol{U = 434.49480874\, m/s}$ Temperature: $\boldsymbol{T = 282.453832572\, K}$ Pressure: $\boldsymbol{p = 31167013.7963\, Pa}$ Species: $\boldsymbol{Y_{N_2} = 1.0}$
Outlet $x = 5$m:	**Supersonic Neumann outflow**
Wall in J and K:	**slip**

This case is run for two resolutions, 401 and 4001 points. These resolutions are comparable to the ones used by Terashima et al. with their higher order scheme. To run the

case with 4001 points, simply edit the script below to replace the value of `maxPts` by 4001. The results are shown in Figures 27 and 28. It can be observed that the additional resolution provides little improvement to the results, and it actually slightly increases the 1-point oscillations observed between the weak compression waves.

Another feature of these results is that the compression waves actually travel backwards in the frame of reference of the pre-shock fluid. This is because for a pre-shock gas with low compressibility, the speed of sound is low (here around 200 m/s) and thus the velocity behind the shock (with respect to the pre-shock fluid) can drop below the speed of sound of the post-shock fluid.

Increasing the accuracy of the iterative solver by decreasing the convergence criterion from 1×10^{-4} to 1×10^{-8} has no influence on the results so we can conclude that most of the oscillations are due to the numerical scheme and not the thermodynamic solver.

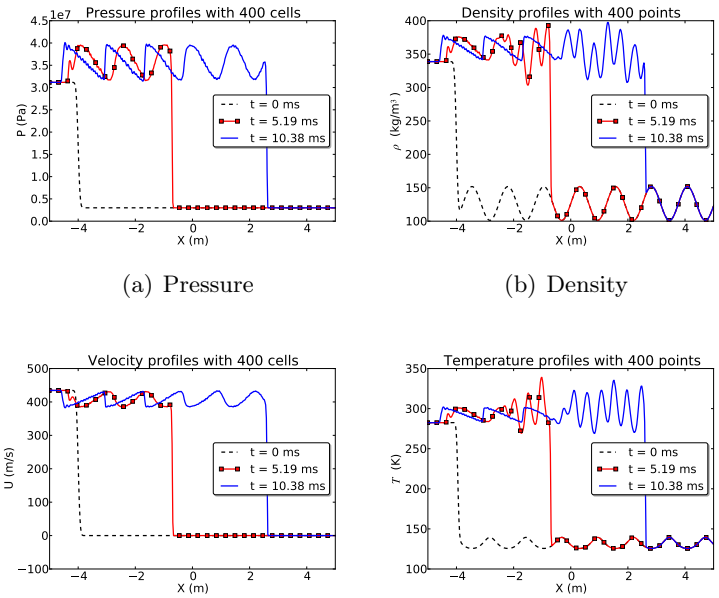

(a) Pressure (b) Density

(c) Velocity (d) Temperature

Figure 27: Results for the strongly non-ideal Shu-Osher test with 401 points.

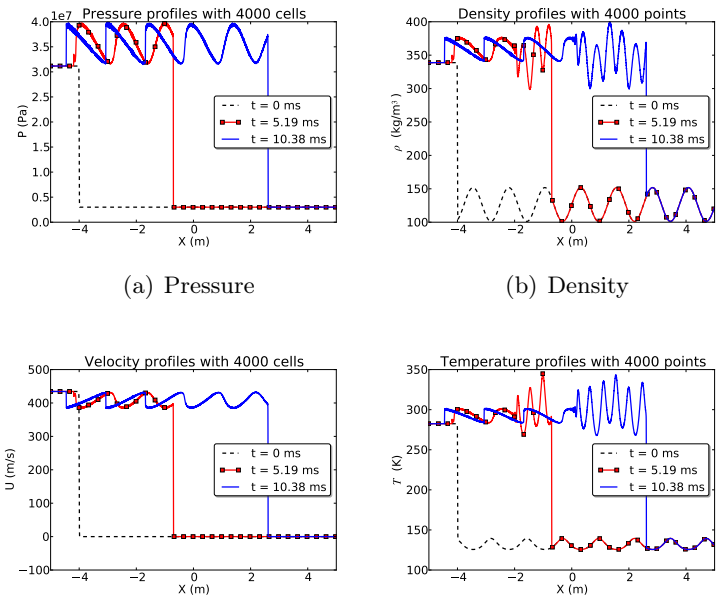

(a) Pressure (b) Density

(c) Velocity (d) Temperature

Figure 28: Results for the strongly non-ideal Shu-Osher test with 4001 points.

3.4.2 Conservative properties

A one-dimensional material convection problem inspired by Johnsen and Colonius [118] is used to investigate the conservative properties of the current flow solver. Unlike Nonomura and Terashima [209] who ran this problem using the stiffened gas equation of state using non-dimensional quantities, the problem introduced here uses realistic physical values for rocket problems. So the convection of a pocket of cryogenic oxygen in a uniform cryogenic hydrogen flow is modeled. The initial conditions are smoothed using the function suggested by Kawai and Terashima [120] since the rocket problems of interest deal with continuous not discrete interfaces between different fluids:

$$U = (1 - f_s)\, U_{\mathrm{H}_2} + f_s U_{\mathrm{O}_2} \quad \text{with} \quad f_s = 0.5 + 0.5\,\mathrm{erf}\left(\frac{s}{C_\varepsilon \Delta x}\right) \tag{3.4.4}$$

where s is the signed distance from the interface, erf is the Gauss error function, Δx is the local grid spacing and C_ε is the smoothing parameter. A value of 3 is usually considered as adequate to smooth the interface [209]. The conditions $U = (p, T, u, Y_{\mathrm{O}_2}, Y_{\mathrm{H}_2})$ in the oxygen

and hydrogen are given by:

$$U_{O_2} = (1.0e7, 100.0, 30.0, 1.0, 0.0) \tag{3.4.5}$$

$$U_{H_2} = (1.0e7, 100.0, 30.0, 0.0, 1.0) \tag{3.4.6}$$

The initial locations of the H_2-O_2 interfaces are $x = \pm 0.0025$ for a domain extending from $x = -0.005$ to $x = 0.005$. Periodic conditions are applied at the edges of the domain.

Since this test case is about fluid interfaces and not about turbulence, most of the simulations run will be with the pure upwind scheme and not the hybrid scheme. Ideally, the pressure, velocity and temperature fields should remain constant as the two fluids are convected by the uniform flow.

Figure 29 shows the time evolution of the L_2-norm of the difference between the primitive fields and the supposedly constant ideal solution for a simulation with the Peng-Robinson equation of state. Overall, the errors observed are slightly worse (10^{-4} versus 10^{-6}) than the ones observed by Nonomura and Terashima for a fully conservative scheme with interpolation on the primitive variables. However, the stiffened gas equation of state used by Nonomura and Terashima does not require the expensive and inherently less accurate iterative method that cubic equations of state use. If the same convection test case is run with a perfect gas equation of state, the errors observed on these primitive fields is close to machine precision around 10^{-16} and hint that the higher errors shown for the real gas case are due to the thermodynamics. Regardless of thermodynamics, the mass and energy conservation are excellent, both below 10^{-14} as expectd given the nature of the scheme. This is very important for combustion applications where small errors in mass conservation could have significant impact on the heat release.

3.5 Miscellaneous computational issues

3.5.1 Real gas iterative solvers

The implementation of the real gas framework is summarized in Figure 31. The two main iterative solvers described in Section 2.5 are apparent within the cubic equation formulation.

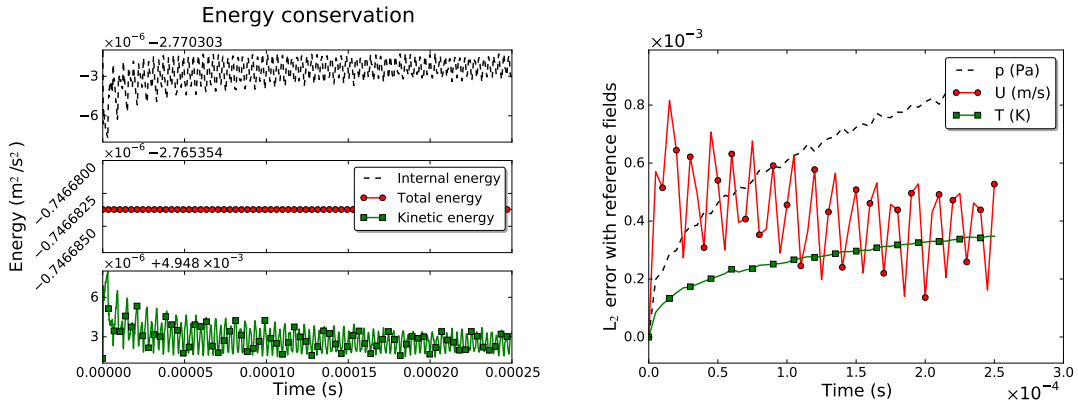

Figure 29: Scheme properties for the trans-critical convection test case. Left: Conservation of energy. Right: L_2-norm of the difference between the computed primitive fields and the constant fields of the analytical solution.

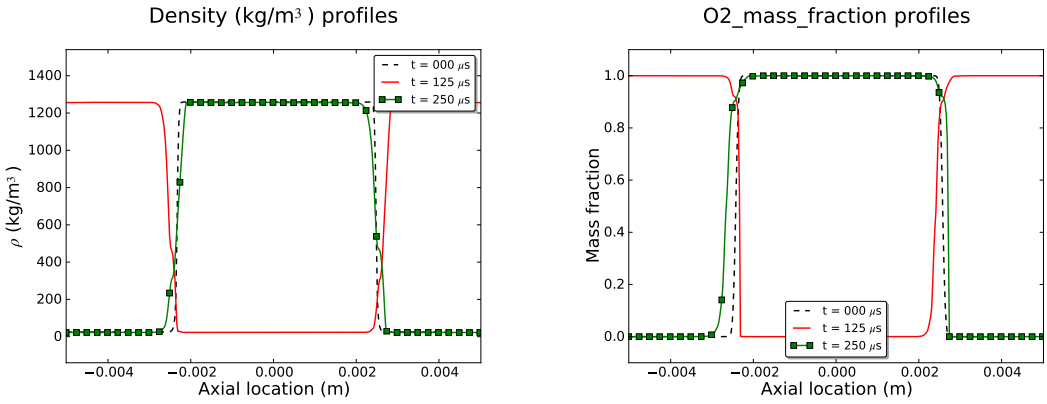

(a) Density

(b) Species

Figure 30: Density (left) and oxygen mass fraction (right) profiles for the trans-critical convection test case.

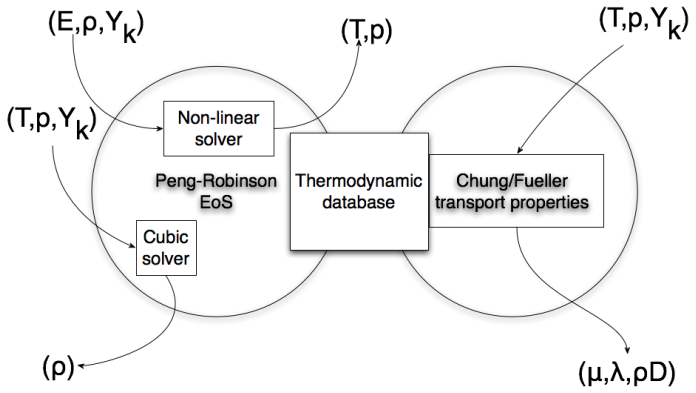

Figure 31: Overview of the real gas framework in LESLIE: both thermodynamic and transport properties are computed from the same database of basic species properties such as critical quantities. The iterative solvers required by the cubic equation of state are represented by squares.

Note that the structure would be the same for any cubic equation, whether it is the Peng-Robinson one as shown in Figure 31, or another one. The performance of these routines, required to convert conservative variables into primitive variables, is crucial to the overall code performance as they represent a significant part of the total computational cost.

The goal of this section is to compare the accuracy and efficiency of the methods described in Section 2.5.7.4. It focuses on the algorithms that solve for T and p from E and ρ but the conclusions are expected to be identical for the enthalpy algorithm given their similarities. In order to perform this comparison, a standalone program randomly generates points of coordinates (T,p,$Y_{k,k=1,N_S}$) and computes the corresponding densities and enthalpies using the equation of state from Eq. 2.5.118 and departure function from Eq. 2.5.123. The previously detailed algorithms are then used to recompute the original T and p, as the mixture composition is assumed constant. The strengths and weaknesses of these algorithms are evaluated by:

- Measuring the average CPU time taken to compute each solution and analyzing the number of iterations (average, standard deviation, maximum) required by each method.

- Evaluating the accuracy on the predicted pressures and temperatures by analyzing

the absolute and relative errors (average, standard deviation, maximum) made by each method.

Measurements are performed over a dataset of 10,000 points and the computations are repeated several times to ensure consistency. The most representative results are obtained by considering two specific datasets:

- A binary mixture of H_2-O_2 at 100 bar, with temperatures ranging from 300 K to 1000 K. This is a purely super-critical mixture, and real gas effects are very limited.
- A binary mixture of H_2-O_2 at 100 bar, with temperatures ranging from 100 K to 400 K. This is a transcritical mixture as the oxygen-rich side is in a compressed liquid state. This is illustrated by Fig. 32 where the compressibility factor Z of the dataset points is shown as a function of the oxygen mass fraction and the temperature. The size and the color of the symbols indicate the importance of real gas effects. Larger symbols imply larger departures from ideal gas.

A binary mixture was chosen for these datasets to make sure the multicomponent formulation in each algorithm was correct. Both algorithms scale similarly for a higher number of species and the binary mixture is representative of a pure mixing problem.

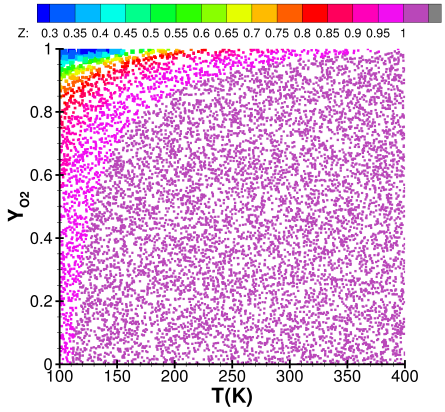

Figure 32: Temperature/mass fraction map of the transcritical H_2-O_2 dataset used for comparing the algorithms converting energy/density to temperature/pressure. Larger symbols imply larger departures from ideal gas.

As mentioned previously, both iterative algorithms are mostly controlled by a convergence criterion. Figures 33(a) and 33(b) display the speed and accuracy of both methods as this convergence criterion is varied. The obvious trends that can be observed from these figures are:

- As expected, computational cost decreases as the convergence criterion increases but the error increases. This is true for both methods and under any conditions.
- The single-variable iteration method is about 50% faster than the dual-variable iteration method under any conditions and for any convergence criterion.
- For the same convergence criterion, the error from the single-variable iteration method is about 15 times smaller than the one from the dual-variable iteration under super-critical conditions and as much as 3 orders of magnitude smaller under trans-critical conditions.
- For both methods, the cost and error are larger under trans-critical conditions than under super-critical conditions.

It is observed that the single-variable iteration scheme is superior in every aspect to the dual-variable iteration scheme. This is mostly due to the fact that in the single-variable method, p and T are perfectly matched through the analytical equation of state for p while for the dual-iteration method, T and p have likely converged at a different rate and do not exactly satisfy the pressure equation of state. Based on an extensive use of these algorithms, the accuracy obtained with the single-variable iteration solver for a convergence criterion of 1×10^{-4} is adequate for fluid mechanics computation. The dual-variabel iteration method requires a convergence criterion of 1×10^{-5} to achieve the same level of accuracy which adds to the cost of this method.

Looking at the distribution of the computational cost in Table 8, it appears that the dual-variable iteration method is suffering from occasional very slow convergences. While the average number of iterations is actually smaller for the dual-variable iteration method than for the single-variable iteration method, the standard deviation is huge as some points

may require 100+ iterations to converge. These points correspond to the trans-critical region, where the derivatives are the stiffest. Moreover, each iteration is more costly for the dual-variable iteration method than for the single-variable iteration method.

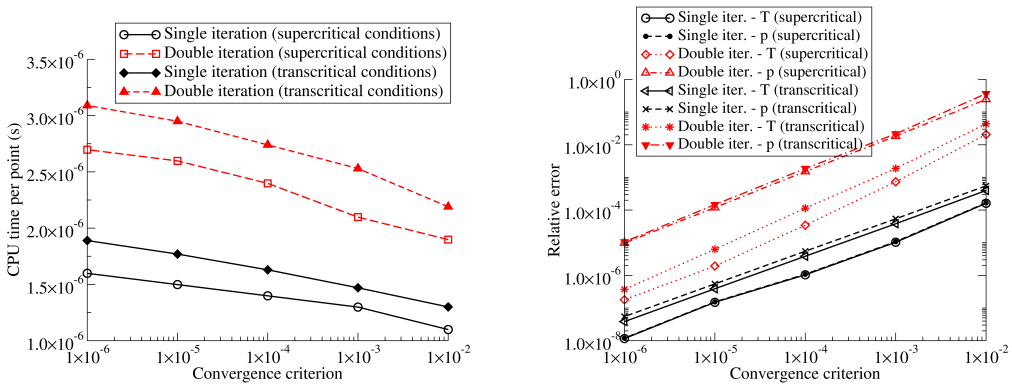

(a) Speed (b) Accuracy

Figure 33: Evaluation of the speed (left) and accuracy (right) for the iterative solvers converting energy/density to temperature/pressure as the convergence criterion is varied.

	CPU time/point	Number of iterations		
		Mean	Standard deviation	Maximum
Single-variable iteration	1.63×10^{-06} s	4.79	0.996	19
Dual-variable iteration	2.74×10^{-06} s	4.27	4.77	133

Table 8: Detailed cost data for the trans-critical dataset for a convergence criterion of 1×10^{-4}.

The full dual-variable iteration solver has many parameters that control it since it essentially performs the main algorithms several times under different sets of parameters. A full parametric study is thus not feasible and the results presented here represent the best performance currently available. It is possible, although unlikely given the extensive testing done, that a better set of parameters exists. In any case, it is doubtful that the performance would be significantly better than what is shown here.

The single-variable iteration solver on the other hand only has 2 main parameters, the convergence criterion and a scaling factor to accelerate the convergence. It is thus possible

to investigate the full influence of these parameters on the cost and accuracy of the method. The influence of the convergence criterion was shown in Figures 33(a) and 33(b) and the dependency on the scaling factor is shown in Figures 34(a) and 34(b). First, it appears that the acceleration levels out for a scaling factor smaller than 1×10^{-4}. In particular, there is essentially no difference between 1×10^{-5} and 1×10^{-6}. If the relative errors are compared for these values of the scaling factor, they are almost identical with maybe a slight edge for 1×10^{-5} for transcritical conditions. Overall the scaling factor has not a large influence on the error, which was to be expected. It is interesting to note, as it was not really apparent in Fig.33(b), that for trans-critical conditions, the error on the pressure computation is significantly larger than for the temperature. The gap is still much narrower than for the dual-variable iteration solver. In view of these findings, a value of 1×10^{-5} for the scaling factor appears optimal for the single-variable iteration solver.

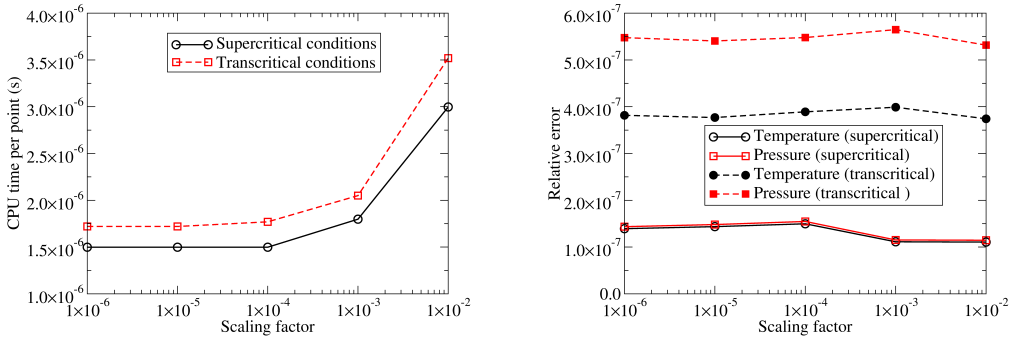

(a) Speed (b) Accuracy

Figure 34: Evaluation of the speed (left) and accuracy (right) for the single-variable iteration solver as the scaling factor is varied. The convergence criterion is set at 1×10^{-5}.

In conclusion, the real gas framework implemented for this work is complete and well suited for CFD applications where compromise between cost and accuracy has to be considered which is the case of full-3D, unsteady LES. The algorithm developed here for the conversion of conservatives variables into primitive variables appears to be an improvement over the previous method. Other solutions were considered, such as the use of Artificial Neural Networks (ANNs) for thermodynamics. However, even though ANNs could deliver

a (T, p) solution faster than the iterative solver, fundamental issues remained with respect to the accuracy. Even with extensive training on a simple binary mixture, the random, albeit small, error that the neural network would produce had fatal consequences for a CFD simulation. Essentially, 1-point small oscillations of pressure were created, which at best could trigger small fluid mechanics structures and at worse grow to significant perturbations. This is unlike the use of neural networks for computing reaction rates where small variations between the output of two very similar states are inconsequential [275]. It could be possible however to use ANNs to compute real gas transport properties since small errors there would have little influence on the flowfield.

3.5.2 Parallel performance and simulation cost

The performance of the flow solver with the real gas thermodynamics has been evaluated on many different architectures from a in-house Linux cluster called *garuda* at the Computational Combustion Laboratory to some of the largest super-computers in the world such as the Cray XE-6 *raptor* at the Air Force Research Laboratory. As mentioned in the previous section, the use of recent features of the FORTRAN language requires the use of updated compilers such as ifort 12.1 recently. Also, over the years, the computer clusters on which the flow solver is run have evolved dramatically. A decade ago, most of the distributed shared memory clusters contained nodes with just 1 or 2 computing cores. But over the last few years, the number of cores per processor has increased rapidly to reach as many as 16 cores per CPU and 64 cores in a node. This is the case for the *FoRCE* cluster evaluated in the following figures. For more details on some of the machines used for this work, the reader is referred to Appendix I.

The following quantities can be used to compare the performances of the flow solver on various architectures:

- COMP: stands for COde Machine Performance. This single number is supposed to represent the absolute performance of a given code on a given machine. It is computed, for a given run, by multiplying the number of cells per computing/processing core by the number of iterations performed and then dividing by the runtime. In an ideal

situation, this number should be constant no matter the number of cores being used, the size of the grid or the duration of the run. It directly indicates on how many cells one iteration can be performed by one core in one second. By extension, the acronym COMP will be used as unit for measuring the performance of the codes. For examples, if a given run yields "3.2 k COMPs", it means the code is able to process one iteration on 3200 cells per core per second, or 3200 iterations on one cell per core per second, or any similar combination. The inverse of COMP, expressed in CPU.s/cell/iteration is also a widely used metric.

- Speed: Refers here to a measure of absolute computational performance by removing the normalization by the number of cores used in the definition of COMP. The speed is usually expressed in cells times iterations computed per second. It represents the raw performance of the code given a grid and a number of cores.

- Speed-up: This compares the speed of a simulation with a reference simulation on a smaller number of cores. The formula is simply $\frac{\text{Speed for n cores}}{\text{Speed for m cores}}$. Ideally, this ratio should be equal to n over m.

- Efficiency: Efficiency is a measure of how close to ideal the speed-up is. It divides the actual speed-up by the idealized speed-up and is usually expressed in percentage. A 100% efficiency means an ideal speed-up, for example a simulation time divided by 2 when doubling the number of cores.

Other metrics would need to be used to compare the performance of different solvers and/or schemes, for example one where the physical time simulated per unit of CPU time.

The performance of the flow solver and its underlying kernel on simpler configurations with cubic uniform grid and simple thermodynamics has been extensively studied in the past [297, 178, 179, 176]. The focus here is on more complex configurations with real gas thermodynamics. For all the cases presented in this section, the hybrid upwind-central scheme is used with a cubic EoS for the thermodynamics.

The reacting LOX-GH_2 simulations presented in Chapter 6 represents the most complex configuration in the current work. The modeling of the trans-critical injection with the

real gas formulation, the finite rate chemistry with the Baurle mechanism (see ChapterH for details) and the complex inflow geometry with a perforated plate as coflow combine all the features of the flow solver on a computational grid with 11 million grid points. In contrast, a simple temporal mixing layer (TML) is used to evaluate the scaling of the real gas formulation alongside the LEM formulation on a 256^3 cells grid. Both setups are run on the Cray XE6 *raptor* with the baseline TML run with 32 processing cores and the baseline LOX-GH_2 injector run with 80 processing cores. In terms of raw performance, the flow solver achieves about 8000 COMPS for the LOX-GH_2 injector, which translates into about 1 month of simulation time with 1024 cores for 10 ms of statistics collection because of a small limiting timestep of 4×10^{-9} s. Together the thermodynamics and the chemistry represent about 75% of the computational cost.

The very good scaling shown in Figure 35 can be explained in two ways. For the TML, the uniform cubic grid can be mapped into blocks of uniform size no matter the number of cores and the simulation is always perfectly load-balanced. For the reacting LOX-GH_2 simulation, a custom mapper for coaxial injector configurations is used and can get close to a uniform size distribution for a wide range of blocks. This explains the peak efficiency obtained with a few hundreds of blocks. As the number of blocks increases, the load balancing is not perfect anymore and the scaling performance decreases slightly. Thanks to a high computational load per cell due to real gas thermodynamics and chemistry coupled to an efficient parallel message passing scheme, the performance degradation is minimal and the efficiency remains above 80% for up to 2000 cores.

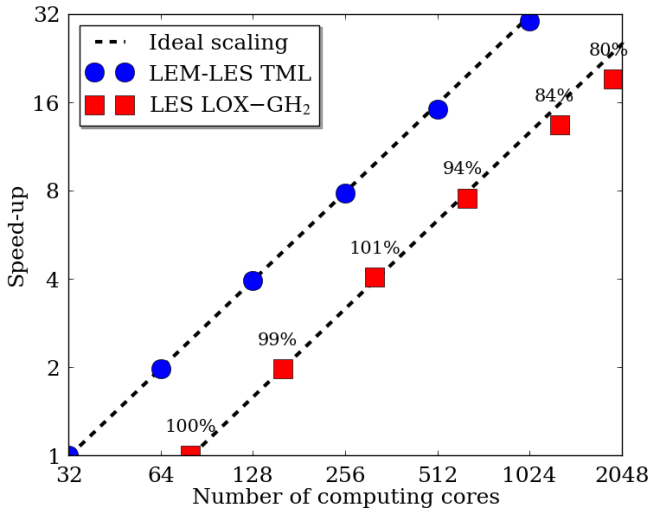

Figure 35: Strong scaling of a real gas TML with LEM-LES and the LOX-GH_2 PSU injector on *raptor* (Cray XE6). Baseline number of processors is 32 for the TML, 80 for the coaxial injector. The run efficiency in % with respect to the baseline run is shown on the graph for the coaxial injector.

CHAPTER IV

GAS-GAS REACTING SHEAR COAXIAL INJECTOR

4.1 Introduction and background

With the focus of this study being on liquid rocket engine applications, a simpler, but still relevant, application is sought after that does not involve the injection of liquid oxygen in a combustion chamber. This simpler application should allow the validation of the hybrid solver in a reacting environment but not include any significant departures from ideal gas behavior.

In this chapter, the focus is on one of the simplest possible setups for a realistic rocket engine. As mentioned earlier in Section 1.2.1, coaxial injectors have been the preferred solution for most launch-vehicle rocket engines over the past 50 years, thanks to their good performance, good reliability and ease of manufacturing. They can be used with liquid oxygen injection and thus can be found in any rocket power cycles such as gas-generator, staged combustion or expander. But they also support gaseous oxygen injection and are an important part of the full flow staged combustion cycle (FFSC), a promising engine cycle for NASA's next generation of Reusable Launch Vehicles (RLVs). A FFSC cycle, as shown in Fig. 36, contains two pre-burners (light red boxes on top of Fig. 36), an oxidizer-rich pre-burner driving the oxidizer turbopump and a fuel-rich pre-burner driving the fuel turbopump. All of the propellants flow into these pre-burners, lowering the required temperature to obtain the necessary enthalpy flux through the turbines: the difference can reach 350 K between a FFSC engine and a fuel-rich staged combustion engine such as the SSME [54]. This makes FFSC cycles more reliable and easier to manufacture with respect to sealing, especially on the oxidizer line [67]. The use of shear coaxial injection elements in these cycles, despite their average gas-gas mixing efficiencies, limits the heat load on the injector plate.

The first combustor under consideration in this chapter contains a single-element coaxial

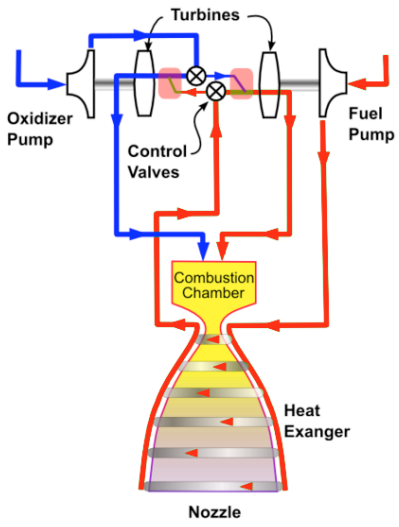

Figure 36: Schematic view of a Full Flow Staged Combustion cycle. Oxidizer line is drawn in blue and fuel line is in red. The pre-burners are represented as light-red boxes next to the turbines.

injector with flow conditions representative of what would be found in the combustion chamber of a FFSC cycle. This is one of the simplest possible setups for a realistic rocket engine. It is important to stress the differences between these gas-gas shear coaxial rocket injectors and more common turbulent non-premixed jet flames extensively studied in laboratories. The large inlet velocities of the rocket injectors not only produce high levels of turbulence, they also make the flow quite compressible, as opposed to the nearly incompressible jet flames usually studied. Also, despite the high strain rates, the low levels of dilution as well as the elevated pressure mean the flame is not lifted as in some similar hydrogen experimental flames [57]. Finally, if hydrogen-oxygen injectors are considered, the experimental data available is very limited under realistic rocket conditions because of the environment inside the chamber. The two most recent works, by Marshall et al. [172] and Conley et al. [43] only provide quantitative data for the heat flux along the outer wall of the chamber. Conley et al. also obtained some limited flame visualization and their configuration will need to be investigated in the future, even though the smaller physical dimensions of the injector increase the range of scales to be considered and thus the computational cost. As part of a NASA evaluation of various state-of-the-art solvers [314], the rig studied by Marshall et

al. was chosen for validation purposes. Following the nomenclature of the 3rd International Workshop on Rocket Combustion Modeling [264], this test case will be referred as the PSU RCM-1 case since experiments on this configuration were conducted at Pennsylvania State University's Cryogenic Combustion Laboratory. The main objective of this experimental campaign was to gain a better understanding of the physical and chemical mechanisms in play for these gas-gas injectors as well as to build a validation database for CFD codes. However, for the first round of tests, optical access was limited and the characterization of the chamber wall heat transfer was the primary goal.

This multi-year effort produced several publications [316, 314, 180] and some of the principal results are recalled in this chapter.

4.2 Description of the PSU-RCM1 experiments and simulations

4.2.1 Experimental configuration

The single-element shear coaxial injector investigated by the Pennsylvania State University (PSU) in their Cryogenic Combustion Laboratory is the focus of this study. This small-scale thrust chamber consists of oxidizer and fuel preburners providing the two streams of reactants for the coaxial injector and is part of NASA's Marshall Center validation campaign for the Constellation Universities Institutes Project (CUIP) [315]. The combustor, referred to as PSU RCM-1, is comprised of a cylindrical chamber instrumented for wall heat flux measurement and a convergent-divergent nozzle. A detailed description of the experimental setup is given in a previous paper [316] whereas additional details on the instrumentation and the measured data can be found elsewhere [230, 264]. A schematic of the rig is shown in Figure 37 alongside the wall temperatures used for the isothermal wall simulations.

Upstream of the main combustion chamber (MCC), an oxidizer-rich pre-burner and a fuel-rich pre-burner provide the hot gases for injection in the MCC. Flow conditions in the pre-burners are summarized in Table 9 while conditions in the MCC can be found in Table 10.

Table 9: Operating conditions of the two pre-burners in the PSU RCM-1 combustor [264].

	Actual run conditions
Oxidizer Preburner	
Gaseous O_2 flowrate (kg/s)	8.99×10^{-2}
Gaseous H_2 flowrate (kg/s)	5.57×10^{-4}
Mixture ratio O/F	161
Pressure (MPa)	5.85
O_2 Mass Fraction in Exhaust	0.945
H_2O Mass Fraction in Exhaust	0.055
Exhaust temperature (K)	700
Fuel Preburner	
Gaseous O_2 flowrate (kg/s)	1.76×10^{-2}
Gaseous H_2 flowrate (kg/s)	1.55×10^{-2}
Mixture ratio O/F	1.13
Pressure (MPa)	6.50
H_2 Mass Fraction in Exhaust	0.402
H_2O Mass Fraction in Exhaust	0.598
Exhaust temperature (K)	811

Table 10: Operating conditions of the main combustion chamber in the PSU RCM-1 combustor.

	Actual run conditions
Gaseous O_2 flowrate (kg/s)	8.55×10^{-2}
Gaseous H_2 flowrate (kg/s)	1.33×10^{-2}
Gaseous H_2O flowrate (kg/s)	2.478×10^{-2}
Mixture ratio O/F	6.43
Pressure (MPa)	5.42
Oxidizer stream density ($kg.m^{-3}$)	28.6
Fuel stream density ($kg.m^{-3}$)	3.46
Oxidizer stream velocity ($m.s^{-1}$)	146
Fuel stream velocity ($m.s^{-1}$)	740
Velocity ratio	5.07
Momentum ratio	1.85

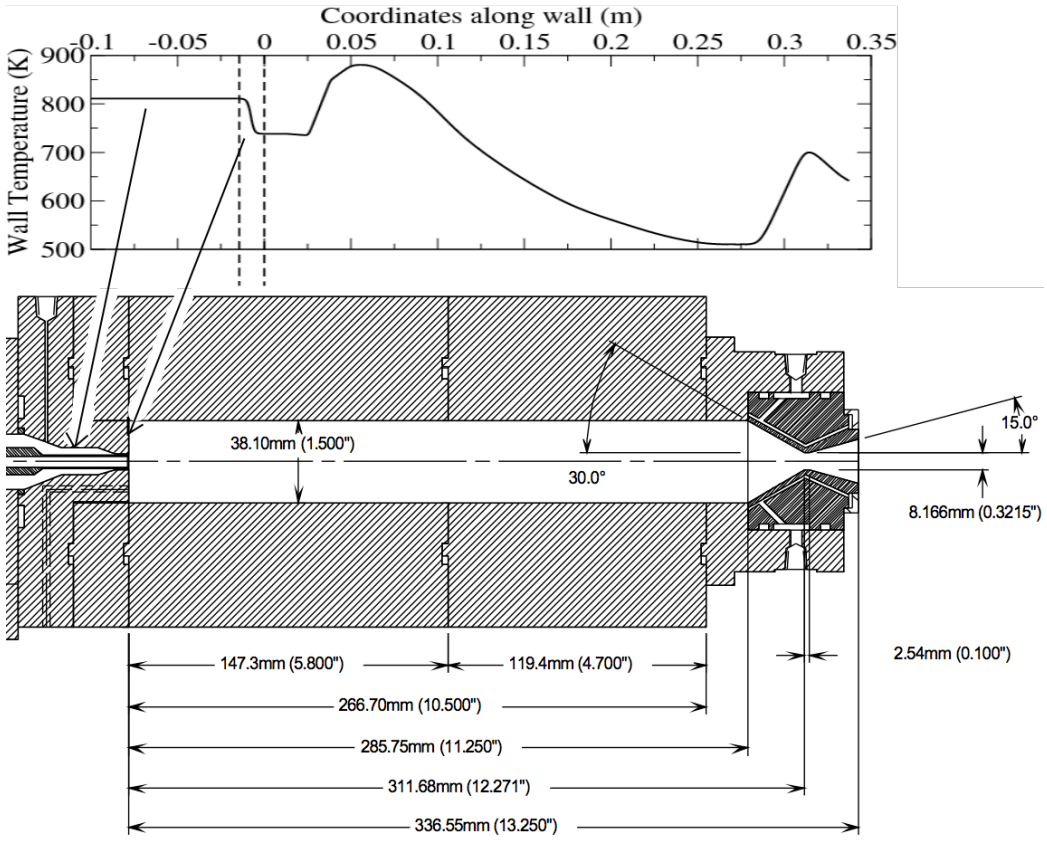

Figure 37: Schematic of the RCM1 combustor [264] with a graph of the temperature alongside the outer wall of the rig. Coordinates along the wall correspond to the distance from the injection plane for the chamber wall. Arrows indicate which wall corresponds to which part of the profile.

Of note, while the target chamber pressure is high (5.5 MPa), the injection temperatures of the reactants (711 K for the oxidizer stream and 800 K for the fuel stream) prevent any significant real gas effects to occur and justify the use of the perfect gas equation of state in the simulations. However the high pressure makes it very difficult to get a complete set of measurements because of the difficulty in gaining optical access of the inside of the chamber. The high-pressure, high-temperature environment in a limited volume imposes very severe constraints on the material used for the walls. Operating conditions and the geometry of the injector reflect those found in an actual staged combustion engine. For reference, the inlet Mach numbers are 0.29 and 0.51 for the oxidizer and fuel post exits and the Reynolds numbers there are respectively 650,000 and 150,000.

Table 11: Main geometrical dimensions in the PSU RCM-1 combustor, in millimeters,

Coaxial injector	
Oxidizer post inner diameter	5.26
Recess with respect to injector face	0.43
Fuel annulus inner diameter	6.30
Fuel annulus outer diameter	7.49
Oxidizer post area (m^2)	2.17×10^{-5}
Fuel annulus area (m^2)	1.29×10^{-5}

Since direct measurements inside the chamber are currently impossible, the main validation data available is the wall heat flux along the cylindrical part of the combustion chamber. Also, while the volume of the chamber is small enough to require active cooling, the distance between the injector centerline and the chamber wall is about twice as large (19 mm) as in a real engine [245]. Thus, the flow confinement experienced in a multi-injector configuration is not correctly represented. conditions along the wall being significantly different. For example, the large recirculation in the corner of the chamber is unlikely to be present in an actual configuration. From a numerical point of view, it artificially increases the convergence time of the simulations and from a physical point of view, it explains why the element-to-wall distance has a major impact on the wall heat flux[245].

Finally, while the wall heat flux is the only available experimental data, it will not be the primary focus of this study. Because of assumptions in the formulation and the grid resolution employed (detailed later), it is acknowledged that the prediction of this wall heat flux, although reasonable, could be improved. The main goal of this study is to demonstrate the ability of the unsteady, three-dimensional LES approach to capture the overall physics of a typical rocket injector flame.

4.3 Numerical setup

4.3.1 Implementation

The staged combustion nature of the PSU RCM-1 rig not only allows the use of the perfect gas equation of state as mentioned in the previous section, it also limits the density gradients between the streams of the reactants at the inflow. In previous works related to cryogenic

injection of H_2 and O_2 [175], the limitations of a central scheme used by the flow solver were highlighted when dealing with such large density gradients. While the density ratio between the injected streams is only about 10 for the present case (compared to well over 100 for a cryogenic injection), previous works have clearly shown the necessity of running a hybrid central-upwind scheme instead of a pure central scheme.

The current fully compressible flow solver uses a finite volume scheme with a 2nd-order time accurate predictor-corrector integration and a 2nd-order accurate hybrid solver for spatial integration as described earlier. This hybrid scheme allows the capture of the large density gradients typically found near the injection plane while keeping the required grid resolution reasonable and keeping the less-dissipative central scheme in the far-field in order to accurately model the turbulence.

Characteristic inflow with constant mass flux and supersonic outflow boundary conditions are employed, respectively at both fuel and oxidizer inlets and for the choked nozzle. Isothermal conditions along the combustor wall use the experimental wall temperature profile, and for the injector walls (including the injector plate), a blended function is used to smoothly go from the injection temperature to the external wall temperature. With the flame expected to sit near the tip of the oxygen post, the wall temperature there is set at about the highest possible temperature sustainable for the wall material, that is 900 K. These boundary conditions are illustrated in Figure 37. Assuming a near uniform grid normal to the wall, the temperature gradient at the wall can be computed as $\left(\frac{\partial T}{\partial y}\right)_{wall} = \frac{-9T_j+8T_{wall}+T_{j-1}}{3\Delta y}$. The heat flux is then obtained by multiplying this gradient by the sum of the molecular and turbulent thermal conductivities, as seen in Equations 2.2.9 and Equations 2.2.10. Given the wall resolution of the current simulations, the turbulent contribution dominates along the outer wall, representing as much as 95% of the total heat flux. As the wall resolution is increased, it is expected that the molecular, laminar heat flux will represent a larger fraction of the heat flux.

4.3.2 Computational grid

The computational domain models the full combustion chamber (a cylinder of 286 mm $\times$ 38.1 mm) and the nozzle (51 mm long with a throat of 8 mm), but a shortened inlet. The very long injector section (152 mm) has been reduced to 50 mm, as can be seen in Figure 38-(a) based on independent simulations of the full upstream configuration. The current inlet allows sufficient development of the initial flat profiles with correct bulk flow conditions. The current simulations have been performed on a baseline, multi-block grid. The outer cylindrical block contains $611 \times 87 \times 65$ grid points while the inner "butterfly" cartesian block contains $611 \times 17 \times 17$ grid points (Figure 38-(c)). Since some of the computational cells in the inlet regions are actually blanked out, the total number of cells is about 3.2 million.

The oxygen post is recessed 0.43 mm from the base of the combustion chamber. At that location, the diameter of the oxygen jet is 5.26 mm. A thin 520 microns sleeve separates it from the annular hydrogen jet near the injection place. The annular gap is 600 microns wide there. The finest resolution is located in the injector post tip region, where grid spacing reaches a minimum value of 43 micrometers in both axial and radial directions ($\Delta x_{\text{tip}} = \Delta y_{\text{tip}} = 43$ microns). The resolved kinetic energy spectrum in this region, shown in Figure 39, demonstrates the recovery of the Kolmogorov -5/3 spectrum, indicating sufficient resolution for a proper LES model. While the resolution is coarser in the rest of the combustor, the local Reynolds number is also lower because of the increased viscosity of burned gases. The wall-normal resolution near the outer wall, where the heat flux was measured experimentally, ranges from 0.7 mm in the corner to 0.2 mm further downstream.

In order to investigate the influence of the grid resolution on the flame structure and on the wall heat flux, a series of axisymmetric simulations was performed since the cost of a full 3D simulation prohibits such parametric study in three dimensions. Three grids were compared:

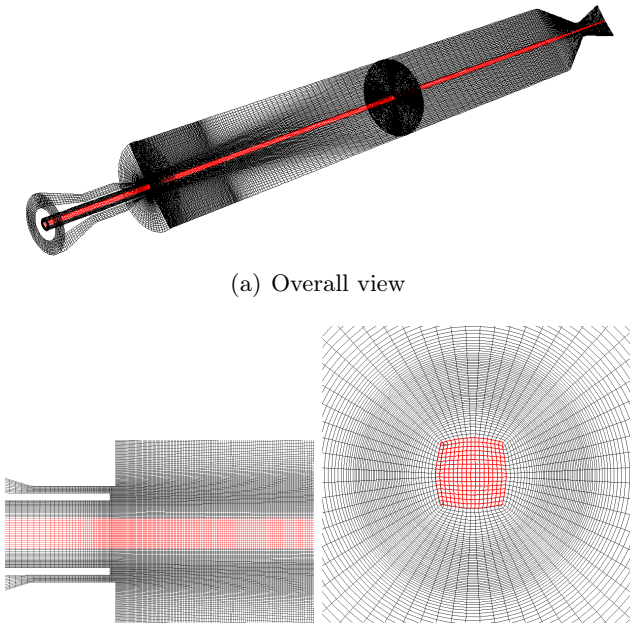

(a) Overall view

(b) Injector near-field (c) Butterfly grid

Figure 38: Views of the baseline grid for the PSU RCM-1 configuration.

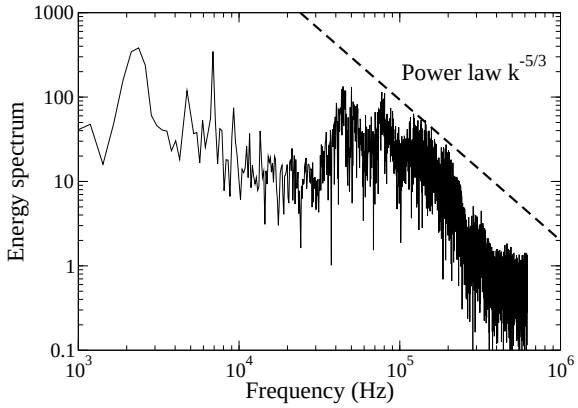

Figure 39: Resolved kinetic energy spectrum in the injector near-field.

- a baseline axisymmetric grid (grid (1)) nearly identical to a slice of the baseline three-dimensional grid, resulting in a grid size of 610×94,
- a finer grid (grid (2)) where only the resolution near the outer wall was improved ($\Delta y_{\text{wall}} = 100$ microns), resulting in a grid size of 610×144,

- an even finer grid (grid (3)) where the resolution was improved throughout the combustor, resulting in a grid size of 916×273. ($\Delta y_{\text{wall}} = 50$ microns, $\Delta x_{\text{tip}} = \Delta x_{\text{tip}} = 20$ microns).

Assuming an azimuthal resolution for these grids in line with the baseline three-dimensional grid, this would translate into 3D grids with respectively 3.2, 5 and 24 million computational cells. While the 5 million grid points simulation could be achieved in a reasonable amount of time on an in-house cluster, the simulation with 24 million points requires a huge increase in computational resources. For comparison, an LES with very high near-wall resolution of the PSU RCM-1 configuration was run as part of the CUIP effort [314] and required more than 2 million CPU hours on 256 million computational cells, with one third of the cells dedicated to the modeling of the injector upstream from the injection plane.

Finally, the same procedure is used to start up the axisymmetric and 3D simulations. After initializing the combustion chamber with a mixture made of 90% H_2O and 10% OH at 3000 K, reactants are introduced in the domain at their injection temperature and the flame auto-ignites without any artificial help. Once the flame is anchored in the wake of the injector inner sleeve, 15 ms of physical time are simulated to wash away the influence of the initialization. As mentioned previously, the simulation is then run for at least 20 ms to collect meaningful statistics, especially in the near-field. When looking at average quantities for the 3D simulations, it has to be noted that on top of temporal averaging, spatial averaging over the azimuthal direction has been performed.

4.3.3 Computational cost

Very good scaling of the performances have been obtained from 32 processors (the smallest number of processors which can run this case because of memory limitations) up to 256 processors with which most of the simulations have been run. Limited testing shows comparable scaling (above 80% efficiency) for 512 and 1024 processors but available computational resources did not allow running under such configuration. While the current flow solver has displayed excellent scalability in basic configurations [177], two additional factors help performance in the PSU RCM-1 case: first, the additional processors allow for a more uniform

mapping of the computational domain, thus improving the load balancing; second, the large cost of the chemistry in each cell means the communication between processors represents a small amount of the total computational cost. This simulation has mostly been run on an in-house Intel 3.2 GHz Xeon cluster but performance on a Cray XT3 is very similar. About 250,000 single-processor hours are required to complete the 20+ ms of simulation used for the statistical analysis reported here.

An issue with the PSU RCM-1 rig is the definition of convergence for the simulations. The volume of the combustor is rather large and the slow recirculation regions and downstream expansion do not improve the convergence rate of the computations. With the usual definition of Flow-Through-Time (FTT: time required for a particle to traverse the domain at a bulk velocity based on the total mass flow and the cross-sectional area), a time of about 8 ms is obtained. The time over which statistics are collected thus corresponds to about 2.5 FTTs. However, in the main region of interest (the first third of the combustor), mean velocities are much higher over a smaller length and characteristic times are much smaller. As an estimate, an axial mean velocity of about 200 m/s (see zone B definition in Section 4.4.1) can be assumed in the first third of the combustor and yields a characteristic time of about $0.125/200 = 0.6$ ms for this region. Consequently, second-order statistics, such as the RMS of the velocities, collected over 20 ms are meaningful in the near-field, high-speed region, but not as much in the recirculation zones (zone C) or further downstream (zone D).

4.4 Three-dimensional study

4.4.1 Steady state flowfield

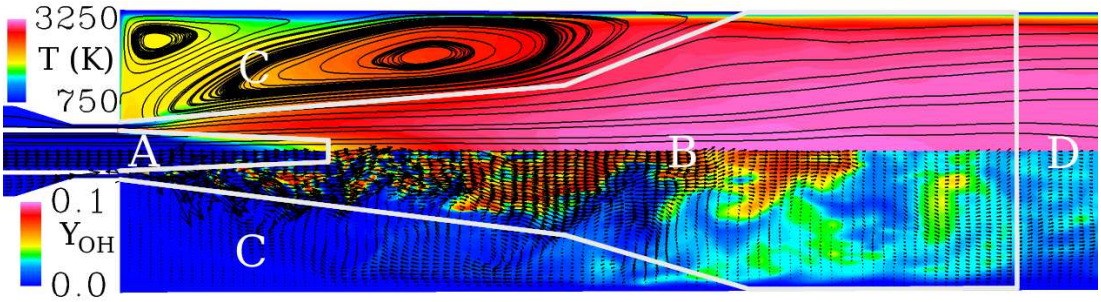

Figure 40: Division of the flowfield in four main regions, using the underlying time-averaged and instantaneous flowfields as guides. The top half of the figure displays the temporally- and spatially-averaged streamlines with the temperature in K as color contours. The bottom half shows the instantaneous velocity vectors as well as the instantaneous OH mass fraction contours. Detailed description of zones A to D is given in the text.

To begin the analysis of the simulations performed in this study, an overview of the PSU RCM-1 flowfield is first presented. The flowfield in the main chamber can be divided into four distinct regions where the dominant physical processes are very different. This is shown in Figure 40, where zone A corresponds to the very-near field of the coaxial injection. It extends downstream up to the end of oxygen core, i.e. around 5 oxygen diameters ($\approx$ 25 mm) downstream of the injection plane. As will be highlighted later, this zone is dominated by purely diffusive flames. Further downstream, as the oxygen jet breaks down, the flame is no longer simply diffusive as the reactants are being premixed with products. This occurs along the centerline for the oxygen while the hydrogen stream mixes with the products convected by the main recirculation bubble. This bubble, along with the smaller one in the corner of the chamber, defines the zone C which confines the coaxial jet to a narrow tube for the first 10 diameters. In this zone B, the flow first accelerates because of the expansion of the burned gases but then dramatically slows down as the cross-section area displaying positive mean axial velocity expands. This flow eventually reattaches to the outer wall (as seen later on in Figure 56) and closes the large recirculation bubble. By this time, secondary combustion is almost complete and the mass fraction of intermediate species such

as OH steadily decreases along the axial direction. The final region D shows very little action up to the convergent-divergent nozzle. From a fluid mechanics point of view, this is a homogeneous, lower-Reynolds ($\mathrm{Re} \approx 5 \times 10^5$) pipe flow and there is only very limited heat release occurring to perturb this flow. It is expected to display strong axisymmetry both instantaneously and on average.

While the dump combustor configuration has been extensively studied before [202, 3, 2], the PSU-RCM1 rig presents a combination of unique features that makes direct comparison with past work difficult: coaxial streams with large velocity ratio, large density difference between the two streams, high levels of heat release. However, it seems likely that the general aspect of the flowfield observed previously would be found again here. Akselvoll and Moin [3] predicted a main recirculation region up to 9 step-heights after the dump plane while Afshari et al. [2] observed a shortening of this main recirculation region in reacting flows. In the current case, the reattachment point appears to be around $X = 0.09$ m based on the axial velocity contours, equivalent to about 6.5 step-heights. In general, in such a dump combustor configuration, reattachment length is expected to be between 5 and 10 step-heights. Akselvoll and Moin also report the secondary vortex in the corner of the chamber. While it is difficult to compare the actual sizes of these recirculation regions with the available literature, the overall flowfield seems in agreement with past experience.

It is interesting to compare the general aspect of the flowfield from the 3D simulation to the axisymmetric studies mentioned in Section 4.3.2, where the 3 grids of increasing resolutions were presented. The axisymmetric simulations are performed using exactly the same options and flow conditions as the baseline three-dimensional simulation. Figure 41 shows the time-averaged fields of hydrogen mass fractions for these 3 grids, with the flow streamlines overlaid. These streamlines highlight that the positive axial flow only fills about half of the chamber diameter. This is in stark contrast with the 3D simulation, where the centerline flow actually reattaches to the outer walls. For the axisymmetric simulations, the outer part of the chamber consists of a large recirculation region that extends from the nozzle to the corner of the chamber. As expected, vortical structures are stronger than in

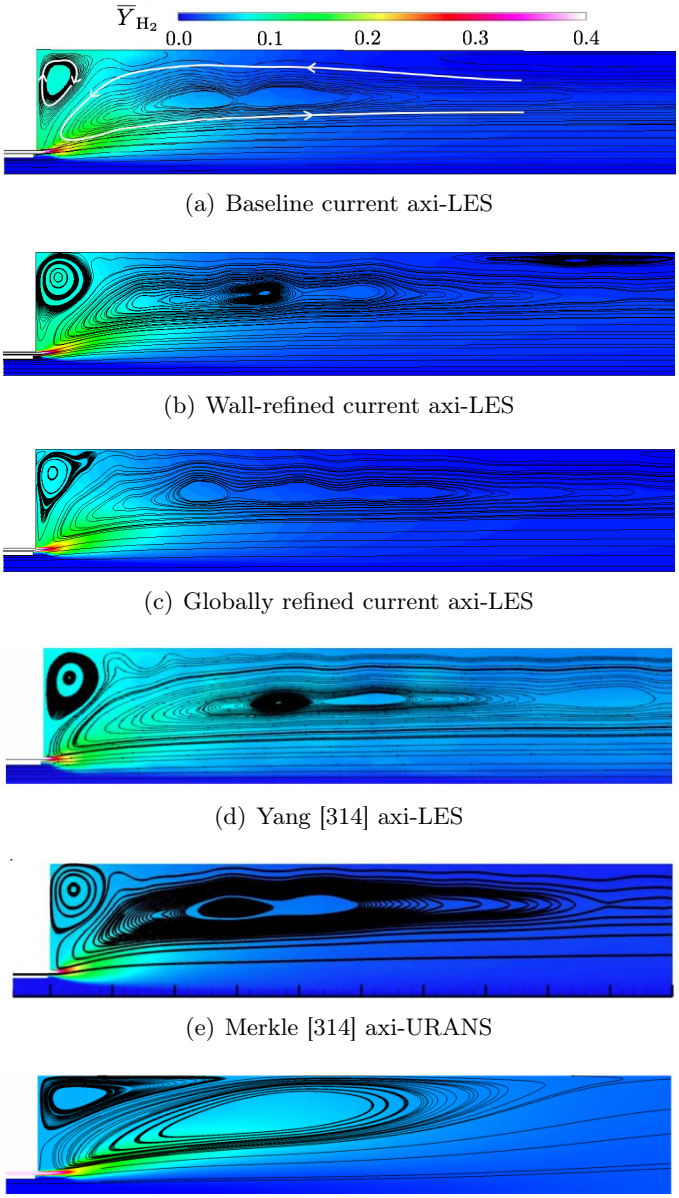

(a) Baseline current axi-LES

(b) Wall-refined current axi-LES

(c) Globally refined current axi-LES

(d) Yang [314] axi-LES

(e) Merkle [314] axi-URANS

(f) Baseline current 3D-LES

Figure 41: Comparison of the time-averaged (over at least 25 ms for the current simulations) hydrogen mass fraction fields and streamlines for the axisymmetric configuration (first 5 figures) and the current 3D configuration.

the three-dimensional case since there is no third dimension to provide additional dissipation and the oxygen jet core extends much further downstream in axisymmetric flow due to the lack of mixing along the centerline. The same features (longer oxygen core compared to 3D, recirculation extending over the whole chamber) are also found in other axisymmetric

unsteady simulations (LES or URANS) of the PSU-RCM1 configuration [314] as can be seen in Figure 41.

The grid resolution study indicates that the secondary, counter-rotating recirculation bubble in the corner of the chamber gets stronger as the resolution increases but the overall flow structure remains relatively unchanged. The impact of this recirculation on the wall heat flux is investigated later when the heat flux predictions between 3D and axisymmetric simulations are compared. The current simulations display a faster consumption of hydrogen than the other axisymmetric simulations from Yang and Merkle, and the increased grid resolution also appears to decrease the amount of hydrogen downstream. Otherwise, the two refined grids show relatively little differences between them, with the wall-refined grid actually displaying slightly higher temperatures in the downstream region, along the oxygen jet as shown in Figure 42. Figure 42 displays the instantaneous and time-averaged, over 15 ms, temperature fields for these three simulations. The instantaneous pictures clearly show more defined,d stronger structures and vortices as the resolution increases. This is characteristic of axisymmetric simulations where there is no third dimension to provide additional dissipation. There is also less cold gas along the wall as the resolution increases. Looking at the time-averaged fields, the recirculation in the corner of the chamber gets stronger as the resolution increases, bringing more hot burned gases into this region. Resolution seems to have no influence on the length of the oxygen core at the centerline, length which is much greater in these axisymmetric simulations than it was in the full three-dimensional simulation. This is similar to what was reported by other axisymmetric simulations in the CUIP effort [314, 151].

So unfortunately, it is impossible to claim that grid independence has been achieved with this axisymmetric study. While the overall flow structure remains the same for all axisymmetric grids, details of mixing and heat transfer have not converged towards a single solution. Moreover, even if grid independence was achieved on axisymmetric studies, the fact that the flow structure differs significantly from the one observed with a comparable 3D grid prevents an extension of the grid independence to the 3D case. With current available

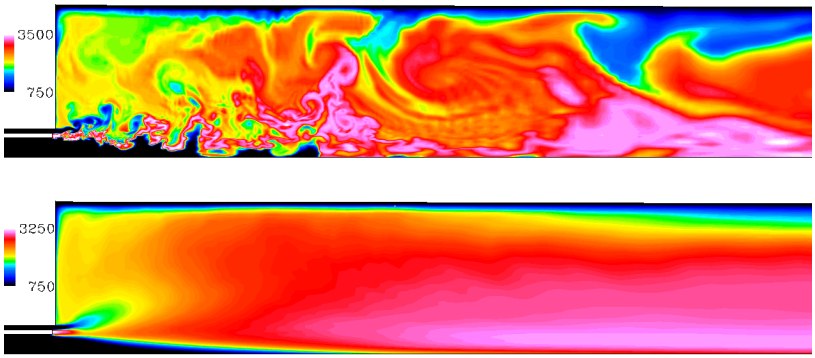

(a) Baseline grid

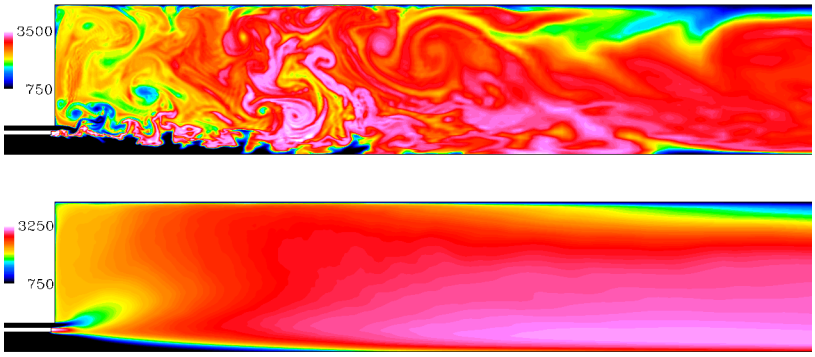

(b) Grid with wall refinement

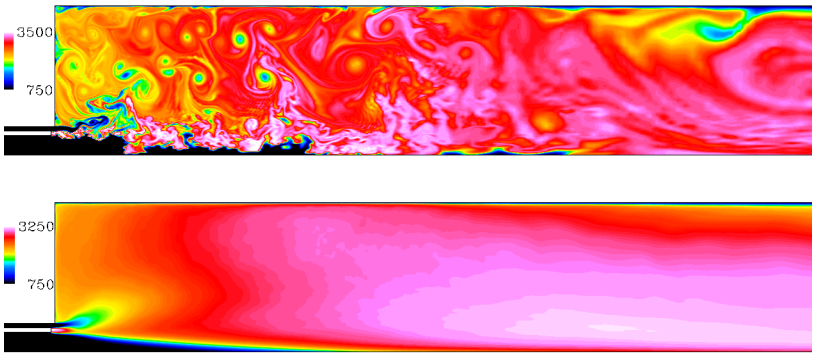

(c) Grid with overall refinement

Figure 42: Temperature fields in K for the three axisymmetric simulations with different grid resolutions.

computational resources, a grid convergence study in 3D is not feasible however.

4.4.2 Influence of the reaction mechanism

There is one final issue that can be explored with the axisymmetric configuration and that is the influence of the reaction mechanism. The 21-step mechanism was a requirement for the CUIP study however, there is interest in investigating simpler alternatives to reduce the computational cost. In particular, reducing the number of species is important for real gas computations as some of the cost increases as $\mathcal{O}(N_S^2)$ because of the mixing terms. As shown in Appendix H.3, the 7-step mechanism from Baurle et al. [13] could be a good candidate for a non-premixed configuration. While the 7-step mechanism is not suited for premixed flames, where it consistently under-predicts the flame speed, it matches well with the O'Conaire mechanism in non-premixed one-dimensional flames, whether at low pressures or under more realistic rocket conditions. Following these encouraging results, the 7-step mechanism is investigated using the axisymmetric finer grid and comparing with the results obtained with the 21-step mechanism. Figure 43 shows the time-averaged, over 25 ms, temperature field alongside streamlines for both simulations. The streamlines help visualizing the flow expansion in the chamber and show very little differences between the two mechanisms. Both display the same very long recirculation region characteristic of axisymmetric simulations, extending up to the convergent nozzle. Some small differences in the near-field can also be observed, in the expansion of the hydrogen stream for example. A more quantitative comparison is provided by Figure 44 with the profiles of density and temperature along the centerline (but obviously not at the centerline given the axisymmetric geometry) for both simulations. It is apparent that slightly less mixing and burning occurs in the case of the 21-step mechanism. The long characteristic tail for the centerline profiles in axisymmetric geometry is even longer for the 21-step mechanism and the effect of this unburned mass of oxygen can be seen in the slightly lower temperature obtained for the 21-step mechanism. Radial profiles of OH mass fraction, shown in Figure 45, show surprisingly little difference between the two simulations. The longer oxygen core for the 21-step mechanism is confirmed by the profiles at X = 0.2 m where the OH is maximum at the centerline for the 7-step

mechanism, indicating the end of the oxygen core. On the other hand, the slightly earlier burning exhibited by the 7-step simulation seems to have an impact on the heat flux profile shown in Figure 46. The 7-step run predicts a slightly higher heat flux between X = 0.05 m and X = 0.1 m, which corresponds to the higher temperature interval observed in Figure 44.

All these results seem to show that the 7-step mechanism qualitatively captures the same behavior as the 21-step mechanism for the flame-holding mechanism and the expansion of the gases in the combustion chamber, at least given the current approximate isothermal wall boundary condition at the tip of the oxygen sleeve. While there are some small differences in the quantitative profiles, it seems that the 7-step mechanism is a valid alternative to the 21-step mechanism, not just for initial transients but also for qualitative if not quantitative comparisons. There are two major advantages in using this mechanism for real gas simulations:

- The elimination of 2 species and the reduced cost of the chemistry integration can decrease the computational cost of the simulations by as much as 40%. In the present case, the 21-step axisymmetric simulation costs 1.7×10^{-4} CPU.s/iteration/cell while the 7-step simulation costs 9.5×10^{-5} CPU.s/iteration/cell. This effect is even more pronounced for real gas simulations given the double loops on species in the real gas framework: eliminating 2 even minor species cuts down the computational cost.

- Since the real gas properties of minor species such as H2O2 cannot be easily modeled, the elimination of these species makes the real gas solver more robust and more accurate. While the effect on the thermodynamics is probably minor, the high-pressure transport properties for these minor species could affect the flame significantly.

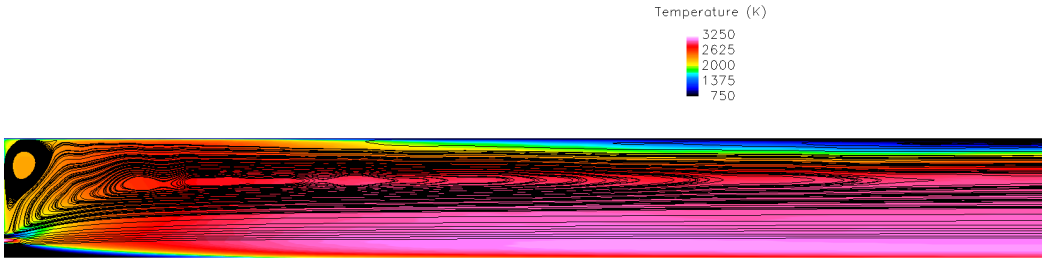

(a) 21-step mechanism

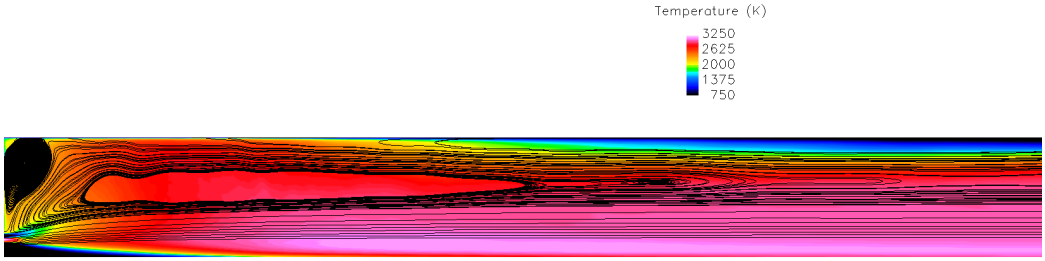

(b) 7-step mechanism

Figure 43: Time-averaged temperature contours and streamlines for the axisymmetric simulation using the finer grid and the 21-step mechanism (top) and the 7-step mechanism (bottom).

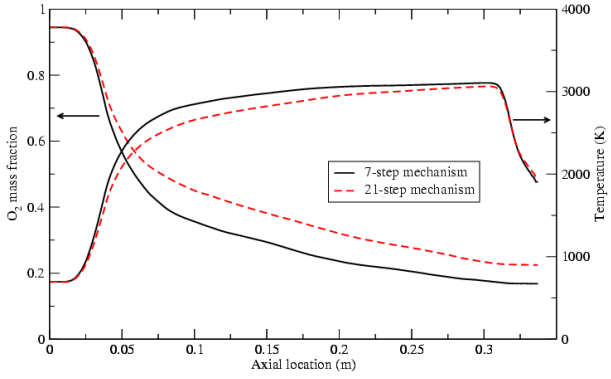

Figure 44: Axial profiles along the centerline of oxygen mass fraction (left scale) and temperature (right scale) for simulation using the finer grid and the 21-step mechanism (dashed lines) and the 7-step mechanism (solid lines).

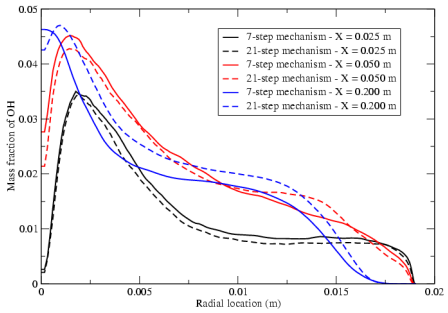

Figure 45: Radial profiles of OH mass fraction at different axial locations for simulation using the finer grid and the 21-step mechanism (dashed lines) and the 7-step mechanism (solid lines).

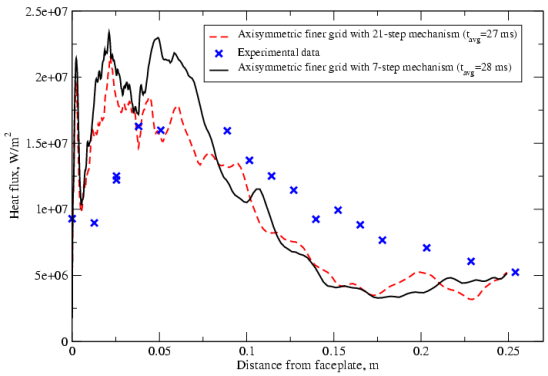

Figure 46: Comparison of the wall heat flux profiles for simulation using the finer grid and the 21-step mechanism (dashed line) and the 7-step mechanism (solid line).

4.4.3 Influence of the combustion closure model

As mentioned in the formulation section, the current study uses the 21-step, 8-species mechanism from Conaire et al. [211]. The numbering of the reaction steps found in Figure 47 follows the original formulation by Conaire et al. Concerning the numerical integration of the system of differential equations, Figure 47 shows that for most of the reactions, the characteristic reaction times are below 1×10^{-9} s, significantly smaller than the LES time-step of about 1×10^{-8} s. As a compromise between the cost and the accuracy of the numerical integration, a simple Euler time-integration with 20 sub-iterations is used instead of solving exactly the system of differential equations. The exact number of sub-iterations was chosen through trial-and-error, focusing on the smoothness of the radical species fields as the number of sub-iterations changes. These fields can show numerical artefacts when the number of sub-iterations is too small. Table 12 summarizes the fluid mechanics and chemical time-steps for the three-dimensional and axisymmetric simulations performed in this chapter.

Table 12: Fluid mechanics (τ_{fl}) and chemical (τ_{chem} timescales for the three-dimensional and axisymmetric simulations shown in this chapter.

	τ_{fl}	τ_{chem}
3D baseline	1×10^{-8} s	5×10^{-10} s
Axi baseline (grid (1))	1×10^{-8} s	5×10^{-10} s
Axi finer (grid (2))	1×10^{-8} s	5×10^{-10} s
Axi finest (grid (3))	2.5×10^{-9} s	1.25×10^{-10} s

This has the consequence of decoupling different chemical reactions: while the slower reactions are solved exactly, the stiffest reactions are essentially assumed to be in quasi-equilibrium state. This fact is illustrated by Figure 47, which compares the characteristic chemical times of the various steps in the mechanism at two temperatures, 1000 K (near-field ignition) and 4000 K (upper bound temperature). In the near-field, it can be seen that the LES time-step is larger than any step except some of the H_2O_2 branching reactions with very large activation energy. However, the simple Euler integration provides a cost-efficient way to capture the majority of the reactions with its time-step 20 times smaller than the

one for the fluid mechanics. It has to be noted that the times presented here are estimates based on the most likely flow conditions at a given temperature.

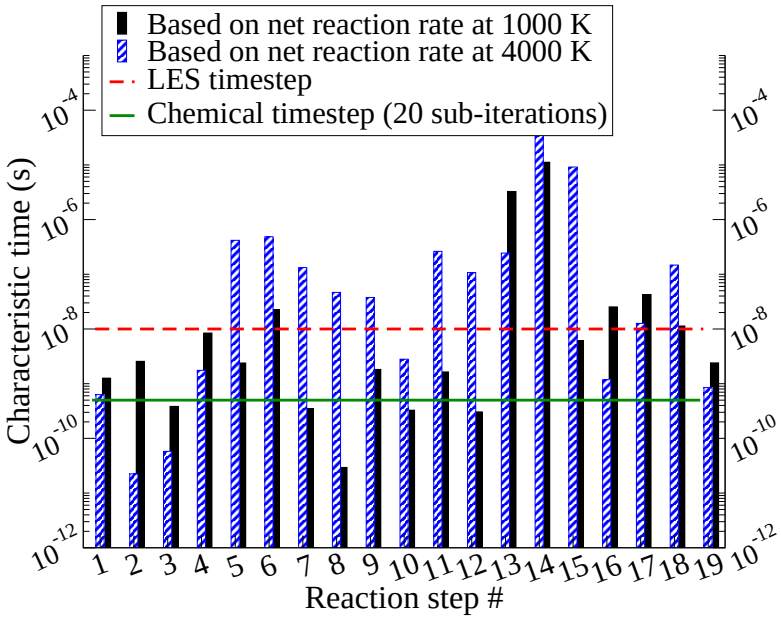

Figure 47: Comparison of the various chemical characteristic times and the time-steps of the flow solver. Longer bars mean larger time scales.

Actual characteristic times observed in the flow field can vary around these values, and very small characteristic times (1×10^{-15}s and smaller) have been observed locally for a short amount of time. These times would be observed for intermediate temperatures in the 2000-3000 K range when enough reactants are present. This makes the mechanism very difficult to integrate using brute force methods such as solving directly the system of differential equations. An additional observation can be made that the hottest regions of the flow present some of the largest characteristic chemical times in the flow since they are close to equilibrium condition. These temperatures are reached in a thin layer around the oxygen jet as well as further downstream where the grid resolution is quite coarse. Other solutions such as the use of artificial neural networks [276] could be investigated in order to find a better compromise between cost and accuracy.

Once the reaction rates, and thus the rates of change of each species, have been evaluated

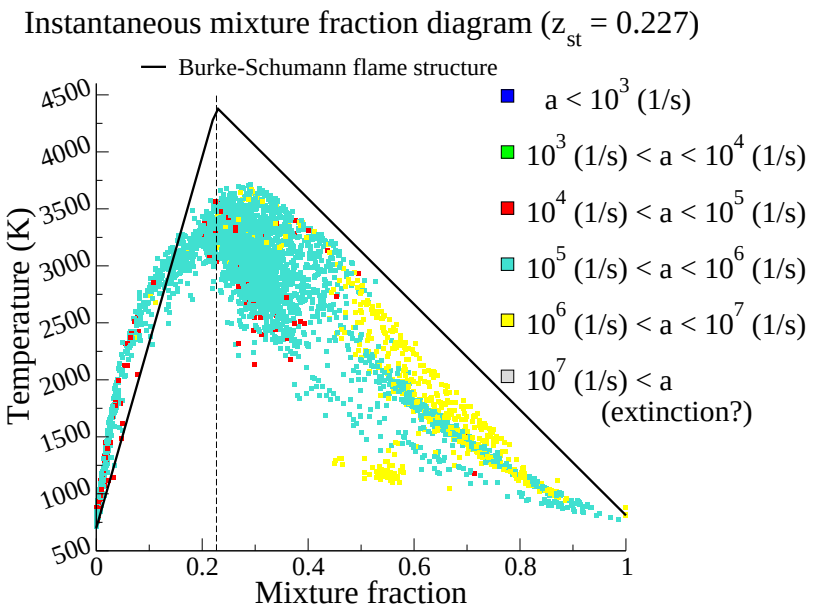

Figure 48: Scatter plot of the instantaneous diffusion flame structure for temperature versus mixture fraction. The points were extracted from a series of instantaneous snapshots and colored/sized by the local oxidizer strain rate.

with this laminar closure model, the coupling with the turbulent mixing remains an issue. The configuration of a typical H_2-O_2 coaxial injector is quite unique as it combines relatively high levels of turbulence (at least on the hydrogen side), fast chemistry and small physical dimensions. The resolution of 50 microns found in the shear layer between the two coaxial streams has important consequences on the closure of the combustion process. The smallest resolved eddies approach the thickness of the main reaction region in the near-field, and thus the importance of sub-grid mixing is diminished. This explains why simple models such as the Eddy Break-Up model [23] fail to model correctly the combustion in this region. With relatively large mixing times compared to the chemical times, a reaction rate based on the former is unable to sustain the flame under the high strain of the mixing layer. Simulations performed with such a combustion model produce lifted flames because the higher levels of turbulent kinetic energy in the shear layer are not large enough to sustain the near-extinction strain rates (5×10^6 1/s for a hydrogen-oxygen flame extinction strain rate of about 4×10^7 1/s according to Sohn et al. [291]) observed there.

The level of unresolved kinetic energy, below 10% of the resolved kinetic energy everywhere except in the near-wall region, provides limited amounts of sub-grid mixing in the diffusion flame. Moreover, as shown in Figure 47, the chemistry appears to slow down enough further downstream that the secondary combustion in the slow moving area between zone B and zone D does not require advanced sub-grid modeling. It seems that for a configuration such as PSU-RCM1, the small physical dimensions, the high-speed streams and the fast H_2-O_2 chemistry combine for a situation where the flame-turbulence interactions are not as critical to the overall flame dynamics as it is in other engines such as gas turbines. Thus the choice of turbulent combustion model is not as important. While additional resolution or more advanced modeling is probably required to improve near-wall behavior, the immediate benefits to the capture of the overall flame physics are not clear due to the decoupling of the turbulent and chemical timescales. Another clue to this phenomenon is the qualitative appearance of the flame when the reaction mechanism is solved exactly using direct integration. While that particular simulation was only run for a short amount of time due to its cost, the major species and main radicals (OH, O, H) fields were mostly identical to the ones obtained with the 20 sub-iterations scheme. This shows that the chemistry captured at a timestep 20 times smaller than the fluid mechanics time-step is qualitatively correct and that the implied decoupling, due to the large Damköhler number, is justified. Most of the flame is likely under quasi-laminar flamelet regime, which explains why the lack of explicit turbulent combustion closure is not critical in this case.

To further illustrate this point, Figure 48 displays the diffusion flame structure in the near-field of the PSU-RCM1 injector. Using the mixture fraction concept, different instances of the instantaneous flame are compared to a simplified Burke-Schumann flame structure which assumes infinite rate chemistry (hence the straight lines) and calorically perfect gas (hence the much higher flame temperature predicted). The local strain rate is computed based on oxidizer-side quantities as recommended by Balakrishnan et al. [9]. It is confirmed that the amount of strain experienced by the flame is large but not close to the theoretical extinction limit. The highest levels of strain are located on the fuel side, which is logical given the low densities on the hydrogen side. As seen earlier, vorticity and strain are limited

on the oxidizer side because of the density gradient and the flame structure on that side is very close to the idealized flame structure. The fuel side of the flame displays much stronger effects from mixing and strain rate, with even some relatively low temperatures associated with mixture fraction not far from the stoichiometric mixture fraction (equal to 0.227 in the PSU-RCM1 case because of the partial premixing of the inlets). These locations are most likely associated with pockets of hydrogen penetrating the oxygen jet, as will be shown later.

4.4.4 Heat flux and recirculation zones

The wall heat fluxes predicted by the current simulations given the chosen grids and combustion model are now investigated. The experimental data from Marshall et al. [172] is plotted in Figure 49 and includes the error bars estimated by the authors. For the three-dimensional simulation, the heat flux profile has been averaged temporally over 20 ms as well as spatially over the azimuthal direction. The individual fluxes in each azimuthal plane are also plotted in order to represent the scatter of the data.

Far downstream, for $X > 0.1$ m, the decay rate of the heat flux is correctly predicted even though magnitudes are off by about 20-25%. Upstream, experiments show a plateau of maximum heat flux between $X = 0.04$ m and $X = 0.08$ m, which corresponds to a recirculation flow along the wall in the current simulation. The current LES over-predicts by about 25% the value of that maximum heat flux, even though its location appears to be correctly captured. This might be due to the high levels of sub-grid kinetic energy convected from the the main shear layer to this wall location. A larger heat flux variability in the azimuthal direction exists around $X = 0.1$ m, as shown by the scatter of the dotted lines on the graph. This is due to the large scale fluctuations of the reattachment point of the main recirculation bubble. In the corner region, for $X < 0.04$ m, wall heat flux is greatly under-predicted because of a combination of low levels of k^{sgs} and relatively low temperatures. Although some axial heat transfer in the combustor walls cannot be ruled out, it might not be able to explain this discrepancy. Somehow, very little hot products are being convected in this secondary recirculation which remains relatively cold. Analysis of the transient flow evolution in the corner shows that this recirculation is always present but evolves very slowly. Unfortunately, the characteristic time of such recirculation zones is very large and is definitely an issue with respect to the actual convergence of the PSU RCM-1 simulations. Also, the shape of the heat flux profile is linked to the k^{sgs} field, as the turbulent heat flux represents a significant portion of the total heat flux with the current grid resolution. The exact near-wall behavior of the sub-grid turbulent kinetic energy is difficult to model, especially in the recirculation region where flow reversals and stagnation

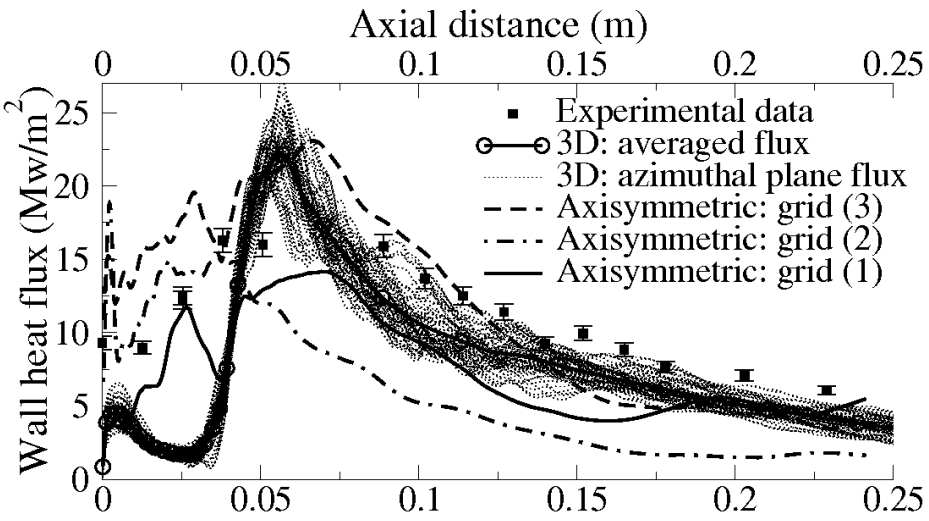

Figure 49: Comparison of the heat flux predictions for the 3D and axisymmetric simulations.

zones occur.

The heat flux prediction with increasing near-wall resolution in the axisymmetric configuration provides more insight on this behavior. The temporally averaged (over at least 25 ms) heat fluxes for the 3 axisymmetric grids are also shown on 49. With the baseline grid (grid (1)), similarly to the 3D grid, a large increase of the heat flux in the corner ($X < 0.05$m) is observed, so that it almost matches the experimental profile in that region. Downstream, the heat flux is even more under-predicted than with the 3D grid and overall, since the predicted heat flux is always lower than the experimental one, the global heat load on the chamber walls is significantly under-predicted. However, one could argue that the shape of the heat flux profile is closer to the experimental profile than with the 3D simulation. But one has to remember that the flow structure obtained with the axisymmetric simulations is very different from the one obtained with the 3D simulation and that the apparent match obtained here is merely a coincidence. This is proven by the heat flux predictions with the refined grids (grids (2) and (3)). As the strength of the recirculation region increases with resolution, the wall heat flux in the corner of the chamber increases and greatly exceeds the experimental values. Further downstream, because of the large recirculation region extending over the whole chamber, the heat flux decays much faster in the axisymmetric configurations than in the 3D configuration and the experimental profile. Similar trends

are observed with the axisymmetric simulations from Yang and Merkle as shown in Figure 50, with a reasonable match of the heat flux profile in the near-field ($X < 0.05$m) and a quick decay further downstream. Looking back at Figure 41, it appears logical that the axisymmetric simulations predict a heat flux maximum closer to the injection plane given the shapes of the recirculation region and the location of the stagnation point between the two recirculation bubbles. That the heat flux predicted in the near-field possibly matches the experimental one needs to be carefully evaluated under various grid resolutions. It could be a simple coincidence as it seems to be here with the baseline axisymmetric grid. Only the flow structure of the 3D simulation predicts correctly the location of the peak heat flux and a moderate improvement of the heat flux magnitude prediction in the near-field can be expected from a three-dimensional simulation using the wall-refined grid. For the current work, as mentioned before, the three-dimensional simulations will be limited to the baseline grid resolution due to available computational resources, which could explain the under-predicted heat flux in the corner. On the other hand, the high-resolution three-dimensional LES simulation by Oefelein shows excellent agreement with the experimental heatflux and predicts a flow structure in reasonable agreement with the current 3D LES simulation, and markedly different from the axisymmetric predictions.

Comparing the averaged flowfield and the instantaneous one at different axial locations yields more insight on these recirculation zones so critical to the heat flux prediction. Figure 52 displays the axisymmetric features of the averaged 3D flow through the temperature field. The same axisymmetric features are observed through the axial mean velocity field shown in Figure 51, where the central jet and its annular counterpart are clearly visible in the first slice along with the secondary recirculation. As the coaxial streams merge and expand, they squeeze both recirculation regions against the walls, resulting in maximum negative velocities near the wall for the main recirculation. At the entrance of zone D, the flow has yet to fully converge towards a perfectly axisymmetric solution. On the other hand, Figure 53 highlights the three-dimensionality of the instantaneous flow. In each figure, the first slice is located in zone A and C, the second slice at the boundary between zone A and

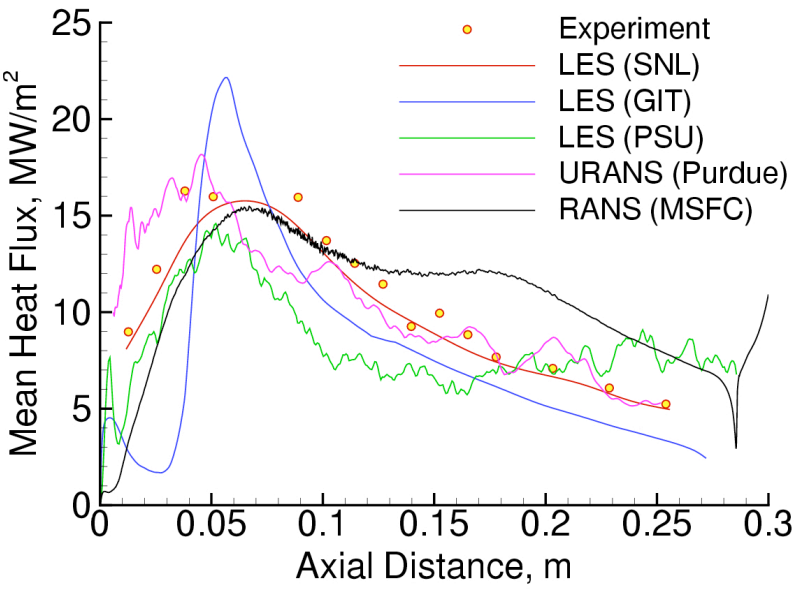

Figure 50: From Tucker et al. [314]: heat flux predictions from different solvers compared with corresponding experimental data. Current work corresponds to LES (GIT). LES (SNL) is the high-resolution LES from Oefelein, LES (PSU) is the axisymmetric LES from Yang, URANS (Purdue) is the axisymmetric unsteady RANS from Merkle and RANS (MSFC) is the axisymmetric RANS from NASA.

zone B, the third and fourth slices in zone B and C respectively, and the final slice at the beginning of zone D. The central jet and its annular counterpart can clearly be identified in the first slice along with the secondary recirculation in the averaged axial velocity field contours (not shown here for brevity). As the coaxial streams merge and expand, they squeeze both recirculation regions against the walls, resulting in maximum negative velocities near the wall for the main recirculation. At the entrance of zone D, the flow has yet to fully converge towards a perfectly axisymmetric solution. In the first slice of Figure 52, the hot gases convected by the main recirculation region are clearly visible, forming an annulus of temperature over 2000 K outside of the tight reacting mixing layer. In general, the temperature field appears more homogeneous than the axial velocity field.

The same recirculating hot products can be found in Figure 53 (a) although they do not form at all a continuous annulus around the main jets. Rather the secondary recirculation appears connected to the main jets at certain occasions. However, this connection is very limited in space and time and is unable to provide the secondary recirculation zone with

significant quantities of fresh hydrogen or hot products from the inner mixing layer. Another difference with the averaged field is that the maximum negative velocities are found in the shear layer between the hydrogen annular jet and the main recirculation region, not near the wall. This is due to the large outer vortices shown in Figure 54. The radial extension of the reacting inner mixing layer is also very apparent in Figure 53, with finger-like structures reaching far away from the centerline. Temperatures above 3000 K are restricted to this inner mixing layer and its surrounding positive axial flow. They highlight how the oxygen jet break-up is far from being axisymmetric. Unlike a simple jet in dump combustor, the coaxial configuration involves much more fluid transport across the centerline. This makes the use of a fully three-dimensional formulation even more critical since an axisymmetric simulation is unable to model a simple confined jet [265].

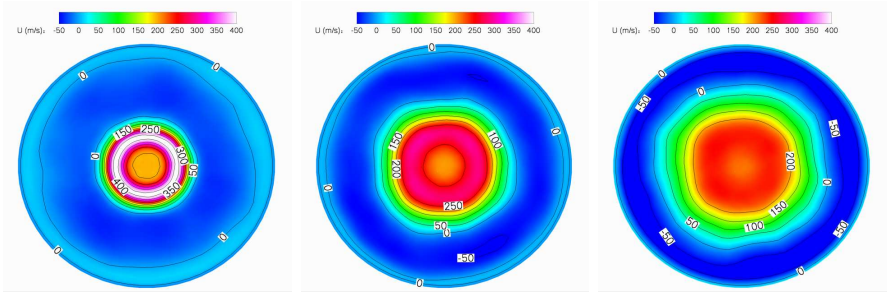

(a) $X = 0.0125$m (b) $X = 0.0250$m (c) $X = 0.0375$m

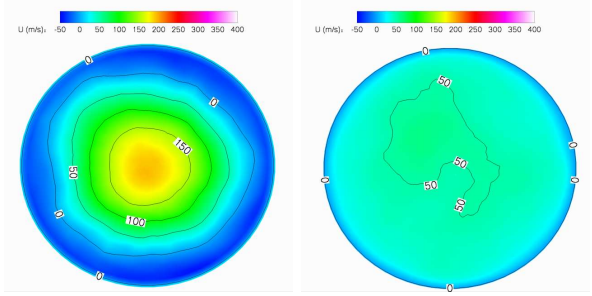

(d) $X = 0.0625$m (e) $X = 0.1250$m

Figure 51: Averaged axial velocity field at various axial locations. The flow is coming towards the reader.

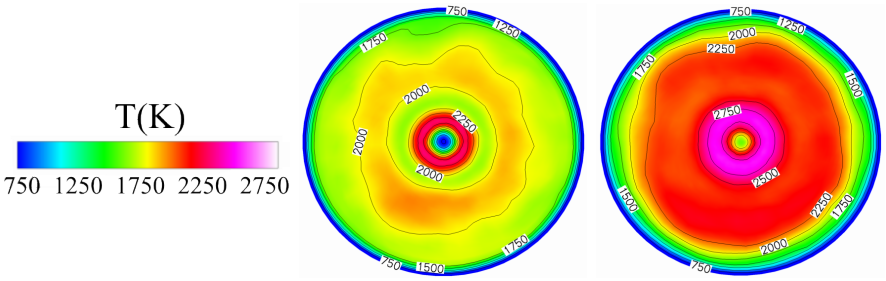

(a) Legend (b) $X = 1.25$cm (c) $X = 2.50$cm

(d) $X = 3.75$cm (e) $X = 6.25$cm (f) $X = 12.50$cm

Figure 52: Averaged temperature field in Kelvins at various axial locations. The flow is coming towards the reader.

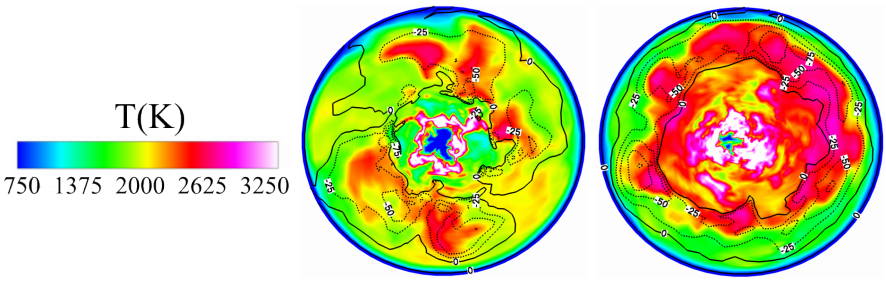

(a) Legend (b) $X = 1.25$cm (c) $X = 2.50$cm

(d) $X = 3.75$cm (e) $X = 6.25$cm (f) $X = 12.50$cm

Figure 53: Instantaneous temperature field in Kelvins at various axial locations with negative axial velocity contours (dashed lines). Solid black lines delimit recirculation regions. The flow is coming towards the reader.

4.4.5 Unsteady flame features

Figure 54 focuses on the breakdown of the oxygen jet. From the tip of the oxygen sleeve to about one diameter downstream, a zone without any large coherent vortical structures can be observed. The very high speed H_2 stream flows straight out of its sleeve while the slow O_2 stream displays only small wrinkles probably caused by the gas expansion near the flame anchor. This anchoring is possible because of a recirculation region right behind the step between the two reactant streams. The recirculation length is two step heights at most. For the remainder of the first diameter, the velocities in this mixing layer remain very low. The flow dynamics then change abruptly when the H_2 annulus starts to get unstable and shed vortices that act as strong perturbation to the oxygen jet. Hydrogen can be seen penetrating the core of the central jet and creating pockets of burned gases further downstream. These pockets appear to be the central mechanism to the oxygen jet break up, more so than pure fluid mechanics shedding. In fact, after three diameters from the injection plane, large scale vortical structures have either broken down or been significantly damped by gas expansion. The remaining pockets of unburned oxygen are surrounded by mostly diffusive flames that will consume them as they move downstream.

Figure 55 attempts to analyze the flame structure around the oxygen jet through another approach. Following the analysis of Amantini et al. [4], the premixedness index is computed:

$$\alpha = \arccos\left(\frac{\nabla Y_{H_2} \cdot \nabla Y_{O_2}}{||\nabla Y_{H_2}|| \times ||\nabla Y_{O_2}||}\right) \tag{4.4.1}$$

Expressed in degrees, it can vary between 0 (pure premixed environment) to 180 (pure diffusive environment). This is the color contour shown in Figure 55. Since it would be meaningless to plot this quantity everywhere, it is only drawn when the value of the mixing index $||\nabla Y_{H_2}|| \times ||\nabla Y_{O_2}||$ is above an arbitrary value. This effectively highlights where primary combustion between H_2 and O_2 occurs. Indeed, it appears that this primary combustion occurs only at the surface of a tube around the oxygen jet; an open tube, and not a closed one as could have been expected since the overall equivalence ratio is slightly rich. In the case of the PSU-RCM1 injector, the premixedness index lies between 90 and 180,

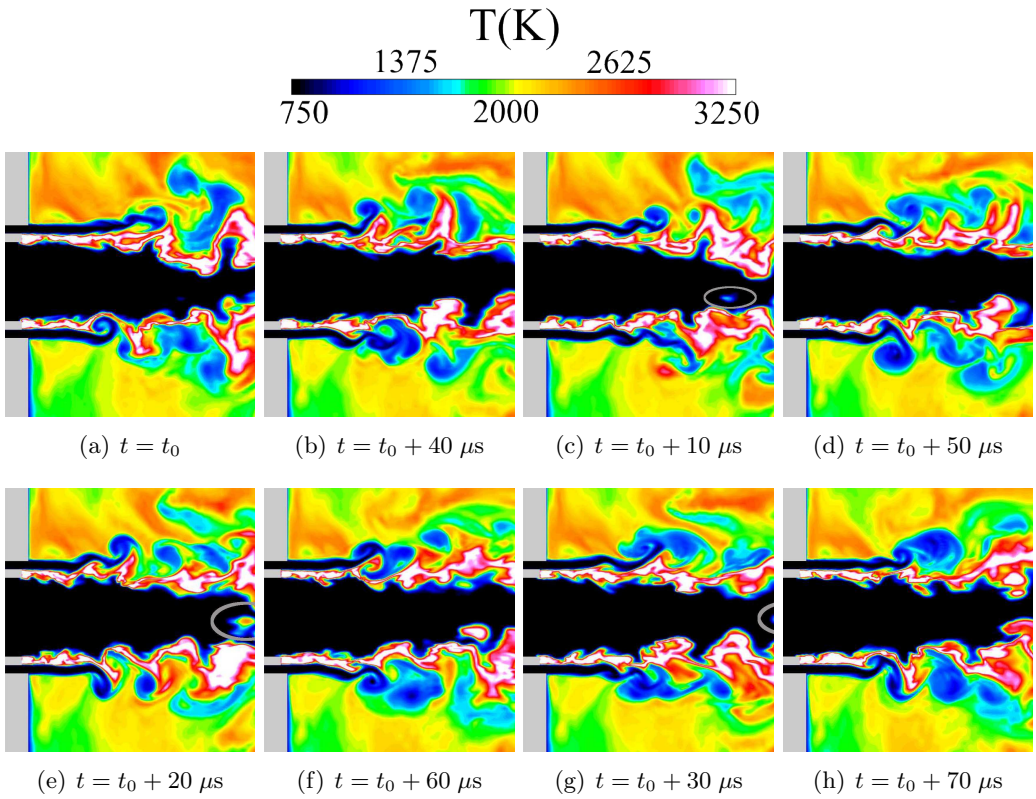

(a) $t = t_0$ (b) $t = t_0 + 40\ \mu$s (c) $t = t_0 + 10\ \mu$s (d) $t = t_0 + 50\ \mu$s

(e) $t = t_0 + 20\ \mu$s (f) $t = t_0 + 60\ \mu$s (g) $t = t_0 + 30\ \mu$s (h) $t = t_0 + 70\ \mu$s

Figure 54: Successive snapshots of the oxygen jet breakdown process, using color contours of the temperature field. The gray ellipses highlight the penetration of hydrogen into the oxygen jet and the subsequent flame that breaks the tip of the jet.

indicating a range from pure diffusion flames (in red in Figure 55) to partially premixed flames (in blue-green). It appears that there is a preferred location in the flow where this moderate amount of premixing occurs. As reported previously, the onset of the vortex shedding of the H_2 annulus flow has major repercussions on the injector dynamics. The large scale structures are able to partially premix the reactants and put the flame under a large strain as seen in next section. But as these vortical structures quickly decay, premixing decreases in the second part of the flame, and once again the primary combustion between H_2 and O_2 takes place in a purely diffusive fashion.

Figure 55 allows us to identify one more interesting feature for this flame. While the velocity vectors are essentially parallel to the diffusion flame, and thus, the stoichiometric line, over the first couple of diameters, they can become perpendicular to the flame when the jet exhibits large wrinkles further downstream. This can probably be linked to the

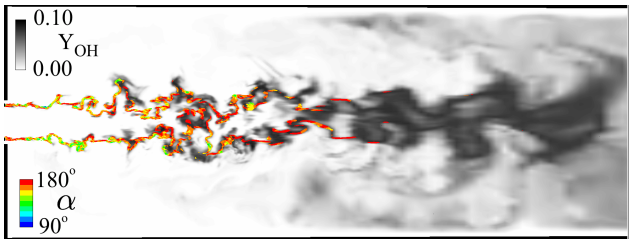

(a) Overall view

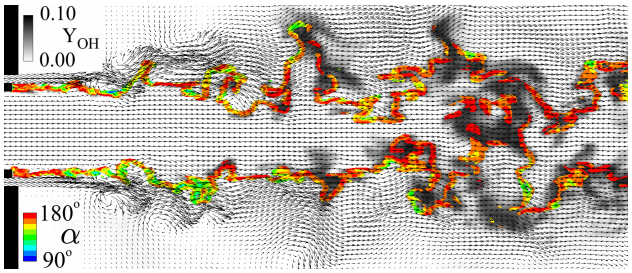

(b) Close-up view

Figure 55: Visualization of the combustion regime for the diffusion flame around the oxygen jet. In both figures, gray-scale contours show OH mass fraction. The color contours show the premixedness index (angle expressed in degrees) but only in regions where the mixing index is large enough. The close-up view includes velocity vectors.

penetration of H_2 in the oxygen jet reported previously, as the hydrogen gets convected before it even reacts with the oxygen. Finally, as the remaining pockets of oxygen are consumed along the centerline, the process is no longer purely diffusive since the flame tube remains open over time. On the outside, secondary combustion between the excess hydrogen and the freshly produced OH provides more heat release, and explains the peak of temperature observed away from the tip of the oxygen core.

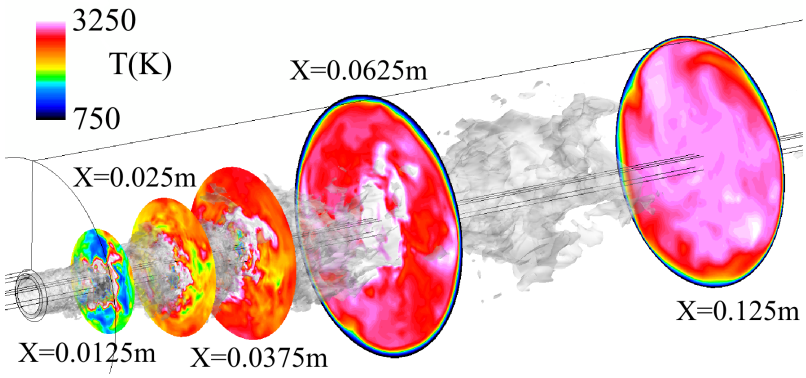

(a) Instantaneous

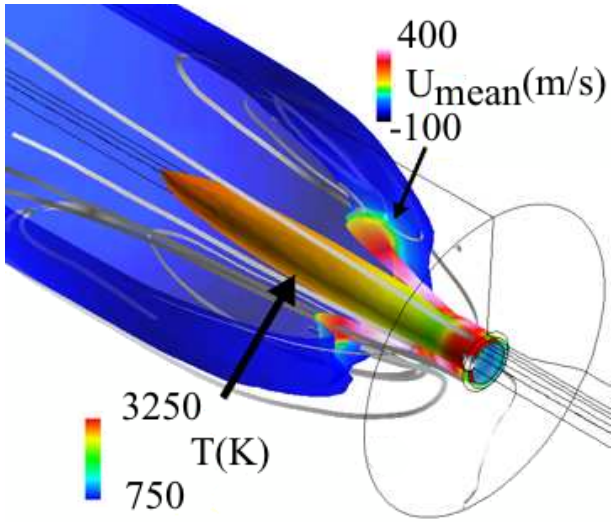

(b) Time-averaged (20 ms)

Figure 56: Three-dimensional view of the flowfield. Top, the instantaneous, non-axisymmetric flow. The gray isosurface is drawn for a mass fraction of OH equal to 0.05. The various slices along the X-plane show the temperature field with the same scale as in previous figures, from 750 K to 3250 K. Bottom, the time-averaged axisymmetric flowfield. The inner isosurface corresponds to an oxygen mass fraction of 0.25 and is colored by temperature according to the scale shown at the bottom. The outer isosurface corresponds to a temperature of 3000 K and is colored by axial velocity according to the scale shown on the right.

4.4.6 Other three-dimensional and dynamic aspects

With Figure 56, the emphasis is put on the three-dimensional features of the transient flow while the time-averaged picture remains perfectly axisymmetric. The different slices in Figure 56 (a) easily relate to the zones previously defined. The first slice, at $X = 0.0125$ m, is in the middle of zone A and displays the large azimuthal variations of the purely diffusive flame. Moving to the second slice at $X = 0.025$ m, the intense and thin diffusion flame has been replaced by the partially premixed flame highlighted previously. Outside the mixing layer, hot burned products alternate with fresh H_2 from the fuel stream, but the further downstream in zone B, the more uniform the outside field becomes. Finally, by $X = 0.125$m, most of the OH has been consumed (end of the gray isosurface) and the uniform flow enters zone D. The strong azimuthal variations observed in the temperature field have a direct impact on the instantaneous heat flux but over the course of the simulation, these variations rightfully cancel out and the axisymmetric field shown in Figure 56 (b) is obtained. The question is whether or not the full 3D formulation is then necessary for such a configuration. We believe the oxygen jet break-up requires a centerline free of any velocity constraint. Around the pockets of unburned oxygen, there is significant radial velocity across the centerline, and thus a non-axisymmetric configuration. While the oxygen jet breakup cannot be attributed solely to vortex shedding, fluid mechanics do play an important role in this process. It should be noted that the transient non-axisymmetric features mentioned previously do not generate any azimuthal, steady instability, such as swirl or tangential acoustic waves. Both recirculation regions remain immobile in the azimuthal direction while pressure traces in 4 diametrically opposed corners of the chamber show no sign of phase delay. Additional analysis of these pressure signals show a dominant frequency around 2.8 kHz, in the range of frequency for the first longitudinal mode.

Figure 57 highlights the transient nature of the heat transfer to the wall. The simulated heat load, that is the integral, over the cylindrical part of the chamber, of the wall heat flux, displays a 30% peak-to-peak amplitude as it oscillates at a frequency of about 2.4 kHz. This relatively high-frequency oscillation could be of acoustic nature as it seems to match the fundamental longitudinal acoustic mode of the chamber, even though the discrepancy with

the pressure spectrum cannot be easily reconciled. It also could be linked to the natural roll-up frequency of the outer shear-layer. Cole et al. [38] have linked the unsteadiness of the reattachment location to the frequency of the shedding over the dump plane. While it is difficult to choose a reference velocity in the coaxial configuration, an estimate of 200 m/s over a step height of 15 mm yields a Strouhal number of $\frac{2400*0.015}{200} \approx 0.18$, about twice as small as what is reported by Cole et al. for a non-reacting, axisymmetric jet in a dump combustor. In the end, a combination of these two effects is possible, with the higher frequency acoustic mode interacting with the lower frequency of the roll-up process to produce the intermediate frequency observed in the heat flux signal.

Looking at the transient signal, a low-frequency oscillation, probably below 100 Hz, could also be present. This frequency is probably too low to be explained by a pure acoustic phenomenon inside the main chamber but it also seems unlikely to be related with the chugging of the feed lines, a low-frequency instability observed in full-scale rocket engines as well as in sub-scale experimental chambers [303]. Such experimental data on the pressure variations at various locations of the combustor should be easier to obtain than a detailed flow visualization and could help obtaining more insight on the physical processes at stake in the chamber. Finally, the difference between the average value of heat load in the experiment and in the current study is slightly less than 20%, which once again seems a reasonable result given our assumptions and our near-wall resolution.

4.5 Conclusions and perspectives

This chapter highlights the results obtained in the simulation of the PSU RCM-1 rig in the context of the evaluation by NASA of several state-of-the-art CFD techniques. With current available computational resources, the present simulations represent a large effort and the focus is on evaluating the quality of the current approach in capturing realistic flame dynamics and accurate heat flux prediction. The influence of closure models and overall resolution has also been included in this discussion. In general, the current unsteady and three-dimensional approach appears to successfully produce a physical flow field, with

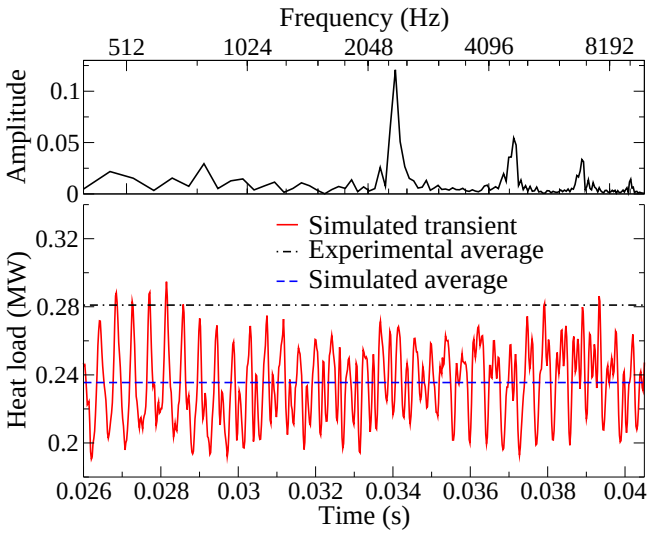

Figure 57: Analysis of the heat load signal: top chart shows the spectrum of the heat load on the chamber walls while the bottom graph shows the evolution of the heat load over time and compares the simulated average with the experimental average.

marked transient and non-axisymmetric features which eventually produce a perfectly axisymmetric time-averaged picture. It appears that the PSU RCM-1 configuration considered in this study presents several characteristics that strongly influence the validation effort. On one hand, the size of the combustor and the lack of flow confinement have a negative effect on the convergence time and thus the cost of our simulation. On the other hand, it seems that the resolution requirements of the fluid mechanics and the fast chemistry allow for a satisfactory implicit modeling of the turbulent combustion using a quasi-laminar finite rate model without requiring a more complex and explicit approach.

The reported wall heat flux cannot be measured directly but needs to be computed from temperature measurements. The conversion from temperature measurements to heat flux data is far from trivial for various reasons:

- The questionable validity of the one-dimensional approximation often used to solve for the heat flux from thermocouples data, as illustrated by the works of Vaidyanathan et al. [319]. deRidder et al. [56] provide a brief overview of the mathematical complexity of the problem.

- The importance of the transient heat flux and the need for the combustion chamber

to reach a state of thermal equilibrium [43].

Thus, with only the wall heat flux for comparison and validation, it is difficult to draw definite conclusions on the cause of the observed discrepancies. While the current results are encouraging, the fine tuning and definite validation of a given turbulent combustion model for rocket engine flows will require more efforts and more detailed experimental data. Such data have started to become available for both gaseous oxygen injection [161] in the form of high-speed visualization and high-speed absorption spectroscopy.

Nonetheless, the current three-dimensional LES formulation, using an hybrid solver, appears capable of predicting the overall physics of the flow, even on relatively coarse grids. It represents a powerful analysis tool that can be extended to other configurations related to rocket engines, especially under conditions where real gas effects could be dominant as will be seen in the next chapters. The possibility of using a 7-step, 6-species mechanism instead of a 21-step, 8-species mechanism was also demonstrated here for H_2-O_2 coaxial configuration which whill allow the computational cost of the reacting real gas simulations to remain reasonable.

Over the last few years, this configuration [147, 145], or very similar ones [332], have been intensely studied but the lack of flow visualization prevents definitive conclusions to be drawn from the many numerical results obtained. However, the consensus echoes the observations made in this chapter: steady or two-dimensional simulations are unable to capture the wall heat flux correctly without fine tuning. And when a good match is obtained, the predicted flowfield does not correspond to the one obtained with three-dimensional unsteady simulations. Fortunately, as reviewed in Section 1.3.2, better experimental data are becoming available that should allow a better validation of CFD solvers. This will be the focus of the next two chapters.

CHAPTER V

LIQUID-GAS NON-REACTING SHEAR COAXIAL INJECTOR

As presented in Section 1.3.3, the experiments from Locke [160] have been selected to validate the current CFD solver. This chapter will focus on LOX-GOX and LOX-GN2 non-reacting studies. The exact experimental setup is first introduced and then a few specificities of the formulation for this mixing case are discussed. A grid independence study is then shown and the LES predictions are compared qualitatively to the experiments through various visualizations. This is followed by quantitative comparisons and the exploration of scaling laws for the dark core length. Finally, a multi-species case is examined in order to validate the LEM-LES for

5.1 Experimental setup

Designing a series of experiments in order to help the validation of Computational Fluid Dynamics (CFD) solvers is not a simple task. It is especially challenging when considering the validation of a LES solver for rocket engine applications:

- Both instantaneous and time-averaged measurements are needed for LES. The validation should be performed on distributions of flow quantities over time as well as their mean values. Experiments usually provide only one type of data.

- In order to keep the geometry simple and the computational cost low, uni-element geometries are usually considered. However, they display a number of features that do not facilitate CFD work. The combustion chambers are usually not cooled and so to sustained the heat load, their volume is artificially large. This reduces the heat transfer from the flame but also creates large recirculation regions in the corners of the chamber. This means large timescales are present in the flowfield, not only in these recirculation regions but also because the mean axial velocity is modest, causing large flow-through-time and slow transients.

- Operating conditions, even when simply considering high-pressure mixing, make it extremely difficult to collect accurate and extensive flow quantities. The challenges faced to build high-pressure combustion chambers with optical access are well summarized by Habiballah et al. [95] and by Santoro et al. [263].

As part of the Constellation University Institutes Project (CUIP) by NASA, an experimental facility was designed in cooperation with computational researchers in order to solve some of the issues mentioned earlier. While the main focus of this facility was the study of reacting oxygen-hydrogen systems under high pressure, some cold flow studies were also conducted. The overall setup is similar to the previously investigated gas-gas configuration (see Chapter 4) with the main difference being that the injection plate is perforated to allow a co-flow around the uni-element injector, thus eliminating the large recirculation regions and their harmful side-effects. As can be seen on Figure 58, there is a large gap (about 4 mm) between the edge of the annular flow and the start of the co-flow. This will allow the coaxial jet to evolve on its own initially. The coaxial configuration was described in Section 1.2.1, in particular in Figure 1 which uses the same conventions than here, while a schematic of the injector plate can be seen in Figure 58. The inner diameter of central jet is D_i=2.0574 mm, which will serve as reference length from here on. The thickness of the sleeve around the central jet is t_{post}=130μm. Details about the dimensions of the chamber and the operating conditions can be found in the original work by Locke [160]. A few details about the operating conditions are given in Table 13.

The perforated plate consists of 78 holes for a total injection area of 8.73×10^{-5} m^2. Modeling each individual hole with a structured grid would significantly increase the complexity and cost of the simulations ans as a first approximation, a uniform flow from a radial distance of 6 mm up to the chamber walls can be thought as an alternative. The injection area increases more than 5 fold to 5.32×10^{-4} m^2 then. The bulk velocities for the coflow reported in Table 13 correspond to this uniform coflow assumption. The exit velocity through individual holes would be more than 5 times higher than these bulk values. The validity of this assumption will be addressed in the next section.

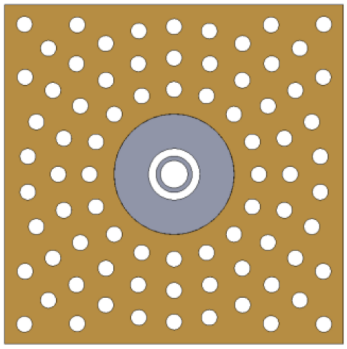

Figure 58: Head-on view of the injector face for the non-reacting LOX-GOX studies as well as the reacting studies from Chapter 6. The gray region represents the footprint of the injector sleeves, identical to the one used for the PSU RCM-1 rig.

Table 13: Operating conditions for the case where sub-critical oxygen is injected into the chamber at super-critical pressure. The reference species is oxygen, whose critical pressure is 50.4 bar and critical temperature is 155 K.

Description	Units	LOX-GOX XP
Main chamber		
Chamber pressure	Pa	5.750×10^{6}
Average density	$kg.m^{-3}$	138
Average velocity	m.s−1	4.57
"Preburner" oxygen background flow		
Mass flowrate	$kg.s^{-1}$	0.268
Inflow density	$kg.m^{-3}$	84.6
Background flow area	m^2	5.32×10^{-4}
Inflow temperature	K	262
Bulk inflow velocity	m.s−1	5.95
Injector inner post oxygen flow		
Mass flowrate	$kg.s^{-1}$	0.0836
Inflow density	$kg.m^{-3}$	1080
Inflow temperature	K	105
Compressibility		0.195
Inflow velocity	$m.s^{-1}$	23.3
Reynolds number		3.6×10^{5}
Injector annular oxygen flow		
Mass flowrate	$kg.s^{-1}$	0.0557
Inflow density	$kg.m^{-3}$	86.9
Inflow temperature	K	269
Compressibility		0.999
Inflow velocity	$m.s^{-1}$	108.4
Reynolds number		2.6×10^{5}
Injector characteristics		
Velocity ratio	$\frac{\text{annulus}}{\text{post}}$	4.35
Mass flow ratio	$\frac{\text{post}}{\text{annulus}}$	1.50
Momentum ratio	$\frac{\text{annulus}}{\text{post}}$	3.10
Momentum flux ratio	$\frac{\text{annulus}}{\text{post}}$	1.44

5.2 Specificities and numerical setup of the mixing study

For the most part, the LES simulations in this chapter will consider a single species and will simply track the mixing of the different inlets through the convection-diffusion of passive scalars. This has a few implications on the formulation used. The passive scalar equations are very similar to the species equations (Eq. 2.2.11):

$$\frac{\partial \bar{\rho}\widetilde{X_k}}{\partial t} + \frac{\partial}{\partial x_i}\left(\bar{\rho}\widetilde{u_i}\widetilde{X_k} + \bar{\rho}\overline{\mathcal{D}}\frac{\partial \widetilde{X}_k}{\partial x_i} + X_{i,k}^{\text{sgs}} + \theta_{i,k}^{\text{sgs}}\right) = 0 \tag{5.2.1}$$

Since there is only one species here, oxygen, the diffusion coefficient $\mathcal{D}$ is simply the self-diffusion coefficient of oxygen. Similarly, the cross-diffusion Dufour and Soret terms are neglected. The localized dynamic procedure (LDKM) is used here to compute these coefficients, but not the turbulent Prandtl and Schmidt numbers, who are assumed to be equal to 0.9 and 1.0 respectively. Note that the value of Sc_t has no influence on the flow here as it only affects the passive scalar fields. For a single species, the filtered pressure expression is also simplified:

$$\bar{p} = \bar{\rho}R_u \sum_{k=1}^{n}\left(\frac{\widetilde{Z}\widetilde{Y_k}\widetilde{T}}{W_k}\right) + \bar{\rho}R_u \sum_{k=1}^{n}\left(\frac{\widetilde{ZY_k}T - \widetilde{Z}\widetilde{Y_k}\widetilde{T}}{W_k}\right) \tag{5.2.2}$$

$$= \bar{\rho}R_g\widetilde{Z}\widetilde{T} + \bar{\rho}R_g\left(\widetilde{ZT} - \widetilde{Z}\widetilde{T}\right) = p(\bar{\phi}) + \bar{\rho}R_g\left(\widetilde{ZT} - \widetilde{Z}\widetilde{T}\right) \tag{5.2.3}$$

The first term on the right hand side contains only resolved variables while the temperature-compressibility correlation may require closure. For thermally perfect gases, $Z = 1$ and there is no need for closure. For non-ideal gases, Selle et al. [273] showed that the unknown thermodynamic variables could be computed from the filtered variables with little error. However, they also showed flows where previously neglected gradients such as $\nabla(\bar{p} - p(\bar{\phi}))$ or $\nabla(\bar{Q}_{i,\text{IK}} - Q_{i,\text{IK}}(\bar{\phi}))$ could have a dominant effect on the momentum or energy equation and suggested closure models for them. For a single-species formulation that does not contain Soret or Dufour effect, only the pressure gradient term might be of significance. For a similar single-species study as this one, Selle and Schmitt [274] decided to not include these models in order to first evaluate their LES approach without modeling specific to non-ideal gas behavior. Finally, for the equations of state, no mixing rules are needed for single species flow. Both Redlich-Kwong and Peng-Robinson EoS are used for this work and will

be compared in the results section. Viscosity and thermal conductivity are computed using the Chung's method for large densities while the diffusion coefficients are computed using the Fuller's approach modified by the high-pressure correction by Riazi and Whitson. For a comparison of the thermodynamic and transport properties predicted by each equation of state, the reader is referred to Appendix D.3. Finally, the hybrid scheme described in Section 3.3 and with the set of parameters $(\epsilon_\rho, \epsilon_p, C_\rho^{\text{cutoff}}, C_p^{\text{cutoff}}) = (0.10, 0.10, 0.25, 0.5)$ is used for the spatial integration of the governing equations. Constant-mass non-reflecting boundary conditions are used at the inflow.

5.3 LOX-GOX simulations

5.3.1 Grid independence and post-processing

A grid independence study is conducted to justify the validity of the current Large Eddy Simulations. For this study, four main grids were investigated and will be referred to as: (a) a "baseline" grid with 3 million grid points (400×120×64) (b) a "I-refined" grid with 5 million grid points (650×120×64) (c) a "IK-refined" grid with 7.5 million grid points (650×120×96) (d) a "coarse" grid with only every other point from the baseline grid. The justification for this last grid comes from Georgiadis et al. [82] who suggest it as another way of establishing the validity of the LES approach for a baseline grid. The solution obtained on this coarse mesh should be at least qualitatively similar to the baseline grid for this baseline resolution to be deemed reasonable. The baseline grid is presented in details in Figures 59 and 60. The overall view shows the transition from a square cross-section to a circular cross-section and further downstream, a convergent-divergent nozzle. As will be detailed later, most of the simulations presented here will not include this nozzle but it is shown here for completeness. The close-up view shows the cartesian grid along the centerline of the domain and the butterfly, cylindrical around it.

Indeed, all grids yield qualitatively similar flows, whose general three-dimensional structure is illustrated in Figure 61. Near the injection plane, streamlines highlight the toroidal

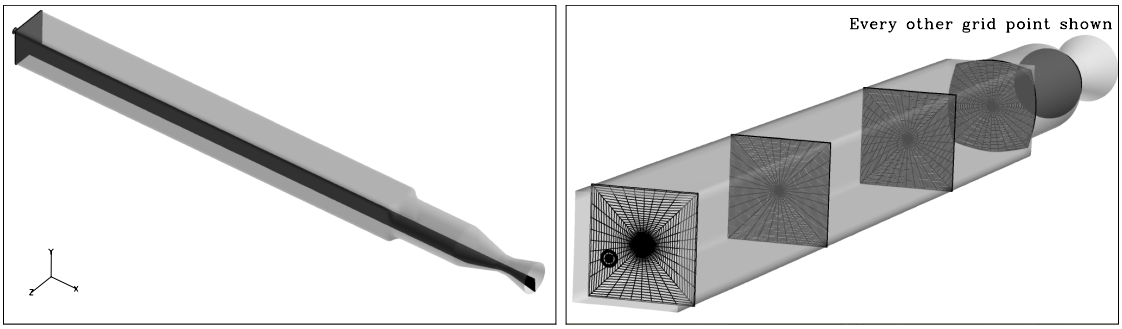

Figure 59: Overall view of the baseline grid for the LOX-GOX simulations.

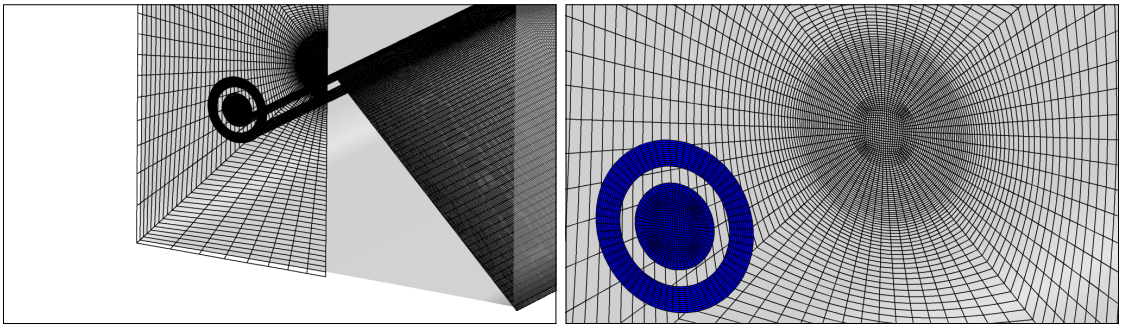

Figure 60: Close-up view of the inlet of the baseline grid for the LOX-GOX simulations.

recirculation region located between the annular jet and the coflow. The isosurface of Q-criterion shows the vortical structures generated by the main shear layer which break down as the central jet starts flapping away from the centerline. Finally, the color contours of the specific heat at constant pressure highlight the thin trans-critical layer at the edge of the compressed liquid oxygen jet. The hybrid scheme captures this thin layer and the very strong density and C_p gradients associated with it. A one-dimensional profile 5 diameters downstream of the injection plane and across the oxygen jet illustrates the large variations of C_p and how the numerical scheme handles it with only a few points across the trans-critical layer. Even the coarse grid resolves this trans-critical layer albeit with significant numerical dissipation, which has consequences on the jet breakup as will be seen in the next section. Moreover, the baseline and refined grids display realistic turbulent spectra as shown in Figure 62. The three velocity components, as well as the kinetic energy spectrum, appear to recover the Kolmogorov -5/3 spectrum, an indication of sufficient resolution for

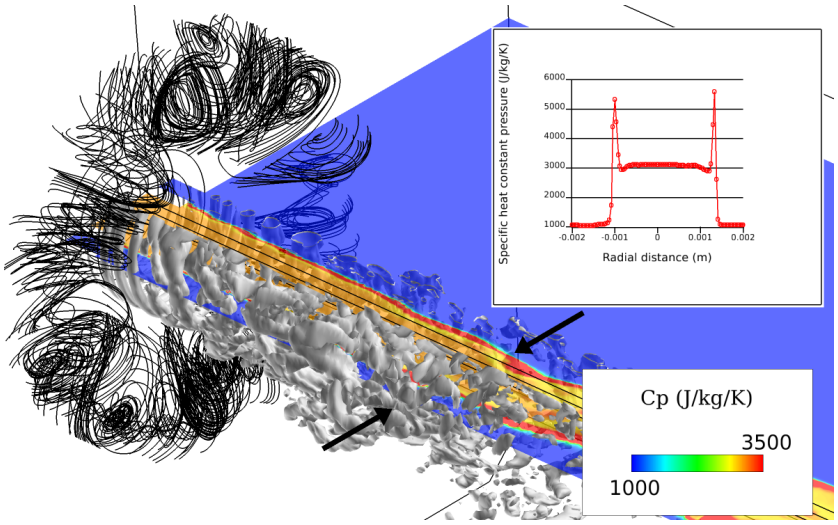

Figure 61: Instantaneous snapshot for the baseline LOXGOX LES simulation

a proper LES model. As mentioned in the Formulation section, all simulations presented here use LDKM for the computation of the model coefficients in the sub-grid kinetic energy transport equation but do not inject inflow turbulence. This assumption is justified by the fact that coaxial jets, especially at large velocity ratios, are less sensitive to inflow conditions than simple jets since the main instability comes from the annular shear layer between the two streams, not the initial perturbation in either stream [327]. Figure 63 shows the time-averaged (over 15 ms) radial profiles for $C_\nu/0.067$ and $C_\epsilon/0.917$ at different axial locations. The main features are local minima around the main shear layer between the two coaxial streams and dissipation peaks at the edge of the oxygen jet.

Another feature for these grids is that by default, they do not include the experimental convergent-divergent nozzle. Such addition can artificially reduce the solver timestep as the non-reacting flow can only be choked through a very small throat. Transient waves can also be generated during the choking process and they take a long time to be dissipated in the chamber. A parametric study using the coarse grid was conducted by replacing the nozzle with an outflow of variable reflectivity at the throat location. No significant differences could be observed in the jet break-up behavior or in the acoustics of the chamber between the simulations with the nozzle, a strongly reflecting outflow and a semi-reflecting outflow.

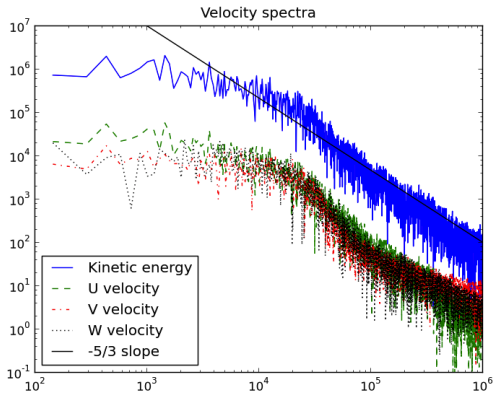

Figure 62: Typical turbulent spectra obtained downstream of the oxygen dark core, at location $(x, y, z) = (0.026\text{m}, 0.002\text{m}, 0.000\text{m})$.

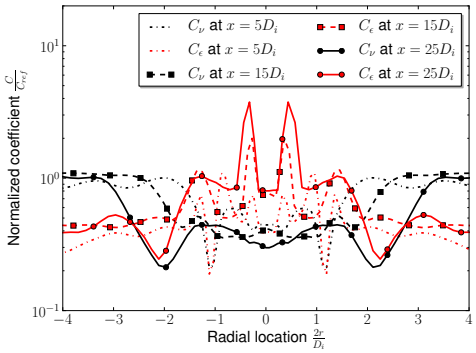

Figure 63: Time-averaged radial profiles of the coefficients of the sub-grid kinetic energy transport equation at three axial locations.

All results presented in this work will thus be without the nozzle being modeled.

Pressure traces and spectra representative from all runs are shown in Figure 64. This highlights the stability of the pressure after 30 ms of simulation, with small fluctuations of less than 0.5% of the mean pressure, highlighting the lack of strong acoustics or strong preferred mode. The pressure spectra show a rather broad peak between 1 kHz and 20 kHz, with minor peaks around 1.5 kHz and 15 kHz. The lower-frequency peak does not correspond to the longitudinal mode of the chamber, which is about 875 Hz, but might to the jet preferred mode, assuming a Strouhal number $St = fR_i/U_i$ of 0.3, which yields a frequency of 1700 Hz. The higher-frequency peak corresponds to a hybrid mode between the jet mode and the very high-frequency shear layer mode. The Strouhal number for this shedding frequency is 0.096, based on the tip thickness and the liquid oxygen velocity. It matches the Strouhal number obtained by Tsohas et al. [312] for a reacting shear coaxial liquid-gas injector with a thin sleeve, the same configuration as the one studied here except non-reacting.

Regarding the choice of thermodynamics, the Redlich-Kwong and the Peng-Robinson EOS show very similar flow structures and statistics as expected for a non-reacting flow. The PR EOS yields a slightly smaller momentum flux ratio for a fixed velocity and temperature as it slightly over-predicts the liquid oxygen density (by 12% at 105 K, the current injection

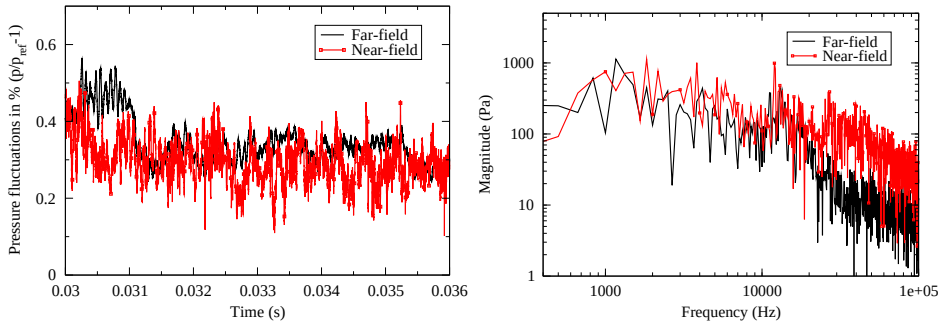

Figure 64: Representative time-trace (top) and power spectrum (left) for the pressure signal at a near-field location $(x, y, z) = (0.041\text{m}, 0.002\text{m}, 0.000\text{m})$ and at a far-field location $(x, y, z) = (0.206\text{m}, 0.000\text{m}, 0.000\text{m})$ for the baseline grid without nozzle.

temperature). On the other hand, the RK EOS over-predicts the specific heats in the compressed liquid region, thus requiring more heat to transition to a super-critical state (the ΔH between the injection temperature and the trans-critical state is about 20% larger for the RK EOS). Both shortcomings seem to have a similar effect on the jet breakup leading to very similar flow structures and dark core length statistics. This absolute effect is likely a slight lengthening of the dark core compared to what more exact thermodynamics would predict. It is hard to quantify exactly how large of an effect this could be but since the relative errors are small, it is likely to have a linear effect on the dark core length and the error is estimated at $\pm 10\%$. This comparison is not shown here for brevity and from this point forward, only results obtained with the Redlich-Kwong equation of state will be shown. Regarding the hybrid scheme, Figure 65 shows the extent of the MUSCL scheme for the baseline grid. It can be seen that there are almost no isolated cells with the MUSCL scheme on as this has a tendency to cause numerical issues around that cell. Instead, the upwind scheme is applied continuously from the liquid core to the edge of the dense fluid region.

Finally, to conclude the qualitative assessment of the current simulations, an attempt at reproducing the backlit images obtained experimentally is shown in Figure 66. Exactly replicating the backlit images from Locke [160] would require to model the light source and then use ray-tracing while accounting for reflection, absorption and scattering across the

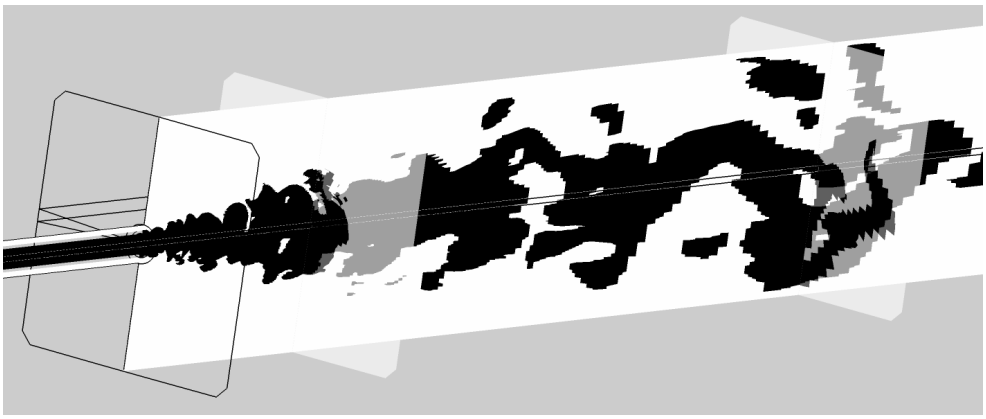

Figure 65: Extent of the upwind scheme shown in black in different slices of the chamber for the baseline grid simulation.

super-critical fluids, a task beyond the scope of this work. Instead, two simple visualizations are shown here to allow qualitative comparison between the experiment and the numerical simulations. The image shown in the middle row of Figure 66 is a simple vertical slice of the computational domain showing the density field as filled grayscale contours and a passive scalar for the central jet fluid which highlights the edges of the jet. The image shown at the top of Figure 66 was generated by taking 200 slices of the computational domain with the fluid density as grayscale index and convoluting them to approximate a line-of-sight integration. A pocket of dense, dark fluid would thus block all light and produce a dark pocket on the resulting image even if the surrounding fluid in the direction of integration was very light. It is however difficult with this technique to pickup the small variations around the jet and qualitatively, the simple slice is actually closer to the experimental image. In any case, this figure shows that the overall flow structure is well captured by the numerical simulations, with finger-like structures emanating from the central jet as well as a spreading rate and a dark core length that seems comparable to the one observed experimentally. As the liquid oxygen is convected downstream, the tip of the jet can get significantly off the centerline before breaking up. The flow downstream of this breakup is highly three-dimensional and turbulent.

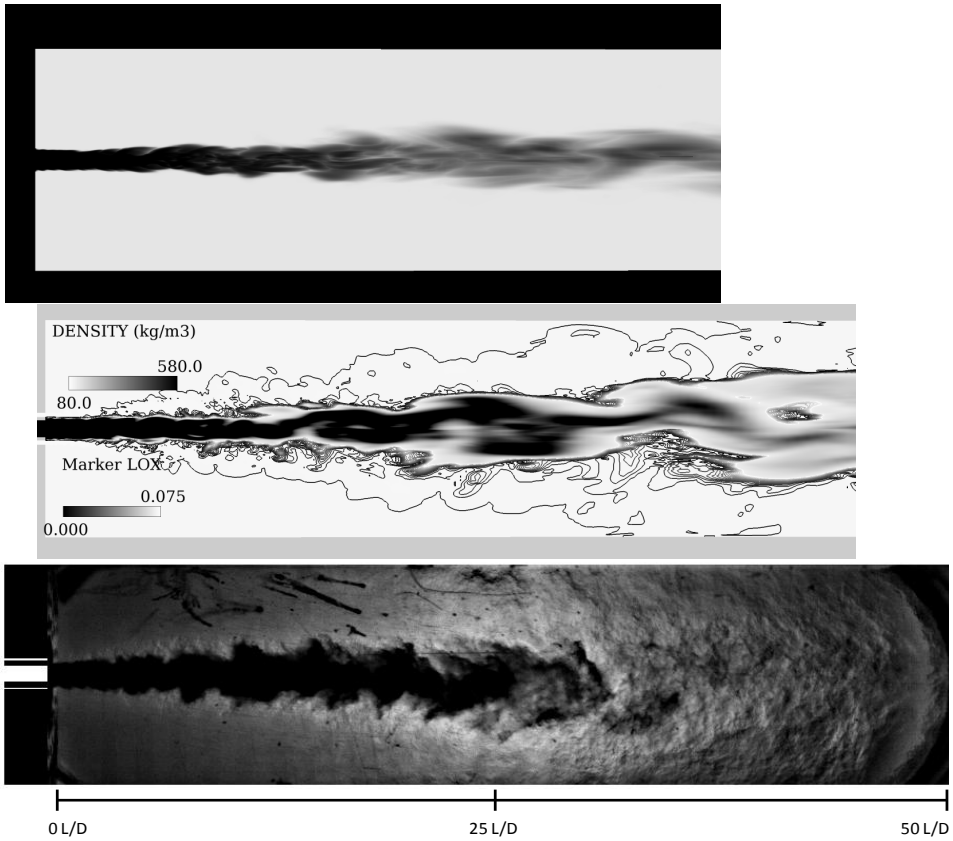

Figure 66: Comparison between the backlit image obtained by Locke [160] (bottom) and images generated using the current simulations: approximated line-of-sight integration using density (top) and vertical slice using density and the liquid oxygen passive scalar (middle).

5.3.2 Visualization of the trans-critical layer

Before moving to the quantitative comparisons with the experimental data, this section will explore in more details the trans-critical layer so specific to the current high-pressure flows. First, the region of large specific heat at constant pressure is shown in Figure 67(a). While the scale is limited at 5000 J/kg/K, locally values can easily exceed 10000 J/kg/K, illustrating the crossing of the pseudo-boiling. It is also seen that in the compressed liquid region, there is a local minimum of C_p before the trans-critical maximum. This is an artifact of the Redlich-Kwong equation of state, as can be seen in Figure 115. It is however barely visible on the radial profiles of C_p and T shown in Figure 68 and is unlikely to play a major in the jet breakup process. It could become more of an issue for lower injection temperature as it would further thicken the thermal boundary layer around the oxygen. This thermal boundary layer, visible in light blue in Figure 67(b) is much thicker than the trans-critical layer based on C_p because of the strong C_p non-linearity. This create a relative large region of dense but not quite liquid region at the edge of the dark core: Figures 68 and 67(c) show this large region with $\rho > 500\text{kg.m}^{-3}$ and . If this phenomenon really occurs physically, it is unclear how light would be absorbed and/or refracted by this layer and this could further complicate the interpretation of the high-speed backlit images obtained experimentally. From a numerical point of view, Figure 68 shows that the C_p maxima can be resolved with as few as 4 to 5 points if need be, but that for many situations, the grid is refined enough to smoothly resolve the specific heat and density variations.

5.3.3 Quantitative comparison of dark core lengths

As mentioned in the introduction, the dark core length is the main metric for coaxial injectors but it is unfortunately not uniquely defined in the experiments. Backlit images of the jet were produced that were then post-processed in order to detect the edges of the darkest region of the flow. Numerically, the dark core length can be linked to the following non-dimensional density:

$$\rho^* = \frac{\rho - \rho^\infty}{\rho^0 - \rho^\infty} = \frac{\rho - 85}{1080 - 85} \tag{5.3.1}$$

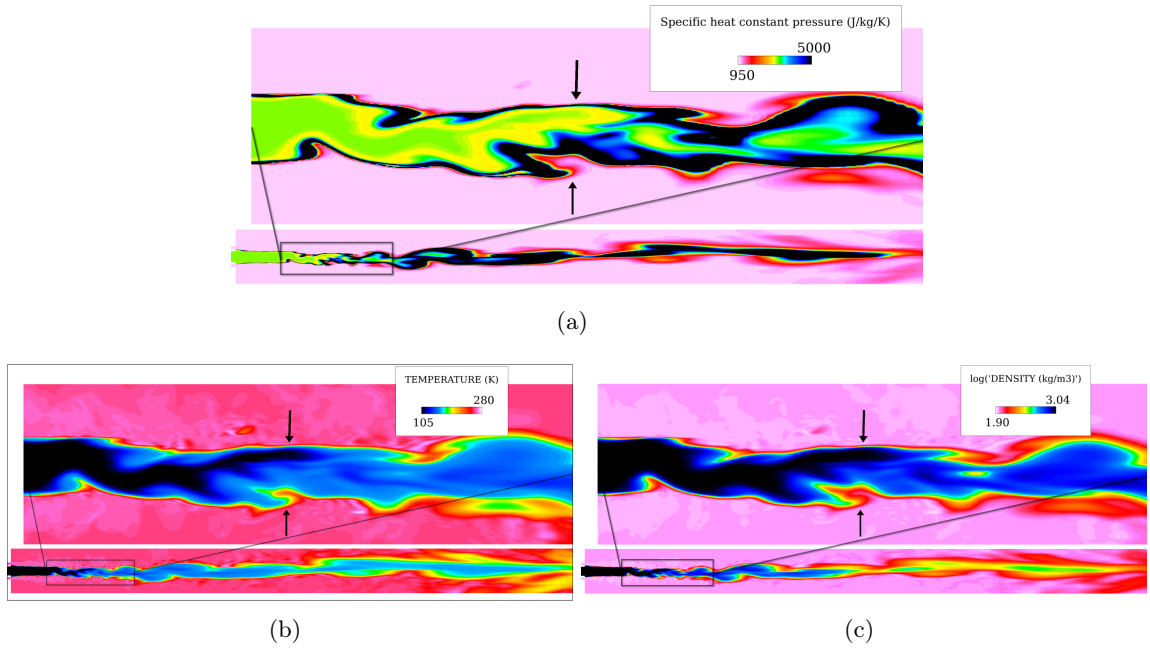

Figure 67: Instantaneous color contours of the specific heat at constant pressure (top), temperature (middle) and logarithm of density (bottom) for the refined grid. The top part of each sub-figure displays a zoomed-in view of the transition region where the jet breaks up. Arrows indicate the location for the radial profiles shown in Figure 68.

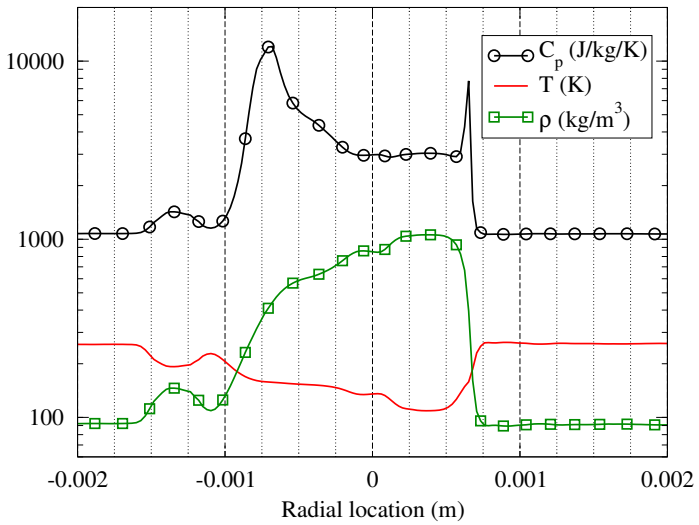

Figure 68: Radial profiles of density, temperature and specific heat at constant pressure on a logarithmic scale. Dotted grid lines are separated by 250 microns to help visualizing the size of the trans-critical layer.

From a thermodynamic point of view, it is expected that values in the range $0.3 < \rho^* < 0.6$ would match what was measured experimentally as densities between 400 and 700 kg.m^{-3} correspond to the trans-critical transition between compressed liquid oxygen and super-critical oxygen fluid. From a fluid mechanics point of view, the jet is expected to be stretched and elongated by the strain over time until the tip of the jet breaks up. Thus, if tracking the edge of the compressed liquid jet through the location of some reference density, the temporal evolution should follow a saw-tooth wave. The periods of steady increases of the dark core length would correspond to the compressed liquid being convected close to the speed of injection and should be followed by sudden drops corresponding to the jet break-up events. This is illustrated by Figure 69 which shows the different temporal evolutions of the dark core length depending on the threshold value chosen. For large ρ^* values, the interface tracked is closed to the potential core and thus there is little change over time. On the other hand, for low values of ρ^*, the fluid is no longer part of the jet and is affected by the surrounding flow without following the convection/break-up described previously. As expected by the thermodynamic arguments, the behavior reported by Locke [160] is recovered here for intermediate values of ρ^*. It is also verified that the upward slopes of the dark core length match the liquid oxygen injection velocity.

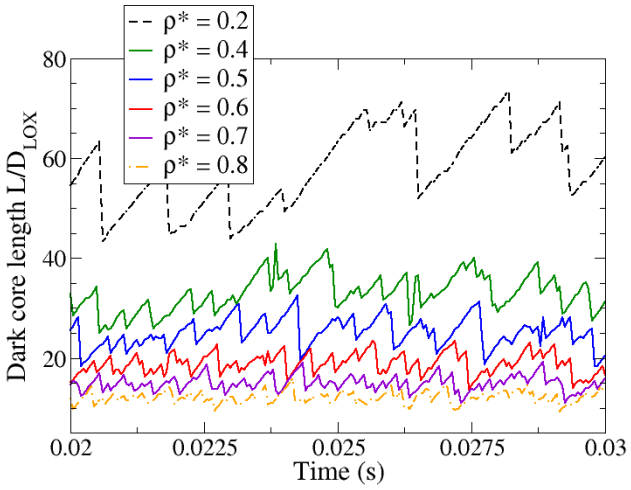

Figure 69: Temporal evolutions of the dark core length for the baseline grid for different threshold values of the non-dimensional density ρ^*.

In this range of realistic non-dimensional densities, a value of 0.55 is chosen to compare the distribution of dark core length predicted by the various LES simulations and obtained by the experiment. This is shown in Figure 70 and the distribution obtained with the coarse grid is discussed first. This grid significantly overestimates the mean dark core length because the poor resolution dissipates most of the vortical structures that help breaking up the oxygen jet. However, by producing a physical, reasonable flowfield with some qualitative agreement with the baseline, this coarse grid fulfills the conditions set by Georgiadis et al. [82] and provides a necessary but not sufficient proof of the validity of the LES approach on the baseline grid.

Figure 70 shows the relatively good agreement obtained between the baseline grid, the most refined grid and the experimental data. These three distributions obtained have a mean around 22.5 L/D_{LOX} and a similar tail on the upstream side. The main difference is that the LES distributions show a tighter distribution around the peak but a shorter tail downstream, indicating fewer events where the jet break-up is delayed and the dark core length reaches more than 25 LOX diameters. Choosing a slightly smaller threshold value would result in a mean displaced to the right and a longer tail downstream, so the quantitative comparison is dependent on the choice of the threshold. The current value of 0.55 appears to be a good choice as it corresponds to a still very compressed liquid ($Z < 0.3$) which is likely to absorb the backlighting of the experimental setup and so should correspond to the jet boundary tracked by the experiment. Quantitatively, the distribution obtained for the baseline grid has a variance of 7.0 and a slight skewness of -0.05. The variance of the experimental distribution appears to be slightly larger while Locke also reports some slight negative skewness. But while Figure 70 is a good indication of the accuracy of the current simulations, one should not focus too much on the alignment of the histograms since they are so dependent on the choice of the threshold value. A time-spectrum from the distributions shown in Figure 70 can also be obtained and compared to the pressure spectra shown earlier in Figure 71. While the sampling resolution of the dark core length data is not very high, it can be seen that dominant frequency, corresponding to the breakup events shown in Figure 69, is comparable to the jet mode identified as the low-frequency pressure

peak. So while the configuration is coaxial, the scaling of the breakup events is probably dominated by the central jet characteristics.

The raw data from the experiment was obtained and post-processed to look at time-averaging over different durations to confirm that the convergence of the simulation was similar to the experiment. By averaging over time the values of each pixel, several averaged snapshots were obtained and the LES flowfield was superimposed over it to compare the flow features. The first information is that the flowfield appears stationary after about 10 ms of averaging. This corresponds to only 1 flow-through-time for the whole chamber but the region of interest is at most 1/4th of the length so this sets a reasonable target for how long the LES statistics need to be collected. The second information concerns the spreading of the coaxial jet, another common metric for evaluating the characteristics of a coaxial injector [149]. The time-averaged field does not represent any direct physical quantity but because of symmetry of the solution, it can display the expansion of the jet in the chamber. Figure 72 illustrates this point by showing the time-averaged processed experimental images with time-averaged density contours from the baseline LES simulation. The LES solution appears to converge towards a stationary solution at the same rate than the experiment, with the 1 ms time-average still showing artifacts from a late jet break-up downstream and the 10 ms time-average showing a monotonic decay with the downstream direction. This suggests that the current LES captures the timescales, the expansion and the extent of the coaxial jet reasonably well. The tangent of the jet divergence angle can be found to be about 0.125, estimated from the time-averaged velocity contours. This value is in line with the spreading rate reported for other high-pressure coaxial jets [149]. Again, comparing a slice of the time-averaged density field with the time-averaged backlit imaging is not a one-to-one comparison but these qualitative features remain relevant and give an indication that the LES solution share many characteristics with the experimental flow field. However, it would be a mistake to quantitatively compare the fields obtained with the current post-processing, as shown in Figure 73. The light intensity along the centerline does not decay at all like the density would for an axisymmetric jet-like flow. This is likely due to the line-of-sight integration which has a tendency to block light even when the fluid is not as dense, thus flattening the

initial profile and producing a sharper divide around the end of the dark core. Note that for this case, the average position of the end of the dark core is about 23 x/D_i. Looking at non-dimensional value of 0.5 for the dark core length, the density profile has a tendency to slightly underpredicts this while the backlit image overpredicts it. This emphasizes the complexity of post-processing this type of backlit imaging. However, the procedure to locate the extent of the dark core is very similar to the one used experimentally and only the exact value of the non-dimensional density is in doubt.

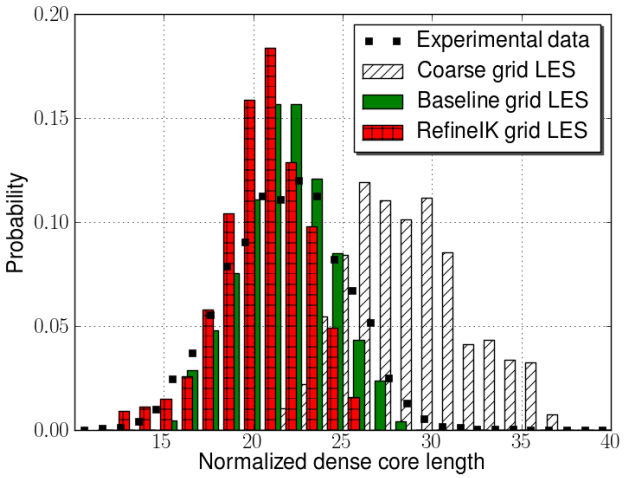

Figure 70: Histogram of the distribution of the normalized dark core length L/D_{LOX} for a threshold $\rho^* = 0.55$ for the coarse, baseline and most refined LES grids.

5.3.4 Scaling laws for dark core length prediction

As mentioned in the previous section, a major difference between the current configuration and what is generally found in the super-critical coaxial injector literature [227, 148, 149, 252, 90, 304] is the presence of a coflow to mimic the presence of other coaxial elements in a real showerhead injector. The baseline grid was run with and without this coflow in order to illustrate its influence on the jet spreading and breakup. An instantaneous snapshot is shown in Fig. 74. This highlights the critical role of coflow and confinement in coaxial jets. While a coflow does confine the coaxial jet, it decreases the shear for the annular jet which means

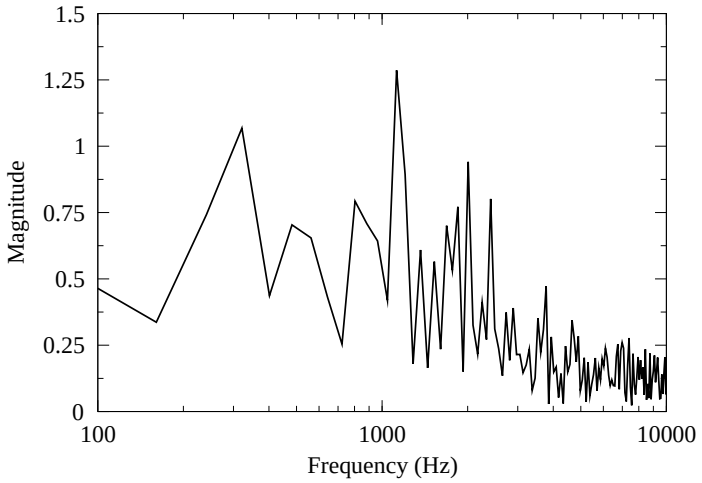

Figure 71: Fourier spectrum of the normalized dark core length L/D_{LOX} for a threshold $\rho^* = 0.55$ for the baseline LES grid.

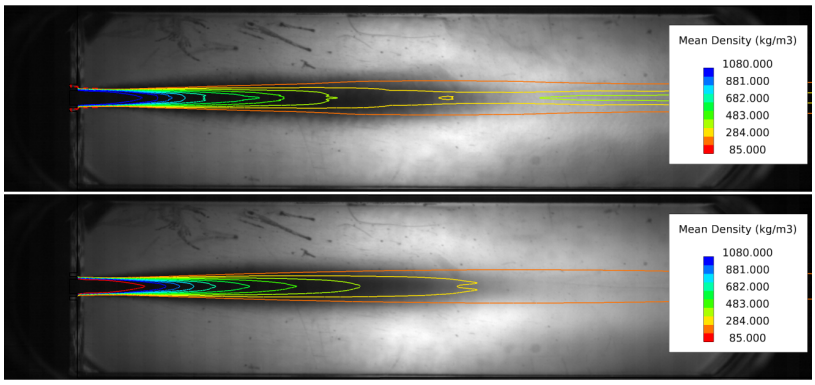

Figure 72: Comparison between the time-averaged experimental backlit imaging and the time-averaged numerical flowfield. Averaging time is 1 ms for the top picture, 10 ms for the bottom one.

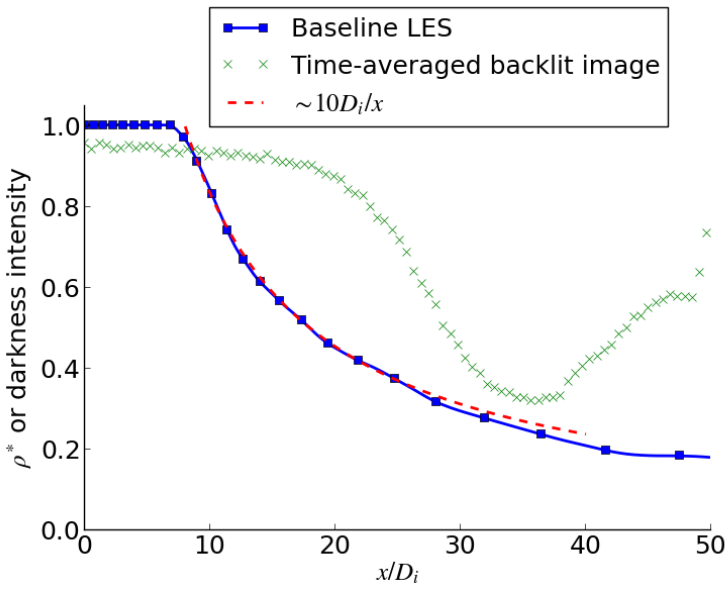

Figure 73: Comparison between non-dimensional density profile along the centerline and the normalized light intensity from the 10 ms time-averaged experimental backlit imaging. The inverse distance correlation is typical of axisymmetric jets.

the shear in the mixing layer between the annular jet and the central jet decays less rapidly. Thus the central jet is subjected to higher shear and will likely break up earlier [160]. On the other hand, when the confinement is provided by solid walls, the shear on the annular jet is increased and the overall mixing is limited. This usually results in longer dark cores [79]. In this case, the coflow seems to act as described but it additionally perturbs the main shear layer through a toroidal recirculation region in the near field, caused by the gap between the coaxial flow and the coflow. This is actually a good approximation to what would happen in a multi-element configuration, although that flow would be even more complex since the coflow would not be uniform in the near-field. This toroidal region is clearly seen as the strong recirculation near the faceplate in Figure 74. It is clear from this Figure that the coflow configuration in this case results in a significantly shorter dark core for the oxygen jet.

Thus it appears that the current LES solver is capable of reproducing the behavior of trans-critical injection through a coaxial element. As mentioned in the introduction, the

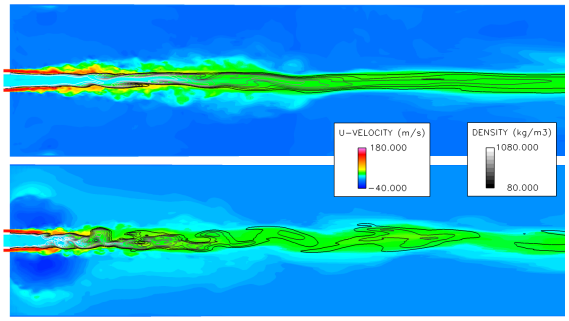

Figure 74: Comparison of the LOXGOX flowfield with (bottom) and without (top) coflow. The instantaneous contours show the axial velocity field in color and the density in grayscale.

prediction of the dark core length for a given injector is a first step towards better understanding and modeling of combustion instabilities in liquid rocket engines [35]. However, experimental data gathered in laboratory sub-scale chambers have limited applicability since the rigs usually cannot match the very large flowrates of real liquid rocket engines. Indeed there is a critical need for scaling laws that reduce the behavior of a coaxial injector to a few parameters [109] and allows the prediction of dark core length for example when the operating conditions are scaled to the ones of a typical engine. These scaling laws use dimensionless numbers such as the momentum flux ratio J or the velocity ratio VR introduced earlier. Values for a full-scale liquid rocket engine can be as high as a momentum flux ratio of 10, a velocity ratio of 40 and a mass flowrate per injection element of 1 kg/s. In Section 1.3.1, a new scaling law was suggested (Eq. 1.3.8), incorporating a shear Reynolds on top of the usual momentum flux ratio dependence. This scaling law was obtained by considering only experiments without co-flow. While some of the physical processes involved in the jet breakup are affected by the presence of a co-flow, within the same configuration with co-flow, it is expected that the trend predicted by the new scaling law should be present. It is straightforward to test this hypothesis with the current numerical setup.

In order to perform this test, one can simply double all injection velocities for given flow conditions. This has two main consequences: (a) the momentum flux ratio is unchanged, and so is the velocity ratio (b) quantities such as the velocity difference, the Reynolds number and the Mach number for each jet are multiplied by 2. The flowrates of course are also

multiplied by 2 and this would be difficult to achieve in a laboratory since they usually operate near-capacity for these kinds of experiments. Additionally, the throat area would also need to be doubled. The flowrates and velocity differences obtained are more typical of full-scale engines but since the non-dimensional scaling parameters stay the same, the dark core length would be same as for the baseline simulation if there was no dependence on Re_s. However, conducting a new simulation on the baseline grid with all injection velocities multiplied by 2 produces a shorter core as can be seen in Figure 75. The average obtained for the threshold value $\rho^* = 0.55$ is also reported on Figure 3 for comparison with the rest of the data available. It can be seen that while the predicted length is well within the range of plausible length for a J of 1.5, the decrease in length compared to the previous simulations correspond to the prediction of Eq. 1.3.8. For a doubling of Re_s, the predicted decrease in $\frac{L_{dc}}{D_i}$ is about 10%, in line with what the LES simulations are showing. This seems to indicate that the simple correlations solely based on J and D_i are probably not sufficient to predict the behavior of coaxial elements in full-scale engines from sub-scale data. This highlights the potential of a validated LES tool to help in the design of experiments exploring new trends and dependencies.

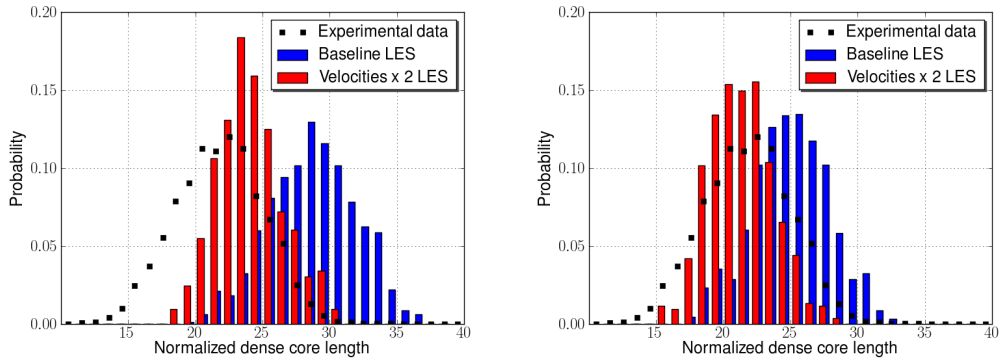

(a) $\rho^* = 0.45$

(b) $\rho^* = 0.50$

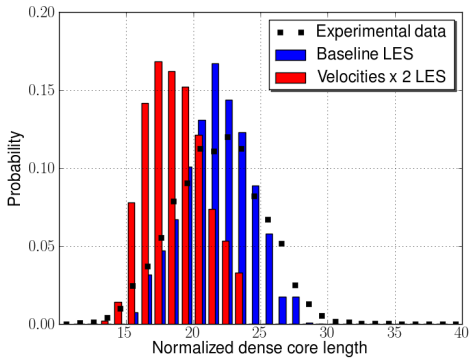

(c) $\rho^* = 0.55$

Figure 75: Comparison of dark core length distributions obtained for the baseline conditions and conditions where all injection velocities where doubled. Significant shortening is obtained for different, realistic threshold values.

5.4 LOX-GN2 simulations

5.4.1 Motivation

This non-reacting case provides a good opportunity to study the effect of the sub-grid model on mixing. However, the experimental conditions with only a single species do not allow testing of the LES-LEM formulation which requires multiple species. Unfortunately, there is currently little multi-species trans-critical or super-critical mixing data for a coaxial configuration, as reviewed in Section 1.3.1.

Oschwald et al. [228] used Raman scattering to investigate the coaxial mixing of LN_2 and H_2. Limited two-dimensional time-averaged maps of the density of each fluid are available for three different operating conditions. Tani et al. [304] investigated the effect of recess and taper on the mixing of nitrogen and helium in a shear coaxial configuration at super-critical pressures. Focusing on the non-tapered cases, the ranges of velocity ratio (≈ 10) and momentum flux ratio (≈ 1) are similar to the rest of the super-critical experimental data available described previously. The main difference is the density ratio of about 100, compared to a range of 1 to 10 for the previous experimental data. The visualization data consists of shadowgraph pictures taken at high speed (shutter speed of 3 μs) that can be averaged to obtain a normalized luminosity contour plot. If the conditions of super-critical pressure or shear coaxial configuration are relaxed, a few more studies of note should be considered. Roy and Segal [256] have performed extensive studies of the mixing of a fluoroketone round jet into ambient nitrogen, going from sub-critical to super-critical pressures and including trans-critical injection. Gautam and Gupta [80, 79] have conducted joint experimental and numerical studies of cryogenic coaxial injectors with LN_2 and He but they only dealt with atmospheric pressure flows. Extensive high-speed schlieren data is available. Finally, Schumaker [269] performed a number of non-reacting shear coaxial experiments involving the mixing of He, H_2 and CH_4 with air. Cinema chemiluminescence and OH PLIF were used to obtain both instantaneous and time-averaged visualization.

In the end, given the scarce available data, instead of moving to a new configuration, the flow conditions of the Locke rig will be modified to maintain the velocity ratio and the momentum flux ratio with different species in the different streams. Since the main

goal of this study is to verify that the Linear-Eddy-Mixing model can be used for trans-critical mixing problems, the species chosen do not need to be very different which would probably requires a dedicated study of the density ratio effects. Also, picking similar species allows only a slight modification of the original flow conditions and thus some qualitative comparison will be possible between the new simulations and the experiments. So for this reason, the outer stream of gaseous oxygen is replaced by a stream of nitrogen. This inert species is also likely to be used in experimental setup, making future comparisons potentially easier. Only small adjustments to the injection temperatures are made for the densities to match and these adjustments have likely little impact on the dark core length statistics. The new operating conditions are listed in Table 14: on top of the lower injection temperature in the annular stream, the Reynolds number there is also slightly increased because of the lower viscosity of nitrogen.

5.4.2 Numerical setup

The first goal of this study is to run very similar grids than the ones run for the LOX-GOX simulations to verify that similar results can be reproduced. A few modifications are made to the computational domain however. The inlets are extended further upstream, up to 0.2 m from the injection plane, in order to eliminate any possibility of unphysical feedback between the inflows and the shear layer. Also, the experimental convergent-divergent nozzle is included at the end of the chamber. As a consequence, the boundary conditions are also slightly modified. The inflow boundary conditions are the constant-mass non-reflecting boundary conditions described in Section 2.7.3. At the outflow, a subsonic boundary condition with a back-pressure of 25 bar is used until the nozzle is choked, and a supersonic boundary condition is used thereafter. An overview of the computational domain is given in Figure 76 and shows the near-uniform, low Mach number at the end of the domain before the convergent-divergent nozzle.

Two grids will be run on this computational domain, a baseline grid and a coarse grid. Both grids are just extensions of the baseline and coarse grids used for the LOX-GOX studies

Table 14: Comparisons of the operating conditions for the trans-critical LOX-GOX case and the trans-critical LOX-GN2 case. The annular stream is made of either oxygen or nitrogen.

Description	Units	LOXGOX XP	LOXGN2
Main chamber			
Chamber pressure	Pa	5.750×10^{6}	5.75×10^{6}
Average density	$kg.m^{-3}$	138	138
Average velocity	m.s−1	4.57	4.57
Preburner background flow			
Composition	(Y_{H_2}, Y_{O_2}, Y_{H_2O}, Y_{N_2})	(0,1,0,0)	(0,1,0,0)
Mass flowrate	$kg.s^{-1}$	0.268	0.268
Inflow density	$kg.m^{-3}$	84.6	84.6
Background flow area	m^2	5.32×10^{-4}	5.32×10^{-4}
Inflow temperature	K	262	262
Bulk inflow velocity	m.s−1	5.95	5.95
Injector inner post oxygen flow			
Mass flowrate	$kg.s^{-1}$	0.0836	0.0836
Post area	m^2	3.3245×10^{-6}	3.3245×10^{-6}
Inflow density	$kg.m^{-3}$	1080	1080
Inflow temperature	K	105	105
Compressibility		0.2	0.2
Inflow velocity	m.s−1	23.28	23.28
Kinematic viscosity	$m^2.s^{-1}$	1.34×10^{-7}	1.34×10^{-7}
Reynolds number		3.6×10^{5}	3.6×10^{5}
Injector annular flow			
Mass flowrate	$kg.s^{-1}$	0.0557	0.0557
Annular area	m^2	5.91×10^{-6}	5.91×10^{-6}
Inflow density	$kg.m^{-3}$	90.74	90.74
Inflow temperature	K	269	234.6
Compressibility		0.94	0.94
Inflow velocity	m.s−1	107.5	107.5
Kinematic viscosity	$m^2.s^{-1}$	2.33×10^{-7}	1.85×10^{-7}
Reynolds number		5.26×10^{5}	6.65×10^{5}
Injector characteristics			
Velocity ratio	$\frac{\text{annulus}}{\text{post}}$	4.62	4.62
Mass flow ratio	$\frac{\text{post}}{\text{annulus}}$	1.50	1.50
Momentum ratio	$\frac{\text{annulus}}{\text{post}}$	3.08	3.08
Momentum flux ratio	$\frac{\text{annulus}}{\text{post}}$	1.73	1.73

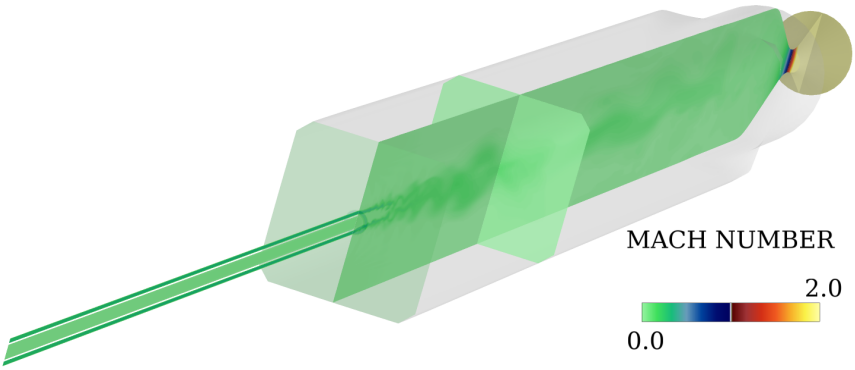

Figure 76: Overview of the computational domain for the LOX-GN2 simulations. The instantaneous Mach number field is shown as color contours and highlights the choked nozzle at the end of the chamber.

and so the minimum spacings remain the same, respectively 40 microns and 80 microns for the baseline and coarse grid. The baseline grid dimensions are (556×121×65,556×17×17) while the coarse grid dimensions are (376×61×33,376×9×9), with the cylindrical mesh listed first, the cartesian mesh second. Other than the multi-species formulation replacing the passive scalar formulation, the simulations run here use the same set of parameters as the LOX-GOX simulations.

5.4.3 Results

5.4.3.1 Overview of LES results

Figure 77 shows the distributions obtained for the coarse grid LES, the baseline grid LES as well as the coarse LEM-LES for a value of the dimensionless density ρ^* of 0.55, while Figure 78 shows the temporal evolution of the dark core length for the two coarse grid simulations. Overall, the same qualitative observations made for the LOX-GOX results can be made again here. The same saw-tooth pattern is observed in the time history of the dark core length and the shape of the distributions is similar to the one recorded experimentally. However, the baseline LES predicts a mean dark core about 5 diameters shorter than for the LOX-GOX case for the same value of ρ^*.

The slightly shorter cores observed in this new configuration could be explained in several

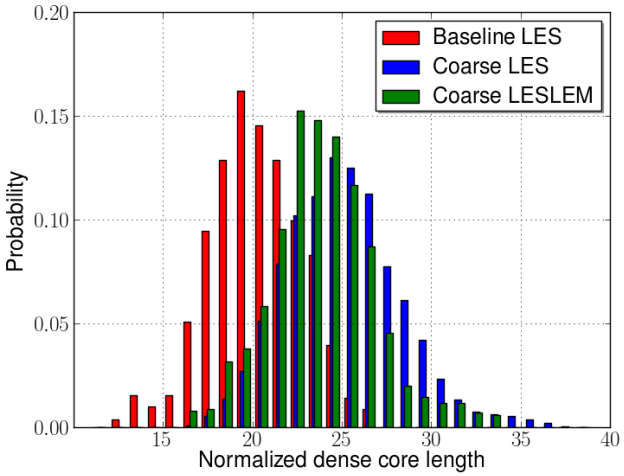

Figure 77: Histogram of the normalized dark core lengths L_{dc}/D_i measured for the LOX-GN2 simulations for a threshold $\rho^* = 0.55$.

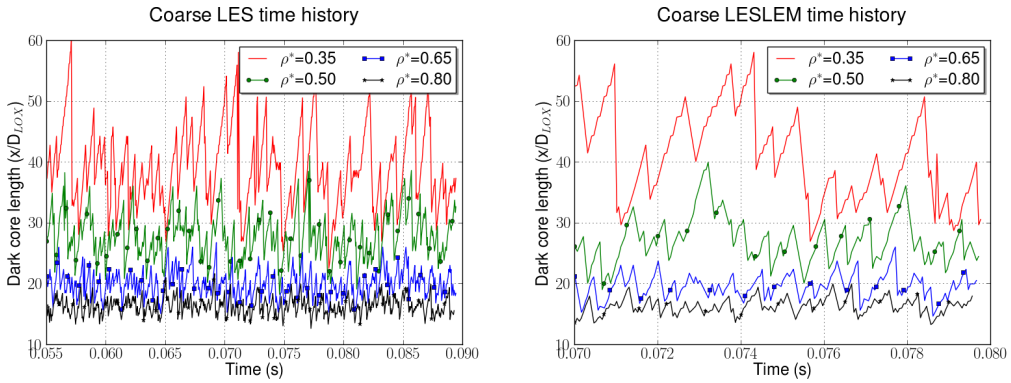

(a) Coarse LES

(b) Coarse LEM-LES

Figure 78: Temporal evolutions the normalized dark core lengths L_{dc}/D_i measured for the coarse grid LOX-GN2 simulations.

ways. While these simulations were performed with a choked nozzle, the influence of the chamber acoustics on the results appear negligible. The acoustic spectra with and without the nozzle are very similar as can be seen in Figure 79 compared to Figure 62. There could be some more fundamental explanation however. The new operating conditions provide a smaller temperature gradient between the central jet and the annular stream and one could think this would result in longer cores since it would take a longer time for the central jet to heat up with the smaller temperature difference. However, in a multi-species configuration, heat diffusion is not the only phenomenon that contributes to the transition from sub-critical fluid to super-critical fluid. The mass diffusion between the compressed liquid oxygen and the super-critical nitrogen is also important. So if mass diffusion is larger than thermal diffusion for this LOX-GN_2 injector, it would contribute to the core length decrease compared to the LOX-GOX, single-species configuration. Figure 80 illustrates this point by showing the contours of the Lewis number which is the ratio of thermal diffusivity to mass diffusion:

$$\mathrm{Le} = \frac{\alpha}{\mathcal{D}} = \frac{\kappa}{\rho C_p \mathcal{D}} \tag{5.4.1}$$

One can observe that the initial mixing between oxygen and nitrogen occurs in a region where the Lewis number is smaller than 1 and thus N_2 and O_2 mix faster than the temperature scalar in the single-species configuration. Since the critical temperature of nitrogen (T_c = 126.2 K) is lower than the one for oxygen (T_c = 154.6 K), the mixture of N_2 and O_2 has a smaller critical temperature than the pure oxygen and thus could reach the trans-critical state quicker under the same temperature gradient. With a temperature gradient slightly lower than for the LOX-GOX configuration, it is not clear if this can fully explain the faster breakup of the oxygen jet. But it highlights the complex physical processes associated with multi-species real gas flows. Also, one cannot discard numerical effects either. It was previously shown in Section 3.4.2 that strong species gradients can be an issue with the upwind solver and that they can generate velocity and pressure fluctuations. It is possible that these fluctuations could increase the inner jet stability and contribute to its faster breakup. However, these fluctuations do not appear too significant in Figure 81 which

shows the same field at the same instant in time than Figure 80. On the other hand, far-field conditions for the LOX-GN_2 case should be very similar to the ones observed for the LOX-GOX case and are unlikely to influence the evolution of the coaxial jet. The densities and flowrates for the annular jet and the coflow are identical between the two cases and since they both display near-ideal behavior ($0.94<Z<1$), there will not be any additional non-linear mixing effect between the nitrogen annular stream and the oxygen coflow. Thus it is likely that the slight differences in dark core lengths find their origins in the small-scale mixing near the trans-critical layer

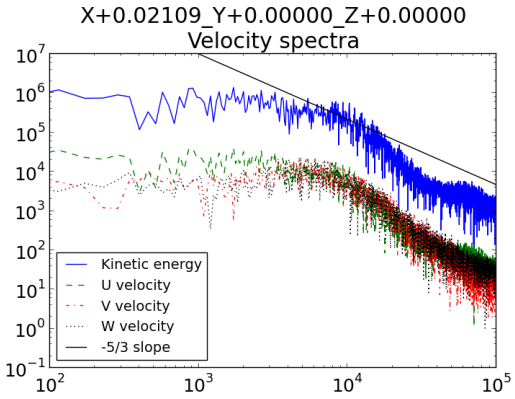

Figure 79: Typical turbulent spectra obtained downstream of the oxygen dark core, at location $(x, y, z) = (0.026\text{m}, 0.002\text{m}, 0.000\text{m})$ for the coarse grid LES simulation.

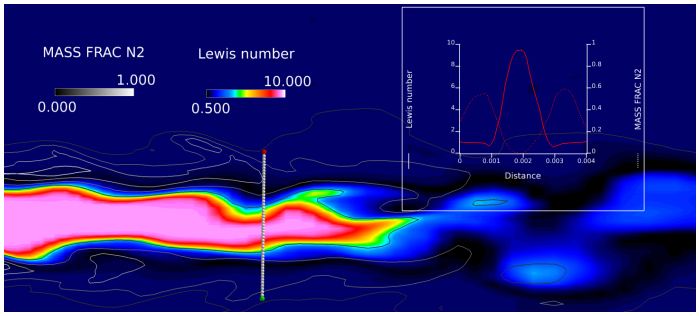

Figure 80: Instantaneous snapshot of the tip of the oxygen jet for the coarse grid LES simulation showing the Lewis number with color contours and the nitrogen mass fraction with grayscale contours. Radial profiles of these quantities across the jet are also shown.

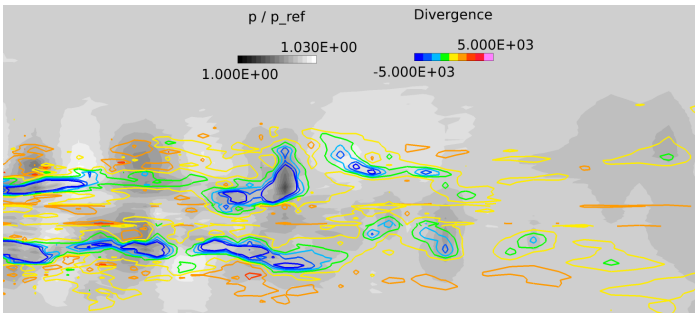

Figure 81: Instantaneous snapshot of the tip of the oxygen jet for the coarse grid LES simulation showing the divergence of velocity with color contours and the normalized pressure ($p_{ref} = 60$ bar) with grayscale contours.

5.4.3.2 LES-LEM results

On top of the comparison on the dark core length statistics shown previously, the instantaneous and time-averaged fields are also compared here with and without LEM as a sub-grid model. Figure 82 shows little differences between the two simulations. The light blue iso-surface representing a density of 500 kg.m^{-3} is slightly shorter for the LEM-LES simulation, confirming the dark core length statistics from Figure 77. The transverse slice shows the mean axial velocity and minute differences can be seen near the inflow. Similarly, the toroidal recirculation region represented by the pink iso-surface of zero axial velocity is nearly identical for both simulations. The instantaneous flow fields show a little more difference, especially when considering the scalar mixing. Figure 83 shows the density fields with a color contours with the mass fraction of the gaseous nitrogen surrounding it in grayscale contours. The jet seems to display a little bit more symmetry with the LEM-LES simulation and the potential cores for each jet have very similar lengths. However, the mixing of the dense, but no longer liquid, fluid downstream of main break-up region ($15 < \frac{x}{D_i} < 25$) appears more efficient for the LEM-LES simulation. These small differences in the mixing details can of course be attributed to the differences between the gradient diffusion model and the Linear-Eddy Model. But under the given flow conditions, it is unlikely that the LEM can capture significantly more physics than the gradient diffusion approach and so it is reassuring that on a statistical level, the only really meaningful level when comparing LES results, the two models yield similar results, with the LEM-LES potentially hinting at the

slightly shorter core obtained with the finer grid.

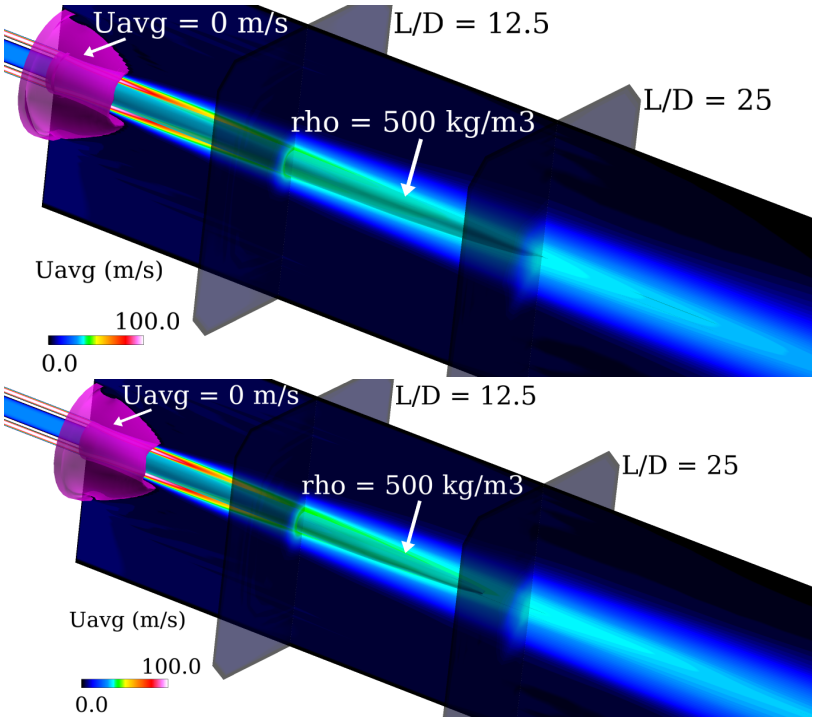

Figure 82: Time-averaged (over 15 ms), three-dimensional overview of the flow fields for the coarse grid LES (top) and LEM-LES (bottom) simulations.

5.4.3.3 Influence of sub-grid model parameters

While the LEM formulation has very few tunable model parameters compared to other sub-grid approaches, it is interesting to investigate the influence of some of the parameters or terms described in Section 2.4. Of particular interest is the amount of turbulence modeled by the LEM model. As explained previously, as the LES grid resolution increases, the unresolved kinetic energy decreases as the cut-off lengthscale gets further into the inertial range. Essentially, the sub-grid experiences a flow with a lower Reynolds number. Also, Lewis and Schmidt numbers vary greatly across the trans-critical layer, for both non-reacting (see Figure 80) and reacting flows (see Figure 6.4). Previous studies [47, 288, 33] have shown that the model parameter C_λ from Eq. 2.4.8 is sensitive to both the Reynolds number and dimensionless numbers involving the mass diffusion coefficient (Schmidt, Lewis or Peclet number).

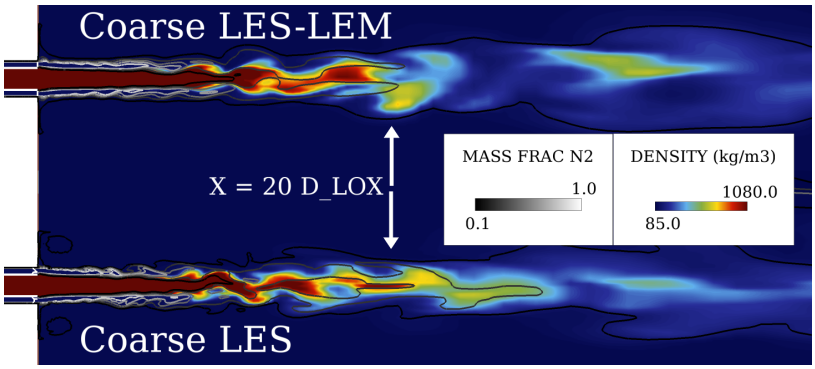

Figure 83: Instantaneous snapshot of density and nitrogen mass fraction in the near-field of the LES and LEM-LES simulations.

Values as low as 0.032 [288] and as high as 1 [47] while Chakravarthy and Menon [33] uses high-Re phenomenological arguments to derive the value of 0.064 which is about the value of 0.067 used by default in the current solver. To investigate the influence of this parameter on the scalar mixing, a LES-LEM simulation with a value of $C_\lambda = 0.5$ is performed. Other than this change, the simulation is identical to the previous LES-LEM simulation. Figure 84 compares the dark core length distributions obtained with the nominal value of C_λ (simulation denoted and a value of 0.5 which increases the stirring frequency by more than an order of magnitude. The distribution obtained with the increased stirring is very skewed, with a long tail towards very long dark cores. What happens is that the increased small-scale mixing in the main shear layer can create the same dense but non-liquid fluid found at the tip of the jet. But this dense fluid in the shear layer actually prevents large vortices to grow in the gaseous nitrogen stream, preventing the significant large-scale mixing that breaks up the jet decisively. Instead the jet slowly diffuses as it moves downstream, resulting in the distribution shown in Figure 84.

Lastly, the contribution to large scale advection by unresolved turbulent eddies as presented in Section 2.4.4 is investigated. It is seen in Figure 84 that the effects are even stronger than the increased stirring. Compounding this effect is the fact that the axial resolution starts decreasing for $X/D_i > 30$, dissipating even more the structures that fail to grow quickly enough upstream.

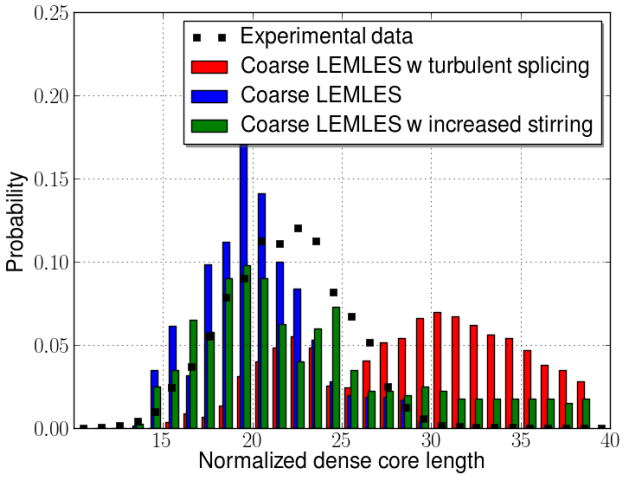

Figure 84: Histogram of the normalized dark core lengths L_{dc}/D_i measured for the LEM-LES LOX-GN2 simulations for a threshold $\rho^* = 0.60$.

5.4.4 Conclusions

For the first time, the Linear-Eddy Model has been applied to a flow with real gas behavior. Given the configuration and the moderate levels of turbulence and sub-grid kinetic energy, it was expected to not produce results drastically different from the gradient-diffusion closure model. Indeed, this was the behavior observed here with the coarse grid LEM-LES results in between the coarse grid and the baseline grid LES results. The sensitivity of two sub-grid model parameters were investigated and it was confirmed that the default values from previous studies are still the recommended ones for real gas flows.

CHAPTER VI

LIQUID-GAS REACTING SHEAR COAXIAL INJECTOR

6.1 Description of the experimental configuration

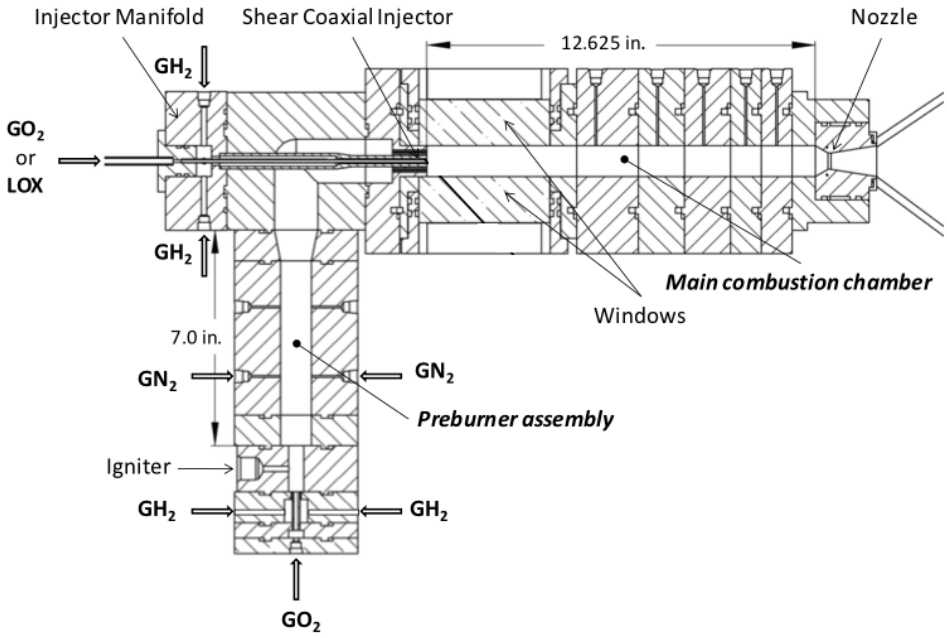

Figure 85: Schematic of the rocket assembly with preburner: window section shown in upstream position. From Locke [160].

The first stage of the validation of the real gas solver was the cold flow studies from the previous chapter. The next stage is to essentially combine all the physics contained in the two previous chapters to study a small-scale reacting flow under conditions very close to those found in an actual rocket engine. As mentioned earlier, the experimental facility used for the mixing studies in the previous chapter was actually designed to perform hot-fire LOX-GH2 runs. The geometry considered here is thus exactly the same as the one described in Section 5.1 and this section will only highlights the differences in flow conditions.

6.2 Numerical implementation and overview results

This section will actually mix descriptions of the various choices made for the grid, the boundary conditions and other physical models and some results produced to justify said results.

6.2.1 Solver options

For all the simulations presented in this chapter, the Peng-Robinson equation of state is used while the viscosity and thermal conductivity are computed using the Chung's method for large densities while the diffusion coefficients are computed using the Fuller's approach modified by the high-pressure correction by Riazi and Whitson. Finally, the hybrid scheme described in Section 3.3 and with the set of parameters

$$(\epsilon_\rho, \epsilon_p, C_\rho^{\text{cutoff}}, C_p^{\text{cutoff}}) = (0.05, 0.05, 0.125, 0.5)$$

is used for the spatial integration of the governing equations. Also, following the analysis in Section 4.4.2, the 7-step mechanism by Baurle et al. [13] with 10 sub-iterations is deemed sufficient for this study. A typical fluid mechanics time-step for the highest resolution run in this chapter is about 6×10^{-9} s, putting the chemical time-step at 6×10^{-10} s.

An additional assumption is made on the thermodynamics and the chemistry. It is assumed that as far as heat release is concerned, there is no real gas effect as the species need to have warmed up before they can react significantly. This can save a significant amount of computational time since the chemical integration solver would require to recompute complex departure functions for specific heats and partial enthalpies for all species at every sub-iteration. In order to assess the validity of such hypothesis, a two-dimensional non-premixed turbulent flame is studied. The setup is similar to a temporal mixing layer (see Appendix A) with two counter-flowing streams at the top and at the bottom of the domain. The top stream contains compressed liquid oxygen at 100 K and the bottom contains a nitrogen-hydrogen mixture at 300 K with a mass ratio of $\frac{9}{1}$ in favor of nitrogen. This nitrogen dilution allows the use of a crude initialization with a Gaussian profile of temperature and products ($Y_{\text{H}_2\text{O}} = 0.1$ and $Y_{\text{OH}} = 0.01$) without creating strong pressure waves at ignition. Obviously

this might have an influence on the magnitude of the differences between simulations but it should not change the qualitative behavior. The operating pressure is set at 85 bar to approach the conditions of the LOX-GH2 rig. The two-dimensional grid is a square of side 6.4 mm and contains 128 cells in both directions, for a resolution similar to the one found in the full three-dimensional simulation of the experimental rig. This means that from a pure physical point of view, the flame modeled is not as accurate as it could be but this should be sufficient to look at the impact of the various assumptions in a configuration comparable to the full three-dimensional simulations. Three simulations are conducted for comparison: the baseline simulation with the full PR EoS formulation, another PR EoS simulation with simplified partial molar enthalpies and specific heats and finally, a simulation with the full RK EoS, which is known to have poor predictions of the specific heats and energies.

First the qualitative differences between the simulations are assessed. Figure 86 shows 3 snapshots for each simulation, at t = 0.125 ms (top row), t = 0.500 ms (middle row) and t = 0.750 ms (bottom row). It appears that there is almost no difference between the two Peng-Robinson simulations, with and without the departure functions in the combustion thermodynamics. The RK EoS simulation shows a few differences at the edge of the flame but the overall behavior is conserved. A more quantitative outlook is given by Figure 87 with the traces of temperature at three different locations near the center of the domain. Due to non-linearities, the RK EoS signal ends up diverging significantly from the PR simulations signals but the overall behavior and range of temperature is conserved. This highlights the difference between the two equations of state for reacting flows. The traces for the Peng-Robinson simulations, on the other hand, are again almost identical. The changes in the combustion thermodynamics are not significant enough to produce any divergence of the solutions over time. This is confirmed by Figure 88 where the momentum thickness of the shear layer is plotted as a representative integrated quantity of the flow. The two PR EoS simulations show very similar growth while the shift displayed by the RK EoS simulation is due to the flame differences as well as the difference in the oxygen density predictions. As a consequence, all reacting simulations shown in this chapter will be performed with the Peng-Robinson formulation but with thermally perfect assumption for the thermodynamics

inside the chemistry. This translates into a 10 to 15% reduction on the computational time for typical three-dimensional simulations.

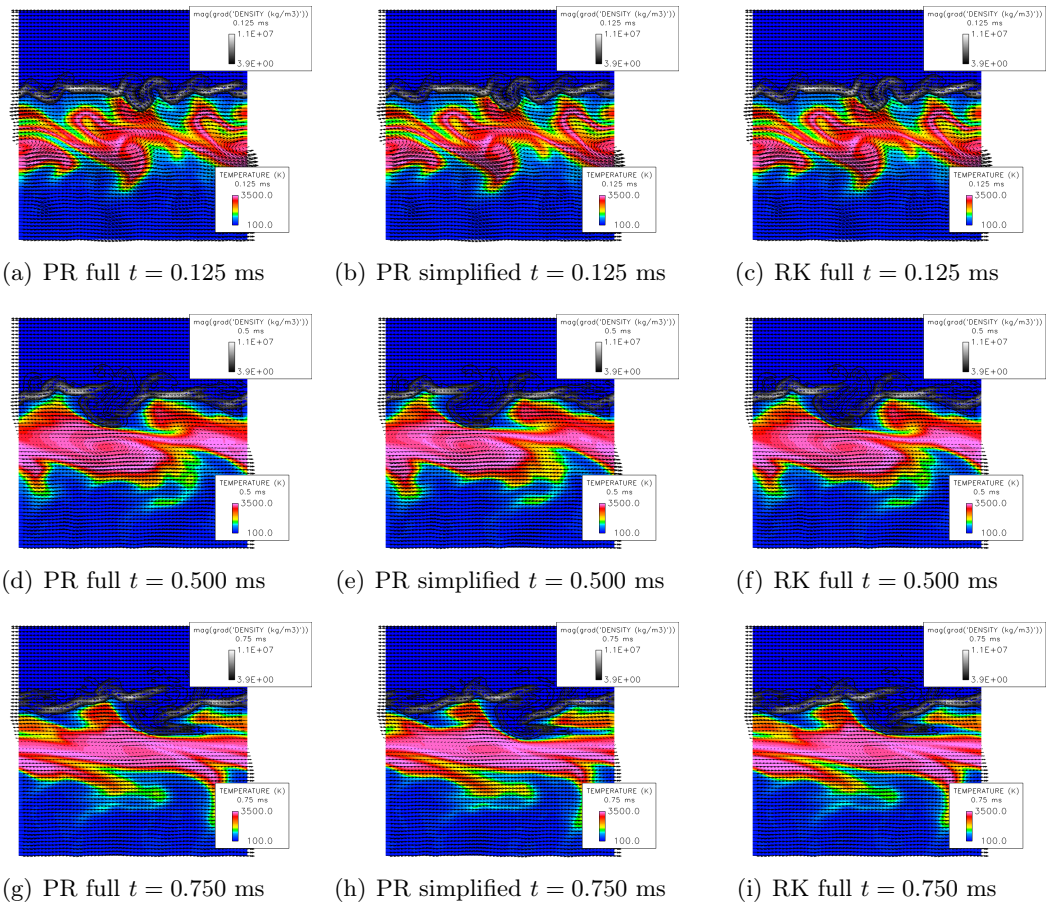

(a) PR full $t = 0.125$ ms (b) PR simplified $t = 0.125$ ms (c) RK full $t = 0.125$ ms

(d) PR full $t = 0.500$ ms (e) PR simplified $t = 0.500$ ms (f) RK full $t = 0.500$ ms

(g) PR full $t = 0.750$ ms (h) PR simplified $t = 0.750$ ms (i) RK full $t = 0.750$ ms

Figure 86: Snapshots of the flowfield for the various thermodynamic models. Velocity vectors are shown in black, grayscale contours of density gradients indicate the trans-critical layer and color contours show temperature fields.

6.2.2 Computational models for the LOX-GH2 geometry

6.2.2.1 Original model and startup strategy

Since the geometry of the LOX-GH2 experiment is absolutely identical to the LOX-GOX one, an initial grid is constructed that is very similar to the baseline LOX-GOX grid. It does contain about 20% more points in order to better resolve the flame and slightly larger gradients. The overall dimensions are thus (460×120×64) for the cylindrical grid and (460×16×16) for

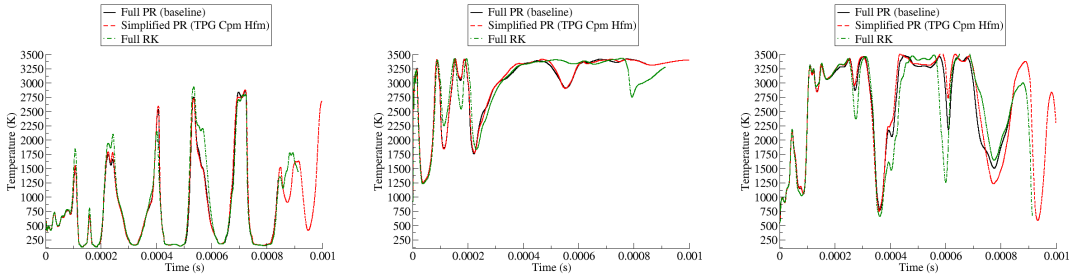

(a) Oxygen side (b) Center (c) Hydrogen side

Figure 87: Time traces for the temperature at locations (0.0mm,0.8mm) (oxygen side), (0.0mm,0.0mm) (center) and (0.0mm,-0.8mm) (hydrogen side).

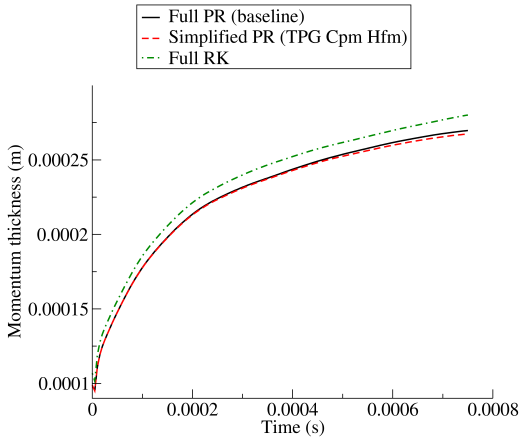

Figure 88: Momentum thickness evolution over time for the two-dimensional reacting LOX-GH2-GN2 mixing layer.

the cartesian grid at the centerline. The minimum grid spacing is located in the main shear layer between the coaxial streams and is equal to about 40 microns. Also, like for the LOX-GOX simulation, this initial LOX-GH2 simulation does not model the full chamber but takes into account the transition from a square cross-section to a circular cross-section and employs a semi-reflecting outflow boundary condition is used before the location of the convergent-divergent nozzle. This boundary condition maintains the operating pressure in the chamber while providing at least some acoustic feedback. The influence of the boundary conditions on the dynamics of the chamber is one of the many additional uncertainties that were not present in the LOXGOX case and which will need to be addressed before validating the LES solver for this application.

Before the first results for this baseline grid are shown, the initialization of the solution is discussed. Because of the large computational cost of such reacting real gas simulation, a cost-effective approach to reliably start up three-dimensional simulations is required. The following steps describe such approach. First an axisymmetric grid is generated in order to get the flame ignited. As this might require a few trials depending on the operating conditions, this is more cost-effective than directly starting with a full 3D grid. The next important item is the initialization of the flowfield. A buffer mixture consisting in this case of water vapor and nitrogen occupies most of the chamber in order to prevent initial mixing of the reactants. This could lead to a significant quantity of flammable mixture that could literally explode and greatly perturb the flowfield. Similarly, one cannot allow significant mixing of hydrogen and oxygen before ignition once the simulation starts. The goal is to promote burning as soon as mixing occurs while making the reaction does not run-off. This is achieved by controlling the temperature seen by the chemical integration solver. An initial range between 800 and 1400 K is usually specified. Gradually, these constraints are loosened over the first few milliseconds of simulation until the temperature seen by the chemistry is the actual flow temperature. Despite these precautions, the high reactivity of the oxygen/hydrogen mixture means that significant pressure oscillations can be generated during this startup/ignition sequence. In order to dampen these oscillations, two main numerical methods are used:

- non-reflecting inflow boundary conditions with varying relaxation coefficients are applied on the different inlets in order to absorb most of the pressure oscillations without affecting too much the inlet conditions
- upwind scheme is applied in the nearly-incompressible oxygen core to damp the pressure oscillations as they propagate through the liquid oxygen

Following this strategy, reliable ignition can be achieved and a steady flame is obtained in the shear layer. However, the axisymmetric simulation cannot be run too long as the oxygen core will extend much farther than it should because of the axisymmetric centerline boundary condition, which does not allow for heat and mass transfer across it. This is the same phenomenon as the one reported in Section 4.4.1 for a gas-gas injector. So, after usually a few milliseconds and at most 10 depending on the flow conditions, the flowfield is rotated and interpolated on a three-dimensional grid. The resolution of each grid does not need to match but usually does as it provides a cleaner initial solution for the three-dimensional simulation.

This strategy is illustrated by the sequence of snapshots shown in Figure 89 and which highlight the transition between the axisymmetric solution and the three-dimensional solution. During this transition, the most notable changes observed are:

- the breakdown of the vortical structures in the main shear layer as vortex stretching, not present in an axisymmetric geometry, takes over
- the shortening of the oxygen core as the vortex rings around it break down
- the large increase in mixing due to the two previous changes. This leads to a large increase in the amount of combustion and heat released in the chamber
- the apparition of sinusoidal, "snake-like" jet instability that is also observed in the experiments

Overall while this transition takes about 1 ms of physical time of three-dimensional simulation, this cost on top of 10 ms of axisymmetric simulation is a very cost-effective way to obtain an initial three-dimensional solution before starting to collect statistics.

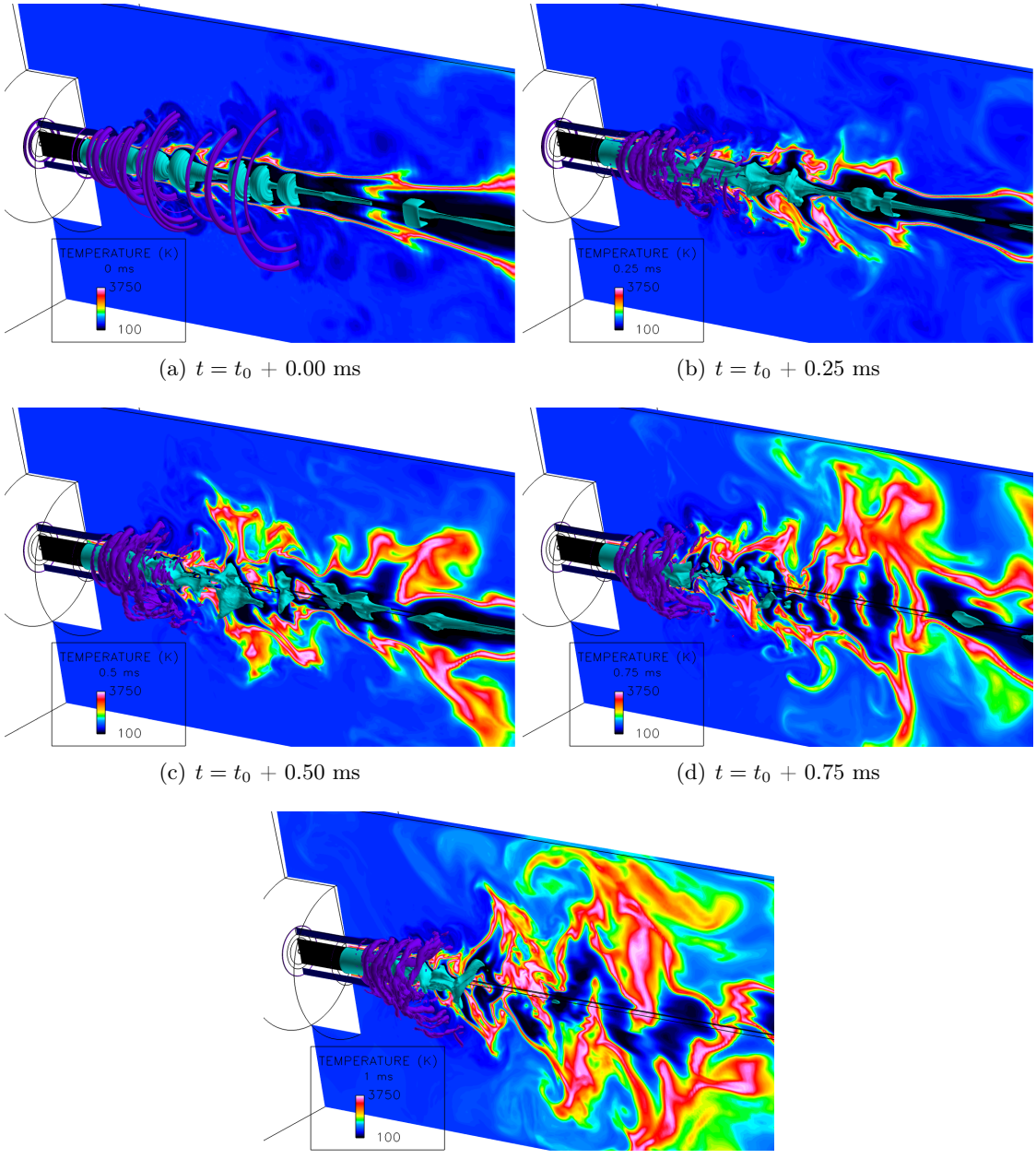

(a) $t = t_0 + 0.00$ ms

(b) $t = t_0 + 0.25$ ms

(c) $t = t_0 + 0.50$ ms

(d) $t = t_0 + 0.75$ ms

(e) $t = t_0 + 1.00$ ms

Figure 89: Transition from axisymmetric solution to three-dimensional solution for the first millisecond of three-dimensional simulation simulation. Each snapshot is 0.25 ms apart and shows temperature color contours, vortical structures in purple and oxygen in light blue.

6.2.3 Multi-physics analysis

A first approximation made when modeling the chamber was to assume the flow conditions given for the injector streams could be applied at the location of the start of the computational domain. The flowrate and temperature measurements are actually performed 3.1 inches, or 79 mm, upstream of the injector and it is suggested that the injection conditions can be significantly different from the upstream conditions. A few additional assumptions are required to perform an analysis of the flow upstream of the injection plane. The whole chamber is made of oxygen-free copper (or oxygen-free high thermal conductivity (OFHC)) and it is assumed as a first approximation that the sleeve around the oxygen jet is made of the same material. The flow upstream of the injection plane, inside the coaxial injector, is considered steady and axisymmetric. The change of area between the coaxial injector and the combustion chamber creates a large impedance that should prevent acoustics from traveling upstream of the injection plane. The natural symmetry of the injector, coupled with the assumed lack of perturbations from the combustion chamber justifies the axisymmetric hypothesis. Thus it appears that a RANS simulation of the injector could realistically model the physics at play there. This means not only the possibility of a small computational cost but also an accurate capture of the boundary layers. This is important since we are interested in the exchange of heat through the oxygen sleeve via two main mechanisms:

- If there is a temperature difference between the two streams, since it can only be measured 3.1 inches upstream of the injector face [160], there could be a significant exchange of heat through the highly conductive copper over this distance. This could significant influence the density (and hence the velocity) of the two streams: close to the critical temperature, small variations of temperature produce large variations of density.

- Since it is assumed the flame is anchored at the tip of the oxygen sleeve, there is probably significant heat transfer from the flame to the sleeve. As a first approximation, and since the melting point of OFHC is around 1350 K, the tip wall temperature is set at 1000 K.

To perform this steady-state analysis, the commercial software ANSYS®Fluent is chosen for its wide range of RANS models and its ability to couple fluid-solid analyses. In order to use a $k-\epsilon$ model easily, a very refined grid is generated, with the first grid point located well inside the viscous sub-layer, at a distance of around 1 wall unit. Each stream is modeled with the Peng-Robinson equation of state and solved using the SIMPLE scheme. The sleeve temperature is initially set at 200 K and generic turbulent profiles are provided at the inflow. The heat conduction through the sleeve is coupled with the turbulent heat transfer in each channel. The tip of the sleeve can optionally be set at 1000 K to model the effect of an isothermal wall. The simulation is then run until convergence. A sample of the results obtained is shown in Figure 90 where the steady-state temperature are displayed independently in each part of the domain. Several conclusions can be drawn from this study, especially after running a few companion LES simulations of the combustion chamber.

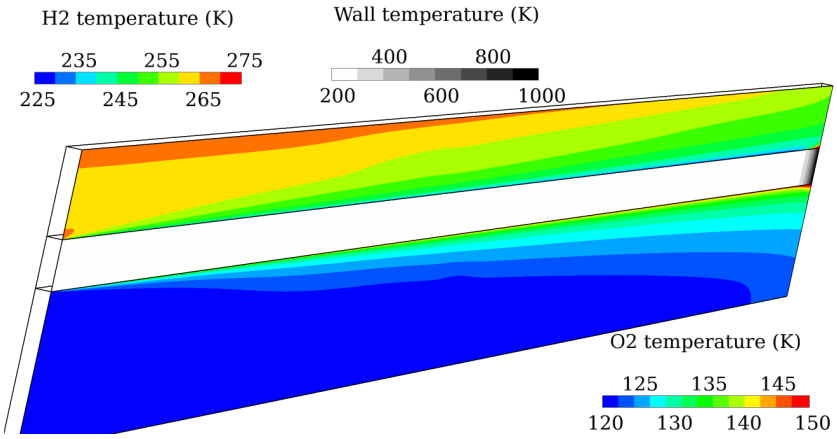

Figure 90: Converged solution of the RANS simulation of the coupled fluid-solid problem upstream of the injection plane. Three different temperature ranges were chosen to highlight the field in each part of the domain: H_2 channel (top), wall (middle), O_2 channel (bottom).

First, even if the tip of the oxygen sleeve is assumed to be as hot as possible, this has little influence on the exit conditions for both streams. Indeed, thanks to the high conductivity of the copper and the cooling from both sides of the sleeve, the wall temperature is only elevated over a few millimeters and this only affect the fluids temperature in the near-wall region. However, it does vaporize the oxygen there and this could influence the stability of

the shear layer downstream. Also, this temperature gradient should only cause a very minor expansion of the tip of the sleeve. Assuming a value of 1.5×10^{-5} K^{-1} for the coefficient of thermal expansion, a gradient of 800 K over 2 mm would simply expands the tip of the sleeve by about 20 microns, which is not likely to affect the flow. Thus, the tip wall temperature has little influence on the injection conditions but might have a role on the location and strength of the flame anchoring. The temperature fields shown in Figure 90 for the hydrogen and oxygen channels thus mostly hold for an adiabatic tip wall too. Following this steady-state analysis, a simulation was conducted with the baseline grid including an isothermal wall boundary condition at the tip of the oxygen sleeve. The wall temperature was set to 1000 K and the solution restarted from a previous baseline simulation. While this created a flame stand-off distance of less than 100 microns from the tip, this was not enough to change the flame anchoring and dynamics in any significant manner. Explicitly extinguishing the flame downstream of the tip for a distance of 2 step heights does not destabilize the flame either and it reattaches itself close to the wall in only a few microseconds. While the current reduced mechanism cannot very accurately predict these extinction/reignition event, this behavior is consistent with what has been reported experimentally and numerically [183, 111]. Thus it appears unlikely that the tip wall temperature can significantly affect the dark core length.

On the other hand, there is significant heat transfer across the sleeve, from the warmer hydrogen to the colder oxygen. As can be seen in Figure 90 this significantly affects the temperature distribution in each stream. In particular, the bulk hydrogen temperature is decreased by at least 10%. This means the hydrogen density increases and since the flowrates are kept constant, the injection velocity for hydrogen is now 10% lower. Effects on the oxygen side are not as dramatic and the bulk of the oxygen temperature does not change much. However, it is likely that the wall temperature causes some local premature vaporization of the oxygen there, which might affect the stability of the boundary layer. This might destabilize the oxygen jet further and could have a decreasing trend on the dark core length, but this is probably a local effect. Anecdotal evidence of turbulent instabilities with an arbitrary wall at constant temperature warm enough to produce significant density changes has been observed in axisymmetric simulations. However, an accurate, transient analysis of

this phenomenon would require detailed unsteady heat transfer through the oxygen sleeve. This is beyond the scope of this work. Even without taking into account the near-wall phenomena, the lowering of the momentum flux of the hydrogen stream however could have an increasing trend on the dark core length. As shown in Table 13, the major parameters of the injection are only slightly affected by these changes in temperature and velocity. It is not expected to affect significantly the dark core length predicted by the LES solver. This is confirmed by Figure 91 which shows the time-averaged fields for two simulations with short inlets and the baseline grid, one with the baseline conditions listed in Table 13 (center column) and one with the conditions predicted by the RANS multi-physics analysis presented above (right column). A stable flame is obtained that qualitatively resembles the experimental visualization and the description of trans-critical flames made by other researchers [30, 207]. The flame structure will be discussed later on in further details but one can note already that the main difference between this flame and a trans-critical flame like MASCOTTE [207] is the influence of the co-flow. The large expansion caused by the sudden volumetric change of the liquid oxygen as it burns is limited by the size of the chamber and the dilution with the co-flow. Thus the flame shell closes rather smoothly unlike the MASCOTTE flame which expands more drastically and ends more abruptly. However, the flame is quantitatively very far from the flame obtained experimentally by Locke with a dark core length of about 5 diameters while Locke reports 38 diameters on average. Clearly, some of the current modeling assumptions are poor and the next sections will continue to explore some of them. As far as the modified inflow RANS-based conditions go, it can be seen that the dark core length remains short but does increase by 1 or 2 diameters but there are no dramatic changes in the overall structure of the flowfield.

6.2.3.1 Co-flow modeling

As stated previously, one major issue is the modeling of the perforated plate. The plate contains 78 holes, distributed in the following manner (see Figure 58):

- A row of 16 holes at a radial location of approximately 6 mm.

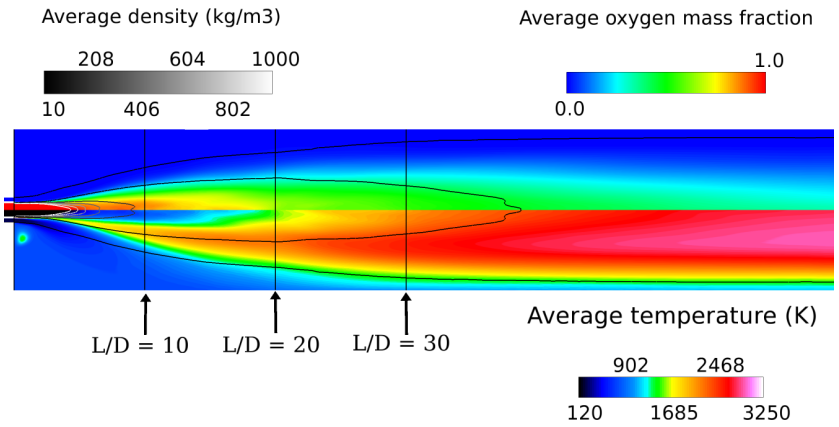

(a) Short inlets with baseline conditions

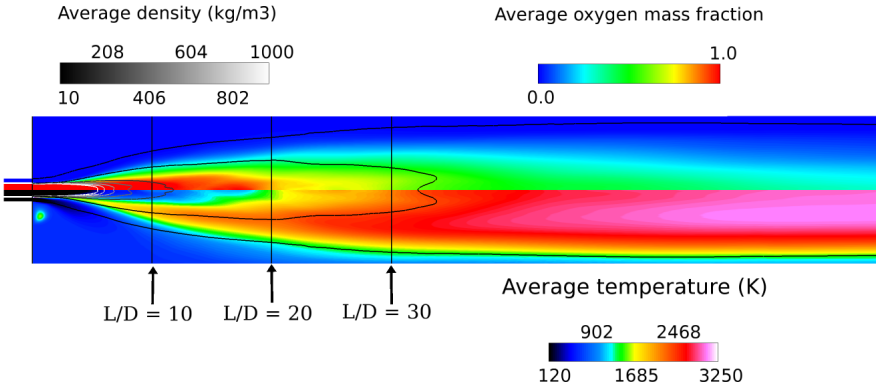

(b) Short inlets with RANS conditions

Figure 91: Comparison of the time-averaged flow-fields (over 8 ms) for simulations with short inlets and either baseline inflow conditions (top) or RANS-based inflow conditions (bottom). upstream of the injection plane. Three different temperature ranges were chosen to highlight the field in each part of the domain: H_2 channel (top), wall (middle), O_2 channel (bottom).

- A row of 20 holes at a radial location of approximately 8.5 mm.
- A row of 26 holes at a radial location of approximately 11 mm.
- The remaining 16 holes are found in 4 groups of 4 holes in the corners of the square cross-section.

Each hole has a diameter of 1.2 mm (0.0047 in). This represents an area of 1.12×10^{-6} m^2 per hole, or 8.73×10^{-5} m^2 overall for the 78 holes. As a first approach, a uniform flow will be assumed from a radial distance of 6 mm up to the chamber wall. This means the effective injection area for the background flow is 5.32×10^{-4} m^2, more than 10 times the area in the experimental rig. With a flowrate of 0.336 $kg.s^{-1}$ and an inflow density of 20.345, this yields a bulk velocity of 31.0 $m.s^{-1}$. A better approximation might be possible with finer grids. Each row of holes would be modeled by an axisymmetric slot, with the third row including the 16 stray holes. This would reduce the total injection area and keep it closer to the actual area of the perforated plate. Using the radial locations previously mentioned, the following dimensions are obtained:

- The first row, of area 1.79×10^{-5} m^2, would be a slot of half-width 237.5 microns, centered at a radial location of 6 mm.
- The second row, of area 2.24×10^{-5} m^2, would be a slot of half-width 209.6 microns, centered at a radial location of 8.5 mm.
- The last row, of area 3.58×10^{-5} m^2 (including the stray holes), would be a slot of half-width 259.1 microns, centered at a radial location of 11 mm.

The issue with this approach is that it requires the grid to remain circular over a larger area and increases skewness in the chamber corner, especially for coarse grids given the small width of the slots.

To illustrate the influence that the coflow can have on the overall flow dynamics, Figure 92 shows a time-sequence of an axisymmetric simulation with a uniform coflow and non-reflecting boundary conditions with a small relaxation coefficient.

The coflow represents an open boundary with potentially low impedance because of the way it is modeled as a uniform flow instead of a perforated plate. Since the inflows are modeled as non-reflecting boundary conditions, the pressure and velocity are allowed to fluctuate at the boundary. While the coaxial inflows are sheltered from the combustion chamber acoustics, the coflow might strongly respond to these acoustic waves if the relaxation coefficient of the boundary (see Section 2.7.3) is too small. Note that due to the coflow composition, there is a weak premixed flame present slightly downstream which explains the constant velocity increase (due to gas expansion) observed in Figure 92.

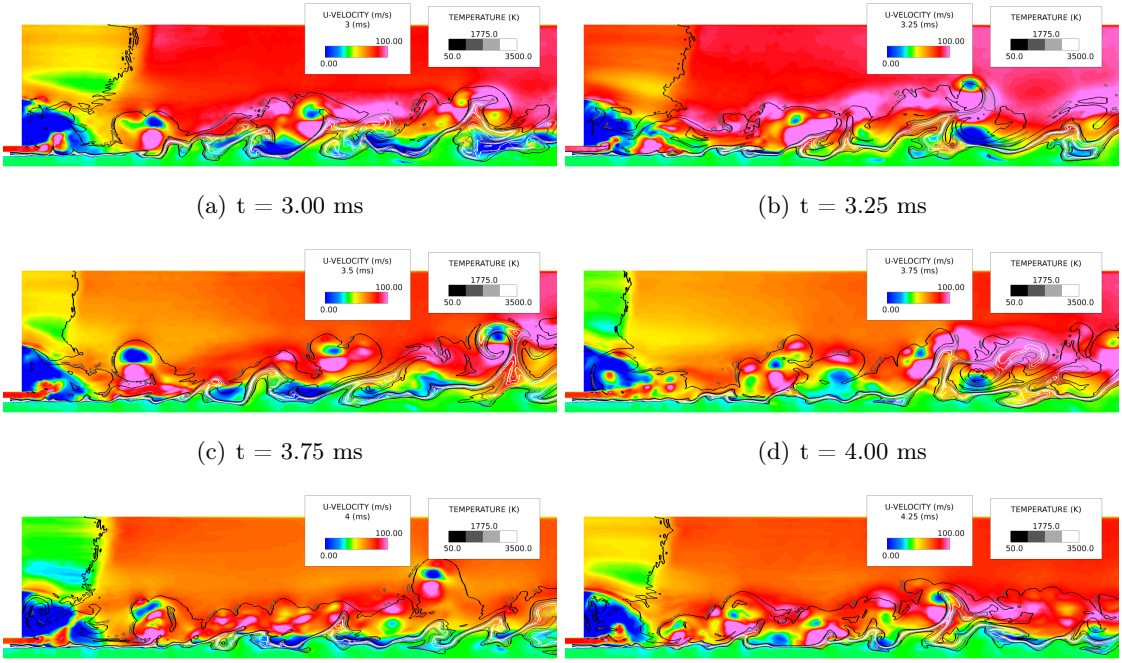

(a) t = 3.00 ms (b) t = 3.25 ms

(c) t = 3.75 ms (d) t = 4.00 ms

(e) t = 4.25 ms (f) t = 4.50 ms

Figure 92: Time-sequence of the pulsating coflow under the influence of the chamber acoustics.

Another issue is the grid transition between a Cartesian geometry, desirable at the centerline to avoid singularities and at the chamber walls to respect the square cross section, and a cylindrical geometry, needed at the boundaries of the injector to capture its circular nature. We choose to use a Cartesian "butterfly" grid along the centerline and a cylindrical

grid outside. We are willing to accept a large amount of stretching and skewness in the corners of the chamber as the flow should be relatively uniform in these regions. So we assume a cylindrical grid up to a radial distance of 6 mm, after which we will start stretching and deforming the grid in the corners. This mapping is a simple function of the ratio of two lengths: the radius of the incircle to the square cross-section (0.5 in = 12.7 mm) and the distance from the center to the edge of the square.

6.2.4 Final computational grid and operating conditions

Following the analysis above, there is a possibility that the high-speed jets through the holes of the plate have enough coherence to penetrate far into the domain and influence the stability of the coaxial jet. Thus a new refined grid with 8.5 M grid points is generated to incorporate the first 2 rows of holes of the perforated plate. The minimum spacing remains similar to the initial grid at around 40 microns. In similar configurations for, respectively, a LOX-CH4 and a LOX-GH2 flame, Schmitt et al. [267] and Ruiz [257] use roughly equivalent resolutions, with minimal spacings around 50 to 100 microns using unstructured grids. This grid is shown in Figure 93(a). The holes are assumed to be rectangular slots for now because of limitations of the current structured grid but the flowrate and velocity for each hole match the experimental values. The first 2 rows of 36 holes should form a shell around the coaxial jet and potentially help delay the breakup of the oxygen jet. The current structured grid does not allow the inclusion of the remaining holes as the grid is skewed and no longer symmetric in the corner of the square cross-section. The same uniform flow boundary conditions is applied there for $r > 11$ mm. In terms of areas, this configuration yields the following:

- The 36 holes represent an area of 4.03×10^{-5} m^2 and the inflow velocity through these holes match excatly the experimental velocity estimated at 188.66 m.s^{-1}.
- The uniform flow in the corners of the chamber represents an area of 2.65×10^{-4} m^2. This replaces the remaining 42 holes and their area of 4.704×10^{-5}.
- The total flow area for the co-flow is thus 3.053×10^{-4} m^2 compared to 8.7×10^{-5} m^2, about 3.5 times larger.

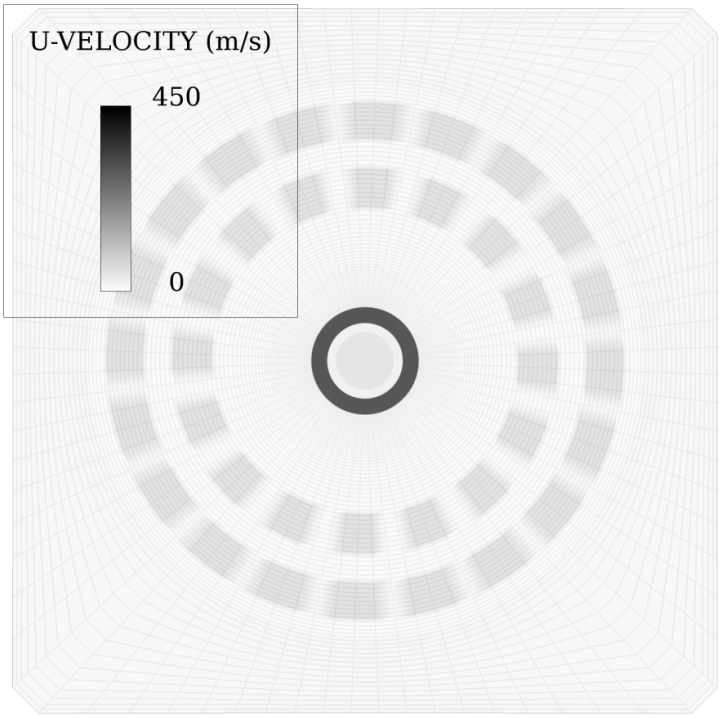

(a) Grid for perforated plate

Figure 93: Head-on view of the refined grid used in modeling the first two rows of holes from the perforated plate. The grayscale contours indicate the injection velocity.

Table 15: Characteristic values for PSU rig acoustics for the LOX-GH2 reacting case with long inlets. The speeds of sound correspond to the values computed with the PR EoS.

Description	Oxygen inlet	Hydrogen inlet	Combustion chamber
Average sound speed (m/s)	590.0	1300.0	1200.0
Characteristic length (m)	7.9×10^{-2}	7.9×10^{-2}	3×10^{-1}
$\left(1-M^2\right)\frac{c}{L}$	7.45×10^{3}	1.31×10^{4}	4.0×10^{3}

One of the sought-after properties of the co-flow is that its volumetric (or molar) content of hydrogen[160] matches the theoretical content of the combustion products of the coaxial injector running slightly fuel rich (O/F = 6). To achieve this, the pre-burner that generates the co-flow is said to run very fuel rich (O/F = 2.1) and to include a significant amount of dilution by nitrogen. Through standalone equilibrium computations using cantera [89], it is straightforward to find the right amount of dilution to obtain 25% of H_2 by volume in the products. These calculations yield a reacting mixture of $(Y_{O_2}, Y_{H_2}, Y_{N_2}) = (0.0698, 0.0332, 0.897)$ and resulting products of $(Y_{H_2}, Y_{H_2O}, Y_{N_2}) = (0.0244, 0.0786, 0.897)$ or $(X_{H_2}, X_{H_2O}, X_{N_2}) = (0.25, 0.09, 0.66)$ at 1000 K. This temperature is higher than the injection temperature of 778 K reported by Locke but it is likely the combustion products will experience significant cooling from the pre-burner to the combustion chamber, given the traveling distance shown in Figure 85.

As mentioned in the previous section, the last temperature measurements upstream of the injection plane occur at $X = -3.1$ in = -78.74 mm. This is the location chosen for the start of a new computational grid. Combined with a semi-reflecting constant-mass boundary conditions in the coaxial inlets, it is expected that the longitudinal pressure oscillations in the feedlines exert less influence on the flow dynamics and the break-up of the oxygen jet. This will depend on how the inlets respond to incoming acoustic waves of various frequencies, and in particular to the characteristic frequencies of the feedlines and the chamber. These frequencies are listed in Table 6.2.4 for future reference.

The experimental conditions and the modified conditions for this final configuration are shown in Table 17 for comparison. However it should be noted that densities and velocities

Table 16: Comparison of density predictions for O_2 and H_2 at their respective injection temperatures (118.3 K and 272 K) for the LOXGH2 PSU rig

Species	Pressure	NIST density	PR EoS density	Relative difference
O_2	65 bar	1010.6 kg.m^{-3}	1122.8 kg.m^{-3}	+11.1%
O_2	80 bar	1016.6 kg.m^{-3}	1131.2 kg.m^{-3}	+11.3%
O_2	95 bar	1022.4 kg.m^{-3}	1140.1 kg.m^{-3}	+11.5%
H_2	65 bar	5.5659 kg.m^{-3}	5.6601 kg.m^{-3}	+1.7%
H_2	80 bar	6.7868 kg.m^{-3}	6.9227 kg.m^{-3}	+2.0%
H_2	95 bar	7.9845 kg.m^{-3}	8.1673 kg.m^{-3}	+2.3%

are not known precisely from the experiment. While the flowrate is easily measured, temperature measurements are more difficult and under the injection conditions, small differences in temperature have a large impact on density and injection velocity. Thus the 10 to 15% adjustment in velocity to match the flowrate despite the over-prediction of density by the PR EoS is deemed acceptable. There have been many reacting studies [42, 267] that have neglected this effect and it is believed that the 10-15% adjustment on the injection velocity is an acceptable compromise to maintain the correct flowrate, the most important parameter and the one usually known with the smallest uncertainty from the experiments.

6.2.5 Coupling between inlets and combustion chamber

In parallel to the multi-physics analysis conducted with the first grid, the influence of the inlet lengths and reflectivities is investigated with the new grid on the pressure oscillations in the combustion chamber. This coupling between the chamber and the feed lines could be one reason why sinusoidal and helicoidal modes are so dominant in the baseline results. To this end, three-dimensional simulations are conducted using either short inlets (10 mm) or long inlets (79 mm), the location of the last temperature probe).

This also highlights the role of the constant-mass, non-reflecting inflow boundary condition as described in Section 2.7.3. With the longer inlet, it is easier for this boundary to absorb lower-frequency perturbations since the reflectivity of the boundary is set proportionally to c/l, with c the speed of sound in the inlet and l the inlet length. If the reflectivity is set too low compared to c/l, while the boundary absorbs perturbations with lower frequency, there is a risk for the mass flux to drift over time. A perturbation of a given frequency is

Table 17: Operating conditions for the final configuration of the LOX-GH2 PSU rig. The reference species is oxygen, whose critical pressure is 50.4 bar and critical temperature is 155 K. The experimental values come from Locke [160] and the simulation conditions take into account the density predicted by the Peng-Robinson equation of state. Two sets of co-flow values are provided for the simulation to differentiate the flow through the modeled holes and the flow through the uniform co-flow on the outer region of the injection plate. The values in the RANS LES column corresponds to the inflow conditions given by the multi-physics RANS study described in Section 6.2.3. These values are always used with a short inlet.

Description	Units	LOXGH2 XP	Baseline LES	RANS LES
Main chamber				
Chamber pressure	Pa	6.343×10^{6}	6.5×10^{6}	6.5×10^{6}
Preburner background flow				
(Y_{H_2}, Y_{H_2O}, Y_{N_2})		(0.0244,0.0786,0.897)	(0.0244,0.0786,0.897)	(0.0244,0.0786,0.897)
Mass flowrate	$kg.s^{-1}$	0.335	0.1546 0.1804	0.1546 0.1804
Mass flux	$kg.m^{-2}.s^{-1}$	3837.3	3837.3 680.7	3837.3 680.7
Inflow density	$kg.m^{-3}$	20.34	20.34 20.34	20.34 20.34
Background flow area	m^2	$8.73e\times10^{-5}$	4.0×10^{-5} 2.7×10^{-4}	4.0×10^{-5} 2.7×10^{-4}
Inflow temperature	K	778	778 778	778 778
Bulk inflow velocity	m.s−1	188.66	188.66 33.47	188.66 33.47
Injector inner post oxygen flow				
Mass flowrate	$kg.s^{-1}$	0.102	0.102	0.102
Mass flux	$kg.m^{-2}.s^{-1}$	30681.3	30681.3	30681.3
Post area	m^2	3.3245×10^{-6}	3.3245×10^{-6}	3.3245×10^{-6}
Inflow density	$kg.m^{-3}$	1010.6	1122.8	1067.5
Inflow temperature	K	118.3	118.3	125.0
Compressibility		0.2	0.19	0.19
Inflow velocity	m.s−1	30.36	27.33	28.7
Kinematic viscosity	$m^2.s^{-1}$	1.12×10^{-7}	1.48×10^{-7}	1.20×10^{-7}
Injector annular flow				
Mass flowrate	$kg.s^{-1}$	0.0168	0.0168	0.0168
Mass flux	$kg.m^{-2}.s^{-1}$	2842.6	2842.6	2842.6
Annular area	m^2	5.91×10^{-6}	5.91×10^{-6}	5.91×10^{-6}
Inflow density	$kg.m^{-3}$	5.566	5.660	6.160
Inflow temperature	K	272	272	250
Compressibility		1.02	1.02	1.01
Inflow velocity	m.s−1	510.72	502.22	461.46
Kinematic viscosity	$m^2.s^{-1}$	1.57×10^{-6}	1.30×10^{-6}	1.13×10^{-6}
Injector characteristics				
Velocity ratio	$\frac{\text{annulus}}{\text{post}}$	16.8	18.37	16.1
Mass flow ratio	$\frac{\text{post}}{\text{annulus}}$	6.05	6.05	6.05
Momentum flux ratio	$\frac{\text{annulus}}{\text{post}}$	1.56	1.70	1.49

thus easier to absorb with a longer inlet. This has an impact on the pressure oscillations in the inlets and to a lesser extent in the chamber, as shown in Figure 94. There, the pressure traces at various locations are plotted for the short inlet case and the long inlet case. The main impact of the long inlets is on the pressure oscillations inside the feed lines, which are significantly reduced. Pressure fluctuations in the chamber are relatively similar, although there is a decrease in the low frequency amplitudes. This is due to a slight delay of the onset of the jet instabilities and a slightly longer dark core. However, qualitatively, the flowfield is not significantly affected. Note also the larger pressure drop across the long inlet compared to the short one. This might also help with the absorption of the pressure disturbances. In the end, the ideal simulation would start from far upstream with physical constant-mass

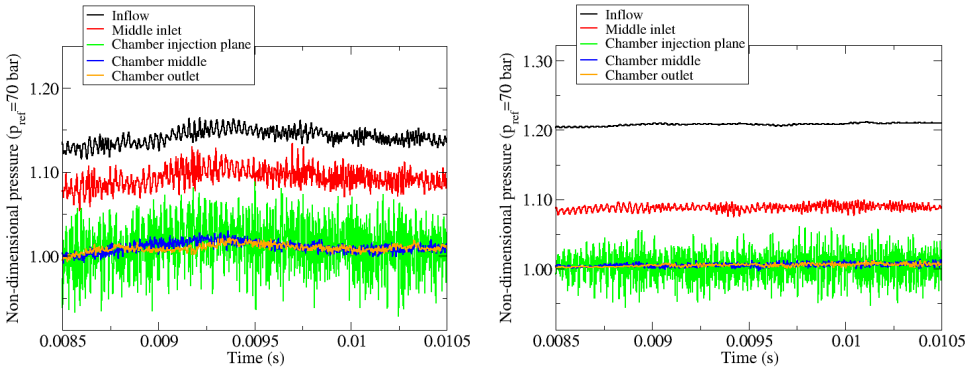

Figure 94: Pressure traces at various relative locations for a three-dimensional simulation with short, 10 mm, inlets (left) and long, 79 mm, inlets (right).

non-reflecting boundary conditions and would take into account the heat transfer between the reactant streams. This simulation is beyond the capabilities of the current solver and beyond the scope of this work. However, based on the results presented in this section, it is unlikely that such simulation would predict a solution dramatically different from the one obtained here.

6.3 Overview of the results with perforated plate

A qualitative comparison with the experimental data available is first presented in Figure 95. It shows a typical backlit image obtained by Locke and a transverse cut of the temperature field predicted by the current LES simulation. In both cases, the dark liquid oxygen jet is surrounded by the bright flame and remains coherent along the centerline for some length. Further downstream, significant amount of oxygen can be seen moving away from the centerline, because of either sinusoidal or helicoidal jet mode. It is unfortunately impossible to tell the difference via the backlit imaging. The main difference appears that the onset of these modes occur much earlier in the three-dimensional simulations than in the experiments. Because of this, and while cold pockets of oxygen appear visible 30 to 40 diameters downstream of the injection plate, the predicted dark core length appears significantly shorter than observed experimentally.

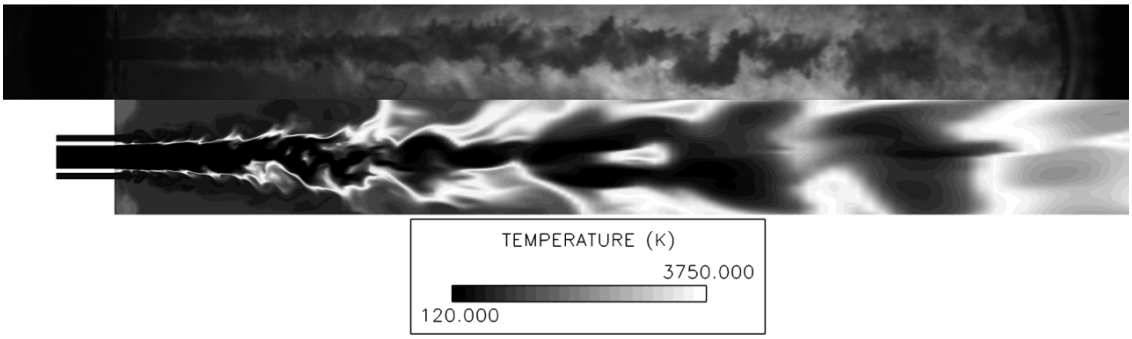

Figure 95: Qualitative comparison between a backlit image of the experimental flame (top) and a cut of temperature field (bottom) for the baseline LES simulation.

Two three-dimensional views, shown in Figures 96 and 97 illustrate the physical processes that precipitate the breakup of the oxygen jet. Figure 96 shows that the jets from the faceplate holes display good coherence for 5 to 10 LOX diameters downstream before quickly breakdown into a more uniform coflow. This coherence helps maintaining the coaxial flow compact and axial, limiting the onset of the helicoidal instabilities and delaying the oxygen jet break-up. However, as soon as the coflow loses its coherence, the main shear layer is destabilized and large scale motions away from the centerline start to appear, which help

breaking up the oxygen jet. For maximum fidelity with the experimental rig, it might thus be necessary of modeling all the holes in the perforated plate. Nonetheless, the role of the co-flow is clearly demonstrated here as it nearly doubles the dark core length reported in Section 6.2.3 to about 15 diameters. However, this is still a poor agreement with the mean value of 38 reported by Locke. Both figures also illustrate the strong sinusoidal and helicoidal modes that are present in the current simulation and which contribute significantly to the heat and mass transfer across the centerline. Comparatively, the backlit images of the experimental flame show a very straight oxygen jet, without any undulation. While it is possible that the baclit image hide such feature in the third dimension, it seems to indicate a fundamental difference in the way the flame evolves around the oxygen jet. In the experiments, the flame essentially shields the jet from the strong vortical structures around it. In the simulation, as shown in Figure 97, the vortical structures manage to interact strongly with the flame and the trans-critical layer that appears as the light blue contour inside the oxygen jet. After a few diameters, the flame becomes much wider and significant vortex pairings occur between the remains of the hydrogen annular stream and the flame.

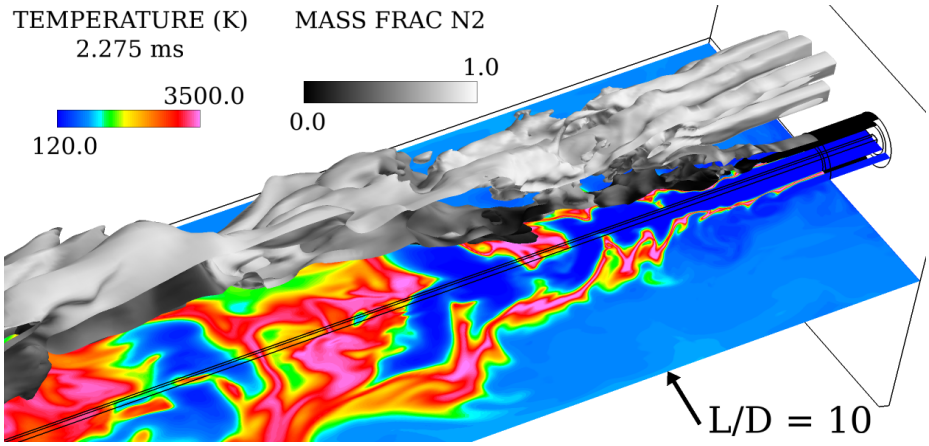

Figure 96: Instantaneous snapshot of the three-dimensional flowfield for the perforated plate case. The temperature field is shown with color contours while the coflow structures are shown through the isosurface of 100 m/s axial velocity. This isosurface is colored by nitrogen mass fraction and is only shown for half of the domain.

Earlier experiments run in a similar rig as the Lock experiments show the influence that

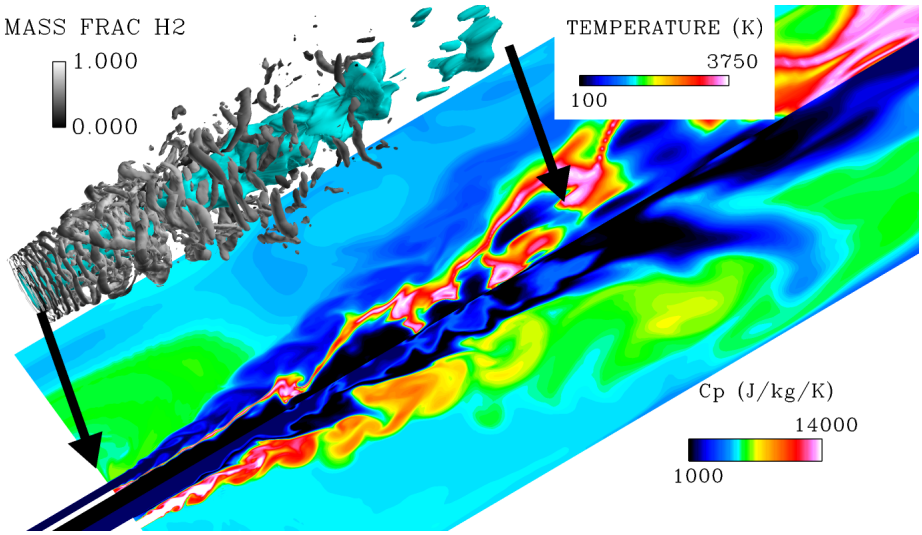

Figure 97: Three-dimensional view of the trans-critical LOX-GH2 flame using colored slices of temperature (top) and specific heat at constant pressure (bottom), as well as a translated view of the oxygen core (light blue isosurface) surrounded by vortical structures.

flow confinement and/or a co-flow can have on the breakup process. Running the same injector under essentially the same conditions but in a smaller chamber and a stronger co-flow, Woodward et al. [338] measured the dark core length observed during a single experiment. The firing lasted for a few seconds with stable pressure for 4 seconds and the visualization rate was low (2.5Hz). However, they also monitored the evolution of the injection conditions during the run: as the LOX injection temperature varied around the critical temperature, the momentum flux ratio would vary accordingly between 1.2 and 1.8. Taken into account only the instances where oxygen was injected at sub-critical temperatures, there is still a large variability in the measured dark core lengths, with L_{dc}/D_i instantaneously ranging from 19 to 30, far below the averaged value of 40 reported by Locke. Table 18 summarizes the operating conditions and observed dark core lengths for both experiments. The combined effect of stronger confinement and stronger co-flow is hard to estimate as there is currently no study, to the author's knowledge, that investigate both of them together in a shear coaxial configuration. Only Gautam et al. [79] studied the effect of confinement in a cold-flow configuration and they found that confinement reduced the heat and mass transfer to the center jet, resulting in longer cores. Even with the current

Table 18: Comparison of experimental conditions and observed dark core lengths between Locke [160] and Woodward et al. [338]. The injector, referred as Case B by Woodward et al., is identical in both experiments.

	Locke	Woodward
Chamber pressure (bar)	63.43	68.9
Chamber cross section (mm^2)	25.4×25.4	19.1×19.1
Co-flow mass flowrate (kg/s)	0.335	0.527
Mixture ratio	6.02	6.0
LOX flowrate (kg/s)	0.102	0.104
LOX temperature (K)	118	125–190
Momentum flux ratio	1.58	1.5–1.8
Normalized dark core length	25–50	19–30

improved modeling of the perforated plate, it is still a crude approximation to the exact experimental configuration and this might significantly affect the coaxial flow dynamics and the predicted dark core length.

In conclusion, the dark core length obtained with the best current LES is still much smaller than the one reported experimentally. Several assumptions on the modeling of the co-flow and the inflow boundary conditions have been investigated and have somewhat improved the predictions but the quantitative agreement remains poor. Qualitatively, sinusoidal and helicoidal modes appear much stronger in the current simulations than in the experiments and strongly contribute to the early break-up of the liquid oxygen jet. The next section will forego further comparisons with the current experimental data and will focus on the physical analysis of the flame structure in order to prepare the investigation of turbulent combustion closure, unfortunately beyond the scope of this work.

6.4 Flame structure

Since the quantitative comparison with the experimental results is not satisfactory, in order to gain more insight on the possible cause of the strong helicoidal shown previously, the flame obtained numerically is compared to the consensual structure illustrated in Figure 98, taken from Candel [30] and slightly modified to facilitate the description of the flame. This Figure shows a composite visualization of the super-critical flame downstream of a shear-coaxial

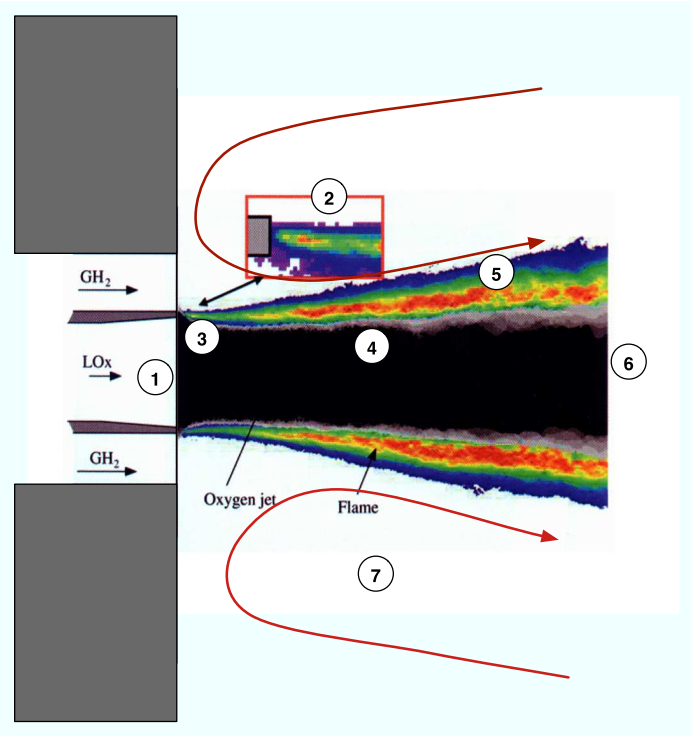

Figure 98: Modified from Candel et al.[30], combined OH* emission (color) and backlighting (grayscale) image in the near-field of a single-element, tapered, shear-coaxial LOX-GH2 injector.

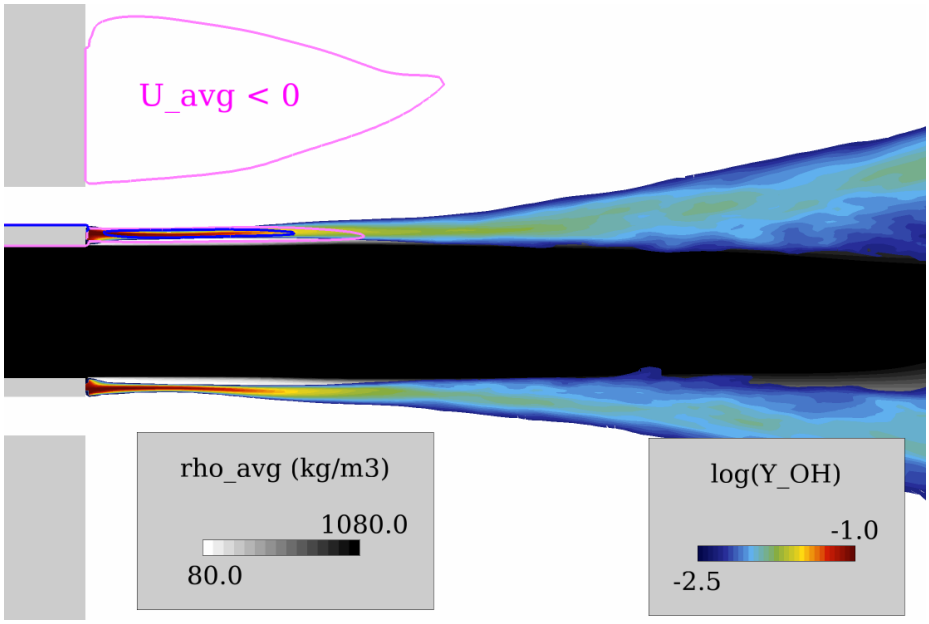

(a) Side view

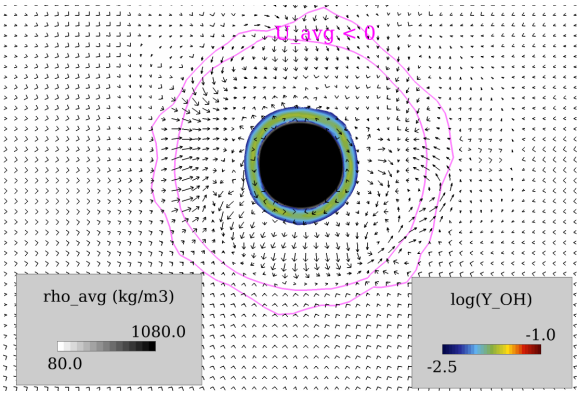

(b) Head-on view

Figure 99: Side (top) and head-on (bottom) view of the trans-critical flame spatial structure using time-averaged data from the current LES. Recirculation regions are shown in pink contours, density is shown in grayscale contours to reproduce the backlit image and the logarithm of the OH mass fraction is shown in color contours to mimic the experimental emission.

injector. The color scale corresponds to a slice of OH* emission and the grayscale to the average backlighting image. The operating conditions correspond to the MASCOTTE case C-60 (60 bar) used as a baseline case for CFD validation at the 3rd International Workshop of Rocket Combustion Modeling (Case RCM-2) [207]. The most important regions of the flow have been identified with a number and can also be identified on Figure 99. This figure attempts to reproduces this visualization using the LES results and also provides a head-on view of the flame. The main difference with the MASCOTTE set-up is once again the presence of a co-flow and it affects some of the following descriptions which are first geared towards Figure 98:

1. At the entrance of the combustion chamber, in **region 1**, the oxygen enters as a compressed liquid jet since the chamber pressure is above the critical pressure of oxygen and the oxygen injection temperature is below the critical temperature of oxygen.

2. **Region 2** corresponds to the close-up view of the tip of the injector. Since the 1990's, it has been shown in many different rigs that the flame was anchored in the small but intense recirculation region downstream of the tip separating the two flows. This does not seem to depend on the geometry of the injector for LOX-GH2 injectors. Whether the injector is recessed, whether the oxygen post is tapered or whether the oxygen post tip is thin or thick, there is no experimental evidence that the flame does not start here. At most, there could be some movement of the anchor point downstream of the tip as discovered by Singla et al. [283]. The stability of this flame anchoring mechanism is a specificity of O_2-H_2 systems. For LOX-GCH4, although latest investigations show the same anchoring mechanism, the flame structure appears to slightly vary with the geometry [260]. For the current simulations, since the tip of the sleeve is adiabatic, the intensity of the flame there is probably overstated.

3. In **region 3** the flame is the thinnest and also the least intense. The oxygen and the hydrogen that had mixed in the wake of the tip have been burned and the shear layer is too thin to mix a lot of reactants. The strain rate is also very large here. Burning here occurs as a pure diffusion flame. Again for the current simulations, there is a

slight decrease in intensity but the recirculation behind the tip is so rich in OH that the emission/concentration remains quite intense here.

4. **Region 4** shows a rather smooth surface of the oxygen jet. In contrast with the picture at subcritical pressures, we cannot see any droplets or ligaments being shed from the jet. However, this does not necessarily mean they cannot exist locally (see the discussion on the mixture supercriticality in the next section), just that they are too small (less than 10 microns in this particular example) to be observed by current visualization techniques [95, 186]. Also we can start to distinguish some density gradients inside the oxygen jet. Two phenomena are probably responsible for these gradients.Most likely, it is caused by the diffusion of hydrogen into the oxygen. At such high pressures, the power of dilution of the two species is very strong, even with the oxygen possibly still a liquid [229]. Also, the oxygen jet can be heated up by the flame and thus becoming supercritical at the edge of the jet.

5. **Region 5** shows the broadening shell flame around the oxygen jet. However, this broadening is limited at supercritical pressures compared to subcritical pressures. It does not usually exceed half the oxygen jet diameter. For subcritical combustion, this is where the atomization would take place, with burning groups of droplets extending the combustion region further away from the jet. But for supercritical chamber pressures, the oxygen jet only displays small scale wrinkles and disturbances. Close-up, one can see "stringy or thread-like structures" [187] growing at the surface and mixing with the hydrogen flow before they could detach from the jet surface. The same broadening is observed with the LES but the concentration/emission of OH does not seem to increase. One has to keep in mind that the experimental OH* emission is integrated over the line-of-sight and thus a quantitative comparison cannot be made with a simple slice of the computational flow-field.

6. Further downstream, in **region 6**, it appears that various kinds of flames [282] or combustion regimes [113] can occur depending on the flow conditions. Palle et al.[233] show that the mass diffusion, thanks to the Soret effect, plays a very important role

and some have suggested the presence of partially premixed flames at least for LOX-GCH4 [282]. Supercritical fluids are known powerful solvents and there could be some intense premixing at the edge of the oxygen jet. Ivancic et al. [113] show that the turbulent time scales and the chemical time scales cover the whole range of the Borghi's turbulent combustion diagram [22]. Depending on the flow conditions, the shell flame can totally embrace an oxygen jet that remains relatively stable or long wavelength helical instabilities [187], especially with recessed injectors [30], can grow and force the breakup of the oxygen jet core. The resulting pockets of unburned oxygen react further downstream.

7. **Region 7** shows the recirculation of hot gases because of the large relative size of the chamber with respect to the injector. While intuitively, this configuration with a rapid hydrogen flow expansion seems quite different from the situation in a multi-element injector, these recirculating gases do mimic in a limited way the co-flow that would be present otherwise. Indeed, some single-element hot-fire testing have been conducted with a real surrounding co-flow, with only limited changes from the freely expanding single-element[21]. The recirculation pattern in the LES is affected by the surrounding co-flow which creates the toroidal recirculation shown in Figure 99.

This qualitative comparison shows that the current LES flame captures most of the documented features of a trans-critical flame. More quantitative investigation is required to understand the specifics of the current flame and what could impact its modeling. To achieve this, a series of plots in the mixture fraction space are presented next. For the current 7-step mechanism, the mixture fraction based on the mass fraction of H is:

$$\mathcal{Z} = MW_{\mathrm{H}} \left(2\frac{Y_{\mathrm{H_2}}}{MW_{\mathrm{H_2}}} + 2\frac{Y_{\mathrm{H_2O}}}{MW_{\mathrm{H_2O}}} + \frac{Y_{\mathrm{H}}}{MW_{\mathrm{H}}} + \frac{Y_{\mathrm{OH}}}{MW_{\mathrm{OH}}} \right) \tag{6.4.1}$$

First a scatter plot of the flame structure in the mixture fraction space is shown in Figure 100(a). This plot is generated by collecting, over a series of instantaneous snapshots, points in the computational domain that are located near the flame. Significant departure is observed from an idealized diffusion flame represented by the black lines of the Burke-Schumann solution. While there are large strain rates recorded along the flame, as high as

1×10^6 1/s, this is not the only factor that explains the shape of the scatter plot. The Burke-Schumann solution not only assumes infinitely fast chemistry but also constant and equal specific heats for all species. While a good approximation for some hydrocarbon combustion, it does not hold here where the specific heat of pure hydrogen is an order of magnitude larger than the one for oxygen. Because of this large specific heat, the temperature increases slowly in the mixture fraction space as one goes from pure hydrogen (Z=1) to a mixture of hydrogen and products. On the other hand, $\frac{\partial T}{\partial Z}$ on the oxygen side is large because of the relatively small oxygen specific heat. This specific heat effect has nothing to do with real gas effects as can be seen when comparing Figure 100(a) and Figure 48. Despite differences in inlet conditions and strain magnitude, the curved shape of the Z-T lines are similar in both cases. The strain does an effect on the fuel side by significantly broadening the possible solutions, resulting in near stoichiometric mixtures at low temperatures. However, some of this mixing effect is also due to the dilution from the preburner flow. This is confirmed by Figure 100(b) where only the water vapor shows significant mixing. All major species show little scatter around the ideal lines, indicating that the chemistry is at least most of the time close to being infinitely fast, and thus unaffected by strain. Despite these large strains on the fuel side (yellow symbols), no sign of extinction is observed in the flow as the strain remains well below typical values of extinction strain rates reported in the literature for H_2-O_2 flames at high pressure. The extinction strain rates are much higher on the hydrogen side than on the oxygen given the large diffusion velocities of H and H_2 and the large density of the oxygen. Several detailed studies on one-dimensional flames under high-pressure conditions have been conducted and give estimates on the values of strain that might start affecting H_2-O_2 flame structure and characteristics. Sohn et al [291] report an extinction strain of 6×10^7 1/s at 70 bar for the fuel side and an extinction strain rate of 5×10^6 1/s at 70 bar for the oxidizer side. Lacaze and Oefelein [140], considering the mean strain rate across the flame, observe no significant influence up to a mean strain rate of 5×10^6 1/s.

Then, a novel way of presenting similar data is shown in Figures 101(a) and 101(b) in the form of heat maps in the mixture fraction-scalar dissipation space. These heat maps

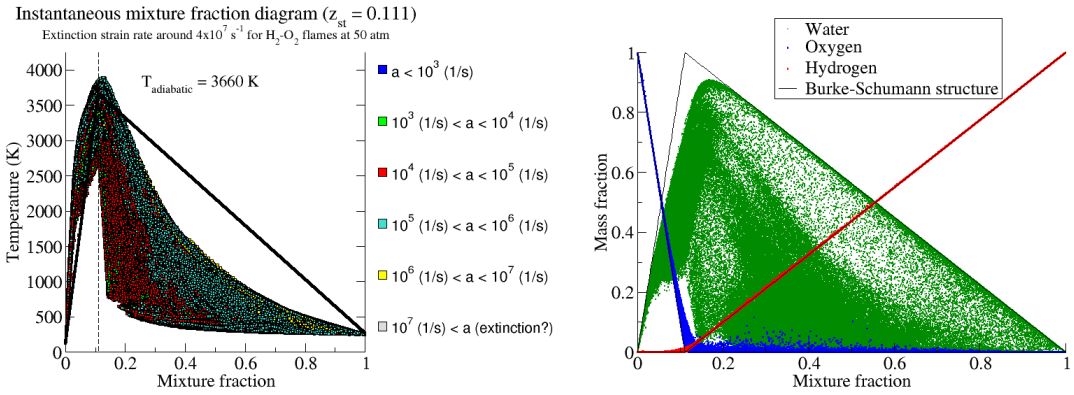

(a) (b)

Figure 100: Scatter plot in the mixture fraction space of the temperature (left) and the major species (right). For the temperature plot, the markers are colored by the magnitude of the strain rate. Ideal Burke-Schumann profiles are shown with black lines.

can be thought as two-dimensional histograms. Values for every cell in the vicinity of the flame are collected over 20 consecutive snapshots. Depending on the value of the mixture fraction and scalar dissipation at that instant, any given point goes into a two-dimensional hexagonal bin. The values of the plotted quantity (say temperature) is accumulated in that bin and the final heat map contains the ensemble average of that quantity for a given $(\mathcal{Z}, \chi)$. The first obvious feature in these heat maps is the detached set that lies near stoichiometry, experiences very large strain rates and scalar dissipation rates and yet display near-adiabatic temperatures. These points correspond to the . This not only shows the influence of the wall temperature boundary condition, it also shows that the thickness of this zone important and should be represented as accurately as possible. Ruiz [257] for example artificially thickens the lip for computational cost reasons but it seems like it could have an influence on the intensity and robustness of the flame, especially with an isothermal wall. Another feature of these plots are the high levels of strain and scalar dissipation rate observed. These levels of scalar dissipation are not usual but have been reported for other super-critical flows [273]. For comparison, Ruiz [257], using non-reacting two-dimensional DNS of a similar coaxial injector, reports scalar dissipation rate as high as 10×10^5 1/s on the fuel side, with a steady decrease towards values below 200 1/s on the oxidizer side. The increase in the scalar

dissipation rate seems to create a broadening of the flame front on the fuel side, but has little effect on the dense oxygen side. The strongest strain rates occur of course in the pure hydrogen stream since this is where the velocity gradients are the largest.

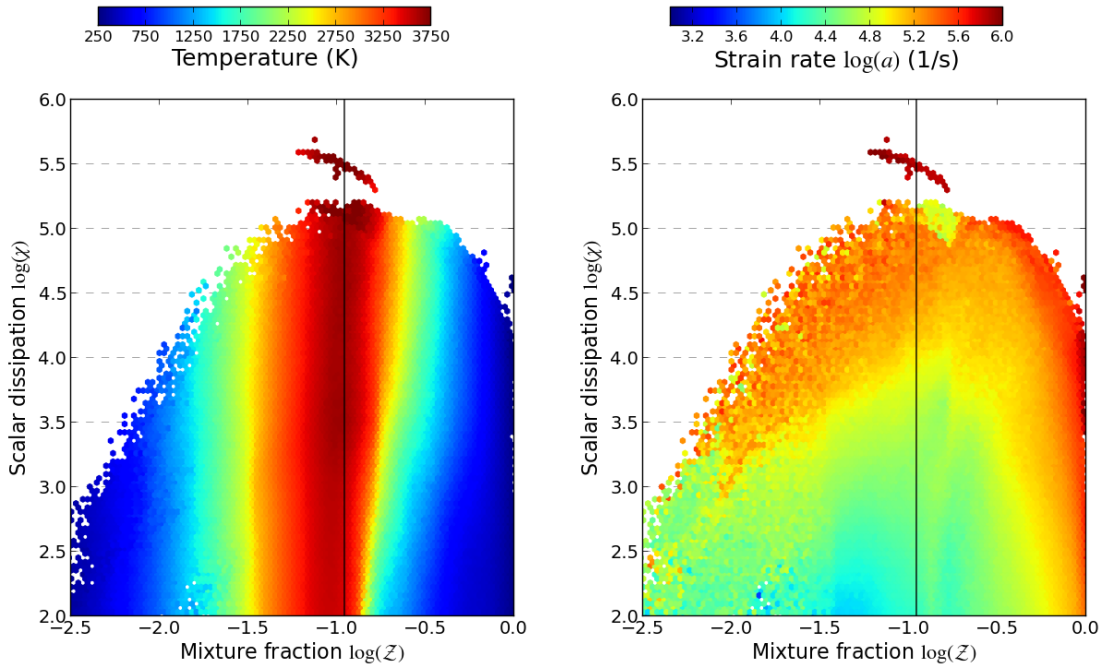

(a) (b)

Figure 101: Heat map plot in the mixture fraction-scalar dissipation space of the temperature (left) and the oxidizer-based strain rate (right, log scale). Values are collected over 20 consecutive snapshots and the ensemble average of the temperature or strain rate is plotted using the colorscale above.

Another way to examine the flame structure is to plot the radial profiles of non-dimensional quantities such as the Schmidt number or the Prandtl. This is done in Figure 6.4 for the near-field, at location $x/D_i = 1$. The diffusion flame structure is clearly apparent there with, starting from left to right:

- the potential liquid oxygen core along the centerline, with very large values of Schmidt and Lewis numbers.
- the dense liquid oxygen bounded by the trans-critical layer, identified by the local

maximum in the specific heat at constant pressure.

- the diffusion flame zone, where the non-dimensional numbers show little departures from classical values.

- the gasous hydrogen layer, characterized by very large specific heat and small values of Lewis and Schmidt numbers.

- the recirculation region with mixes unburned hydrogen with combustion products, resulting in values in-between the flame and the hydrogen stream.

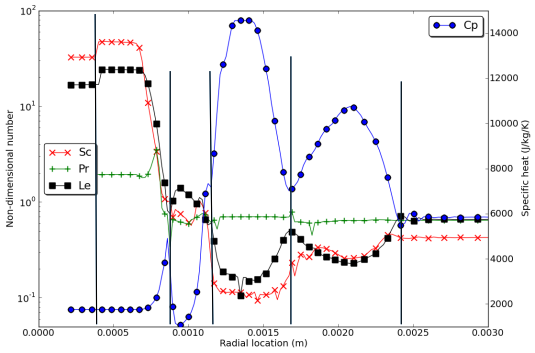

Figure 102: Instantaneous radial profiles of Schmidt number (red crosses), Prandtl number (green pluses), Lewis number (black square) and specific heat at constant pressure (blue circle, right axis) at location $x/D_i = 1$.

Further downstream, because of the significant mixing that occurs, it is much more difficult to clearly identify the different regions of the flame as seen in Figure 6.4. The strength of the vortical structures is illustrated by the peak of Mach number around 0.3, showing clear compressible effects. This occurs relatively far away from the flame. There is a secondary peak of the Mach number in the trans-critical layer because of the low speed of sound there, but it is unclear if this plays a role on the growth of the mixing layer. Figure 6.4 provides a better way to visualize both the diffusion flame in the near-field and the mixing further downstream through a zoomed-in view of the injector near-field. Surrounding the jet of compressed liquid oxygen (gray iso-surface), the Takeno index, or flame index $\overrightarrow{\text{grad}}Y_{\text{H}_2} \cdot \overrightarrow{\text{grad}}Y_{\text{O}_2}$, is shown for regions containing both reactants. Strong

negative values indicate a diffusion flame since the gradients are in opposite directions while strong positive values signify the presence of a premixed flame. Near-zero values are more difficult to interpret but generally indicate some amount of premixing. This Figure is another way of visualizing the capacity of the annular vortical structures to penetrate the flame and to create at least significant partial premixing if not full premixing. While the flame is purely diffusive in Region 2 (leftmost arrow), the flame thickens significantly downstream. While most of the heat release is still associated with the diffusion flame, the creation of pockets of unburned hydrogen (rightmost arrow) surrounded by the flame can create sudden heat release events over a wide area (topmost arrow), possibly triggering the helicoidal modes observed in the simulations.

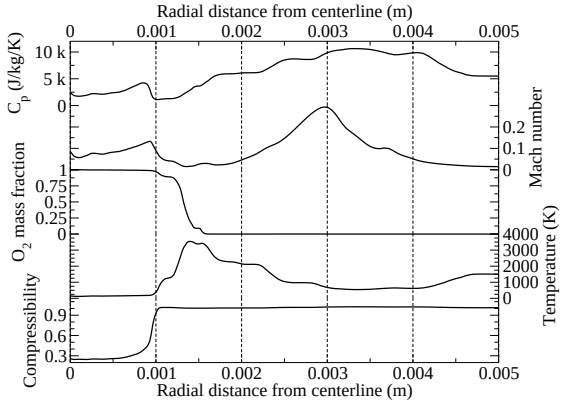

Figure 103: Instantaneous radial profiles of specific heat (1st row), Mach number (2nd row), oxygen mass fraction (3rd row), tempreature (4th row) and compressibility (last row) at location $x/D_i = 5$.

This section seems to illustrate that there are significant flame-turbulence interactions a few diameters downstream of the injection plane. It is difficult to evaluate a posteriori if the current laminar finite-rate combustion model behaves properly under these conditions but it would appear that these interactions are at the source of the sinusoidal and helicoidal modes responsible for the jet breakup, modes that are not observed experimentally.

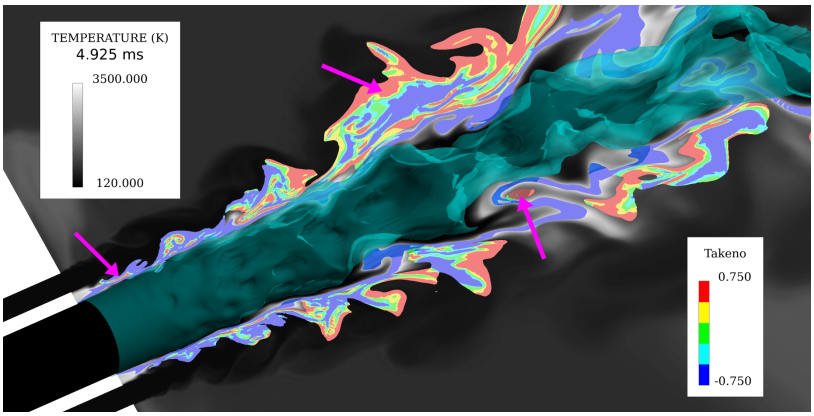

Figure 104: Close-up, three-dimensional view of the flame around the liquid oxygen jet in the injector near-field.

6.5 Conclusions and perspectives

In this chapter, a LOX-GH2 trans-critical flame, in the same configuration as the previous mixing study, is simulated. This time, the Peng-Robinson equation of state is preferred over the Redlich-Kwong equation of state. For the chemistry, a simpler 7-step mechanism is used rather than the baseline 21-step mechanism of the previous PSU RCM-1 study. This was based on the results obtained in that same PSU RCM-1 study showing only slight differences in the flow structure with each mechanism. The fact that there are significant departures from ideal gas for the LOX-GH2 flame here should have little effects on the chemistry itself, thus the PSU RCM1 conclusions should still hold for this LOX-GH2 configuration. The same laminar finite-rate combustion model is used as for the PSU RCM-1 study with 10 sub-iterations to ensure a correct temporal integration of the reaction rates. Initial simulations predicted a very short core of about 10 L_{dc}/D_i compared to about 39 for the experimental data. Several assumptions were investigated to explain this behavior, focusing on the inlet boundary conditions. The flow through the whole coaxial injector was investigated using a multi-physics Reynolds-Averaged Navier-Stokes simulation that took into account the heat transfer between the reactant streams. The main effect of that heat transfer is to lower the effective momentum flux ratio at the injector exit by about 10 to 15%. Simulations conducted with these new inlet conditions show a similar small effect on the dark core length of about 10%. Similarly, the isothermal boundary condition at the tip of the injector

sleeve has little influence on the dark core length. Acoustic coupling was also investigated since the initial simulations only modeled a shortened inlet. LES simulations of the reacting flow with a full inlet (but without heat transfer) showed only a small lengthening of the dark core length and no significant changes in the acoustics of the flow. Finally, the assumption of a uniform co-flow was revisited. For the reacting flow conditions, the injection velocities through the experimental perforated plate are significantly larger, and the resulting jets could have enough coherence to interact with the coaxial flow. So a new computational grid including the first two rows of holes around the coaxial jet is investigated. A strong interaction of the coaxial flow with these jets is observed, with the jets maintaining the coherence of the coaxial flow. This resulted in a significantly longer dark core of about 20 L_{dc}/D_i. This was however still well short of the experimental data. An analysis of the flame structure showed regions of partial premixing downstream of the main diffusion flame while the coaxial flow displayed strong helicoidal instabilities not observed in the experimental flow. These instabilities could be enhanced by very intense and localized bursts of heat release that are observed and could be due to the computation of the turbulent reaction rates.

The current solver has had at least qualitative success with a trans-critical methane-oxygen flame [93] with equivalent thermodynamic and transport properties and much simpler chemistry. This seems to indicate that the current issues are chemistry/combustion related, unless a full modeling of the perforated co-flow is necessary. While the 7-step Baurle reaction mechanism was shown to qualitatively reproduce the results with the 21-step Conaire reaction mechanism for the PSU-RCM1 configuration, the trans-critical LOX-GH2 conditions are even more severe, with higher pressure and pure reactants resulting in very large reaction rates and very stiff equations to solve. Locke [160] actually performed some GOX-GH2 simulations with pure reactants at moderate pressures, but unfortunately, only qualitative data are available but might be used to eliminate at least one factor of the potential error in heat release. Moreover, the simple 1- or 2-step mechanisms used for oxygen-methane combustion do not have to worry about differential- or cross-diffusion issues since they only deal with major species. The current study has ignored multi-component diffusion as well as

cross-diffusion terms such as the Soret and Dufour diffusions. These can have a significant impact on the reaction rates predicted by the reaction mechanisms and hence on the heat release. To a lesser extent, there are uncertainties on the transport properties of radicals such as H, O or H_2O_2, especially under typical liquid rocket engine conditions. Other studies of trans-critical LOX-CH_4 flames [93, 267] have had success in reproducing qualitatively experimental flames, despite using simplified reaction mechanisms and turbulent combustion models. Recently, Ruiz [257] also simulated a trans-critical LOX-GH2 flame using a simplified Burke-Schumann flamelet model and qualitative agreement was obtained on the flame length and structure. This again points to some added complexities of the detailed, finite-rate H_2-O_2 chemistry and this will need to be explored in the future as more complex chemistries will probably be required for the study of combustion instabilities where extinction and reignition events are important. Of course, the next logical step after all the assumptions that were tested in this Chapter is to investigate the influence of a more complex turbulent combustion model such as the Linear Eddy Model (LEM). This was beyond the scope of this work as flow conditions and current grid resolution unfortunately violate the assumptions required for LEM to work correctly. The combination of relatively fine grid at the injector tip and large viscosity due to the flame makes the turbulent sub-grid Reynolds number too small for a proper LEM-LES simulation since the molecular diffusion cannot be neglected with respect to the turbulent diffusion. To be able to use LEM under such conditions, significant changes are required to extend the LEM to these regimes. A few possible approaches will be given in the future work section, Section 7.2.

Finally, an illustration is provided that the solver could inherently predict long dark core length in this configuration but with different inflow conditions. Keeping the same geometry, the hydrogen injection temperature is decreased to 50 K, significantly reducing the hydrogen injection velocity as the mass flow-rate is kept constant. This translates into a significant decrease of the momentum flux ratio and preliminary qualitative comparison of the two cases is presented in Figure 105. While the 50 K case is still in its transient phase, the dark core is much longer with the 50 K injection of hydrogen as what was seen with the 272 K injection, even during the transient phases shown in Figure 89. This is expected

because of the momentum flux ratio dependency. It also seems to display the kind of stability observed experimentally by Locke with a 272 K injection of hydrogen. This case appears to demonstrate that there is no fundamental numerical instability that artificially breaks up the jet and prevents the current LES simulations from predicting a dark core as long as the experiment. However it appears that with the larger momentum flux ratio of the baseline case at 272 K, the mixing and the burning of the reactants is overestimated compared to the experiment. It cannot be concluded that it is solely due to the sub-grid models at this point since there is no proof that the solution obtained at 50 K is more correct than the one obtained at 272 K. And obvisouly, these conclusions cannot be definitive given the transient stage of the 50 K simulation which was only shown for illustrative purpose. Future studies are required to solve the turbulent combustion modeling issue and are proposed in Section 7.2.

A last interesting point is that, despite the same geometry and similar momentum flux ratio, statistics on the reacting dark core length are completely different from the statistics on the non-reacting dark core length, suggesting once again scaling laws much more complex than the ones currently found in the literature.

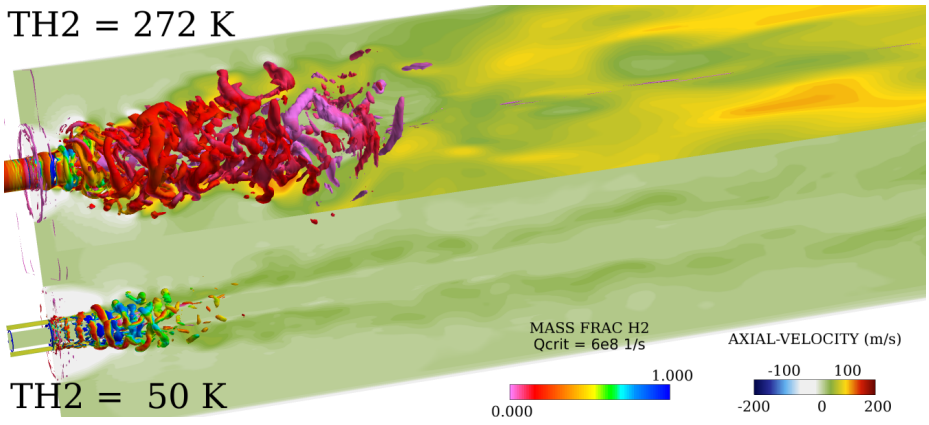

Figure 105: Instantaneous snapshots, after 5 ms of simulation, of the flow field structure for cases 272 K (top) and 50 K (bottom). The velocity field is shown through colored contours on the vertical slice while the Q-criterion displays the vortical structures which are colored by hydrogen mass fraction.

CHAPTER VII

CONCLUSIONS AND FUTURE WORK

7.1 Conclusions

The overall goal of this work was to develop a Large Eddy Simulation solver for a better understanding of liquid rocket engine flows. The objectives identified in the first chapter were meant to break down this development into discrete steps and to study the underlying physics along the way. Here is a summary of the findings reported in this thesis.

The first characteristic of the solver is to be able to handle turbulent flows with large density gradients as encountered in rocket combustion chambers. To solve this issue, an existing hybrid scheme developed for supersonic flows was adapted and evaluated for compressible rocket engine flows with or without real gas effects. While only few modifications were necessary because of the real gas thermodynamics, care was taken to select the most appropriate options for this class of flows: (a) The original approximate Riemann solver is used as it is valid for any equation of state. (b) Davis' approximate evaluation of wavespeeds is selected to limit the computational cost for real gas applications. (c) The local switch sensor between the central and upwind scheme is based on the value of the density gradient and the local compressibility Z. Its parameters were also optimized for shear coaxial flows using temporal mixing layers. The basic properties of the scheme have been verified on simple one-dimensional canonical flows which have highlighted the main characteristics of the hybrid scheme: excellent conservation of mass and energy with a few numerical oscillations in velocity/temperature fields. For a proper modeling of combustion applications, the exact conservation of mass and energy is critical.

Within this framework, a GOX-GH_2 combustor, for which experimental heat transfer data exists, is studied extensively using both axisymmetric and three-dimensional simulations. The simulations highlight the unsteady and three-dimensional characteristics of shear coaxial flows in rocket engines. A simple quasi-laminar model for the turbulent combustion

closure is sufficient to capture a physical flame structure and to obtain a reasonable match with the available experimental data. The resolution and the sub-grid modeling of the heat transfer near the chamber walls have a strong influence on the predicted heat flux. This was observed with the current solver as well as with other state-of-the-art solvers and had a larger influence on the heat flux profile than the overall flow and flame structures. However, the lack of experimental flow visualization prevents from drawing definitive conclusions. Comparative simulations with the current solver do show completely different features between a three-dimensional and an axisymmetric configuration but only few differences between a detailed 21-step mechanism and a simpler 7-step mechanism, despite the high-pressure environment. Finally, this solver needs to be extended for other rocket engine flows where real gas effects cannot be neglected due to low injection temperatures.

To deal with these departures from ideal gas behavior, a single-phase, multi-species formulation using cubic equations of states is selected. The Peng-Robinson EoS and the Redlich-Kwong EoS were implemented alongside calorically perfect and thermally perfect equations of state in a generic thermodynamic framework using FORTRAN 90/03 features to increase modularity. These equations of state have been chosen for the good cost-accuracy compromise they offer, allowing a satisfactory modeling of compressed liquids, super-critical fluids and ideal gases with a single equation. In a similar fashion, high-pressure transport properties can be computed from first principles in place of previous simpler formulations and curvefits. The high-pressure thermodynamic and transport frameworks use the same database of properties and can be swapped for simpler models independently. An important thing to keep in mind when considering whether a real gas EOS should be used for a given application is that there are regions where the compressibility Z differs significantly from 1 not only in the compressed liquid or super-critical fluid quadrants but also in the gas phase and super-heated vapor quadrant. Since the thermodynamics are implemented within a fully-conservative formulation, both temperature and pressure often need to be recomputed from conservative variables such as internal energy and partial densities. Compared to what has been reported in the literature, an improved algorithm was developed to eliminate the need for simultaneous iterative solvers and an optimization of the numerical

parameters was performed to find the best compromise between cost and accuracy. For the boundary conditions, a constant-mass non-reflecting inflow formulation was generalized to any thermodynamic framework.

Verification of the solver performance and accuracy was performed using a series of one-dimensional tests, including an extension of the shock-entropy wave test case by Shu and Osher to super-critical conditions. While the current scheme displays a little bit more dissipation and more numerical oscillations than higher-order alternatives, the main flow features are captured correctly and the conservative properties of the scheme for mass and energy are confirmed with real gas thermodynamics.

With the availability of quality experimental data for a single-element shear coaxial injector, the injection of sub-critical oxygen into super-critical oxygen is investigated numerically and both qualitative and quantitative comparisons are performed. Given the difficulty to reproduce numerically the exact experimental back-lit visualization, the qualitative matches obtained are more important than the quantitative ones. In particular, the overall flow structure, the convergence time of the flow statistics, the shape of the dark core length temporal evolution and statistics are all recovered through a series of three-dimensional Large Eddy Simulations. A demonstration of grid independence and physical turbulent characteristics completes the assessment of the validity of these LES. Additional LES can then be used to investigate physical trends and explore conditions beyond experiments. The importance of the co-flow is shown, a co-flow that is not always present in every experimental setup and could make one-to-one comparisons difficult. An analysis of the available experimental data at super-critical pressures revealed that the dark core length could depend on other parameters than just the momentum flux ratio. Among these parameters, the shear Reynolds number $\mathrm{Re}_s = \frac{\rho_{\mathrm{avg}}|u_i - u_o|t_{\mathrm{post}}}{\mu_{\mathrm{avg}}}$ was considered as it includes dependencies on the flow-rate via ρu, on the geometry via the lip thickness and of course on the shear between the two streams. It is also similar to the Weber number defined for sub-critical pressures. The shear Reynolds number Re_s and the momentum flux ratio J showed at least some degree of independence

in the available data and a non-linear regression yielded the following new correlation:

$$\frac{L_{dc}}{D_i} = 57.20 J^{-0.277} \mathrm{Re}_s^{-0.164} \tag{7.1.1}$$

A numerical experiment was performed to investigate this Re_s dependence and the predicted results agree with this new correlation. This shows how LES can be used to detect and confirm physical trends, which can then be investigated further with actual experiments. Once again, it is more important to focus on the various qualitative matches obtained than on the quantitative agreements. Quantitative validation is difficult to perform given the uncertainties on directly comparing the numerical and experimental visualizations. Also, based on the various simulations performed during this study, the reasons that can explain the good qualitative agreements can be summarized as:

- Shear coaxial flows are a good match for LES since, especially with large velocity ratios, they are less sensitive to inflow conditions than simple jets as the main instability comes from the mixing layer between the two streams, not the initial perturbation in either stream. As a consequence, LES of typical rocket engine coaxial flows does not require very fine grid resolution at the inlet walls or the injection of realistic turbulence.

- Any cubic equation of state is probably good enough for qualitatively capturing the flow structure of typical shear coaxial flows. This study shows that even one of the simplest cubic EOS, the Redlich-Kwong EOS, can accurately capture the dark core length statistics measured experimentally for a non-reacting LES. This is a valuable information since the RK EOS has not been widely used by the CFD community.

- The single-species formulation is a lot simpler than the multi-species one as one does not have to worry about assumptions on additional unclosed terms, mixing rules, binary interaction parameters

- While the presence of a co-flow influences the overall flow structure, the exact modeling of the co-flow does not appear to matter too much given the small velocities involved. This is not always the case as seen with the reacting LOX-GH2 case later on.

- Constant-mass partially-reflecting inflow boundary conditions coupled with inlets of appropriate length (depends on the geometrical configuration) allow for realistic absorption of acoustics and a stable flow in the inlets. While not so important for non-reacting flows, it becomes very important for reacting flows because of the larger pressure fluctuations in the chamber.

Finally, a LOX-GH2 trans-critical flame, in the same configuration as the previous mixing study, is simulated. This time, the Peng-Robinson equation of state is preferred over the Redlich-Kwong equation of state. All along this work, relatively little differences in the resulting flows have been observed when using these two EOS in the flow solver. While the literature recommends the more complex PR EOS over the RK EOS, it is unlikely that the slight differences in properties (no more than 20% on energy or volume) affect the LES predictions significantly given other current uncertainties such as grid resolution, accurate description of the co-flow, turbulent combustion modeling or even uncertainty on the experimental measurements. Looking forward to combustion instabilities however, additional accuracy of the EOS should be desired and the PR EOS is a good starting point given its superior modeling of energies, specific heats and thus acoustic speed. For the chemistry, a simpler 7-step mechanism is used rather than the baseline 21-step mechanism of the previous PSU RCM-1 study, based on the conclusions of that same study. The same laminar finite-rate combustion model is used as for the PSU RCM-1 study with 10 sub-iterations to ensure a correct temporal integration of the reaction rates. Initial simulations predicted a very short core compared to the experimental data. Several assumptions were investigated to explain this behavior, focusing on the inlet boundary conditions. The flow through the whole coaxial injector was investigated using a multi-physics Reynolds-Averaged Navier-Stokes simulation that took into account the heat transfer between the reactant streams but simulations using the output of the RANS model as inlet conditions showed only small improvements in the dark core length. Similarly, the isothermal boundary condition at the tip of the injector sleeve has little influence on the dark core length. Acoustic coupling was also investigated with inlets of different length but again, even a full inlet (but without heat transfer) showed only a small lengthening of the dark core length and no significant

changes in the acoustics of the flow. Finally, the assumption of a uniform co-flow was revisited and the perforated plate surrounding the coaxial element was partially modeled. A strong interaction of the coaxial flow with the holes jets is observed, with the jets maintaining the coherence of the coaxial flow. This resulted in a significantly longer dark core of about 20 L_{dc}/D_i, still almost 50% off the experimental data. An analysis of the flame structure showed regions of partial premixing downstream of the main diffusion flame while the coaxial flow displayed strong helicoidal instabilities not observed in the experimental flow. These instabilities could be enhanced by very intense and localized bursts of heat release that are observed and could be due to the computation of the turbulent reaction rates. To solve this issue and deal with the different combustion regimes that seem to exist in these realistic super-critical flames, better closure models are required.

This is the reason why the Linear-Eddy Mixing (LEM) model was applied for the first time to a case with significant departures from ideal gas thermodynamics. The LEM model has the potential to solve explicitely the issue of sub-grid mixing and combustion for real gas thermodynamics, where many unclosed terms should potentially be taken into account. In the current work, the LEM model was used to revisit the non-reacting LOX-GOX simulations. It was found that the LEM performed well on a coarse grid, where the assumptions of large sub-grid kinetic energy are justified. The sub-grid scalar was visualized and showed a distinct but limited impact of the sub-grid turbulence on scalar mixing. However, for the reacting LOX-GH2 case, finer grid requirements for the fluid mechanics and increased viscosity at the flame significantly reduce the sub-grid kinetic energy and prevent the use of the LEM model as it is.

Before moving on to the recommendations for future work, a few important lessons learned are recalled here to emphasize some important issues for the configurations of interest, i.e. high-pressure shear coaxial elements:

- While configurations with co-flow tend to exhibit less heat and mass transfer across the centerline (unlike PSU RCM-1 for example), even single-element injectors require a three-dimensional modeling for an accurate capture of the flow features.

- Even for non-reacting flows, there are processes whose dependency on time is non-trivial and should be investigated. For example, the temporal evolution of the dark core length is not a simple fluctuation around the time average but follows a buzzsaw-like curve. Obviously, for reacting flows with potential combustion instabilities, capturing such transient phenomena is crucial.

- Based on these two points and on the fact that a coaxial stream is as much a free shear flow as it is a wall bounded flow, Large Eddy Simulation is well-suited to study such configuration without special treatment at the walls.

- In terms of grid resolution, this work as well as a survey of other LES work in the literature indicate that a minimum spacing around 50 microns is a good starting point to resolve the trans-critical layer and/or the high-pressure flame. This still leaves only a few points for resolving either of those thicknesses, which means the spatial scheme needs to be able to handle such large gradients.

- While some physical quantities such as Z or C_p cannot inherently be measured experimentally, they should be investigated numerically as they provide valuable information on the extent and strength of the real gas effects. For the non-reacting trans-critical flow, the dense, non-ideal layer beyond the trans-critical layer seems to play an important role in the mixing process as shown by the LES-LEM results where changes in this layer impacted the dark core length statistics.

- If wall heat transfer is part of the experimental data however, extra care needs to be applied for the near-wall modeling as very different flowfields can produce similar heat transfer profiles as shown in the PSU RCM-1 study.

7.2 Recommendations for future work

A lofty, long-term goal of the CFD community should be to help Large-Eddy Simulations become a design tool for new liquid rocket engines. To achieve this, the accuracy, robustness, fidelity and efficiency of the solver need to be established as formulated by Lin et al. [155]

While some strides have been made, each area still needs to be improved significantly to achieve this goal in the next decade or so.

The most pressing issue is of course accuracy through the quantitative validation of trans-critical reacting flows as quality experimental data become available. For non-reacting flows, while the current agreement between numerical predictions and experimental data is good, the scaling trends potentially detected by the current LES results need to be investigated systematically through experiments. In particular, the experimental effort should focus on two aspects:

- the influence of the co-flow. The same experimental configuration should be first run with and without co-flow to confirm the trend shown in this work and to reconcile the data available in the literature with and without co-flow. Further work will need to be done to quantify the influence of this co-flow based on its geometry (a perforated plate is probably the easiest configuration from a manufacturing and pressure point of view) and flow conditions. This is an important step before moving to multi-element injectors.

- the influence of other parameters than the momentum flux ratio. More systematic studies at conditions closer to full-scale engines should investigate the influence of the shear Reynolds numbers, injector geometry and density or velocity ratios under near-identical thermodynamic conditions. This would ideally be conducted in a joint numerical-experimental in order to identify and analyze new trends most efficiently.

One has to keep in mind however, that not all the non-reacting conclusions can be applied to the scaling of reacting flows since the physics beyond the trans-critical layer are very different in either case. As explained in the conclusions of the reacting LOX-GH2, more work is needed on modeling of the combustion, whether it is related to the laminar or the turbulent aspect of the flame. Therefore, a detailed study of the influence of the reaction mechanism, the chemical integration technique, the transport formulation and the sub-grid combustion model on a spatially-anchored turbulent flame is required. The first recommended configuration is a two-dimensional coaxial flow [185, 280] as it retains most

of the physical features needed to study chemistry-related effects at a fraction of the cost of a three-dimensional simulation. Unlike axisymmetric simulations, the two-dimensional simulation produces more significant flapping and stronger vortex-flame interactions. The two main caveats to this two-dimensional configuration are the volume to heat-release ratio and the two-dimensional turbulence that might conflict with some sub-grid models. The former might require an extension of the dimensions of the two-dimensional chamber for the same linear dimensions of the injector in order to avoid unrealistic combustion instabilities. The latter might delay the study of the sub-grid combustion model influence until a later three-dimensional simulation can be performed with optimal chemical parameters.

Unfortunately as shown previously, the current LEM implementation is not adapted to the kind of diffusion flames that are found around liquid jets due to the low levels of sub-grid kinetic energy. Extension of the current LEM implementation to these regimes might be possible under two conditions: the inclusion of mass diffusion across LES cells [334] and the possibility to have a variable LEM resolution across the computational domain. The former requires tracking the individual species fluxes for the splicing procedure, a large increase in computational complexity and cost. If this extension is not feasible, other sub-grid combustion models should be explored. This is an active field of research for rocket engine applications [347, 174, 134, 135, 140, 133], mostly focused on the flamelet approach. A similar model should be implemented in the current solver to at least provide a direct comparison between the computations of different groups. There are two ways this model could be implemented: either as another method to compute the filtered reaction rate or as a full replacement of the species equations and thus of the thermodynamic module. The latter approach has more upside but its implementation will be more complicated. Also, the capture of preferential diffusion (non-unity, non-constant Lewis number) remains a challenge in flamelet models [326]. An alternative could be a Lagrangian LEM model where each LEM domain corresponds to a fluid particle and thus the amount of turbulence in the LEM domain is not tied to the resolution of the LES grid [237]. Whether or not the LEM can be adapted to this type of flows, it could still be used for turbulent combustion modeling by providing training for various interpolation methods. The use of Turbulent Artificial Neural Networks

(TANN) has already been demonstrated [275]. If proper training using LEM in an opposed-flow configuration [29] can be done including real gas effects, one could use a TANN as a sub-grid combustion modeling for the current rocket applications. However, the stiffness of the H_2-O_2 chemistry at high-pressure is a challenge for the training of neural networks.

Finally, beyond the filtered reaction rate, one must not forget the other unclosed and currently sub-grid terms for super-critical flows. As described in Section 5.2, the most significant terms probably involve gradients such as $\nabla\left(\overline{p(\widetilde{T},\widetilde{\rho},\widetilde{Y_k},\widetilde{T\rho Y_k})}-\bar{p}(\widetilde{T},\widetilde{\rho},\widetilde{Y_k})\right)$. A large amount of work has been conducted by Bellan et al. on temporal mixing layers using DNS [273, 224] and even LES [306, 307] to study these terms. However, there is still a need to investigate the statistical impact of these closure models on spatially developing problems. The LOXGOX configuration studied in this work, with its reliable experimental data and the relatively small grid requirements is a good candidate for such a study. This would be a preliminary to the study of the unclosed terms for reacting flows as explored by Foster and Miller [70].

Other physical models that could be improved are thermodynamic and transport properties as well as heat transfer models. Cubic equations of state are still an active field of research (see Appendix C) and improved models will need to be incorporated in CFD solvers over time. However, even simpler cubic EOS are sufficient to get a qualitative agreement, so the largest issue is the lack of experimental data for mixtures at conditions relevant for rocket engine applications. This means both mixing rules and binary interaction parameters are currently not well defined for typical rocket engine mixtures. Unfortunately both mixing rules and binary interaction parameters can be dependent on the choice of the EOS. Ideally joint numerical-experimental mixing studies will be performed in the future to provide better data and improve thermodynamic and transport properties predictions. For heat transfer, the RANS multi-physics analysis from Chapter 6 showed the potential role of heat transfer in cryogenic coaxial injectors. Therefore a multi-physics LES, through a conjugate gradient approach for example, could improve the modeling of the near-field and of the flame anchoring. In the far-field, the addition of radiation could be considered, especially if wall heat transfer data is available.

The eventual purpose of LES of liquid rocket engines remains to predict the onset of combustion instabilities and help find a way to mitigate or eliminate them [49]. But obviously, experimental data on combustion instabilities in high-pressure combustion chambers are hard to obtain. On top of all the previously mentioned challenges of measurement in a high-pressure rocket configuration, these instabilities can be destructive and unpredictable. One possible way of studying such instabilities is to have a combustion chamber and inlets whose lengths and impedances can be easily varied. Such a chamber is currently under investigation at Purdue University[343] in a configuration not too dissimilar to a rocket engine and operating at moderate, sub-critical pressures. This configuration could be potentially extended to conditions closer to an actual rocket combustion chamber. In more realistic configurations, changes in the inflow conditions can trigger combustion instabilities. It is known that a decrease of the hydrogen injection temperature for an H_2-O_2 injector and this has been observed recently in a sub-scale chamber [210]. However, the data available for such runs is limited to pressure traces for now. The likely explanation is that the decrease in hydrogen temperature implies a decrease in the momentum flux ratio for the injector and thus a longer liquid core more responsive to pressure fluctuations [35]. Such a configuration is currently under investigation with the LESLIE solver [280]. In parallel, multi-element configurations have started to be investigated by the CFD community using three-dimensional, unsteady simulations, looking both at recent experiments [210, 51] and older experiments [117]. But more complex configurations require more work on the implementation and efficiency of the current solver.

While the parallel performance of all simulations presented in this work has been excellent, moving to more complex multi-elements configuration will require some additional development to maintain a reasonable computational cost. An overview of the performance of real gas and rocket engine applications on more complex grids is presented in Appendix K. Compared to the framework used for this work, improvements in the mapping and partitioning of the computational mesh would be welcome. Similarly, while retaining an overall structured grid configuration, the use of grid coarsening [323, 194] far downstream of the injector plate could result in significant computational cost savings without much loss of

accuracy, especially since the propagation of acoustic waves should not be affected. The explicit MacCormack scheme could also be replaced by its semi-implicit version [170, 78] for flow transients. While curvefitting of the thermodynamic properties, especially with neural networks, is not recommended, the use of curvefitting for the transport properties, with either polynomials or neural networks, could slightly improve the computational performance. These improvements are relatively basic and can use tools and models readily available. However they need to be tested to make sure they do not significantly compromise the accuracy of the solution. A more significant improvement would be to use Reduced Basis Modeling [106] to model each inlet stream using ODEs instead of solving the full Navier-Stokes equations there. But this will still allow each injector stream to respond to excitations from the combustion chamber and thus to potentially study combustion instabilities in multi-element configuration at a reasonable cost. While current computational resources at university level limits the size and the complexity of the simulations that can be run in a reasonable amount of time, it is motivating to already see efforts by government agencies such as JAXA to run a full three-dimensional high-fidelity simulation of a whole liquid rocket engine from tanks to nozzle through feedlines, pumps, burners, main chamber.

APPENDIX A

TEMPORAL MIXING LAYER CONFIGURATION

This canonical flow is used several times in the course of this work to assess the influence of physical models or numerical schemes. This chapter presents the initialization for a temporal mixing layer (TML) as well as a few more details on this configuration.

A.1 Theory

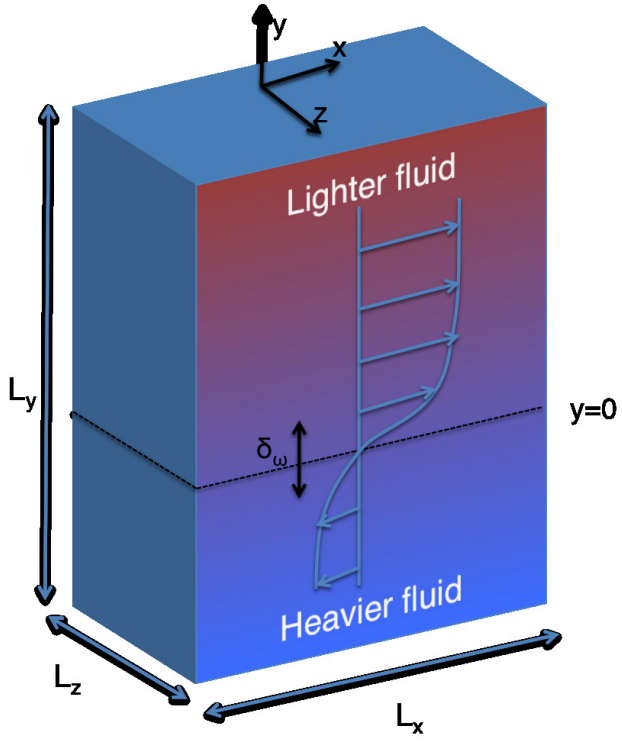

Figure 106: Sketch of the mixing layer configuration. Lighter fluid can be hydrogen or nitrogen while the heavier fluid can be oxygen or heptane.

The temporal mixing layer configuration is represented schematically by Figure 106. The evolution of two counter-flowing parallel streams is simulated in a box with streamwise and spanwise periodic boundary conditions. In the crosswise direction, outflow characteristic

boundary conditions are usually used to allow for pressure waves to exit the domain but slip wall boundary conditions could be used too.

For the initialization of the flow field, the velocity field can be split into two components: a mean flow with two streams flowing in opposite direction and a perturbation field which triggers the inherently unstable mean velocity profile. The mean flow profile can be specified using either an hyperbolic tangent function or an error function, the latter being a little bit steeper but smoother. Based on this velocity profile, it is possible to define the vorticity thickness as:

$$\delta_\omega = \frac{\Delta U}{\left(\frac{\partial \bar{U}}{\partial y}\right)_{\max}} \tag{A.1.1}$$

Depending on the choice of the mean profile, it can be shown that:

$$\frac{\partial \bar{U}}{\partial y} = \frac{U_1 - U_2}{2\delta} \quad \text{with} \quad \bar{U} = U_1 + \frac{1 - \tanh(y/\delta)}{2}\left(U_2 - U_1\right) \tag{A.1.2}$$

$$\frac{\partial \bar{U}}{\partial y} = \frac{U_1 - U_2}{\delta\sqrt{\pi}} \quad \text{with} \quad \bar{U} = U_1 + \frac{1 - \mathrm{erf}(y/\delta)}{2}\left(U_2 - U_1\right) \tag{A.1.3}$$

For the perturbation field, disturbances of the form of Orr-Sommerfeld eigenfunctions are applied in order to stimulate the inherent instability of the initial profile. If only one vortex rollup is desired, the wavelength λ_x of this perturbation is simply half of the domain streamwise length L_x. If pairings are required, this wavelength can be further divided by powers of 2. The ratio between the perturbation wavelength and the initial vorticity thickness determines the growth rate of the instabity since the vorticity thickness is linked to the mean velocity profile by Equation A.1.1. Linear stability analysis is used to compute the most unstable wavelength given a certain velocity and density profile. Early studies by Michalke [195] and Monkewitz et al.[200] showed that the most unstable wavelength given a certain velocity profile for a single-species, incompressible mixing layer and found that a ratio $\frac{\lambda_x}{\delta_{\omega,0}}$ of 7.29 was optimal. However, when a multi-species, compressible flow is considered, the analysis becomes much more complex as the stability curve is not only determined by the velocity profile but also by the density and speed of sound profiles. These additional dependencies also make the stability analysis results in two dimensions independent of the results in three-dimensions. Okong'o and Bellan [221] have conducted extensive stability analyses for the hydrogen-oygen and nitrogen-heptane mixing layers. Since the current

study will focus on these same species couples, the wavelengths computed by Okong'o and Bellan will be used when appropriate. In general, the most unstable wavelength for the nitrogen-heptane layers is close to the ideal value of 7.29, even under conditions where large density gradients and strong departures from ideal gas properties exist. On the other hand, for hydrogen-oxygen layers, the most instable wavelength for given profiles varies over a much wider range. It is also possible to initialize the central mixing layer with isotropic turbulence and let the TML develop from this perturbed field.

In order to maintain the final vortex stationary in the computational domain (akin to a frame of reference moving with the flow), the free stream velocities are computed from a specified value of the convective Mach number:

$$U_1 = \frac{2M_c a_1}{1+\sqrt{\rho_1/\rho_2}a_1/a_2} \quad U_2 = -\sqrt{\frac{\rho_1}{\rho_2}}U_1 \tag{A.1.4}$$

The densities and speeds of sound are computed from the composition, pressure and temperature in the two layers.

On top of the vorticity thickness, other metrics are available in order to monitor the global evolution of the mixing layer. Cortesi et al. [46] review different measures of the global entrainment and find that the momentum thickness is a more reliable measure of the shear layer growth than the vorticity thickness or the velocity thickness based on 95% of the free-stream velocities. The "eddy size" method is also reliable but requires solving for an additional passive scalar. For a stratified, compressible mixing layer, the momentum thickness is defined as [197]:

$$\delta_m = \frac{1}{(\Theta_1-\Theta_2)^2}\int_{-\infty}^{+\infty}(\Theta_2-\langle\rho U\rangle)(\langle\rho U\rangle-\Theta_1)\,\mathrm{d}y \tag{A.1.5}$$

$\Theta_1 = \langle\rho U\rangle_1$ and $\Theta_2 = \langle\rho U\rangle_2$ are the planar-averaged momentums of each stream.

A.2 Initialization procedure

This section assumes that the computational domain is a box of physical dimension $L_x \times L_y \times L_z$ with the free streams parallel to the x-direction as shown in Fig. 106. The steps are the following:

1. Pick how many vortices will be initially in the domain. This sets the ratio $\frac{L_x}{\lambda_x}$, with λ_x the most unstable streamwise wavelength.

2. Set the ratio $\frac{\lambda_x}{\delta_\omega^o}$ where δ_ω^o is the initial vorticity thickness.

3. At this stage, either the domain size L_x is known and the initial vorticity thickness can be computed, or δ_ω^o needs to be set through the mixing layer Reynolds number:

$$\mathrm{Re}^o = \frac{\rho^o \Delta U \delta_\omega^o}{\mu^o} \tag{A.2.1}$$

where the reference properties are simply defined as:

$$\rho^o = \frac{\rho_1 + \rho_2}{2} \tag{A.2.2}$$

$$\Delta U = U_1 - U_2 \tag{A.2.3}$$

$$\mu^o = \frac{\mu_1 + \mu_2}{2} \tag{A.2.4}$$

4. Pick the thermodynamic conditions in each stream: composition, temperature and pressure. Compute the corresponding speed of sound, density, viscosity and compressibilty in each stream.

5. Pick a convective Mach number M_c^o. This sets the velocity in each stream according to the following expressions which attempt to keep the ultimate vortex stationary in the computational domain [198]:

$$U_1 = \frac{2\, M_c^o\, c_{s_1}}{1 + \left(\frac{c_{s_1}}{c_{s_2}}\right)\sqrt{\frac{\rho_1 Z_1}{\rho_2 Z_2}}} \qquad U_2 = -\sqrt{\frac{\rho_1 Z_1}{\rho_2 Z_2}} U_1 \tag{A.2.5}$$

If the velocities were set but not the convective Mach number, it is possible to compute it through:

$$M_c^o = \frac{1}{2}\left(\frac{U_1 - U_c}{c_{s_1}} + \frac{U_2 - U_c}{c_{s_2}}\right) \tag{A.2.6}$$

with

$$U_c = \frac{\frac{U_2}{c_{s_2}} + \frac{U_1}{c_{s_1}}\left(\frac{c_{s_1}}{c_{s_2}}\right)\sqrt{\frac{\rho_1 Z_1}{\rho_2 Z_2}}}{\frac{1}{c_{s_2}} + \frac{1}{c_{s_1}}\left(\frac{c_{s_1}}{c_{s_2}}\right)\sqrt{\frac{\rho_1 Z_1}{\rho_2 Z_2}}} \tag{A.2.7}$$

6. Recalling step 3, if the vorticity thickness is known, the Reynolds number can be computed using Eq. A.2.1 and the mean velocity profile can be set using the error function profile:

$$\bar{U}(y) = U_1 + \frac{1 - \mathrm{erf}(\sqrt{\pi} y / \delta_\omega^o)}{2} (U_2 - U_1) \tag{A.2.8}$$

7. If the vorticity thickness (and the domain length) is unknown, then the Reynolds number needs to be picked and δ_ω^o extracted from it. The domain length is simply $L_x = \frac{L_x}{\lambda_x} \frac{\lambda_x}{\delta_\omega^o} \delta_\omega^o$. The velocity profile is set of course with Eq. A.2.8.

Starting from Equations A.1.2 and A.1.3, and assuming $U_1 = -U_2$, it is possible to non-dimensionalize these velocity profiles as:

$$\bar{U} = \tanh(y/\delta) \tag{A.2.9}$$

$$\bar{U} = \mathrm{erf}(y/\delta) \tag{A.2.10}$$

Assuming a single-species, incompressible mixing layer, the momentum thickness becomes:

$$\delta_m = \int_{-\infty}^{+\infty} \left(1 - \bar{U}^2\right) dy \tag{A.2.11}$$

Consequently, the momentum thickness characteristic of each velocity profile is $\frac{\delta}{2}$ for the hyperbolic tangent and $\frac{\delta}{2}\sqrt{\frac{2}{\pi}}$ for the error function. Since the characteristic vorticity thicknesses for each profile are respectively 2δ and $\sqrt{\pi}\delta$, the ratio $\frac{\delta_\omega}{\delta_m}$ is equal to 4 for the hyperbolic tangent profile and to $\pi\sqrt{2} \approx 4.44$ for the error function profile. As pointed out by Rogers and Moser [255], this ratio is sensitive to the exact shape of the profile and thus varies in time as the mixing layer evolves.

A.3 Further readings

The starting point is the work from Michalke [195] while the basic formulation was described by Moser and Rogers [203]. The simplicity of this configuration, with little or no influence of boundary conditions and its relevance for the physics of mixing makes it ideal as a testbed for physical and numerical models: Vreman et al. [330] used TMLs to test different LES sub-grid models while Ling et al. [156] used TMLs to validate a Lagrangian multi-phase approach.

And of course, as referenced in the main body of this work, the groups of Miller at Clemson et Bellan at the Jet Propulsion Laboratory have used this configuration extensively for multi-phase and real gas developments [197, 222, 273, 307, 70].

APPENDIX B

DATABASE OF THE REAL GAS PROPERTIES

B.1 General database

These properties are used to compute the thermodynamic and the transport properties for this work. This is essentialyl a simple reproduction of the declaration of these variables in the source of the flow solver LESLIE.

```
! Set critical properties of pure species.
! Source of the data is given as often as possible
! NIST: NIST chemistry webbook
! http://webbook.nist.gov/chemistry/
! PGL: Properties of Gases and Liquids
! Oefelein: Real gas subroutines provided by Oefelein

DO ns = 1,nspeci
! H2
! As a quantum gas, many sets of values exist.
  IF (spname(ns) == TRIM(species(1))) THEN
!mm Classical values
!     tc(ns,ns)    =  4.360E+1_wp  ! K NIST
!     pc(ns,ns)    =  2.020E+6_wp  ! Pa NIST
!     vc(ns,ns)    =  5.150E-2_wp  ! m3/kmol NIST
!     omega(ns,ns) =  0.000E-0_wp  ! no units NIST
!mm Standard values
     tc(ns,ns)    =  3.319E+1_wp  ! K NIST
     pc(ns,ns)    =  13.15E+5_wp  ! Pa NIST
     vc(ns,ns)    =  6.640E-2_wp  ! m3/kmol NIST
!mm Actual correct acentric factor value
     omega(ns,ns) = -2.140E-1_wp  ! no units NIST
!mm Use 0 acentric factor for Chung's formulation
!     omega(ns,ns) =  0.000E+0_wp  ! no units NIST
  ENDIF
!H
  IF (spname(ns) == TRIM(species(2))) THEN
!     Tc(ns,ns)    =  404.3E+0_wp  ! K  Ribert_2008a
!     pc(ns,ns)    =   88.2E+5_wp  ! Pa
Ribert_2008a
     Tc(ns,ns)    =  182.6E+0_wp  ! K  Oefelein
     pc(ns,ns)    =  251.9E+5_wp  ! Pa  Oefelein
     vc(ns,ns)    =  16.30E-3_wp  ! m3/kmol ! Oefelein
     omega(ns,ns) =  3.290E-1_wp  ! no units ! Oefel
  ENDIF
!O2
  IF (spname(ns) == TRIM(species(3))) THEN
     tc(ns,ns)    = 154.581E+0_wp ! K SOURCE NIST
     pc(ns,ns)    = 50.4300E+5_wp ! Pa SOURCE NIST
     vc(ns,ns)    = 73.3700E-3_wp ! m3/kmol SOURCE PGL
     omega(ns,ns) = 2.22000E-2_wp ! no units SOURCE NIST
  ENDIF
!OH
  IF (spname(ns) == TRIM(species(4))) THEN
!     Tc(ns,ns)    = 443.7E+0_wp   ! K ! Ribert_2008a
!     pc(ns,ns)    = 85.40E+5_wp   ! Pa ! Ribert_2008a
     Tc(ns,ns)    = 100.7E+0_wp   ! K ! Oefelein
     pc(ns,ns)    = 57.60E+5_wp   ! Pa ! Oefelein
     vc(ns,ns)    = 39.30E-3_wp   ! m3/kmol ! Oefelein
     omega(ns,ns) = 3.290E-1_wp   ! no units ! Oefelein
  ENDIF
!H2O
  IF (spname(ns) == TRIM(species(5))) THEN
     tc(ns,ns)    = 647.14E+0_wp  ! K ! NIST gives 647.096K
     pc(ns,ns)    = 220.64E+5_wp  ! Pa
     vc(ns,ns)    = 55.950E-3_wp  ! m3/kmol
     omega(ns,ns) = 3.4430E-1_wp  ! no units
  ENDIF
!C7H16
  IF (spname(ns) == TRIM(species(6))) THEN
     tc(ns,ns)    = 540.3E+0_wp   ! K SOURCE NIST
     pc(ns,ns)    = 27.36E+5_wp   ! Pa SOURCE NIST
     vc(ns,ns)    = 432.0E-3_wp   ! m3/kmol COMPUTED NIST
     omega(ns,ns) = 3.490E-1_wp   ! no units SOURCE NIST
  ENDIF
!N2
  IF (spname(ns) == TRIM(species(7))) THEN
     tc(ns,ns)    = 126.20E+0_wp  ! K SOURCE NIST
     pc(ns,ns)    = 33.958E+5_wp  ! Pa SOURCE NIST
     vc(ns,ns)    = 8.9000E-2_wp  ! m3/kmol SOURCE NIST
     omega(ns,ns) = 3.9000E-2_wp  ! no units SOURCE NIST
  ENDIF
!CO
  IF (spname(ns) == TRIM(species(8))) THEN
     tc(ns,ns)    = 132.800E+0_wp ! K SOURCE NIST
     pc(ns,ns)    = 34.9350E+5_wp ! Pa SOURCE NIST
```

```
      vc(ns,ns)     = 92.1685E-3_wp ! m3/kmol COMPUTED NIST
      omega(ns,ns) = 5.10000E-2_wp ! no units SOURCE NIST
    ENDIF
  !Fluoroketone
  ! From 3M Novec 649 Fluid properties
    IF (spname(ns) == TRIM(species(9))) THEN
      tc(ns,ns)     = 441.81E+0_wp   ! K SOURCE 3M
      pc(ns,ns)     = 18.646E+5_wp   ! Pa SOURCE 3M
      vc(ns,ns)     = 4.9450E-1_wp   ! m3/kmol SOURCE 3M
      omega(ns,ns) = 4.7100E-1_wp    ! no units SOURCE
    ENDIF
  !O
    IF (spname(ns) == TRIM(species(10))) THEN
  !     Tc(ns,ns)     = 367.4E+0_wp   ! K ! Ribert_2008a
  !     pc(ns,ns)     = 76.00E+5_wp   ! Pa ! Ribert_2008a
      tc(ns,ns)     = 100.7E+0_wp   ! K !
  same as OH
      pc(ns,ns)     = 57.60E+5_wp   ! Pa !
  same as OH
      vc(ns,ns)     = 39.30E-3_wp   ! m3/kmol !
  same as OH
      omega(ns,ns) = 3.290E-1_wp   ! no units !
  same as OH
    ENDIF
  !H2S : hydrogen sulfide, used in a PGL test case
    IF (spname(ns) == TRIM(species(11))) THEN
      tc(ns,ns)     = 373.40E+0_wp   ! K SOURCE PGL
      pc(ns,ns)     =  89.63E+5_wp   ! Pa SOURCE PGL
      vc(ns,ns)     =  98.00E-3_wp   ! m3/kmol SOURCE PGL
      omega(ns,ns) =   9.00E-2_wp   ! no units SOURCE PGL
    ENDIF
  !EE : ethyl ether, used in a PGL test case
    IF (spname(ns) == TRIM(species(12))) THEN
      tc(ns,ns)     = 466.70E+0_wp   ! K SOURCE PGL
      pc(ns,ns)     =  36.40E+5_wp   ! Pa SOURCE PGL
      vc(ns,ns)     = 280.00E-3_wp   ! m3/kmol SOURCE PGL
      omega(ns,ns) =   2.81E-1_wp   ! no units SOURCE PGL
    ENDIF
  !NH3 : ammonia, used in a PGL test case
    IF (spname(ns) == TRIM(species(13))) THEN
      tc(ns,ns)     = 405.50E+0_wp   ! K SOURCE PGL
      pc(ns,ns)     = 113.33E+5_wp   ! Pa SOURCE PGL
      vc(ns,ns)     =  72.40E-3_wp   ! m3/kmol SOURCE PGL
      omega(ns,ns) =   2.56E-1_wp   ! no units SOURCE PGL
    ENDIF
  !CO2 : carbon dioxide
    IF (spname(ns) == TRIM(species(14))) THEN
      Tc(ns,ns)     = 304.12E+0_wp   ! K SOURCE PGL
      pc(ns,ns)     =  73.74E+5_wp   ! Pa SOURCE PGL
      Vc(ns,ns)     =  94.07E-3_wp   ! m3/kmol SOURCE PGL
      omega(ns,ns) =   2.25E-1_wp   ! no units SOURCE PGL
    ENDIF
  !CH4 : methane
    IF (spname(ns) == TRIM(species(15))) THEN
      Tc(ns,ns)     = 190.56E+0_wp   ! K SOURCE PGL
      pc(ns,ns)     =  45.99E+5_wp   ! Pa SOURCE PGL
      Vc(ns,ns)     =  98.60E-3_wp   ! m3/kmol SOURCE PGL
      omega(ns,ns) =   1.10E-1_wp   ! no units SOURCE PGL
    ENDIF
  !C5H12 : 2-methylbutane (isopentane)
    IF (spname(ns) == TRIM(species(16))) THEN
      Tc(ns,ns)     = 460.39E+0_wp   ! K SOURCE PGL
      pc(ns,ns)     =  33.81E+5_wp   ! Pa SOURCE PGL
      Vc(ns,ns)     = 308.30E-3_wp   ! m3/kmol SOURCE PGL
      omega(ns,ns) =   2.29E-1_wp   ! no units SOURCE PGL
    ENDIF
  !Ar : argon
    IF (spname(ns) == TRIM(species(17))) THEN
      Tc(ns,ns)     = 150.86E+0_wp   ! K SOURCE PGL
      pc(ns,ns)     =  48.98E+5_wp   ! Pa SOURCE PGL
      Vc(ns,ns)     =  74.57E-3_wp   ! m3/kmol SOURCE PGL
      omega(ns,ns) =  -0.002E-0_wp   ! no units SOURCE PGL
    ENDIF
  !AIR : air assumed to be 0.7812 nitrogen,
  ! 0.0092 argon and 0.2096 oxygen (in moles)
  ! See Panasiti_1999a
    IF (spname(ns) == TRIM(species(18))) THEN
      Tc(ns,ns)     = 132.5306E+0_wp   ! K SOURCE Panasiti
      pc(ns,ns)     =  37.8600E+5_wp   ! Pa SOURCE Panasiti
      Vc(ns,ns)     =  84.5251E-3_wp   ! m3/kmol SOURCE Panasiti
      omega(ns,ns) =   0.0351E-0_wp   ! no units SOURCE PGL
    ENDIF
  !AC : allyl chloride C3H5Cl for example 11-3 in PGL
  ! http://www.solvaychlorinatedorganics.com
    IF (spname(ns) == TRIM(species(19))) THEN
      Tc(ns,ns)     = 514.1500E+0_wp   ! K SOURCE Solvay web
      pc(ns,ns)     =  48.0000E+5_wp   ! Pa SOURCE Solvay web
      Vc(ns,ns)     = 300.0000E-3_wp   ! m3/kmol SOURCE
      omega(ns,ns) =   0.2000E-0_wp   ! no units SOURCE
    ENDIF
  ! C10H22: n-decane, surrogate for aircraft engine fuel
  ! Pitsch_2008a uses 82.6% C10H22 and 17.4% C9H12 by mass
    IF (spname(ns) == TRIM(species(20))) THEN
      Tc(ns,ns)     = 617.7000E+0_wp   ! K SOURCE PGL
      pc(ns,ns)     =  21.1000E+5_wp   ! Pa SOURCE PGL
      Vc(ns,ns)     = 624.0000E-3_wp   ! m3/kmol SOURCE PGL
      omega(ns,ns) =   0.4900E-0_wp   ! no units SOURCE PGL
    ENDIF
  ! C9H12: 1,2,3-trimethylbenzene,
  ! surrogate for aircraft engine fuel
  ! Pitsch_2008a uses 82.6% C10H22 and 17.4% C9H12 by mass
    IF (spname(ns) == TRIM(species(21))) THEN
      Tc(ns,ns)     = 664.5000E+0_wp   ! K SOURCE PGL
      pc(ns,ns)     =  34.5400E+5_wp   ! Pa SOURCE PGL
      Vc(ns,ns)     = 435.0000E-3_wp   ! m3/kmol SOURCE PGL
      omega(ns,ns) =   0.3670E-0_wp   ! no units SOURCE PGL
    ENDIF
  ! C9H20: nonane, surrogate for Jet-A
  ! Huber_2002a uses 35.0% C9H20 and 65.0% C16H34 by mole
  ! This yields a MWmix of 192.0802 g/mol for Jet-A
  ! and 23.37% C9H20 and 76.63% C16H34 by mole
    IF (spname(ns) == TRIM(species(22))) THEN
```

```
    Tc(ns,ns)     = 594.6000E+0_wp   ! K SOURCE PGL
    pc(ns,ns)     =  22.9000E+5_wp   ! Pa SOURCE PGL
    Vc(ns,ns)     = 555.0000E-3_wp   ! m3/kmol SOURCE PGL
    omega(ns,ns) =   0.4450E-0_wp   ! no units SOURCE PGL
  ENDIF
! C16H34: hexadecane, surrogate for Jet-A
! Huber_2002a uses 35.0% C9H20 and 65.0% C16H34 by mass
! This yields a MWmix of 192.0802 g/mol for Jet-A
! and 23.37% C9H20 and 76.63% C16H34 by mole
  IF (spname(ns) == TRIM(species(23))) THEN
    Tc(ns,ns)     = 723.0000E+0_wp   ! K SOURCE PGL
    pc(ns,ns)     =  14.0000E+5_wp   ! Pa SOURCE PGL
    Vc(ns,ns)     =1034.0000E-3_wp   ! m3/kmol SOURCE PGL
    omega(ns,ns) =   0.7180E-0_wp   ! no units SOURCE PGL
  ENDIF
! C2H6: ethane
  IF (spname(ns) == TRIM(species(24))) THEN
    Tc(ns,ns)     = 305.3200E+0_wp   ! K SOURCE PGL
    pc(ns,ns)     =  48.7200E+5_wp   ! Pa SOURCE PGL
    Vc(ns,ns)     = 145.5000E-3_wp   ! m3/kmol SOURCE PGL
    omega(ns,ns) =   0.0990E-0_wp   ! no units SOURCE PGL
  ENDIF
! C3H8: propane
  IF (spname(ns) == TRIM(species(25))) THEN
    Tc(ns,ns)     = 369.8300E+0_wp   ! K SOURCE PGL
    pc(ns,ns)     =  42.4800E+5_wp   ! Pa SOURCE PGL
    Vc(ns,ns)     = 200.0000E-3_wp   ! m3/kmol SOURCE PGL
    omega(ns,ns) =   0.1520E-0_wp   ! no units SOURCE PGL
  ENDIF
! C2H2: acetylene
  IF (spname(ns) == TRIM(species(26))) THEN
    Tc(ns,ns)     = 308.3000E+0_wp   ! K SOURCE PGL
    pc(ns,ns)     =  61.1400E+5_wp   ! Pa SOURCE PGL
    Vc(ns,ns)     = 112.2000E-3_wp   ! m3/kmol SOURCE PGL
    omega(ns,ns) =   0.1890E-0_wp   ! no units SOURCE PGL
  ENDIF
! CH3: methyl radical
  IF (spname(ns) == TRIM(species(27))) THEN
    Tc(ns,ns)     = 370.9000E+0_wp   ! K SOURCE Palle_06 Joback
    pc(ns,ns)     =  62.0000E+5_wp   ! Pa SOURCE Palle_06 Joback
    Vc(ns,ns)     =  82.5000E-3_wp   ! m3/kmol SOURCE Palle_06 Jo
    omega(ns,ns) =   0.1360E-0_wp   ! no units SOURCE PGL
  ENDIF
! H2O2: hydrogen peroxide
  IF (spname(ns) == TRIM(species(28))) THEN
    Tc(ns,ns)     = 587.1900E+0_wp   ! K SOURCE Palle_06 Joback
    pc(ns,ns)     =  93.5300E+5_wp   ! Pa SOURCE Palle_06 Joback
    Vc(ns,ns)     =  73.5000E-3_wp   ! m3/kmol SOURCE Palle_06 Jo
    omega(ns,ns) =   1.0200E-0_wp   ! no units SOURCE Palle_06
  ENDIF
! HO2: Hydroperoxyl
  IF (spname(ns) == TRIM(species(29))) THEN
    Tc(ns,ns)     = 472.2000E+0_wp   ! K SOURCE Palle_06 Joback
    pc(ns,ns)     =  82.7900E+5_wp   ! Pa SOURCE Palle_06 Joback
    Vc(ns,ns)     =  63.5000E-3_wp   ! m3/kmol SOURCE Palle_06 Jo
    omega(ns,ns) =   0.6200E-0_wp   ! no units SOURCE Palle_06
  ENDIF
ENDDO
```

Finally, Table 19 lists the few non-zero binary interaction parameters used for this study.

Species couple	Interaction parameter	Source
C_2H_6-C_3H_8	0.008	[48]
CH_4-C_3H_8	-0.0029	[48]
CH_4-C_2H_6	-0.0021	[48]
H-O_2	0.0747	
H_2-O_2	0.0747	
H_2-NH_3	0.5620	
H_2-H_2O	0.5620	

Table 19: Non-zero binary interaction parameters used for this study.

B.2 Hydrogen

Hydrogen, like helium and neon, is a quantum gas. This means that quantum effects become significant when the density of the gas is large enough. We recall that cubic equations of state, through the application of the corresponding state principle, simply reflect the modeling of intermolecular forces similar to the Lennard-Jones potential. The van der Waals equation of state actually uses the exact Lennard-Jones potential:

$$V(r) = 4\epsilon\left(\left(\frac{\sigma}{r}\right)^{12} - \left(\frac{\sigma}{r}\right)^{6}\right) \tag{B.2.1}$$

where r is the distance to the molecule center, σ is the finite distance at which the potential is zero (equivalent to a hard sphere radius) and ϵ is the depth of the potential well. It can be shown through quantum mechanics[71] that if we consider two hydrogen atoms in different energy state, the electrostatic interaction between them scales as $\frac{1}{r^3}$ instead of $\frac{1}{r^6}$ for the attractive part of the Lennard-Jones potential (corresponding to the two atoms being in their ground state). r represents the distance between the two atoms. Supposedly, this can be extended to molecular hydrogen. A more generalized treatment is proposed by Hooper et al.[103] where they attempt to estimate the quantum effects on the equation of state of simple fluids. They show that the van der Waals equation of state

$$p = \frac{k_B T}{v - v_0} - \frac{a}{v^2} \tag{B.2.2}$$

where $v_0 = \sigma^3$ represents the excluded volume per particle and $a = 16\pi\sigma^3\epsilon/9$ This equation can be modified, in order to include quantum corrections, into:

$$p = \left(\frac{k_B T}{v - v_0}\right) R(z) - \frac{a}{v^2} \tag{B.2.3}$$

where $R(z)$, quotient of two infinite, rapidly converging series, can be approximated as:

$$R(z) = \frac{1}{1 - \frac{z}{\sqrt{2\pi}}} \tag{B.2.4}$$

with $z^2 = \frac{h^2}{4mk_BT(v-v_0)^{2/3}} = \frac{\pi\lambda_0^2}{2(v-v_0)^{2/3}}$.

The thermal de Broglie wavelength is defined, for a three-dimensional non-relativistic system, as[340]:

$$\lambda_0 = \sqrt{\frac{h^2}{2\pi m k_B T}} \tag{B.2.5}$$

where h is Planck's constant, m is the mass of a gas particle, k_B is Boltzmann's constant and T is the temperature of the gas.

Even when the average interparticle separation is much larger than the thermal wavelength, Yan[340] shows that:

$$\frac{pv}{k_B T} = 1 - \frac{b}{2^{3/2}} \frac{\lambda_0}{gv} \tag{B.2.6}$$

where g is the spin degenerate factor, v is the volume occupied by the particle and b is respectively 1 and -1 for Bose and Fermi systems (for example, the hydrogen atom is a fermion with a spin of 1/2 while the nucleus of deuterium or the nucleus of helium-4 are bosons). Thus the non-ideal factor scales as $\frac{1}{g\sqrt{m}}$: $\frac{\lambda}{v}$ is the measure of the strength of quantum effects in the system. They also show that the Fermi temperature is about 2.4 times the critical temperature. We recall that below the Fermi temperature, a substance gradually expresses more and more quantum effects of cooling. This does not seem to be an absolute rule since molecular oxygen (MW = 16) or carbon monoxide (MW = 14) do not exhibit such effects while neon (MW = 10) do. For more details on how to implement these hydrogen-specific features, the reader is referred to Twu et al. [317], Sadus [259] and Wei et al. [333].

Using the values given in Table 20, we obtain for example specific heats at constant pressure which are very different from the NIST data at low temperatures. This is shown on Fig. 107 where we can see that our real gas model cannot capture the behavior of hydrogen specific heat at low temperatures. We can see that the increase of specific heat at supercritical pressures around the critical temperature is in fact correctly modeled but there is a global trend, both at sub- and supercritical pressures, for much lower specific heat. It has been shown[18] that this effect, first observed (but not understood at the time) by Maxwell, is due to quantum mechanics. Maxwell noticed that the specific heat of hydrogen at low, cryogenic temperatures, instead of following the theoretical values of a diatomic gas, resembled the specific heat of a monoatomic gas. According to quantum mechanics, because of the low mass of hydrogen, its rotational energy levels are widely spaced at these temperatures and thus inhibit the equal partition of energy into rotational motion. Diatomic gases exhibit a more uniform distribution of energy in their rotational

modes, hence the difference in specific heats.

Gunn et al.[94] suggests to use temperature-dependent critical properties for quantum fluids:

$$T_c = \frac{T_c^0}{1 + \frac{21.8}{MW\,T}} \tag{B.2.7}$$

$$p_c = \frac{p_c^0}{1 + \frac{44.2}{MW\,T}} \tag{B.2.8}$$

$$v_c = \frac{v_c^0}{1 - \frac{9.91}{MW\,T}} \tag{B.2.9}$$

where $T_c^0 = 43.6$ K, $p_c^0 = 20.5$ bar and $v_c^0 = 5.15 \times 10^{-2}$ m^3.kmol^{-1} are "classical" critical constants. With these modified critical parameters, it is suggested to use a value of zero for the acentric factor. The influence of such modifications is first presented with a comparison of experimental data[146] and the predicted compressibility values of our current model. Gunn et al. originally used data by Johnston et al.[119] but we are using the more recent data from NIST. Only small deviations have been observed between the two sets of data. This comparison is shown on Fig. 108: we can see that the improvements brought by these redefined parameters are limited. In this example, for the 35 K isotherm, we have thus $T_{c,H_2} = 33.25$ K, $p_{c,H_2} = 12.56$ bar and $v_{c,H_2} = 6.00 \times 10^{-2}$ m^3.kmol^{-1} while, for the 125 K isotherm, we have $T_{c,H_2} = 40.10$ K, $p_{c,H_2} = 17.42$ bar and $v_{c,H_2} = 5.36 \times 10^{-2}$ m^3.kmol^{-1}. If we were to implement these temperature-dependent properties, it would cost us some additional overhead since these properties would need to be recomputed in every cell at every time step. Since the standard formulation along with a zero acentric factor seems to yield acceptable results, we will chose this set of parameters because a negative acentric factor would prevent us from using Chung's formulation for transport properties.

However, without any modification, the Chung's formulation does not yield very accurate results as shown on Fig. 109. While the local minimum associated with the critical temperature appears correctly captured by the standard formulation (blue curve), the viscosity at higher temperatures seems to be under-estimated. The same behavior is observed at low pressures and indicates that "quantum" effects have an influence on the viscosity even at low densities. Maybe this is due to the spin that makes the H_2 molecule asymmetric,

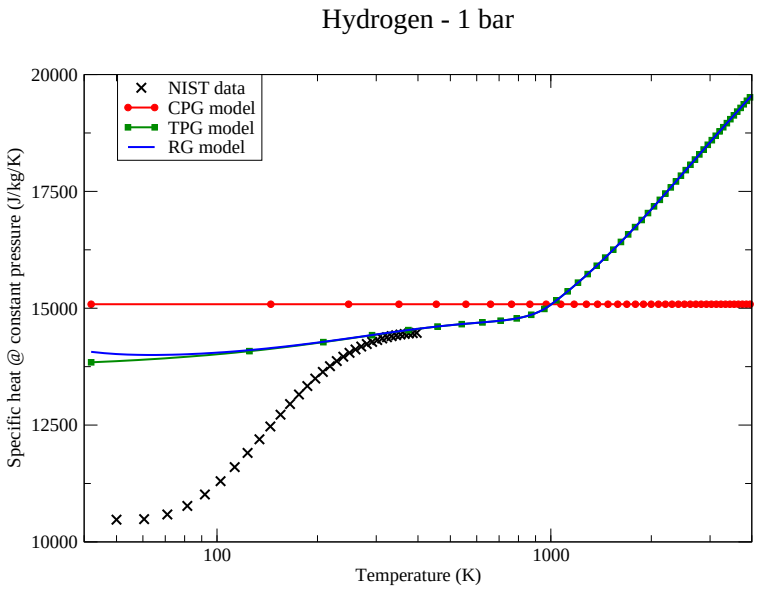

(a) 1 bar

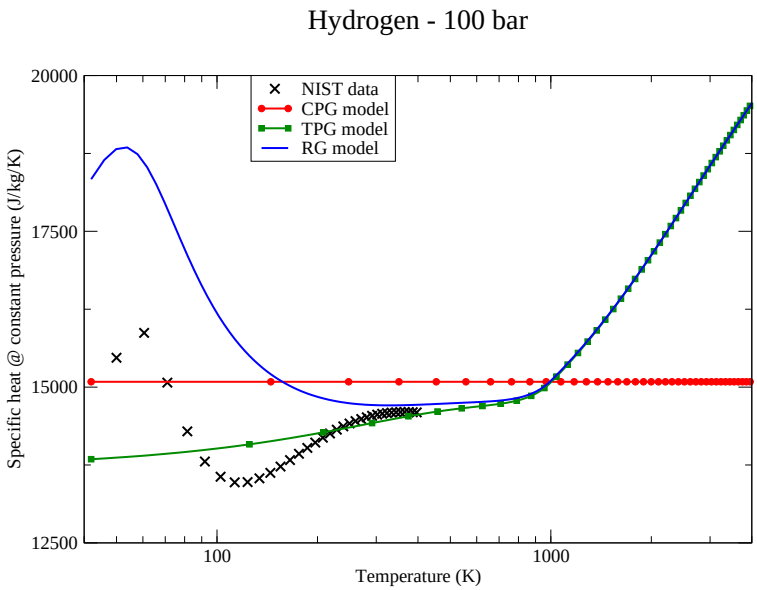

(b) 100 bar

Figure 107: Specific heat at constant pressure for H_2 in function of temperature at sub- and supercritical pressures. Experimental data are from NIST chemistry webbook[146]. The CPG curve corresponds to a constant value used in our flow solver. The TPG curve corresponds to a curvefit from CHEMKIN. The RG curve uses the parameters listed in Table 20.

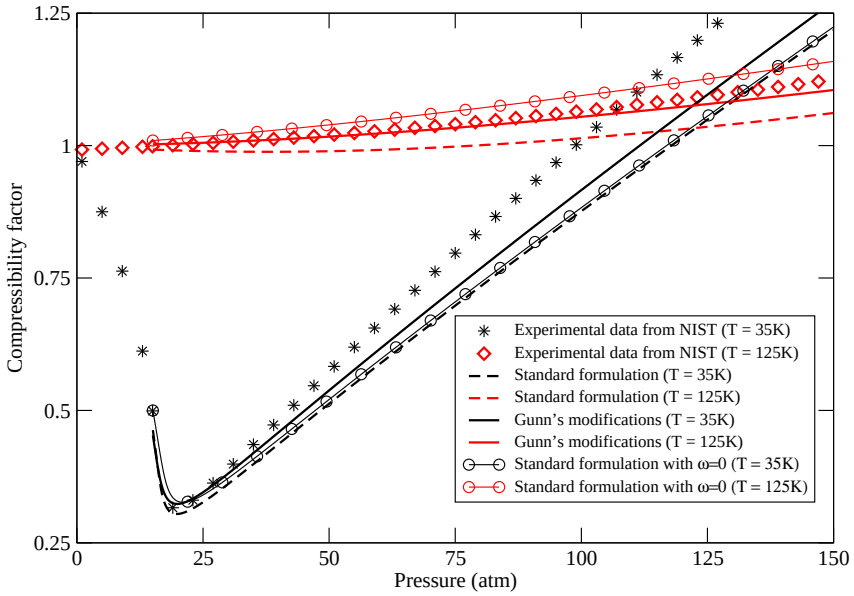

Figure 108: Compressibility chart for hydrogen. Experimental data are from the NIST chemistry web-book[146].

no matter the density. In order to match the experimental data, we suggest two possible modifications to the Chung's viscosities (even the low-density one). One, rather arbitrary (black curve), multiplies the viscosity by a factor $1 + (1 - 0.2\exp^{-(S2-50)/150)})$ while the other (red curve) uses the multiplying factor suggested by Lucas[163] for quantum gases:

$$F_Q^0 = 1.22\, Q^{0.25}\, \left(1 + 0.00385\left[(T_r - 12)^2\right]^{1/MW}\, sign(T_r - 12)\right) \tag{B.2.10}$$

The arbitrary modification yields a very good match to the experimental data but has no physical basis. The Lucas modification gives the correct trend for low-density regime but slightly over-estimates the viscosity near the critical temperature. The next step is to evaluate the cost and accuracy of the full Lucas' methodology even though other researchers[42] have already indicated the relative superiority of the method by Chung for rocket combustion applications.

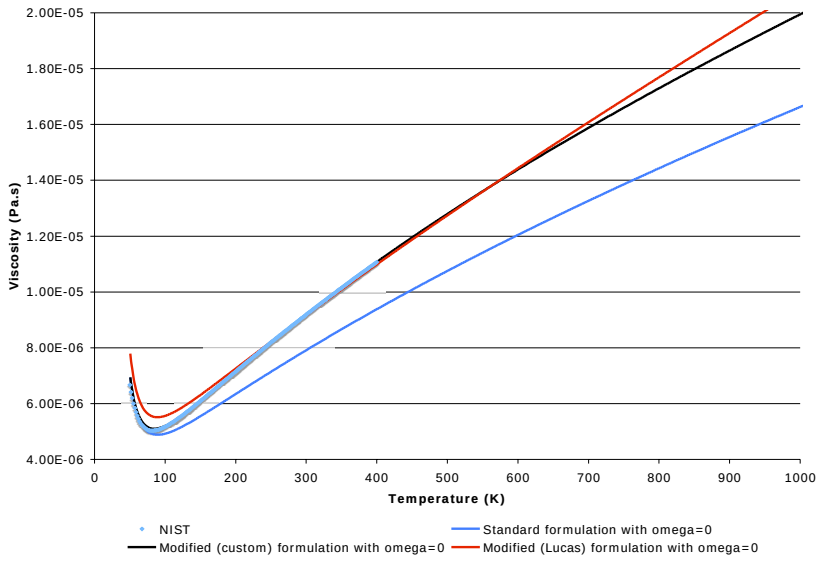

Figure 109: Dynamic viscosity for hydrogen at 100 bar. Experimental data are from the NIST chemistry web-book[146].

Table 20: Values of the standard properties and parameters used in the PR EoS for hydrogen.

Property	Value	Units	Source	Comments	Used
MW	2.016	$g.mol^{-1}$	[146, 231]		
T_c	33.19	K	[146]		X
T_c	33.25	K	[241]		
T_c	33.2	K	[231]		
p_c	13.150	bar	[146]		X
p_c	12.97	bar	[241]		
p_c	13.00	bar	[231]		
ρ_c	30.12	$kg.m^{-3}$	[146]	Yields v_c	X
v_c	$\frac{MW}{\rho_c} = 6.64\times10^{-2}$	$m^3.kmol^{-1}$	[146]	Using MW = 2.0 $g.mol^{-1}$	X
v_c	6.5×10^{-2}	$m^3.kmol^{-1}$	[241, 231]		
s	4.0×10^{-3}	$m^3.kmol^{-1}$		Approximate value similar to N_2	X
Z_c	0.305		[241]		
Z_c	0.306		[231]		
ω	-0.214		[146]		X
ω	-0.218		[241]		
μ_D	0.0	D	[146, 241]		X
κ_R	0.0				X
σ_{LJ}	2.827	Å	[241]		X
$\frac{\epsilon}{k}$	59.7	K	[241]		X
T_b	20.39	K	[146]		
T_b	20.38	K	[241]		

Here again the lack of experimental is problematic and prevent some of these models to be validated. These issues are likely to become more important when considering the injection of hydrogen at very low temperatures, as low as 50 K [210]. Under these conditions, even hydrogen will start to exhibit non-ideal gas behavior and this could have an influence on the stability of the injection and the flame.

APPENDIX C

IMPROVING THE DENSITY PREDICTIONS OF CUBIC EQUATIONS OF STATE

Improving the predictions of cubic equations of state is still an active area of research in the field of thermodynamics and these advances will eventually make their way to CFD as computational resources increase. For a fully conservative formulation with a constant back-and-forth between primitive and conservative variables, the efficiency of cubic equations of states is crucial and particular caution will have to be applied when considering modifications that adds computational cost to increase accuracy. Focusing on the PR EoS, it is known to slightly overpredict densities in the compressed liquid region (by as much as 15% in extreme cases) but there exists some corrections to improve this behavior. An overview of these corrections is presented first below in chronological order before focusing on their actual predictions and detailing their strengths and shortcomings.

Original ideas on volume correction for cubic equations of state can be traced back to the works of Martin [173] and Péneloux et al. [235]. Mathias et al. [182] refined this idea and correlated this volume correction with temperature through a limited database of experimental data:

$$V_m^{corr} = V_m^{PR} + s_m + f_{cm}\left(\frac{0.41}{0.41+\delta_m}\right) \tag{C.0.11}$$

They propose values for the correction term s for a handful of species such as methane, ethane, nitrogen, water or carbon dioxide. It is conceivable to compute such correction terms for other species based on available experimental data. With f_{cm} defined as $V_{cm} - (3.946B_m + s_m)$, this yields:

$$V_m^{corr} = V_m + s_m + (V_{cm} - 3.946B_m + s_m)\left(\frac{0.41}{0.41+\delta_m}\right) \tag{C.0.12}$$

with $\delta_m = -\frac{V^2}{R_u T}\left(\frac{\partial p}{\partial v}\right)_{T,X}$, related to the isothermal compressibility. Simple mixing rules

allow the computation of this modified density for mixture:

$$s_m = \sum_i x_i s_i \tag{C.0.13}$$

$$v_{cm} = \sum_i x_i v_{ci} \tag{C.0.14}$$

This model has seen continuous improvement over the years as more experimental data becomes available [105]. However this was still limited to light hydrocarbons and common molecules such as nitrogen, oxygen and water. For a pure species, Hoyos et al. [105] suggest:

$$v^{corr} = v + \left(\frac{C_1}{C_2}\right) C_2 + C_2 \left(T_r - C_3\right)^2 \tag{C.0.15}$$

with

$$\frac{C_1}{C_2} = 110.07\omega^4 - 83.807\omega^3 + 18.926\omega^2 - 1.6348\omega - 0.0066 \tag{C.0.16}$$

$$C_2 = 2.013645 \times 10^{-3} \ \ \mathrm{m^3.kg^{-1}} \tag{C.0.17}$$

$$C_3 = 0.89 \tag{C.0.18}$$

Thanks to the universal character of C_2 and C_3 (at least for the species considered), an extension of this formulation to a mixture is suggested:

$$v^{corr} = v + \sum_i \sum_j \left(x_i x_j \left(\frac{C_1}{C_2}\right)_{ij} C_2 \right) + C_2 \left(T_{r,m} - C_3\right)^2 \tag{C.0.19}$$

$$\left(\frac{C_1}{C_2}\right)_{ij} = 110.07\, \omega_{ij}^4 - 83.807\, \omega_{ij}^3 + 18.926\, \omega_{ij}^2 - 1.6348\, \omega_{ij} - 0.0066 \tag{C.0.20}$$

with the mixture reduced temperature T_r computed following the mixing rules of Harstad et al. [99]:

$$T_{r,m} = T/T_{c,m} \tag{C.0.21}$$

$$T_{c,m} = \sum_i \sum_j x_i x_j T_{c,ij} \frac{v_{c,ij}}{v_{c,m}} \tag{C.0.22}$$

$$T_{c,ij} = \sqrt{T_{c,i} T_{c,j}} (1 - k_{ij}) \tag{C.0.23}$$

$$v_{c,m} = \sum_i \sum_j x_i x_j v_{c,ij} \tag{C.0.24}$$

$$v_{c,ij} = \frac{\left(\sqrt[3]{v_{c,i}} + \sqrt[3]{v_{c,j}}\right)^3}{8} \tag{C.0.25}$$

However, for low reduced temperatures ($T_r < 0.5$), the predictions of oxygen densities are worse than with the regular Peng-Robinson EoS.

Lin et al. [153] suggest another approach. Under the volume translation formulation, the Volume-Translated Peng-Robinson equation of state (VTPR EoS) can be written as:

$$p = \frac{R_u T}{V + V_t - B_m} - \frac{A_m}{(V + V_t)^2 + 2(V + V_t)B_m - B_m^2} \tag{C.0.26}$$

The parameters A_m and B_m are the same as previously described while the correction volume V_t needs to be modeled. Assuming a simple temperature dependence, V_t can be expressed as:

$$V_t = V_{t,c} f_{V_t}(T_r) = (0.3074 - Z_c) \frac{R_u T_c}{p_c} f_{V_t}(T_r) \tag{C.0.27}$$

With the constraint $f_{V_t}(1) = 1$, a possible expression for the temperature dependency is:

$$f_{V_t}(T_r) = \begin{cases} \beta_{V_t} + (1 - \beta_{V_t}) \exp\left(\chi \left(1 - T_r\right)\right) & \text{if } T_r \leq 1 \\ \beta_{V_t} + (1 - \beta_{V_t}) \exp\left(0.5\chi\right) & \text{if } T_r > 1 \end{cases} \tag{C.0.28}$$

β_{V_t} and χ are two parameters that are determined through curvefitting of experimental data. Lin et al. [154] found that over 91 pure fluids, the best agreement was obtained for:

$$\beta_{V_t} = -2.8431 \exp\left(-64.2184 \left(0.3074 - Z_c\right)\right) + 0.1735 \tag{C.0.29}$$

$$\chi = -99.2558 + 301.6201 Z_c \tag{C.0.30}$$

Frey et al. [72] argue that volume correction formulations that only depend on temperature only improve volume predictions and not other thermodynamic quantities. This can have severe consequences such an unphysical crossovers of isotherms on the pressure-volume diagram of the equation of state. However, for operations away enough from the critical point, this should not be a concern. The main issue with temperature-dependent curvefits is that they focus usually on low-pressure liquid densities and are thus inappropriate for super-critical applications.

An example of more advanced volume translation is given by Frey et al. [73] where the calculation of volume roots is still explicit but no longer purely cubic. And this is actually the issue with all volume translation methods. Even the ones that are only temperature

dependent require extra computation in the real gas formulation. The volume correction needs to be evaluated every time the density from the conservation equation is used in the thermodynamic framework. If it is at a stage

One of the simplest model for volume translation of the Peng-Robinson EoS is proposed by Wang et al. [331]. However it still requires the computation of the saturation properties which involves a new model on top of the equation of state.

A review of a few of the available corrections to the PR EoS is given in Figure 110. At moderate pressures, whether sub- or super-critical, the volume-translation formulation by Lin et al. [153] shows very good performance but without further modifications, it cannot be used blindly at any pressure as seen below. Also, it is interesting to see that the PR EoS, with or without volume-translation, cannot predict the liquid density at atmospheric pressure. This is a known limitation of the formulation. Finally, since some of these formulations are designed for specific temperature and pressure ranges, care must be taken before using them without verifying their performances.

It is possible for example to tweak the formulation by Lin et al. [153] to obtain good volume prediction even at large super-critical pressure conditions (see Figure 111) by adding an explicit pressure dependency or a pseudo-pressure dependency (for applications with a relatively constant pressure). However, the added complexity deteriorates the speed and robustness of the current framework and will not be adopted for this work. There have been many reacting studies [42, 267] that have neglected this effect and it is believed that the 10-15% adjustment on the injection velocity is an acceptable compromise to maintain the correct flowrate, the most important parameter and the one usually known with the smallest uncertainty from the experiments.

Unfortunately, if these corrections improves the tendency of the PR EoS to overpredict the liquid densities, they generally degrade the prediction of all the other thermodynamic properties and only slightly improves the estimation of the transport properties. Thus this correction would need to be implemented in such a way that only the density used for the fluid mechanics part is affected, while the rest of the equations related to the PR

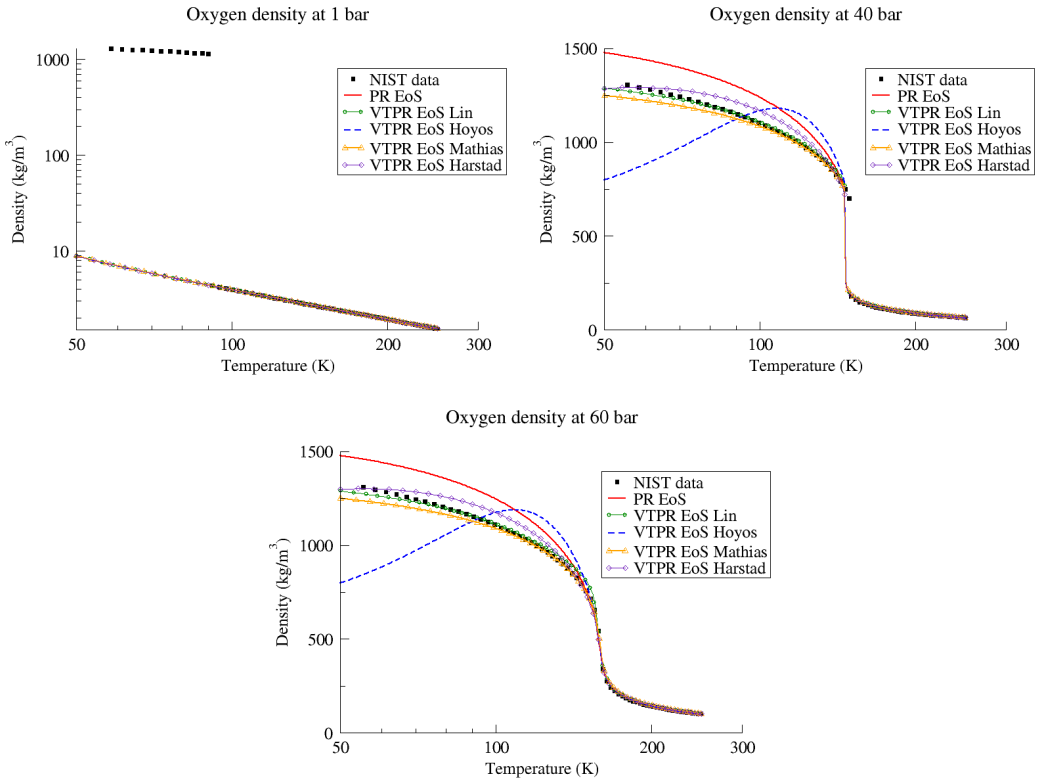

Figure 110: Density predictions for oxygen at 1, 40 and 60 bar for different variants of the PR EoS. Experimental data is given by the NIST database.

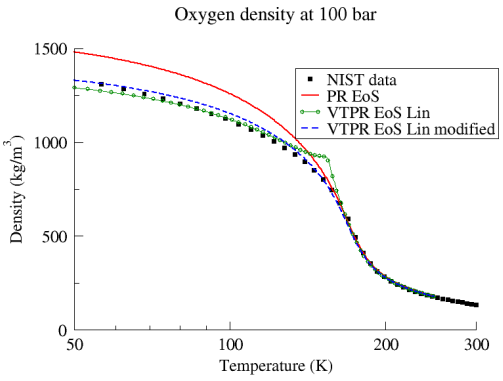

Figure 111: Density predictions for oxygen at 100 bar.

EoS remain unchanged. Another danger of such implementation is that isotherms near the critical point might become ill-defined because of the new temperature dependence. A method to check for this is to make sure the partial derivative of pressure with respect to temperature at constant volume $\left(\frac{\partial p}{\partial T}\right)_v$ never becomes negative. All this is very cumbersome to integrate into the flow solver and is a feature that was not retained for this study even though other similar numerical works have included it for simple binary mixtures [99, 222]. An alternative approach would to consider hybrid three-parameter equations of state such as the one proposed by Cismondi et al. [37] and which have been applied to rocket propellants already [133].

More complex solutions have been suggested such as the use of neural networks for volume translation [144]. The use of neural networks for full computation of the thermodynamics is actually not recommended as the small local fluctuations inherent to neural networks can have very negative effects when computing the pressure for example. The reader is referred to the work of Coquelet et al. [45] and Haghtalab et al. [96] on improving empirical correlations such as the alpha function of the volume correction, the work of Amorim et al. [5] on volume scaling, or the work of Schmid et al. [266] on group contribution methods. Figure 112 gives an overview of the complexity of a group contribution equation of state, but the accuracy obtained is excellent. In the future, some of these advanced thermodynamic models from chemical engineering will have to be implemented in CFD solvers. They show that the thermodynamic aspect of modeling liquid rocket engine flows is still an active research field.

Another way to improve the behavior of the EoS in the sub-critical region is a new computation of the root from the cubic compressibility equation. Instead of always picking the largest real root, Oefelein and Lacaze [219] suggest a new expression for the root used to compute density:

$$Z = Z_1 - (\max(Z_2, Z_3) - \min(Z_2, Z_3)) \tag{C.0.31}$$

In the previous equation, Z_1 represents the root with the largest real part while Z_2 and Z_3 are the other two roots, whether real or imaginary. This new expresssion should have no

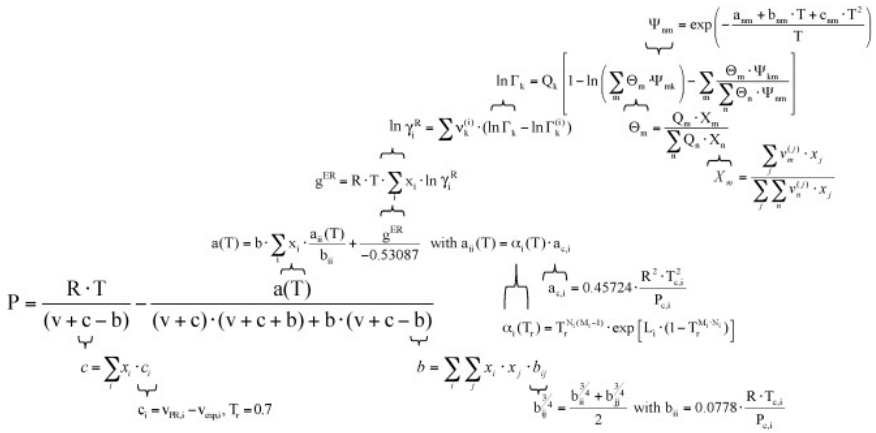

Figure 112: Overview of the VTPR-group contribution equation of state, from Schmid et al. [266]

effect outside the vapor dome since there, $Z_2 = Z_3$.

A final improvement to the accuracy of the predictions of mixture density is to obtain better data on the binary interaction parameters. The experimental data on this is very scarce while the impact of these interaction parameters is easily demonstrated. Consider for example a non-reacting temporal mixing layer, whose formulation is given in Appendix A, with a stream of air with mild real gas effects ($\min(Z) = 0.8$) and a stream of fuel such as hydrogen. A thin layer of water vapor is initialized using a gaussian profile between these two streams and with a maximum mass fraction of 0.1. Water vapor is chosen because it is relevant to hydrogen-oxygen combustion and because it has a strong dipole moment which makes it more likely to interact with other molecules at close range. From the same initialization, the simulation is then run three times using the thermally perfect equation of state, the Peng-Robinson EoS with all binary interaction parameters set to 0 and the Peng-Robinson EoS with non-zero binary interaction parameters as listed in Table 19. The temporal evolution of the momentum thickness (see Eq. A.1.5) is shown in Figure 113 and shows clear difference between the three simulations. The difference between the TPG EoS and the PR EoS can be attributed to the mild departure from ideal gas of the initial conditions but clearly the binary interaction parameters seem to have just as much influence on the growth of the mixing layer. This means that for a reacting flow with many species, the mixing process could be very dependent on these parameters. Figure 114 illustrates

this further by showing the reduced mixing of the water vapor layer with the current set of binary interaction parameters. Being a strongly polar molecule, water vapor is a species that has large interaction parameters and its role in hydrogen-oxygen combustion is critical. For hydrocarbons, while CO_2 has no dipole moment, CO does and so does a few other intermediate species so this would still be an issue.

The influence of the binary interaction parameters is also illustrated in Appendix D.3.2. The same sort of behavior has been observed by Star et al. [294] in a numerical study of the condensation of super-critical fluid injection. They also note that the uncertainty on these interaction parameters is problematic, especially since they are often not measured over a range of temperatures and pressures that correspond to injection conditions for rockets or SCRAMJETs. In case reliable experimental data cannot be obtained, it could be possible to use group contributions [241] to at least estimate if some of the unkown parameters are likely to be non-zero. In any case, this is a topic that requires a lot more effort before numerical predictions can eliminate this source of uncertainty.

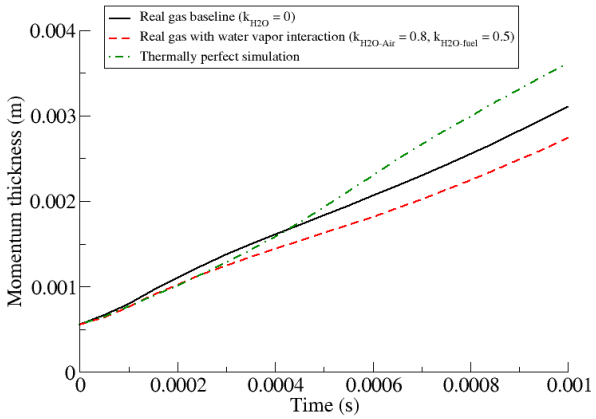

Figure 113: Comparison of the temporal evolution of the momentum thickness of three different TMLs with different thermodynamic formulations.

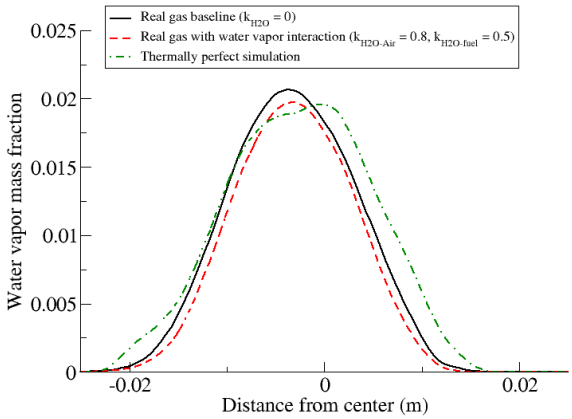

Figure 114: Comparison of the planar-averaged crosswise profiles of water vapor mass fraction of three different TMLs with different thermodynamic formulations.

APPENDIX D

MORE DETAILS ON THE REAL GAS FORMULATION

D.1 Details on the derivation of thermodynamic quantities

This section contains more details on the derivation of some of the quantities introduced in Section 2.5.6 and will help the reader derive the same quantities for similar cubic equations of state.

In order to compute the various quantities required by the real gas solver, the fundamental equations of thermodynamics, valid for any EoS, will be used along with the triple product rule:

$$\left(\frac{\partial x}{\partial y}\right)_z \left(\frac{\partial y}{\partial z}\right)_x \left(\frac{\partial z}{\partial x}\right)_y = -1 \text{ or } \left(\frac{\partial x}{\partial y}\right)_z = -\left(\frac{\partial z}{\partial y}\right)_x \left(\frac{\partial x}{\partial z}\right)_y \tag{D.1.1}$$

The definitions of the massic internal energy e, the massic enthalpy h, the massic Helmholtz free energy a and the massic Gibbs free energy g are given by:

$$e = Ts - pv + \sum_i X_i \mu_i \tag{D.1.2}$$

$$h = e + pv = Ts + \sum_i X_i \mu_i \tag{D.1.3}$$

$$a = e - Ts = -pv + \sum_i X_i \mu_i \tag{D.1.4}$$

$$g = e + pv - Ts = \sum_i X_i \mu_i \tag{D.1.5}$$

$$\tag{D.1.6}$$

As mentioned earlier, with the species mass fractions kept constant, the dependence on

the chemical potentials μ_i dissapears and first-principle partial derivatives yield:

$$+T = \left(\frac{\partial e}{\partial s}\right)_{v,X_i} = \left(\frac{\partial h}{\partial s}\right)_{p,X_i} \tag{D.1.7}$$

$$-p = \left(\frac{\partial e}{\partial v}\right)_{s,X_i} = \left(\frac{\partial a}{\partial v}\right)_{T,X_i} \tag{D.1.8}$$

$$+v = \left(\frac{\partial h}{\partial p}\right)_{s,X_i} = \left(\frac{\partial g}{\partial p}\right)_{T,X_i} \tag{D.1.9}$$

$$-s = \left(\frac{\partial g}{\partial T}\right)_{s,X_i} = \left(\frac{\partial a}{\partial T}\right)_{v,X_i} \tag{D.1.10}$$

A second differentiation of the thermodynamic potentials gives the Maxwell relations:

$$\left(\frac{\partial T}{\partial v}\right)_{s,X_i} = -\left(\frac{\partial p}{\partial s}\right)_{v,X_i} \tag{D.1.11}$$

$$\left(\frac{\partial T}{\partial p}\right)_{s,X_i} = +\left(\frac{\partial v}{\partial s}\right)_{p,X_i} \tag{D.1.12}$$

$$\left(\frac{\partial s}{\partial p}\right)_{T,X_i} = -\left(\frac{\partial v}{\partial T}\right)_{p,X_i} \tag{D.1.13}$$

$$\left(\frac{\partial s}{\partial v}\right)_{T,X_i} = +\left(\frac{\partial p}{\partial T}\right)_{v,X_i} \tag{D.1.14}$$

From the definitions of the specific heats $c_v = T\left(\frac{\partial s}{\partial T}\right)_v$ and $c_p = T\left(\frac{\partial s}{\partial T}\right)_p$ and the

differentiation of the entropy, one can show:

$$\begin{aligned} ds &= \left(\frac{\partial s}{\partial T}\right)_v dT + \left(\frac{\partial s}{\partial v}\right)_T dv \\ &= \frac{c_v}{T} dT + \left(\frac{\partial s}{\partial v}\right)_T dv \qquad \text{(D.1.15)} \\ &= \left(\frac{\partial s}{\partial T}\right)_v dT + \left(\frac{\partial s}{\partial v}\right)_T \left(\left(\frac{\partial v}{\partial T}\right)_p dT + \left(\frac{\partial v}{\partial p}\right)_T dp\right) \\ &= \left(\left(\frac{\partial s}{\partial T}\right)_v + \left(\frac{\partial s}{\partial v}\right)_T \left(\frac{\partial v}{\partial T}\right)_p\right) dT + \left(\frac{\partial s}{\partial v}\right)_T \left(\frac{\partial v}{\partial p}\right)_T dp \\ &= \frac{c_p}{T} dT + \left(\frac{\partial s}{\partial p}\right)_T dp \qquad \text{(D.1.16)} \end{aligned}$$

$$c_p = T\left(\frac{\partial s}{\partial T}\right)_v + T\left(\frac{\partial s}{\partial v}\right)_T \left(\frac{\partial v}{\partial T}\right)_p \qquad \text{(D.1.17)}$$

$$= c_v + T\left(\frac{\partial p}{\partial T}\right)_v \left(\frac{\partial v}{\partial T}\right)_p \qquad \text{(D.1.18)}$$

$$c_p - c_v = -T\left(\frac{\partial v}{\partial T}\right)_p \left(\frac{\partial p}{\partial v}\right)_T \left(\frac{\partial v}{\partial T}\right)_p \qquad \text{(D.1.19)}$$

$$c_p - c_v = -T\frac{\left(\frac{\partial v}{\partial T}\right)_p^2}{\left(\frac{\partial v}{\partial p}\right)_T} = -T\frac{\left(\frac{\partial p}{\partial T}\right)_v^2}{\left(\frac{\partial p}{\partial v}\right)_T} \qquad \text{(D.1.20)}$$

Introducing the thermal expansion coefficient (or expansivity) α_v and the isothermal compressibility κ_T, this can be recast as:

$$c_p - c_v = \frac{{\alpha_v}^2 vT}{\kappa_T} \qquad \text{(D.1.21)}$$

with:

$$\alpha_v = \frac{1}{v}\left(\frac{\partial v}{\partial T}\right)_p = -\frac{1}{v}\frac{\left(\frac{\partial p}{\partial T}\right)_v}{\left(\frac{\partial p}{\partial v}\right)_T} \qquad \text{(D.1.22)}$$

$$\kappa_T = -\frac{1}{v}\left(\frac{\partial v}{\partial p}\right)_T = \alpha_v \left(\frac{\partial T}{\partial p}\right)_v \qquad \text{(D.1.23)}$$

Similarly, it can be shown that the ratio γ of specific heats is:

$$\frac{c_p}{c_v} = \left(\frac{\partial p}{\partial v}\right)_s \left(\frac{\partial v}{\partial p}\right)_T = \frac{\kappa_T}{\kappa_s} \qquad \text{(D.1.24)}$$

with κ_s the adiabatic compressibility.

For an ideal gas, these expressions reduce to:

$$\alpha_v = \frac{1}{T} \quad \kappa_T = \frac{1}{p} \quad c_p - c_v = R \qquad \text{(D.1.25)}$$

D.2 Dual-variable iteration method to compute primitive variables from conservative variables

It is assumed that the internal energy e and the new specific volume v are known at this stage. These values will be superscripted with a "N+1" like e^{N+1}. They are expressed respectively in J.kg^{-1} and m^3.kg^{-1}.

The procedure consists in updating p and T at each iteration using the following algebraic expression:

$$T^k = T^{k-1} + dT \qquad\qquad p^k = p^{k-1} + dp \tag{D.2.1}$$

The two convergence criteria will be de/e and dv/v, with a tolerance fixed at 10^{-6}:

$$de = e^{N+1} - e^k(X^{N+1}, p^k, T^k) \qquad dv = v^{N+1} - v^k(X^{N+1}, p^k, T^k) \tag{D.2.2}$$

The differentiation of pressure and temperature yields:

$$dT = \left(\frac{\partial T}{\partial v}\right)_{e,X}^{k-1} dv + \left(\frac{\partial T}{\partial e}\right)_{v,X}^{k-1} de + \sum_i \left(\frac{\partial T}{\partial X_i}\right)_{v,e,X_{j,i\neq j}}^{k-1} dX_i \tag{D.2.3}$$

$$dp = \left(\frac{\partial p}{\partial v}\right)_{e,X}^{k-1} dv + \left(\frac{\partial p}{\partial e}\right)_{v,X}^{k-1} de + \sum_i \left(\frac{\partial p}{\partial X_i}\right)_{v,e,X_{j,i\neq j}}^{k-1} dX_i \tag{D.2.4}$$

At this stage of the algorithm, the species mass fractions is assumed to be known through the conservation equations. This has two main consequences. First, the above equations do not contain the species summation term anymore. Second, it means there is a direct equivalence between the molar quantities and the massic quantities. That is why the massic quantities with low case letters will be used in this formulation.

Using relations derived previous, and in particular Section D.1, it is possible to compute the derivatives required by the real gas solver:

$$\left(\frac{\partial T}{\partial v}\right)_e = \frac{-1}{\left(\frac{\partial v}{\partial e}\right)_T \left(\frac{\partial e}{\partial T}\right)_v} \qquad \text{(triple product)} \tag{D.2.5}$$

$$= \frac{-\left(\frac{\partial e}{\partial v}\right)_T}{c_v} \qquad \text{(should be 0 for an IG)} \tag{D.2.6}$$

$$= \frac{-1}{c_v}\left(\left(\frac{\partial a}{\partial v}\right)_T + T\left(\frac{\partial s}{\partial v}\right)_T\right) \qquad (e = a + Ts) \tag{D.2.7}$$

$$= \frac{-1}{c_v}\left(-p + T\left(\frac{\partial p}{\partial T}\right)_v\right) \qquad \text{(from (D.1.8) and (D.1.14))} \tag{D.2.8}$$

$$= \frac{p - T\frac{\alpha_v}{\kappa_T}}{c_v} \qquad \text{(indeed 0 for an IG)} \tag{D.2.9}$$

$$\left(\frac{\partial T}{\partial e}\right)_v = \frac{1}{\left(\frac{\partial e}{\partial T}\right)_v} = \frac{1}{c_v} \tag{D.2.10}$$

$$\left(\frac{\partial p}{\partial v}\right)_e = \left(\frac{\partial p}{\partial T}\right)_e \left(\frac{\partial T}{\partial v}\right)_e \quad \text{(chain rule)} \tag{D.2.11}$$

$$= \left(\frac{\partial e}{\partial T}\right)_p \left(\frac{\partial p}{\partial e}\right)_T \left(\frac{\partial e}{\partial v}\right)_T \left(\frac{\partial T}{\partial e}\right)_v \quad \text{(triple product)} \tag{D.2.12}$$

$$= \left(\frac{\partial e}{\partial T}\right)_p \left(\frac{\partial p}{\partial v}\right)_T \frac{1}{c_v} \quad \text{(chain rule and (D.2.10))} \tag{D.2.13}$$

$$= \left(\left(\frac{\partial h}{\partial T}\right)_p + p\left(\frac{\partial v}{\partial T}\right)_p\right) \frac{-1}{v\kappa_T}\frac{1}{c_v} \quad (h = e + pv) \text{ and from (D.1.23)} \tag{D.2.14}$$

$$= (c_p - pv\alpha_v)\frac{-1}{vc_v}\frac{1}{\kappa_T} \tag{D.2.15}$$

$$= -\frac{c_v^*}{c_v}\frac{1}{v\kappa_T} \tag{D.2.16}$$

where a pseudo specific heat at constant volume c_v^* has been introduced as $c_v^* = c_p - pv\alpha_v$. For an ideal gas, $c_v^* = c_v$ and $\left(\frac{\partial p}{\partial v}\right)_e = -\frac{p}{v}$.

$$\left(\frac{\partial p}{\partial e}\right)_v = \left(\frac{\partial p}{\partial T}\right)_v \left(\frac{\partial T}{\partial e}\right)_v = \frac{1}{c_v}\frac{\alpha_v}{\kappa_T} \tag{D.2.17}$$

$$= \frac{p}{c_V T} \text{ (for an ideal gas)} \tag{D.2.18}$$

Similarly, to go from enthalpy and volume to temperature and pressure, we have the following formulation:

$$dT = \left(\frac{\partial T}{\partial v}\right)_{h,X}^{k-1} dv + \left(\frac{\partial T}{\partial h}\right)_{v,X}^{k-1} dh + \sum_i \left(\frac{\partial T}{\partial X_i}\right)_{v,h,X_{j,i\neq j}}^{k-1} dX_i \tag{D.2.19}$$

$$dp = \left(\frac{\partial p}{\partial v}\right)_{h,X}^{k-1} dv + \left(\frac{\partial p}{\partial h}\right)_{v,X}^{k-1} dh + \sum_i \left(\frac{\partial p}{\partial X_i}\right)_{v,h,X_{j,i\neq j}}^{k-1} dX_i \tag{D.2.20}$$

To compute these derivatives, a pseudo specific heat at constant pressure $c_p^* = c_v + \frac{v\alpha_v}{\kappa_T}$ is introduced. This could define a pseudo specific gas constant:

$$R^* = c_p^* - c_v^* = -R + v\alpha_v\left(\frac{1}{\kappa_T} + p\right) \tag{D.2.21}$$

$$(= -R + 2R = R \text{ for an IG}) \tag{D.2.22}$$

$$\left(\frac{\partial T}{\partial v}\right)_h = \frac{-1}{\left(\frac{\partial v}{\partial h}\right)_T \left(\frac{\partial h}{\partial T}\right)_v} \qquad \text{(triple product)} \tag{D.2.23}$$

$$= \frac{-\left(\frac{\partial h}{\partial v}\right)_T}{\left(\frac{\partial h}{\partial T}\right)_v} \tag{D.2.24}$$

$$= \frac{-\left(\frac{\partial e}{\partial v}\right)_T - \left(\frac{\partial (pv)}{\partial v}\right)_T}{\left(\frac{\partial e}{\partial T}\right)_v + \left(\frac{\partial (pv)}{\partial T}\right)_v} \qquad (h = e + pv) \tag{D.2.25}$$

$$= \frac{\left(p - T\frac{\alpha_v}{\kappa_T}\right) - p - v\left(\frac{\partial p}{\partial v}\right)_T}{c_v + v\left(\frac{\partial p}{\partial T}\right)_v} \tag{D.2.26}$$

$$= \frac{-T\frac{\alpha_v}{\kappa_T} + \frac{1}{\kappa_T}}{c_v + \frac{v\alpha_v}{\kappa_T}} \tag{D.2.27}$$

$$= \frac{1 - T\alpha_v}{\kappa_T c_p^*} \qquad \text{(0 for an IG)} \tag{D.2.28}$$

$$\left(\frac{\partial T}{\partial h}\right)_v = \frac{1}{\left(\frac{\partial h}{\partial T}\right)_v} \tag{D.2.29}$$

$$= \frac{1}{c_v + \frac{v\alpha_v}{\kappa_T}} \tag{D.2.30}$$

$$= \frac{1}{c_p^*} \qquad \left(\frac{1}{c_p} \text{ for an IG}\right) \tag{D.2.31}$$

$$\left(\frac{\partial p}{\partial v}\right)_h = \left(\frac{\partial p}{\partial T}\right)_h \left(\frac{\partial T}{\partial v}\right)_h \qquad \text{(chain rule)} \tag{D.2.32}$$

$$= \left(\frac{\partial h}{\partial T}\right)_p \left(\frac{\partial p}{\partial h}\right)_T \left(\frac{\partial h}{\partial v}\right)_T \left(\frac{\partial T}{\partial h}\right)_v \qquad \text{(triple product)} \tag{D.2.33}$$

$$= \frac{c_p}{c_p^*}\left(\frac{\partial p}{\partial v}\right)_T \qquad \text{(chain rule and from (D.2.31))} \tag{D.2.34}$$

$$= \frac{c_p}{c_p^*}\frac{-1}{v\kappa_T} \qquad \left(= -\frac{p}{v} \text{ for an IG}\right) \tag{D.2.35}$$

$$\left(\frac{\partial p}{\partial h}\right)_v = \left(\frac{\partial p}{\partial T}\right)_v \left(\frac{\partial T}{\partial h}\right)_v \tag{D.2.36}$$

$$= \frac{\alpha_v}{c_p^* \kappa_T} \qquad \left(= \frac{p}{c_p T} \text{ for an IG}\right) \tag{D.2.37}$$

Similarly, to go from enthalpy and pressure to temperature and volume, we have the following formulation:

$$dT = \left(\frac{\partial T}{\partial p}\right)_{h,X}^{k-1} dp + \left(\frac{\partial T}{\partial h}\right)_{p,X}^{k-1} dh + \sum_i \left(\frac{\partial T}{\partial X_i}\right)_{p,h,X_{j,i\neq j}}^{k-1} dX_i \tag{D.2.38}$$

$$dv = \left(\frac{\partial v}{\partial p}\right)^{k-1}_{h,X} dp + \left(\frac{\partial v}{\partial h}\right)^{k-1}_{p,X} dh + \sum_i \left(\frac{\partial v}{\partial X_i}\right)^{k-1}_{p,h,X_{j,i\neq j}} dX_i \tag{D.2.39}$$

$$\left(\frac{\partial T}{\partial p}\right)_h = \frac{-1}{\left(\frac{\partial p}{\partial h}\right)_T \left(\frac{\partial h}{\partial T}\right)_p} \qquad \text{(triple product)} \tag{D.2.40}$$

$$= \frac{-\left(\frac{\partial h}{\partial p}\right)_T}{c_p} \tag{D.2.41}$$

$$= \frac{-\left(\frac{\partial g}{\partial p}\right)_T + \left(\frac{\partial (Ts)}{\partial p}\right)_T}{c_p} \qquad (h = g - Ts) \tag{D.2.42}$$

$$= \frac{-v + T\left(\frac{\partial s}{\partial p}\right)_T}{c_p} \tag{D.2.43}$$

$$= \frac{-v - T\left(\frac{\partial v}{\partial T}\right)_p}{c_p} \tag{D.2.44}$$

$$= \frac{-v(1 - T\alpha_v)}{c_p} \qquad (= 0 \text{ for an IG}) \tag{D.2.45}$$

$$\left(\frac{\partial T}{\partial h}\right)_p = \frac{1}{\left(\frac{\partial h}{\partial T}\right)_p} \tag{D.2.46}$$

$$= \frac{1}{c_p} \qquad \left(= \frac{1}{c_p} \text{ for an IG}\right) \tag{D.2.47}$$

$$\left(\frac{\partial v}{\partial p}\right)_h = \left(\frac{\partial v}{\partial T}\right)_h \left(\frac{\partial T}{\partial p}\right)_h \qquad \text{(chain rule)} \tag{D.2.48}$$

$$= \left(\frac{\partial h}{\partial T}\right)_v \left(\frac{\partial v}{\partial h}\right)_T \left(\frac{\partial h}{\partial p}\right)_T \left(\frac{\partial T}{\partial h}\right)_p \qquad \text{(triple product)} \tag{D.2.49}$$

$$= \frac{\left(\frac{\partial e}{\partial T}\right)_v + v\left(\frac{\partial p}{\partial T}\right)_v}{c_p} \left(\frac{\partial v}{\partial p}\right)_T \qquad (h = e + pv, \text{ chain rule and from (D.2.47)}) \tag{D.2.50}$$

$$= -\frac{c_v + v\frac{\alpha_v}{\kappa_T}}{c_p} v\kappa_T \tag{D.2.51}$$

$$= -\frac{c_p^*}{c_p} v\kappa_T \qquad \left(= -\frac{v}{p} \text{ for an IG}\right) \tag{D.2.52}$$

$$\left(\frac{\partial v}{\partial h}\right)_p = \left(\frac{\partial v}{\partial T}\right)_p \left(\frac{\partial T}{\partial h}\right)_p \tag{D.2.53}$$

$$= -\frac{v\alpha_v}{c_p} \qquad \left(= \frac{v}{c_p T} \text{ for an IG}\right) \tag{D.2.54}$$

D.2.1 Derivation of the partial molar volume for the PR EoS

Background information on partial molar quantities is given in Section 2.5.6.6. For the partial molar volume, it is easier to make pressure appear in the partial derivatives:

$$V_{,l} = \left(\frac{\partial \mathcal{V}}{\partial N_l}\right)_{T,p,N_{k,k\neq l}} = \left(\frac{\partial \mathcal{V}}{\partial p}\right)_{T,N} \left(\frac{\partial p}{\partial N_l}\right)_{T,\mathcal{V},N_{k,k\neq l}} \tag{D.2.55}$$

The equation of state expression involving the extensive volume is:

$$p = \frac{NR_uT}{\mathcal{V} - NB_m} - \frac{N^2 A_m}{\mathcal{V}^2 + 2NB_m\mathcal{V} - N^2B_m^2} \tag{D.2.56}$$

$$\left(\frac{\partial p}{\partial \mathcal{V}}\right)_{T,N} = -\frac{NR_uT}{(\mathcal{V} - NB_m)^2} - \frac{N^2A_m\left(2\mathcal{V} + 2NB_m\right)}{\left(\mathcal{V}^2 + 2NB_m\mathcal{V} - N^2B_m^2\right)^2} \tag{D.2.57}$$

$$\left(\frac{\partial p}{\partial \mathcal{V}}\right)_{T,N} = \frac{1}{N}\left(-\frac{R_uT}{(V - B_m)^2} - \frac{2A_m(V + B_m)}{\left(V^2 + 2B_mV - B_m^2\right)^2}\right) \quad = \frac{1}{N}\left(\frac{\partial p}{\partial V}\right)_{T,N} \tag{D.2.58}$$

$$\begin{aligned}\left(\frac{\partial p}{\partial N_l}\right)_{T,\mathcal{V},N_{k,k\neq l}} &= \frac{R_uT}{\mathcal{V} - NB_m} - \frac{-B_lNR_uT}{(\mathcal{V} - NB_m)^2} \\ &- \frac{2\sum_{k=1}^{N_S} A_{lk}N_k}{\mathcal{V}^2 + 2NB_m\mathcal{V} - N^2B_m^2} \\ &+ \frac{\left(-2NB_mB_l + 2\mathcal{V}B_l\right)N^2A_m}{\left(\mathcal{V}^2 + 2NB_m\mathcal{V} - N^2B_m^2\right)^2}\end{aligned} \tag{D.2.59}$$

because:

$$NB_m = N\sum_{k=1}^{N_S}\frac{N_k}{N}B_k = \sum_{k=1}^{N_S} N_kB_k \tag{D.2.60}$$

$$\left(\frac{\partial NB_m}{\partial N_l}\right)_{T,\mathcal{V},N_{k,k\neq l}} = B_l \tag{D.2.61}$$

$$N^2A_m = N^2\sum_{j=1}^{N_S}\sum_{k=1}^{N_S}\frac{N_j}{N}\frac{N_k}{N}A_{jk} = \sum_{j=1}^{N_S}\sum_{k=1}^{N_S} N_jN_kA_{jk} \tag{D.2.62}$$

$$= 2\sum_{j=1}^{N_S} N_jN_lA_{jl} + \sum_{\substack{j=1\\j\neq l}}^{N_S}\sum_{\substack{k=1\\k\neq l}}^{N_S} N_jN_kA_{jk} \tag{D.2.63}$$

$$\left(\frac{\partial N^2A_m}{\partial N_l}\right)_{T,\mathcal{V},N_{k,k\neq l}} = 2\sum_{j=1}^{N_S} N_jA_{jl} \tag{D.2.64}$$

Plugging Eq. D.2.58 and Eq. D.2.59 into Eq. 2.5.111, this finally yields:

$$V_{,l} = -\left(\frac{\partial V}{\partial p}\right)_{T,X}\left(\frac{R_u T}{V-B_m} + \frac{B_l R_u T}{(V-B_m)^2} - \frac{2\sum_{k=1}^{N_S} X_k A_{lk}}{V^2+2VB_m-B_m^2} + \frac{2A_m(V-B_m)B_l}{(V^2+2VB_m-B_m^2)^2}\right) \tag{D.2.65}$$

The partial derivative is easily computed from the original expression for the PR EoS (Eq. 2.5.22):

$$\left(\frac{\partial p}{\partial V}\right)_{T,X} = -\frac{R_u T}{(V-B_m)^2} + \frac{2A_m\left(V+B_m\right)}{\left(V^2+2VB_m-B_m^2\right)^2} \tag{D.2.66}$$

One can then verifies that the sum of the partial molar volumes is equal to the molar volume of the mixture:

$$\begin{aligned}\sum_{l=1}^{N_S} X_l V_{,l} &= -\left(\frac{\partial V}{\partial p}\right)_{T,X}\left(\frac{R_u T}{V-B_m} + \frac{B_m R_u T}{(V-B_m)^2} - \frac{2A_m}{V^2+2VB_m-B_m^2} + \frac{2A_m(V-B_m)B_m}{(V^2+2VB_m-B_m^2)^2}\right)\\ &= -\left(\frac{\partial V}{\partial p}\right)_{T,X}\left(\frac{VR_u T}{(V-B_m)^2} - \frac{2A_m V(V+B_m)}{(V^2+2VB_m-B_m^2)^2}\right)\\ &= +V\left(\frac{\partial V}{\partial p}\right)_{T,X}\left(\frac{\partial p}{\partial V}\right)_{T,X} = V\end{aligned} \tag{D.2.67}$$

D.2.2 Derivation of the partial molar volume for the RK EoS

The equation of state expression involving the extensive volume is:

$$p = \frac{NR_u T}{\mathcal{V}-NB_m} - \frac{N^2 A_m}{\mathcal{V}^2+NB_m\mathcal{V}} \tag{D.2.68}$$

$$\left(\frac{\partial p}{\partial \mathcal{V}}\right)_{T,N} = -\frac{NR_u T}{\left(\mathcal{V}-NB_m\right)^2} - \frac{N^2 A_m\left(2\mathcal{V}+NB_m\right)}{\left(\mathcal{V}^2+2NB_m\mathcal{V}\right)^2} \tag{D.2.69}$$

$$\left(\frac{\partial p}{\partial \mathcal{V}}\right)_{T,N} = \frac{1}{N}\left(-\frac{R_u T}{\left(V-B_m\right)^2} - \frac{A_m(2V+B_m)}{\left(V^2+B_m V\right)^2}\right) \qquad = \frac{1}{N}\left(\frac{\partial p}{\partial V}\right)_{T,N} \tag{D.2.70}$$

$$\begin{aligned}\left(\frac{\partial p}{\partial N_l}\right)_{T,\mathcal{V},N_{k,k\neq l}} &= \frac{R_u T}{\mathcal{V}-NB_m} - \frac{-B_l N R_u T}{\left(\mathcal{V}-NB_m\right)^2}\\ &\quad - \frac{2\sum_{k=1}^{N_S} A_{lk}N_k}{\mathcal{V}^2+NB_m\mathcal{V}}\\ &\quad + \frac{\mathcal{V}B_l N^2 A_m}{\left(\mathcal{V}^2+NB_m\mathcal{V}\right)^2}\end{aligned} \tag{D.2.71}$$

Plugging Eq. D.2.70 and Eq. D.2.71 into Eq. 2.5.111, this finally yields:

$$V_{,l} = -\left(\frac{\partial V}{\partial p}\right)_{T,X}\left(\frac{R_u T}{V-B_m} + \frac{B_l R_u T}{(V-B_m)^2} - \frac{2\sum_{k=1}^{N_S} X_k A_{lk}}{V^2+VB_m} + \frac{A_m V B_l}{(V^2+VB_m)^2}\right) \tag{D.2.72}$$

The partial derivative is easily computed from the original expression for the PR EoS (Eq. 2.5.22):

$$\left(\frac{\partial p}{\partial V}\right)_{T,X} = -\frac{R_u T}{(V-B_m)^2} + \frac{A_m\,(2V+B_m)}{(V^2+VB_m)^2} \tag{D.2.73}$$

One can then verifies that the sum of the partial molar volumes is equal to the molar volume of the mixture:

$$\begin{aligned}\sum_{l=1}^{N_S} X_l V_{,l} &= -\left(\frac{\partial V}{\partial p}\right)_{T,X}\left(\frac{R_u T}{V-B_m} + \frac{B_m R_u T}{(V-B_m)^2} - \frac{2A_m}{V^2+VB_m} + \frac{A_m V B_m}{(V^2+VB_m)^2}\right)\\ &= -\left(\frac{\partial V}{\partial p}\right)_{T,X}\left(\frac{V R_u T}{(V-B_m)^2} - \frac{2A_m V^2 + A_m V B_m}{(V^2+VB_m)^2}\right)\\ &= +V\left(\frac{\partial V}{\partial p}\right)_{T,X}\left(\frac{\partial p}{\partial V}\right)_{T,X} = V\end{aligned} \tag{D.2.74}$$

D.2.3 Derivation of the partial molar enthalpy for the PR EoS

Background information on partial molar quantities is given in Section 2.5.6.6. The derivation starts from the departure function for enthalpy obtained in Eq. 2.5.79:

$$\begin{aligned}H_{,l} = \left(\frac{\partial \mathcal{H}}{\partial N_l}\right)_{T,p,N_{k,k\neq l}} &= \left(\frac{\partial N H^{\mathrm{ig}}}{\partial N_l}\right)_{T,p,N_{k,k\neq l}} + pV_{,l} - R_u T\\ &+ \left(\frac{\partial \frac{1}{2\sqrt{2}NB_m}\ln\left(\frac{V+(1-\sqrt{2})B_m}{V+(1+\sqrt{2})B_m}\right)\left(A_m N^2 - T\frac{\partial A_m N^2}{\partial T}\right)}{\partial N_l}\right)_{T,p,N_{k,k\neq l}}\end{aligned} \tag{D.2.75}$$

Splitting the derivatives:

$$\begin{aligned}H_{,l} &= H_l^{\mathrm{ig}} + pV_{,l} - R_u T\\ &+ N^2\left(A_m - T\frac{\partial A_m}{\partial T}\right)\left(\frac{\partial \frac{1}{2\sqrt{2}NB_m}\ln\left(\frac{\left(V+(1-\sqrt{2})B_m\right)}{\left(V+(1+\sqrt{2})B_m\right)}\right)}{\partial N_l}\right)_{T,p,N_{k,k\neq l}}\\ &+ \frac{1}{N}K_1\left(\frac{\partial\left(A_m N^2 - T\frac{\partial A_m N^2}{\partial T}\right)}{\partial N_l}\right)_{T,p,N_{k,k\neq l}}\end{aligned}$$

$$
\begin{aligned}
H_{,l} &= H_l^{\mathrm{ig}} + pV_{,l} - R_u T \\
&- \left(A_m - T\frac{\partial A_m}{\partial T}\right)\frac{B_l}{2\sqrt{2}B_m^2}\ln\left(\frac{\left(V+(1-\sqrt{2})B_m\right)}{\left(V+(1+\sqrt{2})B_m\right)}\right) \\
&+ \left(A_m - T\frac{\partial A_m}{\partial T}\right)\frac{N}{2\sqrt{2}B_m}\left(\frac{\frac{\partial\left(V+(1-\sqrt{2})B_m\right)}{\partial N_l}}{\left(V+(1-\sqrt{2})B_m\right)} - \frac{\frac{\partial\left(V+(1+\sqrt{2})B_m\right)}{\partial N_l}}{\left(V+(1+\sqrt{2})B_m\right)}\right) \\
&+ \frac{1}{N}K_1\left(\sum_{j=1}^{N_S} 2N_j A_{jl} - T\frac{\partial\sum_{j=1}^{N_S} 2N_j A_{jl}}{\partial T}\right)
\end{aligned}
$$

$$
\begin{aligned}
H_{,l} &= H_l^{\mathrm{ig}} + pV_{,l} - R_u T \\
&- \left(A_m - T\frac{\partial A_m}{\partial T}\right)\frac{B_l}{B_m}K_1 \\
&+ \left(A_m - T\frac{\partial A_m}{\partial T}\right)\frac{1}{2\sqrt{2}B_m}\left(\frac{V_{,l}+(1-\sqrt{2})B_l}{\left(V+(1-\sqrt{2})B_m\right)} - \frac{V_{,l}+(1+\sqrt{2})B_l}{\left(V+(1+\sqrt{2})B_m\right)}\right) \\
&+ K_1\left(2\sum_{j=1}^{N_S} X_j A_{jl} - 2T\sum_{j=1}^{N_S} X_j\frac{\partial A_{jl}}{\partial T}\right)
\end{aligned}
$$

A final regrouping introduces the following quantities and allows for a more readable expression:

$$X^- = \left(V+(1-\sqrt{2})B_m\right) \tag{D.2.76}$$

$$X^+ = \left(V+(1+\sqrt{2})B_m\right) \tag{D.2.77}$$

$$K_1 = \frac{1}{2\sqrt{2}B_m}\ln\frac{X^-}{X^+} \tag{D.2.78}$$

This yields for the partial molar enthalpy:

$$
\begin{aligned}
H_{,l} &= H_l^{\mathrm{ig}} + pV_{,l} - R_u T \\
&+ \left(A_m - T\frac{\partial A_m}{\partial T}\right)\left(\frac{V_{,l} - V\frac{B_l}{B_m}}{X^- X^+}\right) \\
&+ K_1\left(2\sum_{j=1}^{N_S} X_j A_{jl} - 2T\sum_{j=1}^{N_S} X_j\frac{\partial A_{jl}}{\partial T} - \left(A_m - T\frac{\partial A_m}{\partial T}\right)\frac{B_l}{B_m}\right)
\end{aligned}
\tag{D.2.79}
$$

This matches expressions found in the literature [196, 231] based on relationships derived earlier (see Eqs. 2.5.54 and 2.5.59). One can then verifies that the sum of the partial molar

enthalpies is equal to the molar enthalpy of the mixture:

$$\begin{aligned}\sum_{l=1}^{N_S} X_l H_{,l} &= H^{\mathrm{ig}} + pV - R_u T \\ &\quad + \left(A_m - T\frac{\partial A_m}{\partial T}\right)\frac{V - V\frac{B_m}{B_m}}{X^- X^+} \\ &\quad + K_1\left(2A_m - 2T\frac{\partial A_m}{\partial T} - \left(A_m - T\frac{\partial A_m}{\partial T}\right)\frac{B_m}{B_m}\right) \\ &= H^{\mathrm{ig}} + pV - R_u T + K_1\left(A_m - T\frac{\partial A_m}{\partial T}\right) = H\end{aligned} \tag{D.2.80}$$

D.2.4 Derivation of the partial molar enthalpy for the RK EoS

The derivation starts from the departure function for enthalpy obtained in Eq. 2.5.80:

$$\begin{aligned}H_{,l} = \left(\frac{\partial \mathcal{H}}{\partial N_l}\right)_{T,p,N_{k,k\neq l}} &= \left(\frac{\partial N H^{\mathrm{ig}}}{\partial N_l}\right)_{T,p,N_{k,k\neq l}} + pV_{,l} - R_u T \\ &- \left(\frac{\partial \frac{1}{NB_m}\ln\left(\frac{V}{V+B_m}\right)\left(\frac{3A_m N^2}{2}\right)}{\partial N_l}\right)_{T,p,N_{k,k\neq l}}\end{aligned} \tag{D.2.81}$$

Splitting the derivatives:

$$\begin{aligned}H_{,l} &= H_l^{\mathrm{ig}} + pV_{,l} - R_u T - N^2\frac{3A_m}{2}\left(\frac{\partial \frac{1}{NB_m}\ln\left(\frac{V}{V+B_m}\right)}{\partial N_l}\right)_{T,p,N_{k,k\neq l}} \\ &\quad - \frac{1}{NB_m}\ln\left(\frac{V}{V+B_m}\right)\left(\frac{\partial \frac{3A_m N^2}{2}}{\partial N_l}\right)_{T,p,N_{k,k\neq l}}\end{aligned}$$

$$\begin{aligned}H_{,l} &= H_l^{\mathrm{ig}} + pV_{,l} - R_u T + \frac{3A_m B_l}{2B_m^2}\ln\left(\frac{V}{V+B_m}\right) \\ &\quad - \frac{3A_m}{2}\left(\frac{V_l - V\frac{B_l}{B_m}}{V(V+B_m)}\right) \\ &\quad - \frac{1}{NB_m}\ln\left(\frac{V}{V+B_m}\right)\left(\sum_{j=1}^{N_S} 3N_j A_{jl}\right)\end{aligned}$$

This yields for the partial molar enthalpy:

$$H_{,l} = H_l^{\mathrm{ig}} + pV_{,l} - R_u T - \frac{3A_m}{2}\frac{B_l}{B_m}K_1 + \frac{3A_m}{2}\left(\frac{V_l - V\frac{B_l}{B_m}}{V(V+B_m)}\right) + 3K_1\sum_{j=1}^{N_S} X_j A_{jl} \tag{D.2.82}$$

One can then verifies that the sum of the partial molar enthalpies is equal to the molar enthalpy of the mixture:

$$\begin{aligned}\sum_{l=1}^{N_S} X_l H_{,l} &= H^{\text{ig}} + pV - R_u T - \frac{3A_m}{2} K_1 + \frac{3A_m}{2} 0 + 3A_m K1 \\ &= H^{\text{ig}} + pV - R_u T + K_1 \left(A_m - T \frac{\partial A_m}{\partial T} \right) = H \end{aligned} \tag{D.2.83}$$

D.2.5 Derivation of the partial molar specific heats for the PR EoS

Starting from Eq. D.2.79, it is not straightforward to obtain an expression for the partial molar specific heat at constant pressure. It is easier to start from the partial molar internal energy and first compute the partial molar specific heat at constant volume:

$$\begin{aligned} E_{,l} - E_l^{\text{ig}} &= H_{,l} - H_l^{\text{ig}} - pV_{,l} + R_u T \\ &= \left(A_m - T \frac{\partial A_m}{\partial T} \right) \left(\frac{V_{,l} - V \frac{B_l}{B_m}}{X^- X^+} \right) \\ &+ K_1 \left(2 \sum_{j=1}^{N_S} X_j A_{jl} - 2T \sum_{j=1}^{N_S} X_j \frac{\partial A_{jl}}{\partial T} - \left(A_m - T \frac{\partial A_m}{\partial T} \right) \frac{B_l}{B_m} \right) \end{aligned} \tag{D.2.84}$$

$$\begin{aligned} C_{V,l} &= \left(\frac{\partial E_{,l}}{\partial T} \right)_{V,X} \\ &= C_{V,l}^{\text{ig}} - T \frac{\partial^2 A_m}{\partial T^2} \frac{V_{,l} - V \frac{B_l}{B_m}}{X^- X^+} + K_1 \left(-2T \sum_{j=1}^{N_S} X_j \frac{\partial^2 A_{jl}}{\partial T^2} + T \frac{\partial^2 A_m}{\partial T^2} \frac{B_l}{B_m} \right) \end{aligned} \tag{D.2.85}$$

It is easy to verify that the additive rule is verified for the specific heat at constant volume:

$$\sum_{l=1}^{N_S} X_l C_{V,l} = C_V^{\text{ig}} - T \frac{\partial^2 A_m}{\partial T^2} \frac{V - V \frac{B_m}{B_m}}{X^- X^+} + K_1 \left(-2T \frac{\partial^2 A_m}{\partial T^2} + T \frac{\partial^2 A_m}{\partial T^2} \frac{B_m}{B_m} \right) \tag{D.2.86}$$

$$= C_V^{\text{ig}} - K_1 T \frac{\partial^2 A_m}{\partial T^2} = C_V \tag{D.2.87}$$

Moving on to the specific heat at constant pressure, Equation 2.5.88 still applies for the partial molar specific heats:

$$C_{p,l} - C_{V,l} = T \frac{\left(\frac{\partial \alpha_v^2 NV}{\partial N_l} \right)_{p,T}}{N \kappa_T} - T \frac{\alpha_v^2 NV \left(\frac{\partial N \kappa_T}{\partial N_l} \right)_{p,T}}{N^2 \kappa_T^2}$$

It is recalled that the expansivity α_v and the isothermal compressibility κ_T are defined as:

$$\alpha_v = -\frac{\left(\frac{\partial p}{\partial T}\right)_v}{v\left(\frac{\partial p}{\partial v}\right)_T} \tag{D.2.88}$$

$$\kappa_T = -\frac{1}{v\left(\frac{\partial p}{\partial v}\right)_T} \tag{D.2.89}$$

Given the complexity of these derivatives and the associated cost, a simpler model for the partial molar specific heat at constant pressure is assumed here:

$$C_{p,l} - C_{V,l} = -T\frac{\left(\frac{\partial p}{\partial T}\right)^2_{V,X}}{\left(\frac{\partial p}{\partial V}\right)_{T,X}} \tag{D.2.90}$$

For the PR EoS, it can be shown that:

$$\alpha_v = -\frac{1}{V}\frac{R_u\left(V-B_m\right)\left(X^-X^+\right)^2 - \frac{\partial A_m}{\partial T}X^-X^+\left(V-B_m\right)^2}{2A_m\left(V-B_m\right)^2\left(V+B_m\right) - X^-X^+R_uT} \tag{D.2.91}$$

Using Equations 2.5.65 and 2.5.66 leads to the following expression for the partial molar specific heat, which of course satisfies the additive rule:

$$\begin{aligned} C_{p,l} = C^{\text{ig}}_{V,l} &- T\frac{\partial^2 A_m}{\partial T^2}\frac{V_{,l} - V\frac{B_l}{B_m}}{X^-X^+} + K_1\left(-2T\sum_{j=1}^{N_S}X_j\frac{\partial^2 A_{jl}}{\partial T^2} + T\frac{\partial^2 A_m}{\partial T^2}\frac{B_l}{B_m}\right) \\ &- T\frac{\left(X^-X^+R_u\right)^2 + \frac{\partial A_m}{\partial T}\left(V-B_m\right)^2 - R_u\frac{\partial A_m}{\partial T}X^-X^+\left(V-B_m\right)}{2A_m\left(V-B_m\right)^2\left(V+B_m\right) - X^-X^+R_uT} \end{aligned} \tag{D.2.92}$$

D.2.6 Derivation of the partial molar specific heats for the RK EoS

Starting from Eq. D.2.82, it is not straightforward to obtain an expression for the partial molar specific heat at constant pressure. It is easier to start from the partial molar internal energy and first compute the partial molar specific heat at constant volume:

$$\begin{aligned} E_{,l} - E^{\text{ig}}_l &= H_{,l} - H^{\text{ig}}_l - pV_{,l} + R_uT \\ &= -\frac{3A_m}{2}\frac{B_l}{B_m}K_1 \\ &+ \frac{3A_m}{2}\left(\frac{V_l - V\frac{B_l}{B_m}}{V(V+B_m)}\right) \\ &+ 3K_1\sum_{j=1}^{N_S}X_jA_{jl} \end{aligned} \tag{D.2.93}$$

$$C_{V,l} = \left(\frac{\partial E_{,l}}{\partial T}\right)_{V,X}$$

$$= C_{V,l}^{\text{ig}} + \frac{3A_m K_1}{4T}\frac{B_l}{B_m} - \frac{3A_m}{4T}\left(\frac{V_l - V\frac{B_l}{B_m}}{V(V+B_m)}\right) - \frac{3K_1}{2T}\sum_{j=1}^{N_S} X_j A_{jl} \tag{D.2.94}$$

$$= C_{V,l}^{\text{ig}} + \frac{K_1}{2T}\left(\frac{3A_m}{2}\frac{B_l}{B_m} - \frac{3}{2}\left(\frac{\partial A_m}{\partial X_k}\right)_T\right) - \frac{3A_m}{4T}\left(\frac{V_l - V\frac{B_l}{B_m}}{V(V+B_m)}\right) \tag{D.2.95}$$

It is easy to verify that the additive rule is verified for the specific heat at constant volume using 2.5.55:

$$\sum_{l=1}^{N_S} X_l C_{V,l} = C_V^{\text{ig}} - K_1 T\frac{3A_m}{4T^2} = C_V^{\text{ig}} - K_1 T\frac{\partial^2 A_m}{\partial T^2} = C_V \tag{D.2.96}$$

Moving on to the specific heat at constant pressure, Equation 2.5.88 still applies for the partial molar specific heats:

$$C_{p,l} - C_{V,l} = T\frac{\left(\frac{\partial \alpha_v^2 NV}{\partial N_l}\right)_{p,T}}{N\kappa_T} - T\frac{\alpha_v^2 NV\left(\frac{\partial N\kappa_T}{\partial N_l}\right)_{p,T}}{N^2\kappa_T^2}$$

It is recalled that the expansivity α_v and the isothermal compressibility κ_T are defined as:

$$\alpha_v = -\frac{\left(\frac{\partial p}{\partial T}\right)_v}{v\left(\frac{\partial p}{\partial v}\right)_T} \tag{D.2.97}$$

$$\kappa_T = -\frac{1}{v\left(\frac{\partial p}{\partial v}\right)_T} \tag{D.2.98}$$

Given the complexity of these derivatives and the associated cost, a simpler model for the partial molar specific heat at constant pressure is assumed here:

$$C_{p,l} - C_{V,l} = -T\frac{\left(\frac{\partial p}{\partial T}\right)_{V,X}^2}{\left(\frac{\partial p}{\partial V}\right)_{T,X}} \tag{D.2.99}$$

For the RK EoS, it can be shown that:

$$\alpha_v = -\frac{R_u V(V+B_m)^2(V-B_m) + \frac{A_m}{2T}(V+B_m)(V-B_m)^2}{-R_u T V^2(V+B_m)^2 + A_m(2V+B_m)(V-B_m^2)} \tag{D.2.100}$$

Using Equations 2.5.63 and 2.5.64 leads to the following expression for the partial molar specific heat, which of course satisfies the additive rule:

$$C_{p,l} = C_{V,l}^{\text{ig}} + \frac{K_1}{2T}\left(\frac{3A_m}{2}\frac{B_l}{B_m} - 3\sum_{j=1}^{N_S} X_j A_{jl}\right) - \frac{3A_m}{4T}\left(\frac{V_l - V\frac{B_L}{B_m}}{V(V+B_m)}\right) - \frac{1}{4T}\frac{4R_u^2T^2V^2(V+B_m)^2 + A_m^2(V-B_m)^2 + 4A_mR_uT(V-B_m)(V+B_m)V}{A_m(2V+B_m) - R_uT} \tag{D.2.101}$$

D.3 Verification of the real gas formulation

A series of plots of basic thermodynamic properties for various species of interest are presented next.

D.3.1 Single-species properties

D.3.1.1 Oxygen and hydrogen

First, the properties of oxygen and hydrogen for conditions relevant to rocket engine applications are investigated. The operating pressure is chosen as 84.75 bar and the temperature ranges from 120 K to 500 K. For these same conditions, oxygen and hydrogen are in very different thermodynamic states. Figure 115 shows a sample of thermodynamic and transport properties of oxygen under these conditions. The apparition of real gas effects occurs for temperatures as high as 300 K and become more pronounced as the temperature decreases. The crossing of the pseudo-boiling line, or Widom line (see Section 2.5.1) occurs around 170 K as seen by the local maximum of specific heat. This is larger than the critical temperature of 156 K for oxygen. The current formulation with the PR EoS has some difficulties with the density or the viscosity in the compressible liquid domain, but overall, errors are reasonable and always smaller than with an ideal gas formulation. The 10% error in the injection density means the inlet velocity would need to be adjusted by 10% to keep the geometry and the flow-rate constant. And the higher viscosity in the liquid oxygen region would have a small effect on the Reynolds number. The situation for the hydrogen is very different. Since the conditions are very close to a perfect gas (the injection temperature is more than three times the critical temperature of hydrogen), the ideal gas formulation is expected to yield

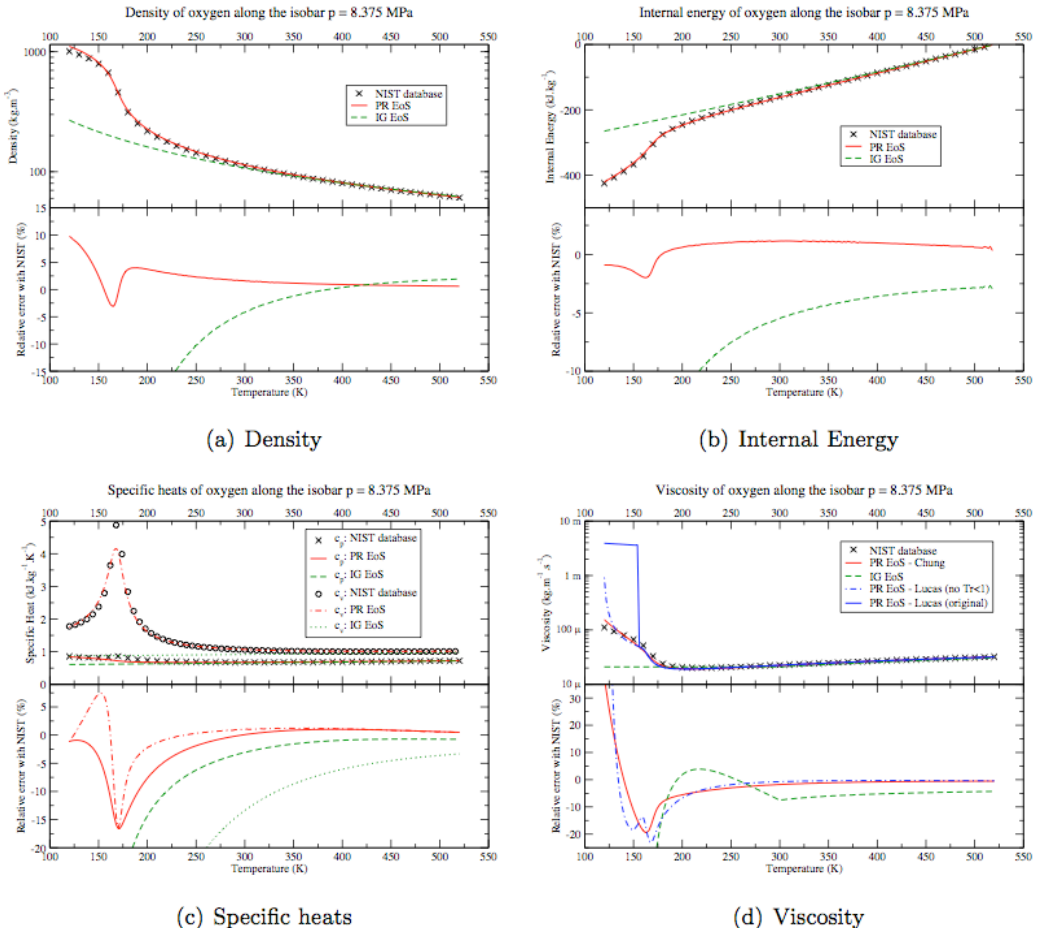

Figure 115: Thermodynamic and transport properties of oxygen at 84 bar and with 120 K $< T <$ 500 K. Bottom part of each graph shows the error of each method relative to the NIST database [146]

properties close to the experimental ones. This is indeed the case as shown in Figure 116. The stairs-like aspect of some curves is due to the limited numerical precision of the NIST database and is only visible because the errors are so small. The PR EoS only improves the prediction of the density by a few percents compared to the IG formulation. For specific heats and internal energy, both formulation produce excellent estimates but there is a large discrepancy for the prediction of the viscosity. H2 is a so-called quantum gas and it is a known limitation of the Chung's formulation that it handles these quantum effects poorly. To the author's knowledge, there exists no consistent fix to this problem that would behave correctly for a mixture of gases. An alternate formulation by Lucas et al. and detailed in Appendix B can better handle these effects but is not as practical nor efficient to use in a CFD solver.

D.3.1.2 Nitrogen

Here, the properties of nitrogen relevant for Chapter 5 are plotted. The pressure is set to 57.5 bar and the temperature ranges between 50 and 350 K. For all properties, the Chung formulation with high pressure corrections is used while the equation of state is varied. The differences between the RK EoS and PR EoS are apparent with the RK EoS providing a better match to the density in the compressed liquid regime but displaying significant error for the specific heat and hence energy. A negative Joule-Thompson coefficient indicate that the fluid would warm when undergoing an adiabatic expansion. Properties for oxygen would be very close to these values given the similarity between the two species.

D.3.2 Multi-component mixtures

Detailed experimental data on multi-component mixtures under conditions where real gas effects are significant are scarce. However, there is a need to properly validate the pseudo-fluid formulation chosen for this work.

The work by Cristancho et al. [48] is considered here. Using magnetically-coupled sinker and balance, they precisely measure a mixture representative of natural gas. One mole of this mixture contains 0.95039 mole of methane, 0.03961 mole of ethane and 0.010000 mole of

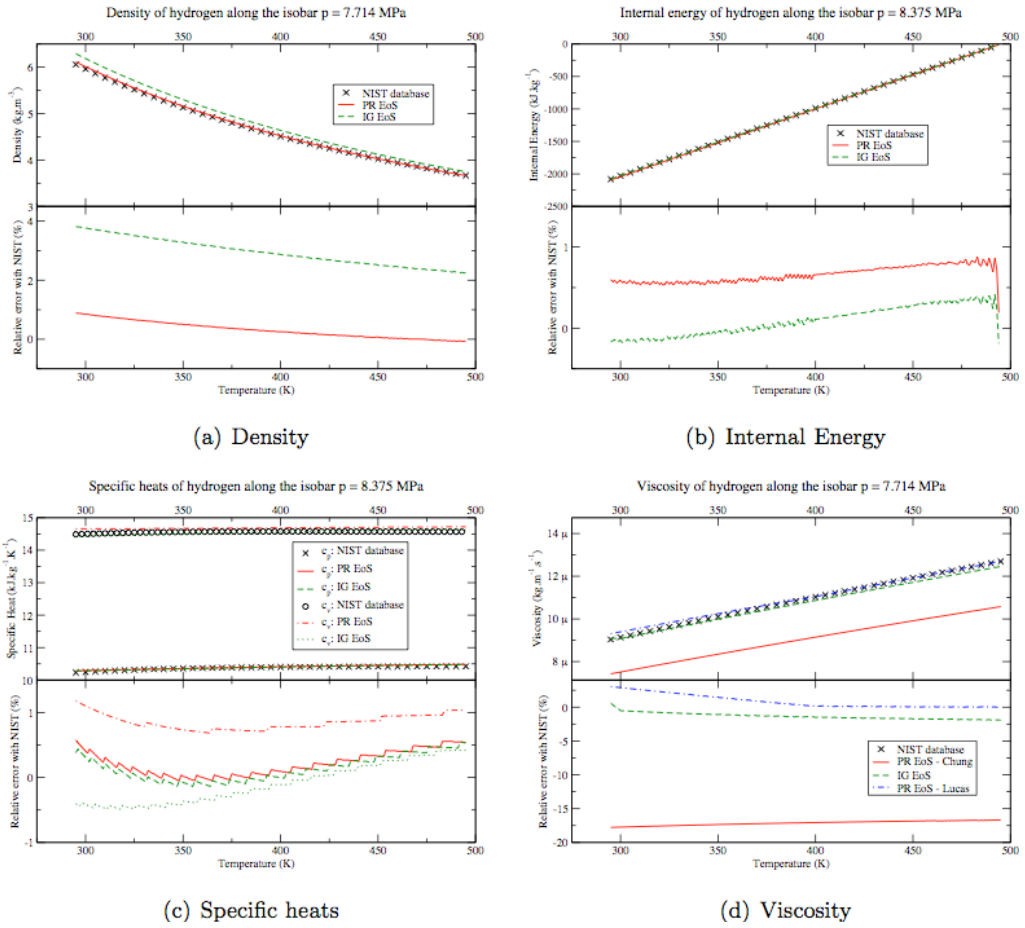

(a) Density

(b) Internal Energy

(c) Specific heats

(d) Viscosity

Figure 116: Thermodynamic and transport properties of hydrogen at 84 bar and with 120 K $< T <$ 500 K. Bottom part of each graph shows the error of each method relative to the NIST database [146].

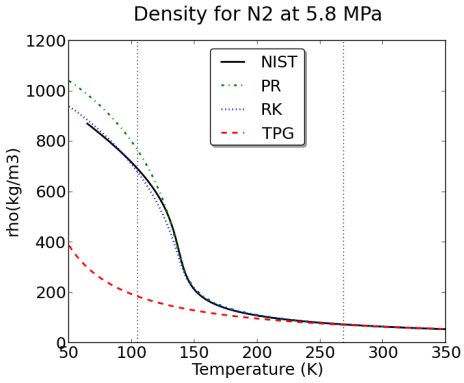

(a) Density

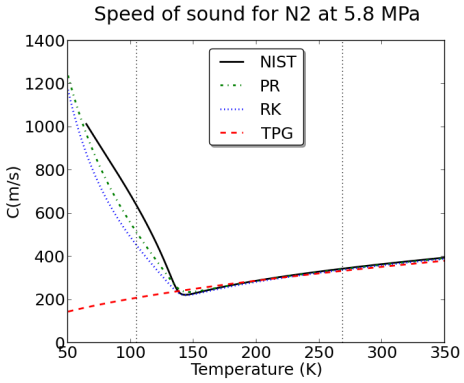

(b) Speed of sound

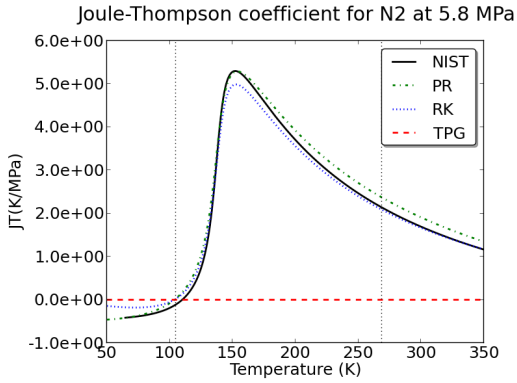

(c) Joule-Thompson coefficient

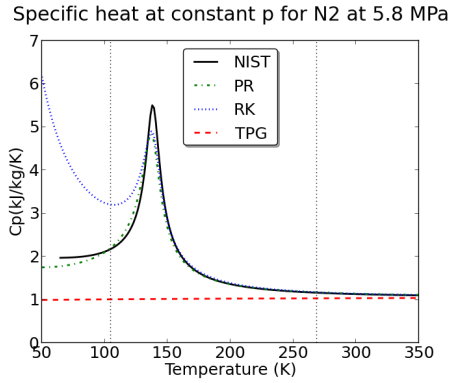

(d) Specific heat

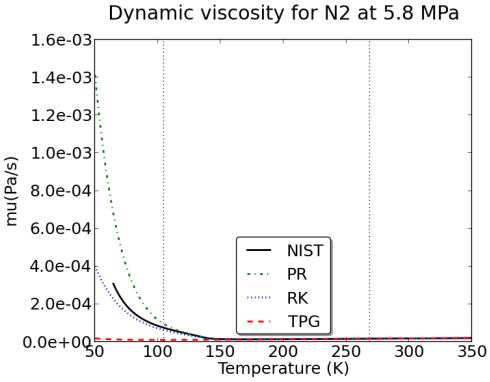

(e) Viscosity

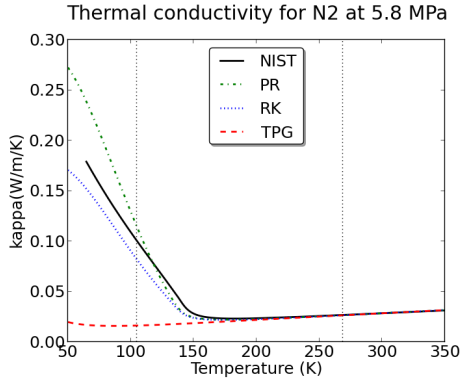

(f) Thermal conductivity

Figure 117: Thermodynamic and transport properties of nitrogen at 57.5 bar and with 50 K $< T <$ 350 K. Vertical lines correspond to the liquid (105 K) and gas (269 K) injection temperatures. The critical temperature of nitrogen is 126 K.

propane. In terms of mass fractions, this translates into 90.331% for methane, 7.0565% for ethane and 2.6125% for propane. Cristancho et al. also provide binary interaction parameters for this mixture based on correlation of experimental data. Figure 118 and Table 21 show the predictions of the current PR EoS formulation and also highlight the influence of the binary interaction parameters. For comparison, multiparameter EoS implemented in commercial softwares [146] can achieve less than 0.04% of error on such experimental data. It is observed that the current formulation does not quite achieve such accuracy but is still within 0.6% of the experimental data. Also, the empirical interaction parameters do not seem to improve at all the predictions of the PR EoS. This experimental data is also useful for verifying the computation of partial molar quantities, in particular the additive rule shown in Eq. 2.5.109. For the conditions (T=350 K, p=4.998 MPa), the partial molar volumes, whose expressions were derived in Section D.2.1, are computed:

$$\begin{aligned} X_{\mathrm{CH4}}V_{,\mathrm{CH4}} + X_{\mathrm{C2H6}}V_{,\mathrm{C2H6}} + X_{\mathrm{C3H8}}V_{,\mathrm{C3H8}} &= 0.95039 \times 0.5584 \times 10^{-3} \\ &+ 0.03961 \times 0.4718 \times 10^{-3} \\ &+ 0.01 \times 0.4072 \times 10^{-3} \\ &= 0.5534 \text{ m3/mol } = \frac{M_{\mathrm{mix}}}{\rho} \end{aligned}$$

The following is obtained for the partial molar enthalpies (see Section D.2.3), knowing that the predicted enthalpy under such conditions is $H = -7.4528 \times 10^4$ J/mol:

$$\begin{aligned} X_{\mathrm{CH4}}H_{,\mathrm{CH4}} + X_{\mathrm{C2H6}}H_{,\mathrm{C2H6}} + X_{\mathrm{C3H8}}H_{,\mathrm{C3H8}} &= -0.95039 \times 7.3853 \times 10^4 \\ &- 0.03961 \times 8.3417 \times 10^4 \\ &- 0.01 \times 1.0347 \times 10^5 \\ &= -7.4528 \times 10^4 \text{ J/mol} = H \end{aligned}$$

The same verification can be performed for the partial molar specific heats.

D.4 Example of code optimization for thermodynamics computation

This simple study was conducted with version 11 of the FORTRAN Intel compiler as the thermodynamic routines were rewritten to accomodate a more modular approach and allow

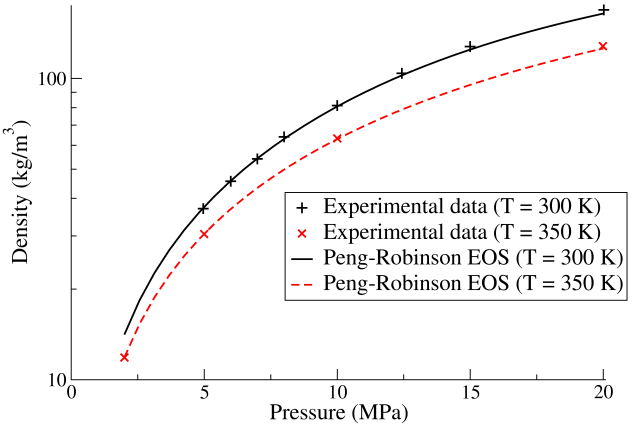

Figure 118: Comparison of experimental data from Cristancho et al. [48] and predictions from the current formulation for a mixture of methane, ethane and propane.

Table 21: Comparison of experimental data from Cristancho et al. [48] and predictions for the current formulation with default interaction parameters (subscript `PR,def`) and with empirical interaction parameters (subscript `PR,bin`).

			ρ (kg.m^{-3})			Relative error (%)	
T (K)	p (MPa)	Z	ρ_{XP}	$\rho_{\text{PR,def}}$	$\rho_{\text{PR,bin}}$	$\varepsilon_{\text{PR,def}}$	$\varepsilon_{\text{PR,bin}}$
300	4.965	0.9033	36.976	37.1883	37.1927	-0.57	-0.59
300	8.002	0.8591	63.008	63.0133	63.0260	-0.01	-0.03
350	2.002	0.9779	11.854	11.8745	11.8748	-0.17	-0.17
350	4.998	0.9506	30.452	30.4957	30.4979	-0.14	-0.15

a seamless integration of the real gas framework. Most thermodynamic models require the computation of curvefits for internal energy/enthalpy and their derivatives. Various methods are considered here:

- Previous method (method #1):

```
DO N = 1, NITER
   DO I = 1, 1000
      IF ( T(I) >= 1.0D3) THEN
         CPS(I,N) = T(I) *  CETTH(5  ,1)
         CPS(I,N) = T(I) * (CETTH(4  ,1) + CPS(I,N))
         CPS(I,N) = T(I) * (CETTH(3  ,1) + CPS(I,N))
         CPS(I,N) = T(I) * (CETTH(2  ,1) + CPS(I,N))
         CPS(I,N) =        (CETTH(1  ,1) + CPS(I,N))
      ELSE
         CPS(I,N) = T(I) *  CETTH(12,1)
         CPS(I,N) = T(I) * (CETTH(11,1) + CPS(I,N))
         CPS(I,N) = T(I) * (CETTH(10,1) + CPS(I,N))
         CPS(I,N) = T(I) * (CETTH(9  ,1) + CPS(I,N))
         CPS(I,N) =        (CETTH(8  ,1) + CPS(I,N))
      ENDIF
   ENDDO
ENDDO
```

  This assumes there is no upper and lower bound on the curvefits. Most of the curvefits are smooth and behave fine outside of the 300-3000/5000 K bounds. For low- or high-temperatures applications, a bounded formulation actually introduces more errors. This means there is only one check for the temperature range. Also, the formulation with the line by line addition and multiplication dates back from the times where compilers were less sophisticated and there were no such things as SSE libraries which greatly speed up these kind of power computations.

- More modern method, more compact and no more IF statement (method #2):

```
DO N = 1, NITER
   DO I = 1, 1000
      M = 7 * (1 - INT(1.D0 + SIGN(0.5D0,T(I)-1.0D3)))
      CPS(I,N) = (CETTH(1+M,1)          &
               +  CETTH(2+M,1) * T(I)    &
               +  CETTH(3+M,1) * T(I)**2 &
               +  CETTH(4+M,1) * T(I)**3 &
               +  CETTH(5+M,1) * T(I)**4 )
   ENDDO
ENDDO
```

- Hybrid method, no more IF statement but still line by line operations (method #3):

```
DO N = 1, NITER
   DO I = 1, 1000
```

```
      M = 7 * (1 - INT(1.D0 + SIGN(0.5D0,T(I)-1.0D3)))
      CPS(I,N) = T(I) *  CETTH(5+M,1)
      CPS(I,N) = T(I) * (CETTH(4+M,1) + CPS(I,N))
      CPS(I,N) = T(I) * (CETTH(3+M,1) + CPS(I,N))
      CPS(I,N) = T(I) * (CETTH(2+M,1) + CPS(I,N))
      CPS(I,N) =        (CETTH(1+M,1) + CPS(I,N))
    ENDDO
  ENDDO
```

- A full vector method, where `MM` has been declared as an array (method #4):

```
  DO N = 1, NITER
    MM = 7 * (1 - INT(1.D0 + SIGN(0.5D0,T-1.0D3)))
    CPS(:,N) = (CETTH(1+MM,1)          &
             +  CETTH(2+MM,1) * T      &
             +  CETTH(3+MM,1) * T**2   &
             +  CETTH(4+MM,1) * T**3   &
             +  CETTH(5+MM,1) * T**4 )
  ENDDO
```

- A full vector method, where the expression for `M` has been integrated inside the curvefit expression (method #5):

```
  DO N = 1, NITER
    CPS(:,N) = (CETTH(1+7 * (1 - INT(1.D0 + SIGN(0.5D0,T-1.0D3))),1)          &
             +  CETTH(2+7 * (1 - INT(1.D0 + SIGN(0.5D0,T-1.0D3))),1) * T      &
             +  CETTH(3+7 * (1 - INT(1.D0 + SIGN(0.5D0,T-1.0D3))),1) * T**2   &
             +  CETTH(4+7 * (1 - INT(1.D0 + SIGN(0.5D0,T-1.0D3))),1) * T**3   &
             +  CETTH(5+7 * (1 - INT(1.D0 + SIGN(0.5D0,T-1.0D3))),1) * T**4 )
  ENDDO
```

Running these methods multiple times over a 1D-array of size 64, the average times shown in Table 22 are obtained. The bottleneck represented by the `IF` statement is apparent and its elimination is the source of the greatest speed-ups. The `-parallel` option requires OpenMP libraries and while it easily speeds up serial code, it is not straightforward to extrapolate this behavior in a MPI-parallel code. For the other combinations of method and compiler, there is relatively little difference between the different options.

Table 22: Optimization of curvefit computation: Time in seconds for 1×10^6 computations on pterodactyl, a machine with a quad-core Xeon L5420 (2.5GHz, 6 MB L2 cache).

	Default	`-O3 -xSSE4.1`	`-O3 -xSSE4.1 -parallel`
Method #1	0.1145	0.0970	**0.0180**
Method #2	0.0785	0.0755	0.0210
Method #3	**0.0755**	0.0765	0.0183
Method #4	0.0786	**0.0735**	0.0720
Method #5	0.143	0.144	0.0254

Of course, this kind of study was conducted for many others portions of the thermodynamic formulation but given the constant progress of the processor architectures and compilerss, they have to be repeated periodically to make sure there is no computational cost to shave and so it is useful to illustrate the process as a sort of best practice. Recently, profiling tools such as Intel's vtune have become much more user-friendly and greatly facilitate the detection of bottlenecks.

APPENDIX E

DERIVATION OF EQUATION OF STATE-INDEPENDENT EQUATIONS

E.1 Primitive form of the one-dimensional Euler equations

The starting point is the governing Euler equations (Eqs. (2.7.1)-(2.7.4) with the right-hand sides set to 0). The following general derivatives of the internal energy are needed to achieve the primitive form:

$$\left(\frac{\partial e}{\partial \rho}\right)_{p,Y_k} = \frac{1}{\rho}\left(\frac{p}{\rho} - \frac{c_p}{\alpha_v}\right) \tag{E.1.1}$$

$$\left(\frac{\partial e}{\partial p}\right)_{\rho,Y_k} = \left(\frac{\partial e}{\partial T}\right)_{\rho,Y_k}\left(\frac{\partial T}{\partial p}\right)_{\rho,Y_k} \tag{E.1.2}$$

$$= \frac{c_v \kappa_T}{\alpha_v} = \frac{c_p \kappa_s}{\alpha_v} \tag{E.1.3}$$

with α_v the thermal expansion coefficient, κ_s the isentropic compressibility and κ_T the isothermal compressibility. The derivatives containing the total energy e_T in Eqs. (2.7.1)-(2.7.4) can be rewritten as:

$$\frac{\partial \rho e_T}{\partial t} = \rho \frac{\partial e}{\partial t} + e\frac{\partial \rho}{\partial t} + \frac{\rho}{2}\frac{\partial u_i u_i}{\partial t} + \frac{u_i u_i}{2}\frac{\partial \rho}{\partial t} \tag{E.1.4}$$

$$\frac{\partial \rho e_T u_j}{\partial x_j} = \rho u_j \frac{\partial e}{\partial x_j} + e\frac{\partial \rho u_j}{\partial x_j} + \frac{\rho u_j}{2}\frac{\partial u_i u_i}{\partial x_j} + \frac{u_i u_i}{2}\frac{\partial \rho u_j}{\partial x_j} \tag{E.1.5}$$

Using the continuity equation, the sum of the derivatives can be simplified to:

$$\frac{\partial \rho e_T}{\partial t} + \frac{\partial \rho e_T u_j}{\partial x_j} = \rho \frac{\partial e}{\partial t} + \frac{\rho}{2}\frac{\partial u_i u_i}{\partial t} + \rho u_j \frac{\partial e}{\partial x_j} + \frac{\rho u_j}{2}\frac{\partial u_i u_i}{\partial x_j} \tag{E.1.6}$$

Using the momentum equation, the kinetic energy terms can be rearranged:

$$\frac{\rho}{2}\frac{\partial u_i u_i}{\partial t} + \frac{\rho u_j}{2}\frac{\partial u_i u_i}{\partial x_j} = \rho u_i \left(\frac{\partial u_i}{\partial t} + u_j \frac{\partial u_i}{\partial x_j}\right) = -u_j \frac{\partial p}{\partial x_j} \tag{E.1.7}$$

This can be combined with the pressure term in Eq. (2.7.3):

$$-u_j \frac{\partial p}{\partial x_j} + \frac{\partial p u_j}{\partial x_j} = p\frac{\partial u_j}{\partial x_j} \tag{E.1.8}$$

This finally yields for the Euler energy equation:

$$\frac{\partial \rho e_T}{\partial t} + \frac{\partial \rho e_T u_j}{\partial x_j} = \rho \frac{\partial e}{\partial t} + \rho u_j \frac{\partial e}{\partial x_j} + p \frac{\partial u_j}{\partial x_j} = 0 \tag{E.1.9}$$

By splitting the time and space derivatives with the partial derivatives shown earlier, the following expression is obtained:

$$\left(\frac{\partial e}{\partial p}\right)_{\rho,Y_k} \left(\rho \frac{\partial p}{\partial t} + \rho u_j \frac{\partial p}{\partial x_j}\right) + \left(\frac{\partial e}{\partial \rho}\right)_{p,Y_k} \left(\rho \frac{\partial \rho}{\partial t} + \rho u_j \frac{\partial \rho}{\partial x_j}\right) \tag{E.1.10}$$

$$+ \left(\frac{\partial e}{\partial Y_k}\right)_{\rho,p,Y_l,l\neq k} \left(\rho \frac{\partial Y_k}{\partial t} + \rho u_j \frac{\partial Y_k}{\partial x_j}\right) + p \frac{\partial u_j}{\partial x_j} = 0 \tag{E.1.11}$$

Once again, this can further be simplified using conservation of mass and species:

$$\left(\frac{\partial e}{\partial p}\right)_{\rho,Y_k} \left(\rho \frac{\partial p}{\partial t} + \rho u_j \frac{\partial p}{\partial x_j}\right) - \rho^2 \frac{\partial u_j}{\partial x_j} \left(\frac{\partial e}{\partial \rho}\right)_{p,Y_k} + p \frac{\partial u_j}{\partial x_j} = 0 \tag{E.1.12}$$

Plugging in Eqs. (E.1.1) and (E.1.3):

$$\frac{\rho c_p \kappa_s}{\alpha_v} \left(\frac{\partial p}{\partial t} + u_j \frac{\partial p}{\partial x_j}\right) + \frac{\partial u_j}{\partial x_j} \left(\frac{\rho c_p}{\alpha_v} - p\right) + p \frac{\partial u_j}{\partial x_j} = 0 \tag{E.1.13}$$

$$\frac{\partial p}{\partial t} + u_j \frac{\partial p}{\partial x_j} + \frac{\partial u_j}{\partial x_j} \frac{1}{\kappa_s} = 0 \tag{E.1.14}$$

Recognizing that for any gas, $\kappa_s = \frac{1}{\rho c^2}$, the general, EoS-independent Euler equations are recovered:

$$\frac{\partial \rho}{\partial t} + \frac{\partial \rho u_i}{\partial x_i} = 0 \tag{E.1.15}$$

$$\frac{\partial \rho u_i}{\partial t} + \frac{\partial}{\partial x_j} \left(\rho u_i u_j + p \delta_{ij}\right) = 0 \tag{E.1.16}$$

$$\frac{\partial p}{\partial t} + u_j \frac{\partial p}{\partial x_j} + \rho c^2 \frac{\partial u_j}{\partial x_j} = 0 \tag{E.1.17}$$

APPENDIX F

ADDITIONAL LOCAL ONE DIMENSIONAL INVISCID RELATIONS

The relation linking the temperature variation with the waves amplitudes can be derived from the continuity equation:

$$\frac{\partial \rho}{\partial t} + \mathcal{L}_2 + \frac{\mathcal{L}_5 + \mathcal{L}_1}{c^2} = 0 \tag{F.0.18}$$

$$\frac{\partial \rho}{\partial t} = \frac{\partial T}{\partial t}\left(\frac{\partial \rho}{\partial T}\right)_{p,Y_k} + \frac{\partial p}{\partial t}\left(\frac{\partial \rho}{\partial p}\right)_{T,Y_k} + \sum_k^{N_S} \frac{\partial Y_k}{\partial t}\rho_{,k} \tag{F.0.19}$$

$$= -\frac{\partial T}{\partial t}\rho\alpha_v + \frac{\partial p}{\partial t}\rho\kappa_T - \sum_k^{N_S} \mathcal{L}_{5+k}\rho_{,k} \tag{F.0.20}$$

$$\frac{\partial T}{\partial t} - \frac{\partial p}{\partial t}\frac{\kappa_T}{\alpha_v} + \frac{1}{\alpha_v}\sum_k^{N_S} \mathcal{L}_{5+k}\frac{\rho_{,k}}{\rho} - \frac{c^2\mathcal{L}_2 + \mathcal{L}_5 + \mathcal{L}_1}{\rho c^2 \alpha_v} = 0 \tag{F.0.21}$$

$$\frac{\partial T}{\partial t} + (\mathcal{L}_5 + \mathcal{L}_1)\left(\frac{\kappa_T}{\alpha_v} - \frac{1}{\rho c^2 \alpha_v}\right) - \frac{\mathcal{L}_2}{\rho\alpha_v} + \frac{1}{\alpha_v}\sum_k^{N_S} \mathcal{L}_{5+k}\frac{\rho_{,k}}{\rho} = 0 \tag{F.0.22}$$

$$\frac{\partial T}{\partial t} + (\mathcal{L}_5 + \mathcal{L}_1)\left(\frac{\kappa_T - \kappa_s}{\alpha_v}\right) - \frac{\mathcal{L}_2}{\rho\alpha_v} + \frac{1}{\alpha_v}\sum_k^{N_S} \mathcal{L}_{5+k}\frac{\rho_{,k}}{\rho} = 0 \tag{F.0.23}$$

$$\frac{\partial T}{\partial t} + \frac{T\alpha_v(\mathcal{L}_5 + \mathcal{L}_1)}{\rho c_p} - \frac{\mathcal{L}_2}{\rho\alpha_v} + \frac{1}{\alpha_v}\sum_k^{N_S} \mathcal{L}_{5+k}\frac{\rho_{,k}}{\rho} = 0 \tag{F.0.24}$$

If the ideal gas EoS is assumed, the following expression is obtained:

$$\frac{\partial T}{\partial t} + \frac{\mathcal{L}_5 + \mathcal{L}_1}{\rho c_p} - \frac{T c^2 \mathcal{L}_2}{\rho c^2} = 0 \tag{F.0.25}$$

$$\frac{\partial T}{\partial t} + \frac{RT(\gamma - 1)(\mathcal{L}_5 + \mathcal{L}_1)}{pR\gamma} - \frac{RT^2 c^2 \mathcal{L}_2}{p\gamma RT} = 0 \tag{F.0.26}$$

$$\frac{\partial T}{\partial t} + \frac{T}{p\gamma}\left((\gamma - 1)(\mathcal{L}_5 + \mathcal{L}_1) - c^2\mathcal{L}_2\right) = 0 \tag{F.0.27}$$

To derive the equation governing the flow rate, one simply combines the continuity equation and the velocity equation:

$$\frac{\partial \rho u_1}{\partial t} = \rho\frac{\partial u_1}{\partial t} + u_1\frac{\partial \rho}{\partial t} = -\frac{\mathcal{L}_5 - \mathcal{L}_1}{c} - \frac{u_1\left(c^2\mathcal{L}_2 + \mathcal{L}_5 + \mathcal{L}_1\right)}{c^2} \tag{F.0.28}$$

$$\frac{\partial \rho u_1}{\partial t} + \frac{(\mathrm{Ma} + 1)\mathcal{L}_5 + (\mathrm{Ma} - 1)\mathcal{L}_1}{c} + u_1\mathcal{L}_2 = 0 \tag{F.0.29}$$

APPENDIX G

EVALUATION OF BULK VISCOSITY EFFECTS IN REAL GAS FLOWS

It is recalled that for a Newtonian, isotropic fluid, the symmetric stress tensor is:

$$\sigma_{ij} = \left(-p + \lambda\left(\frac{\partial u_k}{\partial x_k}\right)\right)\delta_{ij} + \mu\left(\frac{\partial u_i}{\partial x_j} + \frac{\partial u_j}{\partial x_i}\right) \tag{G.0.30}$$

From Eq. G.0.30, one can define the mean, mechanical pressure $\bar{P}$ as:

$$\bar{P} = -\frac{1}{3}\left(\sigma_{11} + \sigma_{22} + \sigma 33\right) = p - \left(\lambda + \frac{2}{3}\mu\right)\nabla \cdot \boldsymbol{u} \tag{G.0.31}$$

The term $\left(\lambda + \frac{2}{3}\mu\right)$ is often dubbed the coefficient of bulk viscosity and will be denoted β from here on out. The dynamic viscosity is of course μ while λ is called the volume (or second) viscosity. Interpretating Eq. G.0.31, the bulk viscosity is connected to the dissipation mechanism when the flow experiences a change of volume. This dampening of volumetric vibrations occur for example during sound absorption. This explains one of the experimental techniques used to evaluate the value of the coefficient of bulk viscosity. In these, the attenuation and dispersion of intense ultronic waves are measured and the attenuation coefficient can be linked to the viscosities [91]. However, the volume viscosity might not even be a thermodynamic property since available data seems to show it is dependent on the frequency of the signal. Even if it is assumed that a frequency independent (or at least low-frequency) value can be obtained, the validity of the Stokes assumption ($\beta = 0$) is in question for polyatomic gases. For dense super-critical fluids or liquids, they do usually display such frequency dependency. Called positive dispersion, it represents an increase of the speed of sound from the classical adiabatic value at low frequency/large wavelength to a high frequency/short wavelength limit as the wavelength approaches the interparticle distance [281].

Another consequence of Eq. G.0.31 is that the mechanical pressure is not equal at every instant to the thermodynamic pressure in a deforming viscous fluid. The mechanical pressure

is a measure of the translational energy of the molecules whereas the thermodynamic pressure is a measure of the total energy. For monoatomic gases, or gases in perfect equilibrium, these two pressures are the same. However, if the relaxation time of the molecules is not small compared to the characteristic time of the flow, then these two pressures will differ and bulk viscosity will play a role. In this sense, the bulk viscosity is not a physical property of a gas, but rather an approximation designed to simulate the effect of thermal relaxation when the governing equations are cast in terms of a single temperature.

As a first approximation to the computation of the bulk viscosity for a mixture of gas, the empirical formula suggested by Giovangigli [84] is used as a good compromise between cost, complexity and accuracy:

$$\beta = \left(\sum_{k=1}^{N_S} X_k \beta_k^{3/4} \right)^{4/3} \tag{G.0.32}$$

The volume viscosity of an individual monoatomic species is assumed to be 0 while the one for a polyatomic species is given by:

$$\beta_k = \frac{k_B \pi}{4} \left(\frac{c_k^{\text{int}}}{c_{V,k}} \right)^2 \frac{Z_{\text{rot}}}{c_k^{\text{int}}} \mu_k \tag{G.0.33}$$

$$= \frac{R_u \pi}{4} \left(\frac{C_k^{\text{int}}}{C_{V,k}} \right)^2 \frac{Z_{\text{rot}}}{C_k^{\text{int}}} \mu_k \tag{G.0.34}$$

For monoatomic species, the rotational relaxation collision number Z_{rot} is 0 and so the bulk viscosity is also 0. The species dynamic viscosity μ_k can be obtained through kinetic theory as long as it includes intermolecular effects through collision integrals. The problem is in the selection of the Lennard-Jones parameters used to compute these collision integrals. Usually, the parameters used to generate these integrals are only loosely related to the actual Lennard-Jones parameters found in the literature. A method such as the Chung et al. method [36] recomputes the Lennard-Jones parameters from the critical properties of a species, making it much easier to have a complete and consistent set of values. The added benefit is that the Chung formulation has been extended to include intermolecular forces effects at high pressures.

The specific heat of internal energy can be estimated as:

$$C_k^{\text{int}}(T) = C_{p,k}(T) - C_p^{\text{tr}} = C_{p,k}(T) - \frac{5}{2} R_u \tag{G.0.35}$$

The molar specific heat at constant pressure for species k, $C_{p,k}$, is obtained from the traditional methods discussed previously (i.e. curvefits for ideal gases, departure functions for real gases).

The rotational relaxation collision number Z_{rot} has a temperature dependency that is function of the depth of the Lennard-Jones potential ϵ:

$$Z_{\text{rot}}(T) = Z_{\text{rot}}(T^o)\frac{F_Z(T^o)}{F_Z(T)} \tag{G.0.36}$$

with

$$F_Z(T) = 1 + \frac{\pi^{3/2}}{2}\left(\frac{\epsilon_k/k_B}{T}\right)^{\frac{1}{2}} + \left(\frac{\pi^2}{4} + 2\right)\left(\frac{\epsilon_k/k_B}{T}\right) + \pi^{3/2}\left(\frac{\epsilon_k/k_B}{T}\right)^{\frac{3}{2}} \tag{G.0.37}$$

A value of the collision numbers at a reference temperature is also required and can be found in classical transport property databases [122].

Few CFD studies have been conducted while taking into account the bulk viscosity and investigating its influence on the flow. Billet, Giovangigli and de Gassowski [19] consider the interaction between a planar shock and a hydrogen bubble. They found significant differences with respect to the shock thickness, the velocity distribution and the flame structure when taking into account the volume viscosity.

A quick numerical investigation was conducted to see if the non-validity of the Stokes' assumption could have an influence on compressible mixing layers involving hydrogen. A two-dimensional mixing layer with significant compressible effects ($M_c = 0.4$) is considered. The only species is hydrogen and standard conditions (298 K, 1 atm) are imposed. The Reynolds number is initialized to a rather low value ($\text{Re}_0 = 400$) in order to have non-negligible viscous terms. This mixing layer is run first with the Stokes' hypothesis then with the model for bulk viscosity described above. Figure 119 shows identical momentum thickness growth for both simulations while actual numbers slightly differ but only by about 0.01%. Figure 120 display some instantaneous snapshots of the flowfield during the second pairing event. Despite large Mach numbers, strong divergence of the velocity field and a bulk viscosity almost 20 times larger than the dynamic viscosity, no quantitative effect can be seen on the flow features or on the mixing layer growth rate.

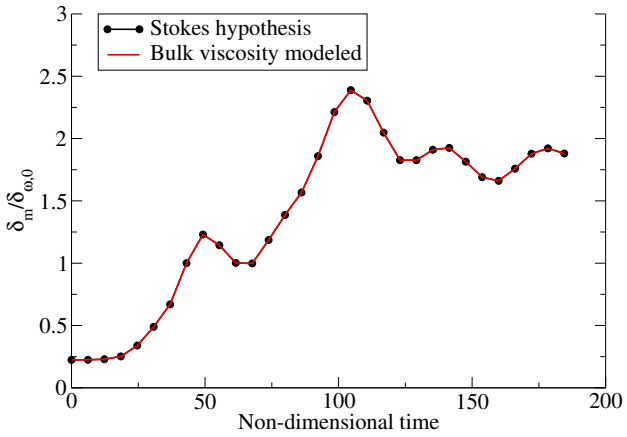

Figure 119: Comparison of the momentum thickness growth of a compressible hydrogen mixing layer with and without taking into account bulk viscosity.

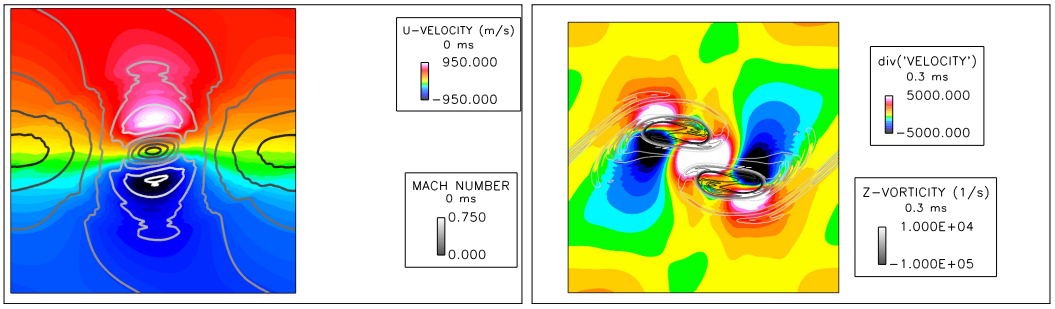

(a) Velocity/Mach number

(b) Velocity divergence/Vorticity

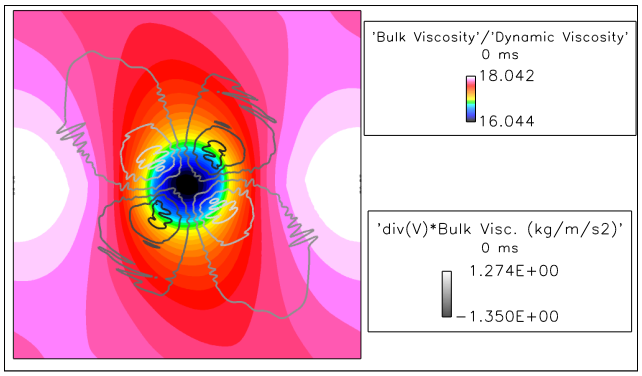

(c) Viscosities ratio/Bulk dilatation

Figure 120: Instantaneous snapshots of the flowfield of a compressible hydrogen mixing layer during the second pairing event. The bulk viscosity is modeled in this simulation.

APPENDIX H

REACTION MECHANISMS FOR H_2-O_2 CHEMISTRY

This section only deals with the reaction mechanisms used in the current study, not with how the reaction rates are computed and how they are coupled with the flow. For more on these issues, the reader is referred to Sections 2.3.6, 2.4 and 3.2.3.

H.1 Background and specificities of H_2-O_2 chemistry

The combustion of hydrogen presents several unique characteristics. As a carbon-free fuel, it will react cleanly with pure oxygen to form water but when reacting with air, the very high flame temperatures usually produce high levels of thermal NO_x. For rocket engines applications however, the production of these pollutants will not be an issue. Not only is the adiabatic flame temperature very large for hydrogen (up to 3000 K in pure oxygen), but its reactivity is also very high, which implies very thin flames and very large flame speeds. The very high specific impulse of the hydrogen-oxygen bipropellant makes it a very popular choice for rocket engine applications. From a chemical kinetics point of view, the absence of carbon and nitrogen in a pure hydrogen-oxygen system means a detailed, exhaustive reaction mechanism can be written using 8 species and about 40 reactions. Following Glassman [87], the oxidation of hydrogen can be described as follows:

1. Initiation reactions:

$$H_2 + M \rightarrow H + H + M \quad \text{(high temperature dissociation)} \tag{H.1.1}$$

$$H_2 + O_2 \rightarrow HO_2 + H \quad \text{(slow dissociation)} \tag{H.1.2}$$

2. Chain reactions with the first family of radicals (O, H and OH):

$$\mathrm{H + O_2 \rightarrow \ + OH} \quad \text{(chain branching reaction)} \tag{H.1.3}$$

$$\mathrm{+ H_2 \rightarrow H + OH} \quad \text{(chain branching reaction)} \tag{H.1.4}$$

$$\mathrm{H_2 + OH \rightarrow H_2O + H} \quad \text{(chain carrying reaction)} \tag{H.1.5}$$

$$\mathrm{+ H_2O \rightarrow OH + OH} \quad \text{(chain branching reaction)} \tag{H.1.6}$$

3. Termination steps with the first family of radicals (O, H and OH):

$$\mathrm{H + H + M \rightarrow H_2 + M} \quad \text{(three-body recombination)} \tag{H.1.7}$$

$$\mathrm{+ \ + M \rightarrow O_2 + M} \quad \text{(three-body recombination)} \tag{H.1.8}$$

$$\mathrm{H + \ + M \rightarrow OH + M} \quad \text{(three-body recombination)} \tag{H.1.9}$$

$$\mathrm{H + OH + M \rightarrow H_2O + M} \quad \text{(three-body recombination)} \tag{H.1.10}$$

4. Through the initial dissociation (H.1.2) or the following chain carrying reaction,

$$\mathrm{H + O_2 + M \rightarrow HO_2 + M} \tag{H.1.11}$$

the hydrogen peroxide pathway can open up via the hydroperoxy radical $\mathrm{HO_2}$:

$$\mathrm{H + H + M \rightarrow H_2 + M} \quad \text{(three-body recombination)} \tag{H.1.12}$$

$$\mathrm{+ \ + M \rightarrow O_2 + M} \quad \text{(three-body recombination)} \tag{H.1.13}$$

$$\mathrm{H + \ + M \rightarrow OH + M} \quad \text{(three-body recombination)} \tag{H.1.14}$$

$$\mathrm{H + OH + M \rightarrow H_2O + M} \quad \text{(three-body recombination)} \tag{H.1.15}$$

These reactions, along with their reverse counterparts, represent one complete version of the chemical path between the hydrogen-oxygen reactants and their combustion products. However, because of the very high reactivity of some hydrogen-based radicals (such as $\mathrm{H_2O_2}$), the resulting mechanism is really stiff to integrate. And because the large pressure dependency of the branching and termination reactions, there is a large uncertainty on some of the reaction rates, especially at high pressure. Esposito et al. [66] show that

at high pressures, uncertainties on diffusion coefficients are much less critical than uncertainties in reaction rates for the basic flame properties such as flame speed or extinction limits. However, their analysis is limited to a 2-step reaction mechanism and it is unclear how this conclusion can be transposed to more complex mechanisms as the ones used in this study. An additional issue with hydrogen-oxygen flames is that without nitrogen as diluent, the assumption of mixture-averaged diffusion is less valid than for a hydrogen-air flame. This mixture-averaged assumption is usually preferred over the multi-component diffusion approach in numerical simulations of complex geometries because of its high computational cost. The same assumption is made for this work and was argumented in Section 2.6. Similarly, Soret and Dufour effects are neglected which has an impact on the predictions of the detailed mechanisms. In any case, there are large uncertainties on the transport properties of radicals such as H, Øor H_2O_2, especially under conditions relevant to rocket engines. All these limitations can have an impact on the reaction rates computed by the mechanisms presented here.

Unlike methane-air flames, the extinction strain rate for hydrogen-air flames increases linearly with pressure up to 50 atm [8] while for hydrogen-oxygen flames it increases linearly up to 100 atm [291]. For non-premixed H_2-O_2 flames, Soret diffusion generally increases the local concentration of Hin the reaction zone, making the flame even more resistant to extinction [341]. In any case, this makes the flame very robust and easy to anchor.

The following sections details the mechanims used for the current CFD applications. Many mechanisms had been considered for rocket engine flows such as the detailed mechanism from Balakrishnan et al. [8] and its derived reduced mechanisms or the recent mechanism by Shimizu et al. [277]. The mechanism of Li et al. [150] is very similar to the Conaire mechanism as it is mostly based on the same experimental data and detailed comparisons by Strohle et al. [298] show that it compares very well with the Conaire mechanism. However, the Conaire mechanism was selected by NASA for the CUIP study. In the end, the detailed mechanisms from Conaire et al. [211] was selected because of its extended range of validity at high pressure while the reduced mechanism from Baurle [13] was selected for its simplicity.

H.2 Baurle 7-step, 6-species mechanism

Various abridged versions of the Jachimowski mechanism [114] have been used over the years, mostly for high-speed flow (SCRAMJET) applications:

- Eklund et al. [63, 201]
- Baurle et al. [13]
- Keistler [123]

These mechanisms simply eliminate the stiff H_2O_2 and HO_2 branches from the detailed mechanism to obtain a 7-step,6-species mechanism. The rates quoted in the literature do not always match and it is not quite clear how these various rates were obtained. Despite the mediocre performance of these reduced mechanisms when considering premixed laminar flame speed predictions [345] as seen in the following sections, they compare well [201, 123] in high-speed, non-premixed configurations with detailed mechanisms such as the ones by Conaire or Li. For the current work, the implementation of Baurle et al. is the one chosen and is summarized in Table 23. For the last two reactions involving three molecules, the third-body efficiencies are taken as 2.5 for H_2, 16 for H_2O and 1 for all other species.

Reaction	A	B	C
$H_2 + O_2 \rightleftharpoons OH + OH$	1.70×10^{13}	0.0	24233
$O_2 + H \rightleftharpoons OH + O$	1.42×10^{14}	0.0	8254
$H_2 + OH \rightleftharpoons H_2O + H$	3.16×10^{07}	1.8	1525
$O + H_2 \rightleftharpoons OH + H$	2.07×10^{14}	0.0	6920
$OH + OH \rightleftharpoons H_2O + O$	5.50×10^{13}	0.0	3523
$H + OH \rightleftharpoons H_2O + M$	2.21×10^{22}	-2.0	0
$H + H \rightleftharpoons H_2 + M$	6.53×10^{17}	-1.0	0

Table 23: Reduced, 7-step, 6-species mechanism as detailed by Baurle et al. [13] for hydrogen flames in supersonic flows. Forward rate constants are given as $k = AT^B \exp -C/T$ with T in Kelvin and A in multiple of $cm^3.mol^{-1}.s^{-1}$. Reverse reaction rates are computed using equilibrium constant from Gibbs energy.

H.2.1 Conaire 21-step, 8-species mechanism

The following mechanism has been proposed by Ó Conaire et al. [211] and validated over a wide range of operating conditions, including pressures as high as 87 atm. The 8 species

involved are: H_2, O_2, H, O, OH, H_2O, HO_2, H_2O_2. It contains 15 regular reversible reactions, 2 reversible reactions with two possible multiple paths for a total of 4 steps (reactions (13) and (15)) and 2 pressure-dependent steps (reactions (20) and (21)). The effective reaction rates for these two steps are:

$$k_0 = A_0 T^{\beta_0} \exp\left(-E_0/R_C T\right) \qquad \text{for the low-pressure limit} \tag{H.2.1}$$

$$k_\infty = A_\infty T^{\beta_\infty} \exp\left(-E_\infty/R_C T\right) \qquad \text{for the high-pressure limit} \tag{H.2.2}$$

$$k = k_\infty \left(\frac{p_r}{1+p_r}\right) F \qquad \text{for the actual rate} \tag{H.2.3}$$

The reduced pressure p_r is $\frac{k_0[M]}{k_\infty}$ and $[M] = \sum_i^{N_S} f_i[M_i]$ is the concentration of the mixture including third-body efficiencies shown in Table 25. In the Troe form used in this mechanism, the coefficient F is given by:

$$\log F = \left[1 + \left(\frac{\log p_r + c}{n - d(\log p_r + c)}\right)^2\right]^{-1} \log F_{cent} \tag{H.2.4}$$

For this mechanism, Conaire et al. [211] suggest to take $F_{cent} = 0.5$ which implies:

$$c = -0.19831 \tag{H.2.5}$$

$$n = 1.1323 \tag{H.2.6}$$

$$d = 0.14 \tag{H.2.7}$$

H.3 Comparisons of H_2-O_2 mechanisms

The two mechanisms presented previously are compared using an opposed diffusion flame modeled with the CHEMKIN OPPDIF module. The inlet conditions are inspired by the PSU-RCM1 configuration with significant preheating but involve pure streams of reactants. The operating pressure is set at 55 bar and the strain rate is small, unlikely to affect the flame structure. The results are shown in Figure 121 and the Baurle profiles compare very well with the detailed mechanism from Conaire. This validates the use of the Baurle mechanism for rocket engine applications even if it produces mediocre results on premixed flames.

Number	Reaction	A	B	C
(1)	$H + O_2 \rightarrow O + OH$	1.915×10^{14}	0.00	8270
(1)	$H + O_2 \leftarrow O + OH$	5.481×10^{11}	0.39	−147
(2)	$H_2 + O \rightarrow OH + H$	5.080×10^{04}	2.67	3170
(2)	$H_2 + O \leftarrow OH + H$	2.667×10^{04}	2.65	2460
(3)	$H_2 + OH \rightarrow H_2O + H$	2.160×10^{08}	1.51	1730
(3)	$H_2 + OH \leftarrow H_2O + H$	2.298×10^{09}	1.40	9220
(4)	$O + H_2O \rightarrow OH + OH$	2.970×10^{06}	2.02	6740
(4)	$O + H_2O \leftarrow OH + OH$	1.465×10^{05}	2.11	−1460
(5)	$H_2 + M \rightarrow H + H + M$	4.577×10^{19}	−1.40	52500
(5)	$H_2 + M \leftarrow H + H + M$	1.146×10^{20}	−1.68	413
(6)	$O_2 + M \rightarrow O + O + M$	4.515×10^{17}	−0.64	59800
(6)	$O_2 + M \leftarrow O + O + M$	6.165×10^{15}	−0.50	0
(7)	$OH + M \rightarrow O + H + M$	9.880×10^{17}	−0.74	51400
(7)	$OH + M \leftarrow O + H + M$	4.714×10^{18}	−1.00	0
(8)	$H_2O + M \rightarrow H + OH + M$	1.912×10^{23}	−1.83	59600
(8)	$H_2O + M \leftarrow H + OH + M$	4.500×10^{22}	−2.00	0
(9)	$HO_2 + H \rightarrow H_2 + O_2$	1.660×10^{13}	0.00	414
(9)	$HO_2 + H \leftarrow H_2 + O_2$	3.164×10^{12}	0.35	27900
(10)	$HO_2 + H \rightarrow OH + OH$	7.079×10^{13}	0.00	148
(10)	$HO_2 + H \leftarrow OH + OH$	2.027×10^{10}	0.72	18500
(11)	$HO_2 + O \rightarrow OH + O_2$	3.250×10^{13}	0.00	0
(11)	$HO_2 + O \leftarrow OH + O_2$	3.252×10^{12}	0.33	26800
(12)	$HO_2 + OH \rightarrow H_2O + O_2$	2.890×10^{13}	0.00	−250
(12)	$HO_2 + OH \leftarrow H_2O + O_2$	5.861×10^{13}	0.24	34800
(13a)	$H_2O_2 + O_2 \rightarrow HO_2 + HO_2$	4.634×10^{16}	−0.35	25500
(13a)	$H_2O_2 + O_2 \leftarrow HO_2 + HO_2$	4.200×10^{14}	0.00	6030
(13b)	$H_2O_2 + O_2 \rightarrow HO_2 + HO_2$	1.434×10^{13}	−0.35	18700
(13b)	$H_2O_2 + O_2 \leftarrow HO_2 + HO_2$	1.300×10^{11}	0.00	−820
(14)	$H_2O_2 + H \rightarrow H_2O + OH$	2.410×10^{13}	0.00	2000
(14)	$H_2O_2 + H \leftarrow H_2O + OH$	1.269×10^{08}	1.31	35900
(15)	$H_2O_2 + H \rightarrow HO_2 + H_2$	6.025×10^{13}	0.00	4000
(15)	$H_2O_2 + H \leftarrow HO_2 + H_2$	1.041×10^{11}	0.70	12100
(16)	$H_2O_2 + O \rightarrow HO_2 + OH$	9.550×10^{06}	2.00	2000
(16)	$H_2O_2 + O \leftarrow HO_2 + OH$	8.660×10^{03}	2.68	9340
(17a)	$H_2O_2 + OH \rightarrow HO_2 + H_2O$	1.000×10^{12}	0.00	0
(17a)	$H_2O_2 + OH \leftarrow HO_2 + H_2O$	1.838×10^{10}	0.59	15500
(17b)	$H_2O_2 + OH \rightarrow HO_2 + H_2O$	5.800×10^{14}	0.00	4810
(17b)	$H_2O_2 + OH \leftarrow HO_2 + H_2O$	1.066×10^{13}	0.59	20400
(18_∞)	$H_2O_2 + M \rightleftharpoons OH + OH + M$	2.951×10^{14}	0.00	24400
(18_0)	$H_2O_2 + M \rightleftharpoons OH + OH + M$	1.202×10^{17}	0.00	22899
(19_∞)	$H + O_2 + M \rightleftharpoons HO_2 + M$	1.475×10^{12}	0.60	59600
(19_0)	$H + O_2 + M \rightleftharpoons HO_2 + M$	3.482×10^{16}	−0.41	−561

Table 24: Reduced 21-step, 8-species mechanism suggested by Ó Conaire et al. [211] for hydrogen-oxygen flames. Forward rate constants are given as $k = AT^B \exp -C/T$ with T in Kelvin and A in multiple of $cm^3.mol^{-1}.s^{-1}$.

Number	Reaction	H_2 efficiency	H_2O efficiency
(5)	$H_2 + M \rightleftharpoons H + H + M$	2.5	12
(6)	$O_2 + M \rightleftharpoons O + O + M$	2.5	12
(7)	$OH + M \rightleftharpoons O + H + M$	2.5	12
(8)	$H_2O + M \rightleftharpoons H + OH + M$	0.73	12
(18)	$H + O_2 + M \rightleftharpoons HO_2 + M$	1.3	14
(19)	$H_2O_2 + M \rightleftharpoons OH + OH + M$	2.5	12

Table 25: Third-body efficiencies for the chosen mechanism.

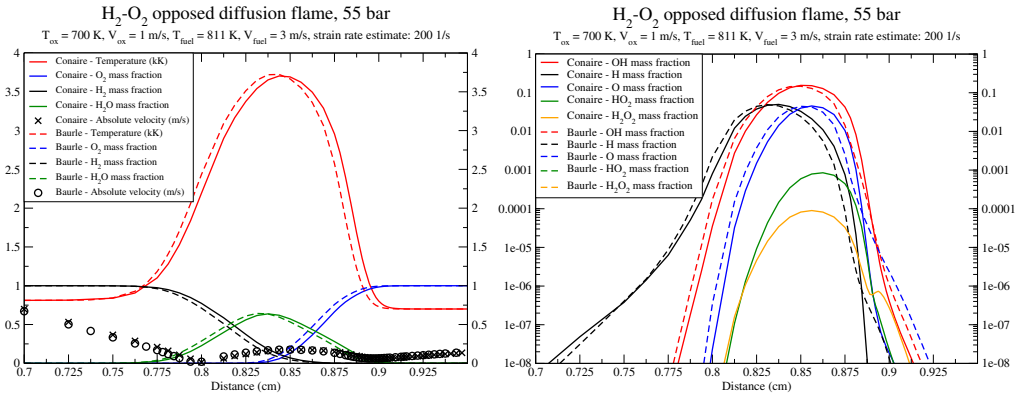

Figure 121: Comparison between the predictions of the Conaire mechanism and the Baurle mechanism for a H_2/O_2 flame at 55 bar.

APPENDIX I

DESCRIPTION OF SOME OF THE SYSTEMS USED IN THIS WORK

I.1 Intel systems available for this study

I.1.1 `garuda`: Woodcrest Xeon E5150

`garuda` is a Linux cluster with 256 nodes connected by a Cisco DDR switch. It is the main computing cluster at the CCL. Each node contains two dual-core Xeon "Woodcrest" E5150 with a frequency of 2.66GHz, for a total of 1024 available computing cores. Each Woodcrest CPU shares 2 GB of DDR2 RAM among its two cores, for a total of 4 GB of RAM per node. The head node, used for compilation, contains two slightly faster Xeon Woodcrest E5160, with a clock speed of 3.0 GHz. Each Woodcrest has 4 MB of L2 cache with a Front Side Bus speed of 1333 MT/s (DDR). These 64-bit machines support MMX, SSE, SSE2, SSE3 and SSSE3. `garuda` is operated by the Computational Combustion Laboratory at the Georgia Institute of Technology.

I.1.2 `pterodactyl`: Harpertown L5420

`pterodactyl` is a small Linux cluster owned by the CCL. It consists of 3 nodes linked by a simple Gigabit Ethernet connection. Each node contains two quad-core Xeon "Harpertown" L5420 with a frequency of 2.50GHz, for a total of 24 available computing cores. Each node contains 16 GB of DDR3 RAM, equivalent to 2 GB of RAM per computing core. Each CPU has 6 MB of L2 cache with a Front Side Bus speed of 1333 MT/s. The thermal envelope is around 50 W. The head node, used for compilation, contains two Xeon Clovertown E5345, with a clock speed of 2.33 GHz, with 4 MB of L2 cache and a Front Side Bus speed of 1333 MT/s.

I.1.3 `endeavor`: Sandy Bride Xeon E5-2670

`endeavor` is a benchmarking cluster owned by Intel and located in DuPont, WA. The part of the cluster that is the focus of this study consists of 360 nodes connected by an unknown

Infiniband switch (probably QDR). Each nodes contains two octo-core Xeon "Sandy Bridge" E5-2670 with a frequency of 2.6 GHz and 64 GB of 1333 MHz (instead of 1600 MHz) DDR3 RAM.

I.2 AMD systems available for this study

I.2.1 `raptor`: Opteron 6136

`raptor` is a large cluster owned by the AFRL and which has been in the top 60 supercomputer in the world for the past 2 years. It consists of 42712 cores with 16 cores per compute node. A Cray interconnect manages the communication between the compute nodes. Each core is clocked at 2.4 GHz. Its peak performance has been evaluated at 410 teraFLOPS.

I.2.2 `FoRCE`: Opteron 6274

`FoRCE` is the main computational cluster at the Georgia Institute of Technology. For this work, the part that was used consisted of 14 nodes containing 4 16-core Opteron 6274 each. The cores were clocked at 2.2 GHz and the compute nodes were linked by a QDR Infiniband switch.

APPENDIX J

HYBRID SWITCH PARAMETERS FOR LARGE DENSITY GRADIENTS FLOWS

The effects of the hybrid switch parameters are first investigated on an ideal gas temporal mixing layer (TML) before moving to a real gas case for verification. For this first TML, the central scheme used is the Gottlieb-Turkel 3rd order scheme [81] as it displayed good stability and accuracy on such uniform grid. This scheme is combined with the 3rd order upwind scheme for the hybrid central-upwind scheme. The two species are nitrogen and heptane in order to provide a significant density gradient across the shear layer. The initial vorticity perturbation follows the formulation given by Ling et al. [156]. The scheme, the switch and the resolution are varied through a series of simulations detailed in Table 26. Through Figures 122 to 127, it is observed that the symmetry of the flowfield is somewhat improved with the global switch instead of the directional switch, especially when the switch is not turned on very much. Note that a non-contiguous hybrid switch produces numerical oscillations that make the solution diverge significantly from the higher resolution solutions. In the end, the directional switch with parameters $(\epsilon_\rho, \epsilon_p, C_\rho^{\text{cutoff}}, C_p^{\text{cutoff}}) = (0.05, 0.05, 0.125, 0.5)$ is recommended for better accuracy while a set of parameters such as $(\epsilon_\rho, \epsilon_p, C_\rho^{\text{cutoff}}, C_p^{\text{cutoff}}) = (0.025, 0.025, 0.0625, 0.25)$ and a global switch can be used for additional stability.

To verify that these parameters also work with real gas equations of state, a hydrogen-oxygen TML is setup at 100 bar with liquid oxygen at 120 K on one side and gaseous hydrogen at 300 K on the other side. The initialization is similar to the previous TML and the directional switch with $(\epsilon_\rho, \epsilon_p, C_\rho^{\text{cutoff}}, C_p^{\text{cutoff}}) = (0.05, 0.05, 0.125, 0.5)$ is used. Sample results are shown in Figures 129 to 132 and they display a smooth solution without numerical oscillations and with crisp finger-like structures that do not show an excessive level of

Table 26: Parameters for the ideal gas TML simulations. A directional switch means the switch is evaluated independently in each direction. A global switch indicates that all fluxes are upwinded at a given point if one direction requires it.

Case	$(\epsilon_\rho, \epsilon_p, C_\rho^{\text{cutoff}}, C_p^{\text{cutoff}})$	Switch	Note
RUN100	(0.10,0.05,0.25,0.5)	Directional	
RUN101	(0.10,0.05,0.25,0.5)	Global	
RUN102	(0.05,0.05,0.125,0.5)	Global	
RUN103	N/A	N/A	Pure central scheme
RUN104	(0.05,0.05,0.125,0.5)	Global	Double resolution
RUN105	N/A	N/A	Pure central scheme (double resolution)

numerical dissipation.

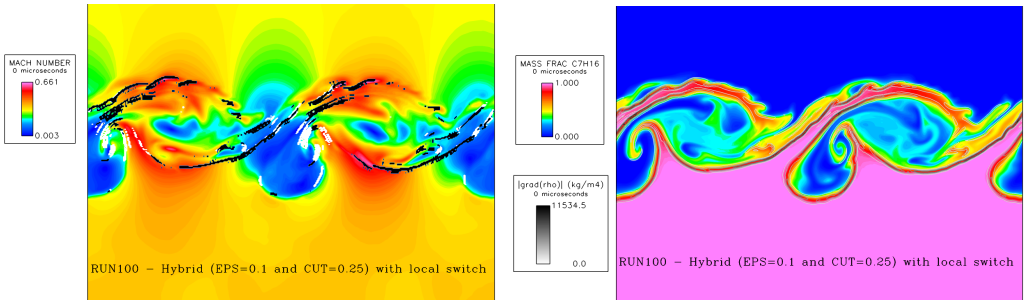

(a) Mach number/Switch (b) Mass fraction/Density gradient

Figure 122: Instantaneous snapshots of the flowfield for RUN100 of the ideal gas TML. On the left, the Mach number is shown with color contours while the upwinding is indicated in white for the I-direction and in black for the J-direction. On the right, the heptane mass fraction is shown with color contours while the density gradient is shown with grayscale contour lines.

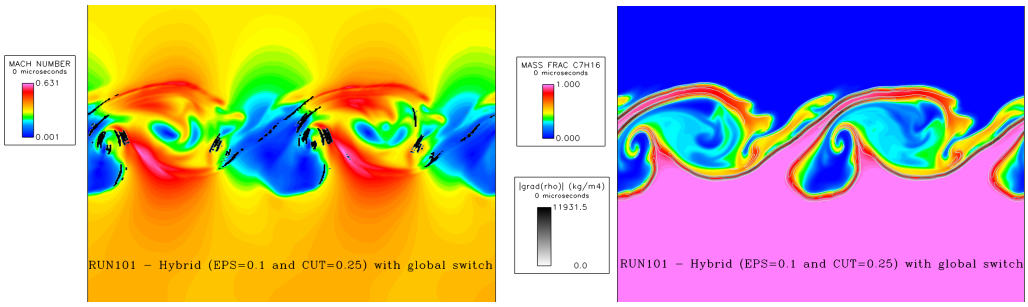

(a) Mach number/Switch (b) Mass fraction/Density gradient

Figure 123: Instantaneous snapshots of the flowfield for RUN101 of the ideal gas TML. On the left, the Mach number is shown with color contours while the upwinding is indicated in white for the I-direction and in black for the J-direction. On the right, the heptane mass fraction is shown with color contours while the density gradient is shown with grayscale contour lines.

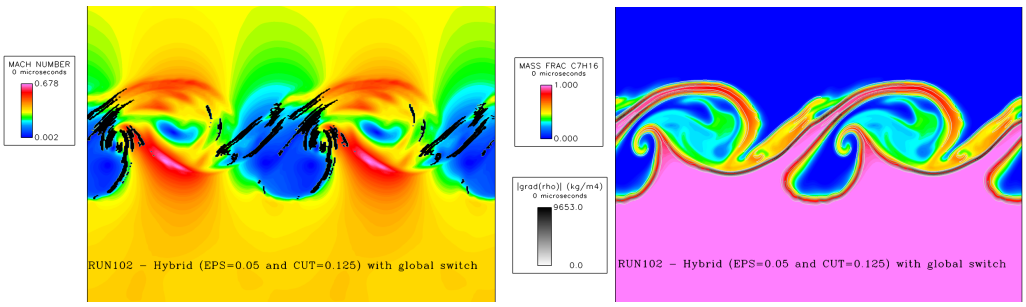

(a) Mach number/Switch (b) Mass fraction/Density gradient

Figure 124: Instantaneous snapshots of the flowfield for RUN102 of the ideal gas TML. On the left, the Mach number is shown with color contours while the upwinding is indicated in white for the I-direction and in black for the J-direction. On the right, the heptane mass fraction is shown with color contours while the density gradient is shown with grayscale contour lines.

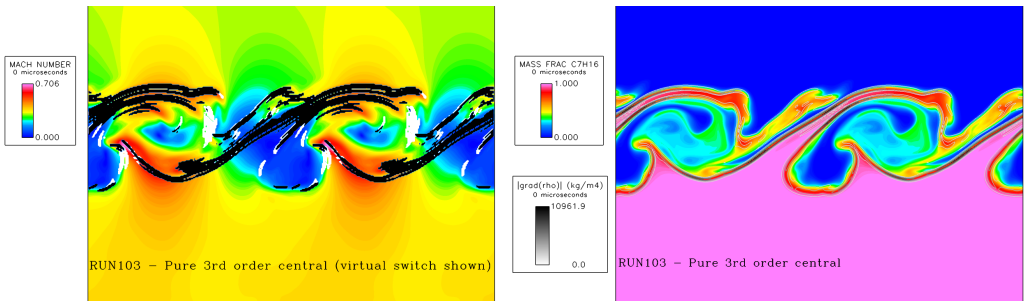

(a) Mach number/Switch (b) Mass fraction/Density gradient

Figure 125: Instantaneous snapshots of the flowfield for RUN103 of the ideal gas TML. On the left, the Mach number is shown with color contours while the upwinding is indicated in white for the I-direction and in black for the J-direction. On the right, the heptane mass fraction is shown with color contours while the density gradient is shown with grayscale contour lines.

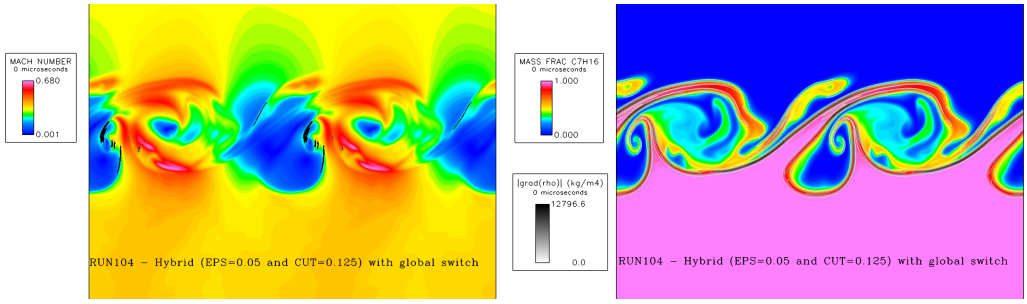

(a) Mach number/Switch (b) Mass fraction/Density gradient

Figure 126: Instantaneous snapshots of the flowfield for RUN104 of the ideal gas TML. On the left, the Mach number is shown with color contours while the upwinding is indicated in white for the I-direction and in black for the J-direction. On the right, the heptane mass fraction is shown with color contours while the density gradient is shown with grayscale contour lines.

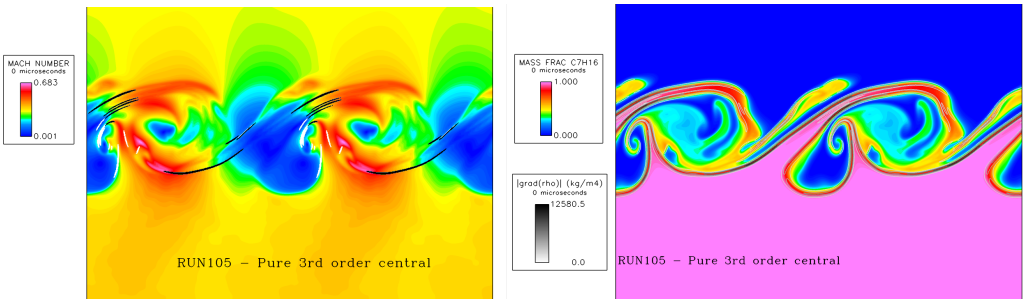

(a) Mach number/Switch (b) Mass fraction/Density gradient

Figure 127: Instantaneous snapshots of the flowfield for RUN105 of the ideal gas TML. On the left, the Mach number is shown with color contours while the upwinding is indicated in white for the I-direction and in black for the J-direction. On the right, the heptane mass fraction is shown with color contours while the density gradient is shown with grayscale contour lines.

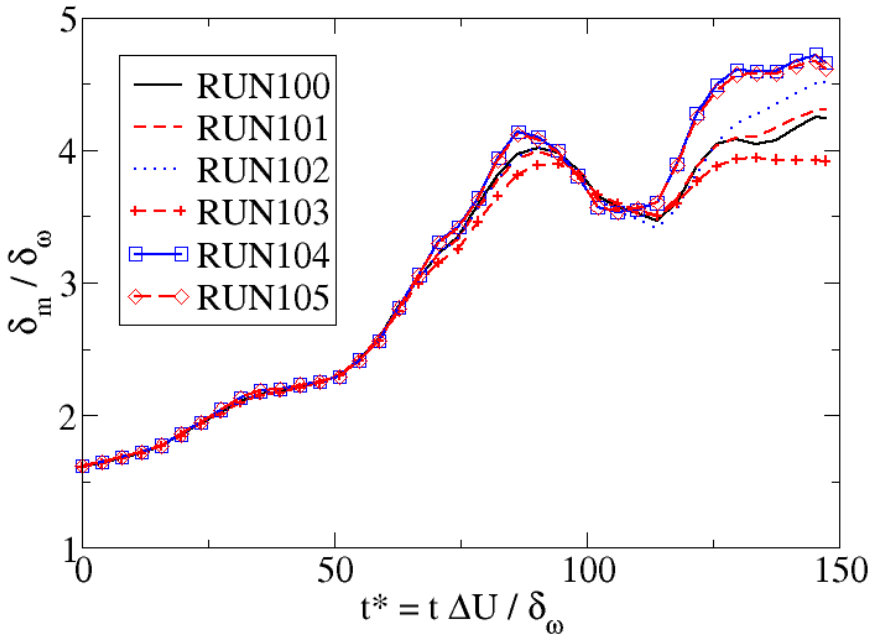

Figure 128: Temporal evolution of the momentum thickness for the ideal TML simulations.

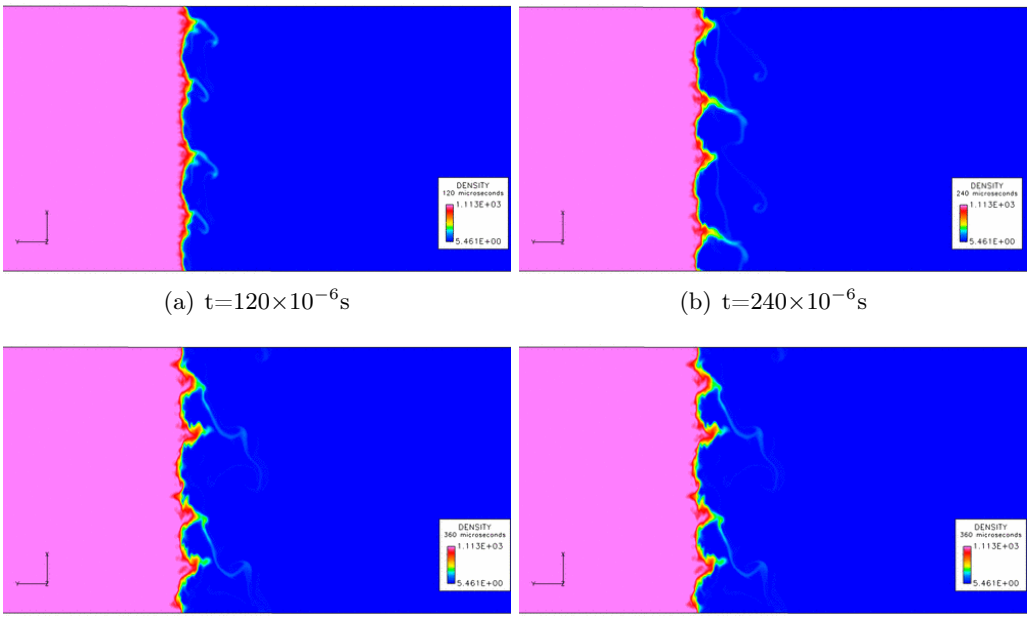

(a) t=120×10^{-6}s (b) t=240×10^{-6}s

(c) t=360×10^{-6}s (d) t=480×10^{-6}s

Figure 129: Instantaneous snapshots of the flowfield for real gas H_2/O_2 TML showing the density field.

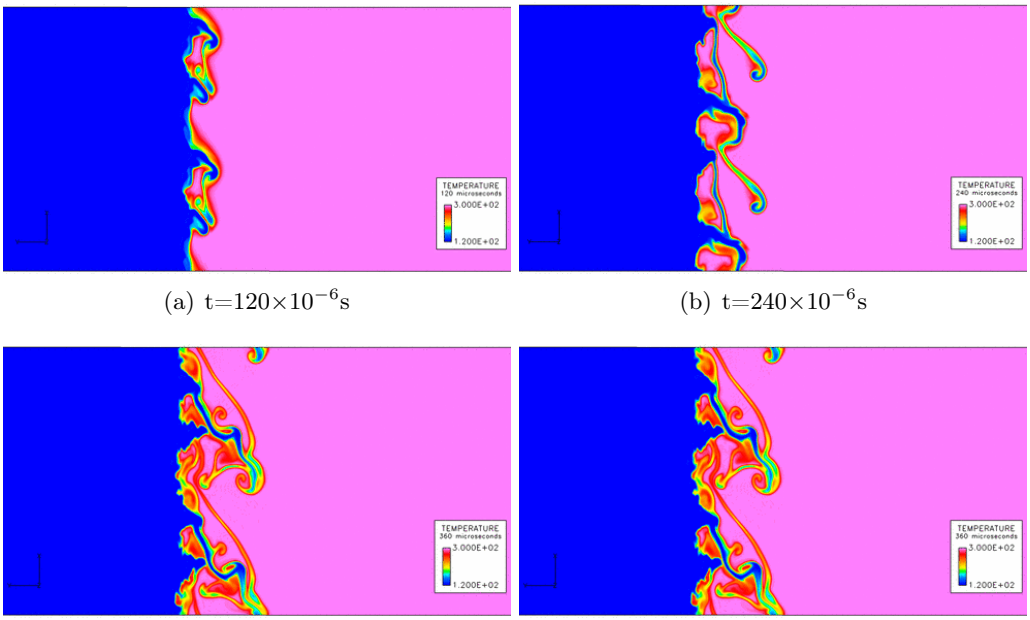

(a) t=120×10^{-6}s (b) t=240×10^{-6}s

(c) t=360×10^{-6}s (d) t=480×10^{-6}s

Figure 130: Instantaneous snapshots of the flowfield for real gas H_2/O_2 TML showing the temperature field.

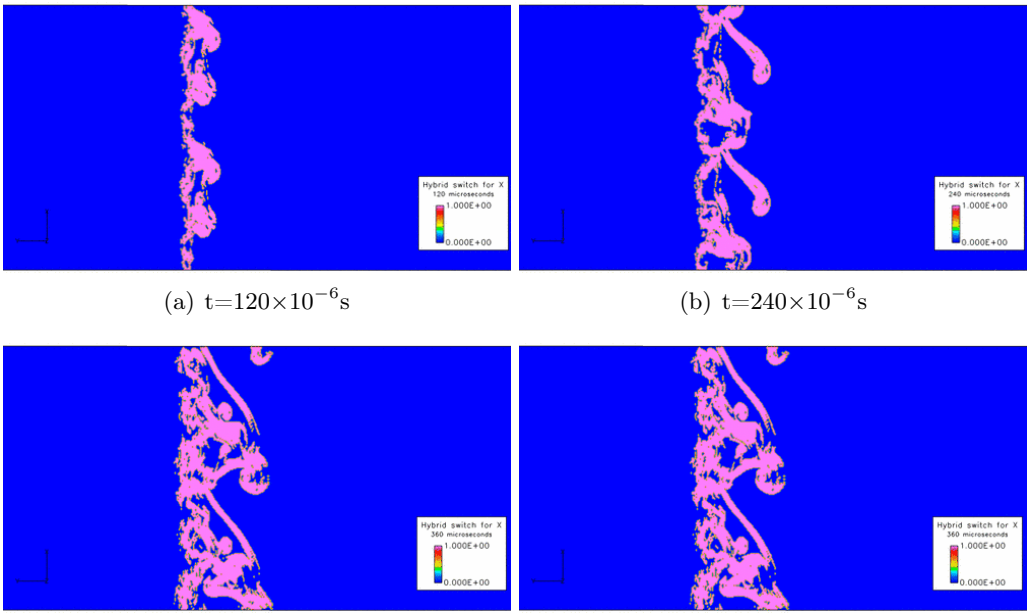

(a) t=120×10^{-6}s (b) t=240×10^{-6}s

(c) t=360×10^{-6}s (d) t=480×10^{-6}s

Figure 131: Instantaneous snapshots of the flowfield for real gas H_2/O_2 TML showing the field of the hybrid switch in the I-direction.

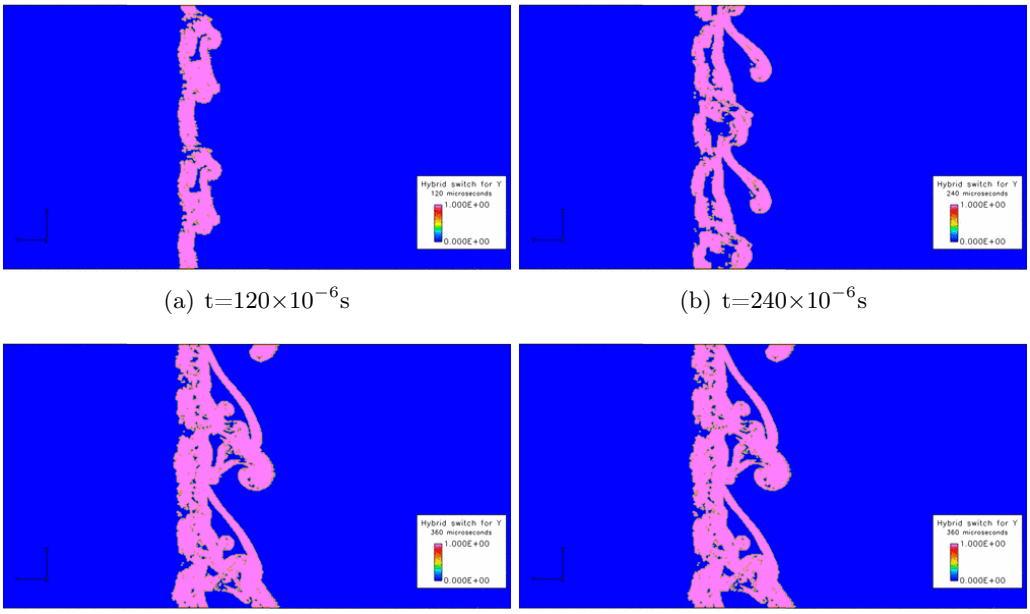

(a) t=120×10^{-6}s (b) t=240×10^{-6}s

(c) t=360×10^{-6}s (d) t=480×10^{-6}s

Figure 132: Instantaneous snapshots of the flowfield for real gas H_2/O_2 TML showing the field of the hybrid switch in the J-direction.

APPENDIX K

COMPUTATIONAL PERFORMANCE FOR COMPLEX GRIDS

The three-dimensional simulations presented in this work used butterfly grids for pipe-like geometries, with a cartesian grid along the centerline and a cylindrical grid around it. These grids were actually manually coded and generated using FORTRAN routines. This is actually relatively straightforward for structured grids with such strong symmetries. Obviously, this grid generation becomes untractable for more complex geometries such as swirlers or multi-element injectors. The methodology developed in this work is perfectly valid for this more complicated configurations as illustrated below.

The worst case scenario is described here, with a multi-block grid coming from a commercial grid generation software whose number of blocks cannot be changed and with a non-reacting flow with simple sub-grid model where the computational load per cell is not very high and balanced communications play a more important role. The flow solver is evaluated on four different machines using a trans-critical jet in cross-flow configuration. This configuration uses the Redlich-Kwong EoS with 3 species and a complex geometry with uneven blocks. The liquid jet fuel is modeled with a mixture of nonane and hexadecance as a surrogate for Jet-A [107] and is injected below the mixture critical temperature which is about 650 K. Representative snapshots of the flowfield is shown in Figure 133. The liquid jet keeps its coherence over a few injector diameters as it penetrates the hot air coflow. The trans-critical layer can be identified by the local maxima displayed by the specific heat at constant pressure: across this layer, the behavior of the fluid goes from liquid-like to gas-like. Strong vortical structures including horshoe-like structures are generated at the base of the liquid jet and further break down into three-dimensional turbulent fluctuations. Overall, the computational domain consists of 2040 blocks for 6.65 M grid points. Since the blocking of the domain is set, increasing the number of cores makes load balancing more and more

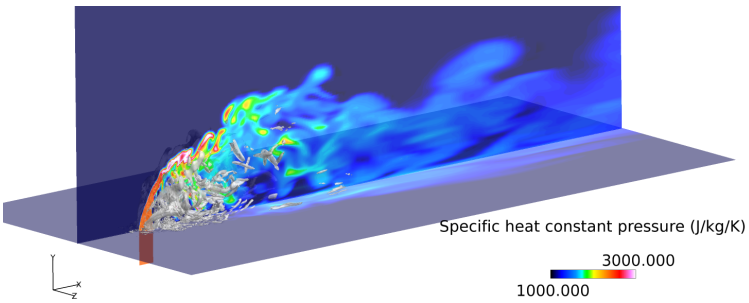

(a) Overall view

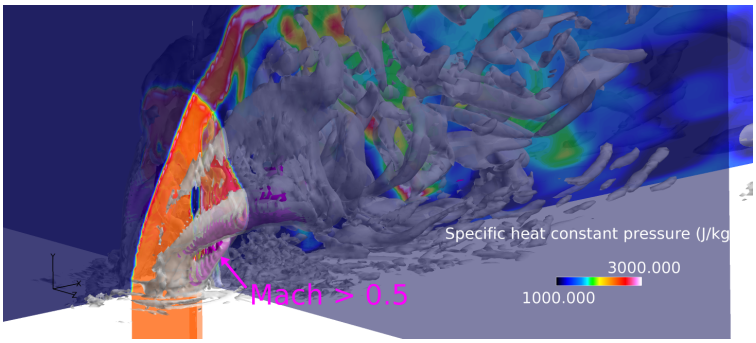

(b) Zoom view

Figure 133: Overall (top) and zoom (bottom) view of the trans-critical injection of a Jet-A surrogate into a crossflow of heated air.

difficult. Table 27 illustrates this point and highlights the fact that the unbalancing is not a linear function of the number of cores used. For this problem, trying to distribute the 2040 blocks over 896 cores with the current algorithm yields a very unbalanced load that has a direct impact on performance as seen in Figure 134. If the scaling was ideal, the COMPs values would remain constant as the number of cores increases. However, there is a significant performance hit as the computational load on each core decreases and the communication between each core becomes more important. This is strongly affected by the unbalancing of the load and results in less than 50% efficiency on all machines when comparing the runs with 64 cores and the runs with 512 cores.

Table 27: Load-balancing for the JICF simulations as the number of cores is varied. Total number of grid points is 6,665,544

Number of cores	Average load	Maximum load	Unbalancing
32	208298	209581	0.62%
64	104149	105618	1.41%
128	52074	55864	7.28%
256	26037	29686	14.01%
512	13018	14784	13.56%
896	7439	12192	63.89%
1024	6509	8160	25.36%

For a multi-element rocket injector, the number of blocks that can be easily generated by a commercial software becomes a limitation of the current mapping approach as illustrated below. A simplified multi-element injector that is a subset of sub-scale Astrium rig [175] is considered. The injector consists of 7 identical elements and each of them is meshed with a grid of about 2 M grid points, for a total of 14 M grid points for this preliminary coarse grid. A couple of snapshots of the grid can be seen in Figure 135 alongside a flowfield from a non-reacting simulation on this same grid. The code will perform close to its optimum if the distribution of blocks sizes is close to a Dirac function, or if at least it has low variance and large negative skewness. On such complex geometries, it is impossible to fully control the sizes of each block but it is possible to mitigate this by assigning several

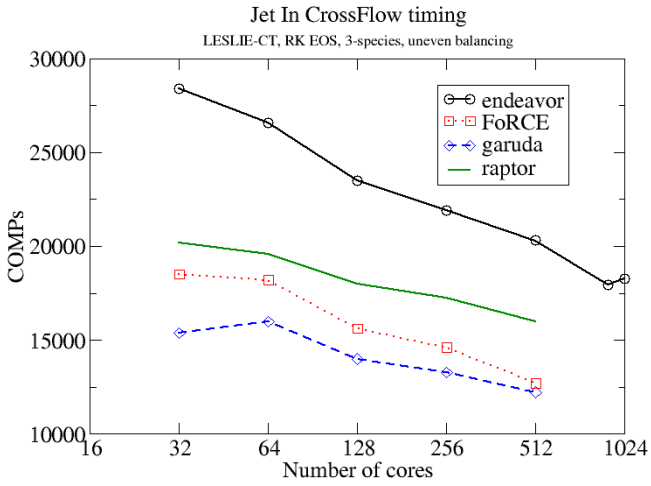

Figure 134: Performance of the current flow solver for a trans-critical jet in cross-flow on various architectures.

blocks to the same processing core so that the final load is as uniform as possible. This is illustrated by Figure 136(a) where the load distribution for all the processing cores is shown for 128, 256 and 512 cores. The curves for 128 and 256 cores look excellent since their right tail is virtually non-existent. Cores with a larger load need to be avoided since they slow down all the other cores. The size of the left tail is less important since a lighter load for a handful of cores simply means these cores will be waiting for the other cores, slightly reducing the overall efficiency. But the distribution for 512 starts showing a larger right tail, indicating a possible drop in performance. This is confirmed by Figure 136(b) where a near-perfect scaling is achieved from 128 to 256 cores but a drop in efficiency is observed for 512 cores. Currently, this blocking and load balancing process is not fully automated and time-consuming, that is why a good scaling for 512 cores is not easily obtained. However, since the average number of cells per core for such simulation would be in the range of optimal performance as previously seen, there is no reason why this cannot be achieved with a more refined pre-processing. This is part of the recommendation for future work along with the use of grid coarsening downstream of the injector plate. One could imagine a single butterfly grid for the full chamber section replacing the many butterfly grids required at the

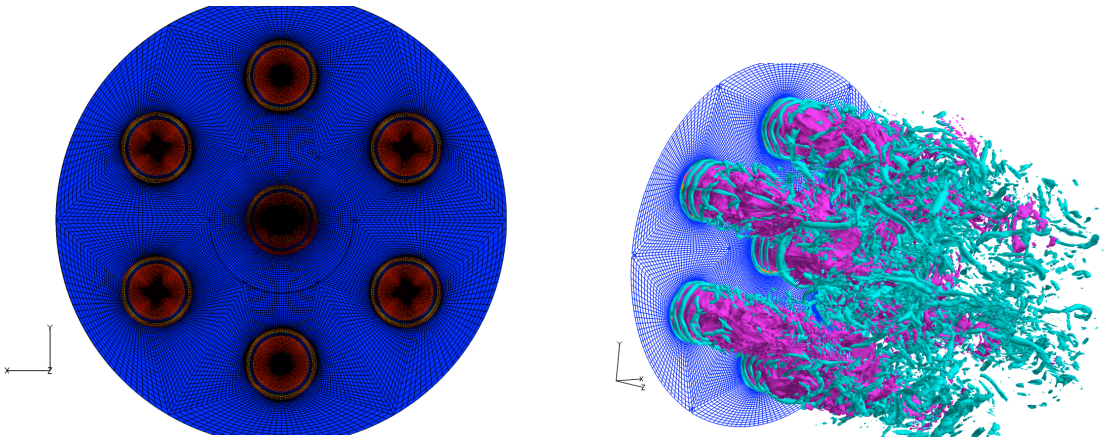

Figure 135: Overview of the current multi-element injector configuration. The 7 elements are meshed using a coarse grid of 14 M points distributed over 1280 computational blocks (left). A sample non-reacting flowfield is shown with pink iso-surfaces outlining the jet cores and cyan iso-surfaces showing vortical structures (right).

inflow. This could reduce the size of the computational grid by as much as 40%.

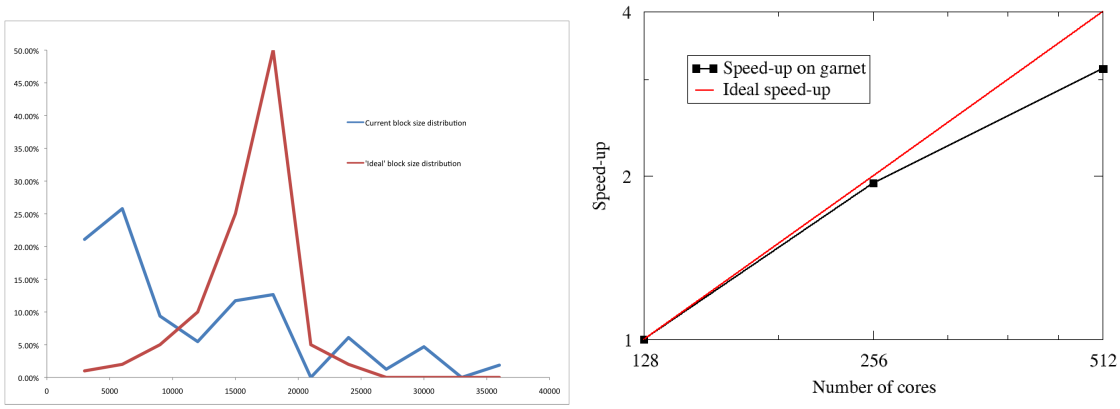

(a) (b)

Figure 136: Load distribution and performance of the current solver on the coarse multi-element shown in Figure 135.

REFERENCES

[1] "Planetary resources." http://www.planetaryresources.com, 2012.

[2] Afshari, A., Jaberi, F. A., and Shih, T., "Large-eddy simulations of turbulent flows in an axisymmetric dump combustor," *AIAA Journal*, vol. 46, pp. 1576–1592, July 2008.

[3] Akselvoll, K. and Moin, P., "Large-eddy simulation of turbulent confined coannular jets," *Journal of Fluid Mechanics*, vol. 315, no. 1, pp. 387–411, 1996.

[4] Amantini, G., Frank, J. H., Bennett, B. A. V., Smooke, M. D., and Gomez, A., "Comprehensive study of the evolution of an annular edge flame during extinction and reignition of a counterflow diffusion flame perturbed by vortices," *Combustion and Flame*, vol. 150, no. 4, pp. 292–319, 2007.

[5] Amorim, J. A., Chiavone-Filho, O., Paredes, M. L. L., and Rajagopal, K., "Modeling high-pressure densities at wide temperature range with volume scaling: Cyclohexane + n-hexadecane mixtures," *Fluid Phase Equilibria*, vol. 259, pp. 89–98, 2007.

[6] Andrews, T. *Phil. Trans. Roy. Soc. Lond.*, vol. 159, pp. 575–590, 1869.

[7] Arnone, A., Liou, M.-S., and Povinelli, L. A., "Integration of navier-stokes equations using dual time stepping and a multigrid method," *AIAA Journal*, vol. 33, pp. 985–990, June 1995.

[8] Balakrishnan, G., Smooke, M. D., and Williams, F. A., "A numerical investigation of extinction and ignition limits in laminar nonpremixed counterflowing hydrogen-air streams for both elementary and reduced chemistry," *Combustion and Flame*, vol. 102, pp. 329–340, 1995.

[9] Balakrishnan, G. and Williams, F. A., "Turbulent combustion regimes for hypersonic propulsion employing hydrogen-air diffusion flames," *Journal of Propulsion and Power*, vol. 10, no. 3, pp. 434–437, 1994.

[10] Balarac, G., Métais, O., and Lesieur, M., "Mixing enhancement in coaxial jets through inflow forcing: A numerical study," *Physics of Fluids*, vol. 19, 2007.

[11] Barlow, R. S., "International workshop on measurement and computation of turbulent non-premixed flames." http://www.sandia.gov/TNF/abstract.html, 2012.

[12] Baum, M., Poinsot, T., and Thévenin, D., "Accurate boundary conditions for multicomponent reactive flows," *Journal of Computational Physics*, vol. 116, pp. 247–261, 1994.

[13] Baurle, R. A. and Girimaji, S. S., "Assumed pdf turbulence-chemistry closure with temperature-composition correlations," *Combustion and Flame*, vol. 134, pp. 131–148, 2003.

[14] Bazargan, M. and Mohseni, M., "Algebraic zero-equation versus complex two-equation turbulence modeling in supercritical fluid flows," *Computers and Fluids*, vol. 60, pp. 49–57, 2012.

[15] Bellan, J., "Supercritical (and subcritical) fluid behavior and modeling: drops, streams, shear and mixing layers, jets and sprays," *Progress in Energy and Combustion Science*, vol. 26, pp. 329–366, 2000.

[16] Bellan, J., "Theory, modeling and analysis of turbulent supercritical mixing," *Combustion Science and Technology*, vol. 178, pp. 253–281, 2006.

[17] Berche, B., Henkel, M., and Kenna, R., "Critical phenomena: 150 years since Cagniard de la Tour," 2009.

[18] Berman, R., Cooke, A. H., and Hill, R. W., "Cryogenics," *Annual Review of Physical Chemistry*, vol. 7, pp. 1–20, 1956.

[19] Billet, G., Giovangigli, V., and de Gassowski, G., "Impact of volume viscosity on a shock/hydrogen bubble interaction," tech. rep., Ecole Polytechnique, February 2007.

[20] Bird, R. B., "Viewpoints on transport properties," *Korean Journal of Chemical Engineering*, vol. 15, no. 2, pp. 105–123, 1998.

[21] Boniface, Y. P., Reeb, A. B., Woodward, R. D., Pal, S., and Santoro, R. J., "Hot-fire studies of lox primary atomization from rocket engin coaxial injectors," in *Eleventh Annual Symposium of the Propulsion Engineering Research Center*, pp. 110–119, Pennsylvania State University, 1999.

[22] Borghi, R., "Turbulent combustion modelling," *Progress in Energy and Combustion Science*, vol. 14, pp. 245–292, 1988.

[23] Brink, A., Mueller, C., Kilpinen, P., and Hupa, M., "Possibilities and limitations of the eddy break-up model," *Combustion and Flame*, vol. 123, no. 1–2, pp. 275–279, 2000.

[24] Brown, P. N., Byrne, G. D., and Hindmarsh, A. C., "VODE, a variable-coefficient ODE solver," *SIAM Journal on Scientific and Statistical Computing*, vol. 10, pp. 1038–1051, September 1989.

[25] Buelow, P. E. O., Venkateswaran, S., and Merkle, C. L., "Stability and convergence analysis of implicit upwind schemes," *Computers and Fluids*, vol. 30, pp. 961–988, 2001.

[26] Byun, D. and Baek, S. W., "Numerical investigation of combustion with non-gray thermal radiation and soot formation effect in a liquid rocket engine," *International Journal of Heat and Mass Transfer*, vol. 50, pp. 412–422, 2007.

[27] Cagniard de la Tour, C., "Exposé de quelques résultats obtenus par l'action combinée de la chaleur et de la compression sur certains liquides, tels que l'eau, l'alcool, l'éther sulfurique et l'essence de pétrole rectifiée," *Ann. Chim. Phys.*, vol. 21, pp. 127–132, 1822.

[28] Calhoon, W. H. and Menon, S., "Subgrid modeling for reacting large eddy simulations," in *34th Aerospace Sciences Meeting and Exhibit*, no. AIAA 96-0516, 1996.

[29] Calhoon, W. H., Zambon, A. C., Sekar, B., and Kiel, B., "Combustor and augmentor combustion modeling for LES based on stochastic model parametrization," in *Proceedings of ASME Turbo Expo 2011*, no. GT2011-45126, pp. 153–167, 2011.

[30] Candel, S., Juniper, M., Singla, G., Scouflaire, P., and Rolon, C., "Structure and dynamics of cryogenic flames at supercritical pressure," *Combustion Science and Technology*, vol. 178, pp. 161–192, January 2006.

[31] Candel, S., Rodriguez, J. I., and Schmitt, T., "Mixing under transcritical flow conditions," Tech. Rep. AFRL-AFOSR-UK-TR-2011-0001, AFRL, 2011.

[32] Carlès, P., "A brief review of the thermophysical properties of supercritical fluids," *Journal of Supercritical Fluids*, vol. 53, pp. 2–11, 2010.

[33] Chakravarthy, V. K. and Menon, S., "Linear-eddy simulations of Reynolds and Schmidt number dependencies in turbulent scalar mixing," *Physics of Fluids*, vol. 13, pp. 488–499, 2001.

[34] Chakravarthy, V. and Menon, S., "Subgrid modeling of premixed flames in the flamelet regime," *Flow, Turbulence and Combustion*, vol. 65, pp. 133–161, 2000.

[35] Chehroudi, B., "Physical hypothesis for the combustion instability in cryogenic liquid rocket engines," *Journal of Propulsion and Power*, vol. 26, pp. 1153–1160, November–December 2010.

[36] Chung, T. H., Ajlan, M., Lee, L. L., and Starling, K. E., "Generalized multiparameter corresponding state correlation for polyatomic, polar fluid transport properties," *Industrial and Engineering Chemistry Research*, vol. 27, pp. 671–679, 1988.

[37] Cismondi, M. and Mollerup, J., "Development and application of a three-parameter RK-PR equation of state," *Fluid Phase Equilibria*, vol. 232, pp. 74–89, 2005.

[38] Cole, D. and Glauser, M., "Applications of stochastic estimation in the axisymmetric sudden expansion," *Physics of Fluids*, vol. 10, pp. 2941–2949, November 1998.

[39] Colonna, P. and Guardone, A., "Molecular interpretation of nonclassical gas dynamics of dense vapors under the van der waals model," *Physics of Fluids*, vol. 18, 2006.

[40] Colonna, P. and Rebay, S., "Numerical simulation of dense gas ows on unstructured grids with an implicit high resolution upwind euler solver," *International Journal for Numerical Methods in Fluids*, vol. 46, pp. 735–765, 2004.

[41] Colonna, P. and Silva, P., "Dense gas thermodynamic properties of single and multicomponent fluids for fluid dynamics simulations," *Journal of Fluids Engineering*, vol. 125, pp. 414–427, May 2003.

[42] Congiunti, A., Bruno, C., and Giacomazzi, E., "Supercritical combustion properties," in *41st Aerospace Sciences Meeting and Exhibit*, no. AIAA 2003-478, (Reno, NV), January 2003.

[43] Conley, A., Vaidyanathan, A., and Segal, C., "Heat flux measurements for a GO_2/GH_2 single-element, shear injector," *Journal of Spacecraft and Rockets*, vol. 44, no. 3, pp. 633–639, 2007.

[44] Cook, A. W., "Enthalpy diffusion in multicomponent flows," *Physics of Fluids*, vol. 21, 2009.

[45] Coquelet, C., Chapoy, A., and Richon, D., "Development of a new alpha function for the peng-robinson equation of state: Comparative study of alpha function models for pure gases (natural gas components) and water-gas systems," *International Journal of Thermophysics*, vol. 25, no. 1, pp. 133–158, 2004.

[46] Cortesi, A. B., Smith, B. L., Yadigaroglu, G., and Banerjee, S., "Numerical investigation of the entrainment and mixing processes in neutral and stably-stratified mixing layers," *Physics of Fluids*, vol. 11, pp. 162–185, January 1999.

[47] Cremer, M. A., McMurtry, P. A., and Kerstein, A. R., "Effects of turbulence lengthscale distribution on scalar mixing in homogeneous turbulent flow," *Physics of Fluids*, vol. 6, p. 2143, 1994.

[48] Cristancho, D. E., Mantilla, I. D., Coy, L. A., Tibaduiza, A., Ortiz-Vega, D. O., and Hall, K. R., "Accurate $p-\rho-t$ data and phase boundary determination for a synthetic residual natural gas mixture," *Journal of Chemical and Engineering Data*, 2010.

[49] Culick, F. E. C., "Unsteady motions in combustion chambers for propulsion systems," AGARDograph AG-AVT-039, NATO Research and Technology Organisation, 2006.

[50] Cutrone, L., De Palma, P., Pascazio, G., and Napolitano, M., "A RANS flamelet-progress-variable method for computing reacting flows or real-gas mixtures," *Computers and Fluids*, vol. 39, pp. 485–498, 2010.

[51] Daimon, Y., Negishi, H., Yamanishi, N., Nunome, Y., Sasaki, M., and Tomita, T., "Combustion and heat transfer modeling in regeneratively cooled thrust chambers (multi-injection flow features)," in *47th AIAA/ASME/SAE/ASEE Joint Propulsion Conference and Exhibit*, no. AIAA 2011-5625, (San Diego, CA), August 2011.

[52] Davis, D. W., *On the behavior of a shear-coaxial jet, spanning sub- to supercritical pressures, with and without an externally imposed transverse acoustic field.* PhD thesis, The Pennsylvania State University, May 2006.

[53] Davis, D. W. and Chehroudi, B., "Measurements in an acoustically driven coaxial jet under sub-, near- and supercritical conditions," *Journal of Propulsion and Power*, vol. 23, pp. 364–374, March–April 2007.

[54] Davis, J. A. and Campbell, R. L., "Advantages of full-flow staged combustion cycle engine system," in *33rd AIAA/ASME/SAE/ASEE Joint Propulsion Conference*, 1997.

[55] Davis, S. F., "Simplified second-order Godunov-type methods," *SIAM Journal on Scientific and Statistical Computing*, vol. 9, pp. 445–469, May 1988.

[56] deRidder, M. and Anderson, W. E., "Heat flux and pressure profiles in an oxygen/hydrogen multielement rocket combustor," *Journal of Propulsion and Power*, vol. 26, pp. 696–705, July–August 2010.

[57] Duwig, C. and Fuchs, L., "Large eddy simulation of a H_2/N_2 lifted flame in a vitiated co-flow," *Combustion Science and Technology*, vol. 180, no. 3, pp. 453–480, 2008.

[58] Echekki, T. and Mastorakos, E., eds., *Turbulent Combustion Modeling*, vol. 95. Springer, 2011.

[59] Edwards, J. R., Boles, J. A., and Baurle, R. A., "Large-eddy/reynolds-averaged navier-stokes simulation of a supersonic reacting wall jet," *Combustion and Flame*, vol. 159, pp. 1127–1139, 2012.

[60] Edwards, J. R., Franklin, R. K., and Liou, M.-S., "Low-diffusion flux-splitting methods for real fluid flows with phase transitions," *AIAA Journal*, vol. 38, pp. 1624–1633, September 2000.

[61] Eggenspieler, G., *Numerical Simulatioon of Pollutant Emission and Flame Extinction in Lean Premixed Systems*. PhD thesis, Georgia Institute of Technology, 2005.

[62] Einfeldt, B., Munz, C. D., Roe, P. L., and Sjögreen, B., "On godunov-type methods new low densities," *Journal of Computational Physics*, vol. 92, pp. 273–295, 1991.

[63] Eklund, D. R., Drummond, J. P., and Hassan, H. A., "Calculation of supersonic turbulent reacting coaxial jets," *AIAA Journal*, vol. 28, pp. 1633–1641, September 1990.

[64] Eppard, W. M., "CFD time-integration strategies for large chemical systems," Final Report F49620-03-1-0208, AFOSR, Blacksburg, VA, March 2006.

[65] Erlebacher, G., Hussaini, M. Y., Speziale, C. G., and Zang, T. A., "Toward the large-eddy simulation of compressible turbulent flows," *Journal of Fluid Mechanics*, vol. 238, no. 1, pp. 155–185, 1992.

[66] Esposito, G. and Chelliah, H. K., "Effect of binary diffusion and chemical kinetic parameter uncertainties in simulations of premixed and non-premixed laminar hydrogen flames," *Combustion and Flame*, 2012.

[67] Farhangi, S., Yu, T., Rojas, L., Sprouse, K., and McKinnon, J., "Gas-gas injector technology for full flow stage combustion cycle application," in *35th AIAA/ASME/SAE/ASEE Joint Propulsion Conference*, no. AIAA 99-31444, (Los Angeles, CA), 1999.

[68] Fosso, A. P., Deniau, H., Sicot, F., and Sagaut, P., "Curvilinear finite-volume schemes using high-order compact interpolation," *Journal of Computational Physics*, vol. 229, pp. 5090–5122, 2010.

[69] Foster, J. W. and Miller, R. S., "A priori analysis of subgrid statistics from direct numerical simulations of high pressure hydrogen-oxygen flames: I subgrid mass flux

vectors," in *7th US National Technical Meeting of the Combustion Institute*, (Atlanta, GA), March 2011.

[70] Foster, J. W. and Miller, R. S., "A priori analysis of subgrid mass diffusion vectors in high pressure turbulent hydrogen/oxygen reacting shear layer flames," *Physics of Fluids*, vol. 24, no. 075114, 2012.

[71] Fowler, M., "Van der waals forces between atoms," 2007.

[72] Frey, K., Augustine, C., Ciccolini, R. P., Paap, S., Modell, M., and Tester, J., "Volume translation in equations of state as a means of accurate property estimation," *Fluid Phase Equilibria*, vol. 260, pp. 316–325, 2007.

[73] Frey, K., Modell, M., and Tester, J., "Density-and-temperature-dependent volume translation for the SRK EOS: 1. pure fluids," *Fluid Phase Equilibria*, vol. 279, pp. 56–63, 2009.

[74] Fuller, E., Schettler, P., and Giddings, J. C., "A new method for prediction of binary gas," *Industrial and Engineering Chemistry Research*, vol. 58, pp. 18–27, May 1966.

[75] Fureby, C., "Comparison of flamelet and finite rate chemistry LES for premixed turbulent combustion," in *45th AIAA Aerospace Sciences Meeting and Exhibit*, no. AIAA 2007-1413, (Reno, NV), January 2007.

[76] Fureby, C., "Towards the use of large eddy simulation in engineering," *Progress in Aerospace Sciences*, vol. 44, 2008.

[77] Fureby, C. and Moller, S.-I., "Large-eddy simulation of reacting flows applied to bluff body stabilized flames," *AIAA Journal*, vol. 33, no. 12, pp. 2339–2347, 1995.

[78] Fürst, J. and Furmanek, P., "An implicit MacCormack scheme for unsteady flow calculations," *Computers and Fluids*, vol. 46, pp. 231–236, 2011.

[79] Gautam, V. and Gupta, A. K., "Simulation of flow and mixing from a cryogenic rocket injector," *Journal of Propulsion and Power*, vol. 23, pp. 123–130, January–February 2007.

[80] Gautam, V. and Gupta, A. K., "Cryogenic flow and atomization from a coaxial injector," *Journal of Propulsion and Power*, vol. 25, pp. 33–39, January–February 2009.

[81] Génin, F., *Study of Compressible Turbulent Flows in Supersonic Environment by Large-Eddy Simulation*. PhD thesis, Georgia Institute of Technology, 2009.

[82] Georgiadis, N. J., Rizzetta, D. P., and Fureby, C., "Large-eddy simulation: Current capabilities, recommended practices, and future research," *AIAA Journal*, vol. 48, pp. 1772–1784, August 2010.

[83] Germano, M., Piomelli, U., Moin, P., and Cabot, W. H., "A dynamic subgrid-scale eddy viscosity model," *Physics of Fluids A*, vol. 3, no. 11, pp. 1760–1765, 1991.

[84] Giovangigli, V., *Multicomponent Flow Modeling*. Modeling and Simulation in Science, Engineering and Technology, Boston: Birkhäuser, 1999.

[85] Giovangigli, V., Matuszewski, L., and Dupoirieux, F., "Detailed modeling of planar transcritical H_2-O_2-N_2 flames," Tech. Rep. 688, Ecole Polytechnique, July 2010.

[86] Giovangigli, V., Matuszewski, L., and Dupoirieux, F., "Detailed modeling of planar transcritical H_2-O_2-N_2 flames," *Combustion Theory and Modelling*, vol. 15, no. 2, pp. 141–182, 2011.

[87] Glassman, I., *Combustion*. Academic Press, third ed., 1996.

[88] Godunov, S. K., "A difference scheme for numerical computation of discontinuous solution of hyperbolic equation," *Math. Sbornik*, vol. 47, pp. 271–306, 1959.

[89] Goodwin, D. G., "An open-source, extensible software suite for CVD process simulation," in *Chemical Vapor Deposition XVI and EUROCVD 14* (Allendorf, M., Maury, F., and Teyssandier, F., eds.), vol. 2003-08, pp. 155–162, The Electrochemical Society, 2003.

[90] Graham, J. J., Leyva, I. A., Rodriguez, J. I., and Talley, D., "On the effect of a transverse acoustic field on a flush shear coaxial injector," in *45th AIAA/ASME/SAE/ASEE Joint Propulsion Conference and Exhibit*, no. AIAA 2009-5142, (Denver, Colorado), August 2009.

[91] Graves, R. E. and Argrow, B. M., "Bulk viscosity: Past to present," *Journal of Thermophysics and Heat Transfer*, vol. 13, pp. 337–342, July–September 1999.

[92] Gryngarten, L. D. and Menon, S., "A generalized approach for sub- and supercritical flows using the local discontinuous galerkin method," *Computational methods in applied mechanics and engineering*, vol. 253, pp. 169–185, 2013.

[93] Guézennec, N., Masquelet, M., and Menon, S., "Large eddy simulation of flame-turbulence interactions in a LOX-CH_4 shear coaxial injector," in *50th AIAA Aerospace Sciences Meeting*, no. AIAA 2012-1267, 2012.

[94] Gunn, R. D., Chueh, P. L., and Prausnitz, J. M., "Prediction of thermodynamic properties of dense gas mixtures containing one or more of the quantum gases," *AIChE Journal*, vol. 12, no. 5, pp. 937–941, 1966.

[95] Habiballah, M., Orain, M., Grisch, F., Vingert, L., and Gicquel, P., "Experimental studies of high-pressure cryogenic flames on the mascotte facility," *Combustion Science and Technology*, vol. 178, no. 1–3, pp. 101–128, 2006.

[96] Haghtalab, A., Mahmoodi, P., and Mazloumi, S. H., "A modified Peng-Robinson equation of state for phase equilibrium calculation of liquefied, synthetic natural gas and gas condensate mixtures," *The Canadian Journal of Chemical Engineering*, vol. 89, pp. 1376–1387, 2011.

[97] Harstad, K. G. and Bellan, J., "Isolated fluid oxygen drop behavior in fluid hydrogen at at rocket chamber pressures," *International Journal of Heat and Mass Transfer*, vol. 41, pp. 3537–3550, 1998.

[98] Harstad, K. G. and Bellan, J., "High-pressure binary mass-diffusion coefficients for combustion applications," *Industrial and Engineering Chemistry Research*, vol. 43, pp. 645–654, 2004.

[99] Harstad, K. G., Miller, R. S., and Bellan, J., "Efficient high-pressure state equations," *American Institute of Chemical Engineers Journal*, vol. 43, no. 6, pp. 1605–1610, 1997.

[100] Harten, A., Lax, P. D., and van Leer, B., "On upstream differencing and godunov-type schemes for hyperbolic conservation laws," *SIAM Review*, vol. 25, pp. 35–61, January 1983.

[101] Hirschfelder, J. O., Taylor, M. H., and Kihara, T., *Molecular Theory of Gases and Liquids*. Wiley, New York, 1954.

[102] Hixon, R. and Turkel, E., "Compact implicit maccormack-type schemes with high accuracy," *Journal of Computational Physics*, vol. 158, pp. 51–70, 2000.

[103] Hooper, M. A. and Nordholm, S., "Generalized van der waals theory. ii quantum effects on the equation of state," *Australian Journal of Chemistry*, vol. 33, pp. 2029–2035, 1980.

[104] Hosangadi, A., Lee, C. P., Kannepalli, C., and Arunajatesan, S., "Three-dimensional hybrid rans/les simulations of a supercritical liquid nitrogen jet," in *44th AIAA/ASME/SAE/ASEE Joint Propulsion Conference and Exhibit*, no. AIAA 2008-5227, (Hartford, CT), July 2008.

[105] Hoyos, B., "Generalized liquid volume shifts for the peng-robinson equation of state for c_1 to c_8 hydrocarbons," *Latin America Applied Research*, vol. 34, pp. 83–89, 2004.

[106] Huang, X. and Baumann, W. T., "Reduced-order modeling of dynamic heat release for thermoacoustic instability prediction," *Combustion Science and Technology*, vol. 179, pp. 617–636, 2007.

[107] Huber, M. L. and Yang, J. C., "A thermodynamic analysis of fuel vapor characteristics in an aircraft fuel tank ullage," *Fire Safety Journal*, vol. 37, pp. 517–524, 2002.

[108] Hulka, J. R., "Scaling of performance in liquid propellant rocket engine combustors," in *20th Memorial Meeting of the Northern Section of the Japan Society for Aeronautical and Space Sciences*, (Sendai, Japan), 2007.

[109] Hulka, J. R., "Scaling of performance in liquid propellant rocket engine combustion devices," in *44th AIAA/ASME/SAE/ASEE Joint Propulsion Conference and Exhibit*, no. AIAA 2008-5113, July 2008.

[110] Huo, H. and Yang, V., "LOX/methane flame stabilization of shear coaxial injector at supercritical conditions," in *7th US National Technical Meeting of the Combustion Institute*, (Atlanta, GA), March 2011.

[111] Huo, H. and Yang, V., "Supercritical LOX/methane combustion of a shear coaxial injector," in *49th AIAA Aerospace Sciences Meeting*, no. AIAA 2011-326, (Orlando, FL), January 2011.

[112] Huzel, D. K. and Huang, D. H., *Modern Engineering for Design of Liquid Propellant Rocket Engines*. Progress in Astronautics and Aeronautics, AIAA, 1992.

[113] Ivancic, B. and Mayer, W. O. H., "Time- and length scales of combustion in liquid rocket thrust chambers," *Journal of Propulsion and Power*, vol. 18, pp. 247–253, March–April 2002.

[114] Jachimowski, C. J., "An analytical study of the hydrogen-air reaction with application to scramjet combustion," NASA Technical Paper 2791, NASA Langley Research Center, 1988.

[115] Jameson, A., Schmidt, W., and Turkel, E., "Numerical solutions of the euler equations by finite volume methods using runge-kutta time-stepping schemes," No. AIAA 81-1259, 1981.

[116] Jang, Y. K.

[117] Jensen, R. J., Dodson, H. C., and Claflin, S. E., "LOX/hydrocarbon combustion instability investigation," NASA Contractor Report 182249, NASA Lewis Research Center, 1989.

[118] Johnsen, E. and Colonius, T., "Implementation of WENO schemes in compressible multicomponent flow problems," *Journal of Computational Physics*, vol. 219, pp. 715–732, 2006.

[119] Johnston, H. L. and White, D. *Trans. ASME*, vol. 70, p. 651, 1948.

[120] Kawai, S. and Terashima, H., "A high-resolution scheme for compressible multicomponent flows with shock waves," *International Journal for Numerical Methods in Fluids*, vol. 66, pp. 1207–1225, 2011.

[121] Kays, W. M., "Turbulent prandtl number – where are we?," *ASME Journal of Heat Transfer*, vol. 116, pp. 284–295, May 1994.

[122] Kee, R. J., Dixon-Lewis, G., Warnatz, J., Coltrin, M. E., Miller, J. A., and Moffat, H. K., "A FORTRAN computer code package for the evaluation of gas-phase, multicomponent transport properties," tech. rep., Sandia National Laboratories, March 1998.

[123] Keistler, P., *A Variable Turbulent Prandtl and Schmidt Number Model Study for Scramjet Applications.* PhD thesis, North Carolina State University, 2009.

[124] Keizer, J., *Statistical Thermodynamics of Nonequilibrium Processes.* New York: Springer Verlag, 1987.

[125] Kerstein, A. R., "Linear-eddy model of turbulent scalar transport and mixing," *Combustion Science and Technology*, vol. 60, pp. 391–421, 1988.

[126] Kerstein, A. R., "Linear-eddy model of turbulent transport III," *Journal of Fluid Mechanics*, vol. 216, pp. 411–435, 1990.

[127] Kerstein, A. R., "Linear-eddy modeling of turbulent transport. part VI: Microstructure of diffusive scalar mixing fields," *Journal of Fluid Mechanics*, vol. 231, pp. 361–394, 1991.

[128] Kerstein, A. R., "Linear-eddy modeling of turbulent transport. part IV: Structure of diffusion-flames," *Combustion Science and Technology*, vol. 81, pp. 75–86, 1992.

[129] Kerstein, A. R., "Linear-eddy modeling of turbulent transport. part VII: Finite-rate chemistry and multi-stream mixing," *Journal of Fluid Mechanics*, vol. 240, pp. 289–313, 1992.

[130] Kerstein, A. R. and Ashurst, W. T., "Propagation rate of growing interfaces in stirred fluids," *Physical Review*, vol. 68, no. 7, pp. 934–937, 1992.

[131] Kerstein, A. R., "Linear-eddy modeling of turbulent transport. part II: Application to shear layer mixing," *Combustion and Flame*, vol. 75, pp. 397–413, 1989.

[132] Khalil, I. and Miller, D. R., "The structure of supercritical fluid free-jet expansions," *AIChE Journal*, vol. 50, pp. 2697–2704, November 2004.

[133] Kim, S.-K., Choi, H.-S., and Kim, Y., "Thermodynamic modeling based on a generalized cubic equation of state for kerosene/LOx rocket combustion," *Combustion and Flame*, vol. 159, pp. 1351–1365, 2012.

[134] Kim, T., Kim, Y., and Kim, S.-K., "Numerical analysis of gaseous hydrogen/liquid oxygen flamelet at supercritical pressures," *International Journal of Hydrogen Energy*, 2011.

[135] Kim, T., Kim, Y., and Kim, S.-K., "Real-fluid flamelet modeling for gaseous hydrogen/cryogenic liquid oxygen jet flames at supercritical pressure," *Journal of Supercritical Fluids*, vol. 58, pp. 254–262, 2011.

[136] Kim, W.-W., *A New Dynamic Subgrid-Scale Model for Large-Eddy Simulation of Turbulent Flows*. PhD thesis, Georgia Institute of Technology, 1996.

[137] Kim, W.-W., Menon, S., and Mongia, H. C., "Large eddy simulations of a gas turbine combustor flow," *Combustion Science and Technology*, vol. 143, no. 1, pp. 25–62, 1999.

[138] Kiselev, S. B. and Ely, J. F., "Generalized crossover description of the thermodynamic and transport properties in pure fluids ii. revision and modifications," *Fluid Phase Equilibria*, vol. 252, pp. 57–65, 2007.

[139] Korucu, A., Foster, J. W., and Miller, R. S., "A priori analysis of subgrid statistics from direct numerical simulations of high pressure hydrogen-oxygen flames: Ii subgrid heat flux vector," in *7th US National Technical Meeting of the Combustion Institute*, (Atlanta, GA), March 2011.

[140] Lacaze, G. and Oefelein, J. C., "A non-premixed combustion model based on flame structure analysis at supercritical pressures," *Combustion and Flame*, vol. 159, pp. 2087–2103, 2012.

[141] Lafon, P., Meng, H., Yang, V., and Habiballah, M., "Vaporization of liquid oxygen (LOX) droplets in hydrogen and water environments under sub- and supercritical conditions," *Combustion Science and Technology*, vol. 180, pp. 1–26, 2008.

[142] Lam, S. H., "Multicomponent diffusion revisited," *Physics of Fluids*, vol. 18, 2006.

[143] Lasheras, J. C. and Hopfinger, E. J., "Liquid jet instability and atomization in a coaxial gas stream," *Annual Review of Fluid Mechanics*, vol. 32, pp. 275–308, 2000.

[144] Laugier, S., Rivollet, F., and Richon, D., "New volume translation for cubic equations of state," *Fluid Phase Equilibria*, vol. 259, 2007.

[145] Lee, D. J., Thakur, A., Wright, J., Ihme, M., and Shyy, W., "Characterization of flow field structure and species composition in a shear coaxial rocket GH_2/GO_2 injector: Modeling of wall heat losses," in *47th AIAA/ASME/SAE/ASEE Joint Propulsion Conference and Exhibit*, no. AIAA 2011-6125, (San Diego, CA), August 2011.

[146] Lemmon, E. W., Huber, M. L., and McLinden, M. O., "NIST standard reference database 23: Reference fluid thermodynamic and transport properties - REFPROP version 8.0," tech. rep., National Institute of Standards and Technology, Gaithersburg, MD, 2007.

[147] Lempke, M., Gerlinger, P., Aigner, M., and Rachner, M., "Steady and unsteady RANS simulations of cryogenic rocket combustors," in *49th AIAA Aerospace Sciences Meeting*, no. AIAA 2011-101, (Orlando, FL), January 2011.

[148] Leyva, I. A., Chehroudi, B., and Talley, D., "Dark core analysis of coaxial injectors at sub-, near-, and supercritical pressures in a transverse acoustic field," in *43rd AIAA/ASME/SAE/ASEE Joint Propulsion Conference and Exhibit*, no. AIAA 2007-5456, (Cincinnati, OH), July 2007.

[149] Leyva, I. A., Rodriguez, J. I., Chehroudi, B., and Talley, D., "Preliminary results on coaxial jet spread angles and the effects of variable phase transverse acoustic fields," in *48th AIAA Aerospace Sciences Meeting and Exhibit*, no. AIAA 2008-950, (Reno, NV), January 2008.

[150] Li, J., Zhao, Z., Kazakov, A., and Dryer, F. L., "An updated comprehensive kinetic model of hydrogen combustion," *International Journal of Chemical Kinetics*, vol. 36, pp. 566–575, October 2004.

[151] Lian, C., Xia, G., and Merkle, C. L., "Effects of back-step height and recirculation zones on unsteady mixing and combustion," in *39th AIAA Fluid Dynamics Conference*, no. AIAA 2009-3897, (San Antonio, TX), June 2009.

[152] Lian, C., Xia, G., and Merkle, C. L., "Solution-limited time stepping to enhance reliability in CFD applications," *Journal of Computational Physics*, vol. 228, pp. 4836–4857, 2009.

[153] Lin, H. and Duan, Y.-Y., "Empirical correction to the Peng-Robinson equation of state for the saturated region," *Fluid Phase Equilibria*, pp. 194–203, 2005.

[154] Lin, H., Duan, Y.-Y., and Min, Q., "Gradient theory modeling of surface tension for pure fluids and binary mixtures," *Fluid Phase Equilibria*, vol. 254, pp. 75–90, 2007.

[155] Lin, J., West, J. S., Williams, R. W., Tucker, P. K., and Chenoweth, J. D., "CFD code validation of wall heat fluxes for a GO_2/GH_2 single element combustor," in *41st AIAA/ASME/SAE/ASEE Joint Propulsion Conference and Exhibit*, no. AIAA 2005-4524, (Tucson, AZ), July 2005.

[156] Ling, W., Chung, J. N., Troutt, T. R., and Crowe, C. T., "Direct numerical simulation of a three-dimensional temporal mixing layer with particle dispersion," *Journal of Fluid Mechanics*, vol. 358, pp. 61–85, 1998.

[157] Liou, M.-S., "A sequel to AUSM, part ii: AUSM$^+$-up for all speeds," *Journal of Computational Physics*, vol. 214, pp. 137–170, 2006.

[158] Liou, M.-S. and Steffen, C. J., "A new flux splitting scheme," *Journal of Computational Physics*, vol. 107, pp. 23–39, 1993.

[159] Liu, T., *Shear-Coaxial Injection And Mixing Of Cryogenic Fluids Under Supercritical Conditions*. PhD thesis, The Pennsylvania State University, 2007.

[160] Locke, J. M., *High speed diagnostics for characterization of oxygen/hydrogen rocket injector flowfields*. PhD thesis, The Pennsylvania State University, May 2011.

[161] Locke, J. M., Pal, S., Woodward, R. D., and Santoro, R. J., "Toward time-resolved measurements in a gaseous hydrogen/oxygen rocket," in *45th AIAA/ASME/SAE/ASEE Joint Propulsion Conference and Exhibit*, no. AIAA 2009-5395, 2009.

[162] Lou, H. and Miller, R. S., "On ternary species mixing and combustion in isotropic turbulence at high pressure," *Physics of Fluids*, vol. 16, no. 5, pp. 1423–1438, 2004.

[163] Lucas, K., *Phase Equilibria and Fluid Properties in the Chemical Industry*, p. 573. Frankfurt: Dechema, 1980.

[164] Lund, T. S., Ghosal, S., and Moin, P., "Numerical experiments with highly-variable eddy viscosity models," in *Engineering Applications of Large Eddy Simulations* (Piomelli, U. and Ragab, S., eds.), vol. 162 of *FED*, pp. 7–11, ASME, 1993.

[165] Lux, J. and Haidn, O., "Effect of recess in high-pressure liquid oxygen/methane coaxial injection and combustion," *Journal of Propulsion and Power*, vol. 25, pp. 24–32, January–February 2009.

[166] Lux, J. and Haidn, O., "Flame stabilization in high-pressure liquid oxygen/methane rocket engine combustion," *Journal of Propulsion and Power*, vol. 25, pp. 15–23, January–February 2009.

[167] Lynch, E. D., Lariviere, B., Talley, D. G., and Menon, S., "Alrest high fidelity modeling program approach," in *French/German/United States Joint Symposium on Liquid Rocket Combustion Instabilities*, (London, UK), June 2011.

[168] Ma, Z. Y., Foster, J. W., and Miller, R. S., "A priori analysis of subgrid statistics from direct numerical simulations of high pressure hydrogen-oxygen flames: Iii subgrid pressure," in *7th US National Technical Meeting of the Combustion Institute*, (Atlanta, GA), March 2011.

[169] MacCormack, R., "The effects of viscosity in hyper-velocity impact cratering," No. AIAA 69-354, 1969.

[170] MacCormack, R., "A numerical method for solving the equations of compressible viscous flow," *AIAA Journal*, vol. 20, pp. 1275–1281, September 1982.

[171] Mahle, I., Sesterhenn, J., and Friedrich, R., "Turbulent mixing in temporal compressible shear layers involving detailed diffusion processes," *Journal of Turbulence*, vol. 8, no. 1, 2007.

[172] Marshall, W. M., Pal, S., Woodward, R. D., and Santoro, R. J., "Benchmark wall heat flux data for a go_2/gh_2 single element combustor," in *41st AIAA/ASME/SAE/ASEE Joint Propulsion Conference and Exhibit*, no. AIAA 2005-3572, (Tucson, AZ), July 2005.

[173] Martin, J. J., "Equations of state – applied thermodynamics symposium," *Industrial and Engineering Chemistry*, vol. 59, pp. 34–52, December 1967.

[174] Masi, E. and Bellan, J., "The subgrid-scale scalar variance under supercritical pressure conditions," *Physics of Fluids*, vol. 23, 2011.

[175] Masquelet, M., "Simulations of a sub-scale liquid rocket engine: Transient heat transfer in a real gas environment," Master's thesis, Georgia Institute of Technology, December 2006.

[176] Masquelet, M., Gallagher, T., Génin, F., and Menon, S., "Performance of codes developed by the computational combustion laboratory on blue gene/p," CCL Technical Report 2009-001-1, Georgia Tech Computational Combustion Laboratory, 2009.

[177] Masquelet, M., Génin, F., and Menon, S., "Update to the 107.leslie3d code for the SPEC MPI2007 benchmark," tech. rep., Georgia Tech Computational Combustion Laboratory, 2008.

[178] Masquelet, M. and Menon, S., "Large eddy simulation of flame-turbulence interactions in a GH_2-GO_2 shear coaxial injector," in *44th AIAA/ASME/SAE/ASEE Joint Propulsion Conference and Exhibit*, no. AIAA 2008-5030, (Hartford, CT), 2008.

[179] Masquelet, M. and Menon, S., "Benchmarking of various systems for future hpc capabilities at georgia tech," CCL Technical Report 2009-03-1, Georgia Tech Computational Combustion Laboratory, 2009.

[180] Masquelet, M. and Menon, S., "Large eddy simulation of flame-turbulence interactions in a shear coaxial injector," *Journal of Propulsion and Power*, vol. 26, September–October 2010.

[181] Masquelet, M., Menon, S., Jin, Y., and Friedrich, R., "Simulation of unsteady combustion in a LOX-GH_2 fueled rocket engine," *Aerospace Science and Technology*, vol. 13, pp. 466–474, December 2009.

[182] Mathias, P. M., Naheiri, T., and Oh, E. M., "A density correction for the Peng-Robinson equation of state," *Fluid Phase Equilibria*, vol. 47, pp. 77–887, July 1989.

[183] Matsuyama, S., Shinjo, J., Mizobuchi, Y., and Ogawa, S., "A numerical investigation on shear coaxial LOX/GH_2 jet flame at supercritical pressure," in *44th Aerospace Sciences Meeting and Exhibit*, no. AIAA 2006-761, (Reno, NV), January 2006.

[184] Matsuyama, S., Shinjo, J., Ogawa, S., and Mizobuchi, Y., "LES of H_2/O_2 coaxial jet flames in a multiple-injector combustor," in *49th AIAA Aerospace Sciences Meeting*, no. AIAA 2011-325, (Orlando, FL), January 2011.

[185] Matsuyama, S., Shinjo, J., Ogawa, S., and Mizobuchi, Y., "LES of high-frequency combustion instability in a single element rocket combustor," in *50th AIAA Aerospace Sciences Meeting*, no. AIAA 2012-1271, (Nashville, TN), January 2012.

[186] Mayer, W. O. H., Schick, A., Vielle, B., Chauveau, C., Gökalp, I., Talley, D., and Woodward, R., "Atomization and breakup of cryogenic propellants under high-pressure subcritical and supercritical conditions," *Journal of Propulsion and Power*, vol. 14, no. 5, pp. 835–842, 1998.

[187] Mayer, W. O. H. and Smith, J. J., *Liquid Rocket Thrust Chambers: Aspects of Modeling, Analysis, and Design*, vol. 200 of *Progress in Astronautics and Aeronautics*, ch. Fundamentals of Supercritical Mixing and Combustion of Cryogenic Propellants, pp. 339–367. AIAA, 2004.

[188] Mayer, W. O. H., Telaar, J., Branam, R., Schneider, G., and Hussong, J., "Raman measurements of cryogenic injection at supercritical pressure," *Heat and Mass Transfer*, vol. 39, pp. 709–719, 2003.

[189] McMillan, P. F. and Stanley, H. E., "Fluid phases: Going supercritical," *Nature Physics*, vol. 6, pp. 479–480, 07 2010.

[190] Meng, H. and Yang, V., "A unified treatment of general fluid thermodynamics and its application to a preconditioning scheme," *Journal of Computational Physics*, vol. 189, pp. 277–304, 2003.

[191] Menon, S. and Calhoon, W., "Subgrid mixing and molecular transport modeling for large-eddy simulations of turbulent reacting flows," *Proceedings of the Combustion Institute*, vol. 26, pp. 59–66, 1996.

[192] Menon, S. and Kim, W.-W., "High reynolds number flow simulations using the localized dynamic subgrid-scale model," no. AIAA 1996-0425, 1996.

[193] Menon, S., McMurtry, P., and Kerstein, A. R., "A linear eddy mixing model for large eddy simulation of turbulent combustion," in *LES of Complex Engineering and Geophysical Flows* (Galperin, B. and Orszag, S., eds.), Cambridge University Press, 1993.

[194] Menon, S. and Srinivasan, S., "Challenges for multiscale large-eddy simulation of application systems: Gas turbine to scramjet," in *SCIDAC*, 2011.

[195] Michalke, A., "On the inviscid instability of the hyperbolic tangent velocity profile," *Journal of Fluid Mechanics*, vol. 19, no. 4, pp. 543–556, 1964.

[196] Miller, R. S., "Long time mass fraction statistics in stationary compressible isotropic turbulence at supercritical pressure," *Physics of Fluids*, vol. 12, pp. 2020–2032, August 2000.

[197] Miller, R. S. and Bellan, J., "Direct numerical simulation and subgrid analysis of a transitional droplet laden mixing layer," *Physics of Fluids*, vol. 12, pp. 650–671, March 2000.

[198] Miller, R. S., Bellan, J., and Harstad, K. G., "Direct numerical simulations of supercritical fluid mixing layers applied to heptane-nitrogen," *Journal of Fluid Mechanics*, vol. 436, pp. 1–39, 2001.

[199] Miller, R. S. and Lou, H., "Effects of Soret and Dufour diffusion on conditional expectations in isotropic turbulent mixing at supercritical pressure," *Bulletin of the American Physical Society, 53th Annual Meeting of the Division of Fluid Dynamics of the American Physical Society, Washington, D.C., November 19-21*, 2000.

[200] Monkewitz, P. A. and Huerre, P., "Influence of the velocity ratio on the spatial instability of mixing layers," *Physics of Fluids*, vol. 25, pp. 1137–1143, July 1982.

[201] Montgomery, C. J., Zhao, W., Adams, B. R., Eklund, D. R., and Chen, J.-Y., "Supersonic combustion simulations using reduced chemical kinetics mechanisms and ISAT," in *AIAA Computational Fluid Dynamics Conference*, no. AIAA 2003-3547, 2003.

[202] Morrison, G. L., Tatterson, G. B., and Long, M. W., "Three-dimensional laser velocimeter investigation of turbulent, incompressible flow in an axisymmetric sudden expansion," *Journal of Propulsion and Power*, vol. 4, pp. 533–540, November–December 1988.

[203] Moser, R. D. and Rogers, M. M., "Mixing transition and the cascade to small scales in a plane mixing layer," *Physics of Fluids A*, vol. 3, pp. 1128–1134, May 1991.

[204] Nannan, N., Guardone, A., and Colonna, P., "On the fundamental derivative of gas dynamics in the vapor-liquid critical region of single-component typical fluids," *Fluid Phase Equilibria*, 2012.

[205] Nelson, C. C. and Menon, S., "Unsteady simulations of compressible spatial mixing layers," in *36th Aerospace Sciences Meeting and Exhibit*, no. AIAA-98-0786, (Reno, NV), January 1998.

[206] Nickalls, R. W. D., "A new approach to solving the cubic: Cardan's solution revealed," *The Mathematical Gazette*, vol. 77, pp. 354–359, 1993.

[207] Nicole, A., Vingert, L., and Habiballah, M., "Test case RCM-2: MASCOTTE single injector - 60 bar," in *3rd International Workshop Rocket Combustion Modeling*, (Vernon, France), pp. 10–19, Snecma, Space Engine Division, March 2006.

[208] Nicoud, F. and Ducros, F., "Subgrid-scale stress modelling based on the square of the velocity gradient tensor," *Flow, Turbulence and Combustion*, vol. 62, pp. 183–200, 1999.

[209] Nonomura, T., Morizawa, S., Terashima, H., Obayashi, S., and Fujii, K., "Numerical (error) issues on compressible multicomponent flows using a high-order differencing scheme: Weighted compact nonlinear scheme," *Journal of Computational Physics*, vol. 231, pp. 3181–3210, 2012.

[210] Nunome, Y., Onodera, T., Sasaki, M., Tomita, T., Kobayasho, K., and Daimon, Y., "Combustion instability phenomena observed during cryogenic hydrogen injection temperature ramping tests for single coaxial injector elements," in *47th*

AIAA/ASME/SAE/ASEE Joint Propulsion Conference and Exhibit, no. AIAA 2011-6027, (San Diego, CA), August 2011.

[211] Ó Conaire, M., Curran, H. J., Simmie, J. M., Pitz, W. J., and Westbrook, C. K., "A comprehensive modeling study of hydrogen oxidation," *International Journal of Chemical Kinetics*, vol. 36, no. 11, pp. 603–622, 2004.

[212] O'Connell, J. P. and Haile, J. M., *Multicomponent Thermodynamics: Fundamentals for Ap- plications*. Cambridge University Press, 2000.

[213] Oefelein, J. C., "LES of supercritical LOX-H2 injection and combustion in a shear coaxial uni-element rocket," in *41st Aerospace Sciences Meeting and Exhibit*, no. AIAA 2003-0479, (Reno, NV), January 2003.

[214] Oefelein, J. C., "Thermophysical characteristics of shear-coaxial LOX-H_2 flames at supercritical pressure," *Proceedings of the Combustion Institute*, vol. 30, pp. 2929–2937, 2005.

[215] Oefelein, J. C., "Mixing and combustion of cryogenic oxygen-hydrogen shear-coaxial jet flames at supercritical pressure," *Combustion Science and Technology*, vol. 178, pp. 229–252, 2006.

[216] Oefelein, J. C. and Aggarwal, S. K., "Toward a unified high-pressure drop model for spray simulations," in *Proceedings of the Center for Turbulence Research*, (Stanford, CA), pp. 193–205, 2000.

[217] Oefelein, J. C. and Yang, V., "Analysis of transcritical spray phenomena in a turbulent mixing layer," in *34th Aerospace Sciences Meeting and Exhibit*, no. AIAA 1996-0085, (Reno, NV), January 1996.

[218] Oefelein, J. C. and Yang, V., "Modeling high-pressure mixing and combustion processes in liquid rocket engines," *Journal Propulsion and Power*, vol. 14, no. 5, pp. 843–857, 1998.

[219] Oefelein, J. C. and Lacaze, G., "Robust treatment of mass conservation and EOS for non-dilute flames at high-pressures." NASA MSFC report, June 2010.

[220] Okong'o, N. and Bellan, J., "Consistent boundary conditions for multicomponent real gas mixtures based on characteristic waves," *Journal of Computational Physics*, vol. 176, pp. 330–344, 2002.

[221] Okong'o, N. and Bellan, J., "Real-gas effects on mean flow and temporal stability of binary-species mixing layers," *AIAA Journal*, vol. 41, pp. 2429–2443, December 2003.

[222] Okong'o, N. and Bellan, J., "Perturbation and initial reynolds number effects on transition attainment of supercritical, binary, temporal mixing layers," *Computers and Fluids*, vol. 33, pp. 1023–1046, 2004.

[223] Okong'o, N. and Bellan, J., "Turbulence and fluid-front area production in binary-species, supercritical, transitional mixing layers," *Physics of Fluids*, vol. 16, pp. 1467–1492, May 2004.

[224] Okong'o, N. and Bellan, J., "Small-scale dissipation in supercritical, transitional mixing layers," in *47th AIAA Aerospace Sciences Meeting*, no. AIAA 2009-807, 2009.

[225] Okong'o, N., Bellan, J., and Harstad, K. G., "Direct numerical simulations of O_2/H_2 temporal mixing layers under supercritical conditions," *AIAA Journal*, vol. 40, no. 5, pp. 914–926, 2002.

[226] Okong'o, N., Harstad, K. G., and Bellan, J., "Direct numerical simulations of O_2/H_2 temporal mixing layers under supercritical conditions," in *40th AIAA Aerospace Sciences Meeting and Exhibit*, no. AIAA 2002-0779, (Reno, NV), January 2002.

[227] Oschwald, M. and Schik, A., "Supercritical nitrogen free jet investigated by spontaneous Raman scattering," *Experiments in Fluids*, vol. 27, pp. 497–506, 1999.

[228] Oschwald, M., Schik, A., Klar, M., and Mayer, W., "Investigation of coaxial LN_2/GH_2-injection at supercritical pressure by spontaneous raman scattering," in *35th AIAA/ASME/SAE/ASEE Joint Propulsion Conference*, no. AIAA 1999-2887, (Los Angeles, CA), 1999.

[229] Oschwald, M., Smith, J. J., Branam, R., Hussong, J., Schik, A., Chehroudi, B., and Talley, D., "Injection of fluids into supercritical environments," *Combustion Science and Technology*, vol. 178, pp. 49–100, 2006.

[230] Pal, S., Marshall, W. M., Woodward, R. D., and Santoro, R. J., "Wall heat flux measurements for a uni-element GO_2/GH_2 shear coaxial injector," in *Third International Workshop on Rocket Combustion Modeling*, (Paris, France), March 2006.

[231] Palle, S., *On Real Gas and Molecular Transport Effects in High Pressure Mixing and Combustion*. PhD thesis, Clemson University, December 2006.

[232] Palle, S. and Miller, R. S., "Analysis of high-pressure hydrogen, methane and heptane laminar diffusion flames: thermal diffusion factor modeling," *Combustion and Flame*, vol. 151, pp. 581–600, 2007.

[233] Palle, S., Nolan, C., and Miller, R. S., "On molecular transport effects in real gas laminar diffusion flames at large pressure," *Physics of Fluids*, vol. 17, October 2005.

[234] Park, T. S., "LES and RANS simulations of cryogenic liquid nitrogen jets," *Journal of Supercritical Fluids*, vol. 72, pp. 232–247, 2012.

[235] Péneloux, A., Rauzy, E., and Frèze, R., "A consistent correction for redlich-kwong-soave volumes," *Fluid Phase Equilibria*, vol. 8, no. 1, pp. 7–23, 1982.

[236] Petit, X., Ribert, G., and Domingo, P., "Large eddy simulation of supercritical fluid injection," in *50th AIAA Aerospace Sciences Meeting*, no. AIAA 2012-1268, (Nashville, TN), January 2012.

[237] Pit, F., Mory, M., and Bruel, P., "Modélisation par la Fonction Densité de probabilité du mélange de produits inertes ou réactifs par une turbulence homogène," in *18ème Congrès Francais de Mécanique*, (Grenoble, France), August 2007.

[238] Pitsch, H., Desjardins, O., Balarac, G., and Ihme, M., "Large-eddy simulation of turbulent reacting flows," *Progress in Aerospace Sciences*, vol. 44, pp. 466–478, August 2008.

[239] Pitzer, K. S., "The volumetric and thermodynamic properties of fluids. i. theoretical basis and virial coefficients," *Journal of the American Chemical Society*, vol. 77, pp. 3427–3433, July 1955.

[240] Poinsot, T. J. and Lele, S. K., "Boundary conditions for direct simulations of compressible viscous flows," *Journal of Computational Physics*, vol. 101, pp. 104–129, 1992.

[241] Poling, B. E., Prausnitz, J. M., and O'Connell, J. P., *The Properties of Gases and Liquids, Fifth Edition*. McGraw-Hill, 2001.

[242] Pons, L., Darabiha, N., Candel, S., Ribert, G., and Yang, V., "Mass transfer and combustion in transcritical non-premixed counterflows," *Combustion Theory and Modelling*, vol. 13, no. 1, pp. 57–81, 2009.

[243] Pope, S. B., *Turbulent Flows*. Cambridge University Press, 2000.

[244] Poschner, M. and Pfitzner, M., "CFD-simulation of supercritical LOX/GH2 combustion considering consistent real gas thermodynamics," in *Proceedings of the European Combustion Meeting 2009*, 2009.

[245] Preclik, D., Knab, O., Görgen, J., and Hagemann, G., *Liquid Rocket Thrust Chambers: Aspects of Modeling, Analysis, and Design*, vol. 200 of *Progress in Astronautics and Aeronautics*, ch. 15: Simulation and Analysis of Thrust Chamber Flowfields: Cryogenic Propellant Rockets, pp. 527–551. AIAA, 2004.

[246] R Core Team, *R: A Language and Environment for Statistical Computing*. R Foundation for Statistical Computing, Vienna, Austria, 2012. ISBN 3-900051-07-0.

[247] Rehab, H., Villermaux, E., and Hopfinger, E., "Flow regimes of large-velocity-ratio coaxial jets," *Journal of Fluid Mechanics*, vol. 345, pp. 357–381, 1997.

[248] Riazi, M. R. and Whitson, C. H., "Estimating diffusion coefficients of dense fluids," *Industrial and Engineering Chemistry Research*, vol. 32, pp. 3081–3088, 1993.

[249] Ribert, G., Zong, N., Yang, V., Pons, L., Darabiha, N., and Candel, S., "Counterflow diffusion flames of general fluids: Oxygen/hydrogen mixtures," *Combustion and Flame*, vol. 154, pp. 319–330, 2008.

[250] Richecoeur, F., *Expérimentations et simulations numériques des interactions entres modes acoustiques transverses et flammes cryotechniques*. PhD thesis, Ecole Centrale Paris, November 2006.

[251] Richecoeur, F., Ducruix, S., Scouflaire, P., and Candel, S., "Effect of temperature fluctuations on high frequency acoustic coupling," *Proceedings of the Combustion Institute*, vol. 32, pp. 1663–1670, 2009.

[252] Rodriguez, J. I., Graham, J. J., Leyva, I. A., and Talley, D., "Effect of variable phase transverse acoustic fields on coaxial jet forced spread angles," in *47th AIAA Aerospace Sciences Meeting*, no. AIAA 2009-231, (Orlando, FL), January 2009.

[253] Rodriguez, J. I., Leyva, I. A., Graham, J. J., and Talley, D., "Mixing enhancement of liquid rocket engine injector flow," in *45th AIAA/ASME/SAE/ASEE Joint Propulsion Conference and Exhibit*, no. AIAA 2009-5143, (Denver, Colorado), August 2009.

[254] Roe, P. L., "Approximate riemann solvers, parameter vectors, and difference schemes," *Journal of Computational Physics*, vol. 43, no. 2, pp. 357–372, 1981.

[255] Rogers, M. M. and Moser, R. D., "Direct simulation of a self-similar turbulent mixing layer," *Physics of Fluids*, vol. 6, pp. 903–924, February 1994.

[256] Roy, A. and Segal, C., "Experimental study of fluid jet mixing at supercritical conditions," *Journal of Propulsion and Power*, vol. 26, pp. 1205–1211, November–December 2010.

[257] Ruiz, A., *Unsteady Numerical Simulations of Transcritical Turbulent Combustion in Liquid Rocket Engines*. PhD thesis, INP Toulouse, 2012.

[258] Ruiz, A., Cuenot, B., Selle, L., and Poinsot, T., "The flame structure of a turbulent supercritical hydrogen/oxygen flow behind a splitter plate," in *47th AIAA/ASME/SAE/ASEE Joint Propulsion Conference and Exhibit*, no. AIAA 2011-6121, (San Diego, CA), August 2011.

[259] Sadus, R. J., "Influence of quantum effects on the high-pressure phase behavior of binary mixtures containing hydrogen," *Journal of Physical Chemistry*, vol. 96, pp. 3855–3860, 1992.

[260] Salgues, D., Mouis, A.-G., Lee, S.-Y., Kalitan, D., Pal, S., and Santoro, R. J., "Shear and swirl coaxial injector studies of LOX/GCH4 rocket combustion using non-intrusive laser diagnostics," in *44th Aerospace Sciences Meeting and Exhibit*, no. AIAA 2006-757, (Reno, NV), January 2006.

[261] Sankaran, V., *Sub-grid Combustion Modeling for Compressible Two-Phase Reacting Flows*. PhD thesis, Georgia Institute of Technology, Atlanta, GA, July 2003.

[262] Sankaran, V. and Oefelein, J. C., "Advanced preconditioning strategies for chemically reacting flows," in *45th AIAA Aerospace Sciences Meeting and Exhibit*, (Reno, NV), January 2007.

[263] Santoro, R. J., Pal, S., Woodward, R. D., and Schaaf, L., "Rocket testing at university facilities," in *39th Aerospace Sciences Meeting and Exhibit*, no. AIAA 2001-16582, (Reno, NV), January 2001.

[264] Santoro, R. J. and Pal, S., "Test case RCM-1: Penn State preburner combustor," in *3rd International Workshop Rocket Combustion Modeling*, (Vernon, France), pp. 1–9, Snecma, Space Engine Division, March 2006.

[265] Schlüter, J. U., "Influence of axisymmetric assumptions on large eddy simulations of a confined jet and a swirl flow," *International Journal of Computational Fluid Dynamics*, vol. 18, pp. 235–246, April 2004.

[266] Schmid, B. and Gmehling, J., "Revised parameters and typical results of the vtpr group contribution equation of state," *Fluid Phase Equilibria*, vol. 317, pp. 110–126, 3 2012.

[267] Schmitt, T., Méry, Y., Boileau, M., and Candel, S., "Large-eddy simulation of oxygen/methane flames under transcritical conditions," in *Proceedings of the Combustion Institute*, vol. 33, pp. 1383–1390, 2011.

[268] Schmitt, T., Selle, L., Ruiz, A., and Cuenot, B., "Large-eddy simulation of supercritical-pressure round jets," *AIAA Journal*, vol. 48, pp. 2133–2144, September 2010.

[269] Schumaker, S. A., *An Experimental Investigation of Reacting and Nonreacting Coaxial Jet Mixing in a Laboratory Rocket Engine*. PhD thesis, University of Michigan, 2009.

[270] Schumann, U., "Subgrid scale model for finite difference simulations of turbulent flows in plane channels and annuli," *Journal of Computational Physics*, vol. 18, pp. 376–404, 1975.

[271] Schumann, U., "Realizability of reynolds-stress turbulence models," *Physics of Fluids*, vol. 20, no. 5, pp. 721–725, 1977.

[272] Segal, C. and Polikhov, S. A., "Subcritical to supercritical mixing," *Physics of Fluids*, vol. 20, May 2008.

[273] Selle, L. C., Okong'o, N., Bellan, J., and Harstad, K. G., "Modelling of subgrid-scale phenomena in supercritical transitional mixing layers: an *a priori* study," *Journal of Fluid Mechanics*, vol. 593, pp. 57–91, 2007.

[274] Selle, L. C. and Schmitt, T., "Large-eddy simulation of single-species flows under supercritical thermodynamics conditions," *Combustion Science and Technology*, vol. 182, no. 4-6, pp. 392–404, 2010.

[275] Sen, B. A., *Artificial Neural Networks based subgrid chemistry model for turbulent reactive flow simulations*. PhD thesis, Georgia Institute of Technology, December 2009.

[276] Sen, B. A., Hawkes, E. R., and Menon, S., "Large eddy simulation of extinction and reignition with artificial neural networks based chemical kinetics," *Combustion and Flame*, vol. 157, no. 3, pp. 566–578, 2010.

[277] Shimizu, K., Hibi, A., Koshi, M., Morii, Y., and Tsuboi, N., "Updated kinetic mechanism for high-pressure hydrogen combustion," *Journal of Propulsion and Power*, vol. 27, pp. 383–395, March–April 2011.

[278] Shu, C.-W., "High order weighted essentially nonoscillatory schemes for convection dominated problems," *SIAM Review*, vol. 51, no. 1, pp. 82–126, 2009.

[279] Shu, C.-W. and Osher, S., "Efficient implementation of essentially non-oscillatory shock-capturing schemes, II," *Journal of Computational Physics*, vol. 83, pp. 32–78, 1989.

[280] Sierra, P., Masquelet, M., and Menon, S., "Large-eddy simulation of a reactive shear coaxial injector configuration," in *51st AIAA Aerospace Sciences Meeting*, 2013.

[281] Simeoni, G. G., Bryk, T., Gorelli, F. A., Krisch, M., Ruocco, G., Santoro, M., and Scopigno, T., "The Widom line as the crossover between liquid-like and gas-like behaviour in supercritical fluids," *Nature Physics*, vol. 6, no. 7, pp. 503–507, 2010.

[282] Singla, G., Scouflaire, P., Rolon, C., and Candel, S., "Transcritical oxygen/-transcritical or supercritical methane combustion," *Proceedings of the Combustion Institute*, vol. 30, pp. 2921–2928, 2005.

[283] Singla, G., Scouflaire, P., Rolon, C., and Candel, S., "Planar laser-induced fluorescence of OH in high-pressure cryogenic LOx/GH_2 jet flames," *Combustion and Flame*, vol. 144, pp. 151–169, 2006.

[284] Singla, G., Scouflaire, P., Rolon, J.-C., Candel, S., and Vingert, L., "OH planar laser-induced fluorescence and emission imaging in high-pressure LOX-methane flames," *Journal of Propulsion and Power*, vol. 23, pp. 593–602, May–June 2007.

[285] Smagorinsky, J., "General circulation experiments with the primitive equations," *Monthly Weather Review*, vol. 91, pp. 99–164, March 1963.

[286] Smith, J. M., Van Ness, H. C., and Abbott, M. M., *Introduction to Chemical Engineering Thermodynamics*. New York: Mc Graw Hill, 2001.

[287] Smith, J. J., Schneider, G., Suslov, D., Oschwald, M., and Haidn, O., "Steady-state high pressure LO_x/h_2 rocket engine combustion," *Aerospace Science and Technology*, vol. 11, no. 1, pp. 39–47, 2007.

[288] Smith, T. M. and Menon, S., "Model simulations of freely propagating turbulent premixed flames," *Proceedings of the Combustion Institute*, vol. 26, pp. 299–306, 1996.

[289] Smith, T. M. and Menon, S., "The structure of premixed flames in a spatially evolving turbulent flow," *Combustion Science and Technology*, vol. 119, no. 1-6, pp. 77–106, 1996.

[290] Smith, T. M., *Unsteady Simulations of Turbulent Premixed Reacting Flows*. PhD thesis, Georgia Institute of Technology, March 1998.

[291] Sohn, C. H., Chung, S. H., Lee, S. R., and Kim, J. S., "Structure and acoustic-pressure response of hydrogen-oxygen diffusion flames at high pressure," *Combustion And Flame*, vol. 115, no. 3, pp. 299–312, 1998.

[292] Sone, K., "Unsteady simulations of mixing and combustion in internal combustion engines," Master's thesis, Georgia Institute of Technology, Atlanta, GA, August 2001.

[293] Sozer, E., Hassan, E. A., Yun, S., Thakur, S., Wright, J., Ihme, M., and Shyy, W., "Turbulence-chemistry interaction and heat transfer modeling of H_2/O_2 gaseous injector flows," in *48th AIAA Aerospace Sciences Meeting*, no. AIAA 2010-1525, 2010.

[294] Star, A. M., Edwards, J. R., Lin, K.-C., and Jackson, T. A., "Modeling of condensation in injection of supercritical fuels," in *44th Aerospace Sciences Meeting and Exhibit*, no. AIAA 2006-810, (Reno, NV), January 2006.

[295] Stiel, L. I. and Thodos, G., "Force constants for polar substances: Their prediction from critical properties," *AIChE Journal*, vol. 10, pp. 266–269, 1964.

[296] Stone, C., *Large-Eddy Simulation of Combustion Dynamics in Swirling Flows*. PhD thesis, Georgia Institute of Technology, Atlanta, GA, 2003.

[297] Stone, C. and Menon, S., "Large-eddy simulations on distributed shared memory clusters," *Journal of Parralel Distributed Computing*, vol. 64, pp. 1103–1112, 2004.

[298] Ströhle, J. and Myhrvold, T., "An evaluation of detailed reaction mechanisms for hydrogen combustion under gas turbine conditions," *International Journal of Hydrogen Energy*, vol. 32, pp. 125–135, 2007.

[299] Stryjek, R. and Vera, J. H., "PRSV - an improved peng-robinson equation of state for pure compounds and mixtures," *Canadian Journal of Chemical Engineering*, vol. 64, pp. 323–333, April 1986.

[300] Sun, M.-B., Wang, Z.-G., Liang, J.-H., and Geng, H., "Flame characteristics in supersonic combustor with hydrogen injection upstream of cavity flameholder," *Journal of Propulsion and Power*, vol. 24, pp. 688–696, July–August 2008.

[301] Takahashi, S. *Journal of Chemical Engineering Japan*, vol. 7, p. 417, 1974.

[302] Takahashi, S. and Hongo, M., "Diffusion coefficients of gases at high pressures in the CO_2-C_2H_4 system," *Journal of Chemical Engineering Japan*, vol. 15, pp. 57–59, 1982.

[303] Tamura, H., Sakamoto, H., Takahashi, M., Sasaki, M., Onodera, T., Tomita, T., and Mayer, W. O. H., "Observation of LOX/hydrogen combustion flame in a rocket chamber during chugging instability," in *39th AIAA/ASME/SAE/ASEE Joint Propulsion Conference and Exhibit*, no. AIAA 2003-4756, (Huntsville, AL), July 2003.

[304] Tani, H., Teramoto, S., and Nagashima, T., "Injector geometry effects on cryogenic coaxial jets at supercritical pressures," in *46th AIAA/ASME/SAE/ASEE Joint Propulsion Conference and Exhibit*, no. AIAA 2010-6738, (Nashville, TN), July 2010.

[305] Tannehill, J. C., Anderson, D. A., and Pletcher, R. H., *Computational Fluid Mechanics and Heat Transfer - Second Edition*. Washington: Taylor & Francis, 1997.

[306] Taskinoglu, E. and Bellan, J., "A posteriori study using a dns database describing fluid disintegration and binary-species mixing under supercritical pressure: Heptane and nitrogen," *Journal of Fluid Mechanics*, vol. 645, pp. 211–254, 2010.

[307] Taskinoglu, E. and Bellan, J., "Subgrid-scale models and large-eddy simulation of oxygen stream disintegration and mixing with a hydrogen or helium stream at supercritical pressure," *Journal of Fluid Mechanics*, 2011.

[308] Terashima, H., Kawai, S., and Yamanishi, N., "High-resolution numerical method for supercritical flows with large density variations," *AIAA Journal*, vol. 49, pp. 2658–2672, December 2011.

[309] Teshome, S., *Droplet Combustion and Non-Reactive Shear-Coaxial Jets with and without Transverse Acoustic Excitation.* PhD thesis, UCLA, 2012.

[310] Thompson, K. W., "Time dependent boundary conditions for hyperbolic systems, ii," *Journal of Computational Physics*, vol. 89, pp. 439–461, 1990.

[311] Toro, E. F., Spruce, M., and Speares, W., "Restoration of the contact surface in the HLL Riemann solver," *Shock Waves*, vol. 4, no. 1, pp. 25–34, 1994.

[312] Tsohas, J. and Heister, S. D., "CFD simulations of liquid rocket coaxial hydrodynamics," in *45th AIAA/ASME/SAE/ASEE Joint Propulsion Conference and Exhibit*, no. AIAA 2009-5387, 2009.

[313] Tsonopoulos, C. and Heidman, J. L., "High-pressure vapor-liquid equilibria with cubic equations of state," *Fluid Phase Equilibria*, vol. 29, pp. 391 – 414, 1986.

[314] Tucker, P. K., Menon, S., Merkle, C. L., Oefelein, J. C., and Yang, V., "Validation of high-fidelity CFD simulations for rocket injector design," in *44th AIAA/ASME/SAE/ASEE Joint Propulsion Conference and Exhibit*, no. AIAA 2008-5226, (Hartford, CT), July 2008.

[315] Tucker, P. K., Rybak, J. A., Hulka, J., Jones, G. W., Nesman, T., and West, J. S., "The NASA constellation university institutes project: Thrust chamber assembly virtual institute," in *42nd AIAA/ASME/SAE/ASEE Joint Propulsion Conference and Exhibit*, no. AIAA 2006-4524, (Sacramento, CA), 2006.

[316] Tucker, P. K., Menon, S., Merkle, C. L., Oefelein, J. C., and Yang, V., "An approach to improved credibility of CFD simulations for rocket injector design," in *43rd AIAA/ASME/SAE/ASEE Joint Propulsion Conference and Exhibit*, no. AIAA 2007-5572, (Cincinnati, OH), July 2007.

[317] Twu, C. H., Sim, W. D., and Tassone, V., "Getting a handle on advanced cubic equations of state," *Chemical Engineering Progress*, vol. 98, pp. 58–65, November 2002.

[318] Vaidyanathan, A., Gustavsson, J. P. R., and Segal, C., "Oxygen/hydrogen-planar-laser-induced fluorescence measurements and accuracy investigation in high-pressure combustion," *Journal of Propulsion and Power*, vol. 25, pp. 864–874, July–August 2009.

[319] Vaidyanathan, A., Gustavsson, J. P. R., and Segal, C., "One- and three-dimensional wall heat flux calculations in a O_2/H_2 system," *Journal of Propulsion and Power*, vol. 26, pp. 186–188, January–February 2010.

[320] van der Waals, J. D., *Over de continuiteit van den gas - en vloeistoftoestand.* PhD thesis, Leiden, 1873.

[321] van Leer, B., "Towards the ultimate conservative difference scheme iii. upstream-centered finite-difference schemes for ideal compressible flow," *Journal of Computational Physics*, vol. 23, pp. 263–275, 1977.

[322] van Leer, B., "Towards the ultimate conservative difference scheme v. a second-order sequel to godunov's method," *Journal of Computational Physics*, vol. 32, pp. 101–136, 1979.

[323] Vanella, M., Piomelli, U., and Balaras, E., "Effect of grid discontinuities on large-eddy simulation statistics and flow fields," *Journal of Turbulence*, vol. 9, no. 32, pp. 1–23, 2008.

[324] Vasudevan, R., "Thermal diffusion coefficient modeling for high pressure combustion simulations," Master's thesis, Clemson University, December 2007.

[325] Venkateswaran, S. and Merkle, C. L., "Analysis of preconditioning methods for the euler and navier-stokes equations," in *Von Karman Institute Lecture Series*, Von Karman Institute, March 1999.

[326] Verhoeven, L. M., Ramaekers, W. J. S., van Oijen, J. A., and de Goey, L. P. H., "Modeling non-premixed laminar co-flow flames using flamelet-generated," *Combustion and Flame*, vol. 159, no. 1, pp. 230–241, 2012.

[327] Villermaux, E. and Rehab, H., "Mixing in coaxial jets," *Journal of Fluid Mechanics*, vol. 425, pp. 161–185, 2000.

[328] Vingert, L., Gicquel, P., Lourme, D., and Menoret, L., *Coaxial Injector Atomization*, vol. 169 of *Progress in Astronautics and Aeronautics*, ch. 6. AIAA, 1995.

[329] Vreman, B., Geurts, B., and Kuerten, H., "Realizability conditions for the turbulent stress tensor in large-eddy simulation," *Journal of Fluid Mechanics*, vol. 278, pp. 351–362, 1994.

[330] Vreman, B., Geurts, B., and Kuerten, H., "Large-eddy simulation of the turbulent mixing layer," *Journal of Fluid Mechanics*, vol. 339, no. 1, pp. 357–390, 1997.

[331] Wang, L.-S. and Lu, H.-C., "A unified model for representing densities and viscosities of hydrocarbon liquids and gases based on Peng-Robinson equation of state," *The Open Thermodynamics Journal*, vol. 3, pp. 24–33, 2009.

[332] Wang, X., Cai, G., and Huo, H., "Numerical study of high-pressure GO_2/GH_2 combustion of a single-element injector," *Science China Technological Sciences*, vol. 55, no. 10, pp. 2757–2768, 2012.

[333] Wei, Y. S. and Sadus, R. J., "Equations of state for the calculation of fluid phase equilibria," *AIChE Journal*, vol. 46, pp. 169–196, 2000.

[334] Weydahl, T., *A framework for mixing-reaction closure with the Linear Eddy Model*. Phd, Norwegian University of Science and Technology, Trondheim, Norway, June 2010.

[335] Wong, D. S. H. and Sandler, S. I., "A theoretically correct equations mixing rule for cubic of state," *American Institute of Chemical Engineers Journal*, vol. 38, pp. 671–680, May 1992.

[336] Wong, V. C., "A proposed statistical-dynamic closure method for the linear or nonlinear subgrid-scale stresses," *Physics of Fluids A*, vol. 4, no. 5, pp. 1080–1082, 1992.

[337] Woodward, R. D. and Talley, D. G., "Raman imaging of transcritical cryogenic propellants," in *34th Aerospace Sciences Meeting and Exhibit*, no. AIAA 1996-0468, (Reno, NV), January 1996.

[338] Woodward, R. D., Pal, S., Farhangi, S., Jensen, G. E., and Santoro, R. J., "LOX/GH_2 shear coaxial injector atomization studies: Effect of recess and non-concentricity," in *45th AIAA Aerospace Sciences Meeting and Exhibit*, (Reno, NV), January 2007.

[339] Woosley, S. E., Kerstein, A. R., Sankaran, V., Aspden, A. J., and Ropke, F. K., "Type Ia supernovae: Calculations of turbulent flames using the linear eddy model," *The Astrophysical Journal*, vol. 704, pp. 255–273, 2009.

[340] Yan, Z., "General thermal wavelength and its applications," *European Journal of Physics*, vol. 21, pp. 625–631, 2000.

[341] Yang, F., Law, C. K., Sung, C. J., and Zhang, H. Q., "A mechanistic study of soret diffusion in hydrogen-air flames," *Combustion and Flame*, vol. 157, pp. 192–200, 2010.

[342] Yorizane, M., Yoshimura, S., Masuoka, H., and Yoshida, H. *Industrial and Engineering Chemistry Fundamentals*, vol. 22, p. 458, 1983.

[343] Yu, Y. C., *Experimental and analytical investigations of longitudinal combustion instability in a continuously variable resonance combustor CVRC*. PhD thesis, Purdue, 2009.

[344] Zabaloy, M. S. and Vera, J. H., "The peng-robinson sequel. an analysis of the particulars of the second and third generations," *Industrial and Engineering Chemistry Research*, vol. 37, pp. 1591–1597, 1998.

[345] Zhukov, V. P., "Testing of H2-O2 kinetic schemes in CFD calculations," in *Proceedings of the European Combustion Meeting*, 2009.

[346] Zong, N., Meng, H., Hsieh, S.-Y., and Yang, V., "A numerical study of cryogenic fluid injection and mixing under supercritical conditions," *Physics of Fluids*, vol. 16, pp. 4248–4261, December 2004.

[347] Zong, N., Ribert, G., and Yang, V., "A flamelet approach for modeling of liquid oxygen (LOX)/methane flames at supercritical pressures," in *46th AIAA Aerospace Sciences Meeting and Exhibit*, no. AIAA-2008-946, (Reno, NV), January 2008.

[348] Zong, N., Ribert, G., and Yang, V., "Supercritical combustion of liquid oxygen (LOX) and methane stabilized by a splitter plate," in *45th AIAA Aerospace Sciences Meeting and Exhibit*, (Reno, NV), January 2007.

[349] Zong, N. and Yang, V., "An efficient preconditioning scheme for real-fluid mixtures using primitive pressure-temperature variables," *International Journal of Computational Fluid Dynamics*, vol. 21, pp. 217–230, June–July 2007.

VITA

Matthieu Masquelet was born in "La Ville Rose" of Toulouse on April 24th, 1980 but spent most of his life around Paris with his loving family: his father Marc, his mother Elisabeth and his sister Marion. He attended "Lycée de Montgeron" for high school, "Lycée Saint-Louis" in Paris for prep school before obtaining a Mechanical engineering degree from "École des Mines de Nancy" in 2002. He then decided to learn more about propulsion, CFD and the American way of life by leaving France and joining the Computational Combustion Laboratory as a graduate research assistant under the supervision of Professor Suresh Menon. Over 10 years, he worked on many different projects, found the time to learn how to play ice hockey and to become a decent photographer. More importantly, he found the love of his life in the person of Reah Rogers who he married three times between 2010 and 2012. They are expected to move to the state of New York to continue their adventures once Matthieu completes his degree.